The Growth and Stability of Stress Corrosion Cracks in Large-Diameter BWR Piping

Volume 2: Appendixes

MASTER
DO NOT MICROFILM
COVER

Keywords:
Crack Growth
BWR Pipe Cracking
Intergranular Stress Corrosion Cracking
Fracture Mechanics

EPRI

EPRI NP-2472
Volume 2
Project T118-1
Final Report
July 1982

Prepared by
General Electric Company
San Jose, California

DISTRIBUTION OF THIS DOCUMENT IS UNLIMITED

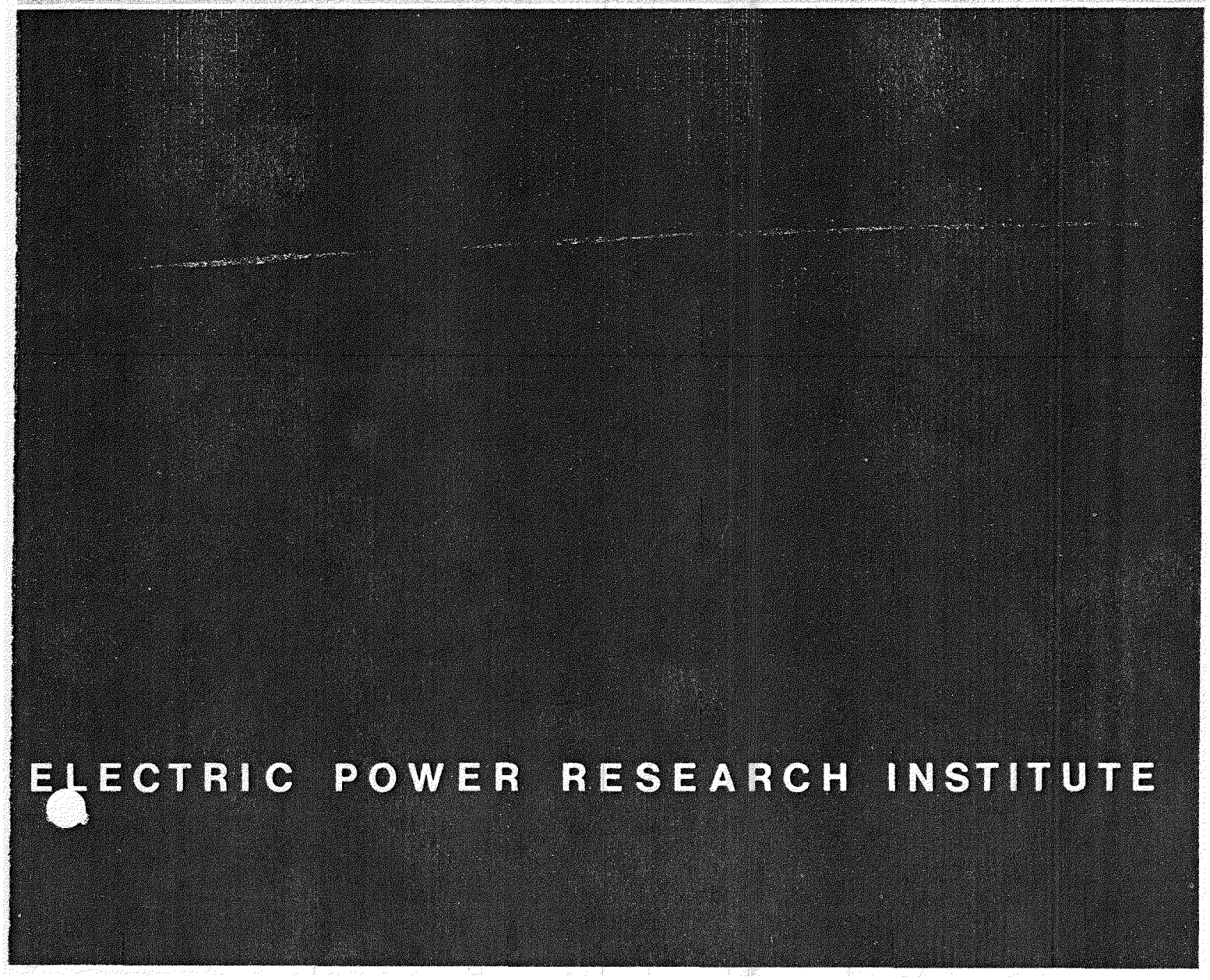

DISCLAIMER

This report was prepared as an account of work sponsored by an agency of the United States Government. Neither the United States Government nor any agency Thereof, nor any of their employees, makes any warranty, express or implied, or assumes any legal liability or responsibility for the accuracy, completeness, or usefulness of any information, apparatus, product, or process disclosed, or represents that its use would not infringe privately owned rights. Reference herein to any specific commercial product, process, or service by trade name, trademark, manufacturer, or otherwise does not necessarily constitute or imply its endorsement, recommendation, or favoring by the United States Government or any agency thereof. The views and opinions of authors expressed herein do not necessarily state or reflect those of the United States Government or any agency thereof.

DISCLAIMER

Portions of this document may be illegible in electronic image products. Images are produced from the best available original document.

EPRI-NP--2472 Vol. 2

DE82 905835

The Growth and Stability of Stress-Corrosion Cracks in Large-Diameter BWR Piping. Volume 2. Appendixes

NP-2472, Volume 2
Research Project T118-1

Final Report, July 1982

Prepared by

GENERAL ELECTRIC COMPANY
Nuclear Engineering Division
175 Curtner Avenue
San Jose, California 95125

Principal Investigators
D. A. Hale
J. D. Heald
R. M. Horn
C. W. Jewett
J. N. Kass
H. S. Mehta
S. Ranganath
S. R. Sharma

Prepared for

BWR Owners Group

and

Electric Power Research Institute
3412 Hillview Avenue
Palo Alto, California 94304

EPRI Project Manager
D. M. Norris

Nuclear Power Division

DISTRIBUTION OF THIS DOCUMENT IS UNLIMITED

ORDERING INFORMATION

Requests for copies of this report should be directed to Research Reports Center (RRC), Box 50490, Palo Alto, CA 94303, (415) 965-4081. There is no charge for reports requested by EPRI member utilities and affiliates, contributing nonmembers, U.S. utility associations, U.S. government agencies (federal, state, and local), media, and foreign organizations with which EPRI has an information exchange agreement. On request, RRC will send a catalog of EPRI reports.

Copyright © 1982 Electric Power Research Institute, Inc. All rights reserved.

NOTICE

This report was prepared by the organization(s) named below as an account of work sponsored by the Electric Power Research Institute, Inc. (EPRI) and the BWR Owners Group. Neither EPRI, members of EPRI, the BWR Owners Group, the organization(s) named below, nor any person acting on behalf of any of them: (a) makes any warranty, express or implied, with respect to the use of any information, apparatus, method, or process disclosed in this report or that such use may not infringe privately owned rights; or (b) assumes any liabilities with respect to the use of, or for damages resulting from the use of, any information, apparatus, method, or process disclosed in this report.

Prepared by
General Electric Company
San Jose, California

EPRI PERSPECTIVE

PROJECT DESCRIPTION

This work is part of a four-year BWR Owners Group Program that addresses intergranular stress corrosion cracking (IGSCC) in austenitic stainless steel piping. This project (RPT118-1) considers the safety margin of circumferentially flawed pipe. Volume 1 reports the research in a summary paper format, with the technical details left to the appendixes of Volume 2 that constitute the bulk of this report.

PROJECT OBJECTIVE

The project objectives are (1) to assess the margins of safety, (2) to develop remedies to mitigate cracking, and (3) to apply remedies.

PROJECT RESULTS

This was a good program with results that have high potential for positive impact on the industry. General Electric Company's two-page Executive Summary is a fair evaluation of the accomplishments. In my assessment, the major accomplishments are (1) the definition of critical crack size that shows large margins of safety above that given in Section XI of the ASME Code, (2) the development of IGSCC growth-rate design curves that allow end-of-life calculations, and (3) the design of the large pipe test currently under way to verify the analysis.

Douglas M. Norris, Project Manager
Nuclear Power Division

ABSTRACT

This report presents the results of a research program conducted to evaluate the behavior of hypothetical stress corrosion cracks in large diameter austenitic piping. The program included major tasks, a design margin assessment, an evaluation of crack growth and crack arrest, and development of a predictive model. As part of the margin assessment, the program developed diagrams which predicted net section collapse as a function of crack size. In addition, plasticity and dynamic load effects were also considered in evaluating collapse. Analytical methods for evaluating these effects were developed and were benchmarked by dynamic tests of 4-in.-diameter piping. The task of evaluating the growth behavior of stress corrosion cracks focused on developing constant load and cyclic growth rate data that could be used with the predictive model. Secondly, laboratory tests were performed to evaluate the conditions under which growing stress corrosion cracks would arrest when they intersected stress corrosion resistant weld metal. The third task successfully developed a model to predict the behavior of cracks in austenitic piping. This model relies on crack growth data and the critical crack size predicted by the net section collapse approach. Full scale pipe tests were initiated to confirm the model's predictions which in turn could be used to formulate an in-service inspection plan for cracked piping allowing continued plant operation.

ACKNOWLEDGMENTS

The following people made significant technical contributions to this program during its duration:

M. M. Bensch
T. A. Caine
R. M. Chrenko
W. L. Clarke, Jr.
R. L. Cowan
R. B. Davis
J. G. DeBriere
T. P. Diaz
T. Gerber
D. A. Hale
P. P. Hallila
J. D. Heald
R. M. Horn
A. J. Jacobs
C. W. Jewett
J. N. Kass
C. H. Lange
H. S. Mehta
S. Ranganath
P. S. Ryan
S. R. Sharma
W. Vanderputten
S. Yukawa

CONTENTS

Volume 1

CONTENTS

Volume 2

APPENDIXES

EXECUTIVE SUMMARY

The research program described in this report investigated the behavior of hypothetical stress corrosion cracks in large diameter austenitic piping. As a result of this work, a method was developed to predict the behavior of cracked pipes. Application of this method demonstrated that very large flaws could be tolerated and as a result showed that a large diameter, welded Type-304 stainless steel pipe, which might contain a stress corrosion crack, has several critical advantages over a small diameter pipe. A large pipe has a more favorable weld residual stress, a weld geometry that would lead to crack arrest, lower sensitization, and a larger wall thickness. The predictions for large pipe can be used to establish an in-service inspection plan for continued plant operation.

The predictive method was supported by several other results. First, failure analysis diagrams for austenitic piping were develped. These diagrams, based on net section collapse, indicate substantial margin to failure in cracked piping under expected conditions and are consistent with experimental and field data. Good agreement with elastic-plastic fracture mechanics predictions was also found. Methods were developed to evaluate the nonlinear dynamic response of a large piping system with a cracked pipe section. These methods were used to quantify the extra structural margin over that determined using linear elastic analysis for piping designed to the ASME Code limits. Thirdly, dynamic pipe tests were performed and confirmed that the elastic-plastic dynamic analysis methods predict the dynamic response of cracked pipe sections. Net section collapse criterion was also confirmed as a conservative estimate of the load capacity of flawed pipes.

As part of the task to evaluate crack growth and crack arrest, finite element methods were developed to better characterize the stress intensity factors for circumferential cracks in pipes subjected to highly nonlinear residual stress distributions. Secondly, laboratory test specimens were used to substantiate arrest of growing stress corrosion cracks in Type-308L weld metal. Constant load crack growth rates, needed for the predictive methodology, were measured

as a function of sensitization in oxygenated high temperature water. Crack growth rates were found to increase with increasing degree of sensitization. Two crack growth rate curves were developed: an expected growth rate curve and a conservative upper bound curve. Cyclic crack growth rates were measured under in-service conditions. The crack growth rate per cycle was a strong function of loading frequency. The growth per cycle increased with decreasing frequency. The cyclic crack growth rates were less dependent on sensitization than those measured under constant load. Finally, confirmatory pipe tests were started in the General Electric Pipe Test Laboratory. Both 4-in.- and 16-in.-diameter pipes, representative of field pipes, are being used to verify the predictive methodology.

Appendix A

FAILURE ANALYSIS DIAGRAMS FOR STATIC LOADING
(H. S. Mehta)

A.1 SUMMARY AND CONCLUSIONS

The Net Section Collapse criterion has been applied to assess quantitatively the margin-to-failure for Boiling Water Reactor (BWR) pipes and safe ends containing part-through and through-wall circumferential cracks, subjected to combinations of membrane and bending stresses expected under normal operation condition. Calculations have been performed for Type-304 stainless steel and Inconel, and the results are plotted in the form of failure analysis diagrams. Various crack shapes are considered in the analysis and the analytical predictions are compared with field and experimental data. The conclusions are summarized below:

1. Failure analysis diagrams for Type-304 stainless steel and Inconel indicate substantial margins to failure in pipes and piping components under normal conditions.

2. Consideration of realistic crack shapes in the analysis shows additional safety margin in field pipe cracks.

3. Experimental and field data are consistent with analytical predictions.

4. Comparison with predictions from elasto-plastic fracture mechanics estimation scheme shows good agreement.

5. The predicted margin is not very sensitive to flow stress. Conservative estimates can be made by using code minimum properties to estimate flow stress.

A.2 INTRODUCTION

Cracking due to IGSCC has been observed in Type-304 stainless steel piping and Inconel safe ends used in BWR applications. These cracks are mainly located in the Heat-Affected Zones (HAZs) next to the welds and are generally circumferential in orientation. Even in the presence of the cracks, the pipes have a substantial margin to failure because of the ductile failure mode. The purpose of this investigation was to determine the critical circumferential crack size at which failure can be expected in a pipe for normal conditions expected in service. This will enable the comparison of an existing flaw to the corresponding critical flaw parameters and assess the safety margin.

The critical flaw parameters can be conveniently represented in a failure analysis diagram which relates the length and depth of a crack at the point of incipient failure to the applied stress in the pipe. The failure analysis diagram can then be used to make a safety assessment and also to predict "leak before break" margin.

For materials where brittle fracture is a failure mode, the critical flaw parameters can be determined on the basis of Linear Elastic Fracture Mechanics (LEFM). However, for ductile materials like stainless steel, failure criteria based on LEFM are not valid since failure is characterized by gross yielding and subsequent plastic instability. In the analysis presented here, failure is predicted using the net section collapse criterion. It is assumed that a pipe with a circumferential crack is at the point of incipient failure when the net section at the crack forms a plastic hinge. Plastic flow is assumed to occur at a critical stress level, σ_f, called the flow stress of the material. The criterion is simple to apply and has been shown to be effective in predicting failure of stainless steel pipes containing circumferential cracks (A-1,A-2).

The net section collapse criterion is first applied to a pipe containing a circumferential crack of constant depth. For a given external bending moment and axial stress in the pipe, a set of critical crack lengths and depths at which collapse occurs are determined. The results are depicted graphically in the form of a failure analysis diagram on which the axes are nondimensional forms of crack length and depth.

The constant crack depth assumption, however, is conservative since the field cracks generally have variable depths. Therefore, to consider the effect of variable depths, a polynomial function of circumferential angle is used to characterize the crack and the failure moment is then calculated. Failure margins predicted by variable crack depth modeling are then compared with margins predicted using a constant depth assumption. Predictions of the net section collapse load approach are compared with the field cracking incidents and the results of an experimental study. Finally, the predictions are compared with those made using elasto-plastic methods.

A.3 ANALYSIS USING THE NET SECTION COLLAPSE CRITERION

A.3.1 Constant Depth Cracks

Consider a circumferential crack of length, ℓ, and constant depth, d, located on the inside surface of a pipe (Figure A-1). In order to determine the point at which collapse occurs, it is necessary to apply the equations of equilibrium assuming that the cracked section behaves like a hinge. For this condition, the stress state and the cracked section is as shown in Figure A-1 where the maximum stress is the flow stress of the material σ_f. The angle, β, at which stress inversion occurs can be determined by considering equilibrium in the longitudinal direction. Let P_m be the primary membrane stress in the longitudinal direction in the uncracked section of the pipe and P_b be the primary bending stress (mainly due to the dead weight and seismic loading). Equilibrium of longitudinal forces gives the following equation:

$$\beta = \frac{\sigma_f \left(\pi - \alpha \frac{d}{t}\right) - P_m \pi}{2\sigma_f} \qquad \text{(A-1)}$$

where

t = pipe thickness

and

α = half the crack angle as shown in Figure A-1.

Consider the equilibrium of moments about the axis of the pipe. Equating the collapse moment to the external moment over the uncracked section gives the following relationship:

$$\frac{2\sigma_f}{\pi} \left(2 \sin \beta - \frac{d}{t} \sin \alpha\right) = P_b \ . \qquad \text{(A-2)}$$

Note that above equations are valid in the range of $0 \leq \alpha \leq \pi - \beta$. Similar equations can be developed for $\pi - \beta < \alpha \leq \pi$.

Equations A-1 and A-2 together define the combinations of α and d/t for which failure by collapse is predicted under the given applied stresses P_m and P_b. It should be noted that secondary and peak stresses have no effect on the limit load and therefore are not included in the analysis. These equations can be solved by considering a given value of crack depth and determining the angle α at which failure occurs for specified values of P_m, P_b, and σ_f.

The flow stress, σ_f, is in general a function of the yield stress, σ_y, and ultimate stress, σ_u, of the material. For the purpose of this analysis, the flow stress was approximated by $(\sigma_u + \sigma_y)/2$. When actual material properties were not available, minimum strength properties given in the ASME Code (A-3) were used.

Figure A-2 shows a failure analysis diagram developed for stainless steel piping with the curves shown for two stress levels - one corresponding to the normal operation condition and the other corresponding to the design condition which included limiting earthquake loads. The value of flow stress was assumed as 48.0 ksi based on strength properties given in the ASME Code. For the normal operation condition, the primary stress of interest is the axial membrane stress due to internal pressure. This stress was assumed to be 6 ksi. Other primary stresses were negligible. For the design condition (which includes the operating basis seismic loads), the ASME Code stress limit is $(P_m + P_b) = 1.5\ S_m$ (S_m for stainless steel = 16.9 ksi). It should be noted that this is the maximum stress permitted by the code and, in reality, the calculated stresses are well below the code limits.

The failure analysis daigram of Figure A-2 indicates that stainless steel pipes can tolerate large circumferential cracks without failure. For example, under normal operation condition, a through-wall crack extending through 55% of the circumference is tolerated. This is consistent with field experience with stainless steel piping in the BWR operation.

A.3.2 Variable Depth Cracks

The safety margins indicated by the curves shown in Figure A-2 are inherently conservative because the cracks in the analysis are idealized as having constant depth equal to the maximum depth of the actual crack. To represent field cracks more closely, the variation in crack depth was modeled. The profiles of circumferential cracks observed in the field in BWR piping are quite varied. Figure A-3 shows some typical examples of circumferential crack profiles (A-4,A-5). These profiles are considered in the selection of varying depth circumferential crack geometries in the following analysis.

Consider a part-through variable depth crack of the type shown in Figure A-4a. The crack depth can be characterized as a second-order polynomial function of circumferential angle θ, i.e., crack depth $d = a + b\theta + c\theta^2$. The constants a, b, and c can be suitably chosen to represent a particular crack profile. For example, $b = c = 0$ represents a constant depth circumferential crack considered in the previous analysis.

The net section collapse criterion was applied in a manner similar to that for constant depth crack. Thus, angle β can be determined considering force equilibrium:

$$\beta = \frac{\sigma_f \left[\pi - \frac{1}{t}\left(a\alpha + \frac{1}{2} b\alpha^2 + \frac{1}{3} c\alpha^3\right)\right] - \pi P_m}{2\sigma_f} \qquad \text{(A-3)}$$

Similarly equilibrium of moments about axis of the pipe can be applied to provide the relationship between the collapse moment and the crack parameters.

Figure A-5 shows the failure analysis diagram for stainless steel obtained by considering variable crack depth modeling. This figure compares the failure diagram for stainless steel obtained under the constant crack depth assumption and the variable depth example for the same loading condition. The assumed variation in crack depth is depicted in Figure A-6. Clearly by considering a more realistic crack depth variation significantly improved safety margins can be demonstrated.

A.3.3 Compound Cracks

This type of crack displayed in Figure A-4b extends through the complete circumference with the leaking portion extending through angle 2ν of the circumference. The crack depth in the nonleaking portion is assumed as constant and equal to 'd' to facilitate representation on a failure analysis diagram. As before, equilibrium of forces and moments are used to locate the neutral axis and to determine the collapse moment. The mathematical expressions for β and the bending stress P_b corresponding to collapse are as follows:

$$\beta = \frac{(\pi - \nu)\left(1 - \frac{d}{t}\right) - \frac{\pi P_m}{\sigma_f}}{2 - \frac{d}{t}} \qquad \text{(A-4)}$$

$$P_b = \frac{2\sigma_f}{\pi} \left[\left(1 - \frac{d}{t}\right) (\sin \beta - \sin \nu) + \sin \beta\right] \qquad \text{(A-5)}$$

Figure A-7 shows a failure analysis diagram for Type-304 stainless steel. Note that the abscissa in this case is ν/π, i.e., fraction of circumference of the through-wall crack, rather than α/π as in previous cases. The results are shown for two cases: Normal operation (P_m = 6.0 ksi, P_b = 0); Design condition (P_m = 6.0 ksi, $P_m + P_b = 1.5\ S_m$). As expected, the critical crack depth indicated for $\nu/\pi = 0$ in Figure A-7 coincides with that indicated for $\alpha/\pi = 1.0$ in Figure A-2.

4.3.4 Analysis of Inconel Safe Ends

The analysis performed for Inconel safe ends is the same as that performed for stainless steel. The flow stress magnitude is different in that the material is inherently stronger than the stainless steel. The flow stress as determined using yield and ultimate stress values of SB166 from ASME Code (A-3) is 54.1 ksi. Figure A-8 depicts the failure analysis diagram. This diagram shows both constant depth and variable depth cracks.

It is noted that the normalized safety margin for Inconel (Figure A-8) is somewhat lower than that for stainless steel (Figure A-5). However, this is due to the higher applied bending moment for the same specified ASME Code limits for Inconel safe ends (S_m for Inconel = 23.2 ksi at 550°F compared to 16.9 ksi for stainless steel). For the same given crack geometry, internal pressure and bending moment, an Inconel component is expected to tolerate a larger crack due to a higher value of flow stress.

A.4 COMPARISON WITH FIELD DATA

Available field observed data on circumferential cracks in austenitic pipes and safe ends are examined on the failure analysis diagrams in order to make a qualitative estimate of typical safety margins. Figure A-9 shows a plot for these data (A-5) on the failure analysis diagram. The nominal pipe size in these data varies from 2 inches to 10 inches. Also shown are the two curves, one corresponding to normal operation (solid line) and the other (dotted line) corresponding to design limits. It is seen that the field data on cracks is well within the safe region. Moreover, the data shows a tendency for the pipe to leak before the collapse load point is reached, thus indicating a strong trend for a "leak before break" condition.

Figures A-10 and A-11 show the failure analysis diagrams for a field-cracked Inconel safe end. Figure A-10 shows the plot of nonleaking safe ends. The values of P_m and P_b were those predicted for normal operation. The leaking safe end was represented on Figure A-11 since it was a compound crack. For comparison purposes, other safe ends are also plotted in the same figure. It is seen that even the leaking safe end, which is cracked to a full depth for approximately 30% of the circumferential and cracked to 75% of the depth for the remaining circumference is still within the safe region.

Thus, it can be concluded from the review of field data that there is considerable safety margin present and that a leak-before-break condition is favored.

A.5 COMPARISON WITH EXPERIMENTAL DATA

Predictions using the net section collapse criterion are compared with the experimental failure pressure and moment load determined from data in a low cycle fatigue study (A-6). Figure A-12 shows the failure analysis diagrams with the experimental data point shown therein. The spread in the limit line defining the safe area represents the possible range of bending stress at the time of collapse of the pipe section. It is seen that the net section collapse criterion gives a conservative prediction.

A.6 COMPARISON WITH ELASTO-PLASTIC FRACTURE MECHANICS PREDICTIONS

The criteria used in the assessment of the strength of circumferentially cracked pipes were based on the concept of a critical net section flow stress. The existence of a critical net section stress for crack initiation in a Center-Cracked Panel (CCP) has been justified by Smith (A-7) using the results of fully plastic solutions developed by Shih, et al. (A-8,A-9). By relating the crack opening displacement, thereby J, to the net section stress, he concluded that except for a slight panel width dependence, the net section stress at crack initiation in a CCP is essentially constant for highly ductile materials like stainless steel.

Only a limited number of elasto-plastic fracture mechanics solutions are currently available pertaining to circumferentially cracked pipes. Reference A-10 provides estimation scheme solutions for the case of a cylinder with a 360° part-through crack and subjected to a uniform axial load. The case of an axially loaded pipe with a through-wall crack has been treated in Reference A-11 using nine-noded Lagrangian shell elements and a bi-linear stress-strain relationship. These solutions were used to develop failure predictions for comparison with net section collapse approach.

Initiation, i.e., attainment of J_{IC}, was conservatively used as the failure criterion in determining the failure flaw size. The room temperature J_{IC} values for Type-304 stainless steel reported in the literature (A-12,A-13) range from 4500 to 7800 in.-lb/in.^{2}. Therefore, the failure flaw size calculations were based on two values of J_{IC}, viz., 4000 and 8000 in.-lb/in.^{2}. The failure flaw size predictions from net section collapse approach were based on a flow stress of 52.5 ksi which is the average of the room temperature yield and ultimate stress for Type-304 stainless steel given in the ASME Code (A-3).

Figure A-13 shows the failure flaw depths for a 360-deg flaw in a pipe subjected to a remote uniform axial stress of 16 ksi. This value of axial stress was chosen for the convenience of interpolation between the given J versus σ curves in Reference A-10. For the same axial stress, Figure A-13 also shows the net section collapse prediction line. It is seen that the net section collapse prediction compares well with the initiation based failure predictions.

Figure A-14 shows failure predictions for a 26-in. diameter pipe with a through-wall crack. The J versus axial stress plot for this size pipe with a quarter circumference through-wall flaw is given in Reference A-11. The plot shows an axial stress of 22 ksi corresponding to J = 4000 in.-lb/in.^{2}. In other words, the predicted failure flaw size is one-fourth the circumference for an axial stress of 22 ksi and J_{IC} of 4000 in.-lb/in.^{2}. This point is shown as (0) in Figure A-14. Since the plot in Reference A-11 extended only up to J = 5500 in.-lb/in.^{2}, the axial stress corresponding to J_{IC} = 8000 in.-lb/in.^{2} could not be obtained. The net section collapse line corresponding to an axial stress of 22 ksi is also shown in Figure A-14. A comparison of the two predictions in Figure A-14 shows that the net section collapse prediction is slightly nonconservative. However, it should be noted that the elasto-plastic fracture mechanics prediction is based on the conservative criteria that defines crack initiation as failure. If stable ductile crack growth is taken into account, it is expected that the two predictions would be closer together.

At present, elasto-plastic fracture mechanics solutions are not available for part-through flaws that are not fully circumferential and for loadings such as bending or axial plus bending. Therefore, this comparison was limited to flaw geometries that are either 360-deg part-through or through-wall and to axial loading only. However, this limited comparison shows that failure flaw predictions based on net section collapse are comparable to those obtained using elasto-plastic fracture mechanics.

A.7 SENSITIVITY OF PREDICTIONS TO FLOW STRESS

A key parameter used in the development of the failure analysis diagram is the flow stress. To determine the sensitivity of the critical flaw size to the flow stress value used in the analysis, evaluations were performed for two values of flow stress. Figure A-15 shows a comparison of the failure diagrams developed with the two different flow stresses. The difference in the two flow stresses used is about 10%. The differences in the critical flow parameters for the two cases are not significant. In any case, conservative values can be obtained by using ASME Code minimum strength properties (A-3).

A.8 REFERENCES

A-1. "Mechanical Fracture Predictions for Sensitized Stainless Steel Piping with Circumferential Cracks," Final Report, September 1976 (EPRI Report NP-192).

A-2. "Review and Assessment of Research Relevant to Design Aspects of Nuclear Power Plant Piping Systems," Nuclear Regulatory Commission, July 1977 (NUREG-0307).

A-3. ASME Boiler & Pressure Vessel Code, Section III, Division 1, Nuclear Power Plant Components.

A-4. C. F. Chang, W. A. Ellington, and J. Y. Park, "Effect of Residual Stress and Microstructures on Stress Corrosion Cracking in BWR Piping," Corrosion/76, Houston, Texas, March 1976.

A-5. H. H. Klepfer, et al., "Investigation of the Cause of Cracking in Austenitic Stainless Steel Piping," General Electric Company, July 1975 (NEDO-21000-1).

A-6. E. Kiss, J. D. Heald, and D. A. Hale, "Low Cycle Fatigue of Prototype Piping," General Electric Company, January 1970 (GEAP-10135).

A-7. E. Smith, "Theoretical Justification for the Association of a Critical Net-Section Stress with Fracture Initiation at a Crack Tip," International Journal of Pressure Vessels and Piping, Vol. 8, 4, July-August 1980, pp. 303-311.

A-8. C. F. Shih and J. W. Hutchinson, "Fully plastic solutions and large-scale yielding estimates for stress crack problems," J. Eng. Mat. Tech., ASME, Series H, 98 (1976), pp. 289-295.

A-9. C. F. Shih and V. Kumar, "Estimation technique for the prediction of elastic-plastic fracture of structural components of nuclear systems," Semiannual report on Electric Power Research Institute Contract RP1237-1, June 1979.

A-10. Monthly Management Letter No. 27 from GE CR&D to Dr. D. M. Norris, Jr., EPRI Project RP1237-1, October 1980.

A-11. "Crack Opening and Stability Analyses for Flawed Stainless Steel Piping," by C. F. Shih, et al., First Interim Report, EPRI Contract No. T118-8, September 1980.

A-12. "EPRI Ductile Fracture Research Review Document," EPRI Report No. NP-80-10-LD, December 1980.

A-13. W. H. Bamford and A. J. Bush, "Fracture Behavior of Stainless Steel," Elastic Plastic Fracture, ATSM STP 668, pp. 553-577.

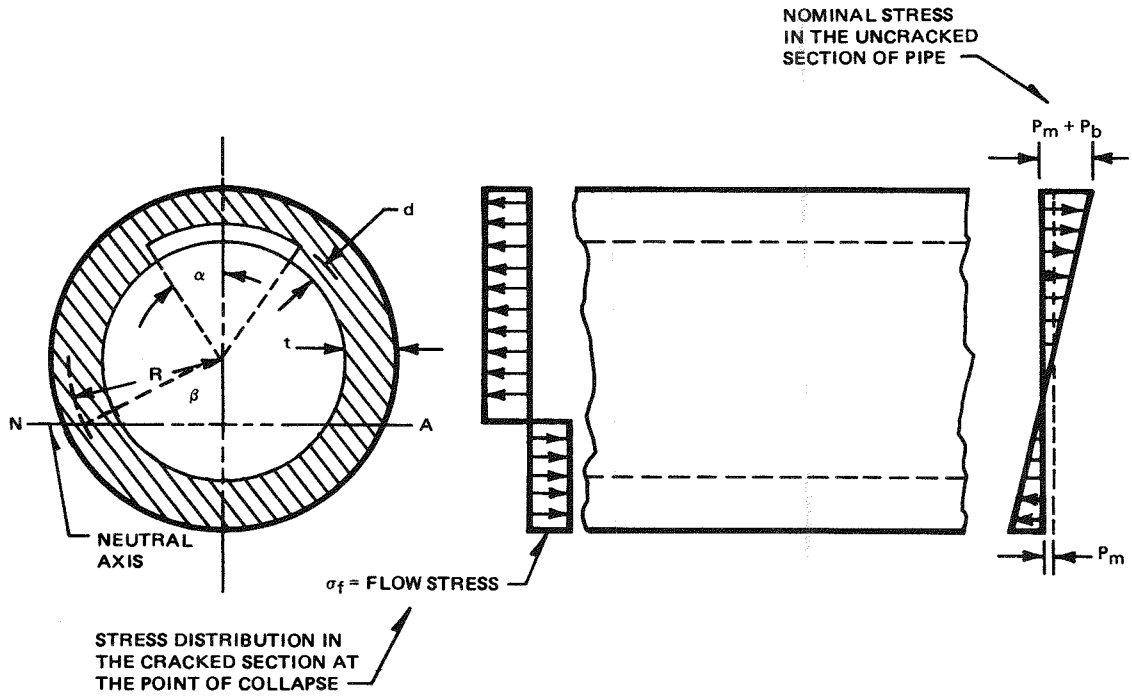

Figure A-1. Schematic Showing Stress Distributed in a Cracked Pipe at the Point of Collapse

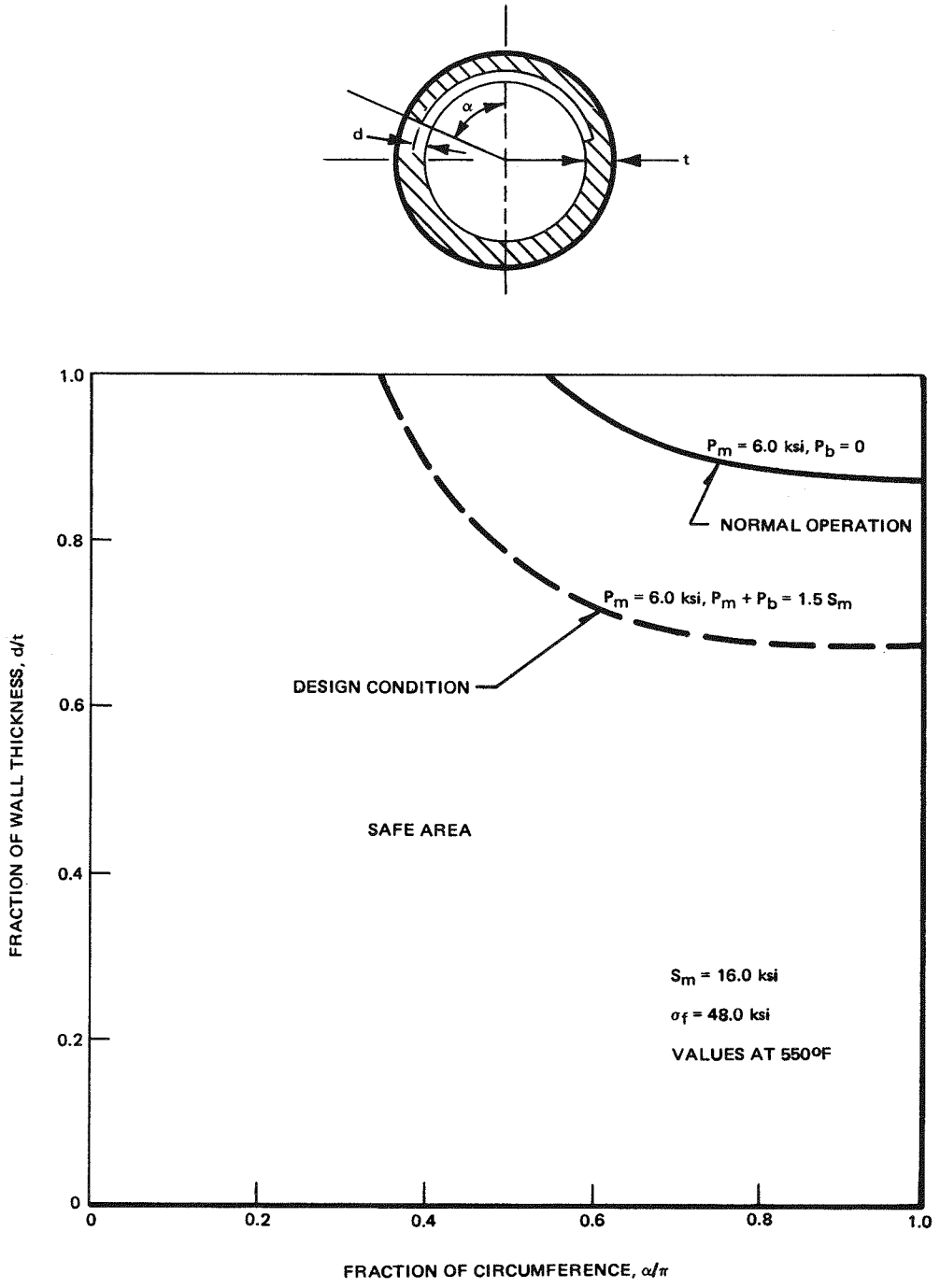

Figure A-2. Failure Analysis Diagram for Stainless Steel Piping Using Constant Depth Crack Assumption

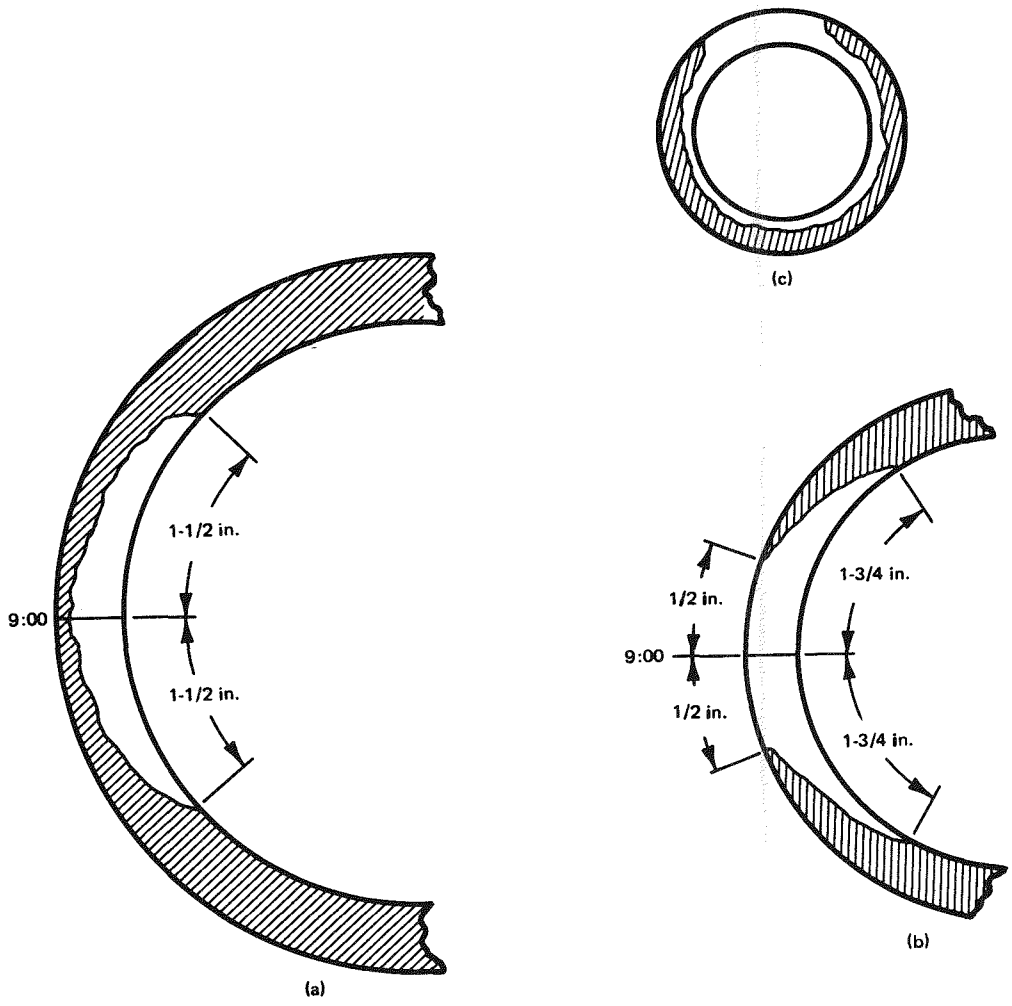

Figure A-3. Some Examples of Field Observed Circumferential Cracks

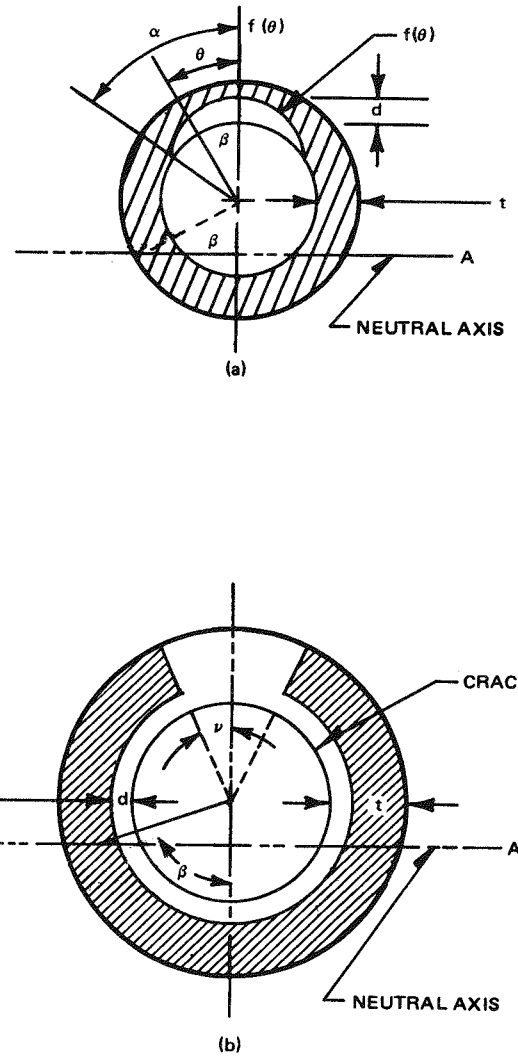

Figure A-4. Geometry Considered in (a) Variable Depth Crack Analysis and (b) Compound Crack Analysis

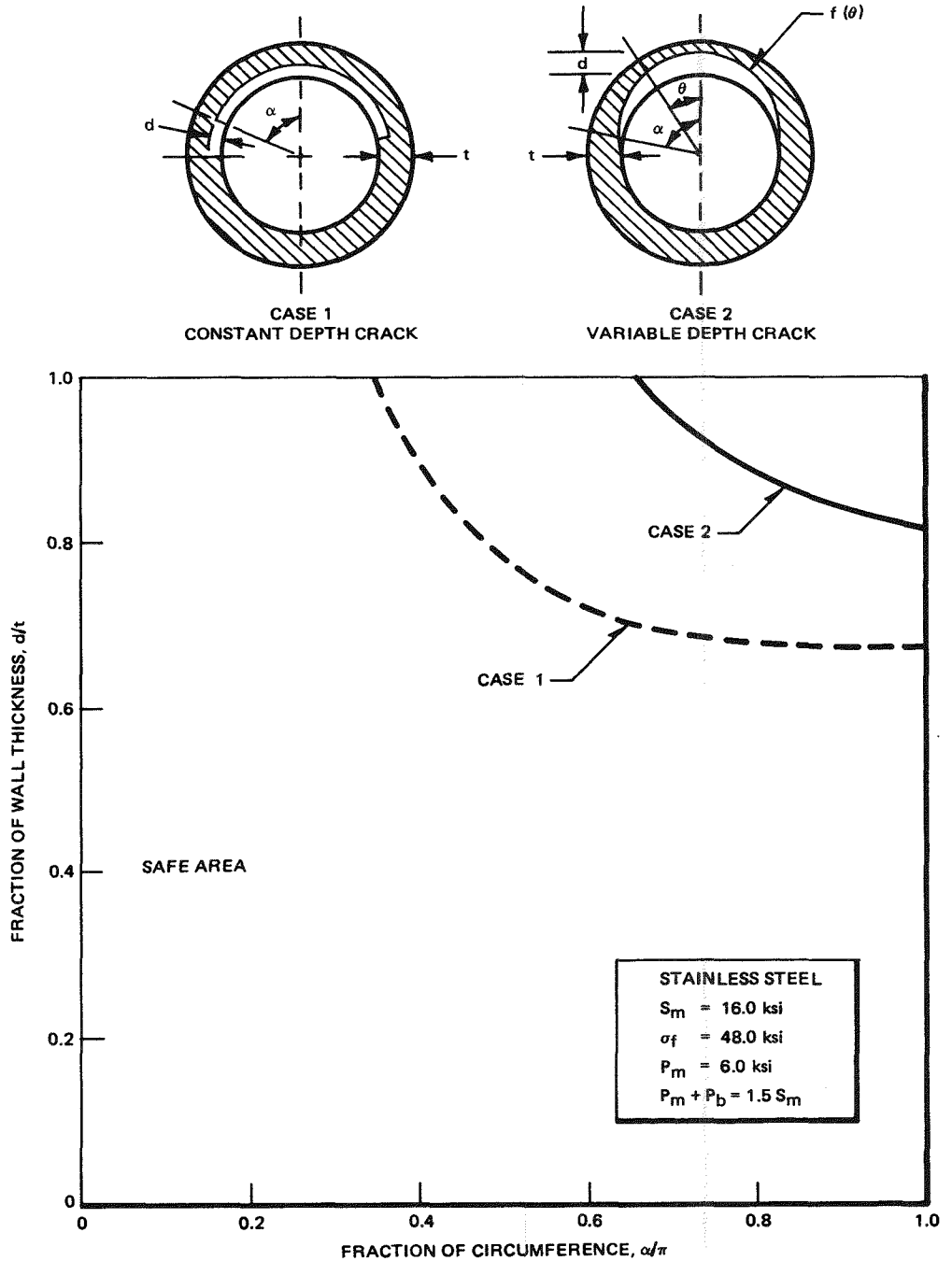

Figure A-5. Failure Analysis Diagram Comparison Between Constant and Variable Crack Depth Assumptions - Stainless Steel

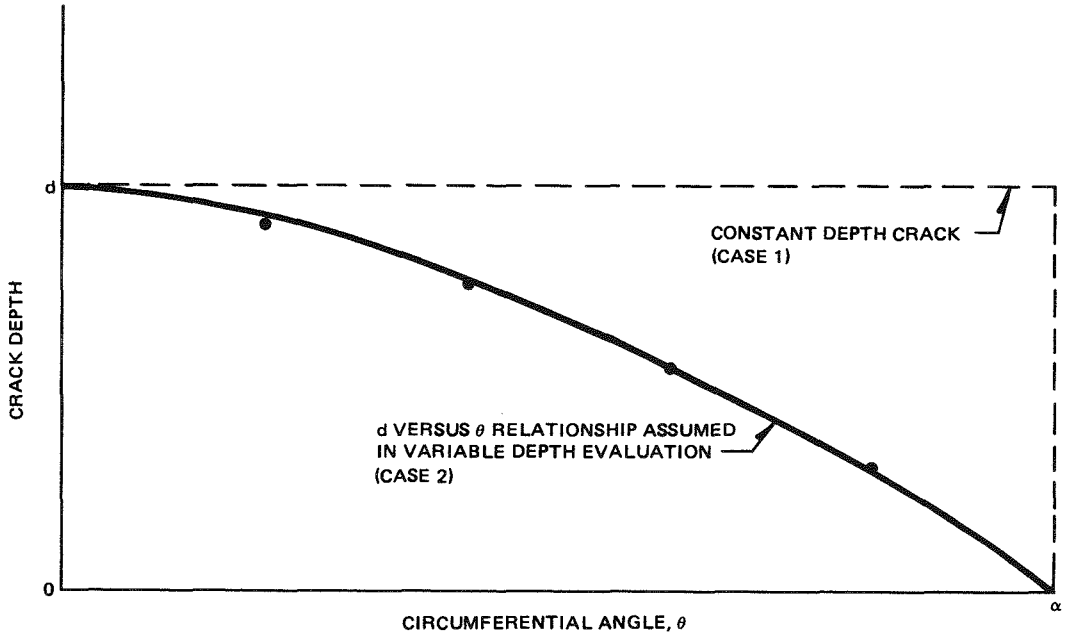

Figure A-6. Assumed Crack Depth versus θ Relationship for Variable Depth Crack

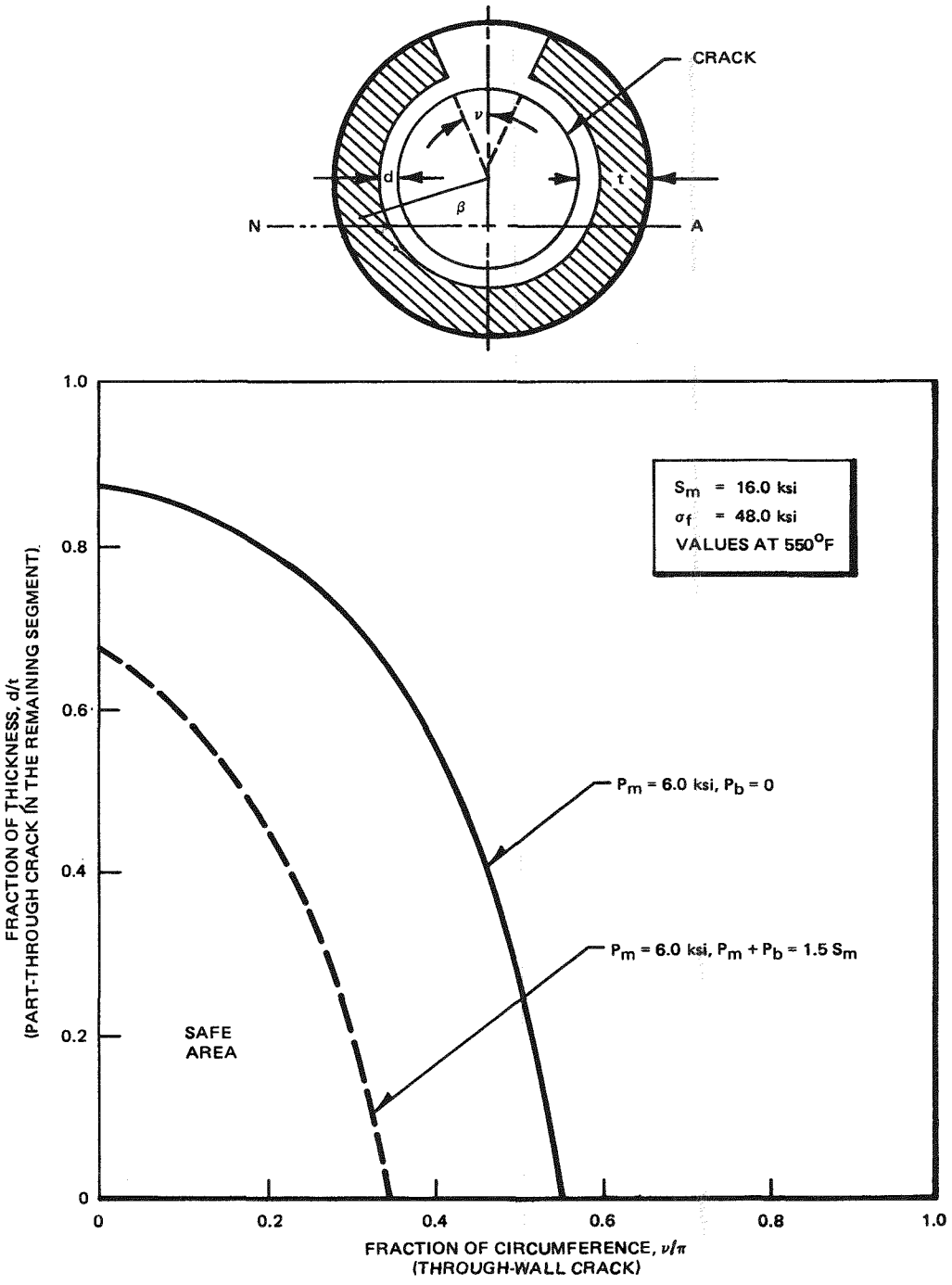

Figure A-7. Failure Analysis Diagram for Compound Crack - Stainless Steel

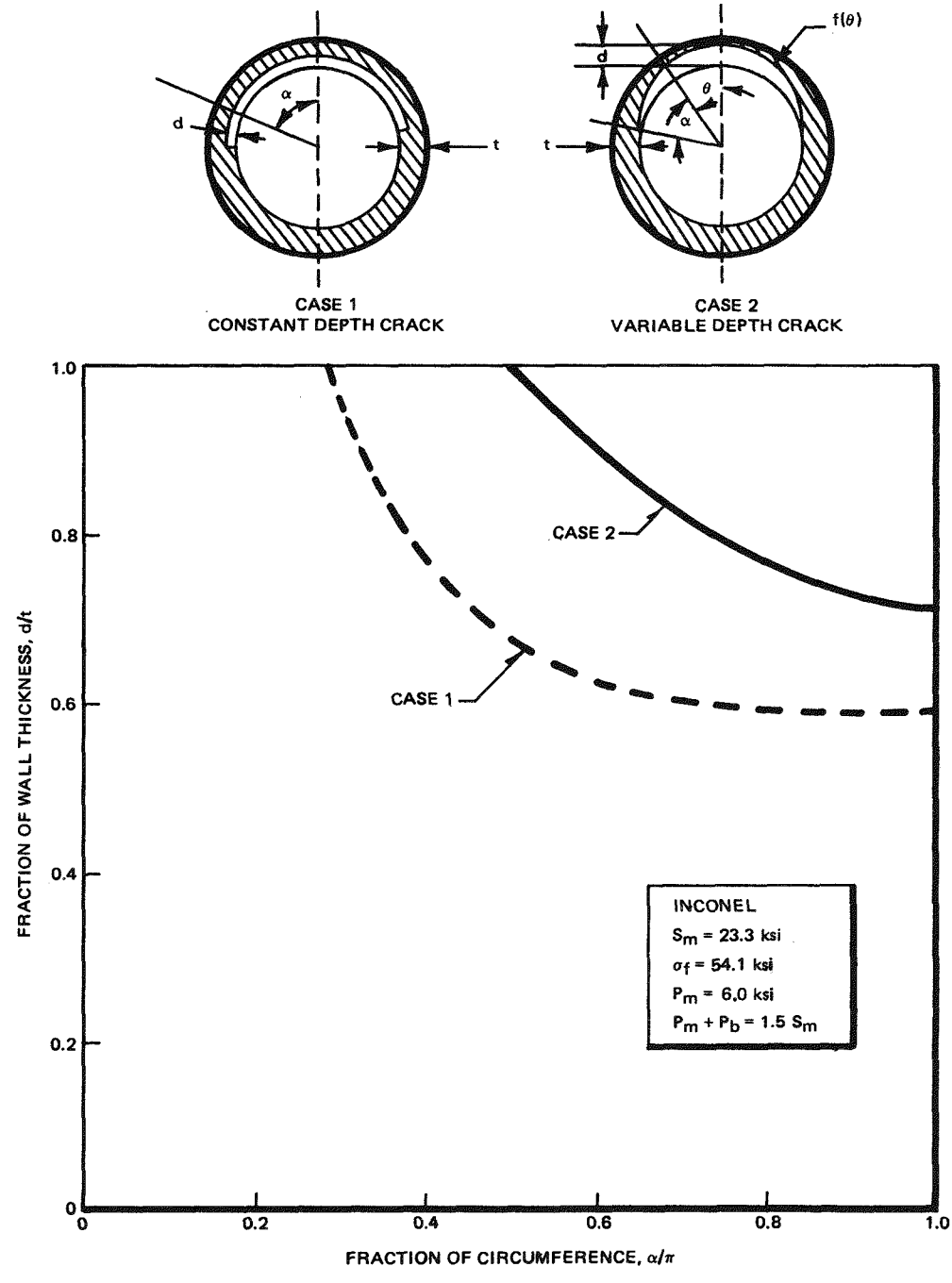

Figure A-8. Failure Analysis Diagram Comparison Between Constant and Variable Crack Depth Assumptions - Inconel

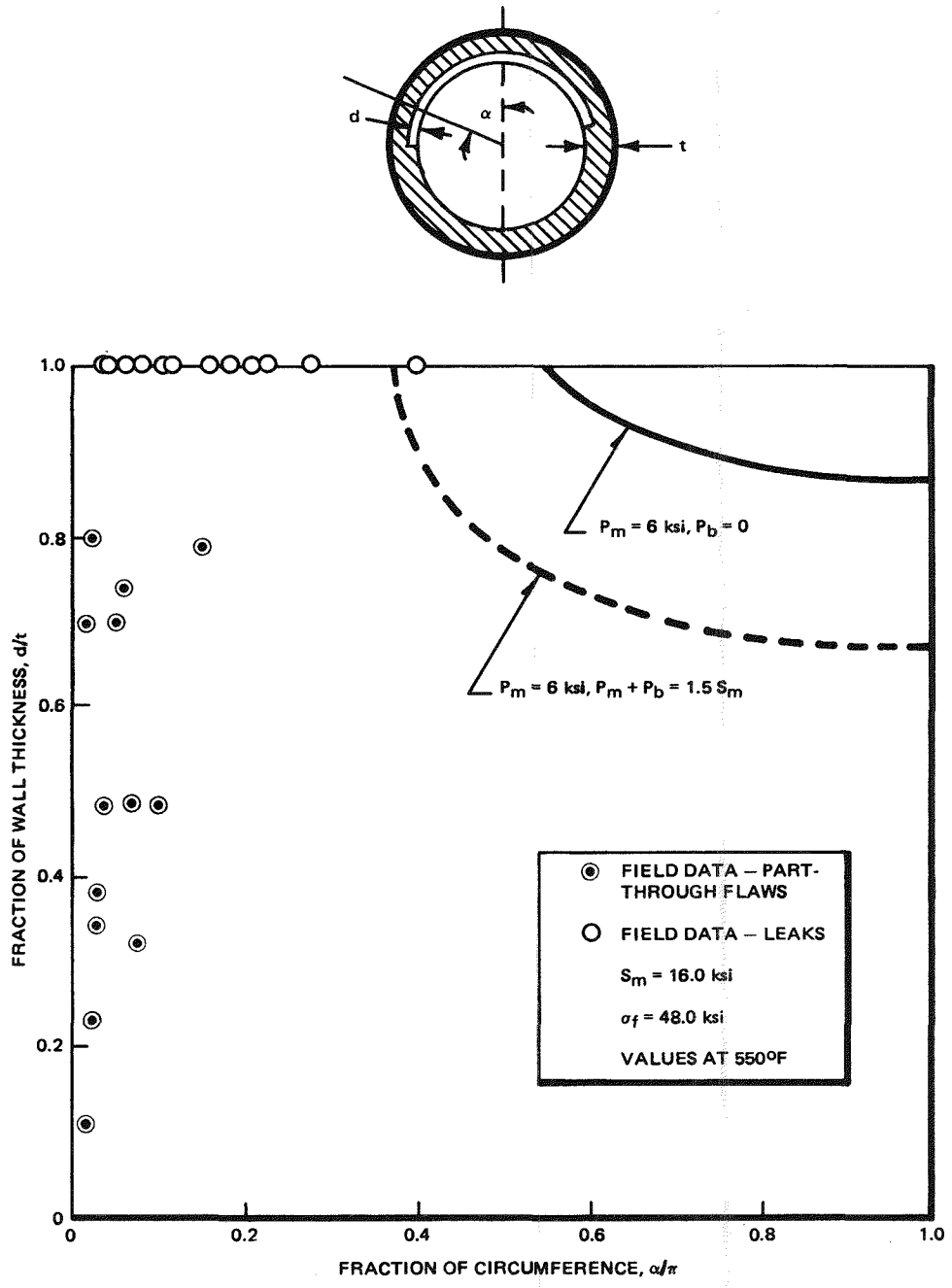

Figure A-9. Comparison with Field Data - Stainless Steel Piping

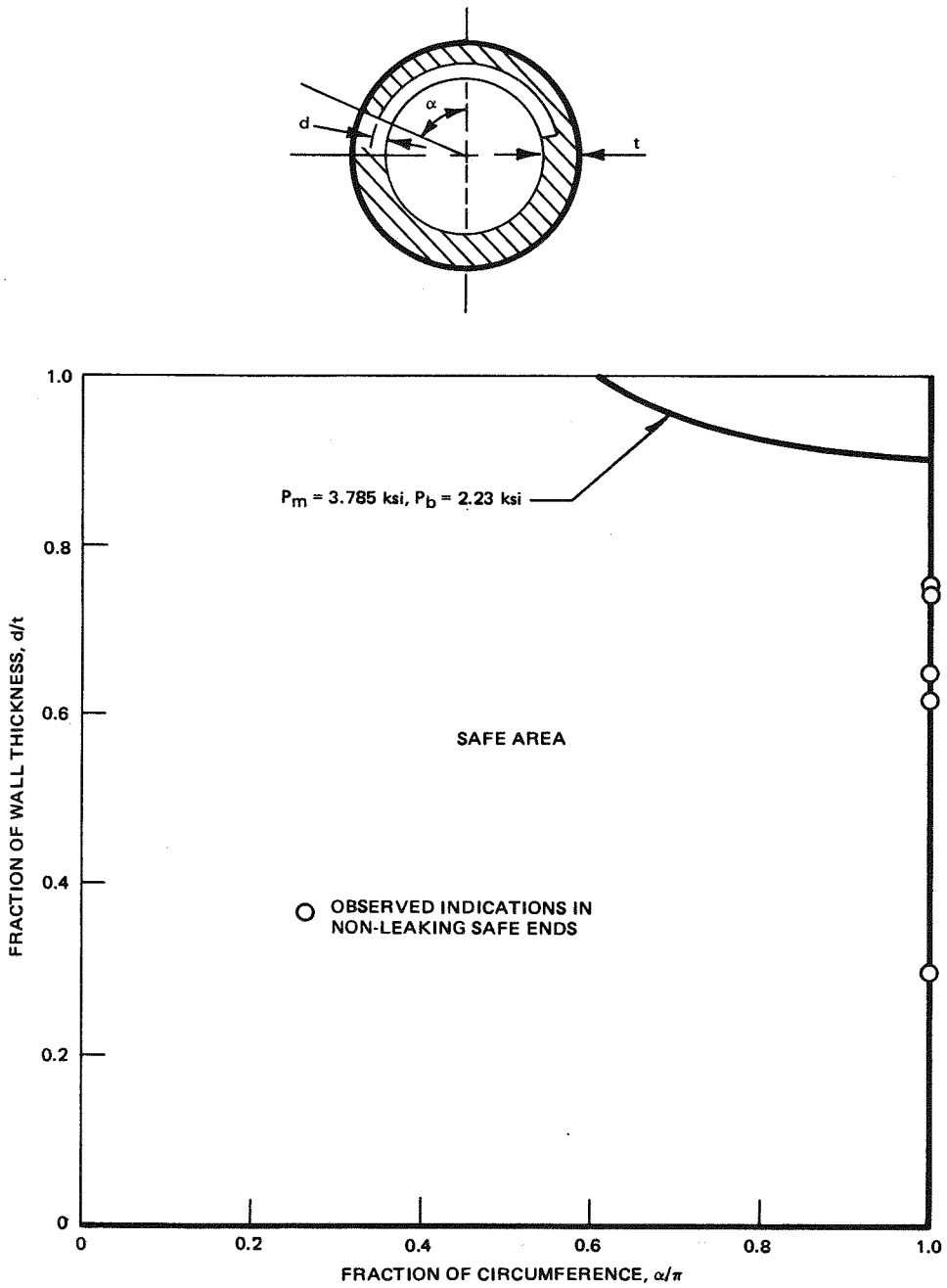

Figure A-10. Failure Analysis Diagram - Normal Operation for Field Observed Cracking in Safe Ends

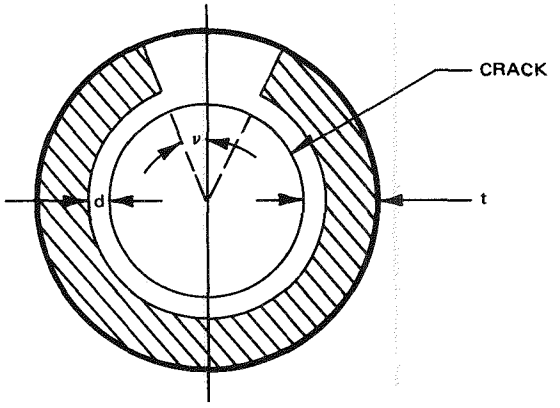

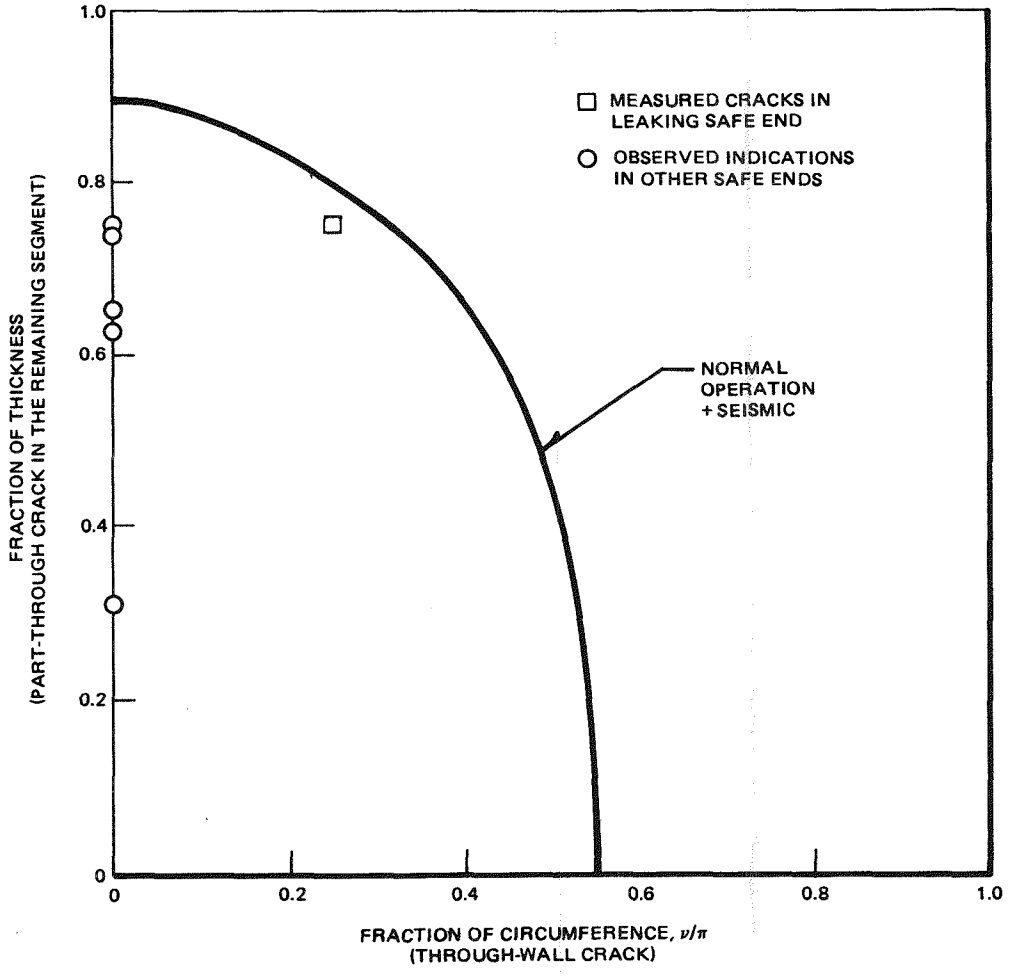

Figure A-11. Failure Analysis Diagram for Normal Operation for Field Observed Cracking in Safe Ends Considering Compound Crack

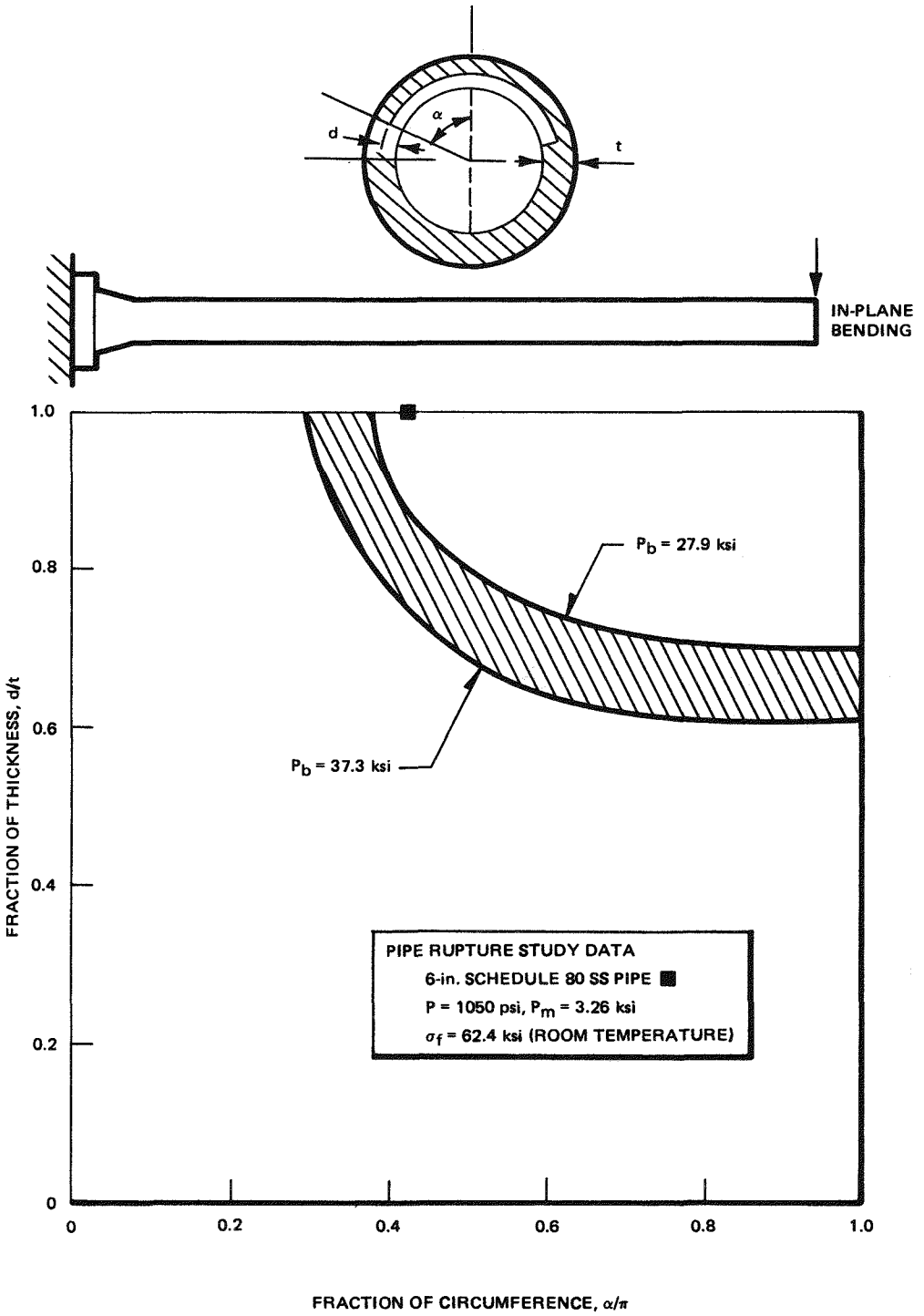

Figure A-12. Application of Net Section Collapse Criteria to Low Cycle Fatigue Study Data

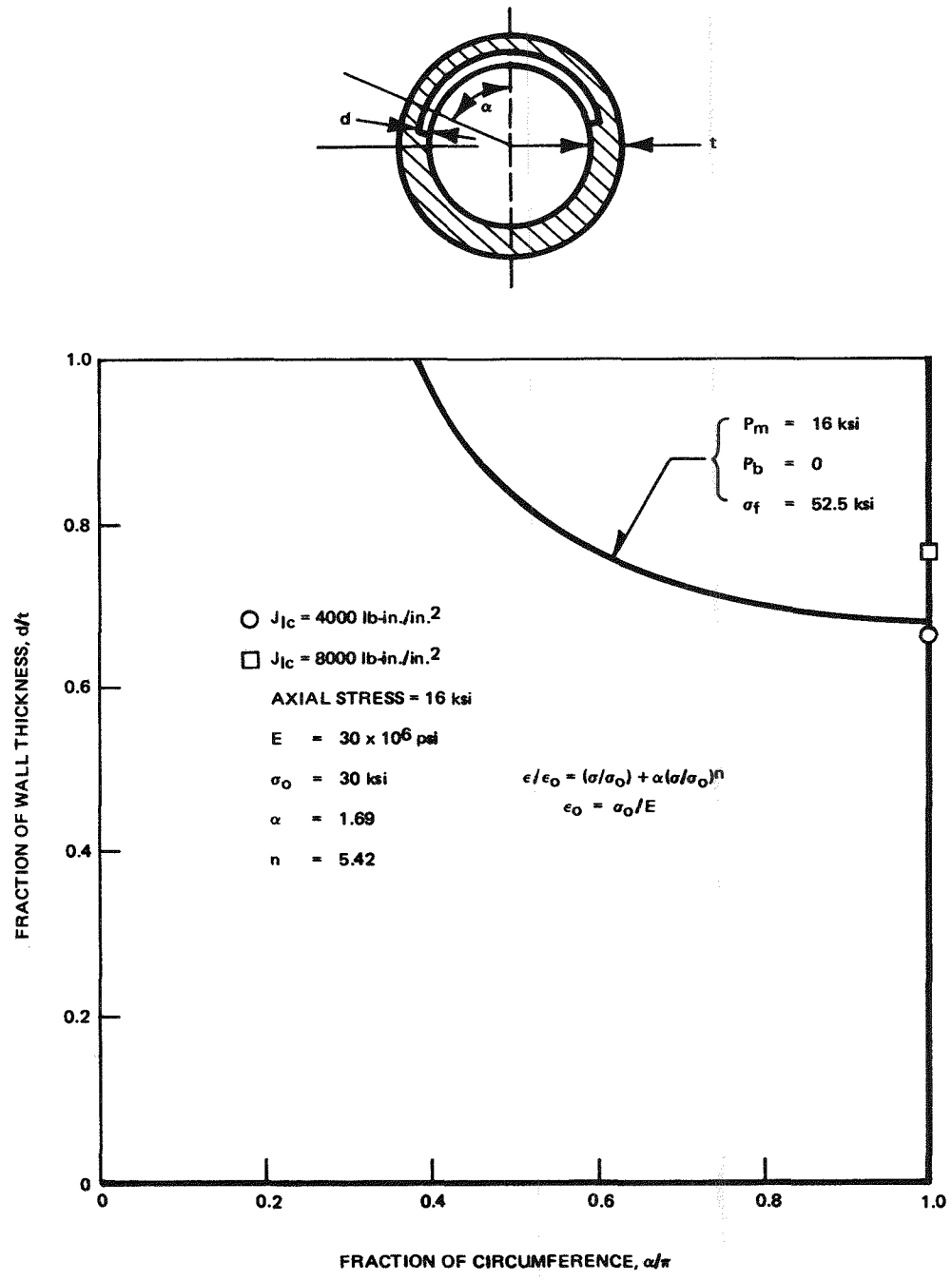

Figure A-13. Comparison of Allowable Flaw Sizes Between Net Section Collapse and Estimation Scheme Procedure - 360-deg Flaw Case

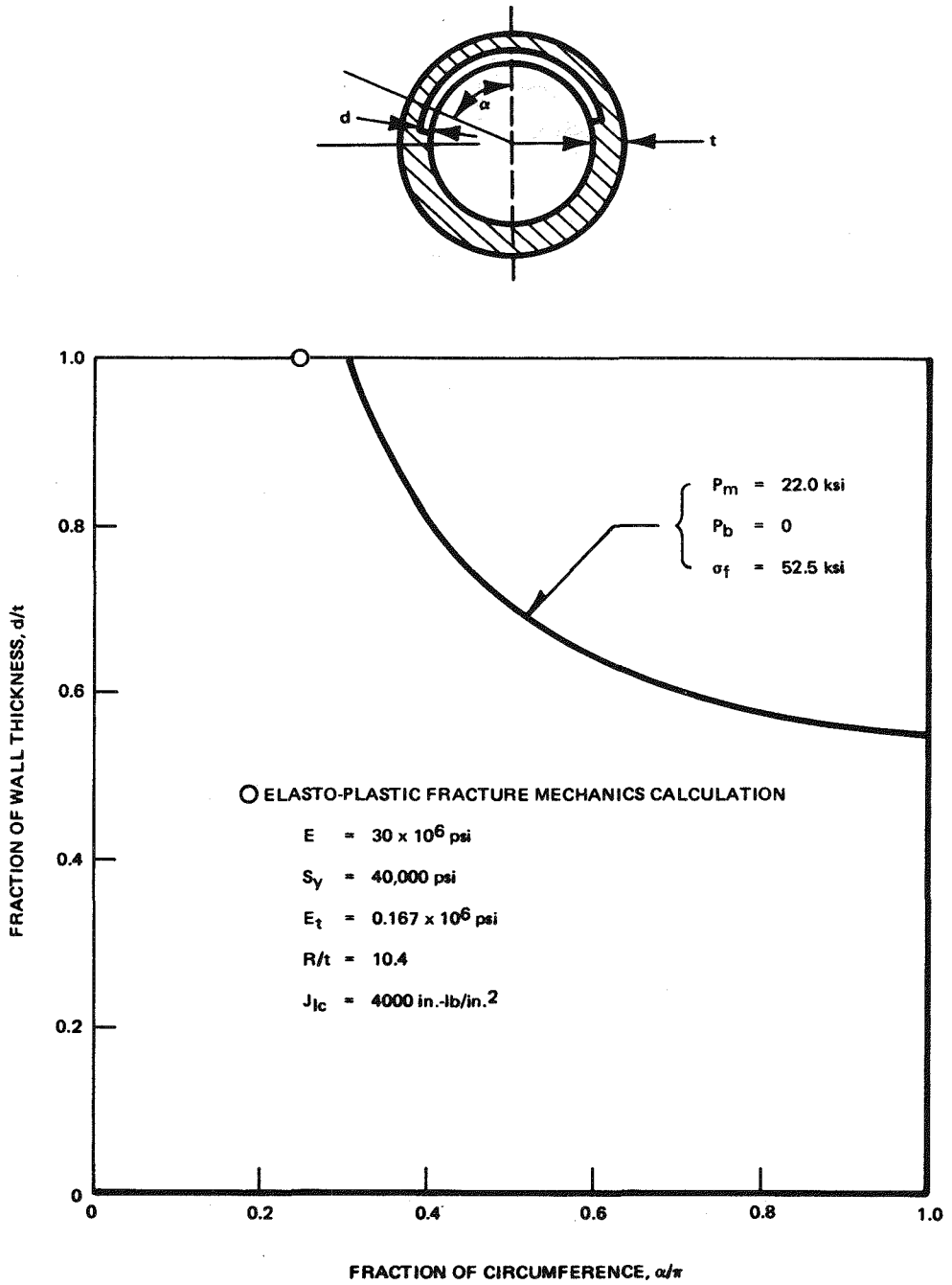

Figure A-14. Comparison of Allowable Flaw Sizes Between Net Section Collapse and Estimation Scheme Procedure - Through-Wall Flaw Case

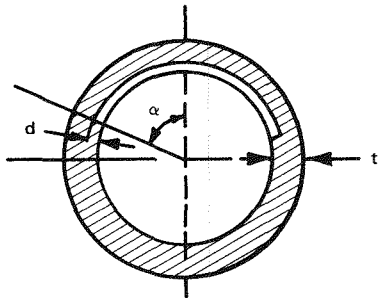

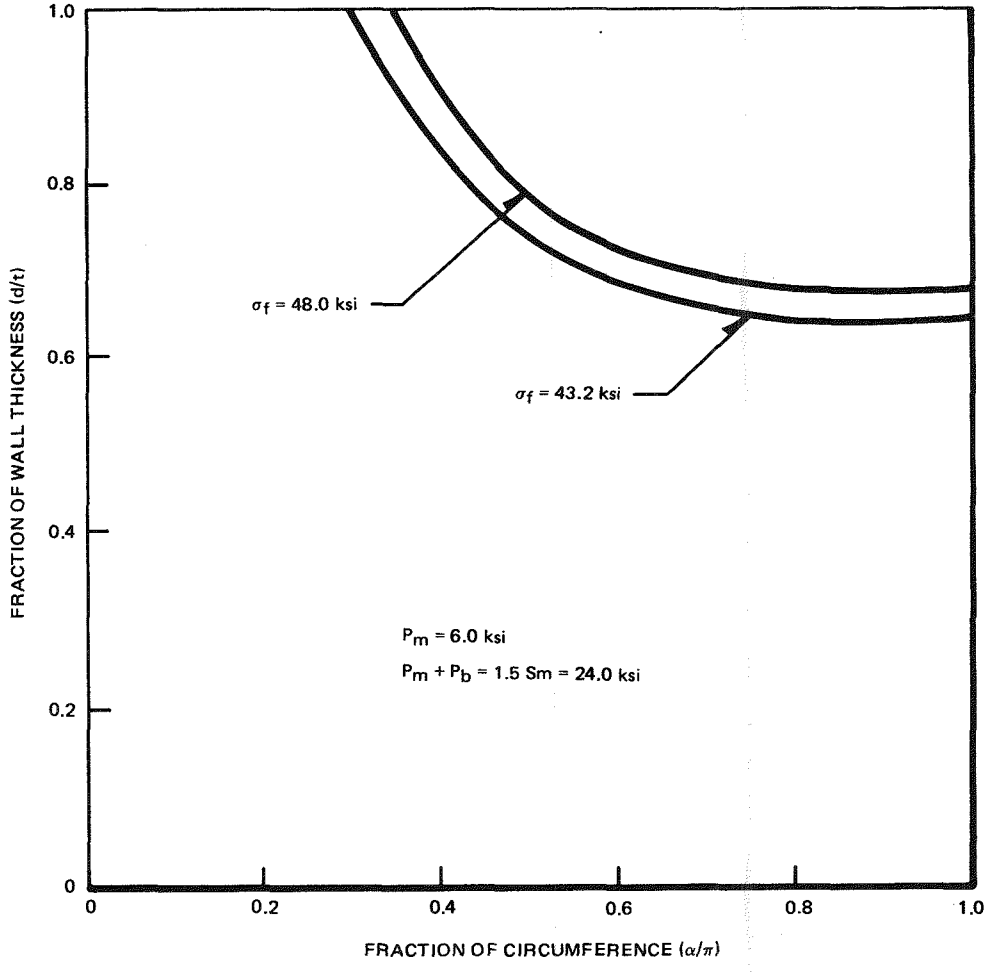

Figure A-15. Comparison of Critical Flaw Sizes for Different Values of Flow Stress

Appendix B

FAILURE MARGIN ANALYSIS FOR DYNAMIC LOADS
(S. R. Sharma)

B.1 INTRODUCTION

The net section collapse approach to estimate safety margins in cracked pipe components, as described in Appendix A, is appropriate for loads which are essentially static in nature such as during the Reactor Pressure Vessel (RPV) steady state normal operation. However, when the loading on the piping is impulsive or vibratory in nature, failure analysis using static equivalent of the maximum dynamic loads obtained from a conventional linear elastic analysis of the piping is considered to be unduly conservative. This is true because the failure of a highly ductile cracked austenitic stainless steel piping requires considerable plastic deformations prior to the onset of plastic instability at the reduced section. The dynamic loads experienced by the piping during an abnormally high loads situation such as the "safe shutdown earthquake" loads during the RPV faulted conditions (B-1) are generally rapidly varying and contain a limited number of high amplitude peaks of short enough duration to restrict large scale plastic deformations. Furthermore, in the presence of plastic deformations, the nonconservative nature of the dynamic system, when the material hysteresis provides an effective means for the dissipation of system kinetic energy, actually assures lower dynamic force response of the system than that predicted by a purely linear elastic analysis. The conservatism associated with the use of elastic analysis to predict safety margins in structures subjected to impulsive loads has been discussed by Subramanian and Kennedy (B-2,B-3). One of the key conclusions of their studies is that the structures exhibiting even moderately ductile behavior possess inherently higher safety margins under dynamic loading than those indicated by linear elastic analysis. This can be demonstrated through a materially nonlinear dynamic analysis of a simple structure as follows.

Consider, for example, the dynamic model of a simple piping system as shown in Figure B-1. The model represents a 10-in. Schedule 80, Type-304 stainless steel piping system with a horizontal span of 15 feet and a vertical unsupported span length of 5 feet. It was assumed that a continuous circumferential flaw of depth-to-pipe-wall thickness ratio of 0.5 is present in the vicinity of the pipe support. To account for the change in the local stiffness of the cracked pipe element due to

the presence of this flaw, its pipe wall thickness was appropriately reduced. The material bilinear stress-strain curve used in the analysis is shown in Figure B-2.

The first natural mode frequency of the system was determined to be 11.1 Hz. The free end of the model was subjected to a forcing function of the form shown in Figure B-1 with frequencies in the range of 11 to 64 Hz. Both linear and nonlinear dynamic responses of the system were determined using the in-house structural dynamics computer program COMET02 which is discussed separately later in this report.

Figures B-3 and B-4 show the comparative results of these analyses. In Figure B-3 M_e and M_{ep} are the absolute maximum moments obtained from linear-elastic and elastic-plastic dynamic analyses, respectively. M_s is the static moment for the applied force equal to the maximum amplitude of the forcing function, t_n is the first mode natural time period of the system, and t_d is the time period of the forcing function. Figure B-4 shows the relationship between the ratios M_e/M_{ep} and t_d/t_n. Although the maximum moments obtained from the two analyses depend upon the forcing function frequency, the moments calculated using elastic-plastic material behavior are significantly lower than the elastically calculated moments, especially in the region where the forcing function frequency approaches the first natural mode frequency of the system, i.e., the resonant conditions.

Using the maximum moments obtained from these analyses for a given t_d/t_n ratio and applying the net section collapse criterion comparative failure margin diagrams developed for the two cases are shown in Figures B-5 and B-6. Figure B-5 indicates failure of the cracked pipe component containing the postulated flaw if the loads on the piping are calculated assuming linear-elastic material behavior. However, the actual loads experienced by the piping are significantly lower when the actual nonlinear material behavior is considered. Consequently, the postulated flaw is still shown to be within the safe regime.

Figure B-6 shows the failure diagram for the loads corresponding to t_d/t_n ratio of 0.33. Although the postulated flaw falls within the safe regime in both the elastic and elastic-plastic analyses cases, higher safety margins to failure are indicated for the nonlinear analysis.

It is evident from the above discussion, that a realistic assessment of safety margins in ductile structures subjected to dynamic loading must include the effects of plastic deformations on the dynamic force response of the structure.

It is for this purpose that this study was initiated to meet the following specific objectives:

1. develop a systematic approach and methods to evaluate the nonlinear dynamic response of a large piping system containing postulated flaws at given locations,

2. demonstrate the applicability of the analytical methods by performing an elastic-plastic dynamic analysis of a complex piping system containing a postulated flaw and subjected to a representative seismic excitation, and

3. quantify extra safety margins in cracked piping by comparison with results from a conventional linear elastic analysis of the piping system.

The following sections of this report describe the development and application of the analytical methods to perform failure analysis of cracked piping under dynamic loading.

B.2 ANALYSIS METHODS

In the design of typical power plant piping systems, the various service loads considered are the pressure, hydraulic, dead weight, thermal, and the dynamic loads such as hydraulic transients and seismic loads. However, the design of a typical Boiling Water Reactor (BWR) piping system is generally controlled by the dynamic loads due to the design basis earthquake loads since primary (load controlled) stresses due to other loads during the RPV normal operation are usually low. Therefore, the method of seismic analysis itself and the ways in which the seismic analysis results are used in subsequent analyses play a central role in the design of piping systems. Because of this importance of the seismic analysis and its consequences, it is useful to briefly review the dynamic analysis methods generally applied in piping system design.

The analysis of a piping system for a seismic event essentially involves applying the expected motion time histories or acceleration response spectra to the piping supports and anchor points and performing a linear elastic dynamic analysis. The anchor point motion time histories, in turn, are obtained from a soil-structure interaction analysis of the total system, i.e., the major equipment systems, associated buildings, and other interacting structures. The soil-structure interaction study of the total system utilizes a plant unique free-field earthquake ground motion time history which conforms to the Nuclear Regulatory Commission Regulatory Guide 1.60, Design Response Spectra. This analysis sequence is shown schematically in Figure B-7.

In the design of major power plant piping systems the two analysis methods generally followed are the acceleration response spectra and the time history analysis methods (B-4 - B-6). The response spectra method deals with the evaluation of the maximum system dynamic response without regard to the phase and amplitude relationships in time. Analysis proceeds with the transformation of the equations of motions of the multi-degree-of-freedom system to normal coordinates yielding a set of uncoupled equations of motion. Equation of motion of any normal mode then is exactly equivalent to a single-degree-of-freedom system. Each degree of freedom system gives the maximum response for the applied anchor point motion histories. The total system response can be evaluated by the superposition of all modal contributions. Since phase and amplitude relations cannot be preserved, usually the "square root of the sum of the squares" method is used for superposition. Obviously this analysis method is inherently conservative because it gives only the maximum possible system response. However, it has the advantage of simplicity and is also the least expensive in terms of computer time.

The time history analysis of linear elastic systems also proceeds by first writing the set of uncoupled equations of motions of the multi-degree system. The eigen solution of these equations provides the system natural frequencies and the normal mode shapes. The time-dependent response of the system vibrating in each of its normal modes when subjected to the given anchor point motion is then determined. The total solution is obtained from the superposition of all time-dependent modal responses thus preserving the phase and amplitude relationships. Since the participation of higher modes toward the over-all system response is minimal, generally a cut-off frequency (typically taken as 40 or 50 Hz for seismic analysis) is assumed with considerable savings in computer time for large piping systems.

It is clear that the above described methods can be applied only to systems whose equations of motion are linear. If, on the other hand, the system exhibits any nonlinearity, structural or material, the most straightforward approach is the direct time integration of the equations of motions. This method, although rarely applied in routine design, has the advantage, at least in theory, that it provides the true system response. However, it requires a large number of computations and is the most expensive in terms of computer time. Also, on the practical side, the usual problem of solution convergence and accuracy associated with the numerical methods employed can prove difficult.

For the evaluation of safety margins to failure of a cracked pipe component, the dynamic loads on the piping using any one of the conventional elastic analysis

methods described above are bound to be highly conservative. If the dynamic excitation levels are such that plastic deformations can be expected, the actual dynamic loads that the cracked pipe element experiences can be significantly lower. In order to make realistic failure predictions, therefore, it becomes mandatory to perform a nonlinear dynamic analysis of the cracked piping system which includes both structural as well as material nonlinearities. The analysis method developed here proceeds in two separate steps. First, an elastic-plastic analysis of the cracked pipe segment is performed to determine its local stiffness characteristics. Second, the nonlinear seismic analysis of the total piping system is performed where the cracked pipe element in the dynamic model is represented by an element of equivalent stiffness, determined in the first step. It should be noted here that the analysis method being followed is consistent in approach to the ASME Code, Appendix F methods, i.e., inelastic system analysis and inelastic component analysis (B-1).

B.2.1 Evaluation of Cracked Pipe Element Stiffness

Although the presence of relatively shallow, part-through flaws in piping may not significantly alter the over-all system dynamic response, deeper or through flaws would have a significant effect on the response, at least locally, of the cracked pipe segment because of the reduced stiffness. Moreover, the reduced section of the cracked pipe allows for the plastic deformations to take place at lower dynamic loads as compared to the adjoining uncracked elements further affecting its response. Therefore, in the dynamic analysis model, the simulation of the cracked pipe element stiffness is essential to obtain its correct response. The purpose of this analysis is, therefore, to determine the stiffness characteristics of the cracked pipe element which could later be incorporated in the total dynamic analysis model.

The stiffness characteristics of the cracked pipe element in terms of an equivalent moment-curvature relationship were determined from a materially nonlinear finite element analysis using the in-house computer code ADINA01 (B-7). The two flaw configurations analyzed were (1) fully circumferential flaw with depth-to-pipe-wall thickness ratio of 0.67 and (2) a 180-deg through flaw. The pipe dimensions were 12.78 inch o.d. and 11.38 inch i.d. typical of recirculation line piping. The finite element models for these analyses were made up of three-dimensional isoparametric elements with up to 20 nodes per element to represent the element displacement function as well as its geometry. It should, however, be noted that no attempt was made to simulate the crack tip singularities in the model; rather, the emphasis was placed on determining the over-all load-deflection relationship of the cracked pipe segment.

A bilinear material stress-strain relationship based on actual data for Type-304 stainless steel at 550°F (Figure B-7) was used. The loading of the model consisted of a constant internal pressure of 1050 psi and a moment incremented in steps to a maximum giving an average of about 10% outer fiber strain.

From the load-deflection histories obtained from these analyses, the moment-curvature relationships for the cracked pipe segment were developed. These moment-curvature diagrams for the two flaw configurations were analyzed and their comparison with the uncracked case are shown in Figures B-8 and B-9. It is perhaps worth noting that, as shown in Figure B-8, the effect on the bending stiffness of the pipe of a fully circumferential flaw, even with a depth equal to two-thirds the wall thickness, is not too significant. On the other hand, the 180-deg through flaw markedly reduces the local bending stiffness (Figure B-9) of the pipe due to the shift of neutral axis of the section. Since the dynamic loads on the piping due to earthquake type of excitation are predominantly bending in nature, part-through circumferential flaws may not, therefore, provide as much relief in these loads due to plastic deformations as the through flaws.

B.2.2 Nonlinear Dynamic Analysis

Following a review of the various computer programs available for applications to structural nonlinear dynamics problems, it was decided that the in-house computer code COMET02 generally met the present analysis requirements. The COMET02 program is a much expanded and modified version of the COMET program described in detail in Reference B-8. The current version of COMET02 is specifically optimized for applications to piping analysis and can accept a general three-dimensional piping layout with both structural and material nonlinearities. Application of this program to nonlinear dynamic problems, such as pipe whip, and comparison of results with experimental data are described in References B-8 and B-9. The program is based upon the component element method in dynamics (B-8) and as such differs significantly in element logic, solution techniques, and program organization from conventional finite element programs for nonlinear dynamic analyses. A brief discussion of the program theory and its other significant aspects adapted from References B-10 and B-11 follows:

In the component element method, the discretization of a given structural model is represented through the assemblage of such elements as a beam in bending, axial force or torsional element, spring, damper, gap, friction elements, etc. The element logic is based upon the reciprocity relationships stating that the coupling coefficients between the element extensions and the generalized coordinate

displacements are also the coupling coefficients between the element forces and the generalized coordinate forces. Using this principle, the generalized coordinate displacement solution in time proceeds with the current coordinate displacement values to determine the element deformations. From the characteristic load-deflection relationship for the element which may be nonlinear and may also include hysteresis, the element internal loads are obtained. Using the coupling coefficients, the internal loads are converted to element nodal forces which, when combined with the externally applied loads and assembled, provide the global nodal force vector. Using the system mass matrix, the set of equations of motion can now be solved for the nodal acceleration vector. Numerical integration of the acceleration vector provides the generalized coordinate displacement vector at the next time step. To illustrate this further, the logic for the beam in bending element included in the COMET02 element library (Figure B-10) is discussed below.

Consider the straight beam element in bending as shown in Figure B-10.a(i). The slope of the beam midway between the coordinate locations i and u to a second order approximation is given as

$$\theta_{ij} = (z_j - z_i)/\ell_{ij}$$

where ℓ_{ij} is the length of the beam between coordinate i and j and z_i and z_j are the displacements orthogonal to the beam axis at coordinate locations i and j, respectively, and are given as

$$z_i = \left(z_{ix}^2 + z_{iy}^2 + z_{iz}^2\right)^{1/2}$$

and

$$z_j = \left(z_{jx}^2 + z_{jy}^2 + z_{jz}^2\right)^{1/2}$$

in which z_{ix}, z_{iy}, and z_{iz} are the displacements of the orthogonal set of a generalized coordinates parallel to a global Cartesian coordinate system at i, etc. Similarly,

$$\theta_{jk} = (z_k - z_j)/\ell_{jk}$$

Defining extension of the element as the change in slope, we have

$$\delta = \theta_{jk} - \theta_{ij} = z_i/\ell_{ij} + z_j \left[- \left(\frac{1}{\ell_{ij}} + \frac{1}{\ell_{jk}} \right) \right] + z_k/\ell_{jk}$$

The curvature, κ, of the beam is then given as

$$\kappa = \frac{\delta}{\left[\frac{1}{2} (\ell_{ij} + \ell_{jk}) \right]}$$

Once the curvature of the beam has been determined, the element force (moment), M, is obtained from the moment-curvature relationship for this element. As a result of the reciprocity relationship, the coordinate reaction moments are given as:

$(M)\ (1/\ell_{ij})$ at coordinate i

$(M) \left[- \left(\frac{1}{\ell_{ij}} + \frac{1}{\ell_{jk}} \right) \right]$ at coordinate j

and

$(M)\ [1/\ell_{jk}]$ at coordinate k.

These are the element nodal forces at time t which can now be resolved into their orthogonal components parallel to the generalized coordinates at locations i, j, and k.

The logic for other elements shown in Figure B-10 is also similarly derived.

The material and structural nonlinearities of the system are simulated by defining the equivalent force-displacement relationships for each element. For example, the material nonlinearity for the beam in bending is handled by the moment curvature relationship for the beam as shown in Figure B-11. In the case of a combined structural and material nonlinearity, as for example, in a gap or pipe restraint element, the nonlinearities are handled as shown in Figure B-12. For a load which continuously increases to a peak value and then drops, the unloading is along the

line with the initial elastic slope. However, if the load drops such that the gap opens, the element forces are held at their zero values. Subsequent load cycles follow the curve as shown in Figure B-12(b).

The program uses the explicit (central difference) scheme for step-by-step numerical integration of the equations of motions. After computing the element forces at time t, these forces are combined with the externally applied forces to determine the global nodal force vector (Q). The global nodal acceleration vector is then determined from

$$\{\ddot{z}\}_t = [M]^{-1} \{Q\}_t$$

where $[M]^{-1}$ is the inverse of the system mass matrix. Since the mass matrix is constant and does not involve any nonlinearity, for these calculations it needs to be inverted only once before the direct time integration of the equations of motion proceeds. This is in contrast to the scheme followed in finite element methods where the equilibrium equations (for implicit time integration) are written as;

$$[K]_t \{\Delta z\} = \{f\}_{t+\Delta t} - [M] \{\ddot{z}\}_{t+\Delta t} - [C] \{\dot{z}\}_{t+\Delta t} - [K]_t \{z\}_t$$

where

$[K]_t$ = Stiffness matrix at time t

$\{\Delta z\}$ = Incremental displacement vector associated with time step Δt

$\{f\}_{t+\Delta t}$ = External force vector at time $t + \Delta t$

$[M]$ = Constant mass matrix

$\{\ddot{z}\}_{t+\Delta t}$ = Nodal acceleration vector at time $t + \Delta t$

$[C]$ = Constant damping matrix

$\{\dot{z}\}_{t+\Delta t}$ = Nodal velocity vector at time $t + \Delta t$

$\{z\}_t$ = Nodal displacement vector at time t

The solution of the above equations provides the nodal displacement increments for the time increment, Δt. However, if the stiffness matrix is nonlinear, it must be reformed at each time step especially if the element stiffness is changing rapidly, for instance, closing of the gaps, impact of pipes with restraints, etc., thus considerably adding to the computational costs. In the element component method, however, no such computations are required. In the finite-element method using implicit time integration scheme, the time step can be comparatively large. However, to assure the solution accuracy, an iterative solution is generally required. The component element method, on the other hand, uses an explicit time integration scheme to compute the nodal displacements as

$$\{z\}_{t+\Delta t} = 2\{z\}_t - \{z\}_{t-\Delta t} + (\Delta t)^2 \{\ddot{z}\}_t$$

This numerical scheme does not require any iterations. However, the solution stability and accuracy must be assured by selecting a small enough time step.

The advantage of this scheme for the solution of nonlinear equations of motion is that it is an efficient algorithm requiring no matrix inversion or iterations for convergence. However, for accuracy and the stability of solution, time-step size may need to be quite small, especially in systems with relatively high stiffness and small masses.

B.2.3 Nonlinear Seismic Analysis of a Cracked Piping System

The analysis methods described above were applied for a nonlinear seismic analysis of an actual power plant piping system. The analysis objectives were to evaluate and compare the actual dynamic force response of the cracked piping system to the response predicted by a linear elastic seismic analysis and thus quantify the inherent extra safety margins to failure of cracked structures exhibiting ductile behavior and subjected to a dynamic loading.

For the purpose of this analysis, the dynamic model used with the computer program COMETO2 is shown in Figure B-13. This model represented the inlet side of a power plant recirculation loop piping. This piping system was selected for analysis because it is representative of the large-diameter stainless steel piping system in BWRs. The dynamic model is an assemblage of the straight and restrained end beam elements in bending, axial force and torsional elements and the snubber support elements. The snubber support element is essentially a linear spring element with provision for a maximum fracture load. The various postulated flaw configurations

and flaw locations (Figure B-14) combinations considered in separate analyses are given below.

Case 1: A fully circumferential part-through flaw of depth equal to 67% of the pipe wall thickness located next to the elbow.

Case 2: A 180-deg through flaw located next to the elbow.

Case 3: Same flaw as in Case 1 but located at the safe end/vessel nozzle junction.

Case 4: Same flaw as in Case 2 but located at the safe end/vessel nozzle junction.

The simulation of the cracked pipe elements in the over-all dynamic model was carried out by using the beam element with stiffness characteristics as defined by the moment-curvature relationships determined earlier and shown in Figures B-8 and B-9. For the rest of the elements, a bilinear representation of the material stress-strain curve (Figure B-2) was used. This stress-strain relationship is based upon the actual data for Type-304 stainless steel at 550°F.

In a time history seismic analysis of a piping system the prescribed earthquake motions of the piping support points are generally given in terms of acceleration time histories. The integrated displacement solution in these analyses, however, may, and generally does, contain a drift if the initial and the end conditions of the applied motions have residual velocity and displacement values. For this reason, if the structure is multiply supported, the contribution of these "pseudo-static" displacement components must be eliminated by applying a so-called "base-line correction" to obtain the true dynamic force response of the system. To avoid this problem in the present analyses, the prescribed seismic motions of the piping support points were, instead, given in terms of displacement time histories.

Although an actual earthquake event can last up to 20 seconds or more in duration, for the purpose of these demonstration analyses, displacement time histories of 1-sec spans out of a total time of 20 seconds were used to minimize the computational expenses. Figures B-15 to B-17 show the actual displacement time histories used in the analyses. These time histories were extracted from the Operating Base Earthquake (OBE) time histories typically used in the design and analysis of a BWR piping system. Each of these time histories represents the two equal but orthogonal

translational motion components of the earthquake in the two horizontal directions for a given piping support point. These displacement time histories were applied simultaneously to all of the piping system support points, i.e., the snubbers and the nozzle-to-vessel junctions - a total of 13 separate points - as shown in Figure B-13. The response of the system to various levels of earthquake severity were determined by linearly scaling the motion time histories prior to their application to the model. For the comparison of results, the linear elastic response of the system to an earthquake input of 1.0 OBE was also determined from a separate analysis.

B.3 DISCUSSION OF ANALYSES RESULTS

A summary of the analyses results for the various combinations of flaw configuration, flaw location, and the level of earthquake intensity is given in Table B-1. The actual time-dependent force response of the cracked pipe element for these cases is shown in Figures B-17 to B-23. In Table B-1, the ratio M_e/M_{ep} - where M_e is the maximum absolute value of the dynamic moment obtained from a conventional linear elastic analysis and M_{ep} is the maximum absolute value of the moment determined from the nonlinear dynamic analysis - provides a measure of the overestimation of dynamic loads on ductile structures when analyzed on a purely linear elastic basis. For the five separate cases analyzed, the ratio M_e/M_{ep} ranges from a value of 1.55 to 2.39, demonstrating, as expected, that the actual loads experienced by the cracked piping are significantly lower than those predicted by the linear elastic analysis.

It is also clear that as the extent of plastic deformations increase with the increasing dynamic loads, the ratio, M_e/M_{ep}, also increases. For example, compare cases 4 and 5 in Table B-1. For identical flaw configurations and their locations, the ratio, M_e/M_{ep}, increases from 1.69 to 2.39 as the seismic loads increase from 5.0 OBE to 10.0 OBE. The same effect is evident from the analysis results of a simple piping system discussed earlier and shown in Figures B-3 and B-4. In this sense the system is self-correcting, that is to say, as the dynamic loading increases, higher safety margins to failure can be demonstrated through an elastic-plastic dynamic analysis of the structure.

Using the maximum values of the dynamic loads determined above, a quantitative assessment of safety margins to failure can be obtained by performing a failure analysis of cracked piping using a suitable failure criterion. The failure criterion used for these analyses here is the net section collapse criterion discussed separately in Appendix A. In this approach, the failure mode is assumed

to be the formation of a plastic hinge leading to plastic instability at the reduced section. Plastic fracture mechanics considerations of crack initiation and extension leading to crack instability are not explicitly included. The validity of this approach and the supporting data are given in Reference B-12 and are also discussed in Appendix A. A comparison of failure predictions for cracked Type-304 stainless steel piping based upon this approach and a J-integral (B-13) based criterion are given in Appendix A and Reference B-14. Basically, the supporting data shows, that for highly ductile piping containing deep flaws, the difference in the loads at crack initiation and at the limit load conditions is within 5 to 10% of each other. This is easily within the uncertainty limits of any failure analysis. The net section collapse criterion, therefore, represents a reasonable engineering approach to define failure of cracked stainless steel piping.

A major advantage of this approach is the simplicity of its application which essentially involves performing a lower bound limit load analysis of the cracked piping circumventing the need for a more involved J-integral (B-15,B-16) based analysis for the evaluation of crack initiation, stable tearing, and crack instability loads. Also, this analysis does not require the determination of any new material properties such as the J_{Ic} or the J-resistance curve. The required material property, i.e., the "flow stress" can generally be taken as the average of the material yield and the ultimate stress at temperature. Another advantage of this approach is that it can also be applied to define failure of cracked piping when the loading is cyclic in nature. This has been demonstrated by the analysis of dynamic pipe test specimens discussed in Appendix C. On the other hand, the application of a J-integral based analysis for cyclic loading with alternate plasticity is still uncertain although some studies in this area have been reported (B-17,B-18).

Using the net section collapse criterion, the failure analyses for the three selected combinations of crack configuration, location and the level of seismic excitation were performed. The comparative results of these failure analyses using maximum values of the dynamic loads obtained from linear-elastic and elastic-plastic dynamic analyses, in the form of failure diagrams, are shown in Figures B-24 and B-25. Figure B-24 depicts the case of a circumferential flaw crack-depth-to-pipe-wall thickness ratio, a/t, of 0.67, located adjacent to the pipe elbow (Figure B-13) and subjected to 10 times the OBE displacement time histories. The failure diagram predicts failure for the postulated flaw when the dynamic loads are calculated with the assumption of linear-elastic material behavior. However, if the actual elastic-plastic material behavior is assumed in the dynamic loads calculations, the flaw is shown to be within the safe regime. Similar failure predictions for a through-flaw

with length equal to half the pipe circumference are shown in Figure B-25. In this case again, whereas the loads from linear elastic dynamic analysis would predict a definite failure, the postulated flaw is shown to be just at the point of failure if loads from elastic-plastic dynamic analysis are used.

Although a quantitative statement regarding the safety margins to failure for the specific case of a given flaw configuration, its location, the material properties, piping system layout, and the severity of the dynamic loading is unique and, therefore, must be dealt with on a case-by-case basis, based upon the analyses results reported here, the following general conclusions can, nevertheless, be made:

1. The actual dynamic force response of structural system, exhibiting ductile behavior, is significantly lower than that predicted by conventional dynamic analysis based upon the assumption of linear-elastic material behavior. Consequently, a failure analysis, based upon elastically calculated dynamic loads, can substantially underpredict the structural capability. A realistic evaluation of safety margins to failure in cracked piping subjected to dynamic loading, therefore, requires that the dynamic loads must be obtained from a nonlinear dynamic analysis of the piping system using actual material properties.

2. The difference between the safety margins to failure evaluated using the elastically calculated dynamic loads and the loads obtained from elastic-plastic dynamic analysis increases with increasing severity of the dynamic input. For example, compare cases 4 and 5 in Table B-1. For identical flaws located at the safe end/nozzle junction, the ratios of elastically calculated moment to the moment obtained from elastic-plastic analysis, M_e/M_{ep}, are 2.39 for a seismic excitation of five times the OBE and 1.69 for one-half of this value of the seismic input. The same effect was demonstrated by the analysis of a simple piping system discussed earlier and shown in Figures B-3 and B-4.

These differences consequently manifest themselves in the failure predictions of the cracked piping as shown graphically in Figures B-24 and B-25 highlighting the inadequacy of linear-elastic analysis. The need for a nonlinear dynamic analysis, therefore, becomes more urgent as the severity of the dynamic excitation increases.

B.4 REFERENCES

B-1. "ASME Boiler and Pressure Vessel Code," Section III, Division 1, Nuclear Power Plant Components, 1980 ed.

B-2. C. V. Subramanian and R. P. Kennedy, "Technical Basis for the SRSS Method of Condensing Dynamic Responses," General Electric Company, Executive Summary Report and Supplement, April 1978.

B-3. R. P. Kennedy, R. D. Campbell, K. L. Merz, and R. B. Narver, "Combining Multiple Dynamic Responses by SRSS Method," EDAC 134-240-7R, May 1978.

B-4. R. C. Clough and J. Penzien, "Dynamics of Structures," McGraw-Hill, Inc., New York, 1975.

B-5. N. M. Newmark and E. Rosenbluth, "Fundamentals of Earthquake Engineering," Prentice-Hall, Inc., New Jersey, 1971.

B-6. R. W. Wu, F. A. Hussain, and L. K. Liu, "Seismic Response Analysis of Structural Systems Subjected to Multiple Support Excitation," Nuclear Engineering and Design, 47, 1978, pp. 273-282.

B-7. K. J. Bathe, "ADINA - A Finite Element Program for Automatic Dynamic Incremental Nonlinear Analysis," Massachusetts Institute of Technology (Report 82448).

B-8. "Analysis of Pipe Whip" Final Report, Electric Power Research Institute, Palo Alto, November 1979 (EPRI NP-1208).

B-9. K. H. Lu, "FAULT01 - User's Manual," General Electric Company, August 1978 (NEDE-23922).

B-10. S. Levy and J. P. D. Wilkinson, "Component Element Method in Dynamics," McGraw-Hill, Inc., New York, 1976.

B-11. G. Esswein, S. Levy, M. Triplett, G. Chan, and N. Varadarajan, "Pipe Whip Dynamics," ASME Special Publication, 1978.

B-12. "Mechanical Fracture Predictions for Sensitized Stainless Steel Piping with Circumferential Cracks," Final Report EPRI NP-192, Electric Power Research Institute, September 1976.

B-13. J. R. Rice, "A Path Independent Integral and Approximate Analysis of Strain Concentration by Notches and Cracks," J. App. Mech., June 1968, pp. 379-386.

B-14. S. Ranganath and H. S. Mehta, "Engineering Methods for the Assessment of Ductile Fracture Margins in Nuclear Power Plant Piping," Paper to be presented at Sec. Int. Sym. on El.-Pl. Frac. Mech., ASTM, 6-9 October 1981.

B-15. P. C. Paris, H. Tada, A. Zahoor, and H. Ernst, in "Elastic-Plastic Fracture," ASTM STP 668, 1979, pp. 5-36.

B-16. J. W. Hutchinson and P. C. Paris, in "Elastic-Plastic Fracture," ASTM STP668, 1979, pp. 37-64.

B-17. N. Dowling and J. A. Begley, in "Mechanics of Crack Growth," ASTM STP590, 1976, pp. 82-103.

B-18. B. N. Leis and A. Zahoor, in "Fracture Mechanics," ASTM STP700, 1980, pp. 65-96.

Table B-1

SUMMARY RESULTS OF NONLINEAR DYNAMIC ANALYSIS OF THE PIPING SYSTEM FOR VARIOUS FLAW CONFIGURATIONS, FLAW LOCATIONS, AND SEISMIC CONDITIONS

Flaw Configuration	Location	OBE Time-History Scaling Factor	Maximum Absolute Moment from Elastic Analysis, Me (in-lbf)	Maximum Absolute Moment from Elastic-Plastic Analysis, Mep (in-lbf)	Ratio M_e/M_{ep}
$\alpha/\pi = 1.0$ $a/t = 0.67$	Elbow	10.0	2.0×10^6	1.29×10^6	1.55
$\alpha/\pi = 1.0$ $a/t = 0.67$	Safe-End	10.0	4.3×10^6	2.08×10^6	2.07
$\alpha/\pi = 0.5$ $a/t = 1.0$	Elbow	5.0	1.0×10^6	0.55×10^6	1.82
$\alpha/\pi = 0.5$ $a/t = 1.0$	Safe-End	5.0	2.15×10^6	0.9×10^6	2.39
$\alpha/\pi = 0.5$ $a/t = 1.0$	Safe-End	2.5	1.08×10^6	0.64×10^6	1.69

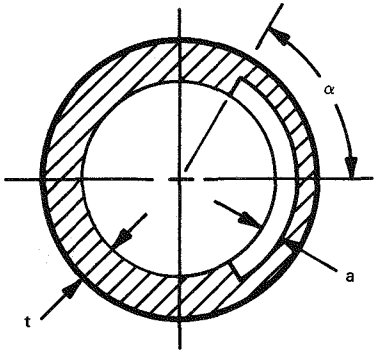

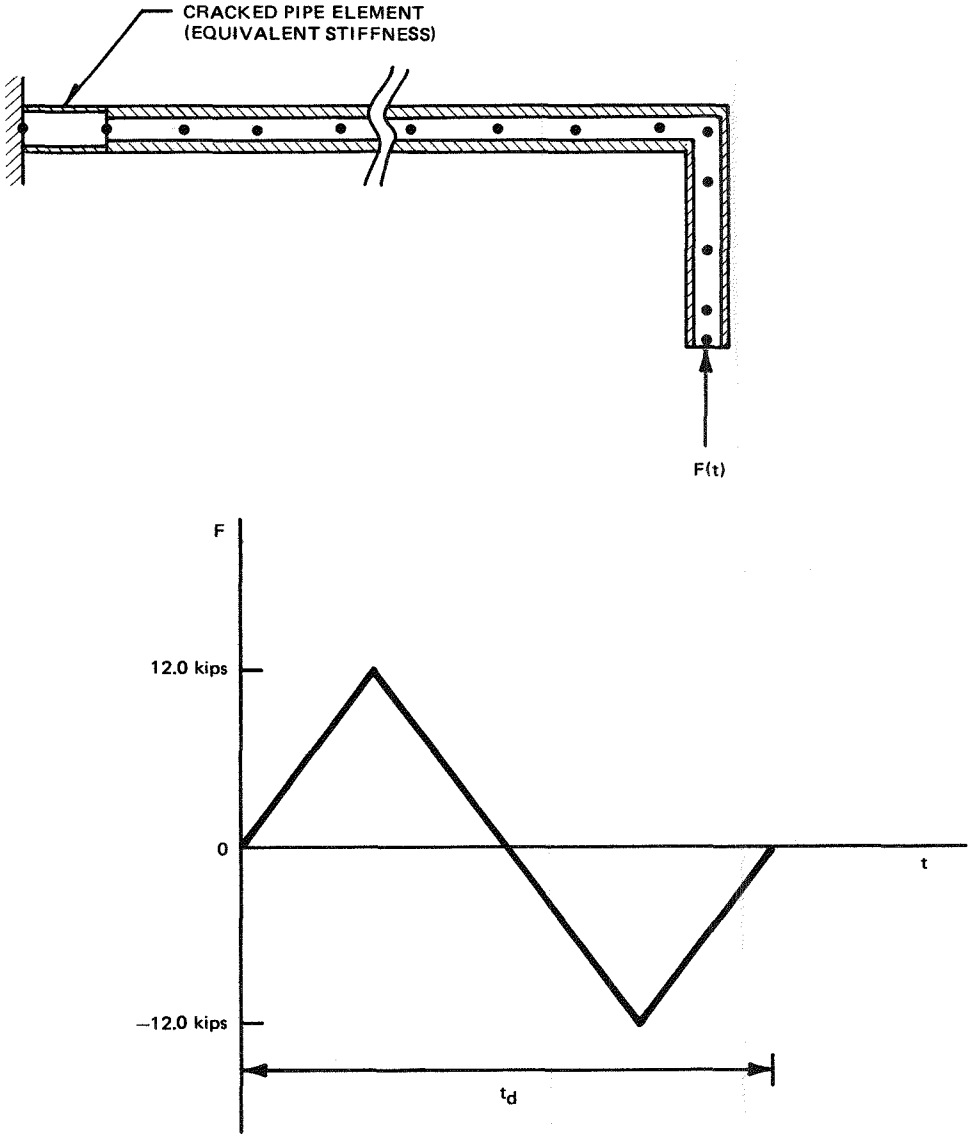

Figure B-1. Piping System Model and the Forcing Function for Dynamic Analysis

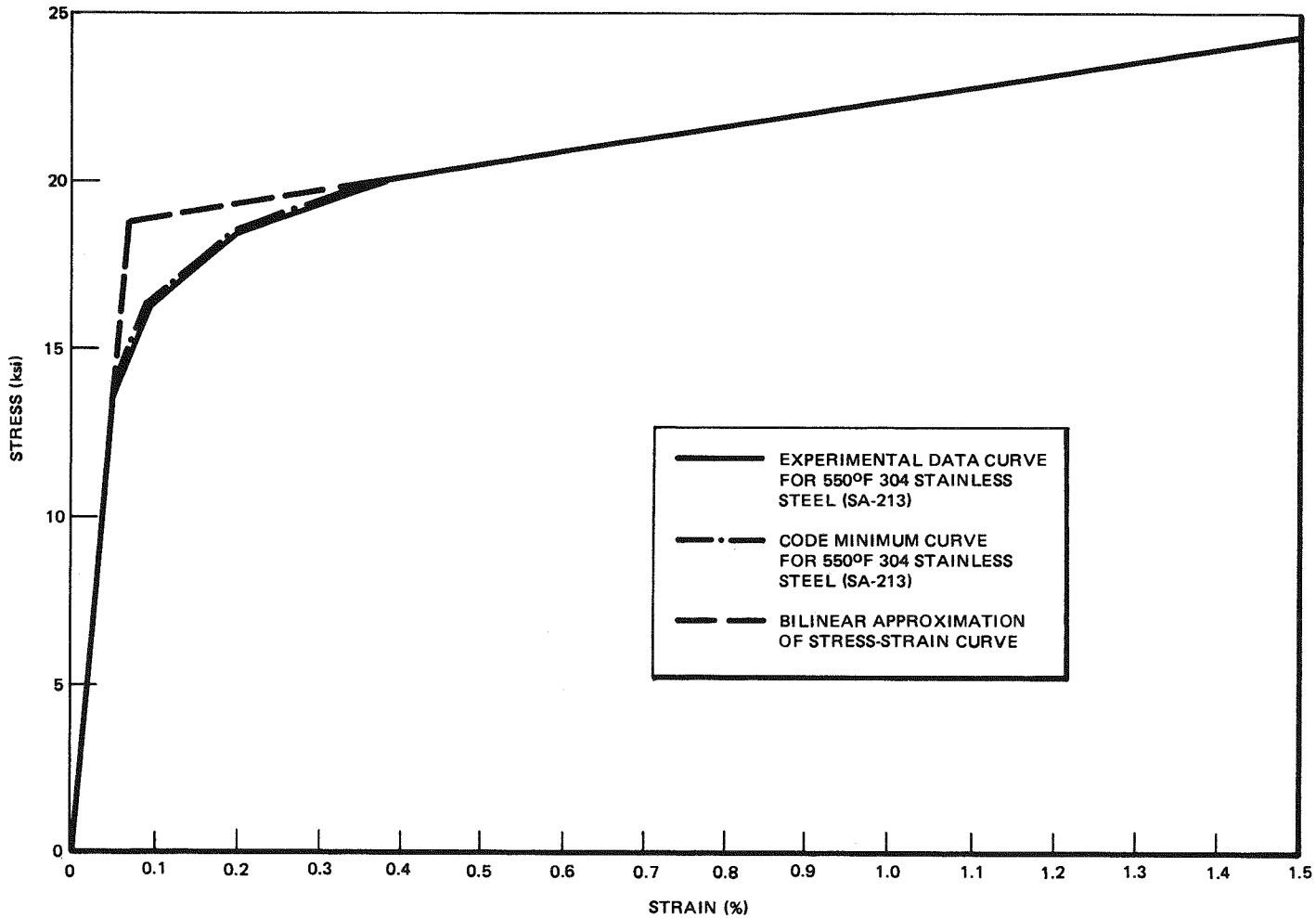

Figure B-2. Material and Bilinear Stress-Strain Curve for Type-304 Stainless Steel at 600°F

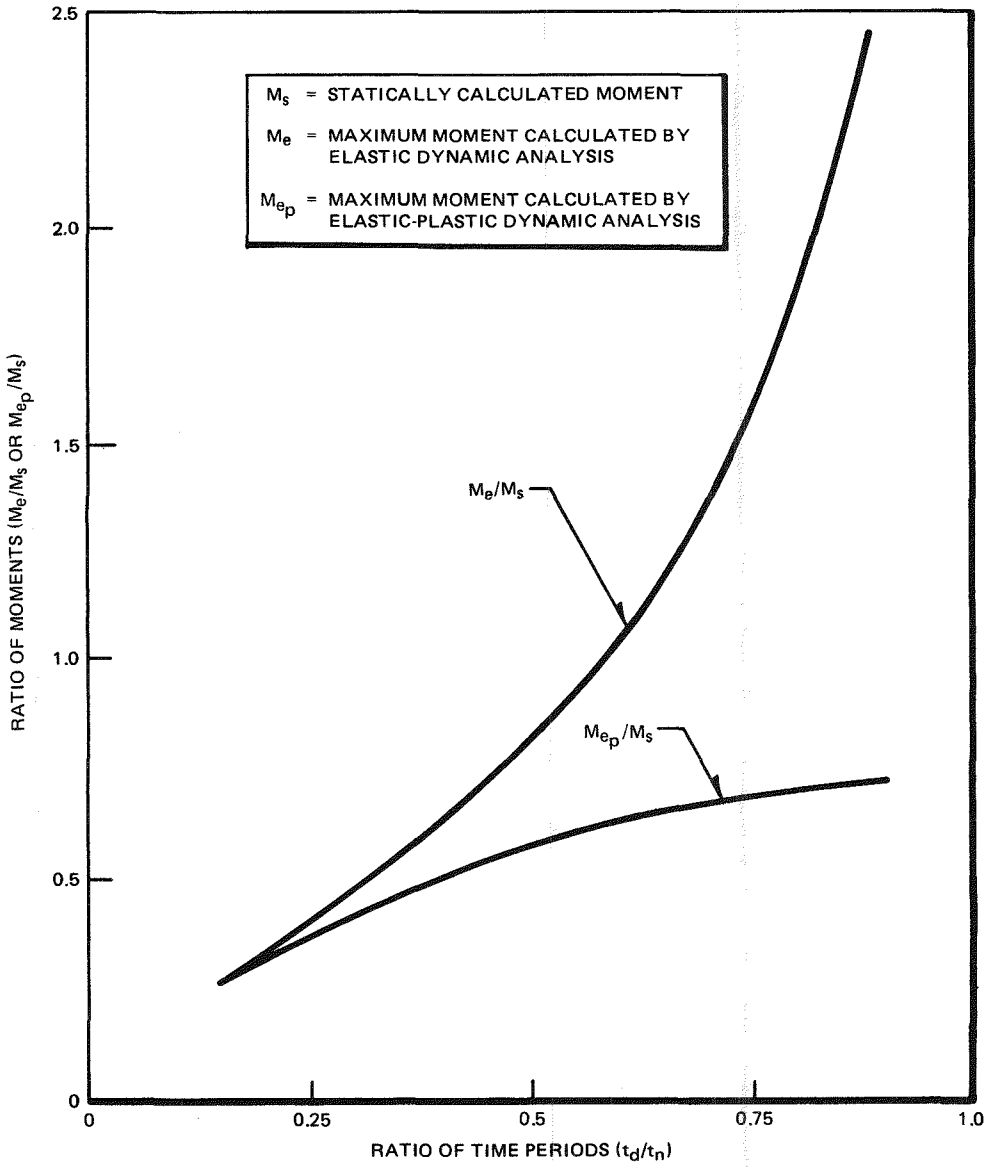

Figure B-3. Comparison of Moments Obtained from Elastic and Elastic-Plastic Dynamic Analyses

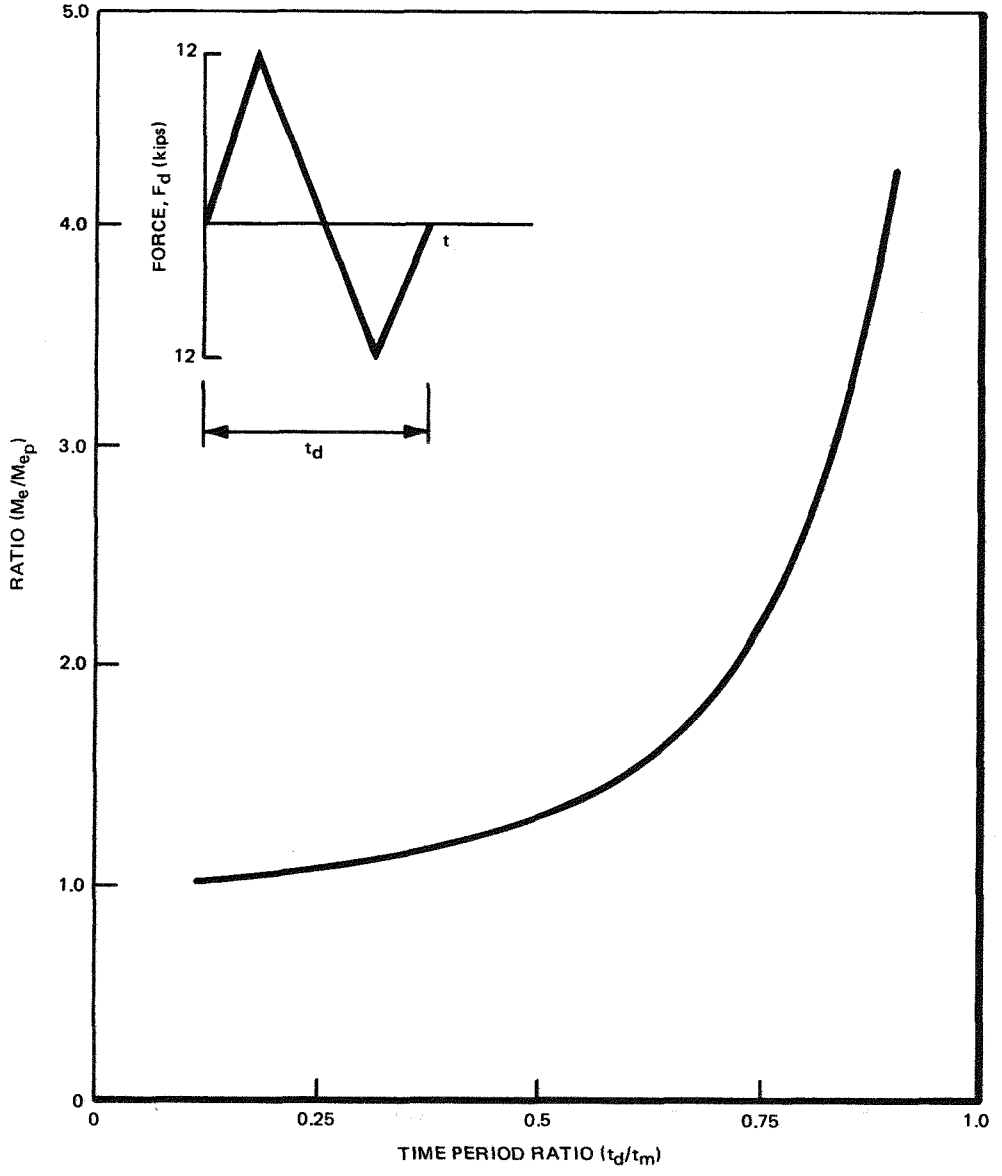

Figure B-4. Ratio of Moments Obtained from Elastic and Elastic-Plastic Dynamic Analyses

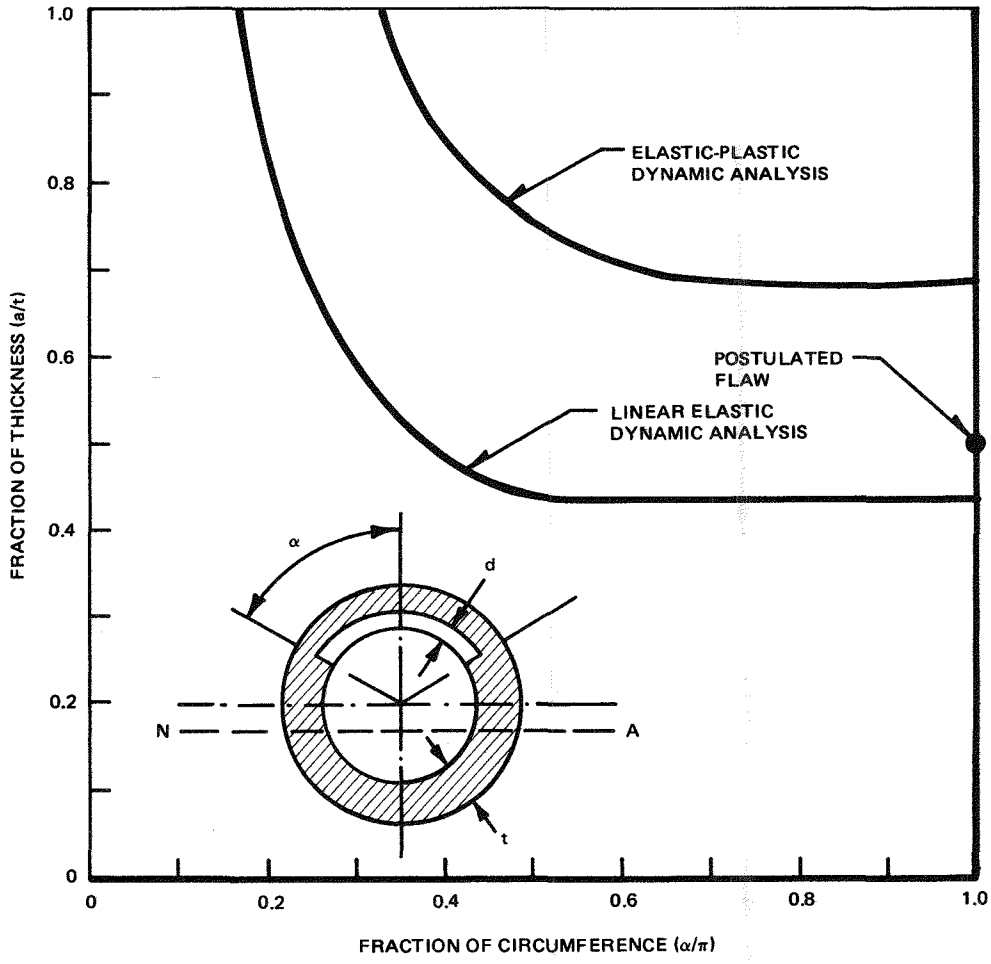

Figure B-5. Failure Diagram for Moments Obtained from Elastic and Elastic-Plastic Dynamic Analyses (t_c/t_n = 0.67)

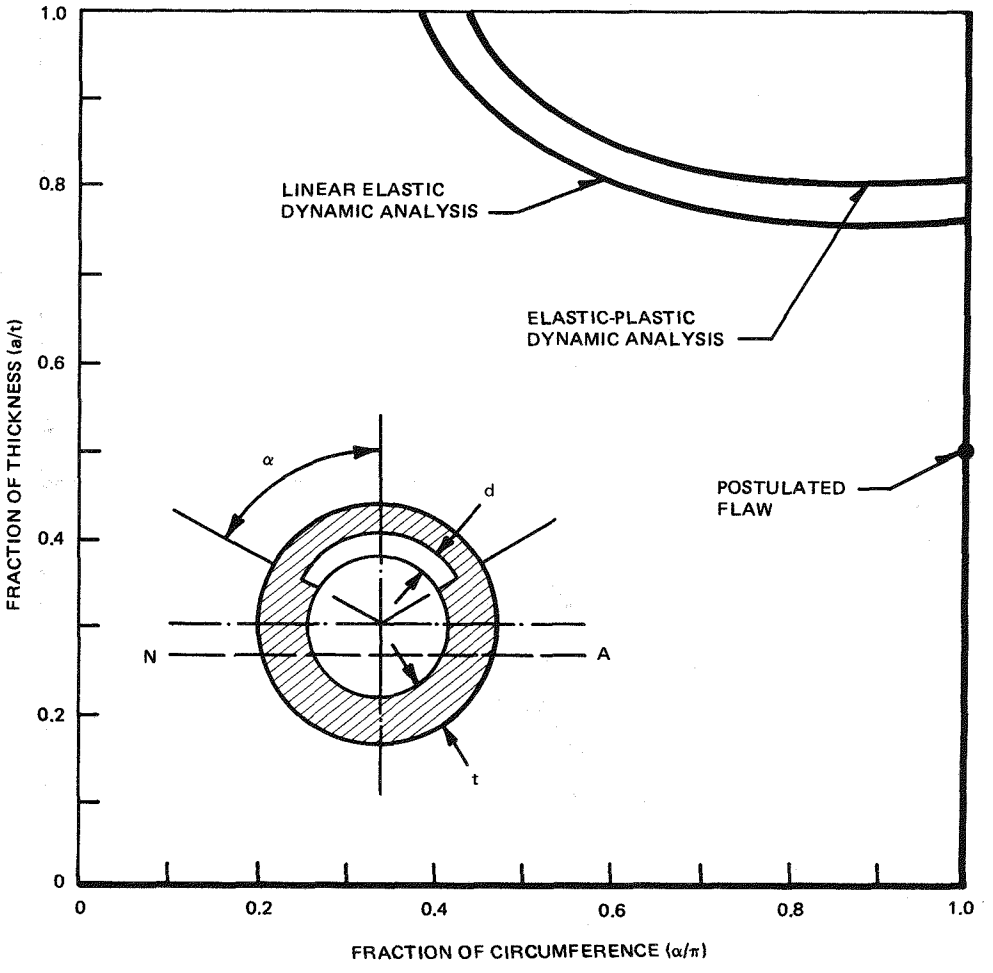

Figure B-6. Failure Diagram for Moments Obtained for Linear Elastic and Elastic-Plastic Analyses (t_d/t_n = 0.33)

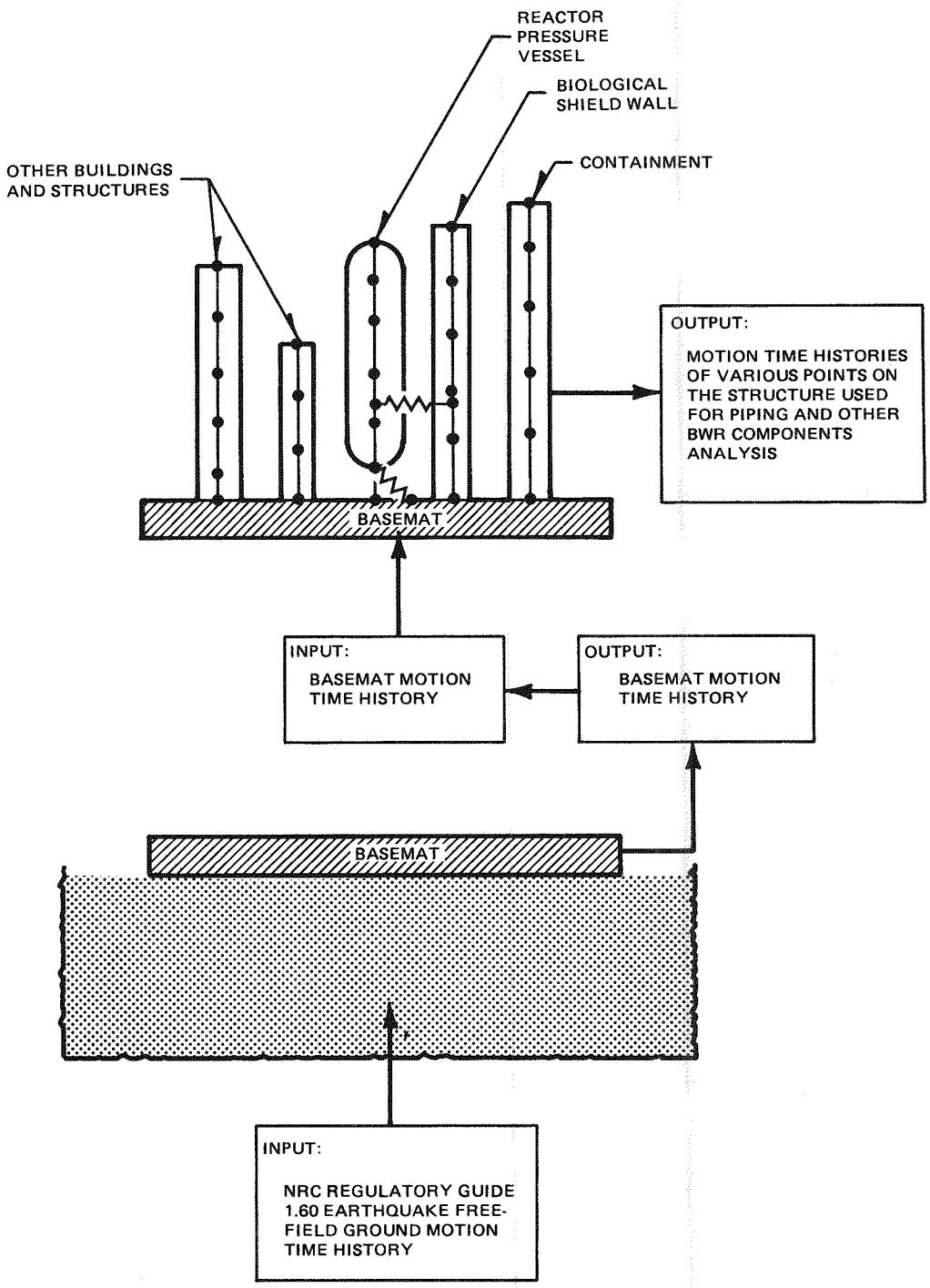

Figure B-7. Schematic Representation of Soil-Structure Interaction Analysis

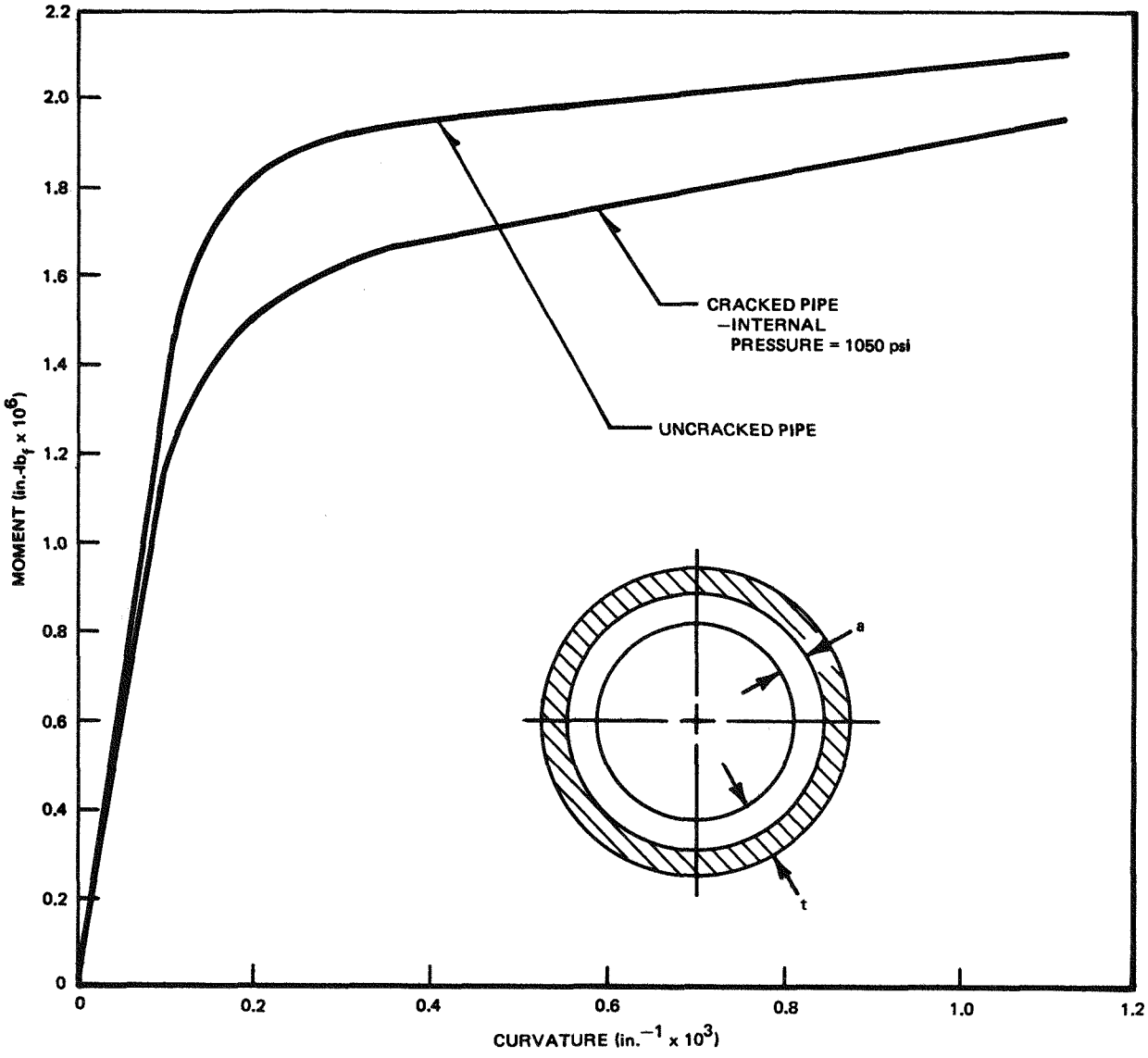

Figure B-8. Moment-Curvature Relationship for the Circumferential Flaw with a/t = 0.67

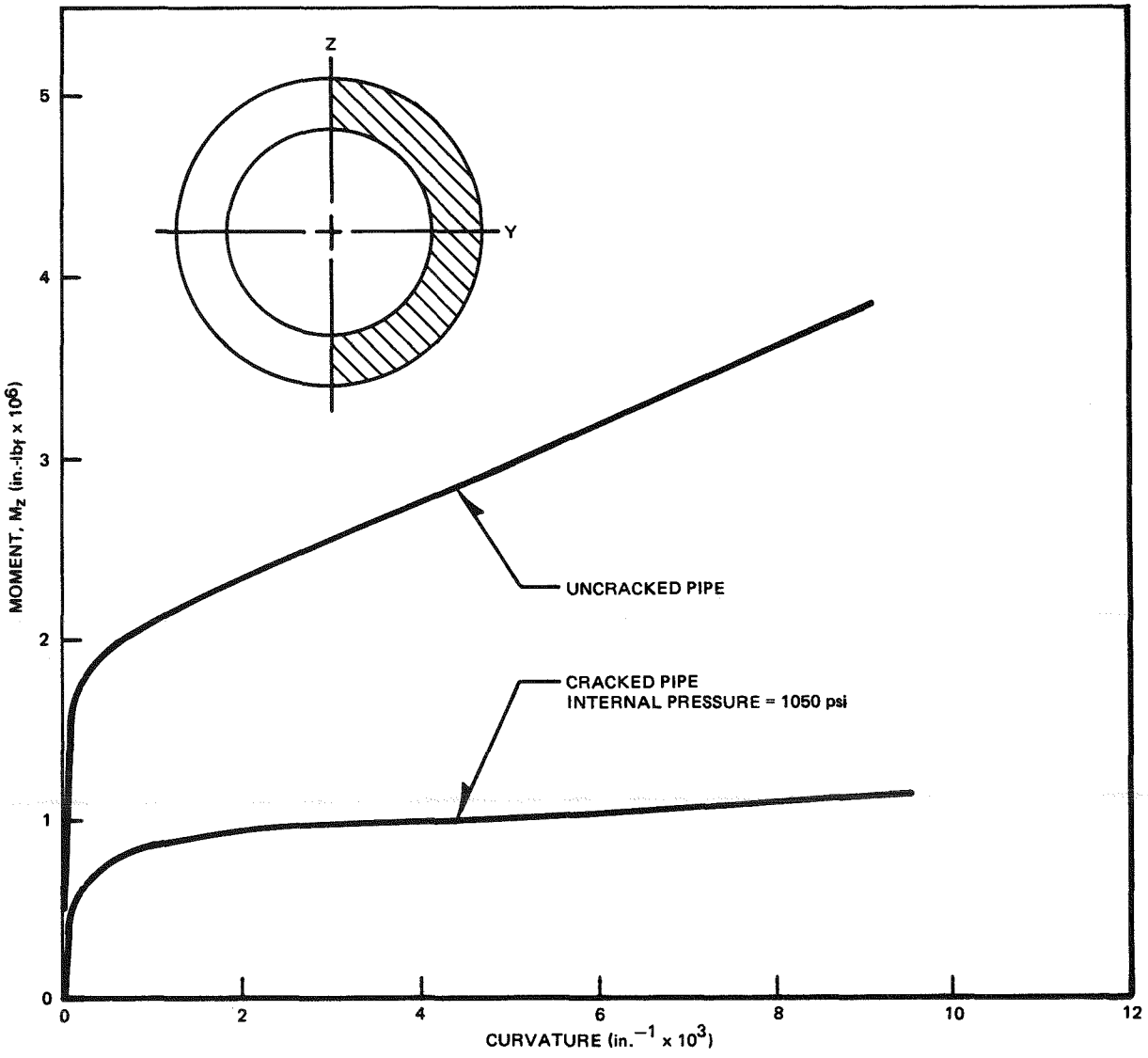

Figure B-9. Moment-Curvature Relationship for Pipe Section with a 180-deg Through Flaw

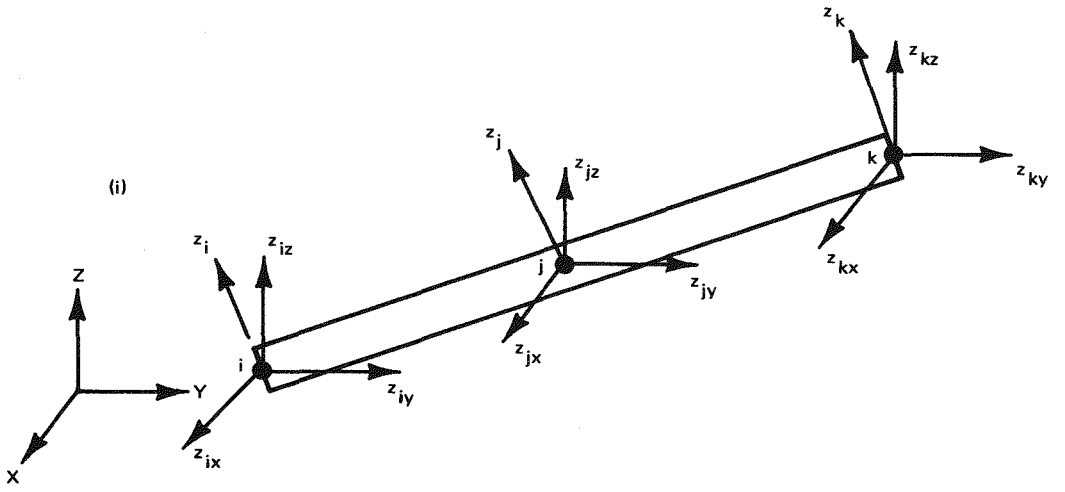

STRAIGHT BEAM ELEMENT

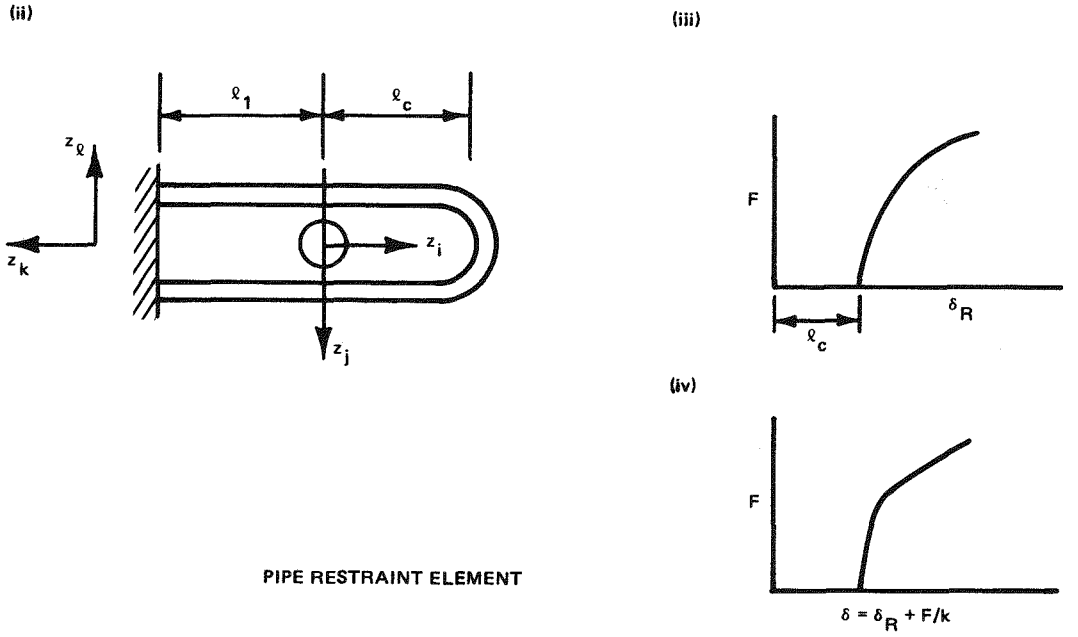

PIPE RESTRAINT ELEMENT

Figure B-10(a). Straight Beam and Pipe Restraint Elements in COMET02

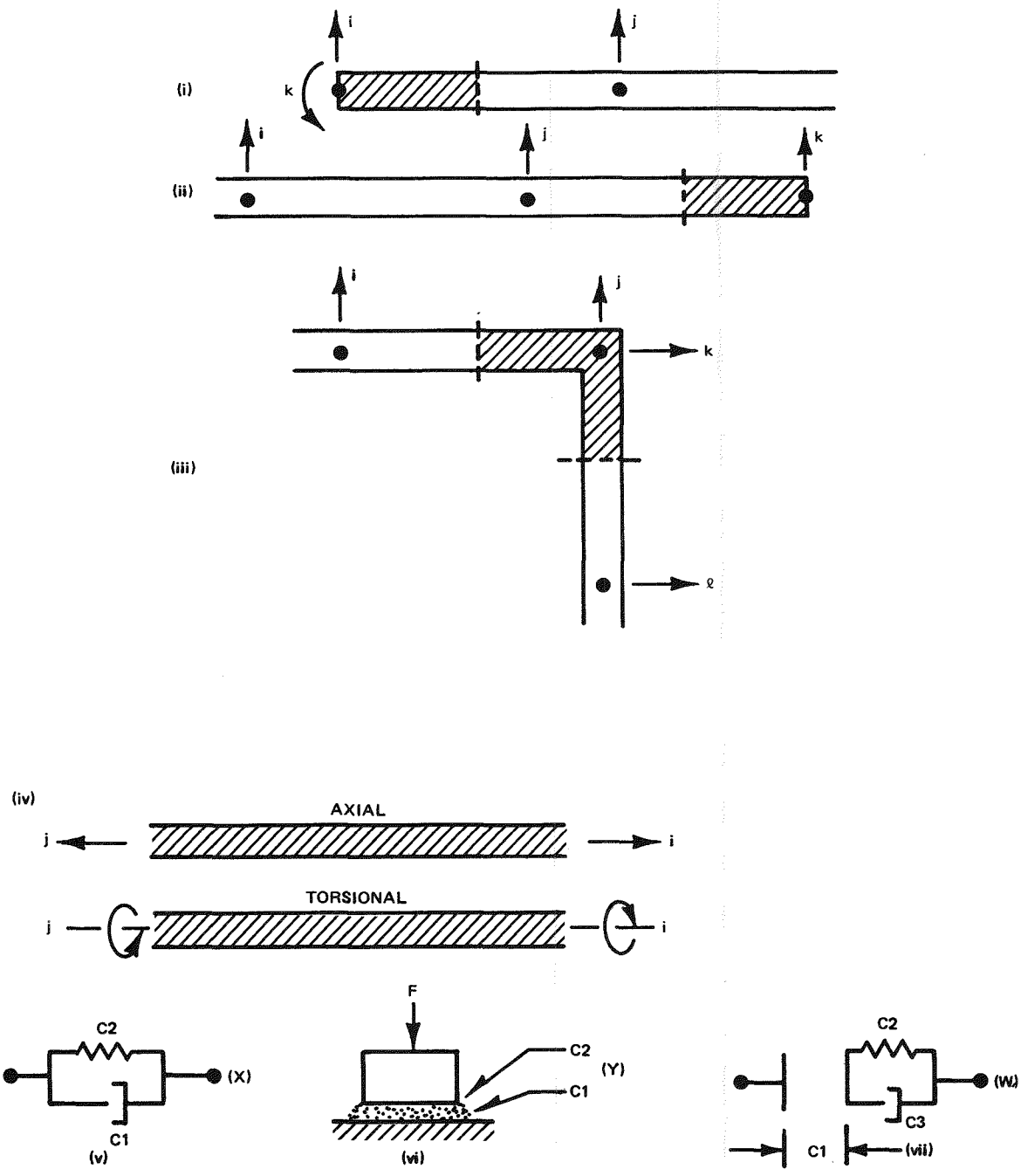

Figure B-10(b). Available Elements in Computer Code COMET02

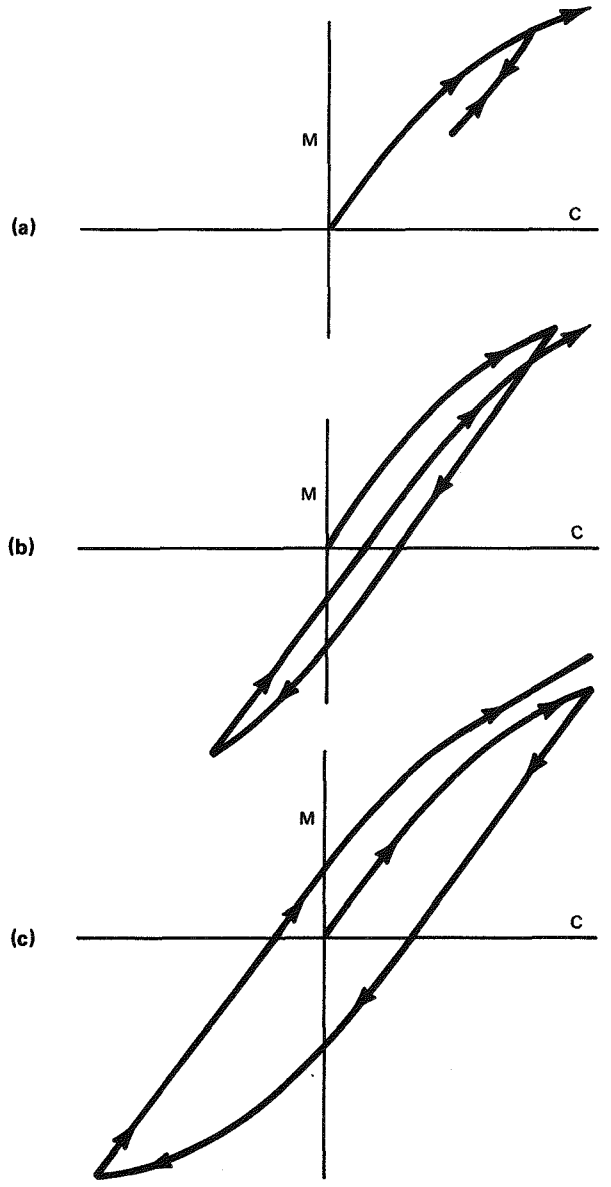

Figure B-11. Moment-Curvature Relationships for Loading and Unloading for Simple Beam Element

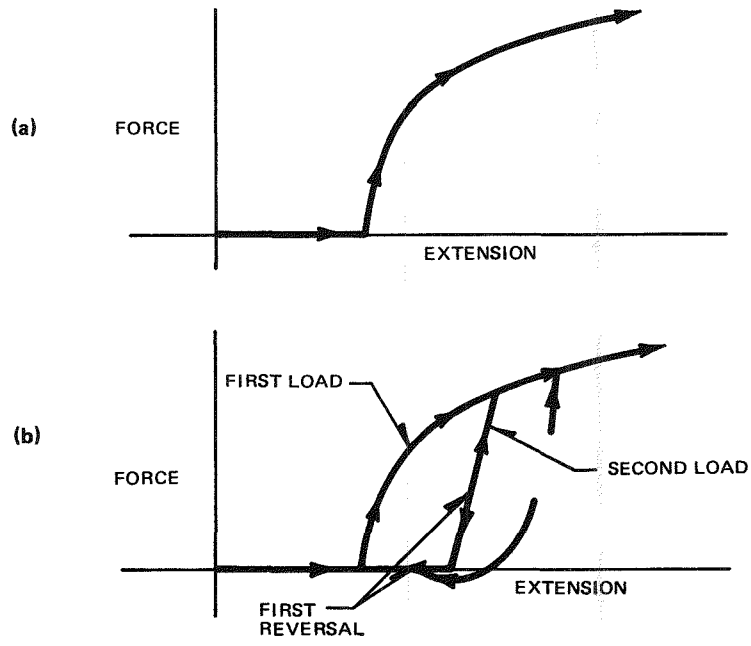

Figure B-12. Loading and Unloading of a Pipe Restraint Element

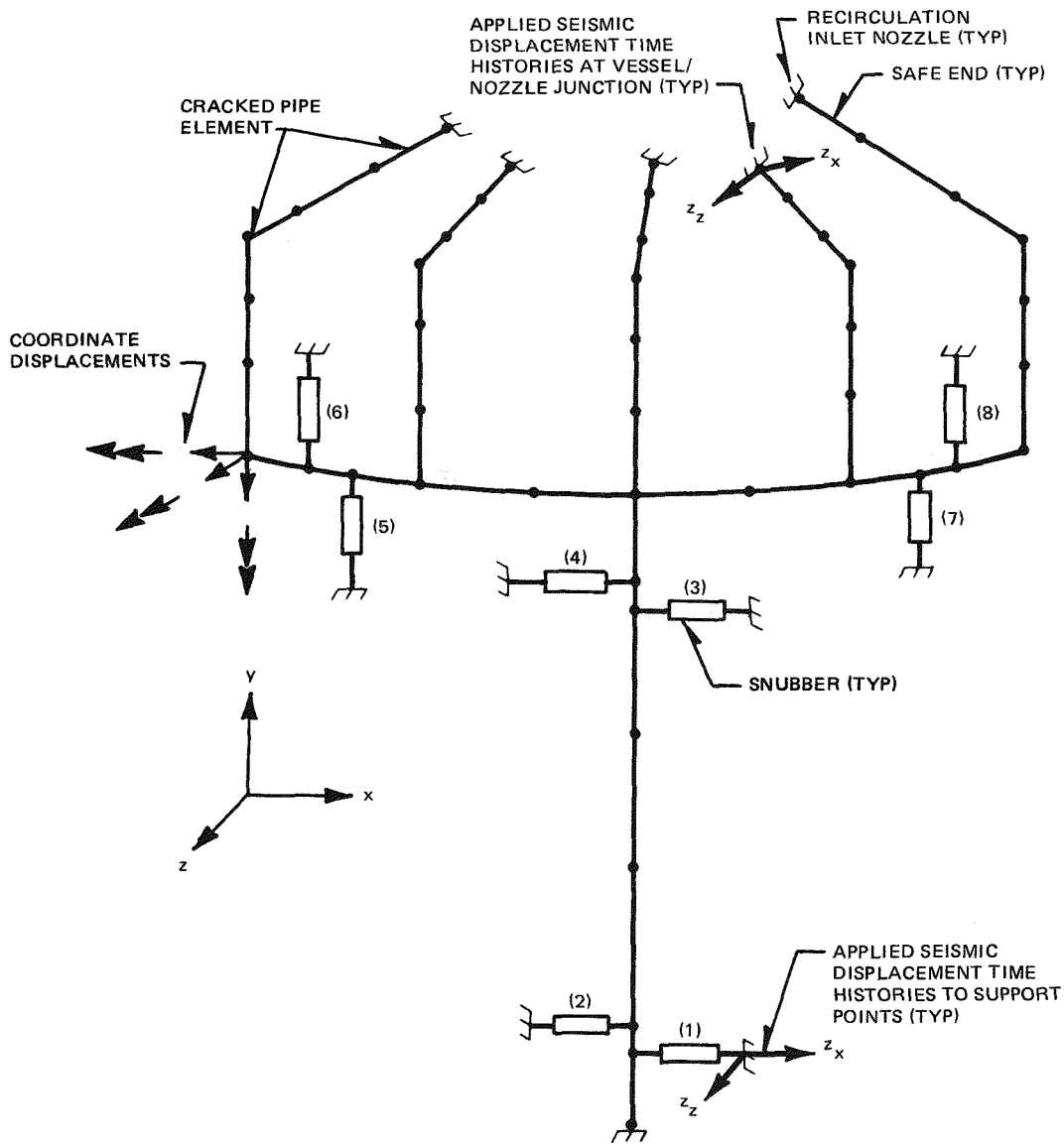

Figure B-13. Finite Element Model of the Recirculation Piping for Nonlinear Dynamic Analysis

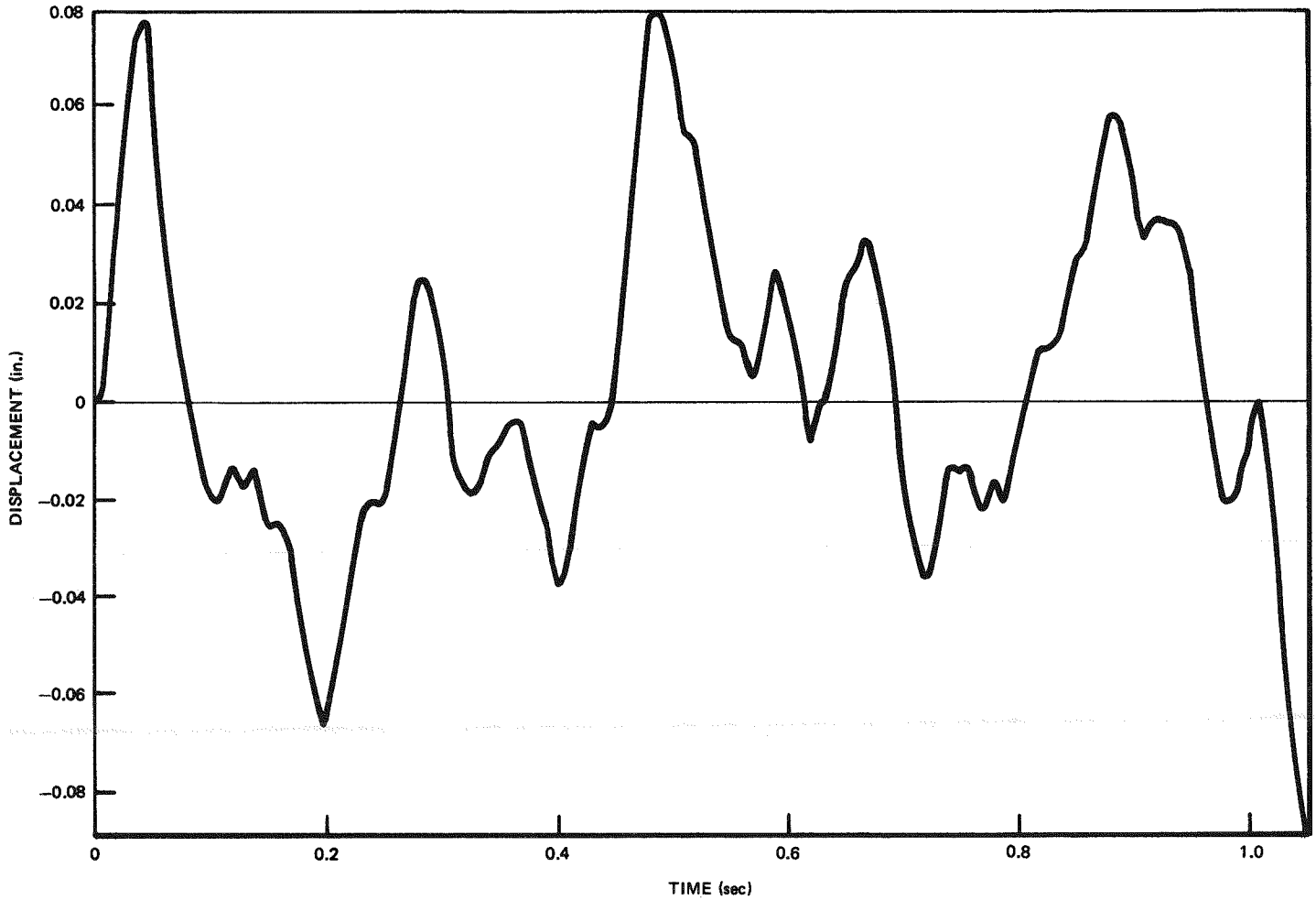

Figure B-14. Operating Base Earthquake Displacement Time History Applied at Nozzle/Vessel Junctions and the Snubber Supports 5 to 8

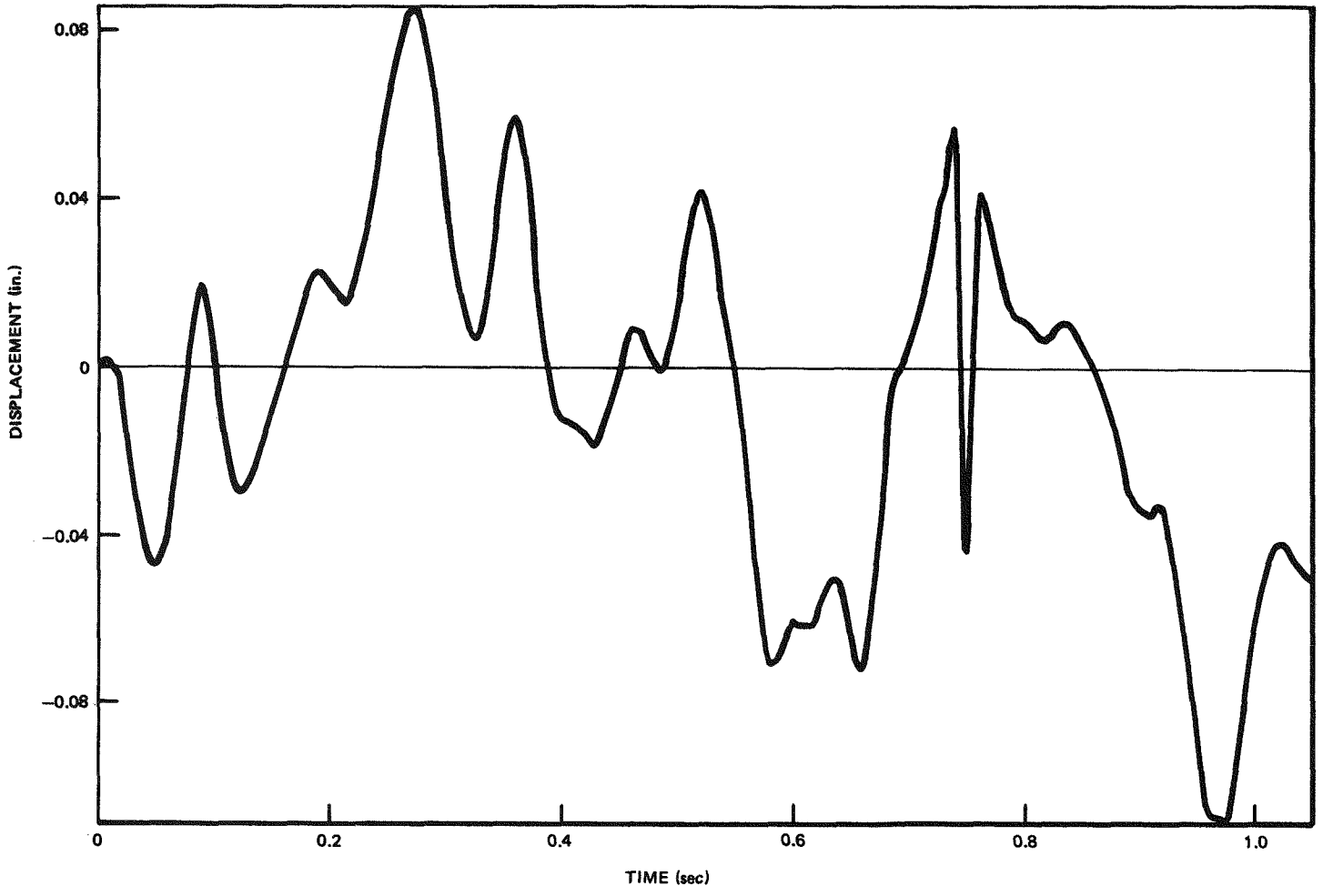

Figure B-15. Operating Base Earthquake Displacement Time History Applied to Snubber Supports 3 and 4

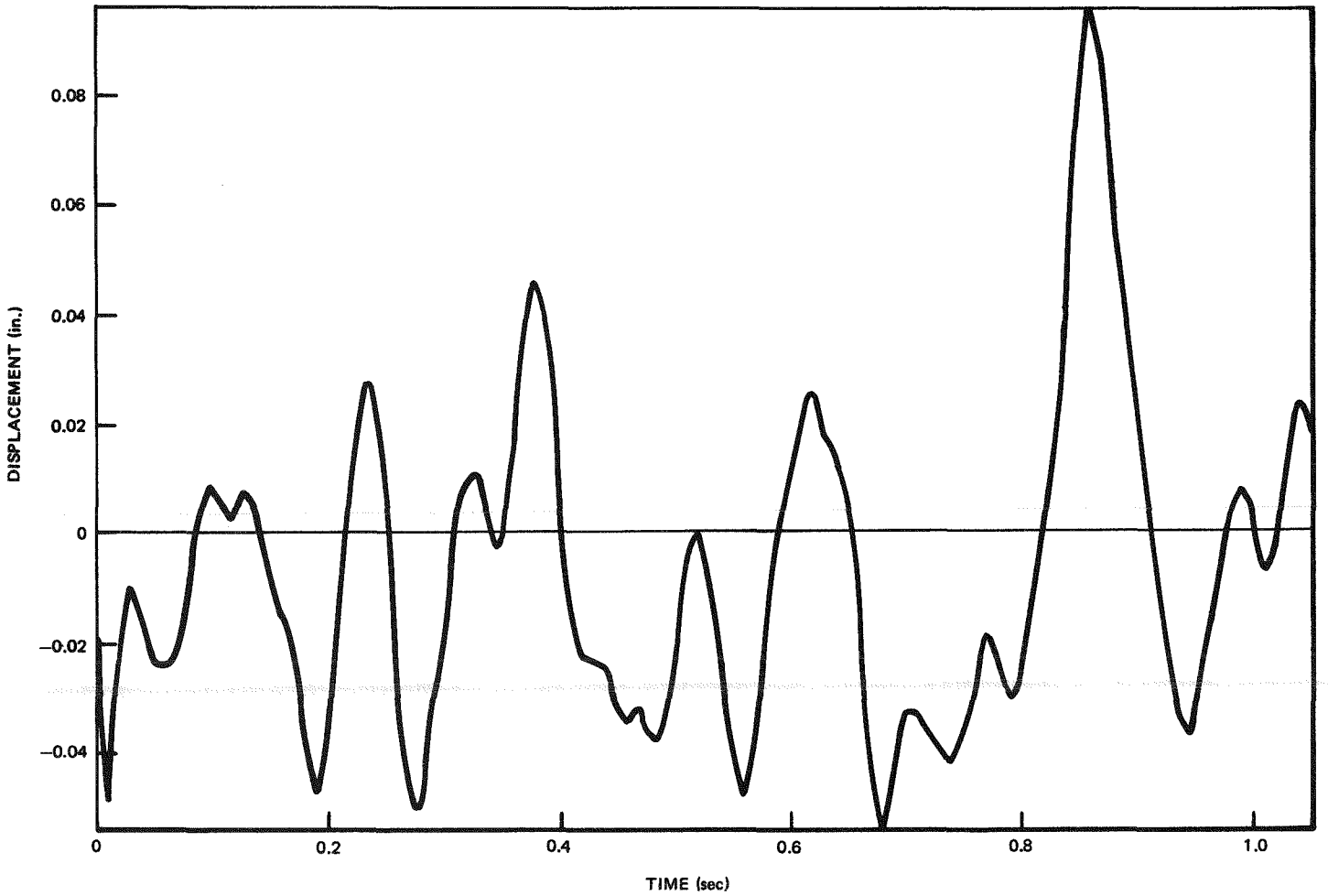

Figure B-16. Operating Base Earthquake Displacement Time History Applied to Snubber Supports 1 and 2

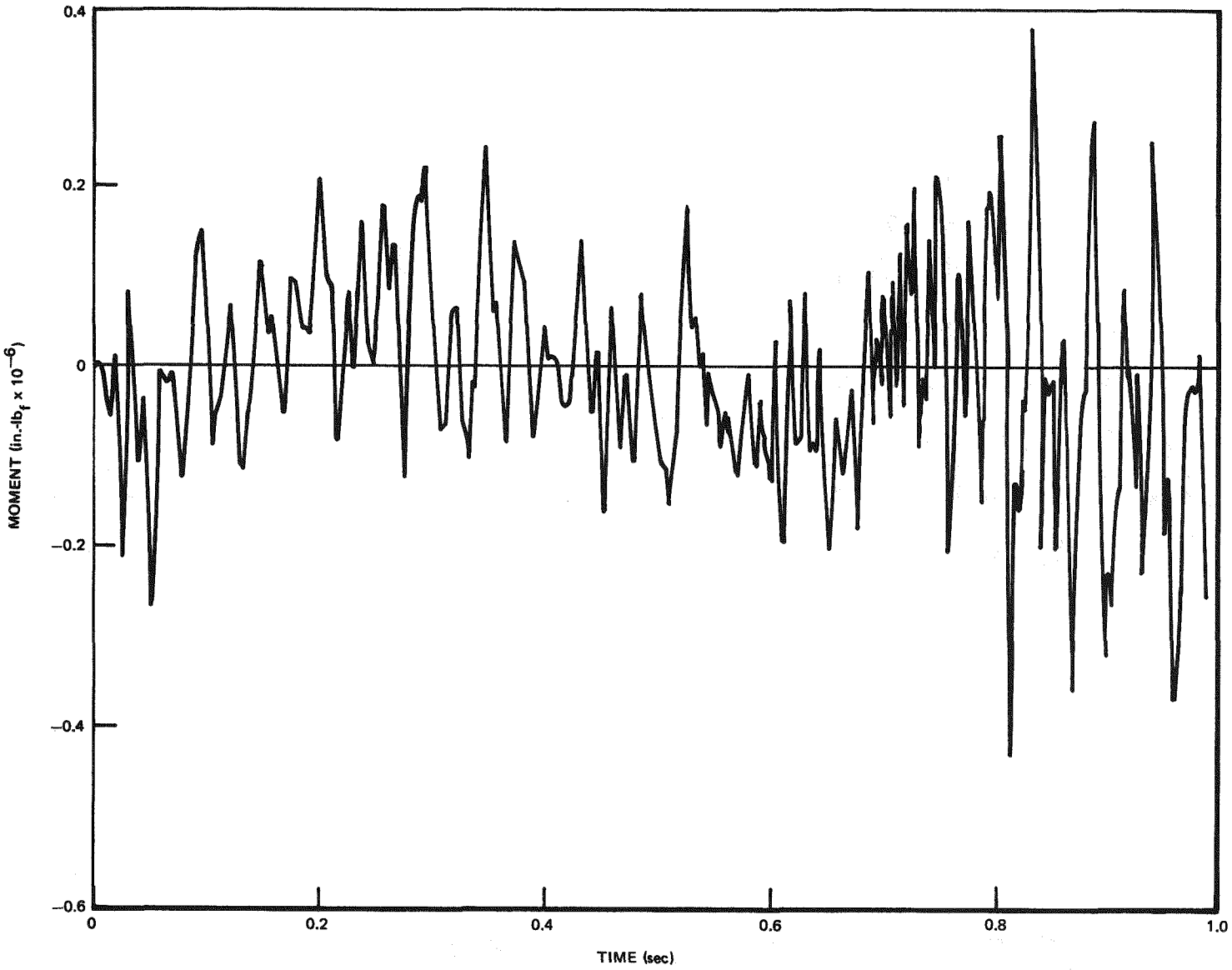

Figure B-17. Moment Response of the Piping System at the Safe End Location for Operating Base Earthquake Conditions - Linear-Elastic Analysis

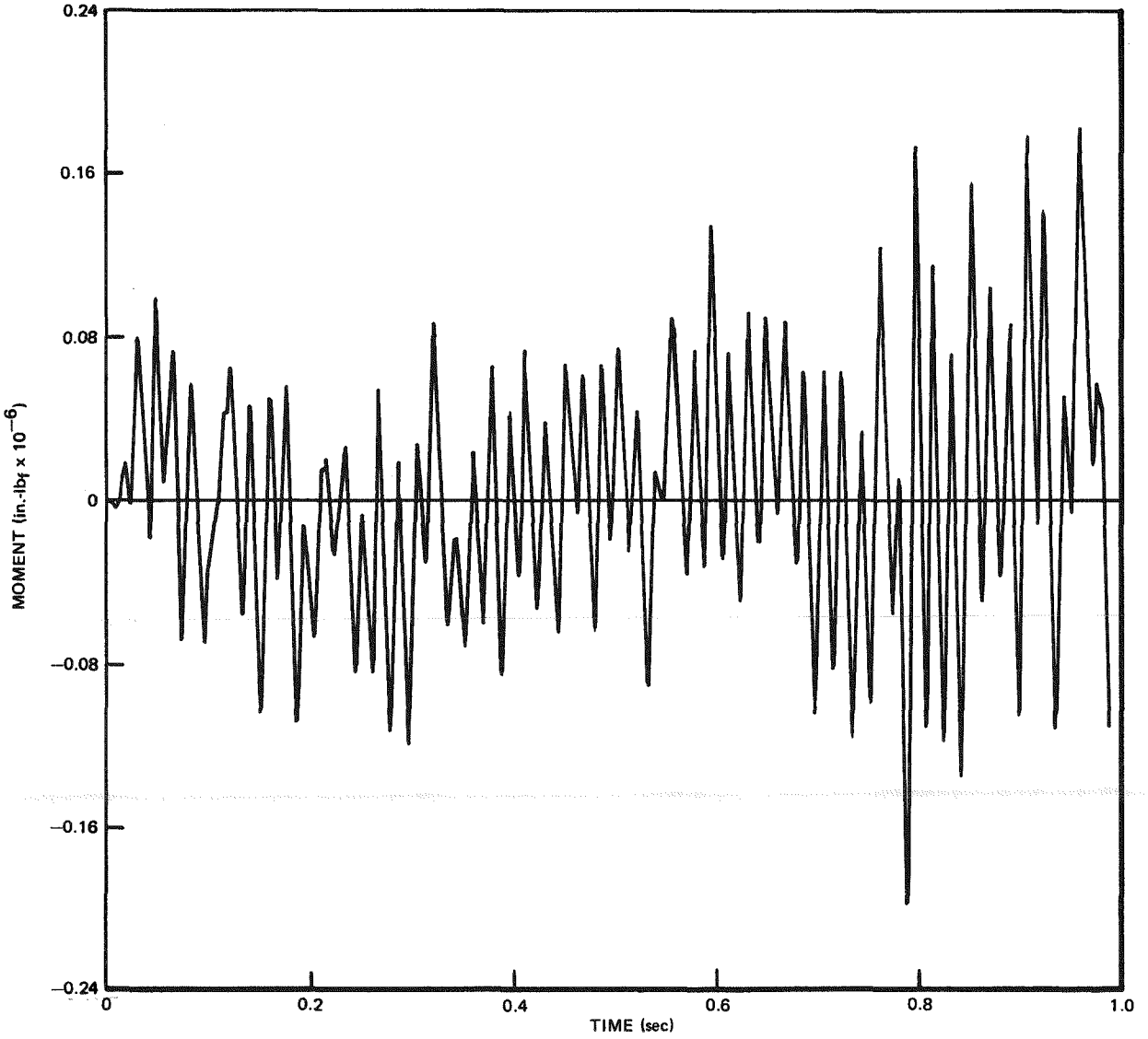

Figure B-18. Moment Response of the Piping System at the Elbow Location to Operating Base Earthquake Conditions, Linear-Elastic Analysis

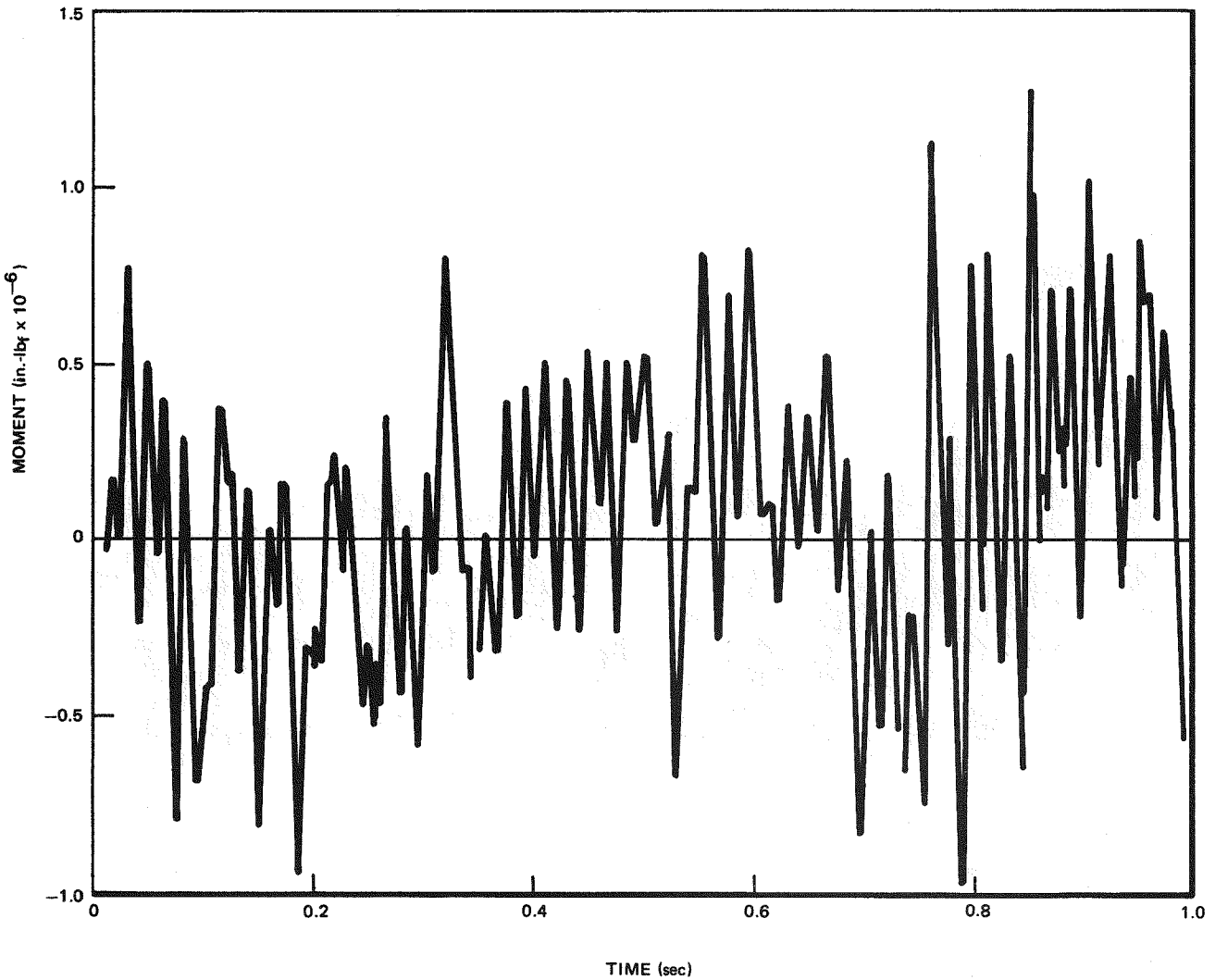

Figure B-19. Moment Response of the Cracked Pipe Element to Ten Times the Operating Base Earthquake Conditions - Elastic-Plastic Analysis (Circumferential flaw of depth to pipe wall thickness ratio of 0.67 - adjacent to the elbow.)

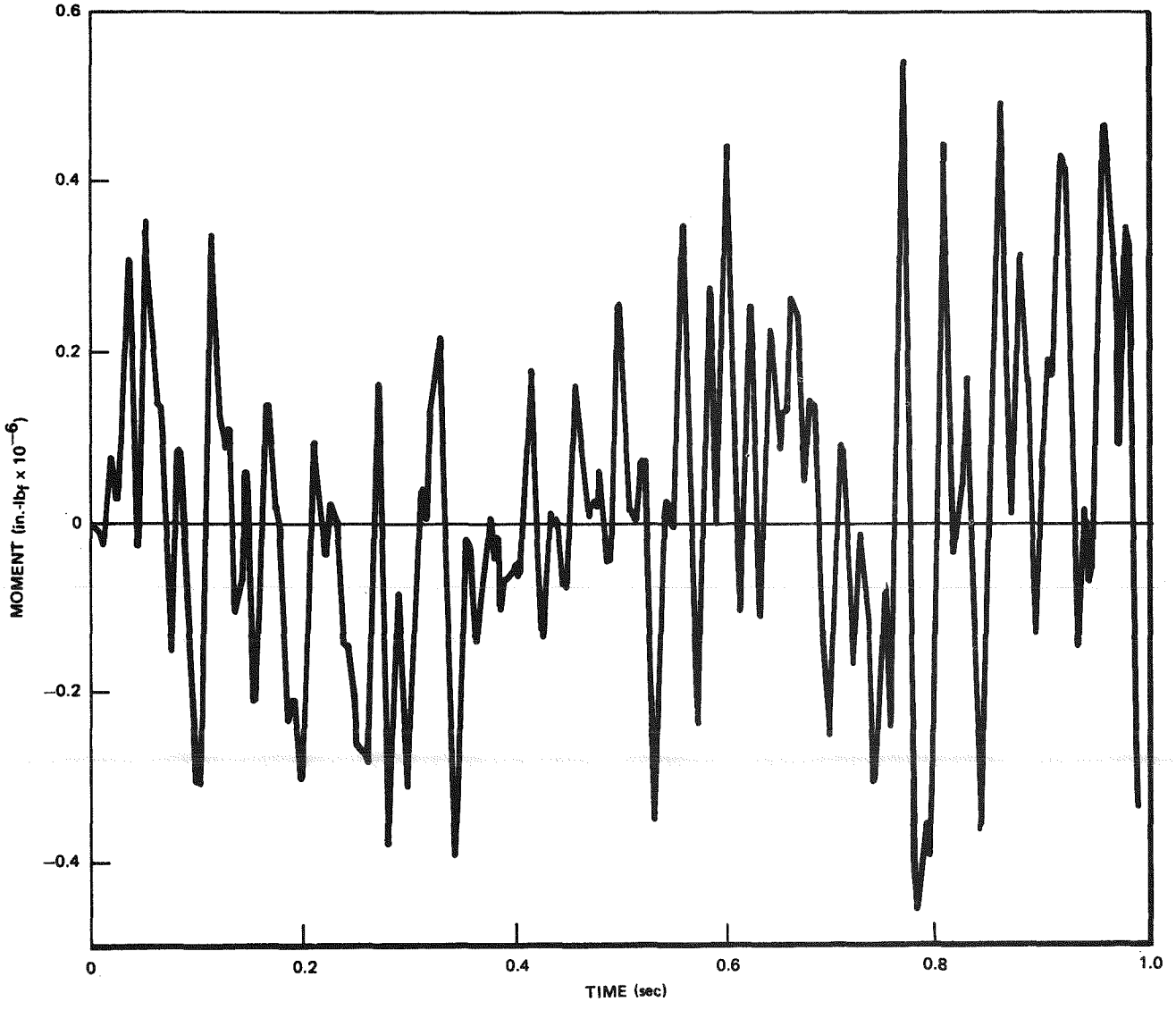

Figure B-20. Moment Response of the Cracked Pipe Element to Five Times the Operating Base Earthquake Conditions - Elastic-Plastic Analysis (180-deg through flaw adjacent to the elbow)

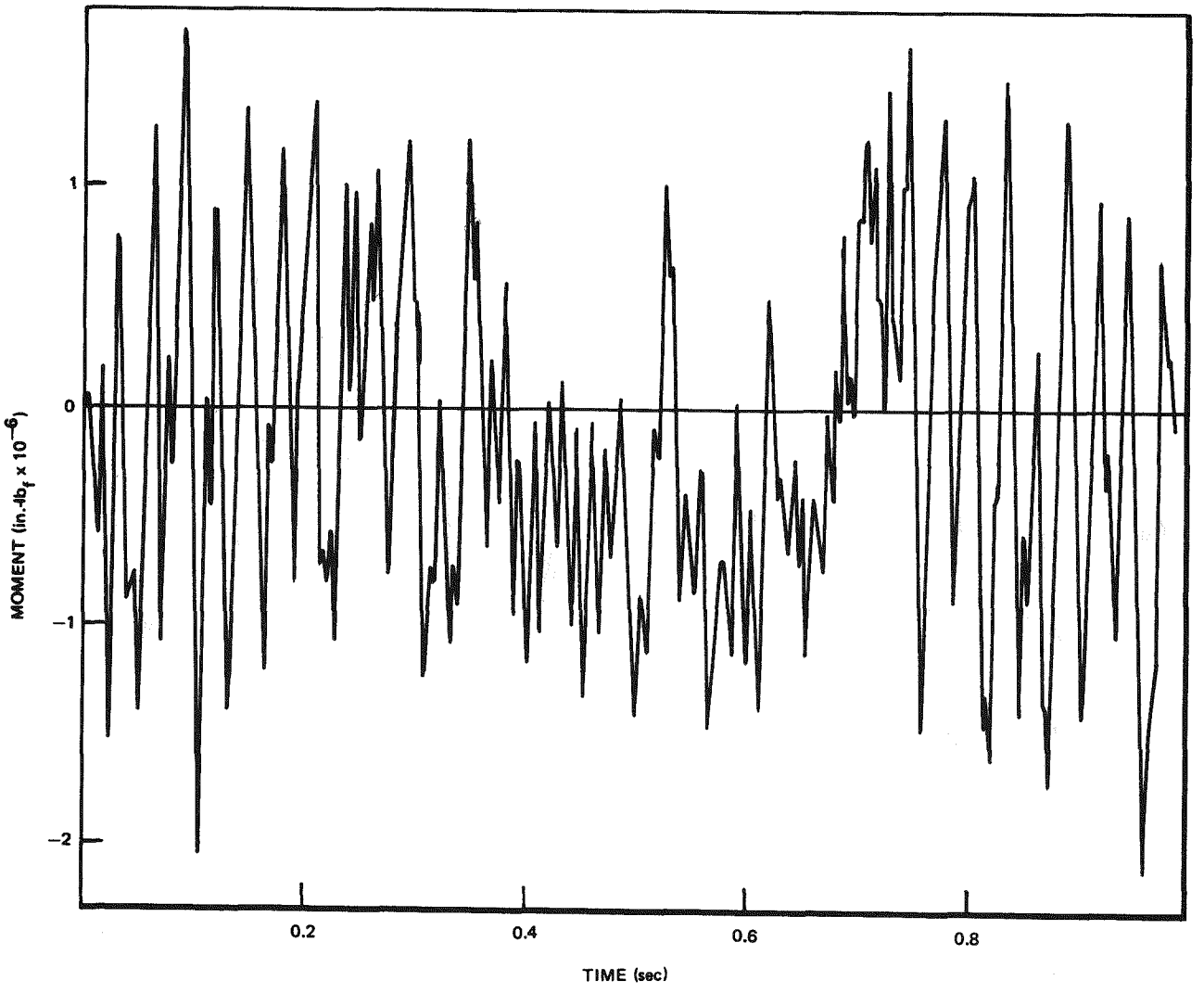

Figure B-21. Moment Response of the Cracked Pipe Element to Ten Times the Operating Base Earthquake Conditions - Elastic-Plastic Analysis (circumferential flaw with depth to pipe thickness ratio of 0.67 - safe end location)

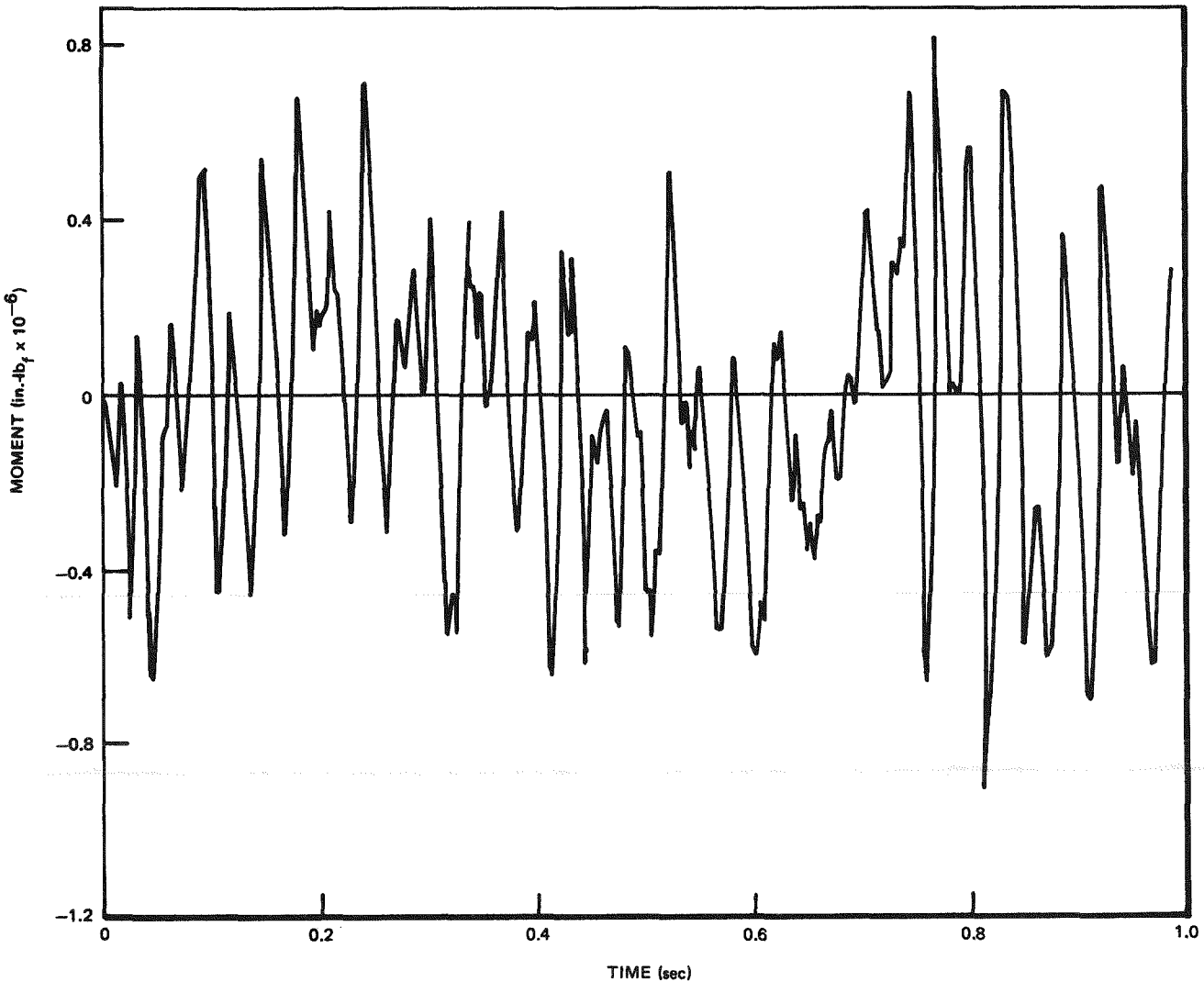

Figure B-22. Moment Response of the Cracked Pipe Element to Five Times the Operating Base Earthquake Conditions - Elastic-Plastic Analysis (180-deg through flaw - safe end location)

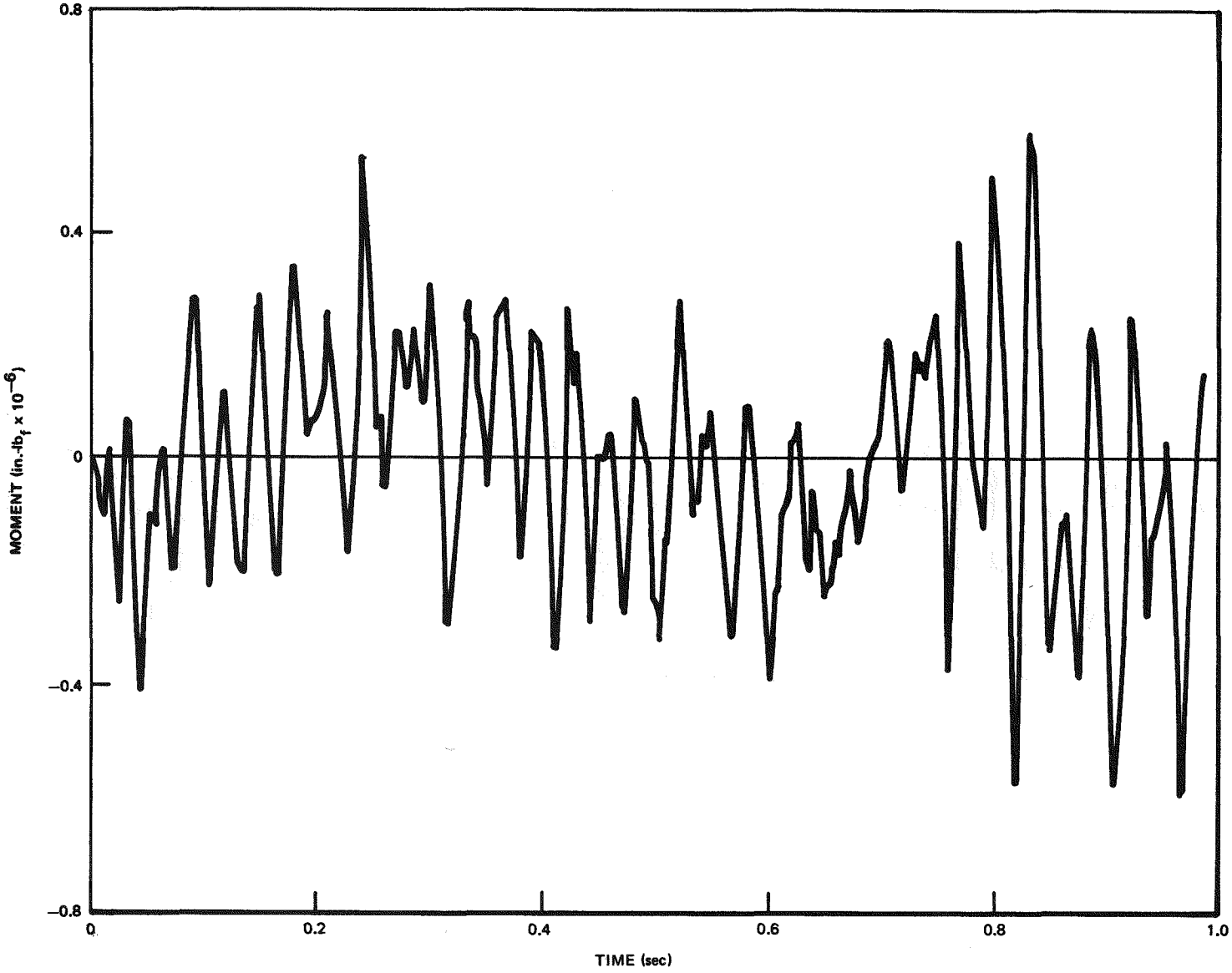

Figure B-23. Moment Response of the Cracked Pipe Element to 2.5 Times the Operating Base Earthquake Conditions - Elastic-Plastic Analysis (180-deg through flaw - safe end location)

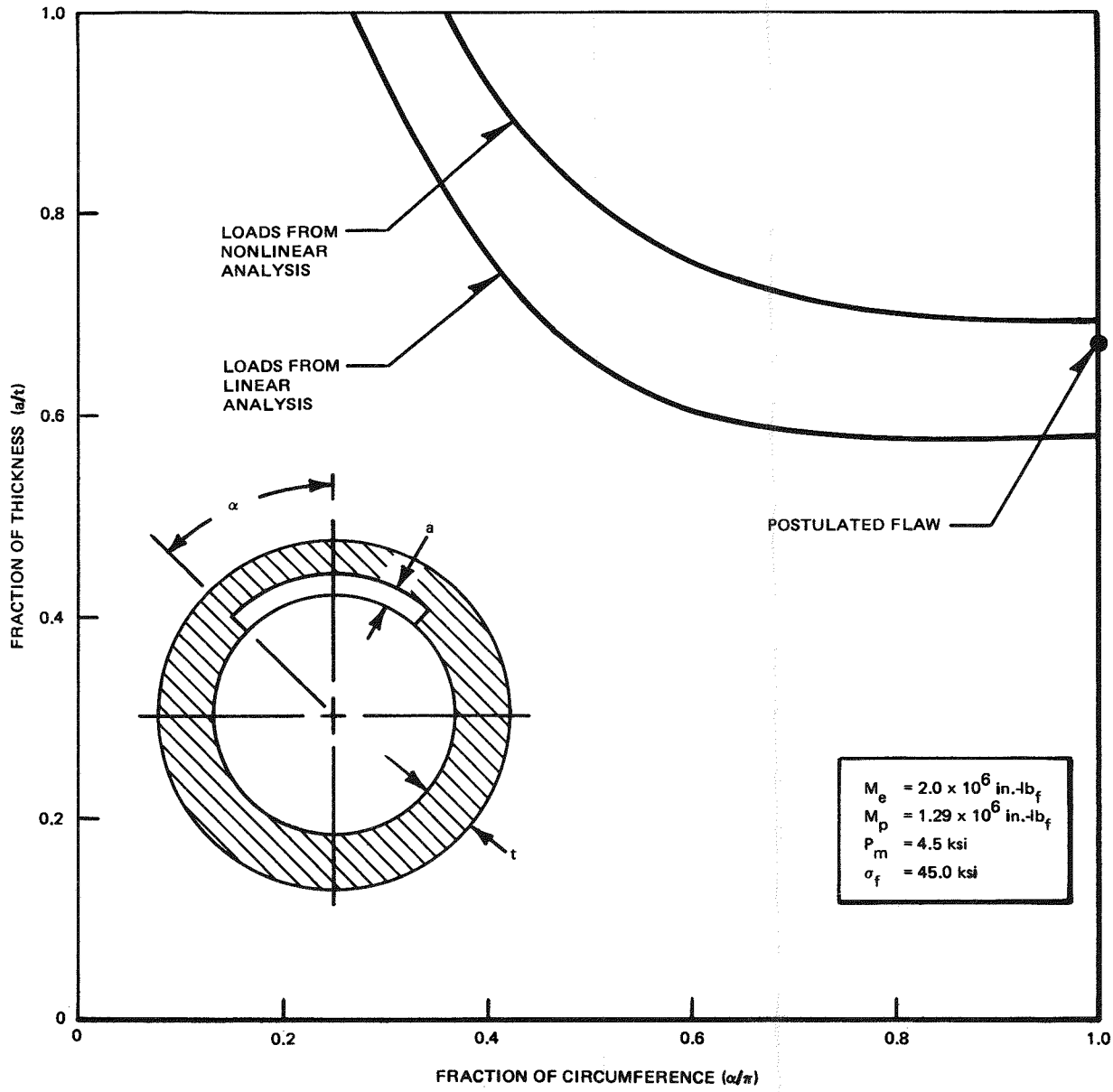

Figure B-24. Failure Diagram for the Circumferential Flaw Located at Elbow - 10.0 OBE Conditions

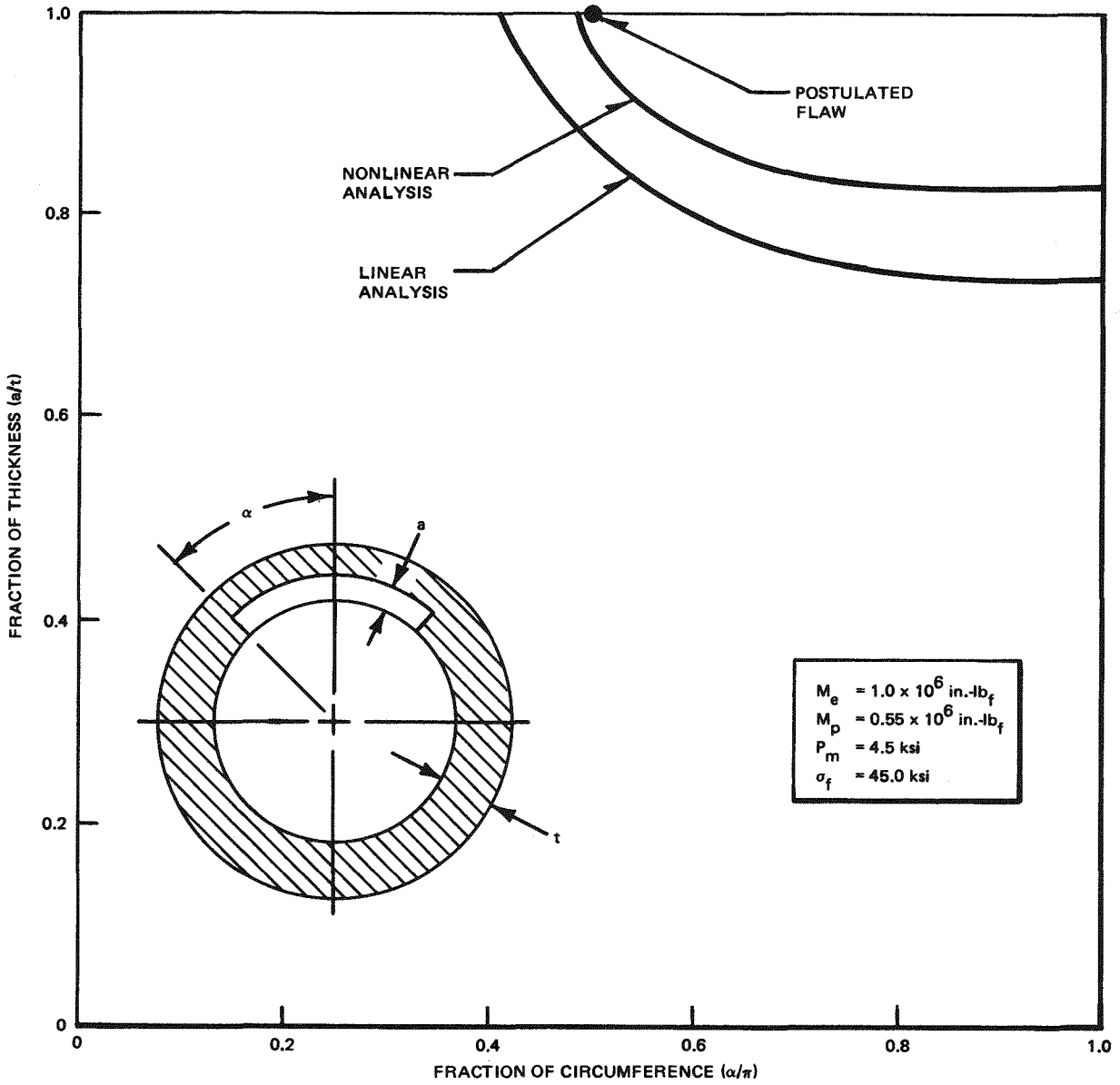

Figure B-25. Failure Diagram for the Through Flaw Located at Elbow - 6.0 OBE Conditions

Appendix C

CONFIRMATORY DYNAMIC PIPE TESTS

(D. A. Hale and J. D. Heald; S. R. Sharma)

C.1 SUMMARY

A series of dynamic pipe tests was conducted involving notched sections of 4-in. Schedule 80 stainless steel and Inconel 600 pipe. The specimen configuration consisted of a four-point bending beam with concentrated end masses sized to give an elastic first mode frequency near that of field-installed piping systems (15 Hz). The specimens were loaded using sinewave excitation at this first mode natural frequency.

The response of the specimen was measured and compared to predictions from an elastic-plastic dynamic analysis which had been previously developed under another task of this same program. In addition, the specimen loads at failure were compared to those loads which would be expected based upon a net section collapse failure criteria.

The dynamic test results confirmed that the elastic-plastic dynamic analysis did a reasonably good job of predicting the dynamic response of flawed pipe components subjected to seismic type excitation.

Furthermore, these tests demonstrated that net section collapse does not occur under dynamic loading conditions which simulate the natural frequencies of as-installed Light Water Reactor (LWR) piping systems and that a net section collapse criterion can be used as a conservative estimate of the load capacity of flawed pipe sections provided the change in flaw shape due to crack growth is properly accounted for.

Finally, these tests showed that at bending moments near those which would be calculated from a net section collapse criterion, significant plastic deformation and rapid fatigue crack growth take place which ultimately lead to full-wall penetration.

C.2 INTRODUCTION

In the design of a typical boiling water reactor piping system, the various service loads considered are the pressure, hydraulic, dead weight, thermal, and seismic loads. However, the design is generally controlled by the dynamic loads due to seismic events since primary stresses due to the other loads during normal operation are usually low. Therefore, the seismic analysis itself and the ways in which the seismic results are used in subsequent analyses play a central role in the design of piping systems.

The analysis of a piping system for a seismic event essentially involves applying the expected anchor point motion time histories (or acceleration response spectra) and performing a linear elastic dynamic analysis. The anchor point motion time histories, in turn, are obtained from a soil-structure interaction analysis of the total system, i.e., the reactor pressure vessel and the associated buildings and other interacting structures. The soil-structure interaction study of the total system utilizes a plant unique free-field earthquake ground motion time history which envelops the Nuclear Regulatory Commission Regulatory Guide 1.60 Design Response Spectra. In this approach, the effects of system nonlinearity (plasticity) are ignored in the dynamic analysis of the piping structure.

This approach is acceptable for the original piping design, since the stresses are generally in the elastic range. However, it may be overly conservative in situations where significant plastic deformations can be expected, such as in piping systems with cracks or relatively high dynamic loads during a faulted event. In such cases, the available safety margins may be significantly higher than those which can be shown by a purely linear elastic dynamic analysis.

Thus, the work reported in this appendix is an attempt to quantify the degree of conservatism inherent in this approach. The program is a combined analytic/experimental effort involving dynamic tests of pipes containing known crack geometries. The two key objectives for the design and execution of these dynamic tests were (1) experimentally determine the response of a cracked piping system subjected to a severe dynamic loading, and (2) provide experimental verification and benchmark the dynamic failure margin analysis methods developed and reported in Appendix B by correlating the analytical predictions with experimental data.

Incorporating these objectives, the test pipe configuration was designed to be representative of a typical piping system span with its first natural mode frequency in the range of 10 to 15 Hz. During the test, the pipe specimen, containing

a flaw, was driven at its first natural mode frequency by applying a sinusoidal anchor point motion. The test, therefore, simulated extremely severe dynamic loading conditions, compared to a real piping system subjected to a motion time history spectrum containing multiple frequencies and amplitudes. The response of a real piping system is due to a composite of all these frequencies rather than that due to a single resonant frequency impressed for a large number of cycles. Clearly, the dynamic pipe test involves more conservative loading conditions than those expected in a real piping system. By demonstrating consistency between the analysis and test results, the added margin due to plasticity effects under dynamic loading can be validated.

C.3 TEST DESIGN CRITERIA

The dynamic pipe test was designed with several goals in mind. First, the specimen configuration was selected to simulate as-installed field piping in terms of dynamic response (i.e., natural frequency) so that the time scale of the specimen response, and, of any accompanying strain/load rates, was reasonably close to that of real piping. Secondly, the manner in which the dynamic loads were applied to both the specimen and field piping (i.e., resonant inertial loadings in response to a deflection controlled excitation) should be the same.

C.3.1 Specimen

The dynamic pipe specimen geometry was a straight pipe section, loaded in four-point bending, with concentrated end weights (Figure C-1) attached to the free ends. The specimen dimensions and end-weight sizes were selected to produce a first mode natural frequency of 10 to 15 Hz, which is within the range of values expected for field-installed piping systems. The center test section was a short section of 4-in. Schedule 80 pipe which was welded on both ends to trunnion pieces (Figure C-2). These trunnion pieces were solid so that the center test section could be pressurized (water at 1,050 psig) during testing.

A notch was machined in the middle of this center test section. Three notch geometries were used (Figure C-3). The first notch geometry was a full-circumference flaw with a depth equal to 33% or 66% of the through-wall thickness (Type I). The second was a notch of a depth 90% through the wall, with a length equal to 50% of the pipe circumference (Type II). Both these notch types were machined from the outside of the pipe using Electrical Discharge Machine (EDM) techniques to produce a notch with a sharp tip radius (less than 0.002 inch). The third notch geometry was a "natural" Stress Corrosion (SC) crack in the heat-affected zone of a weld (Type III). This notch was produced by environmental testing of welded Type-304

stainless steel pipe in General Electric's San Jose Pipe Test Laboratory under severely accelerated conditions which produce stress corrosion cracking. The goal here was to produce a full-circumference, very deep stress corrosion crack.

C.3.2 Test Fixture and Loading System

Special fixturing was designed to allow the pipe test specimen to be subjected to a controlled input deflection level using a sinewave waveform at excitation frequencies up to 50 Hz. Figure C-4 is a schematic of the actual test setup.

The General Electric Seismic Test Facility (San Jose, California) was modified to accommodate these tests. An existing hydraulic power supply provided the high-flow/high-pressure hydraulic fluid (150 gal/min at 3,000 psig) required for these moderate-frequency, large-stroke amplitude tests.

Two load cylinders were provided with independent control systems which were synchronized to apply equal input deflections to the pipe test specimen through trunnion bearing sets. This allowed the specimen to rotate freely about these load points while undergoing a controlled vertical deflection. The deflection of each individual load cylinder was monitored using a Linear Variable Differential Transformer (LVDT). These two LVDT signals served as the primary feedback control variable in the closed-loop, servo-controlled loading system. The ends of the specimen were free to respond to the inertial loading of the end weights.

A high-speed strip chart recorder system was used to record the following system parameters:

a. Input Displacement Excitation; Cylinder 1 and 2; (δ_1, δ_2)

b. Bending Load Cell Bridges, both specimen arms; (P_1, P_2)

c. Accelerometer signal, one end weight; (a)

d. Clip gage-crack mouth opening stretch; (CMOS)

e. Nominal center test section strain; (ε_n)

In addition, high speed movies were made of selected tests to provide additional test information.

Figure C-5 is a more detailed view of the central area of the test fixture and pipe test specimen. The two load cylinders can be seen with their associated individual high-flow electrohydraulic servo valves. The center test section was stainless steel with carbon-steel extension arms on either side (carbon steel was selected

merely to minimize specimen costs). The trunnion bearings, which allowed the specimen to rotate freely about the input load points, are visible in the figure as are the side restraint bearings, which limited any out-of-plane movements of the specimen. The clip gage, used to monitor crack mouth opening stretch, was attached to the center test section across the EDM notch, using special knife edges.

During testing the center test section was pressurized with room temperature water to 1,050 psig, using the tubing lines and accumulator shown in Figure C-5. Barely visible in this photo are the two bending bridges, which served as primary load cells for this test. These were full four arm strain gage bridges which were initially calibrated against NBS* traceable standard load cells. They were permanently attached to each extension arm and reused from test to test.

Figure C-6 is a more global view of the test fixture itself. The large steel boxes on either end of the test fixture are safety shields which surrounded the large weights located on both ends of the specimen. These end weights represented a large source of kinetic energy during dynamic testing. The steel boxes ensured that these end weights were safely confined at all times.

C.3.3 Test Matrix

A total of eight test specimens covering two materials and three notch geometries were included in the test matrix (Table C-1). Three flaw geometries were included in the test matrix. These flaw geometries were chosen to produce several widely separated points on the failure diagram previously developed under the analysis portion of this program (Figures B-5 and B-6).

With the exception of the one Type III Specimen (SS-8), which was procured from the Pipe Test Laboratory, all test specimens were fabricated from one of two heats whose pertinent mechanical and chemical properties are summarized in Table C-2.

C.3.4 Cyclic Stress-Strain Properties

One of the key inputs needed in the aforementioned elastic-plastic dynamic analysis (Appendix B) is a cyclic stress-strain curve. The analysis is sensitive to the chosen values of material yield strength and to the tangent modulus. Therefore, tensile specimens were machined from the 304 SS library material and used to

*National Bureau of Standards

generate cyclic stress-strain data. The tensile specimen geometry was a 3.25-in.-long bar with a 0.125-in.-diameter by 1.25-in.-long gage section which was cut parallel to the pipe axis. These tests were run in strain control through a fully reversed, imposed strain range.

The results are summarized in Figure C-7. A bilinear stress strain curve was fitted to these results - the resultant idealized curve derived from these results is shown in Figure C-8.

C.4 SMALL-SCALE TESTS: METHODS AND RESULTS

Prior to the start of full-size dynamic pipe testing, several exploratory tests were run using small-diameter Type-304 stainless steel tubing to explore important test parameters and techniques (Figure C-9).

A closed-loop, servo-controlled testing machine was used to provide the input displacement excitation. The specimens used were sections of 0.25-in., 0.50-in., or 1.00-in.-outside diameter (o.d.) tubing with a concentrated end mass fastened to the free end. The other end was gripped through a 90-deg elbow in the actuator of the testing machine. The gripped end was instrumented with strain gages in a bending bridge configuration and calibrated to measure the end load applied to the tube at the end-weight location. The tube lengths and end mass size were selected to produce a first mode natural frequency of 2 to 4 Hz. Two of these specimens were notched near the gripped end, using a tubing cutter.

These specimens were loaded using two different procedures. In the first procedure, called resonant following, the frequency of the input excitation was adjusted at each individual loading step to obtain the maximum response from the specimen/mass system.

Typical data from four tests run using this technique on 0.50-in.-o.d. by 0.065-in. wall tubing are shown in Figure C-10. The maximum measured peak-to-peak moment is plotted in terms of the applied input deflection. Two of these four tests were notched (50% and 75% through the wall) and two were not.

The straight line in Figure C-10 represents the linear elastic line established by these test data. For runs 1, 2, and 3, the specimen did not fail prior to the time that the maximum test machine input deflection was reached. However, for run 4, the specimen failed in the notched cross section at a fairly low deflection value. Post-test examination of this specimen indicated that a great deal of fatigue crack

growth had occurred prior to failure. This is not surprising, given the fact that this resonant-following technique consumes a significant number of cycles at each loading step due to two factors. First, as with any scanning technique, one must start below the anticipated peak and sweep up and past the peak. This in itself requires a number of cycles. Just as important, though, is the fact that even when exciting this simple system at the exact resonant frequency, a number of additional cycles (usually 20 to 50) were required before the system response built to its maximum value.

Two other tube sizes were also tested using this same procedure. This data is compared in Figure C-11 with the unnotched case from Figure C-10. Also shown in Figure C-11 is the nominal elastically calculated bending stress (Mc/I) as a function of input excitation deflection level. The straight dotted line represents a best fit to the initial elastic portions of the three data curves. The line at a bending stress of 40,000 psi represents a good approximation of the cyclic yield stress for Type-304 stainless steel.

The second test procedure used consisted of holding the input excitation frequency constant at the initial elastic first mode natural frequency. One specimen was tested in this manner. The results are compared to a companion specimen tested using the resonant following technique in Figure C-12. The lower line in Figure C-12 was generated at a fixed excitation frequency of 4.82 Hz, except for the last data point, which was obtained by tuning the excitation frequency to the first mode natural frequency corresponding to this deflection level (4.50 Hz), i.e., changing to the resonant following procedure.

C.5 FULL-SIZE DYNAMIC PIPE TESTS

C.5.1 Test Methods

The primary purpose of these full-size pipe tests was to confirm the validity of the Dynamic Analysis Methods discussed in Appendix B thereby demonstrating additional margin for dynamic loading situations. Therefore, test techniques and procedures were tailored to allow these tests to be performed in a manner consistent with the analysis procedures, bearing in mind the lessons learned from the small-scale tests.

The analysis was performed at a fixed frequency which corresponded to the elastic first mode natural frequency. This analysis did not follow the decrease in system natural frequency which accompanies increasing plasticity in the cracked cross

section. While the resonant-following technique, evaluated in the small scale tests, produced maximum system response, it was not consistent with the analysis approach which these tests were designed to critique. Therefore, the test mode technique deemed most appropriate for these full-scale pipe tests was the fixed frequency mode represented by the "constant frequency" data in Figure C-12.

All the full-size pipe tests were run at the "elastic" first mode natural frequency, i.e., at the frequency which produced maximum system response during initial low level frequency sweeps. No further adjustment of the input frequency followed. The specific steps were (1) to experimentally determine the as-installed first mode natural frequency, f_n, of the pipe specimen using a low-level input excitation, and (2) to use this value, f_n, for all subsequent loading steps. This approach had the additional practical advantage of minimizing the fatigue duty on the next test specimen.

Figure C-13 represents an overview of the control circuitry assembled for these tests. Basically, this system provided the COMMAND input to the closed-loop, servo-controlled hydraulic system which actually loads the pipe specimen. The COMMAND waveform used was a sine function. The amplitude of this sinewave was manually set to the level desired for each test step. However, the high-speed/ high-force capability of the hydraulic loading system could easily damage the test specimen and/or fixture, unless these forces are applied in a carefully controlled, gradual fashion. Therefore, a "soft" startup/shutdown module was incorporated which ramped the COMMAND sinewave from 0 to 100% of the desired input level in 3 seconds at startup and ramped it down from 100 to 0% in 1 second at shutdown. The frequency of the COMMAND sinewave could be varied manually or automatically. For this particular constant frequency test mode, the frequency was varied manually during the low-level resonance search phase of the test and remained constant for subsequent test steps.

The actual system shutdown for these tests was done manually. The test operator constantly monitored the response of the test specimen (i.e., the output signal from one of the load cell bridges on the specimen extension arm) and allowed it to build up to the maximum possible level associated with each given input step. The manual shutdown button was then actuated activating the "soft" shutdown process.

This procedure is idealized in Figure C-14. The top data track represents the input (cylinder stroke) and the bottom track represents specimen response (load cell bridge). The region from (A) to (B) in Figure C-14 shows the gradual buildup in system response which occurs during the constant amplitude portion of the test. The soft shutdown would be activated at (B) when the system response had reached its maximum.

A typical test sequence, then, would consist of the following steps (Figure C-15):

Step I: Determine as-installed first mode natural frequency of pipe specimen plus end weights. A very small input excitation amplitude is applied to the specimen. The frequency of this input sinewave is slowly increased (manually), starting at 10 Hz, until the maximum system is obtained. This maximum response frequency, f_n, is then used for all subsequent load steps.

Step II: An input deflection amplitude is selected, based upon the Elastic-Plastic (E-P) dynamic analysis (Appendix B), which should result in a system response which is near the upper end of the elastic region.

Step III: Going to the E-P analysis again, a high level response point is selected to confirm the plastic portion of the E-P dynamic analysis prediction curve.

Step IV: An excitation level is selected from the E-P prediction curve which should produce a moment sufficient to "fail" the specimen, i.e., a moment which exceeds the predicted failure moment derived from a net section collapse criterion.

Ideally, then, the test sequence would consist of three to four steps with the last step sufficiently high to cause failure. It was felt that this approach would yield enough data points to critique the E-P dynamic analysis while minimizing the fatigue duty cycle on the specimen itself.

C.5.2 Test Results

C.5.2.1 Bending Load Verification. As previously mentioned, the individual bending load cells on each arm of the test specimen were statically calibrated. However, since the dynamic bending load was one of the two critical parameters

being measured in this experiment, an independent check of the accuracy of these load readings was performed based upon measurements of the end weight accelerations (Figure C-4).

Figure C-16 is a comparison of the peak-to-peak bending load value measured by the North load cell and the bending moment calculated from accelerometer readings taken on the North end weight. Note that this acceleration calculation was made using a "virtual" end weight size which accounted for the distributed weight of the extension arm itself. Generally, the accelerometer-based load was within 10% of the corresponding load cell reading. Only one pipe (SS-10), out of the six represented in Figure C-16, shows a substantial ($\sim$20%) difference between the two sets of load readings. This discrepancy could be due to operational difficulty in the trunnion bearings.

If these bearings bound or seized during dynamic operation, they could attenuate the bending moment being generated by the oscillating end weight so that the true bending moment transmitted to the center test section was less than that measured by the bending load cells. Extreme care was exercised during fabrication of the test fixture and specimens to minimize misalignment in these bearings.

However, in order to determine whether this was a valid concern, strain gages were applied to the center test section in each specimen in locations away from the notched cross section. A linear strain distribution was assumed in this cross section and a stress distribution and accompanying gross section moment were calculated using the bilinear stress strain curve shown in Figure C-8.

Moments calculated from the strain measurements described above are shown as the "predicted" line in Figure C-17. Also shown in Figure C-17 is the actual test data from the five specimens having deep cracks that required relatively low loads for fracture (SS-1, 3, 9, IN-1 and IN-2). The individual specimen data plotted here represents the measured dynamic bending moment amplitude and the corresponding measured dynamic strain amplitude at a location which is within the center test section but away from the machined notch.

Figure C-17 shows reasonable agreement between the moments which would be predicted, based upon gross section strain gage readings, and those actually measured.

Disagreement is noted only in those three specimens (SS-6, SS-8, and SS-10) which were loaded to the highest loads (and concomitant highest fixture displacements).

This apparent discrepancy is discussed in more detail in the discussion of the results from these particular specimens in a later section.

The conclusions of these checks is that the load readings are reasonably accurate.

C.5.2.2 Pipe Tests. Pertinent data for all eight specimens tested are summarized in Table C-3. The actual dynamic test data are plotted in terms of bending load versus input displacement excitation in Figure C-18. The offset in the data in Figure C-18 is due to the initial static moment which existed in the center test section due to the dead weight of the end weights and distributed weight of the extension arms. The open data points for each specimen represent intermediate loading steps. The solid point represents final specimen "failure," i.e., through-wall penetration.

These data for the 2/3 x 360° and 90% x 180° flaw configurations are replotted in slightly different format in Figures C-19 and C-20, respectively. Here, the static moment offset in the data in Figure C-18 is removed and the resultant data compared to the predicted response from the elastic-plastic dynamic analysis (Appendix B). The open points in Figures C-19 and C-20 represent intermediate load steps while the solid points represent specimen failure. The cyclic stress-strain curve shown in Figure C-8 was used for both the stainless steel and Inconel specimens.

C.6 DISCUSSION

C.6.1 Elastic-Plastic Dynamic Analysis

One of the two primary goals of this test program was to critique the E-P dynamic analysis developed and discussed in Appendix B. The open symbol (non-failure) data in Figure C-19 show very good agreement between the test data and the E-P analysis for the case of a 2/3 x 360° flaw configuration. The solid (failure) data points which are plotted in Figure C-19 fall below the E-P analysis. These failure points represent the moment/input deflection conditions existing in the pipe at the instant when full-wall penetration occurred. Obviously, in order for full-wall penetration to occur, the original machined flaw has grown, thereby changing dramatically in shape. This change in flaw shape is the reason that the failure points in Figure C-19 fall below the E-P analysis curve. Figure C-21 shows the final fracture surface for specimen SS-10 (a 1/3 x 360° flaw). The specimen was heat-tinted at the conclusion of dynamic testing, to define the extent of the final crack, and then pulled apart.

The dark "beach marks" near the top of the photo define the shape that the fatigue crack front assumed during the time it was propagating through-wall. The beach mark which defines the shape of the crack at the instant of through-wall penetration is highlighted in Figure C-21 with a dashed line. The cross-hatched area defines the position of the flaw at the end of testing. Note that a great deal of cracking took place following through-wall penetration while the test is being shut down.

One of the critical elements in the E-P dynamic analysis is a moment-curvature diagram for the specific flaw geometry being analyzed (see Figure B-8). Therefore, it is not surprising that the failure or through-wall data points (shown previously in Figures C-17, C-18 and C-19), which are associated with a significantly changed (during test) flaw geometry than that covered by the E-P analysis, fall below the prediction line. This problem of changing flaw geometry will become even more important when looking at net section collapse moments. However, it appears that based upon Figure C-19, the E-P analysis does a good job of predicting specimen response for those cases where the flaw is close to the geometry being analyzed.

C.6.2 Net Section Collapse Failure Criteria

The other primary goal of this program was to determine whether a net section collapse criterion, which has been used primarily in quasi-static loading situations to date, is appropriate and conservative as a failure criterion for dynamic loading of flawed pipes.

It was recognized early in this program that since the net section collapse process is inherently dependent upon the development of large strains, and, therefore, deformations, the time scale of these deformation events would likely play a key role in application of net section collapse to dynamic loading situations.

The net section collapse moments for the three flaw configurations tested in this program are compared to the failure data from Figure C-18 in Figure C-22. The value of 70.9 ksi used for the flow stress in this calculation is the average of the material yield and ultimate strengths (Table C-2). Figure C-22 would seem to indicate that the net section collapse criterion calculated based on the initial flaw geometry does not give a conservative lower bound for the load-carrying capability of flawed pipe. However, as previously noted and illustrated by Figure C-21, the flaw configurations which corresponded to the failure points in Figures C-18 and C-22 were substantially different than the original assumed flaw configurations used in the net section collapse calculations. Clearly, the net section collapse

calculations must be corrected to account for the fatigue crack growth which unavoidably accompanied the high cyclic loadings in the flawed cross section.

The first element needed to perform this correction is an equation to allow calculations of net section collapse moments for flaws of arbitrary geometries. Figure C-23 summarizes the parameters used in the derivation of this equation. Basically, a second order polynomial is used to describe the arbitrary flaw geometry. The resulting moment equation is

$$M = (2\,\sigma_F\,t\,R_N^2)\left[-\sin\alpha = 2\sin\beta + \frac{1}{t}\left[a\sin\alpha + b\,(\cos\alpha + \alpha\sin\alpha - 1) + c\,(2\alpha\cos\alpha + (\alpha^2 - 2)\sin\alpha)\right]\right]$$

where

$$\beta = \frac{(\pi-\alpha)}{2} + \frac{1}{2t}\left(a\alpha + \frac{b\alpha^2}{2} + \frac{c\alpha^3}{3}\right) - \frac{P_M\cdot\pi\cdot R\cdot T}{2\cdot\sigma_F\cdot R_N\cdot t}$$

P_M = primary membrane stress in remote, uncracked cross section

R = average radius in remote, uncracked cross section

T = full-wall thickness of remote, uncracked cross section.

The second element needed is a scheme for determining what values of measured loads and input deflections are to be associated with a given flaw geometry. While specimen loads, deflections, and strains were recorded on each cycle of each loading step, the manner in which the flaw geometry is varied was assessed by a post-test examination of fracture surface described above (Figure C-21).

As previously mentioned, high speed movies were taken of selected tests. These movies provided the key in allowing cross-correlations to be made between the analog recordings of cyclic load, deflection, and strain data, and the instant of full-wall penetration. The beach mark data obtained from post-test fracture surface examinations, such as Figure C-21, allowed the exact shape of the flaw at the instant of through-wall penetration to be defined. Therefore, an accurate estimate of net

section collapse moment could then be made based upon a flaw geometry corrected to account for fatigue crack growth.

This correction method was applied to specimen SS-10. As noted in Figure C-22, the predicted net section collapse moment based upon the original 1/3 x 360° machined flaw would be 260.5 in.-kip. However, based upon the revised through-wall flaw geometry (Figure C-21), the corrected predicted net section collapse moment is 177 in.-kip.

The next step is to compare to observed moments to this corrected prediction described above. The actual moment which is developed in the specimen during the last load step was found to be highly dependent upon the response characteristics of the pipe. Therefore, some independent way for choosing the proper value of the varying moment was needed. This was provided by the high speed movies. These movies of the last load step for SS-10 showed that full-wall penetration occurred on cycle 34. Examination of the data traces for this exact cycle of the last load step gave a value for the average maximum bending moment of 248 in.-kip based upon the load cell readings. Note that this value of 248 in.-kip exceeds the corrected prediction of 177 in.-kip.

However, if the possible uncertainty in the true bending moment which is suggested by Figure C-17, is accounted for, the moment at full wall penetration could be as low as 190.1 in.kip. Nevertheless, for either of these two values, the load-carrying capability of this now severely cracked pipe was still 7 to 43% greater than would be predicted from the net section collapse criteria corrected for true flaw shape.

Specimen SS-1 was also analyzed using this approach. The predicted net section collapse moment, based upon the original 2/3 x 360° machined flaw, would be 120.8 in.-kip. The corrected predicted moment based upon the observed through-wall geometry was 69 in.-kip. The actual moment which existed at the instant of through-wall penetration was 117 in.-kip. Therefore, once again the net section collapse criterion results in a conservative prediction of the load-carrying ability of this badly cracked pipe section. An attempt was made to use this approach to analyze the two 90% x 180° flaw specimens (IN-2 and SS-3). However, the very small size of the ligament (10% of wall is 0.030 inch) resulted in no discernible evidence of fracture shapes on either fracture surface, precluding any further analysis.

These two examples, then, demonstrate that net section moments greater than those which would be predicted based upon a net section collapse criterion were developed during dynamic loading at the 12 Hz loading frequency used during these tests.

Other investigators (C-1) have shown up to 20% increases in yield strength in Type-304 stainless steel loaded at high strain rates. In the present situation, this would translate into a 7% increase in flow stress. However, this is still not enough to account for the effects observed here.

C.6.3 Fatigue Crack Growth Under Dynamic Loading Conditions

Examination of the post-test fracture surfaces revealed very high cyclic crack growth rates during the few cycles immediately before and after full wall penetration. For example, the single cycle striation/beach marks visible in Figure C-21 represent growth rates of 1 to 3 x 10^{-4} inch/cycle.

It is interesting to assess dynamic specimen response, during the time these rapid growth rates were occurring. Figure C-24 shows the actual analog data traces from the last load step of specimen SS-10. The top trace represents input excitation (LVDT Stroke); the second trace, specimen response (bending load cell); the third trace, gross (i.e., uncracked) section strain in the center test section and the bottom trace, crack mouth opening stretch (clip gage).

The input trace shows the soft startup wherein the input displacement to the specimen was increased in a linear fashion from 0 to 100% over a 3-sec time period. Therefore, at the nominal 12 Hz frequency used for this test, full input excitation was applied to the specimen by cycle 36 (Ⓐ in Figure C-24).

The specimen response to this input excitation, as measured by either the bending load cell trace or the nominal section strain gage trace, initially increased in a linear fashion until cycle 11 when a clear break in the rate of increase of specimen response per unit increase in input excitation is noted (Ⓑ in Figure C-24). From cycle 11 to cycle 36, the input excitation to the specimen increased over 300%, yet, the specimen response had only increased ∿30%. Clearly, some process(es) was active here which became controlling above some threshold which was exceeded on cycle 11.

In order to attempt to understand this phenomenon, the analog data in Figure C-24 was digitized on a cycle-by-cycle basis for additional analysis. The resultant data is plotted in Figure C-25. Here three different quantities are plotted versus

the peak-to-peak bending load: (1) peak-to-peak value of the Crack Mouth Open Stretch (CMOS), (2) the mean or midpoint value of CMOS, and (3) a "pseudo-compliance" which is the ratio of peak-to-peak CMOS signal to the peak-to-peak bending load signal. These three quantities were calculated on every third cycle as noted in Figure C-25.

The midpoint CMOS signal, which is a measure of permanent specimen deformation, showed a clear break point at cycle 12. This is significant because, while it was impossible to differentiate permanent specimen deformation caused by plastic yielding from that caused by a change in flaw shape due to crack growth, it does show that some process, which resulted in a permanent specimen deformation, became active when a threshold value of some kind was exceeded on cycle 11 or 12. The maximum value of bending load which would be calculated based on the cycle 11 load data is 205 in.-kip. This is approximately 80% of the 260 in.-kip net section collapse moment which would be calculated based on the original 1/3 x 360° flaw. However, the SS-10 data for the previous load step shows some evidence (i.e., an offset in the CMOS signal at the end of the load step, and an increase in the elastic pseudo-compliance) that crack propagation may have begun on the previous load step. The significance of this is that if the crack at the start of this last load step had been somewhat larger than the assumed original 1/3 x 360° geometry, the 205 in.-kip bending moment value might correspond to the net section collapse moment for the actual flaw.

Similar data from specimen SS-9 (a 2/3 x 360° flaw) is shown in Figure C-26. This data is taken from the second to last load step applied (specimen failed on next load step). Once again a clear breakpoint is seen early in the soft startup process. The value of maximum moment corresponding to this breakpoint is 114 in.-kip. This is 94% of the net section collapse moment for the original 2/3 x 360° flaw.

Examination of the data traces for specimens SS-1, SS-8, and IN-1 revealed this same "breakpoint" type behavior late in the test.

This suggests, then, that at bending moments near the net section collapse moment, either rapid fatigue growth and/or substantial plastic deformation was occurring. The former is consistent with the results from the post-test fracture surface exams. Either process alone or in combination with the other is energy intensive, would consume system energy, and would result in a condition of diminishing return in that continuing increases in input excitation energy produce little or no corresponding increase in specimen response.

C.7 CONCLUSIONS

The dynamic test results confirm that the elastic-plastic dynamic analysis, developed and discussed in Appendix B, does a reasonably good job of predicting the dynamic response of flawed pipe components subjected to seismic type excitation.

Net section collapse does not occur under dynamic loading conditions which simulate the natural frequencies of as-installed LWR piping systems.

However, a net section collapse criterion can be used as a conservative estimate of the load capacity of flawed pipe sections provided the change in flaw shape due to crack growth is properly accounted for.

At bending moments, near those which would be calculated from a net section collapse criterion, significant plastic deformation and rapid fatigue crack growth take place which ultimately lead to full-wall penetration.

C.8 REFERENCES

C-1. M. F. Kanninen, et al., "Third Semi-Annual Progress Report, Instability Predictions for Circumferentially Cracked Large Diameter Type 304 Stainless Steel Pipes under Dynamic Loading," Batelle Columbus Laboratories, January 31, 1981.

Table C-1

DYNAMIC PIPE TEST, TEST MATRIX

Specimen ID	Material[a]	Notch Geometry[b]
SS-1	T-304 SS	66% through wall x 360° (Type I)
SS-3	T-304 SS	90% through wall x 180° (Type II)
SS-6	T-304 SS	33% through wall x 360° (Type I)
SS-8	T-304 SS	Natural Stress Corrosion Crack in Weld Heat-Affected Zone (Type III)
SS-9	T-304 SS	66% through wall x 360° (Type I)
SS-10	T-304 SS	33% through wall x 360° (Type I)
IN-1	Inconel 600	66% through wall x 360° (Type I)
IN-2	Inconel 600	90% through wall x 180° (Type II)

[a]See Table C-2

[b]See Figure C-3

Table C-2

PHYSICAL AND MECHANICAL PROPERTIES, LIBRARY PIPE MATERIAL

Type-304 Stainless Steel (ASTM A-312)
Heat 95405

Chemical Analysis

	% Vendor Certifications	ASME Code Requirements
Carbon	0.070	0.08 maximum
Manganese	1.82	2.0 maximum
Phosphorus	0.024	0.04 maximum
Sulfur	0.029	0.03 maximum
Silicon	0.38	0.75 maximum
Chromium	18.36	18-20 maximum
Nickel	8.06	8-11 maximum
Molybdenum	0.19	--
Copper	0.24	--
Columbium	0.16	--

Physical Properties

Yield Strength	48.3 ksi	30 ksi (minimum)
Tensile Strength	93.5 ksi	75 ksi (minimum)
Elongation	52%	35% (minimum)

Table C-2

PHYSICAL AND MECHANICAL PROPERTIES, LIBRARY PIPE MATERIAL (Continued)

Inconel 600 (ASTM B-167)
Heat 75000

Chemical Analysis

	% Vendor Certifications	ASME Code Requirements
Carbon	0.068	0.15 maximum
Manganese	0.31	1.0 maximum
Phosphorus	0.01	--
Sulfur	0.002	0.015 maximum
Silicon	0.29	0.5 maximum
Titanium	0.21	--
Molybdenum	0.000	--
Nickel	74.52	72 minimum
Chromium	15.8	14-17
Copper	0.09	0.5 maximum
Cobalt	0.06	--
Iron	8.7	6-10

Physical Properties

Yield Strength	35.2 ksi	30 ksi (minimum)
Tensile Strength	80.5 ksi	80 ksi (minimum)
Elongation	59%	35% minimum

Table C-3

DYNAMIC PIPE TEST, TEST PARAMETER SUMMARY

Specimen No.	Material	Flaw Type	Total Number of Load Steps	"Failure" (based on full wall penetration) Data: Average Anchor Point Deflection Amplitude (mils)	"Failure" (based on full wall penetration) Data: Average Maximum Bending Moment (in.-kip)	Remarks
SS-1	Type-304 SS	2/3 x 360°	4	87	117	
SS-3		90% x 180°	2	32	83	
SS-6		1/3 x 360°	13	248	247	
SS-8		Natural SCC	5	166	248	Unable to fail specimen
SS-9		2/3 x 360°	4	61	124	
SS-10	Type-304 SS	1/3 x 360°	4	171	248	
IN-1	Inconel 600	2/3 x 360°	6	53	128	
IN-2	Inconel 600	90% x 180°	3	23	70.4	

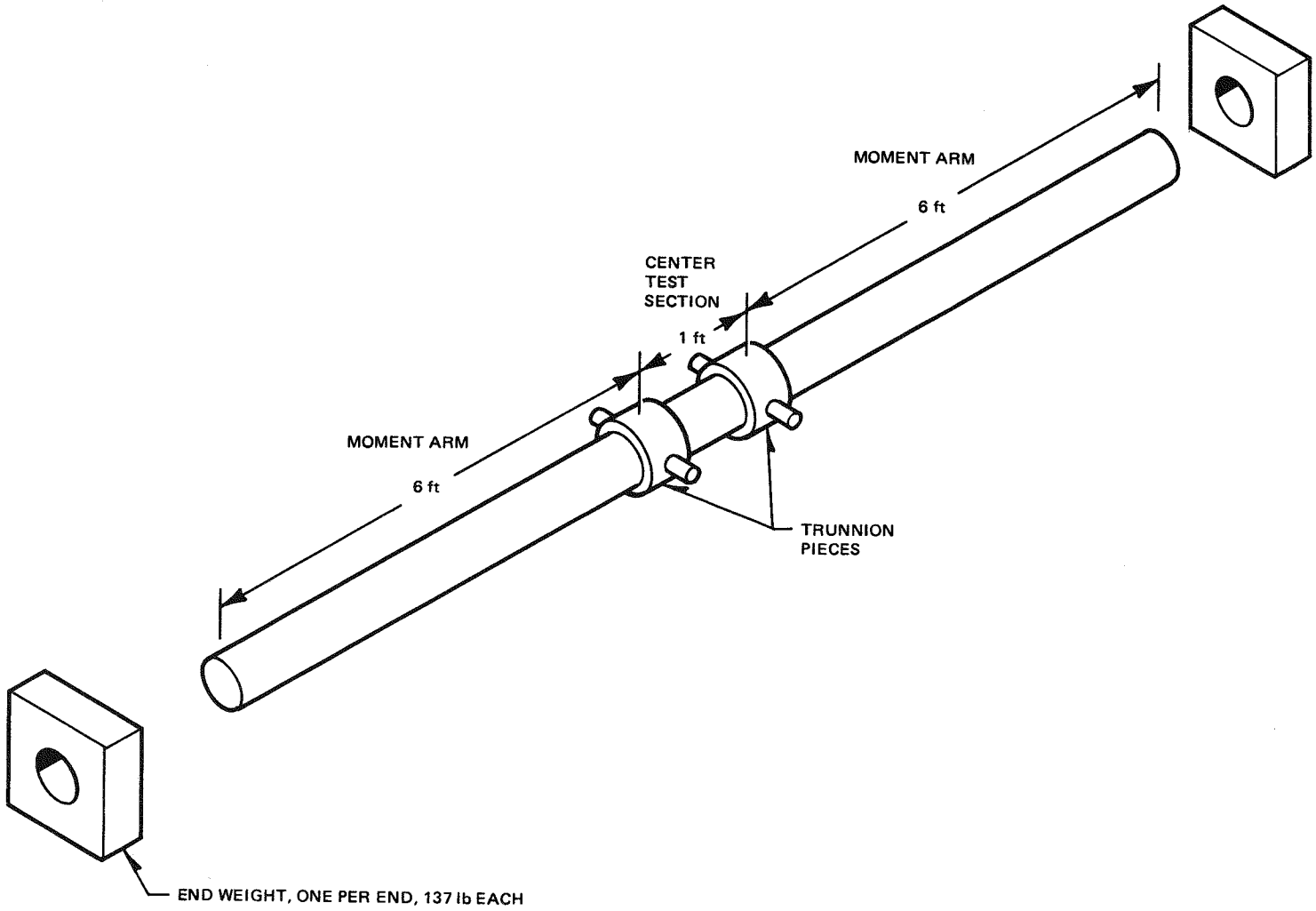

Figure C-1. Pipe Specimen Overview

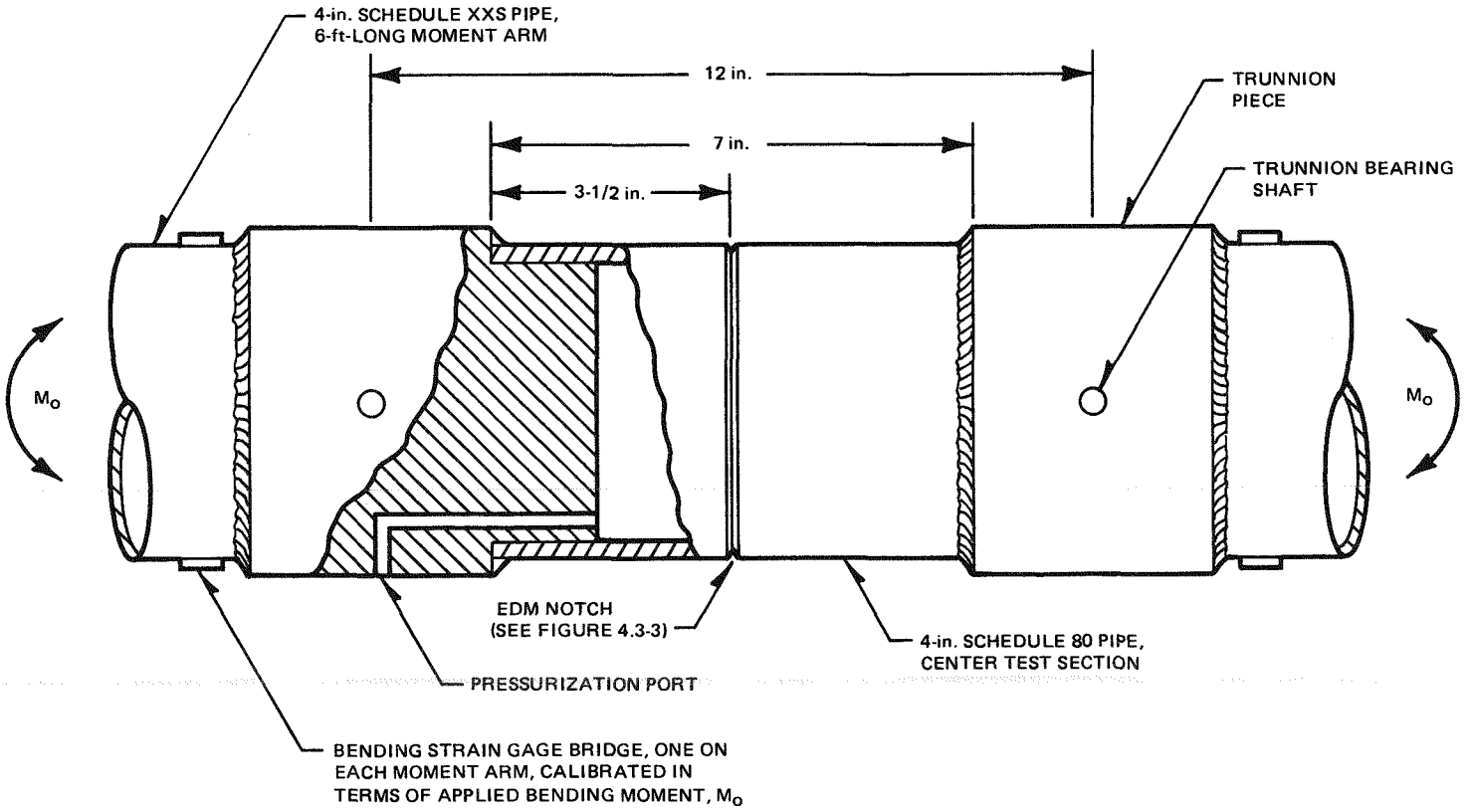

Figure C-2. Pipe Test Specimen, Details of Center Test Section

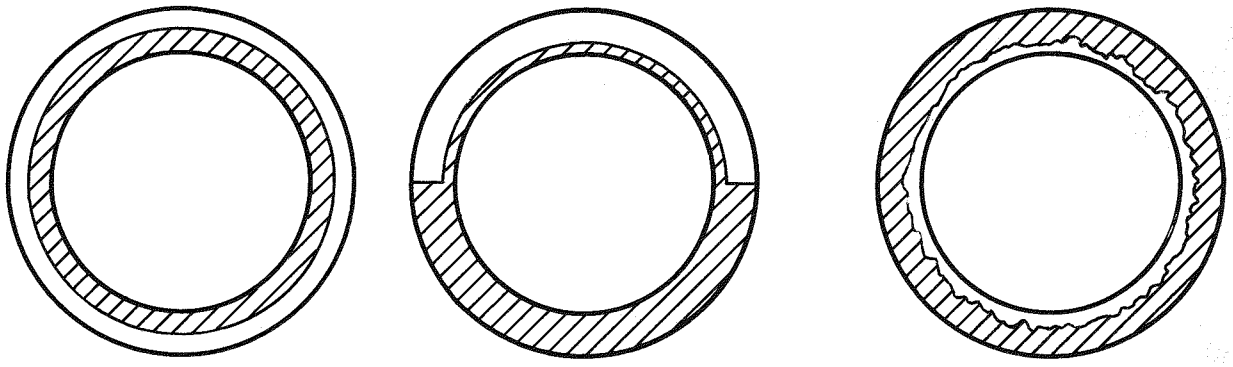

TYPE I

360° AROUND, 33% AND 66% THROUGH WALL

TYPE II

180° AROUND, 90% THROUGH WALL

TYPE III

360° AROUND, VARIABLE DEPTH DUE TO NATURAL STRESS CORROSION CRACK IN WELD HAZ

Figure C-3. Details of EDM'd Notch in Center Test Section

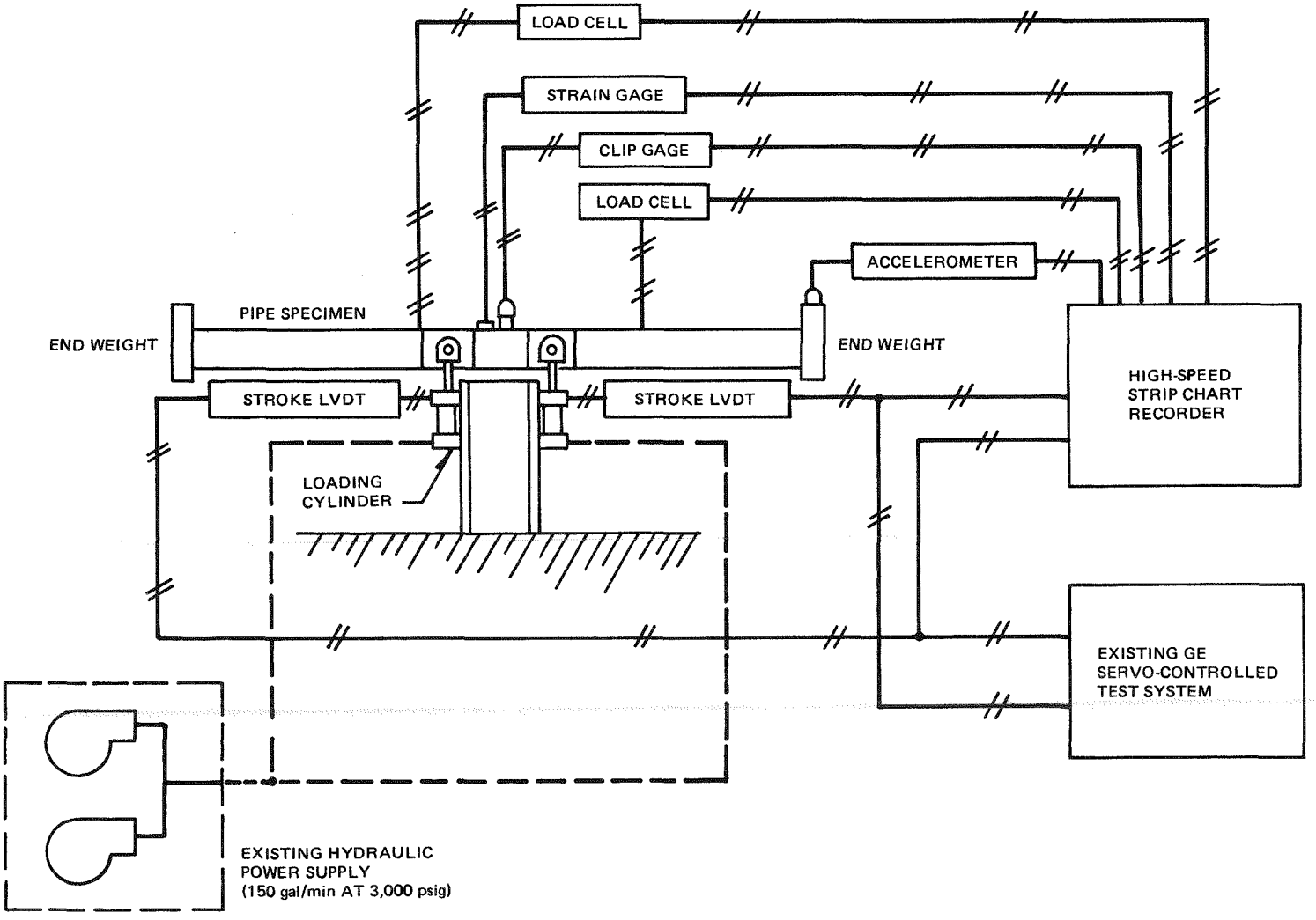

Figure C-4. Dynamic Pipe Test, System Schematic

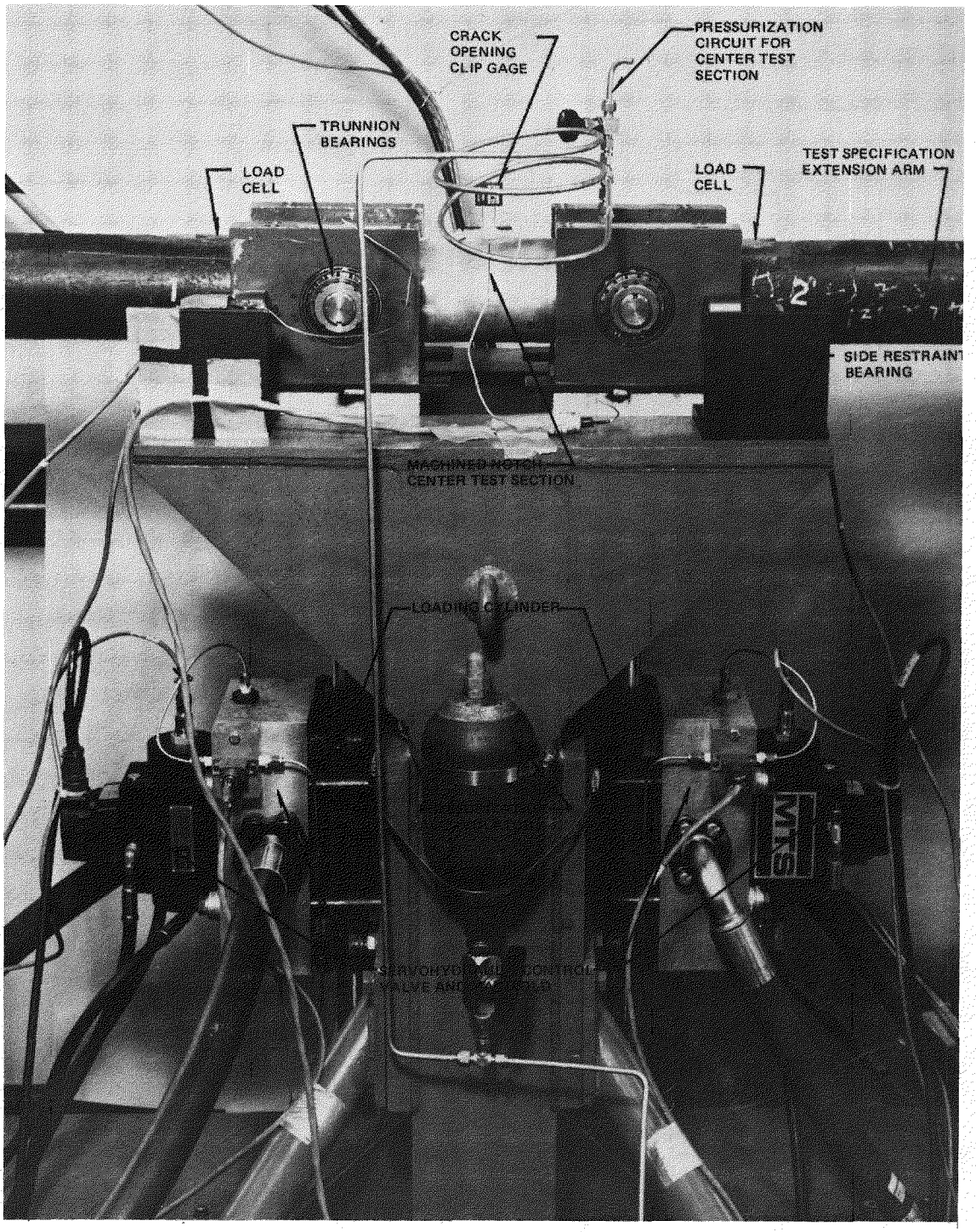

Figure C-5. Dynamic Pipe Test, Fixture Details

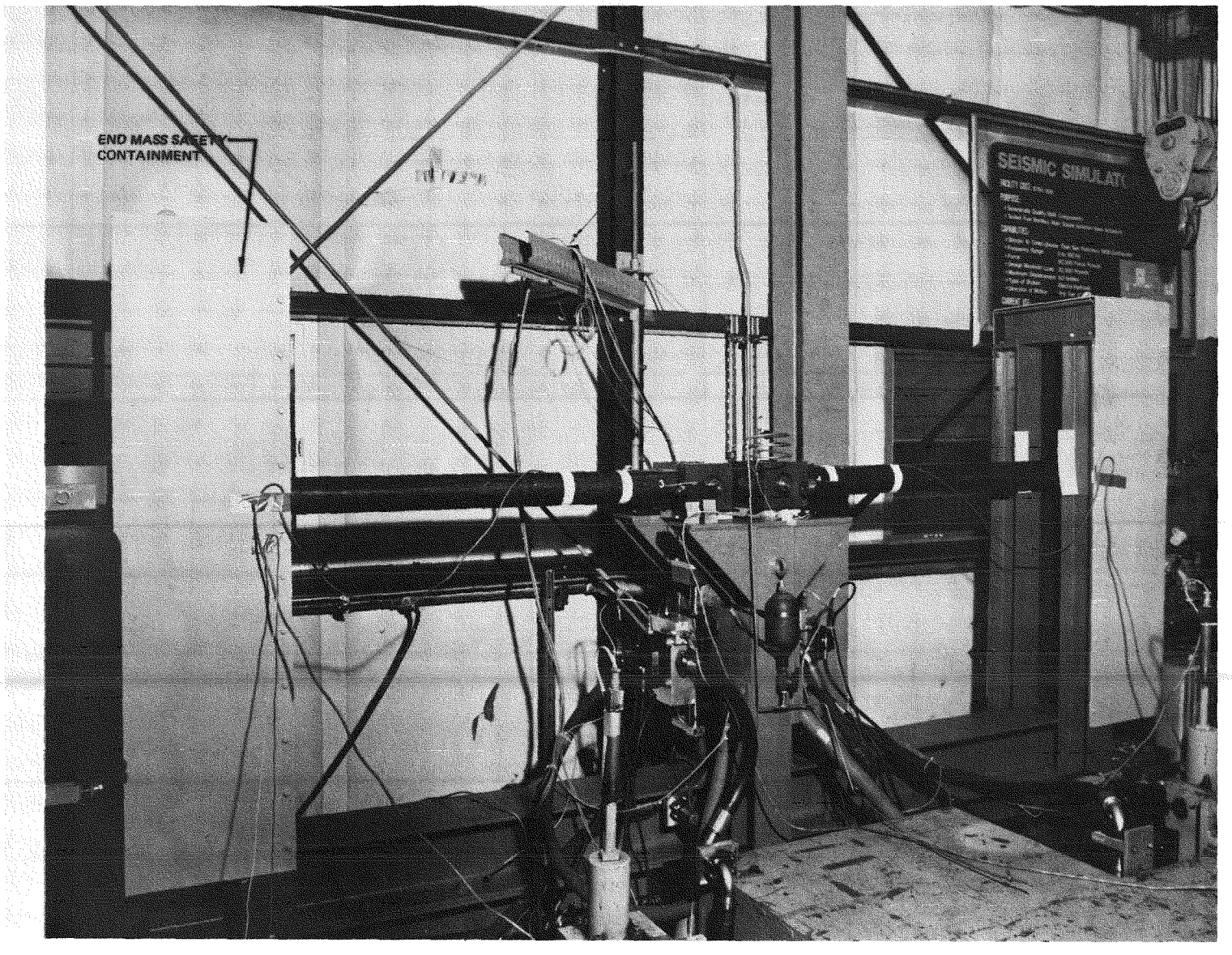

Figure C-6. Dynamic Pipe Test, Test Fixture

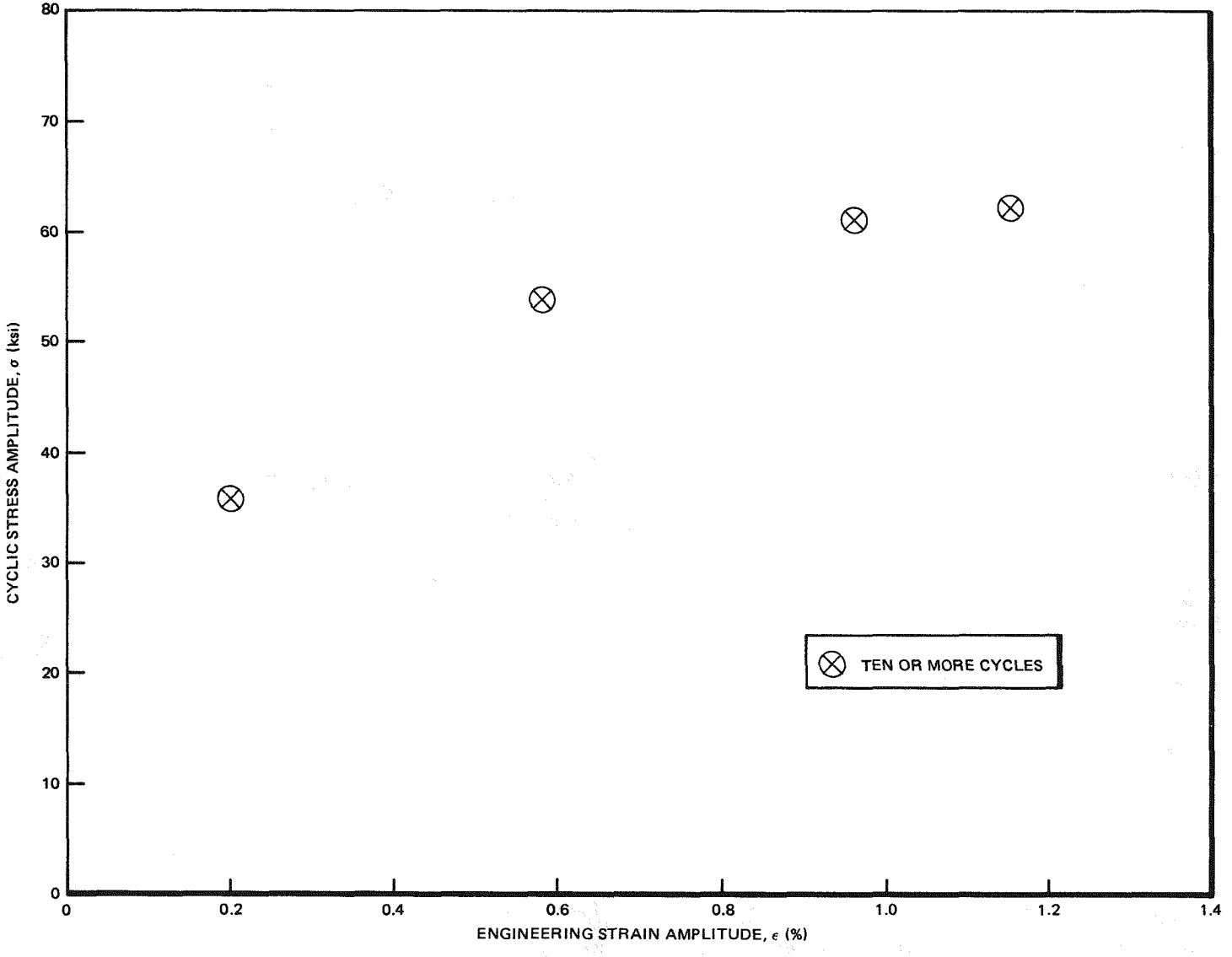

Figure C-7. Room Temperature Cyclic Stress-Strain Curve for Type-304 Stainless Steel - Heat 95405

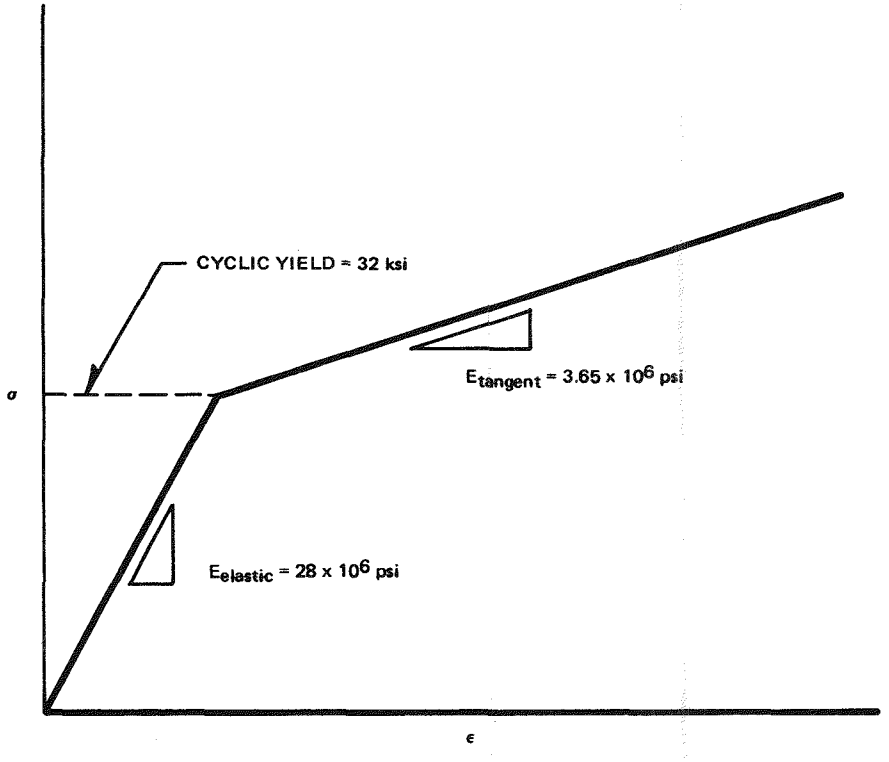

Figure C-8. Idealized Room Temperature Elastic/Plastic Cyclic Stress Strain Curve for 304 SS, Used as Input for All Dynamic Analyses

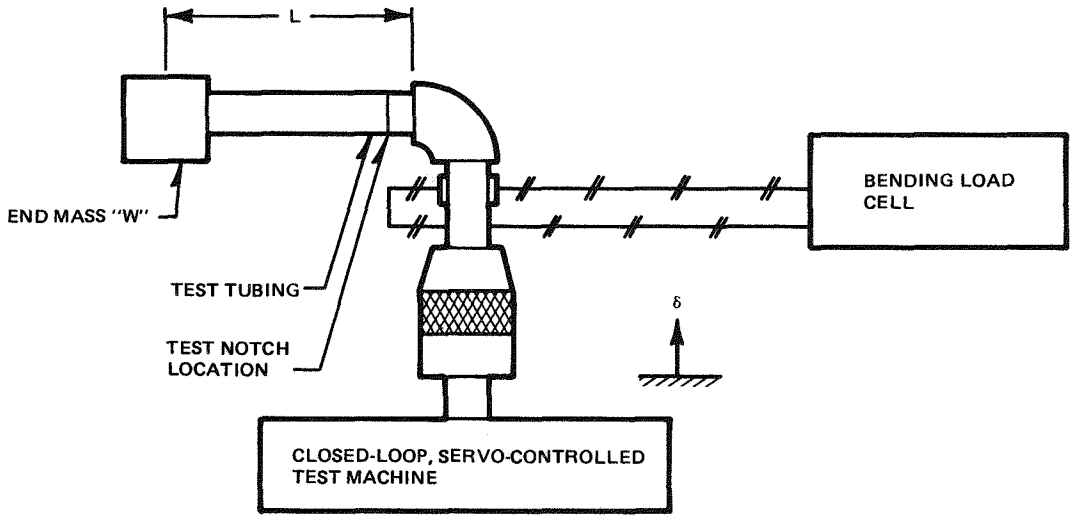

TEST CONDITIONS

TUBE* SIZE (in.)	END MASS "W" (lb)	TUBE LENGTH L (in.)	MEASURED ELASTIC FIRST MODE FREQUENCY (Hz)
0.25 o.d. x 0.035 WALL	4.19	11	4.10
0.50 o.d. x 0.065 WALL	4.19	44	2.10
1.00 o.d. x 0.049 WALL	4.19	74.5	2.31
1.00 o.d. x 0.049 WALL	4.19	44	4.82

*TYPE-304 STAINLESS STEEL

Figure C-9. Small Specimen Test Configuration

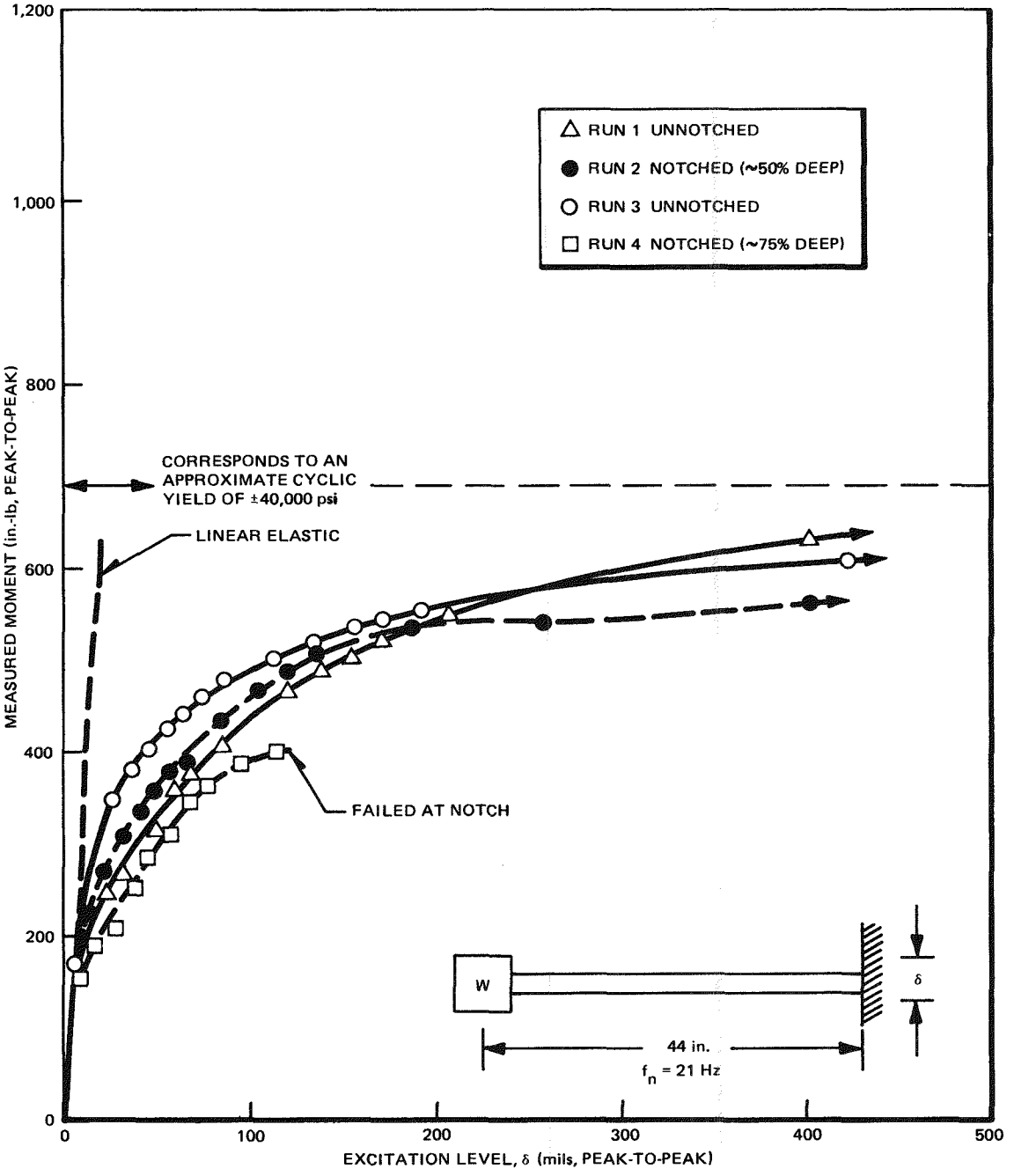

Figure C-10. Small-Scale Test Results, Type-304 Stainless Steel, 0.50-in.-o.d. x 0.065-in. Wall Tubing, Resonant Following Technique

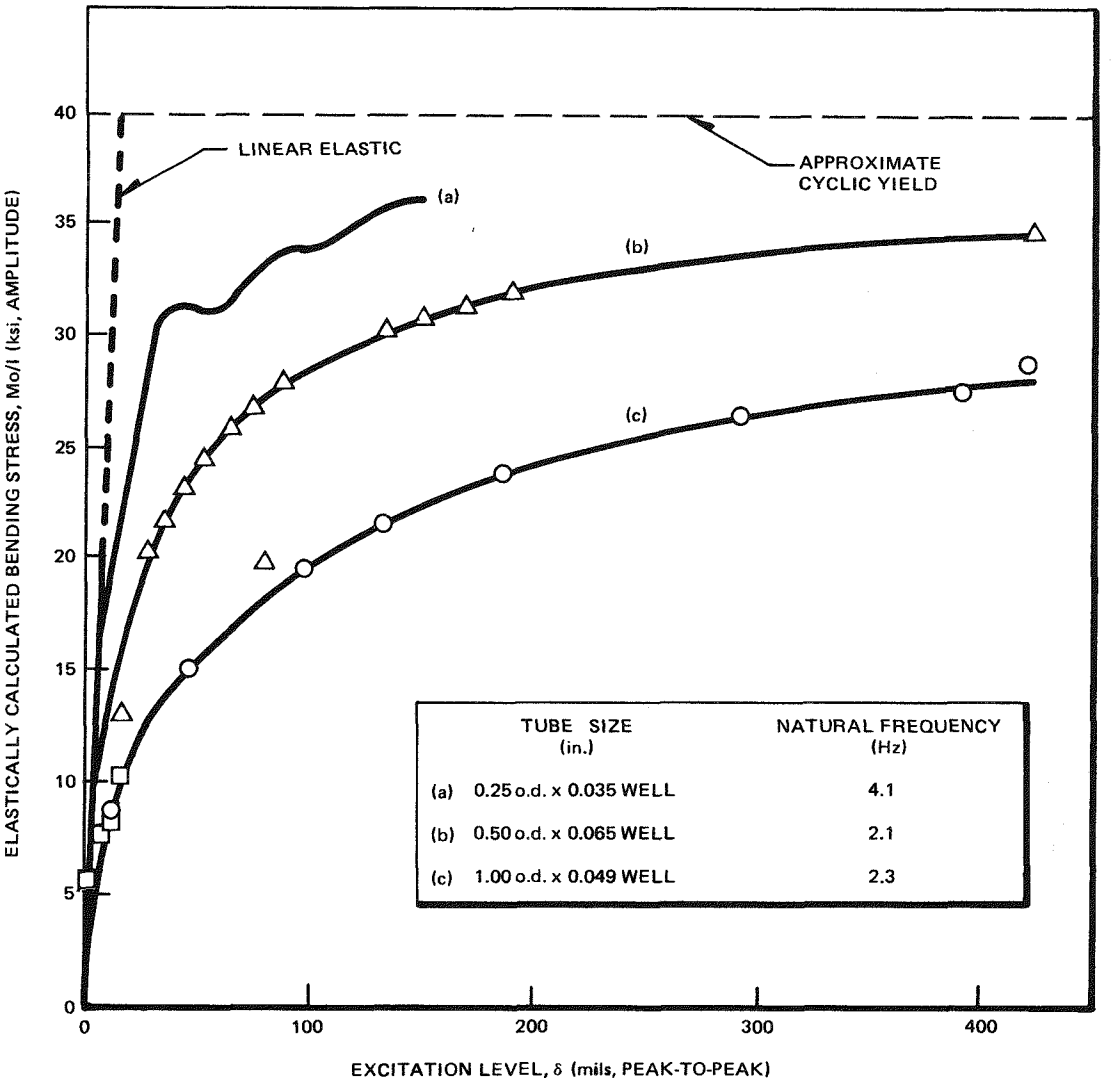

Figure C-11. Small-Scale Test Results, Type-304 Stainless Steel Tubing, Size Effects, Resonant Following Technique

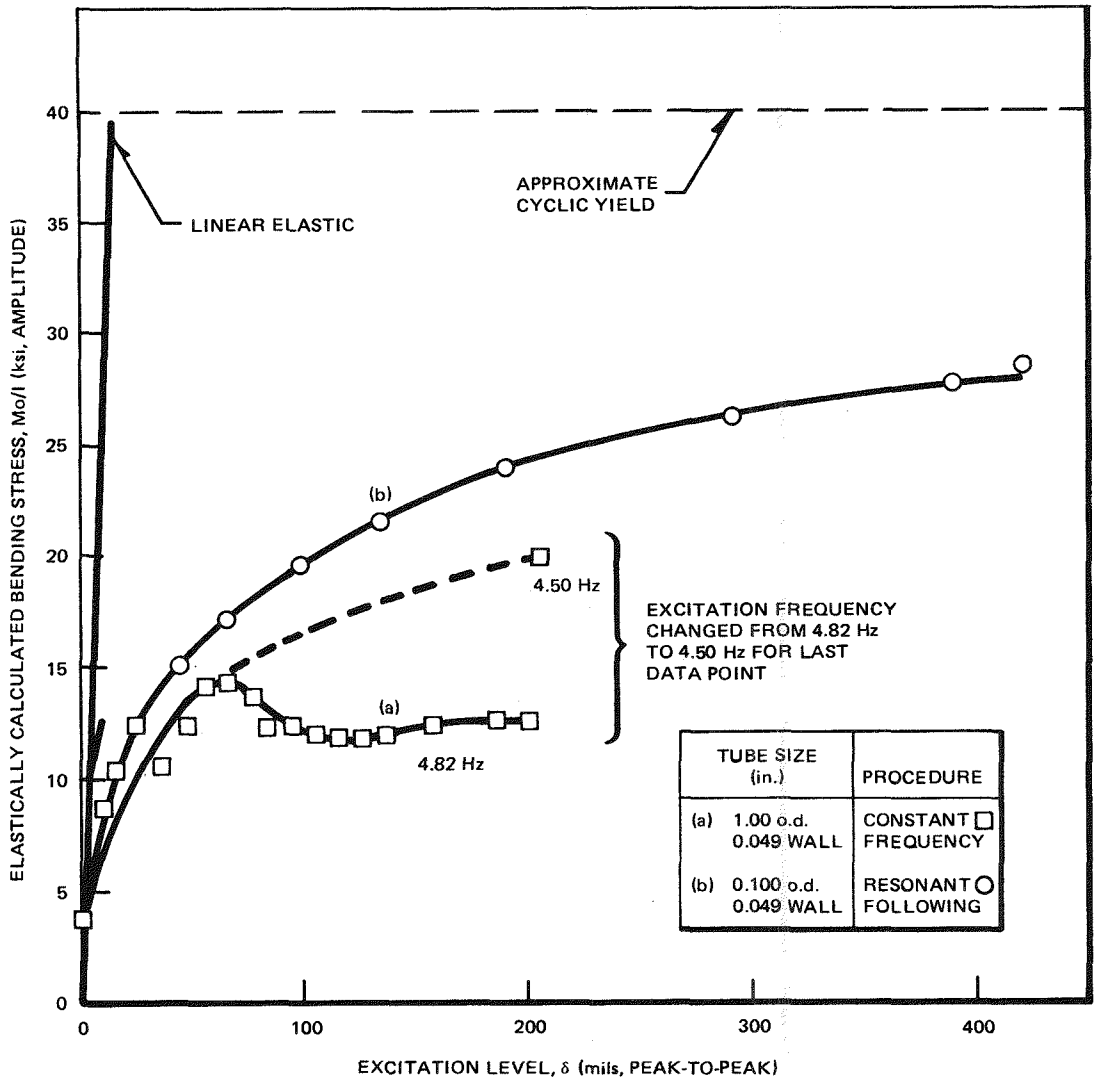

Figure C-12. Small-Scale Test Results, Type-304 Stainless Steel Tubing, Resonant Following versus Constant Initial Frequency

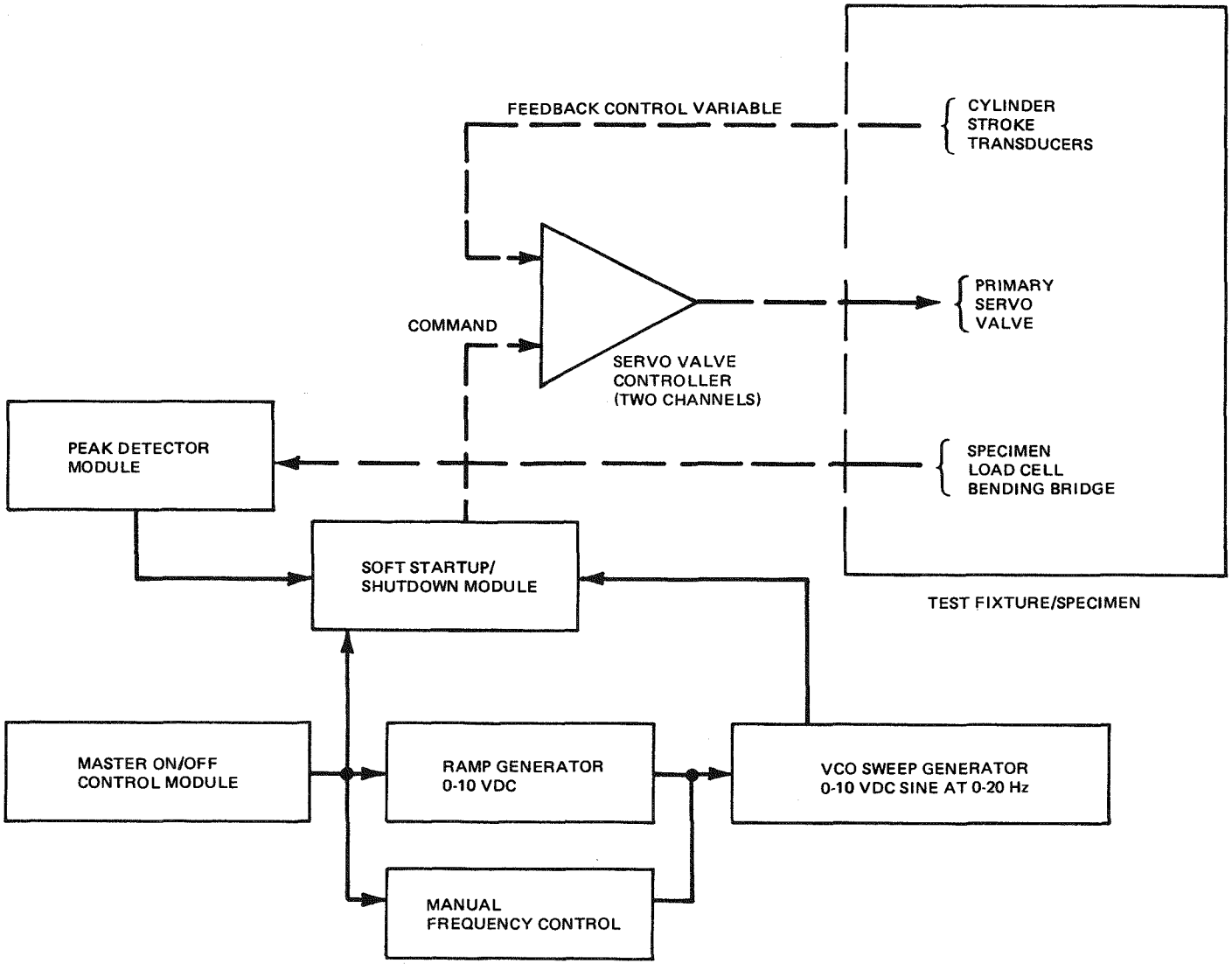

Figure C-13. Dynamic Pipe Test, Control Schematic

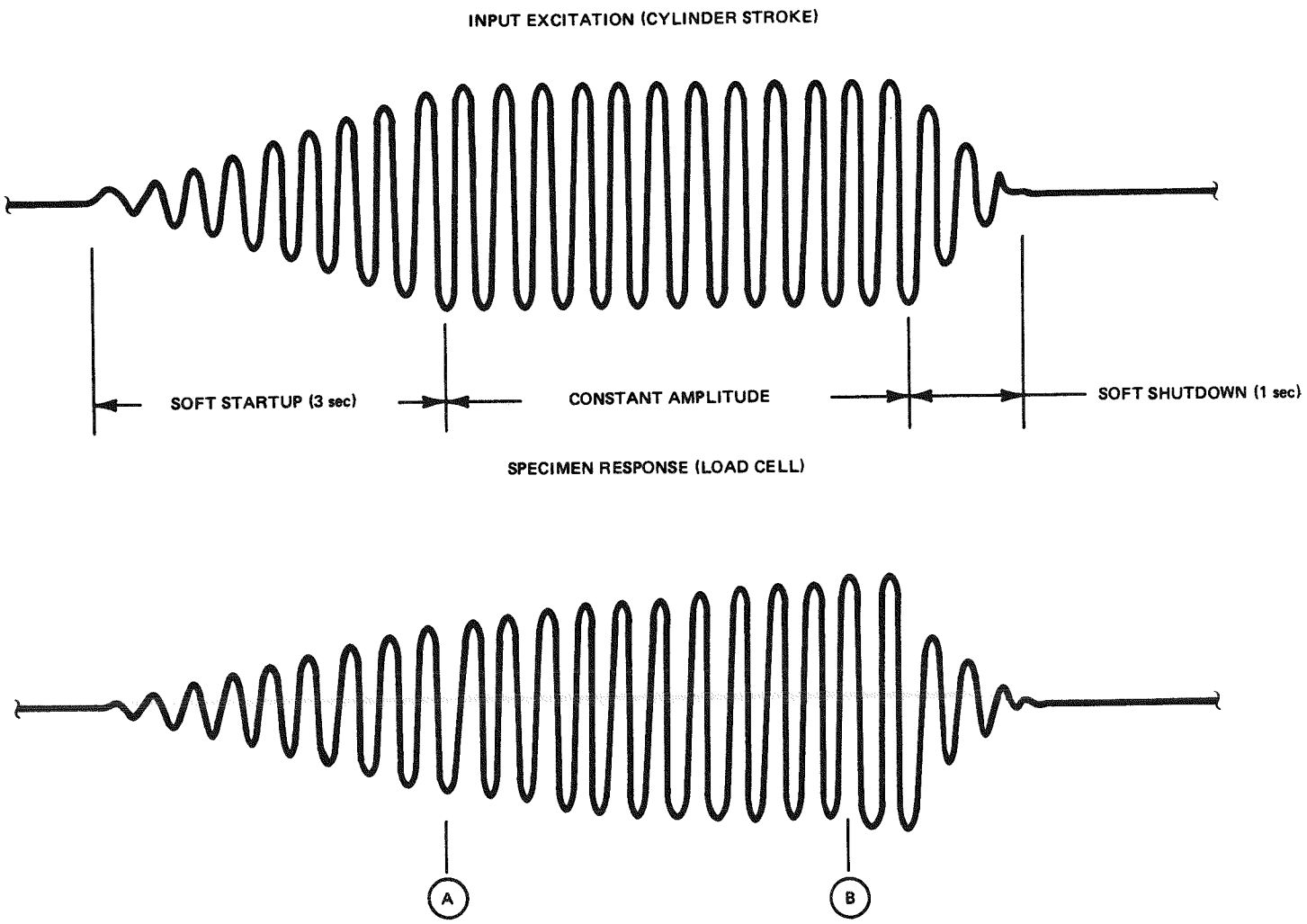

Figure C-14. Ideal Dynamic Pipe Test Sequence

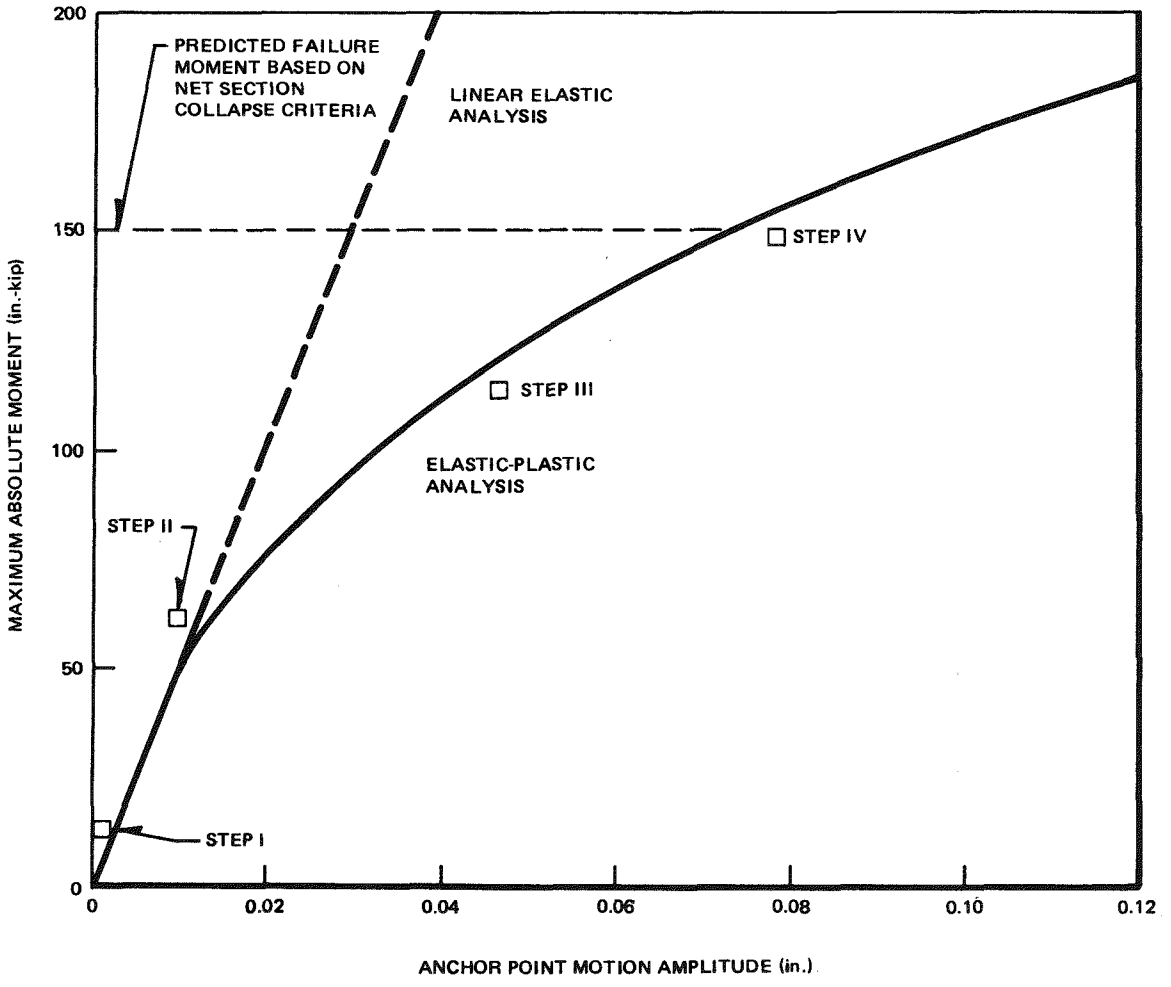

Figure C-15. Typical Dynamic Pipe Test Sequence

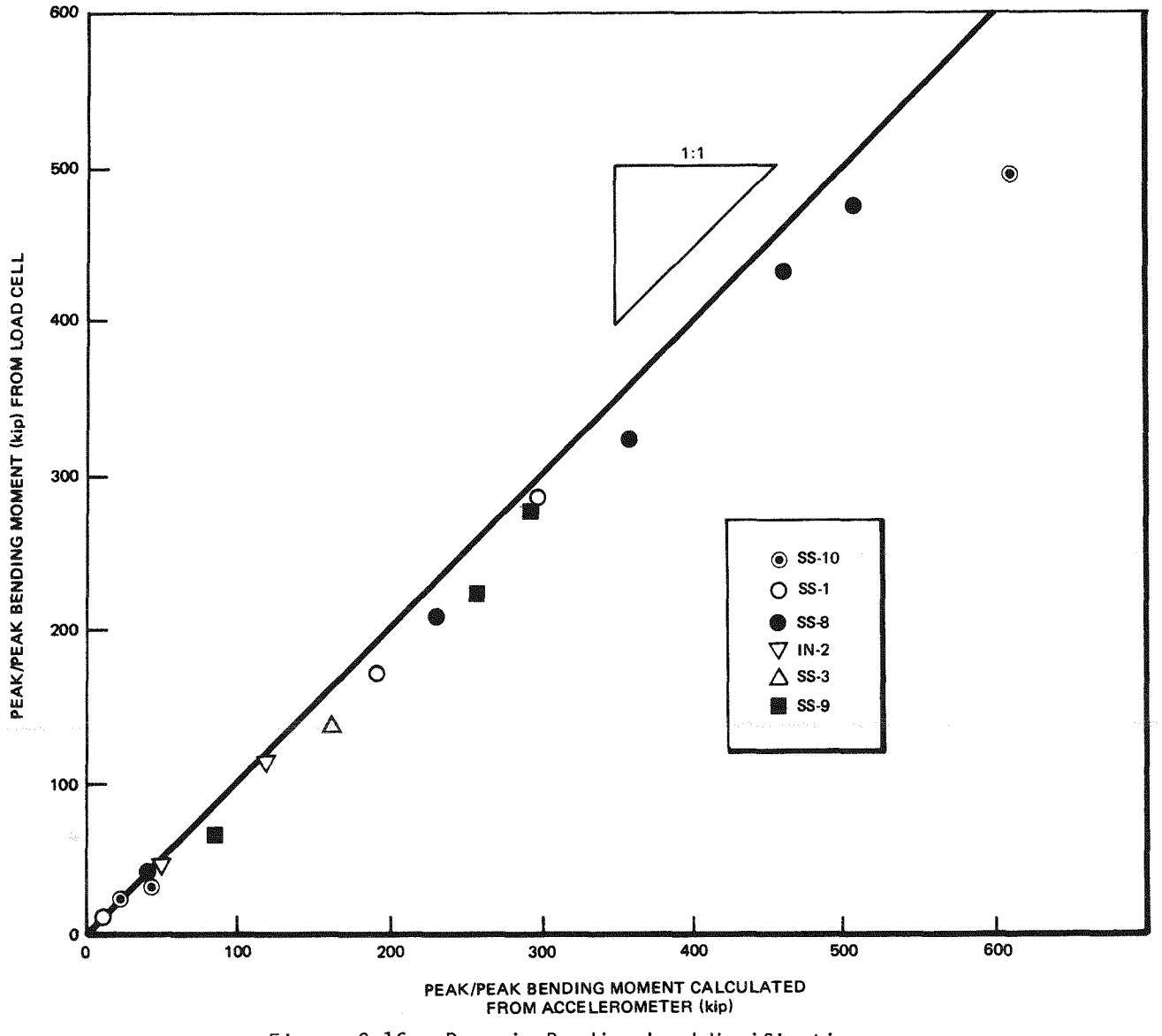

Figure C-16. Dynamic Bending Load Verification

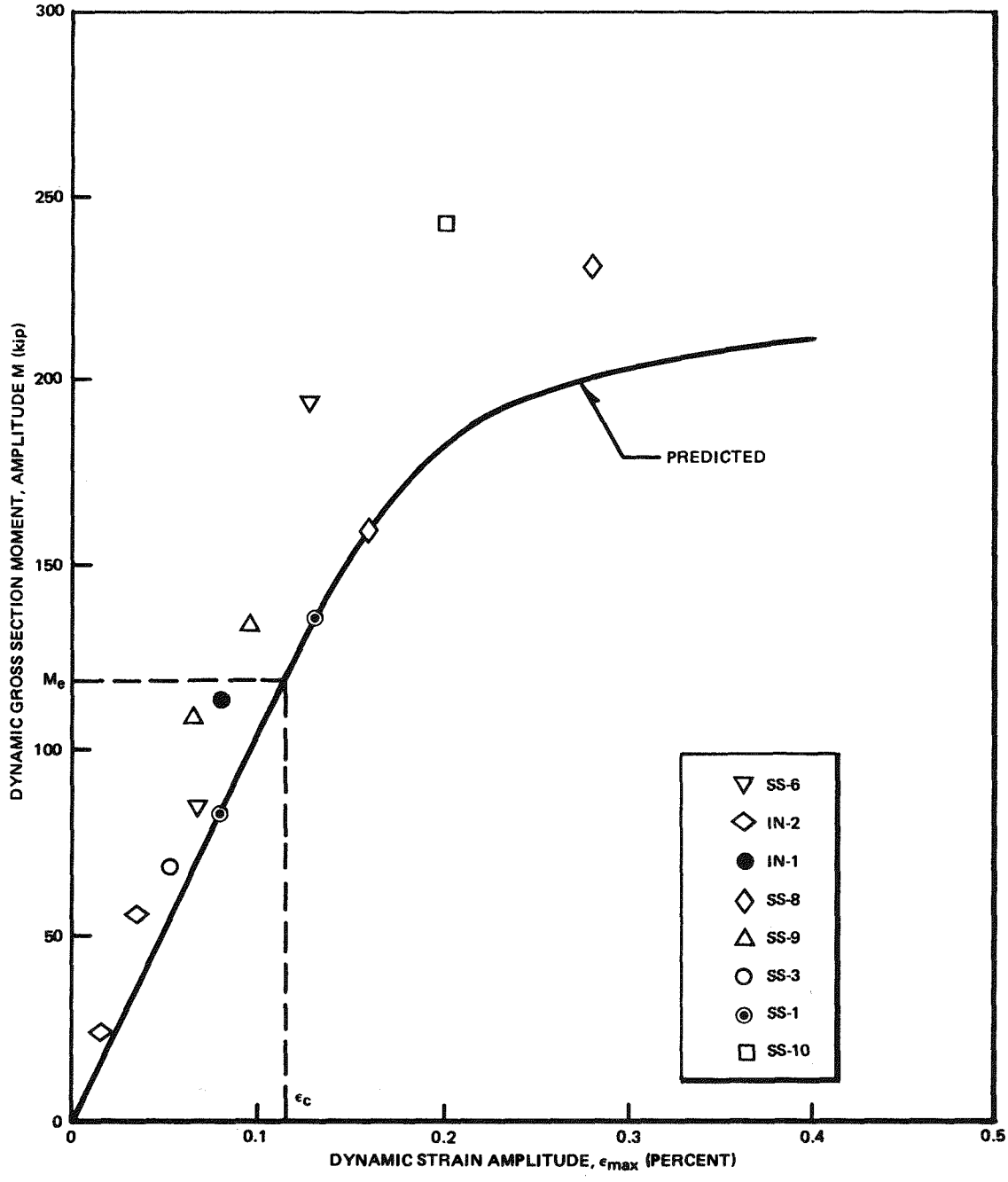

Figure C-17. Comparison of Predicted Gross Section Moment in Center Test Section, versus Actual, Based upon Strain Gage Readings

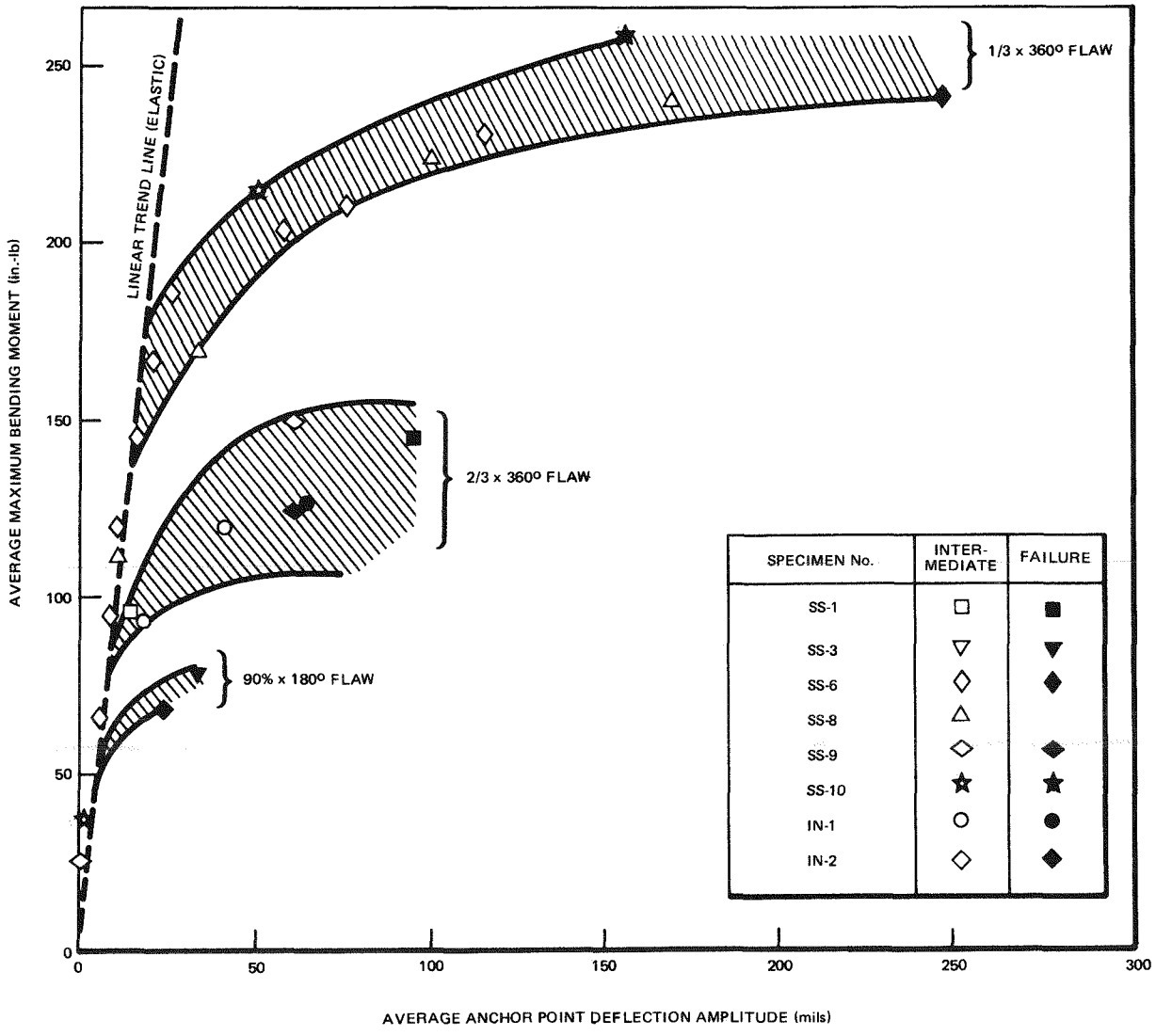

Figure C-18. Dynamic Pipe Test, Response/Failure Data

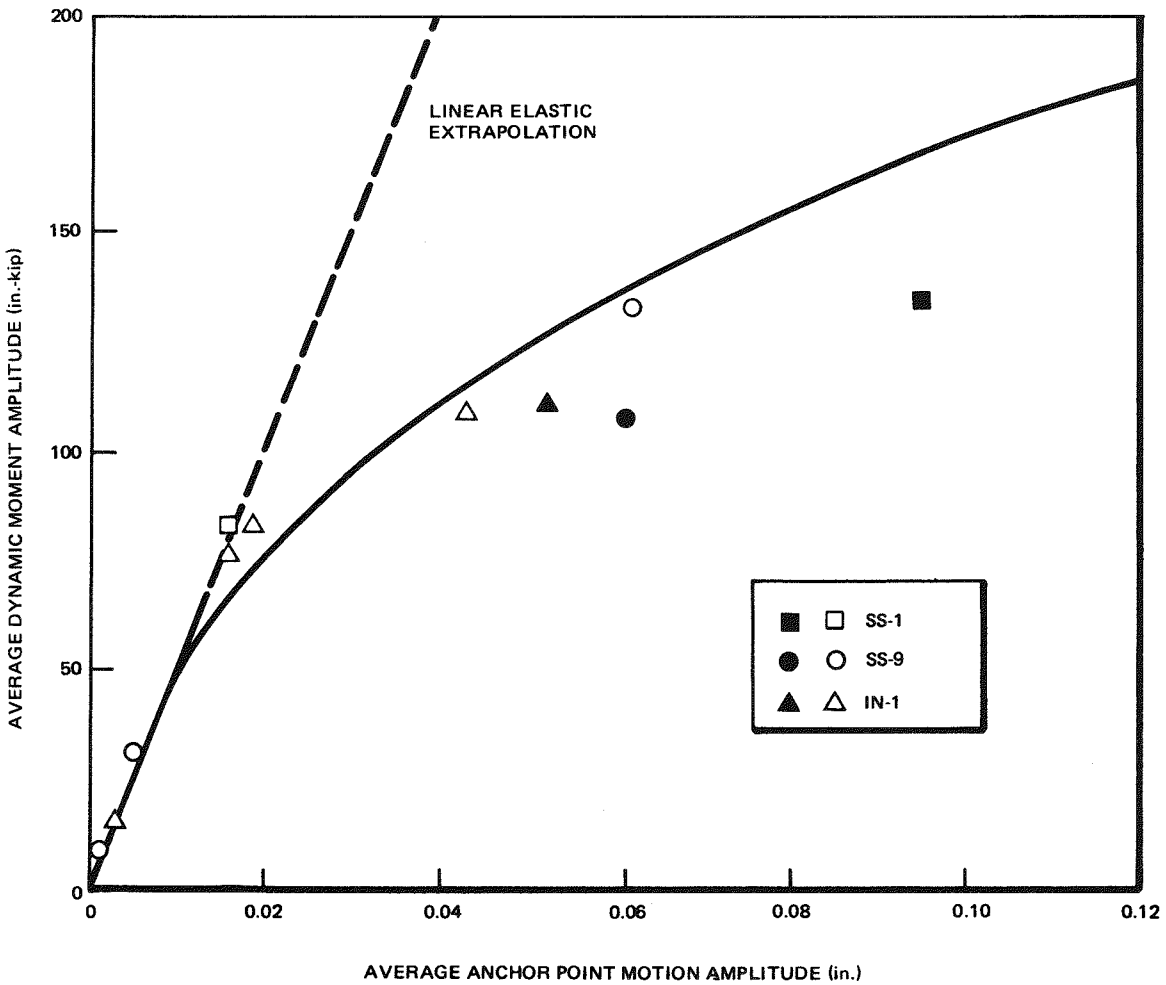

Figure C-19. Comparison of Dynamic Pipe Test Results to Elastic-Plastic Dynamic Analysis-Predicted Response, 2/3 x 360° Flaw, f_n - 12 Hz

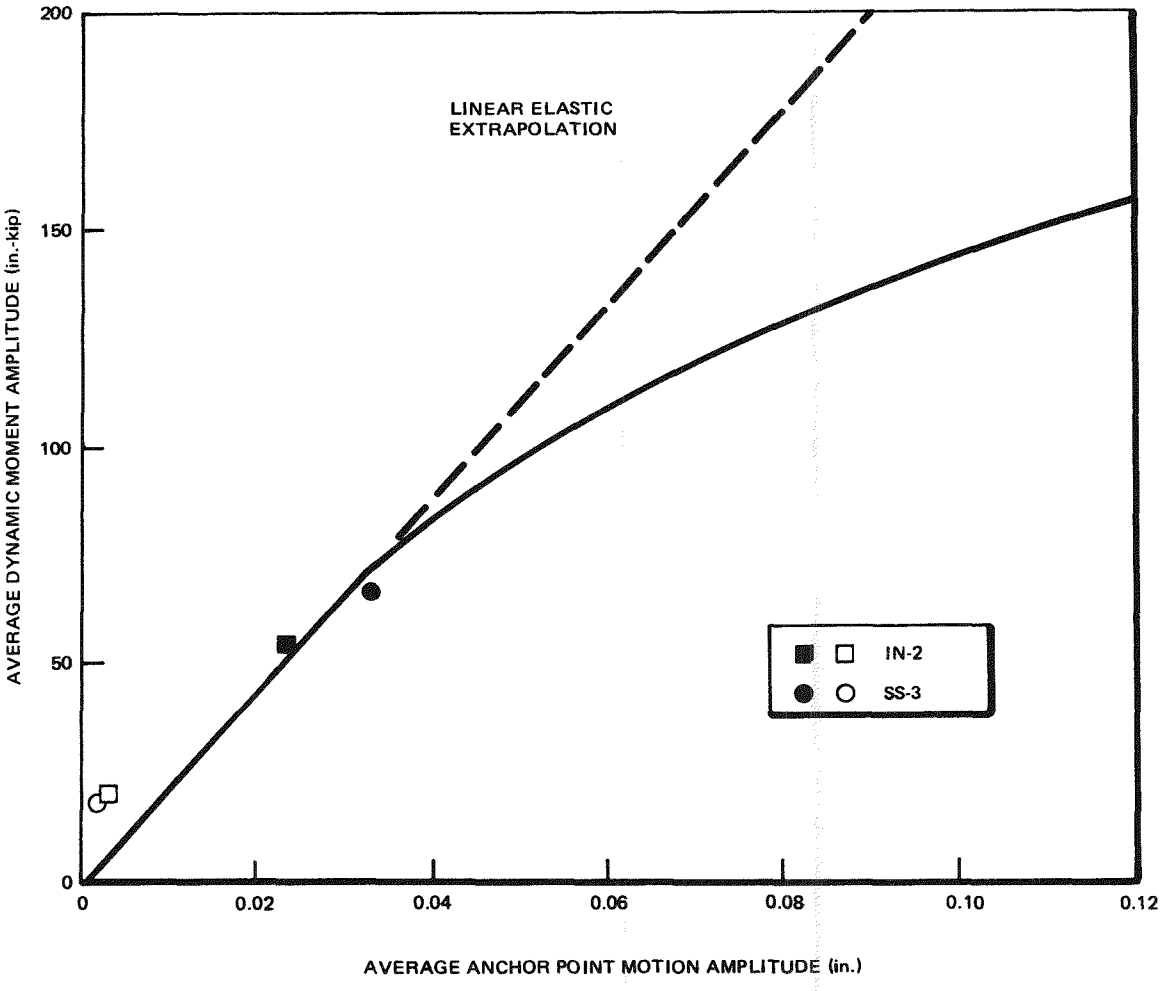

Figure C-20. Comparison of Pipe Test Results to Elastic-Plastic Dynamic Analysis-Predicted Response, 90% x 180° Flaw, f_n = 12 Hz

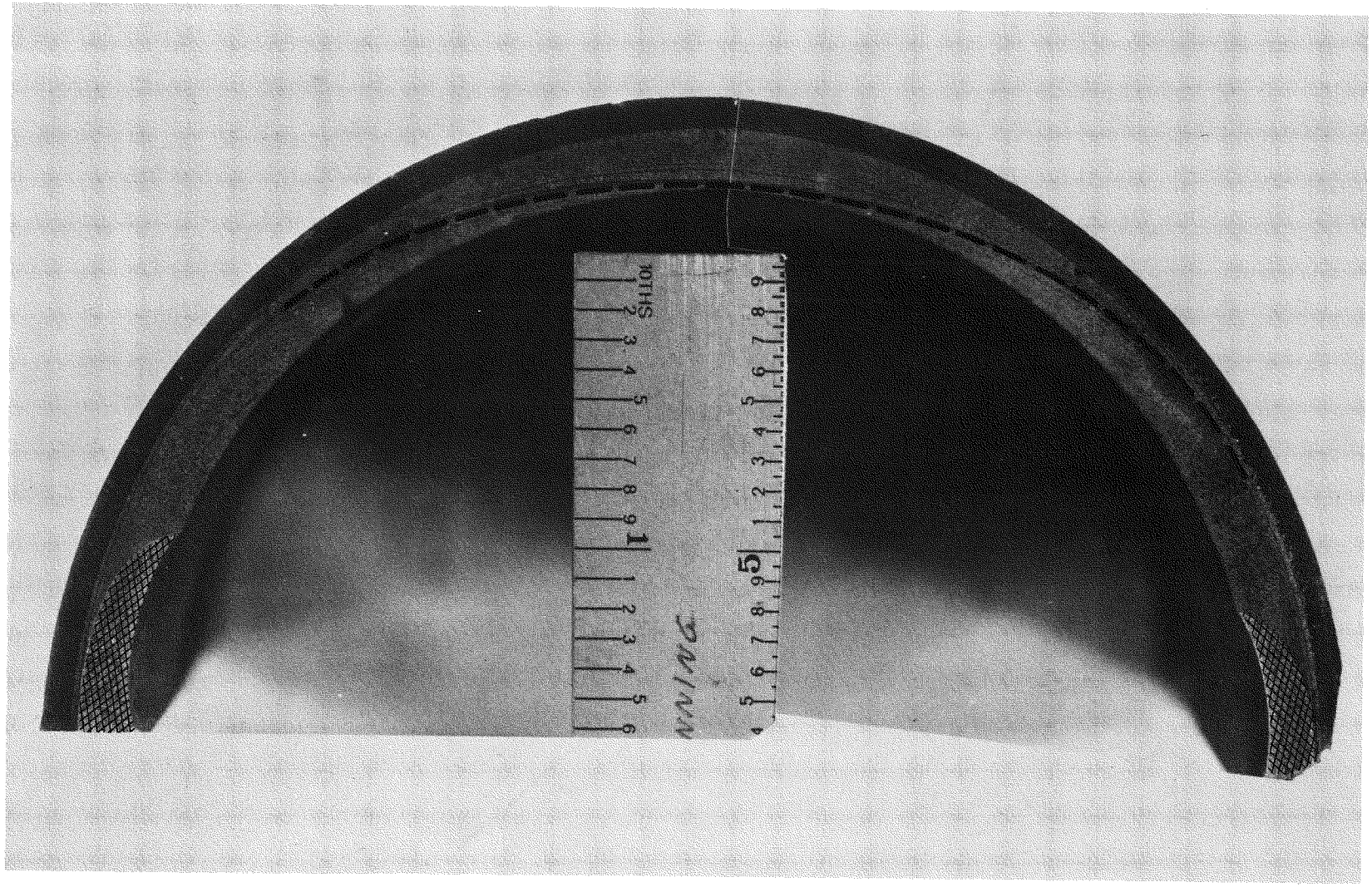

Figure C-21. Post-Test Fracture Surface, Specimen SS-10

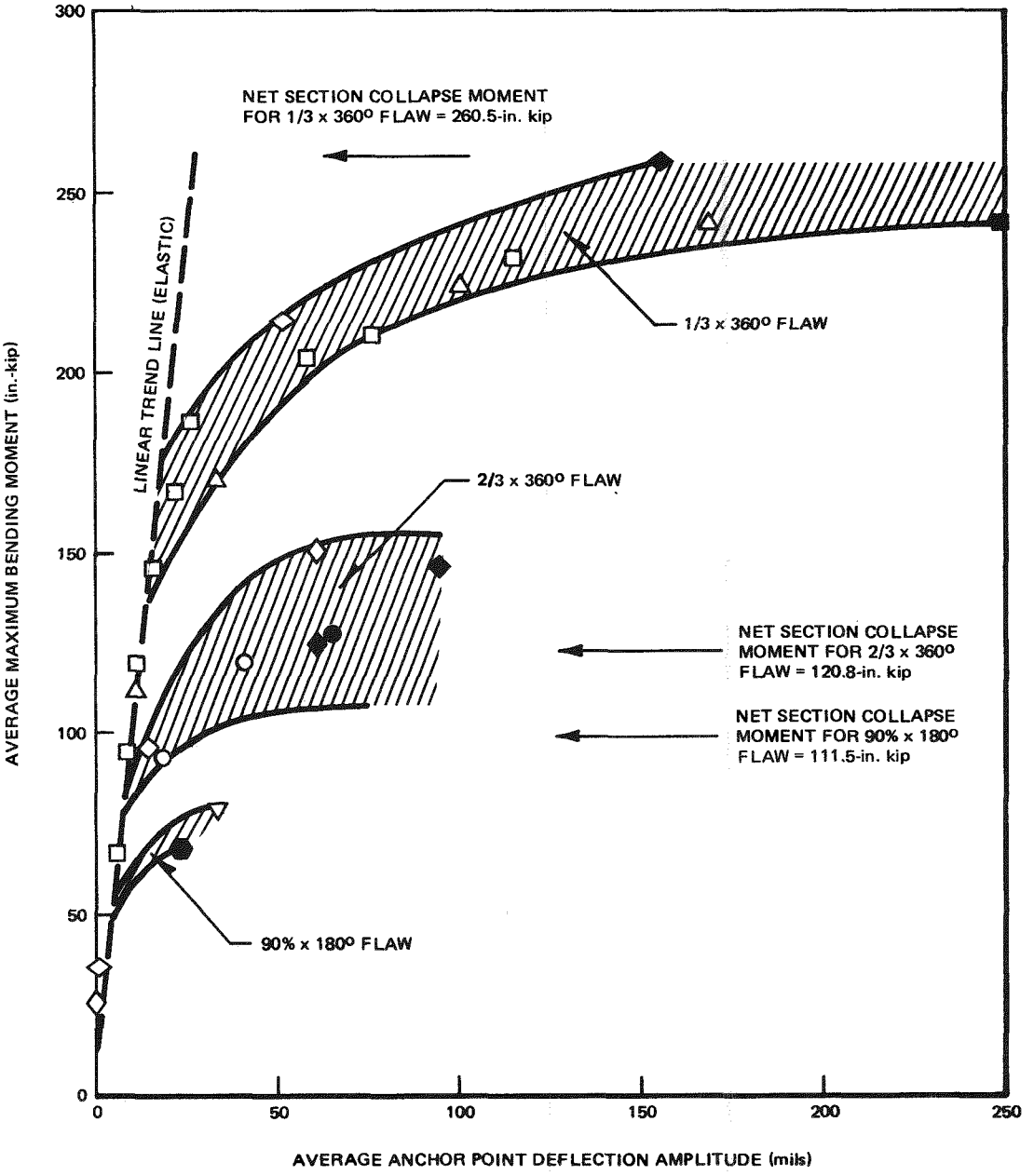

Figure C-22. Dynamic Pipe Test, Response/Failure Data Compared to Calculated Net Section Collapse Moment (based on FS = 70.9 ksi)

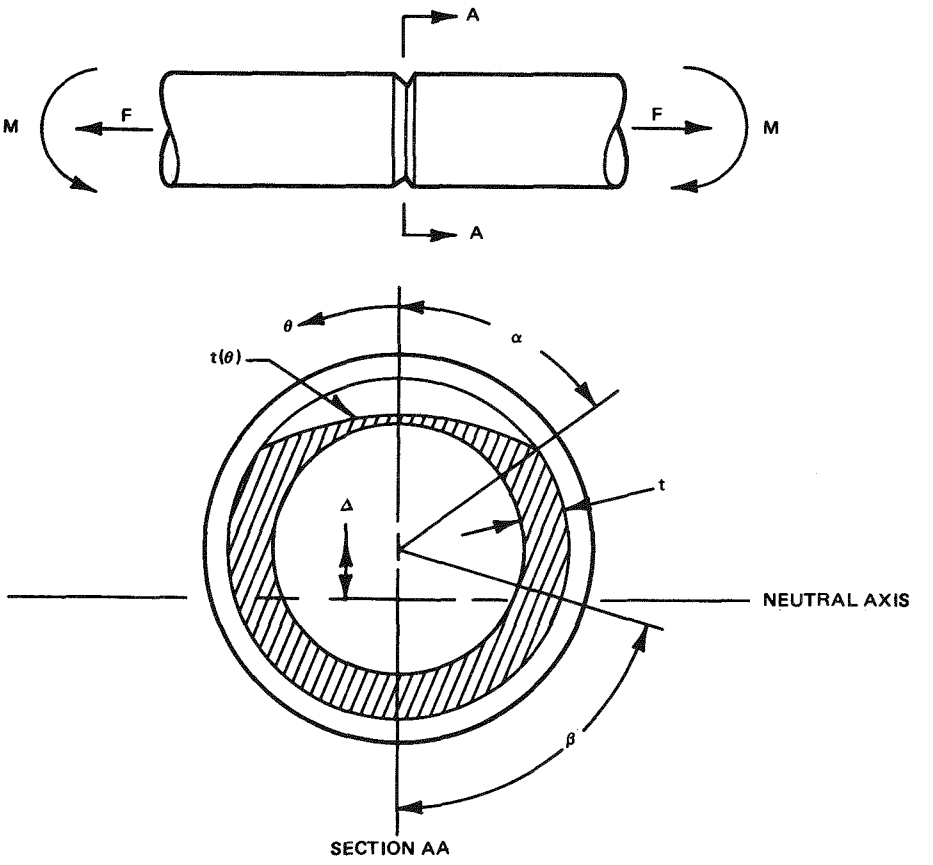

R_N = AVERAGE RADIUS OF ORIGINAL MACHINED FLAW

t = NOMINAL WALL THICKNESS OF ORIGINAL MACHINED FLAW

β = HALF ANGLE IDENTIFYING NEUTRAL AXIS LOCATION

α = HALF ANGLE DEFINING LIMIT OF ARBITRARY FLAW

$t(\theta) = a + b\theta + c\theta^2$

Δ = SHIFT IN NEUTRAL AXIS FROM AXIS OF SYMMETRY

Figure C-23. Net Section Collapse Moment Calculation for Arbitrary Flaw Geometries in a Pipe Loaded in Combined Bending and Axial Loads

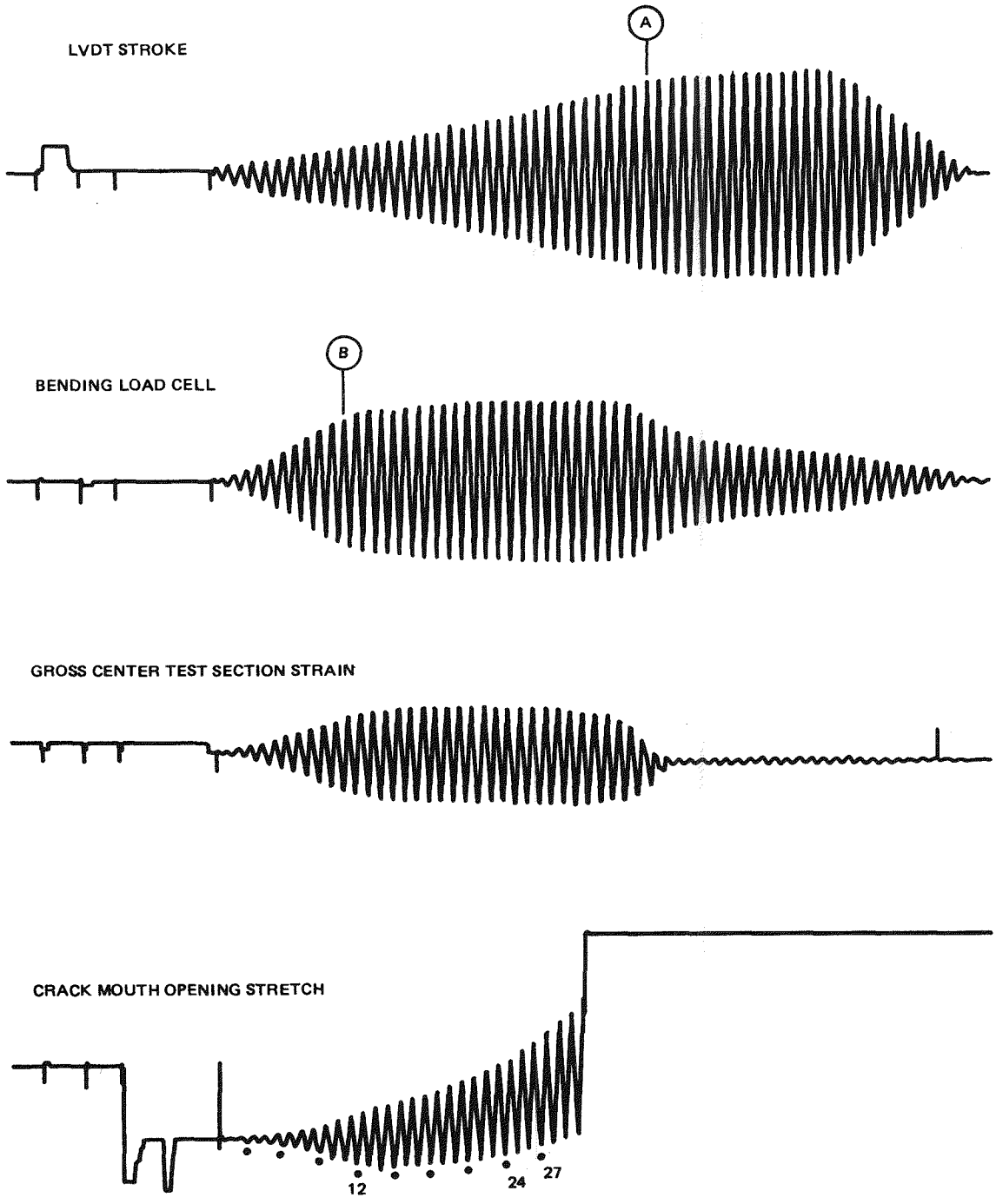

Figure C-24. Typical Dynamic Test Data, Specimen SS-10, Load Step 4

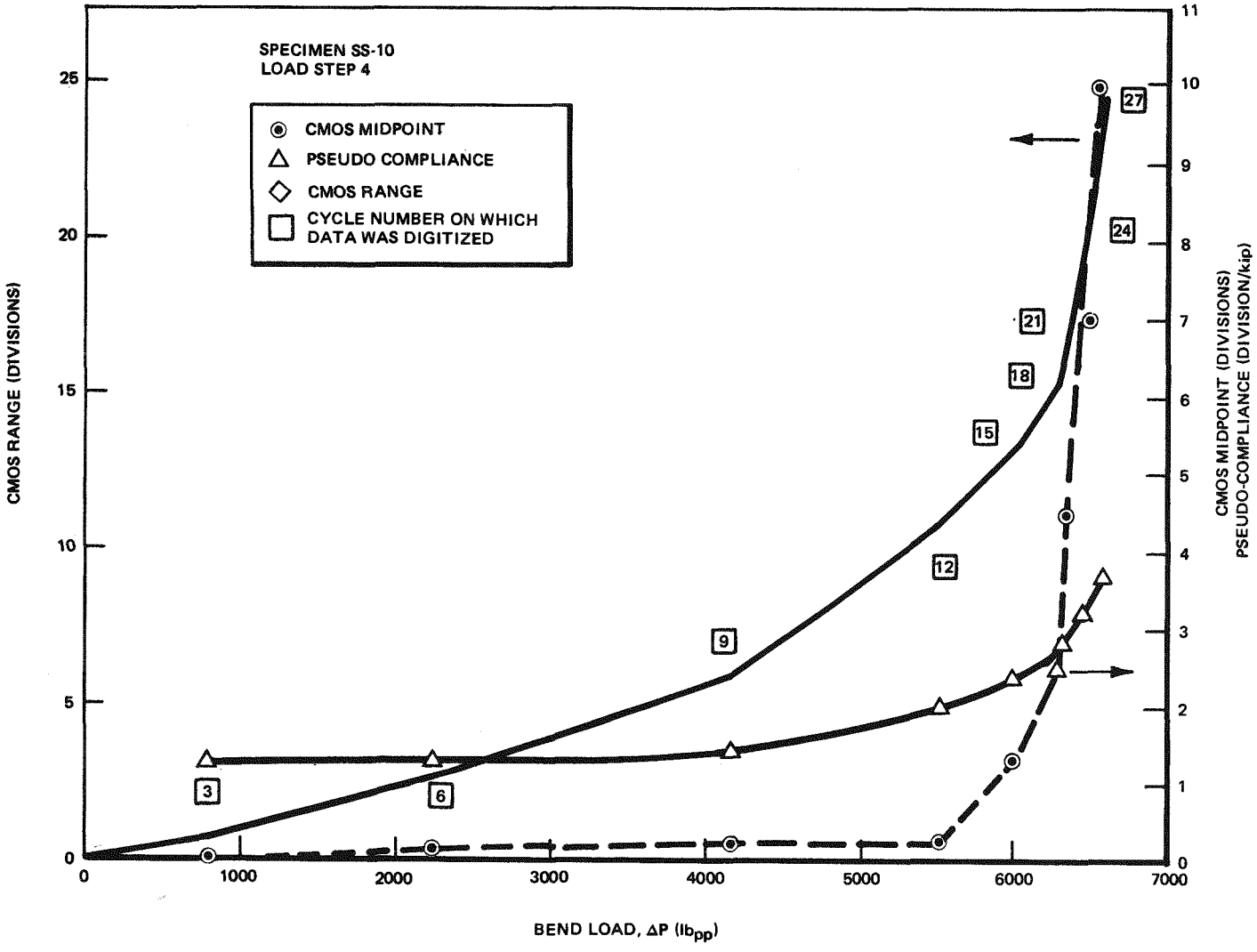

Figure C-25. Cross Correlation of Digitized SS-10 Data

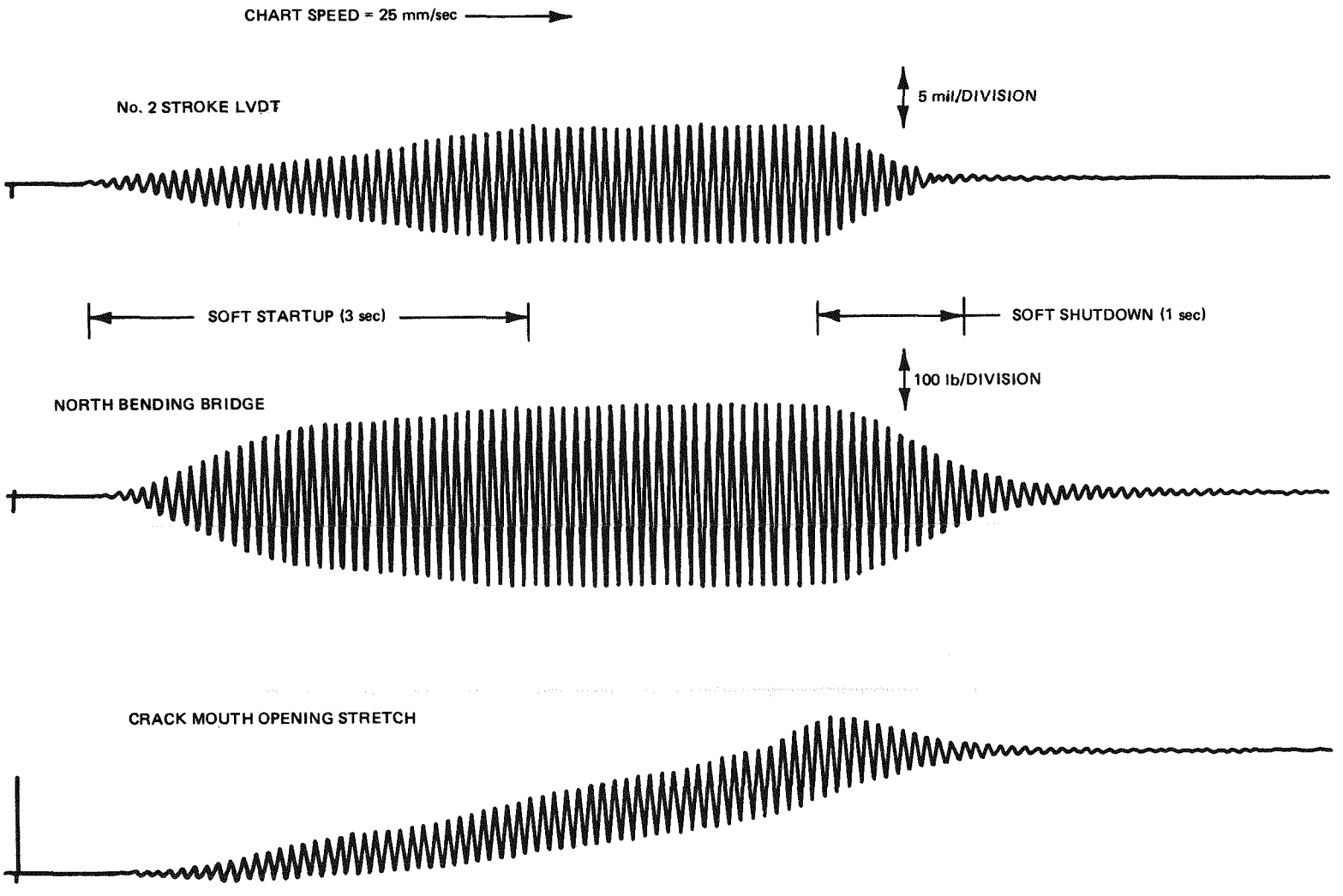

Figure C-26. Typical Dynamic Pipe Test Data, Specimen SS-9, Load Step 3

Appendix D

PREDICTION OF LEAK RATES
(S. Ranganath)

D.1 INTRODUCTION

Reliable prediction of leak rates from cracks in pipes, using analytical models is extremely difficult because of uncertainty in field conditions as well as in the physical processes that govern leakage from cracks. For example, the estimate of the crack opening area is dependent on the previous stress-strain history, material yield properties, and other restraints from the system that might limit crack opening displacement. Similarly, leakage from a crack is also a function of the actual geometrical details and other friction effects. For example, the presence of a tight crevice will inhibit leakage from a crack. Also, when leakage does occur from a pressurized pipe, there is very rapid change of phase and steam formation. Precise prediction of the leak rate under two-phase blowdown conditions is extremely difficult. Finally, experimental data on leak rates from piping with well-defined crack configurations is limited. Therefore, there is not enough leak rate data to verify the predictions of the analytical models. There are EPRI-sponsored programs underway to address the two key issues on leak rates - prediction of the crack opening area as a function of the applied loading and the prediction of the leakage rate for a given crack opening area. While the results of these programs will ultimately enable more accurate prediction of leak rates in piping, simpler models are useful in the interim to derive general conclusions on the influence of crack length and pipe size on leak rates in piping. This section provides simplified methods for the assessment of crack opening area in piping. Once the crack opening area is known, the leak rate can be estimated based on assumed values of the friction factor and the blowdown model. Since most power plants have restrictions on the unidentified leak rates (such as leaks from pipe cracks) above which the plant has to be shut down, the maximum through-wall crack that would leak the limiting leak rate (generally 5 gallons per minute) can be estimated.

D.2 DETERMINATION OF CRACK OPENING AREA

The method used to predict the crack opening area is based on the Goodier-Field approximation (D-1) using the Dugdale model (D-2) for a through-crack in a plate.

Consider a through-crack of length 2ℓ in an infinite plate subjected to a uniform stress σ. It can be shown by Linear Elastic Fracture Mechanics (LEFM) analysis that the crack opening displacement at the center of the crack is

$$\delta = 2v = \frac{4\sigma\ell}{E} \tag{D-1}$$

where E is the Young's modulus, and v is the displacement at the center.
From LEFM it can also be shown that the crack opening profile is elliptical and the crack opening area is given by the area of the ellipsi

$$A_e = \frac{\pi}{4} (\delta) (2\ell) = \frac{2\sigma\ell^2}{E} \tag{D-2}$$

This represents the crack opening area under LEFM conditions. However, in ductile materials there is some yielding at the crack tip. Dugdale's strip yield model assumes that there is a finite "strip" adjacent to the crack that is at yield stress and there is no stress singularity at the end of the yield zone. Figure D-1 shows the crack configuration in a plate including the plastic zone. The assumption of no singularity at the end of the strip yield zone leads to relationship

$$a = \ell \sec \left(\frac{\pi\sigma}{2\sigma_y}\right) \tag{D-3}$$

where 2a is the apparent crack length including the plastic zone which is subject to the yield stress σ_y. From Reference D-1, the displacement v(x) is given by

$$v(x) = \frac{\sigma_y \ell \sec \theta_2}{E} f(\theta) \tag{D-4}$$

where

$$f(\theta) = \cos\theta \ \ell n \left[\frac{\mathrm{Sin}^2(\theta_2-\theta)}{\mathrm{Sin}^2(\theta_2+\theta)}\right] + \cos\theta_2 \ \ell n\left[\frac{(\mathrm{Sin}\,\theta_2 + \mathrm{Sin}\theta)^2}{(\mathrm{Sin}\,\theta_2 - \mathrm{Sin}\theta)^2}\right]$$

and $$\theta_2 = \frac{\pi\sigma}{2\sigma_y}$$

and $$\cos\theta = \frac{x}{\ell} \cos\theta_2$$

The crack opening area, including plasticity effects, is then given by

$$A_p = 4 \int_0^{\ell} v(x)dx \tag{D-5}$$

Equation D-5 can be integrated numberically and expressed in terms of the elastic crack opening area A_e given in Equation D-2:

$$A_p = \frac{2\sigma \ell^2}{E} F(\sigma/\sigma_y) \qquad \text{(D-6)}$$

where F is a plasticity correction factor which is a function of the stress ratio σ/σ_y. The remaining term in Equation D-6 is the crack opening area based on LEFM analysis. Figure D-2 shows the plasticity correction factor F as a function of σ/σ_y. It is seen that for stress levels approaching σ_y the plasticity correction factor can be significant.

The analysis described so far is strictly valid for a crack in an infinite plate. The Dugdale solution shows, as expected, that for stress levels, $\sigma = \sigma_y$, the plastic zone becomes infinite. However, the Dugdale approach is not valid for a finite width plate or for a pipe. For example, in a finite width plate with a through-crack, the plastic zone extends through the entire width of the plate when the limit load is reached. However, the Dugdale model would predict a much smaller plastic zone even though the plate is at limit load. Similar problems arise in characterizing circumferential through-cracks in piping. An approximation which eliminates this difficulty is to use the limit load in place of the yield stress and use the same expressions (Equation D-6) for the crack opening area. This is similar to the use of the limit load in the British R6 two-criteria approach. In pipes with circumferential through-wall cracks under bending loads the estimation of the crack opening area is even more difficult because of curvature effects and the flattening of the shell. Nevertheless, for this discussion we will assume that the use of the flat plate solution with the plasticity factor (Equation D-6) is valid provided that the nominal stress corresponding to limit load is used in place of the yield strength in the correction factor.

D.3 DETERMINATION OF LEAK RATES AND ASSESSMENT OF LEAK-BEFORE-BREAK MARGIN

As discussed earlier, the unidentified leakage rate in a nuclear power plant is limited to 5 gpm. Leak rates above this value would require plant shutdown. For a given pipe size and stress level, the through-wall crack length required for a 5 gpm leak rate can be calculated. This represents the maximum through-wall crack, ℓ, that could exist without requiring mandatory shutdown. One can also calculate the crack length, ℓ_c, at which failure is expected under the given applied stress. The ratio of the crack length for a 5 gpm leak rate to the crack length for failure, ℓ/ℓ_c, is a measure of the leak-before-break margin for the pipe. The ratio ℓ/ℓ_c for different pipe sizes will be calculated in this discussion assuming that under steady

state conditions the membrane stress in the pipe is at $S_m/2$. This is a reasonable assumption since pipes are sized such that the hoop stress at design pressure is under S_m. In calculating the critical flaw size, the flow stress is assumed to be $3S_m$. Leak rates will be calculated using Moody's data (D-3) which suggested a flow rate per unit area of 55 lb/sec-in^2 for blowdown of saturated water at 1000 psi. Assuming that the flow rate is dependent on the crack opening area only, the required area for 5 gpm leak in a saturated water line is 0.0126 in^2. Assuming a membrane stress of $S_m/2$ (8.45 ksi for 304 stainless steel at 550^{o}F) the crack length to provide the area A_p = 0.0126 in^2 was calculated from Equation D-6. Since the crack length is not known a priori, it is calculated first using LEFM analysis (Equation D-2). The plasticity correction factor was determined using the ratio of the applied stress to the limit load corresponding to the crack length and stress. This calculation was performed iteratively until convergence was reached. Table D-1 shows the crack length for a 5 gpm leak rate for three different pipe sizes. The critical crack sizes are also shown in the same table. It is seen that the crack length for 5 gpm leak, ℓ, remains essentially unchanged (the small differences are due to the plasticity correction factor). On the other hand, the critical crack length, ℓ_c, increases linearly with pipe diameter. The ratio ℓ/ℓ_c decreases with pipe size indicating that through-cracks in large diameter pipes would be detected by the leakage monitoring systems well before critical conditions are reached. Thus, the leak-before-break margin is much higher in larger diameter piping. In developing Table D-1, the leak rates of Reference D-3 were used. Even if the actual leak rate/unit area is different, the conclusions of this section on the higher leak-before-break margin in larger diameter pipes remains unchanged.

D.4 SUMMARY

Simple techniques are developed for the estimation of the crack opening area due to a through-wall crack in a pipe. Plasticity correction factors are computed using the Goodier-Field analysis to obtain a more realistic estimate of the crack opening area. Crack length, ℓ, for a leak rate of 5 gpm is calculated for three different pipe sizes assuming a steady state stress level of $S_m/2$. The critical crack length, ℓ_c, is also determined for the three pipe sizes. It is shown that the ratio, ℓ/ℓ_c, decreases with pipe size, showing that through-cracks in larger diameter pipes can be discovered by leak detection systems well before critical conditions are reached. Thus, the leak-before-break margin is shown to be much higher in large diameter piping.

D.5 REFERENCES

D-1. J. N. Goodier, and F. A. Field, "Plastic Energy Dissipation in Crack Propagation," Fracture of Solids, Interscience Publishers, 1962.

D-2. D. S. Dugdale, "Yielding of Sheet Steels Containing Slits," Journal of the Mechanics and Physics of Solids, 8, 1960, p. 100.

D-3. F. J. Moody, "Maximum Two-Phase Vessel Blowdown from Pipes," General Electric Company, April 1965 (APED-4827).

Table D-1

EFFECT OF PIPE SIZE ON THE RATIO OF THE
CRACK LENGTH FOR 5 GPM LEAK RATE AND THE CRITICAL CRACK LENGTH
(Assumed Stress $\sigma = S_m/2$)

Nominal Pipe Size	Crack Length for 5 GPM Leak (in.)	Critical Crack Length ℓ_c in.	ℓ/ℓ_c
4-in. Sch 80	4.50	6.54	0.688
10-in. Sch 80	4.86	15.95	0.305
24-in. Sch 80	4.97	35.79	0.139

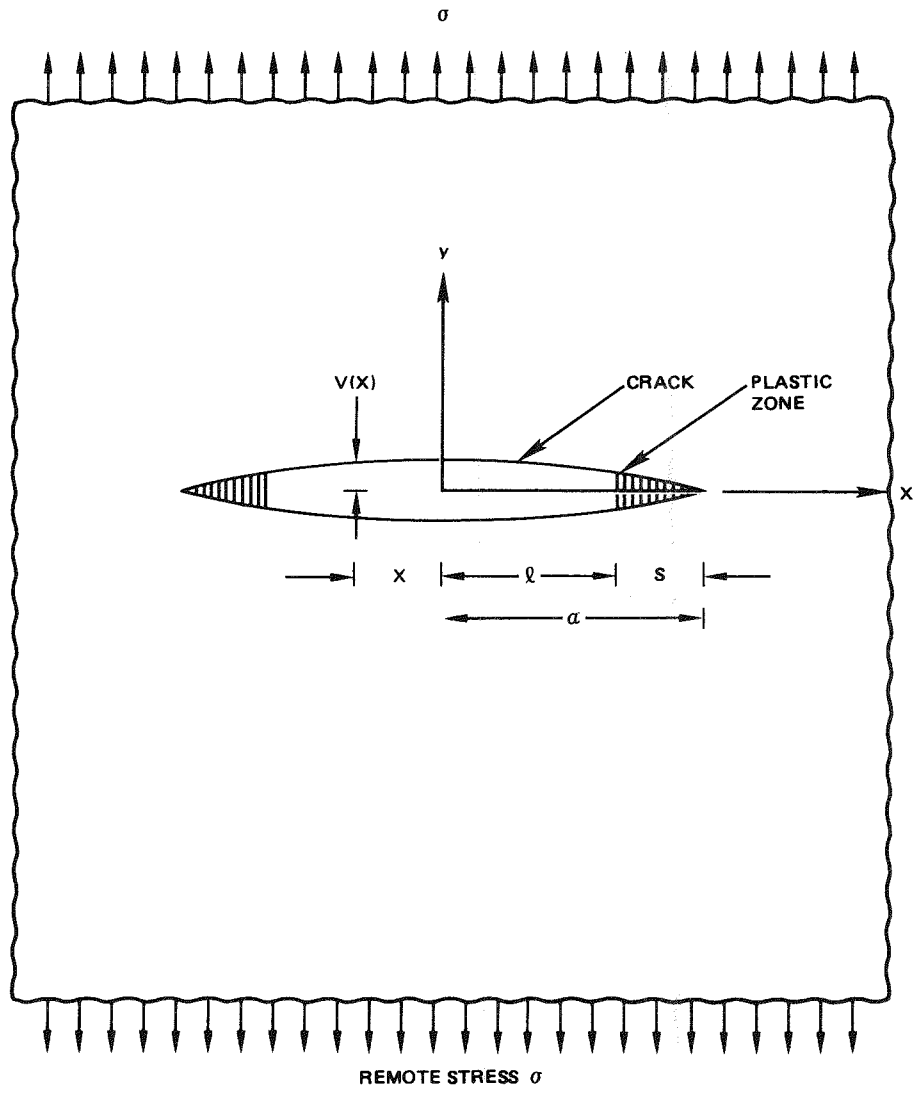

Figure D-1. Plastic Zones at the Crack Tip in an Infinite Plate

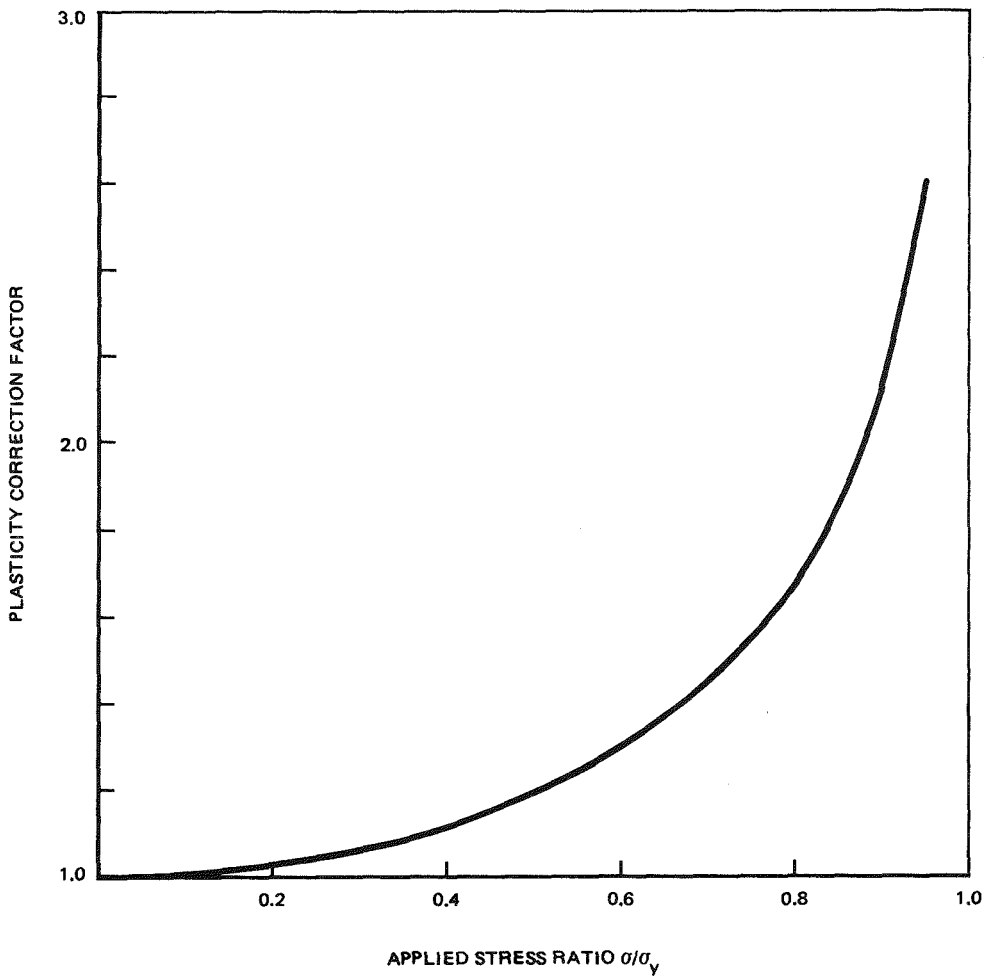

Figure D-2. Plasticity Correction Factor for Determining Crack Opening Area

Appendix E

COMPILATION OF THROUGH-WALL RESIDUAL STRESS DATA LARGE DIAMETER STAINLESS STEEL PIPING

E.1 SUMMARY

Characterization of through-wall residual stresses in the vicinity of the weld fusion line has been performed by several investigators. Both Argonne National Laboratory (ANL) and General Electric Research and Development Laboratory developed through-wall residual stress data reported in RP449 (E-1,E-2). Both sets of measurements were made using strain gage techniques. The GE data was taken 0.12 inch from the fusion line while the ANL data was taken 0.31 inch from the weld center line.

In addition, Argonne performed residual stress measurements on a 20-in. diameter, 1.125-ft wall thickness pipe as part of program T114 (E-3). The data from these measurements are plotted in Figure E-1. In a more recent program, General Electric Corporate Research and Development used strain gage methods to characterize the residual stresses at four azimuths in a reference pipe as part of program RP1394-1 (T113-1) (E-4). These measurements were made 0.098 inch from the fusion line. The data is plotted in Figure E-2.

Finally, Southwest Research Institute performed residual stress measurements on a 28-in. diameter Schedule 80 reference weld (E-5). The technique used was slightly different than that used by ANL and GE in earlier studies in that following initial sectioning with strain gages in place, careful machining was used to remove material to develop through-wall data. The procedures used are described in the reports. Figure E-3 displays the data from four azimuths at a location 0.13 inch from the weld fusion line. It should be noted that the measured mid-thickness stresses derived from measurements were highly compressive (significantly above yield) and that the through-wall distribution is not self equilibrating. This makes the absolute magnitude of the stresses questionable.

All the data collected in the above references is very similar in shape. It is tensile on the inside surface with a magnitude of 30 ksi. The residual stresses

become compressive at a position approximately 10% through the wall with the magnitude of the compressive stresses reaching at least yield strength levels in compression.

E.2 REFERENCES

E-1. A. J. Giannuzzi, "Studies on AISI Type 304 Stainless Steel Piping Weldments for Use in BWR Application," EPRI Report NP 944 Project 449-2, Final Report, December 1978.

E-2. W. J. Shack, W. A. Ellingson, and L. E. Pahis, "Measurement of Residual Stresses in Type 304 Stainless Steel Piping Butt Weldments," EPRI Report NP-1413, Project 449-1, Final Report June, 1980.

E-3. Argonne National Laboratory - Data from Research Project T114.

E-4. D. C. Bertossa, et al., "Techniques to Mitigate BWR Pipe Cracking in Existing Plants (Induction Heat Stress Improvement)," 4th Semi-Annual Progress Report, June 1980 - December 1980, NEDC-25146-3, December 1980.

E-5. S. C. Gregory, "Residual Stress Measurements in a Manually Welded 304 Stainless Steel Pipe Joint - 28-in. Diameter Reference Weld," SWRI Project 02-5672-005, February 1981.

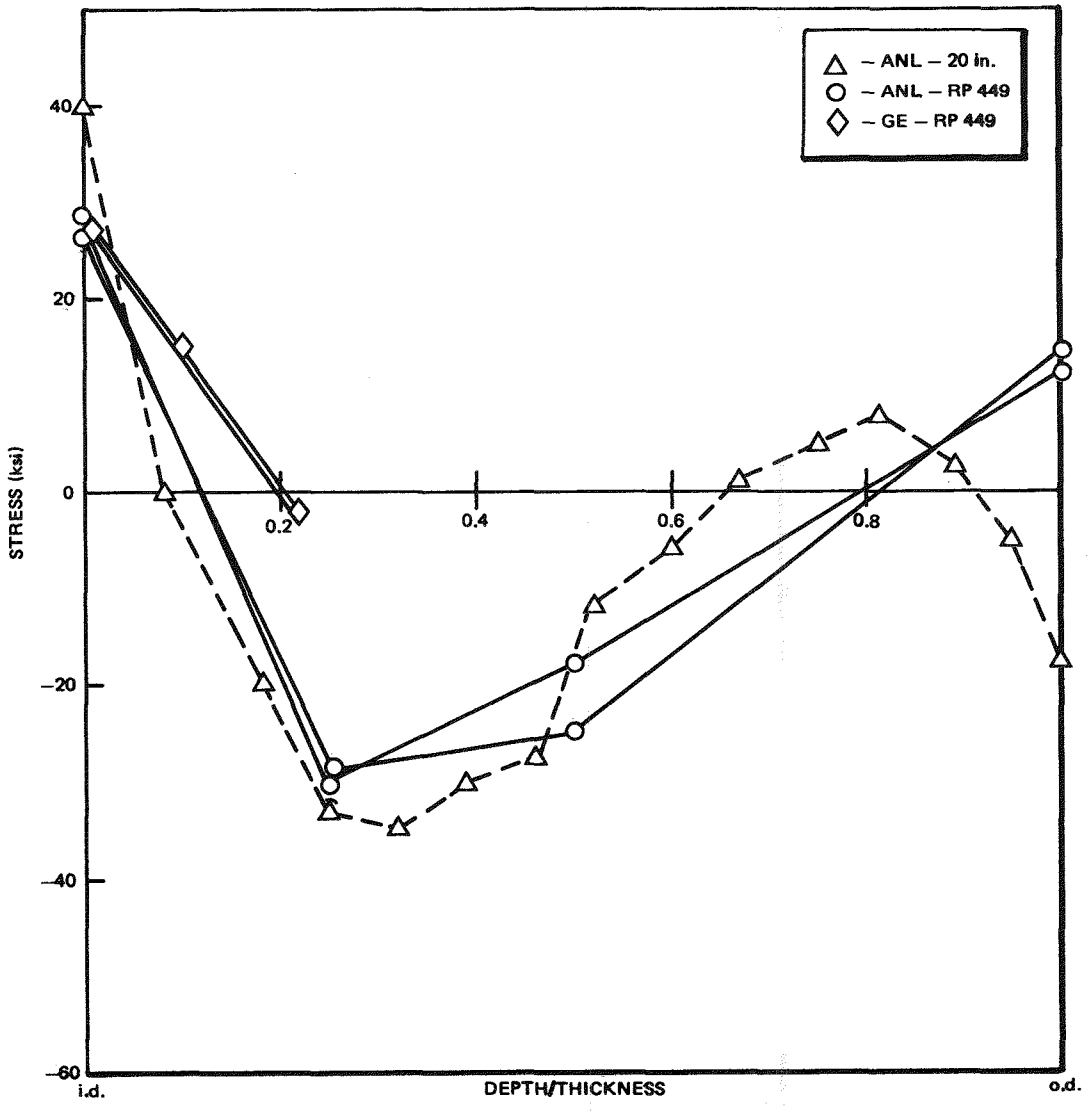

Figure E-1. Through-Wall Residual Stress Measurements on 20-in. and 26-in. Diameter Pipes

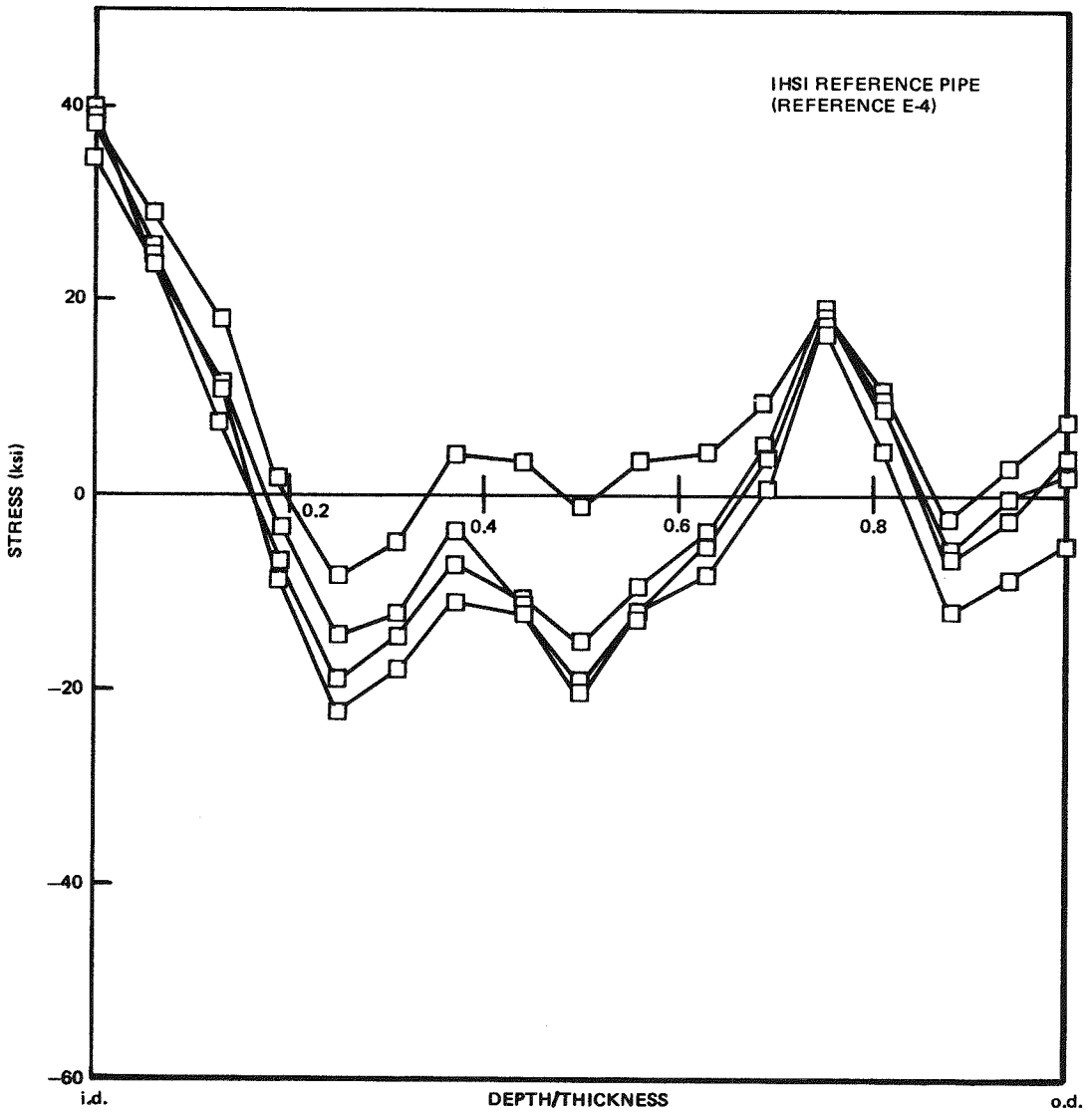

Figure E-2. Through-Wall Residual Stress Data from the IHSI Reference Pipe

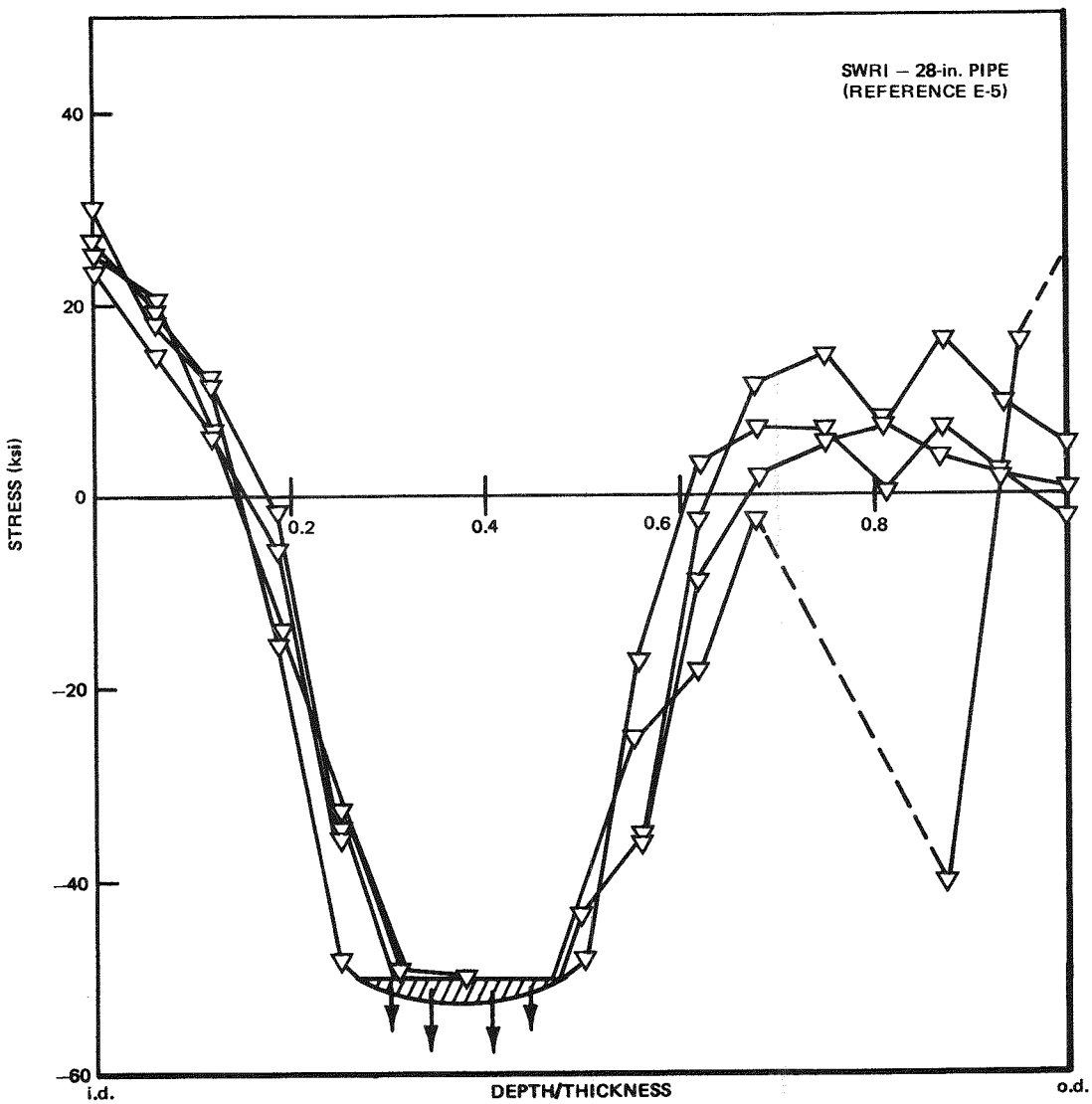

Figure E-3. Through-Wall Residual Stress Data Determined by Southwest Research Institute on a 28-in. Reference Pipe

Appendix F

FRACTURE MECHANICS MODELING
(S. R. Sharma)

F.1 INTRODUCTION

Linear elastic fracture mechanics (LEFM) evaluation of a flaw in welded austenitic stainless piping, in general, requires consideration of crack propagation due to a combination of fatigue crack growth and stress corrosion cracking mechanisms. The fatigue crack growth is due to the stress cycling associated with the piping system pressure and temperature transients specified in the design requirements of the system for its various operating modes. The crack propagation due to intergranular stress corrosion cracking (IGSCC) on the other hand can occur if a special combination of metallurgical, environmental and high sustained stress conditions exists (F-1 – F-3). The material "sensitization" to IGSCC in Type-304 stainless steel is related to the presence of chromium-depleted zones along the grain boundaries in the matrix, which provide a preferential path for the crack to propagate. Sensitization generally occurs as a result of thermal or mechanical treatment of the material, such as welding or high cold work. The two other factors necessary for IGSCC to occur are provided by the oxygenated water environment and by high sustained stresses including weld residual stresses.

Although these two mechanisms of crack growth interact, an analytical evaluation requires their separation into two independent processes. The crack growth analysis process proceeds in two separate steps. Fatigue crack growth calculations are based upon the range of applied stress intensity factor (ΔK), the number of cyclic events, and the experimental data on the material cyclic crack growth rate. On the other hand, stress corrosion crack growth is based on the sustained load stress intensity factor (K_I), the total time of exposure to the environment, and the experimental time-dependent crack growth data. Computations of the total crack extension over a specified time period enable the establishment of in-service inspection periods, and could also form a basis for the acceptance of a discovered flaw to allow continued service of the system. For this purpose, reliable crack growth predictions are essential, involving not only the sound experimental data base on material crack growth rates, but also the realistic methods for obtaining

K_I-solutions for fracture analysis. This appendix characterizes the methods for obtaining K_I solutions for piping components. In certain instances, this requires using finite element methods to characterize the stress intensity factor for highly non-linear weld residual stress distributions.

F.2 CHARACTERIZATION OF K_I USING EXISTING SOLUTIONS

For simple cases of circumferential flaws in pipes under a uniform tensile or a moment loading, the stress intensity factor solutions for axisymmetric problems can be obtained directly or approximated from the solutions listed in various handbooks (for example, F-4 and F-5). For more complex loading conditions such as the nonlinear stress distribution through the pipe wall thickness, general methods such as the boundary integral equation/influence function (F-6 – F-8) or the polynomial superposition method (F-9) can be used. Buchalet and Bamford (F-9) approximated an arbitrary stress distribution across the section thickness by a third-order polynomial expansion series. The numerical solutions for the stress distributions corresponding to each term of the series were then obtained for various combinations of flaw configuration and specimen geometry. The K_I-solution for a given flaw and loading can then be obtained by first expressing the given stress distribution in terms of a third-order polynomial series and then superposing the K_I-solutions for each term of this series.

The K_I-solutions obtained by Buchalet and Bamford (F-9) or those obtained using boundary integral method (for example, Labbens and Pellisier (F-6)), are based upon the superposition principal in LEFM. The formal proof of this principle for a flaw in an elastic solid under load and displacement-controlled loading conditions is due to Bueckner (F-10). Although a discussion on the generalization of this proof to include thermal and residual stress loadings is given by Heaton (F-11), an independent proof for this generalization is presented later in this report. The procedure generally followed to determine K_I as a function of crack depth for a circumferential flaw in a pipe is to first determine the total stress distribution, $\sigma_z^T(r)$, by superposing the various stresses, i.e.,

$$\sigma_z^T(r) = \sigma_z^P(r) + \sigma_z^U(r) + \sigma_z^\theta(r) + \sigma_z^R$$

where $\sigma_z^P(r)$ are load controlled stresses such as pressure, $\sigma_z^u(r)$ are displacement-controlled stresses such as restrained thermal expansion of the pipe, $\sigma_z^\theta(r)$ are thermal stresses due to temperature gradients, and $\sigma_z^R(r)$ are weld residual

stresses. By treating the total stress distribution obtained in this fashion as load-controlled, the total K_I^T-solutions are obtained using either of the two-methods mentioned above, i.e.,

$$K_I^T = K_I(\sigma^T) = K_I(\sigma^P + \sigma^U + \sigma^\theta + \sigma^R)$$

It is assumed here that the K_I-solution for the displacement-controlled portion of stresses is identical to the load-controlled situation. This is acceptable for most practical problems involving long piping systems since K_I for displacement-controlled loading approaches the K_I-solution for a load-controlled situation with increasing specimen length. The solutions developed by Buchalet and Bamford are therefore applicable to most piping systems.

F.3 DEVELOPMENT OF METHODS FOR USE WITH COMPLEX WELD RESIDUAL STRESS DISTRIBUTIONS

An alternate approach for determining K_I^T for stress fields made up of a combination of load-controlled, thermal, and residual stresses is to determine the K_I-solution for each of the stress distribution separately and then combining these K_I-solutions to obtain K_I^T, i.e.,

$$K_I^T = K_I^P + K_I^\theta + K_I^R$$

Since most of the load- and displacement-controlled stresses in piping are usually of the uniform tensile or bending type, the K_I-solutions for circumferential flaws for these cases are available (F4 - F6, F9). However, the through-wall thickness weld residual stress distributions can be highly complex. In such cases, the representation of these stresses by a third-order polynomial expansion or by any other simple function may not be adequate.

For such cases numerical solutions for K_I can be obtained using the following finite element methods.

F.3.1 Numerical Evaluation of Stress Intensity Factors Using Finite Element Methods

An exact determination of the stress intensity factor requires a rigorous solution of the elasticity problem formulated for the given crack configuration, structural geometry, and the loading conditions. Except for some simple idealized cases, the exact solutions for practical engineering problems involving complicated geometries and loading conditions are tedious and difficult to obtain if not completely impossible. It is for this reason, that the finite element methods have found extensive application for the numerical evaluation of fracture parameters not only in the linear elastic regime (F-12 – F-21), but also in the elastic-plastic regime

(F-22, F-23). In most finite element methods developed for structural analysis, the displacements over the finite element size are defined in terms of polynomial functions. Therefore, the behavior of the structure in the region of the crack-tip containing the inverse square root r singularity in the stress field cannot be modeled exactly.

A straightforward approach to overcome this problem is to use a highly refined finite element mesh in the vicinity of the crack tip (F-12 – F-14). However, this has the disadvantage of enormously increasing the computational costs and time required for data preparation. A number of special crack-tip elements embodying the exact singularity in the strain field have also been developed (F-15 – F-17). However, these elements lack the constant strain and rigid body motion modes, and present difficulty in application to thermal stress problems (F-18).

One of the more recent developments in the area of finite element applications to LEFM problems is the use of quadratic isoparametric elements in which the correct crack tip singularity is simulated by shifting the midside nodes to the quarter points (F-18 – F-20). The eight-noded area element for plane stress, plane strain, or axisymmetric applications, and the twenty-noded general three-dimensional isoparametric element in the nonsingular formulations satisfy the essential convergence criteria of inter-element compatibility, constant strain modes, displacement continuity over the domain and the rigid body motion modes (F-18, F-21). These elements can, therefore, be employed for thermal stress analysis without restrictions (F-18, F-24). Using the eight-noded isoparametric element, K_I-solution for two-dimensional problems can be obtained as follows (F-18).

In reference to Figure F-1, it can be shown that the displacement in the y-direction along edge 1-5-2 of the finite element with the midside node located at quarter point is given as

$$u = -\frac{u_2}{2}\left(-1+2\sqrt{\frac{x}{\ell}}\right)\left(2-2\sqrt{\frac{x}{\ell}}\right)+\frac{u_1}{2}\left(-1+2\sqrt{\frac{x}{\ell}}\right)\left(2\sqrt{\frac{x}{\ell}}\right)$$
$$+ u_5\left(4\sqrt{\frac{x}{\ell}}+4\frac{x}{\ell}\right)$$

where k_i refers to the displacement of k^{th} node in the y-direction. The crack-tip displacement in y-direction is given by Williams' expression as

$$u = \frac{K_I}{2G}\left(\frac{r}{2\pi}\right)^{1/2}(\kappa+1)\ ,\ (\text{at } \theta = \pi)$$

where G is material shear modulus, r is radial distance from the crack-tip, $\kappa = (3-4\nu)$ for plane strain, $\kappa = (3-\nu)/(1-\nu)$ for plane stress conditions, and ν is the Poisson's ratio.

Matching the preceding two equations, the following relationship for K_I can be derived as (with $u_2 = 0$ for symmetry)

$$K_I = \left(\frac{2G\sqrt{2\pi}}{(k+1)}\right)(4u_5 - u_1)\left(\frac{1}{\sqrt{\ell}}\right) \qquad \text{(F-1a)}$$

Using the above expression, K_I for a given flaw size can be readily determined from the displacement solution obtained from finite element analysis of the structure for any prescribed loading including a temperature loading.

F.3.2 Determination of K_I for Flaws in the Residual Stress Fields of Welded Pipe

The analysis method described here for developing the K_I-solutions for flaws in the weld residual stress fields is based upon the equivalence of the thermo-elastic and residual stress problems. Both cases have a prescribed displacement field, resulting from either an imposed temperature gradient field or previous nonuniform plastic deformations, and applied over the volume of the structure. Therefore, both problems can be considered as "initial stress" or "initial strain" problems. This is in contrast to the displacement-controlled (second boundary value problem of elasticity) where the loading of the structure is in the form of a prescribed set of displacements over the structure boundary such as restrained thermal expansions in piping systems or the relative displacement of piping support points from the stress-free configuration. Furthermore, whereas displacement controlled loading requires an external reaction force to satisfy equilibrium requirements, in an initial stress problem the structure is in a free-standing self-equilibrium.

Consider the specific case of a 26-in.-diameter butt-welded pipe. A typical weld residual stress distribution through the pipe wall thickness based upon the experimental data reported in Appendix E is shown in Figure F-2. The axial variation of the residual stress at the inside pipe surface is also shown in Figure F-2. It is worthwhile to mention here, that as far as the determination of K_I for a circumferential flaw is concerned, only the axial residual stress distribution $\sigma_z^w(r)$, over the crack plane (in the uncracked body configuration) is important. How this stress varies in the axial direction is of no consequence. This observation follows from the proof of the superposition principle discussed in Section F.3.3.

The numerical solutions for K_I were obtained using finite element methods described earlier. The finite element model used for this analysis is shown in Figure F-3. Since direct inclusion of residual stresses in the finite element model in terms of an initial strain field presents difficulties, the K_I-solutions were obtained by solving the equivalent thermo-elastic stress problem which requires an appropriate temperature field as the imposed loading. The selection of the required temperature field to simulate the thermal axial stress field presents no difficulty if the relationship for thermal axial stresses in pipe due to a temperature gradient field $\theta = \theta\ (t/t_o)$, is considered, i.e.,

$$\sigma_z^{\theta} = \beta\ [\theta^* - \theta]$$

or

$$\theta = \beta\theta^* - \frac{1}{\beta}\sigma_z^{\theta}$$

where θ^* is a constant, t is the radial distance from the inside surface of the pipe, t_o is the pipe wall thickness and $\beta = E/(1-\nu)$ where E is the material elastic constant and ν is the Poisson's ratio. The constant term ($\beta\theta^*$) in the above expression can be taken as zero since in residual stress problems the surface is free of applied displacements and, therefore, the constant temperature term does not contribute to the thermal stress field, i.e.,

$$\theta = -\left(\frac{1}{\beta}\right)\sigma_z^{\theta}$$

The above expression immediately suggests that the required temperature field simulates a given weld residual stress field, i.e., the required temperature field is of the same form as the given residual stress field.

The numerical solutions for K_I for the flaw aspect ratios a/t_o of up to 0.8 obtained using the above approach are shown in Figure F-4. The negative value of K_I in the flaw aspect ratio range of 0.3 to 0.6 strongly indicates that if no other loading is applied, a propagating IGSCC crack cannot indefinitely advance and would eventually arrest as soon as the applied K_I value drops below the threshold K_I for IGSCC (K_{ISCC}) value.

F.3.3 Superposition Principle in Linear Elastic Fracture Mechanics in the Presence of Thermal Stresses

The methods developed rely on the application of Bueckner's superposition principles (F-10). To discuss the applicability to these fracture problems where

the applied loading on the cracked body includes thermo-elastic stresses, this principle must first be reviewed as applied to a general three-dimensional boundary value problem of elasticity in the absence of residual stresses. In the following discussion, identical notation will be used where a repeated index implies summation over the values 1, 2 and 3 and the indices following a comma imply differentiation.

Consider an elastic body as shown in Figure F-5a with a volume V and a boundary surface S under the action of prescribed tractions T_i on S_1, displacements u_i on S_2 ($S_1+S_2=S$), and the body forces X_i on v. The response of the body to the applied T_i, u_i and X_i is a displacement field ${}^{o}u_i$ and the corresponding strains ${}^{o}\varepsilon_{ij}$ and stress ${}^{o}\sigma_{ij}$ where

$$\varepsilon_{ij} = \frac{1}{2}(u_{i,j} + u_{j,i})$$

and

$$\sigma_{ij} = \lambda\delta_{ij}\,\varepsilon_{kk} + 2\mu\varepsilon_{ij}$$

where λ and μ are the Lame's constants for linear elasticity.

Now consider an identical body with prescribed loading, i.e., T_i, u_i and X_i, unchanged but containing a crack of surface C as shown in Figure F-5b.

Let ${}'u_i$, ${}'\varepsilon_{ij}$ and ${}'\sigma_{ij}$ be the displacements, strains, and stresses for this body configuration. The work done by the applied forces in going from the uncracked to the cracked configuration with surface conditions held constant is given as:

$$\Delta W = \int_{S_1} \left(T_i\,{}'u_i - T_i\,{}^{o}u_i\right) ds + \int_{v} \left(X_i\,{}'u_i - X_i\,{}^{o}u_i\right) dv$$

$$= \int_{S_1} \left({}'\sigma_{ij}\,{}'u_i - {}^{o}\sigma_{ij}\,{}^{o}u_i\right) n_j\, ds + \int_{v} \left(X_i\,{}'u_i - X_i\,{}^{o}u_i\right) dv$$

where we have used $T_i = \sigma_{ij}n_j$ with n_j as the components of the outer normal vector to the boundary surface. Transforming the surface integral in the above equation to the volume integral using Gauss' theorem and using the equilibrium equations, i.e.,

$$\sigma_{ij,j} + X_i = 0$$

the above equation reduces to

$$\Delta W = \int_V \left({}'\sigma_{ij}\ {}'u_{i,j} - {}^o\sigma_{ij}\ {}^o u_{i,j} \right) dv$$

which gives

$$\int_V \left({}'\sigma_{ij}\ {}'\varepsilon_{ij} - {}^o\sigma_{ij}\ {}^o\varepsilon_{ij} \right) dv, \text{ since } \sigma_{ij} \text{ is a symmetric tensor.}$$

The change in the stored elastic strain energy of the body for going from the uncracked to cracked configuration is given as

$$\Delta U = \int_V \frac{1}{2} \left({}^o\sigma_{ij}\ {}^o\varepsilon_{ij} - {}'\sigma_{ij}\ {}'\varepsilon_{ij} \right) dv$$

The total change in the system potential energy is, therefore,

$$\Delta V = \Delta W + \Delta U = \frac{1}{2} \int_V \left({}'\sigma_{ij}\ {}'\varepsilon_{ij} - {}^o\sigma_{ij}\ {}^o\varepsilon_{ij} \right) dv = G\ C \qquad \text{(F-1b)}$$

where G is defined as the strain energy release rate and C is the crack surface area. Using Irwin's model for fracture of solids, the crack instability occurs when

$$G \geq G_c \qquad \text{(F-1c)}$$

where G_c, the critical strain energy release rate, is a material property. For two-dimensional problems, G is related to other fracture parameters such as the stress intensity factor, K_I, or the path independent J-integral of Rice (F-25) through the relationships,

$$\frac{K_I}{E'} = J = G$$

where $E' = E$ for the plane stress and $E' = E/(1-\nu^2)$ for plane strain conditions, E is the material elastic modulus and ν is the Poisson's ratio.

As shown by Bueckner (F-10), the total change in system potential energy, ΔV in Equation 1(a) is also given by the following expression:

$$V = \frac{1}{2} \int_C (-T_i^*) \left({}'u_i - {}^o u_i \right) dS$$

where T_i^* are the tractions acting over the crack surface C resulting from the stresses ${}^o\sigma_{ij}$ in the uncracked body configuration (Figure F-5a), i.e., $T_i^* = {}^o\sigma_{ij} n_j$ on C as illustrated in Figure F-5c.

Since ${}^{o}u_i$ remains the same in going from one side of the section to the other while T_i^* changes sign, $\int_C T_i^* \, {}^{o}u_i \, ds = 0$, and the above relationship reduces to

$$V = \frac{1}{2} \int_C - T_i^* \, {}^{'}u_i \, ds \tag{F-2}$$

Equation F-2 underlines Bueckner's superposition principle in linear elastic fracture mechanics. This principle states that if Equations F1a-c characterize fracture, then, for the purpose of evaluating fracture conditions, the response of the cracked body under the action of applied T_i, u_i and X_i is identical to the response of the same body with tractions $(- T_i^*)$ applied over the crack surface C with T_i, u_i and X_i set to zero over their respective domains. This well known principle serves as a basis for determining the fracture parameters such as the K_I solutions using such methods as the boundary integral Equation F-6 or the polynomial superposition method F-9.

Consider now a general thermal stress problem as shown in Figure F-6a. In this case, in addition to the prescribed T_i, u_i and X_i, a temperature field $\theta=\theta(x_i)$ is prescribed on V+S of the body. The temperature θ is the instantaneous temperature at every point x_i of the body and is defined as the temperature above a uniform reference temperature θ_o at which the body is stress free in the absence of all applied forces and displacements.

The field equations of static thermo-elasticity for a linear, homogeneous isotropic material are

$$\sigma_{ij} = \lambda\delta_{ij} \, \varepsilon_{kk}^T + 2\mu\varepsilon_{ij}^T - \beta\delta_{ij}\theta \tag{F-3}$$

$$\varepsilon_{ij}^T = \frac{1}{2}\left(u_{i,j}^T + u_{j,i}^T\right) \tag{F-4}$$

and

$$\sigma_{ij,j} + X_i = 0 \tag{F-5}$$

where u_i^T, ε_{ij}^T are the total displacements and total strains with $u_i^T = u_i + u_i^\theta$ and $\varepsilon_{ij}^T = \varepsilon_{ij} + \varepsilon_{ij}^\theta$ where u_i^θ and ε_{ij}^θ are the thermal displacement and thermal strain components, respectively, λ and μ are the Lame's constants and $\beta = \alpha E/(1-2\nu)$ and where α is the material thermal expansion coefficient. Substitution of Equations F-3 and F-4 in F-5 yields the Navier's equation of equilibrium as

$$\mu u_{i,jj}^T + (\lambda+\mu) \, u_{j,ij}^T + X_i^\theta = 0 \tag{F-6}$$

where

$$X_i^\theta = X_i - \beta\theta_{,i}$$

Also, if T_i are the tractions specified over S, then substitution of $T_i = \sigma_{ij}n_j$ and Equation F-4 in Equation F-3 yields

$$\left(\lambda\, u^T_{k,k}\, \delta_{ij} + \mu u^T_{i,j} + \mu u^T_{j,i}\right) n_j = T_i^\theta = T_i + \beta\theta n_i \qquad \text{(F-7)}$$

Equations F-6 and F-7 together allow the transformation of a thermo-elastic problem into a boundary value problem with prescribed tractions and body forces and are known as Duhamel-Neumann analogy (F-26 - F-28). According to this analogy, the solution of a thermo-elastic problem with prescribed tractions T_i on S, body forces X_i on V and temperatures θ on (V+S) is equivalent to the solution of a boundary value problem with modified $T_i^\theta = T_i + \beta\theta n_i$ and $X_i^\theta = X_i - \beta\theta_i$, and with $\theta=\theta\ (x_i) \equiv 0$ on V+S as shown in Figure F-6b.

Consider now the case of an elastic body with and without a crack in it as shown in Figure F-7a and F-7c. The only loading prescribed for the body is a temperature field θ with $T_i=0$ on S and $X_i=0$ on V. Using Duhamel-Neumann analogy, these problems can be transformed into boundary value problems as shown in Figure F-7b and F-7d. Let ${}^o u_i^\theta$, ${}^o\varepsilon_{ij}^\theta$, and ${}^o\sigma_{ij}^\theta$ be the thermal displacements, strains and stresses in the uncracked body configuration and ${}'u_i^\theta$, ${}'\varepsilon_{ij}^\theta$, and ${}'\varepsilon_{ij}^\theta$ be the thermal displacements, strains, and stresses in the cracked body configuration.

Referring to Figure F-7b and F-7d, the work done by T_i^θ and X_i^θ in going from the uncracked to cracked body configuration can be written as

$$\Delta W^* = \int_{S+C} T_i^\theta\, {}'u_i^\theta\, ds - \int_S T_i^\theta\, {}^o u_i^\theta\, ds + \int_V X_i^\theta \left({}'u_i^\theta - {}^o u_i^\theta\right) dv$$

Transforming the surface integrals into the volume integrals in the above equations, and noting that $\sigma^*_{ij,j} + X_i^\theta = 0$ for equilibrium, and also that σ^*_{ij} is a symmetric tensor, we have

$$\Delta W^* = \int_V \left({}'\sigma^*_{ij}\, {}'\varepsilon_{ij}^\theta - {}^o\sigma^*_{ij}\, {}^o\varepsilon_{ij}^\theta\right) dv$$

The change in the stored elastic strain energy is given as

$$\Delta U^* = \frac{1}{2} \int_V \left({}^o\sigma^*_{ij}\, {}^o\varepsilon_{ij}^\theta - {}'\sigma^*_{ij}\, {}^o\varepsilon_{ij}^\theta\right) dv$$

Then

$$\Delta V^* = \Delta W^* + \Delta U^* = \frac{1}{2} \int_v \left({}'\sigma^*_{ij} \; {}'\varepsilon^\theta_{ij} - {}^o\sigma^*_{ij} \; {}^o\varepsilon^\theta_{ij} \right) dv$$

and since

$$\sigma^*_{ij} = \sigma^\theta_{ij} + \beta\theta\delta_{ij}, \text{ we have}$$

$$\Delta V^* = \frac{1}{2} \int_v \left({}'\sigma^\theta_{ij} \; {}'\varepsilon^\theta_{ij} - {}^o\sigma^\theta_{ij} \; {}^o\varepsilon^\theta_{ij} \right) dv + \frac{1}{2} \int_v \beta\theta\delta_{ij} \left({}'\varepsilon^\theta_{ij} - {}^o\varepsilon^\theta_{ij} \right) dv$$

or

$$\Delta V^* = \Delta V + \frac{1}{2} \int_v \beta\theta \left({}'\varepsilon^\theta_{kk} - {}^o\varepsilon^\theta_{ii} \right) dv \qquad \text{(F-8)}$$

Following Bueckner's (F-10) argument, it can be shown that,

$$\Delta V^* = -\frac{1}{2} \int_C \left(T^*_i - T^\theta_i \right) {}'u^\theta_i \, ds$$

where

$$T^*_i = \left({}^o\sigma^\theta_{ij} + \beta\theta\delta_{ij} \right) n_j$$

and

$$T^\theta_i = \beta\theta n_i$$

Therefore,

$$\Delta V^* = -\frac{1}{2} \int_C \left({}^o\sigma^\theta_{ij} \, n_j \right) {}'u^\theta_i \, ds = -\frac{1}{2} \int_C {}^oT^\theta_i \; {}'u^\theta_i \, ds \qquad \text{(F-9)}$$

Comparing equations F-8 and F-9,

$$\Delta V = -\frac{1}{2} \int_C {}^oT^\theta_i \; {}'u^\theta_i \, ds - \frac{1}{2} \int_v \beta\theta \left({}'\varepsilon^\theta_{kk} - {}^o\phi^\theta_{kk} \right) dv$$

Consider now the volume integral on the right hand side of the above equation, i.e.,

$$I = \int_v \beta\theta \left({}'\varepsilon^\theta_{kk} - {}^o\varepsilon^\theta_{kk} \right) dv \qquad \text{(F-10)}$$

The dilational strains ε^θ_{kk} (= $\Delta v/v$) represent the change in the body volume due to a temperature rise θ, from the reference temperature θ_o at which the body is initially stress free. Let θ^* be the average body temperature given as

$$\theta^* = \frac{1}{V} \int_V \theta\,(X_i)\, dv$$

and let $\theta=\theta^*+\theta'$. The volumetric expansion of both the cracked and uncracked bodies is simply $3\alpha\theta^* = \varepsilon_{kk}^{\theta^*}$ and, therefore, Equation F-10 can be written as

$$I = \int_v \beta\theta \left({}^{'}\varepsilon_{kk}^{\theta'} - {}^{o}\varepsilon_{kk}^{\theta'} \right) dv$$

In the above equation now, the volumetric strain, $\varepsilon_{kk}^{'\theta}$, is due to only the temperature gradients. The thermal strains (and the corresponding thermal stresses), in this sense, are the "internal" strains and stresses which exist in a free standing body due only to the incompatible displacement field imposed by a temperature gradient field. Since internal strains do not cause any change in the volume of the body (F-26, F-29), the above integral vanishes and Equation F-9 reduces to

$$\Delta V = -\frac{1}{2} \int_C {}^{o}T_i^{\theta}\, {}^{'}u_i^{\theta}\, dS \qquad \text{(F-11)}$$

which is identical to Equation F-2. This shows that Bueckner's superposition principle in LEFM is equally valid when applied to cracked bodies under thermal or "internal" stress loading such as the residual stresses.

It is worth noting here that although the solution method for determining the fracture parameters for thermal or residual stresses is identical to the load-controlled case, the situation in fact is more akin to a displacement-controlled loading. This is because of the self-equilibrating nature of the stresses associated with the purely thermal or residual stresses which do not work and, therefore, feed no energy to the propagating crack. This can be illustrated by considering a free-standing structure with internal stresses as shown in Figure F-8a. The internal stresses could be due to temperature gradients or the residual stresses such as due to the previous non-uniform plastic deformations. If a section S_c is passed through this structure (Figure F-8b), the traction vector T and the moment vector (ρXT) (where ρ is an arbitrary position vector) when integrated over the new surface S_c must vanish to satisfy the equilibrium requirements. The net work done by T or (ρXT), therefore, in going from the uncracked to cracked configuration is also zero. This implies that the fracture parameters such as K or G cannot indefinitely increase with increasing crack length and, therefore, crack arrest can be assured. As shown by Chell (F-30), for edge and center cracked plates under a quadratic temperature distribution, K_I in

fact goes to zero as the crack aspect ratio, a/t, goes to one. This is in contrast to a load controlled situation where crack arrest, in general, cannot be assured.

F.4 APPLICATION OF METHODS TO LARGE DIAMETER PIPING CONTAINING A FULLY CIRCUMFERENTIAL FLOW

Consider now a fully circumferential IGSCC flow located in the sensitized region of the weld heat-affected zone of a butt-welded Type-304 stainless steel piping. Figure F-9 shows the stress distribution (F-31) in the HAZ of a 26-in.-diameter butt-welded pipe expected during the steady-state normal operation of the piping system. As shown in this figure, the total stress distribution is a combination of weld residual stress and the applied stresses. The applied stress consists of the pressure stress (load controlled) and the stresses due to differential thermal expansion of the piping system (displacement-controlled).

The determination of the overall stress intensity is broken down into two steps. First, for the combined pressure and restrained thermal expansion loads, K_I as a function of flaw depth was obtained using Buchalet and Bamford's solution (F-9), as shown in Figure F-10.

Concurrently, K_I for the complex weld residual stress distribution was determined using finite elements methods as described in the previous section. The resultant K_I is displayed in Figure F-11. (This is the same as Figure F-4 with an expanded scale.) These two solutions are then superimposed to develop the over-all stress intensity for radial crack growth. The total K_I, including the pressure and other stresses, is displayed in Figure F-12. This stress intensity can be used in conjunction with the crack growth rates to determine the crack depth as a function of time for the large diameter pipes.

F.5 REFERENCES

F-1. R. L. Cowan and G. M. Gordon, "Proceedings of the International Conference on Stress Corrosion Cracking and Hydrogen Embrittlement," Unieux, Firming, France, June 1973.

F-2. R. W. Staehle, "Proceedings of Conference, Fundamental Aspects of Stress Corrosion Cracking," Ohio State University, Department of Metallurgical Engineering, September 11-15, 1967.

F-3. W. Hubner and F. J. E. Johansson, "International Quarterly Scientific Reviews Journal," Vol. II, Nos. 1 and 2, 1974, p. 158.

F-4. D. P. Rook and D. J. Cartwright, "Compendium of Stress Intensity Factors," H.M.S. Stationary Office, London (1976).

F-5. H. Tada, P. Paris, and G. Irwin, "The Stress Analysis of Cracks Handbook," Del Research Corp. (1973).

F-6. R. Labbens, T. A. Pellissier, and J. Heliot, "Mechanics of Crack Growth," ASTM STP 590, pp. 368-389 (1976).

F-7. P. M. Besuner, "The Influence Function Method for Fracture Mechanics and Residual Fatigue Life Analysis of Cracked Components under Complex Stress Fields," Nucl. Eng. Design, Vol. 43, No. 1, p. 115, 1979.

F-8. D. O. Harris, "Influence of Crack Growth Kinetics and Inspection on the Integrity of Sensitized BWR Piping Welds," EPRI, September 1979 (NP-1163).

F-9. C. B. Buchalet and W. H. Bamford, "Mechanics of Crack Growth," ASTM STP 590 pp. 385-402 (1976).

F-10. H. F. Bueckner, "The Propagation of Cracks and the Energy of Elastic Deformation," Trans., ASME, Aug. 1958, pp. 1226-1230.

F-11. M. D. Heaton, "On the Calculation of Stress Intensity Factors due to Thermal and Residual Stress Field Fields," CEGB NWR Report No. NW/SSD/RR/158/76.

F-12. G. P. Anderson, V. L. Ruggels, and G. S. Stibor, "Use of Finite Element Computer Programs in Fracture Mechanics," Int. J. Fract. Mech. 7, pp. 63-76 (1971).

F-13. W. K. Wilson and D. G. Thompson, "On the Finite Element Method for Calculating Stress Intensity Factors for Cracked Plates in Bending," Engr. Fract. Mech., Vol. 2, pp. 97-102, 1971.

F-14. S. K. Chan, I. S. Tuba, and W. K. Wilson, "On the Finite Element Method in Linear Fracture Mechanics," Engr. Fract. Mech., Vol. 2, pp. 1-17 (1970).

F-15. E. Byskov, "The Calculations of Stress Intensity Factors Using Finite Elements Method with Cracked Elements," Int. J. Fract. Mech., Vol. 6, pp. 159-167 (1970).

F-16. D. M. Tracey, "Finite Elements for Determination of Crack Tip Stress Intensity Factors," Engr. Fract. Mech., Vol. 3, pp. 255-265 (1971).

F-17. S. G. Papaioannou, P. D. Hilton, and R. A. Lucas, "A Finite Element Method for Calculating Stress Intensity Factors and its Application to Composite," Engr. Fract. Mech., Vol. 6, pp. 807-823 (1974).

F-18. R. S. Barsoum, "On the Use of Isoparametric Finite Elements in Linear Elastic Fracture Mechanics," Int. J. Num. Meth. Engng., Vol. 10, pp. 25-37 (1976).

F-19. R. D. Henshell and K. G. Shaw, "Crack Tip Elements are Unnecessary," Int. J. Num. Meth. Engng., Vol. 9, pp. 495-507 (1975).

F-20. S. E. Benzley, "Representation of Singularities with Isoparametric Finite Elements," Int. J. Num. Meth. Engng., Vol. 8, pp. 537-545 (1974).

F-21. O. C. Zienkiewicz, "The Finite Element Methods," McGraw-Hill (U.K.), 3rd ed. (1977).

F-22. "Development of a Plastic Fracture Methodology," Report EPRI NP-1734, Electric Power Research Institute (1981).

F-23. "Methodology for Plastic Fracture," Report EPRI NP-1735, Electric Power Research Institute (1981).

F-24. T. K. Helen and F. Cesari, "On the Solution of the Centre Cracked Plate with a Quadratic Thermal Gradient," Eng. Frac. Mech., Vol. 12, pp. 469-478, (1979).

F-25. J. R. Rice, "A Path Independent Integral and the Approximate Analysis of Strain Concentration by Notches and Cracks," J. App. Mech., June 1968, pp. 379-386.

F-26. Y. C. Fung, "Foundations of Solid Mechanics," Prentice-Hall Publications (1965).

F-27. S. P. Timoshenko and J. N. Goodier, "Theory of Elasticity," McGraw-Hill Book Co., 3rd ed. (1970).

F-28. S. S. Manson, "Thermal Stress and Low Cycle Fatigue," McGraw-Hill Book Co. (1966).

F-29. J. D. Eshelby, "The Continuum Theory of Lattice Defects," Solid State Physics, Vol. 3, Academic Press Inc. Publishers (1956).

F-30. G. G. Chell, "Incorporation of Residual and Thermal Stress in Elastic-Plastic Fracture Mechanics Design," Advances in Elasto-Plastic Fracture Mechanics, L. H. Larson, Editor, Applied Science Pub. (1980).

F-31. R. M. Horn, et al., "The Growth and Stability of Stress Corrosion Cracks in Large Diameter BWR Piping," First Semi-Annual Report NEDC-24750-1, December 1979.

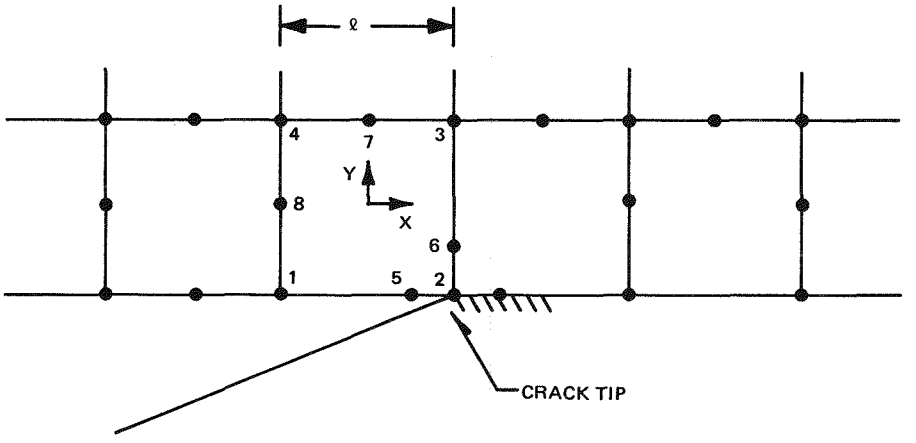

Figure F-1. Application of Eight-Noded Isoparametric Finite Element in Linear Elastic Fracture Mechanics (LEFM)

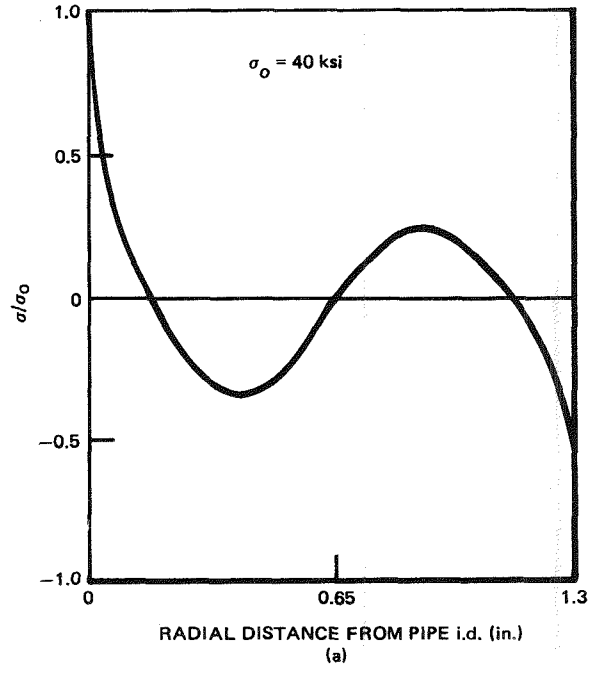

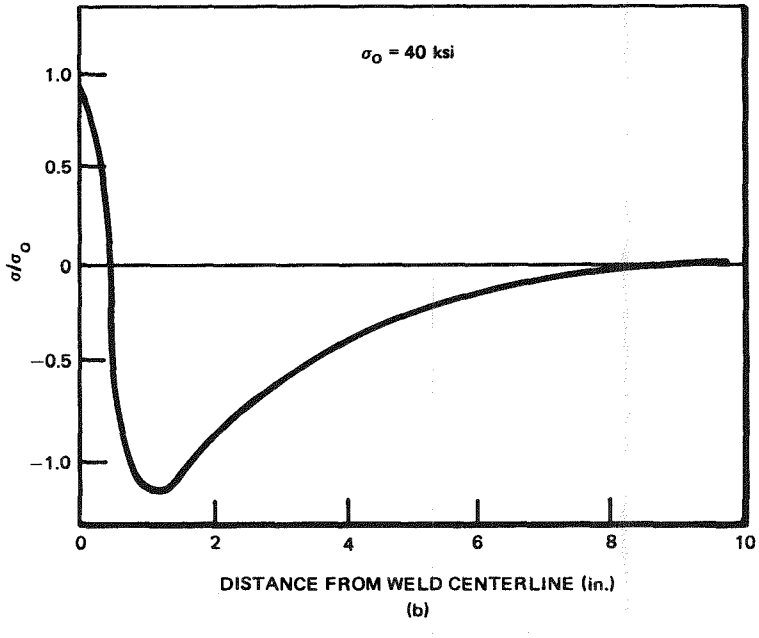

Figure F-2. Residual Stress Distribution in a Butt-Welded 26-in.-Diameter Pipe (from Reference 33)

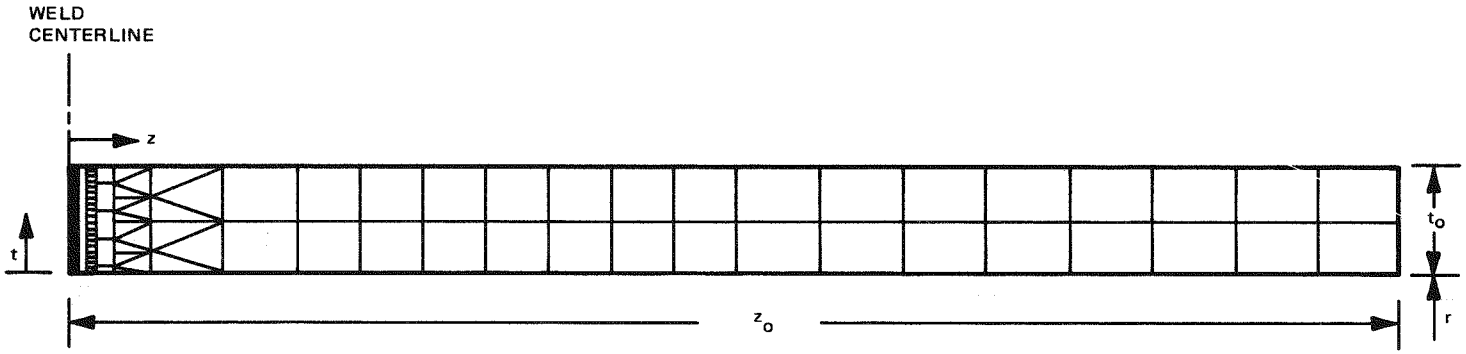

Figure F-3. Finite Element Model of the Pipe

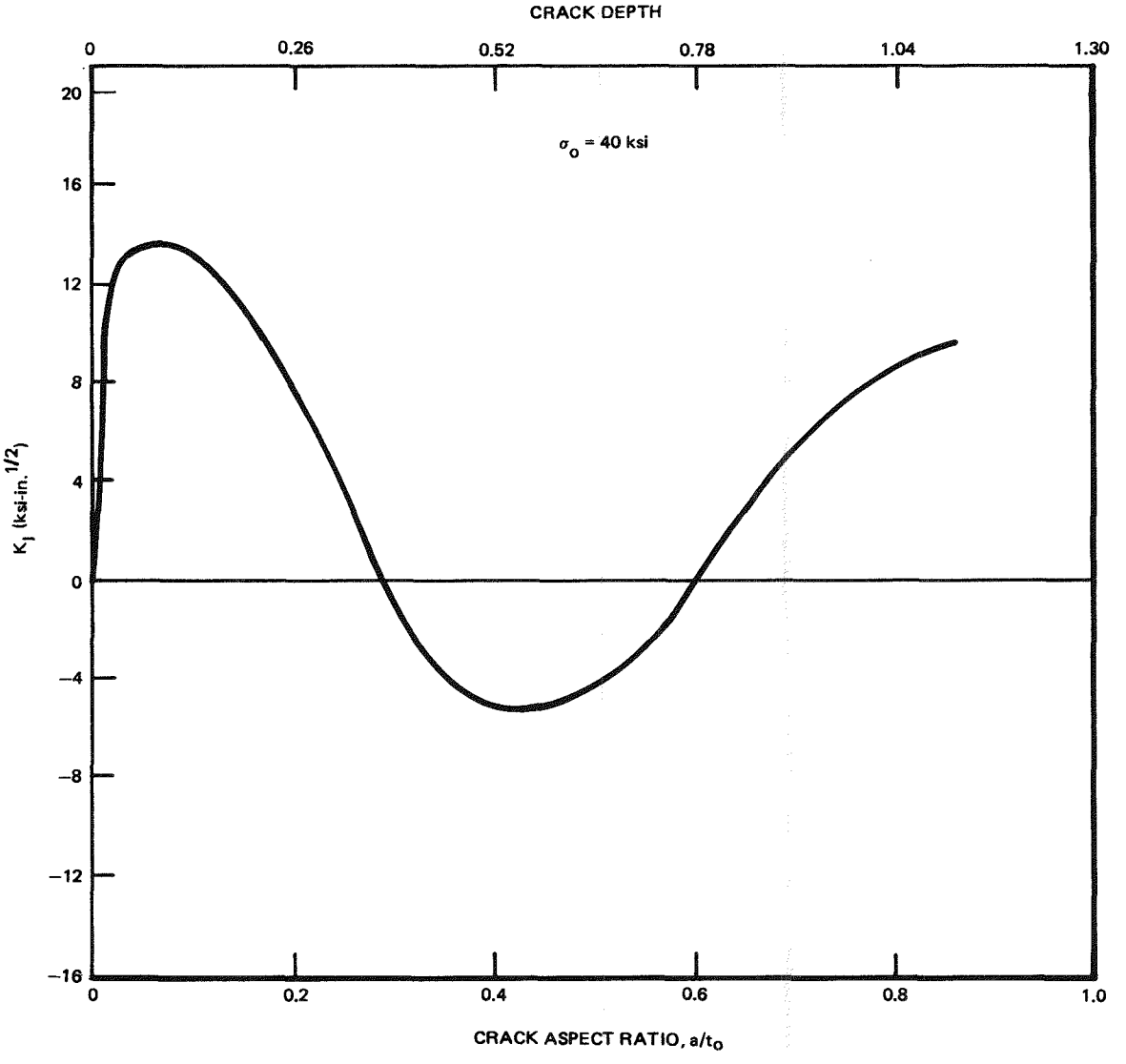

Figure F-4. Stress Intensity Factors for a Circumferential Flaw in Weld Residual Stress Field of a Butt-Welded Pipe (R/to = 10)

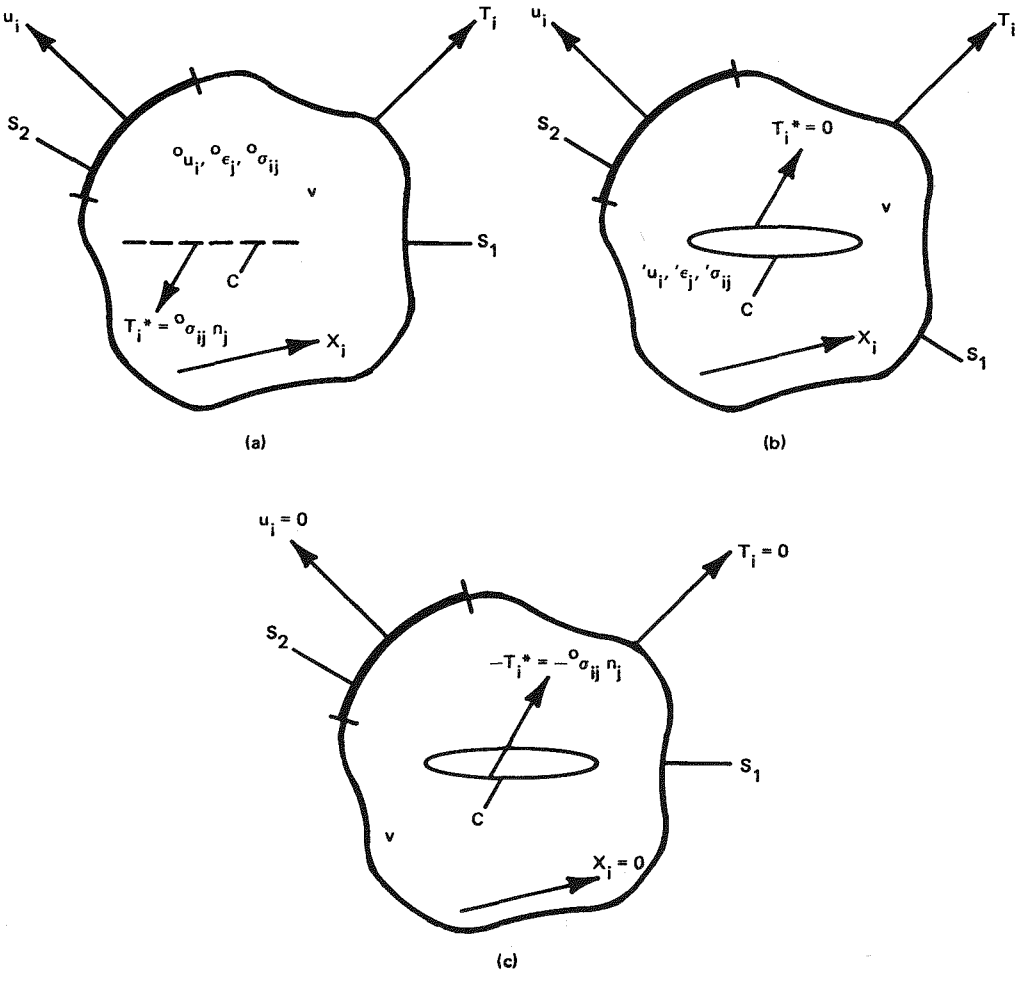

Figure F-5. Cracked and Uncracked Elastic Body Under the Action of Applied Surface Transactions Boundary Displacements and Body Forces

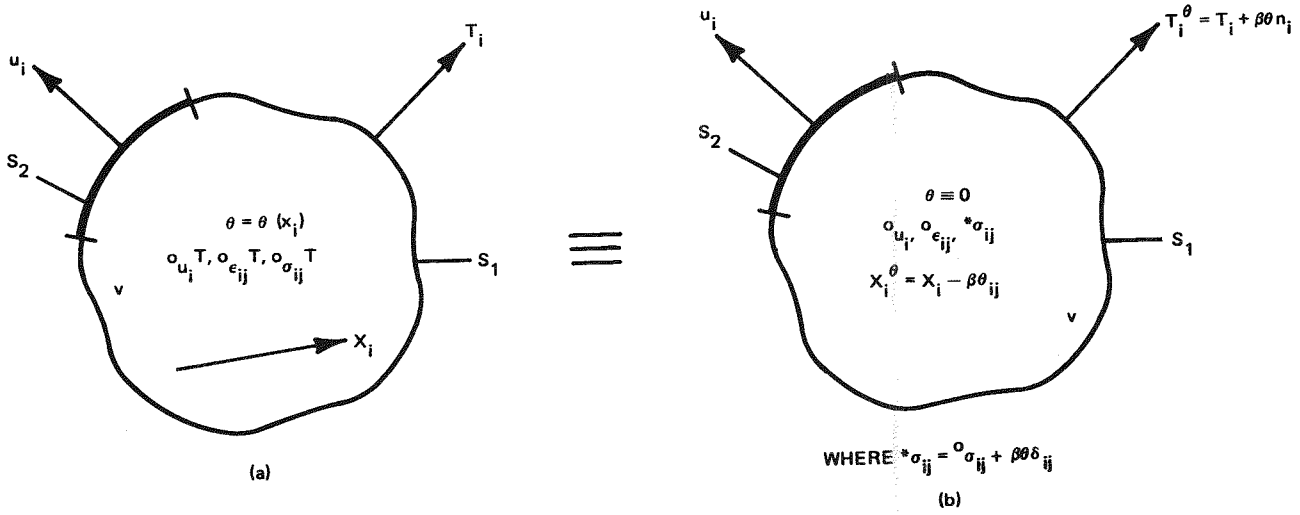

Figure F-6. Duhamel-Neumann Analogy in Thermo-Elasticity

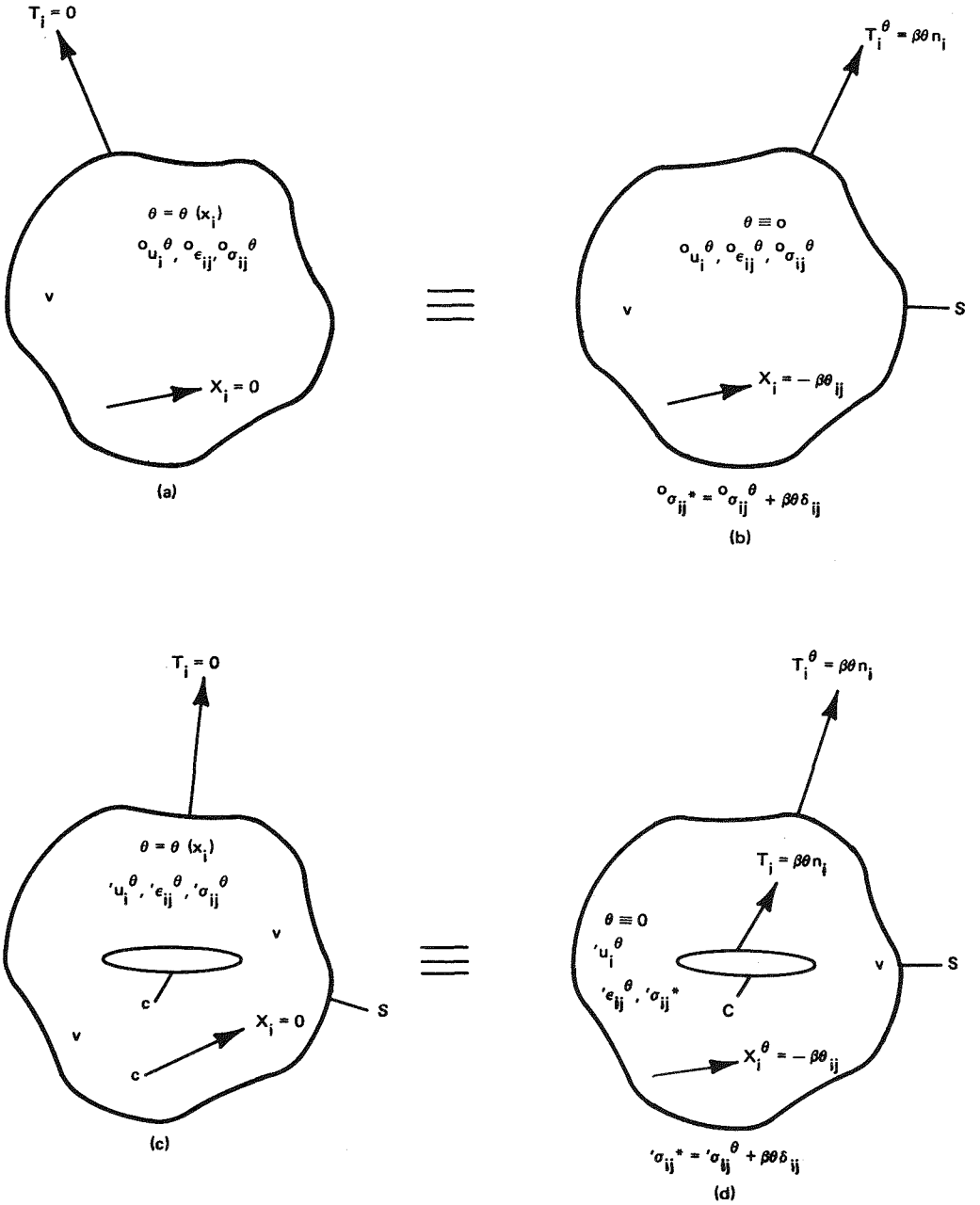

Figure F-7. Transformation of a Thermo-Elastic Problem for a Body with and without a Crack to a Boundary Value Problem Using Duhamel-Neumann Analogy

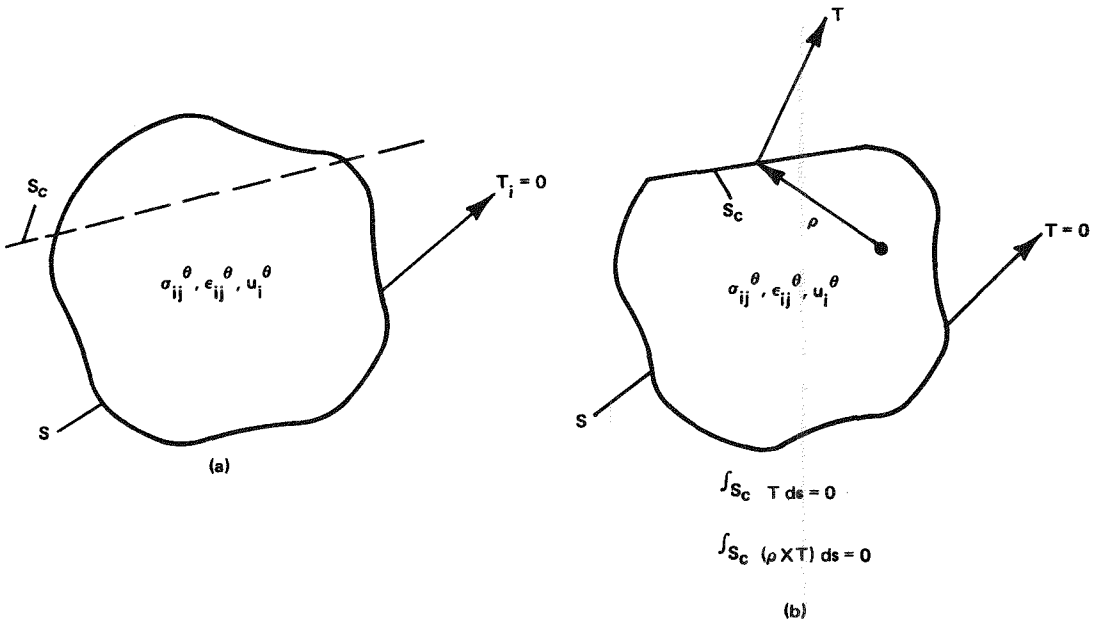

Figure F-8. Equilibrium Conditions for Thermal or Residual Stress Problem

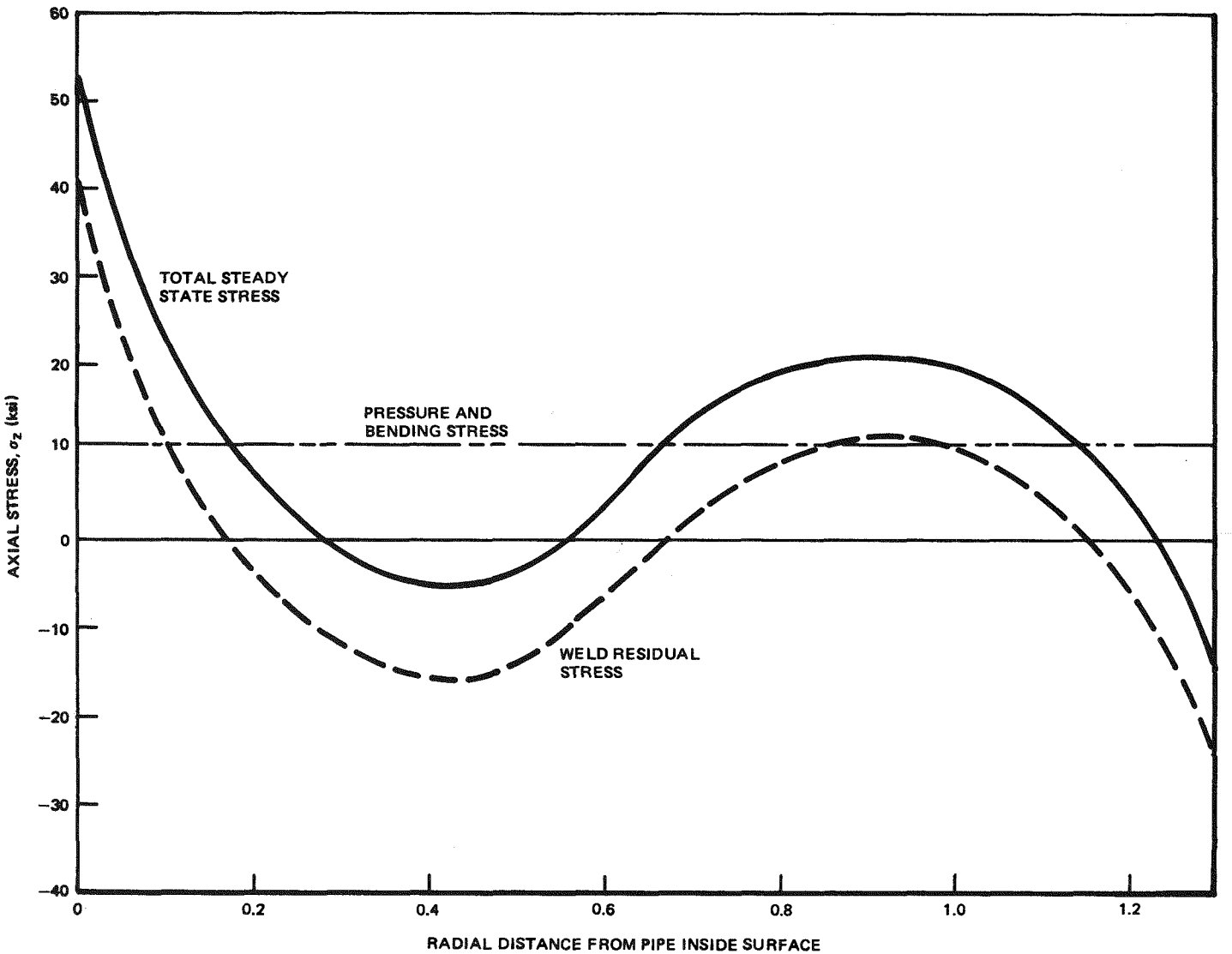

Figure F-9. Axial Stresses in a Butt-Welded 26-in.-Diameter Pipe During the System Normal Operation

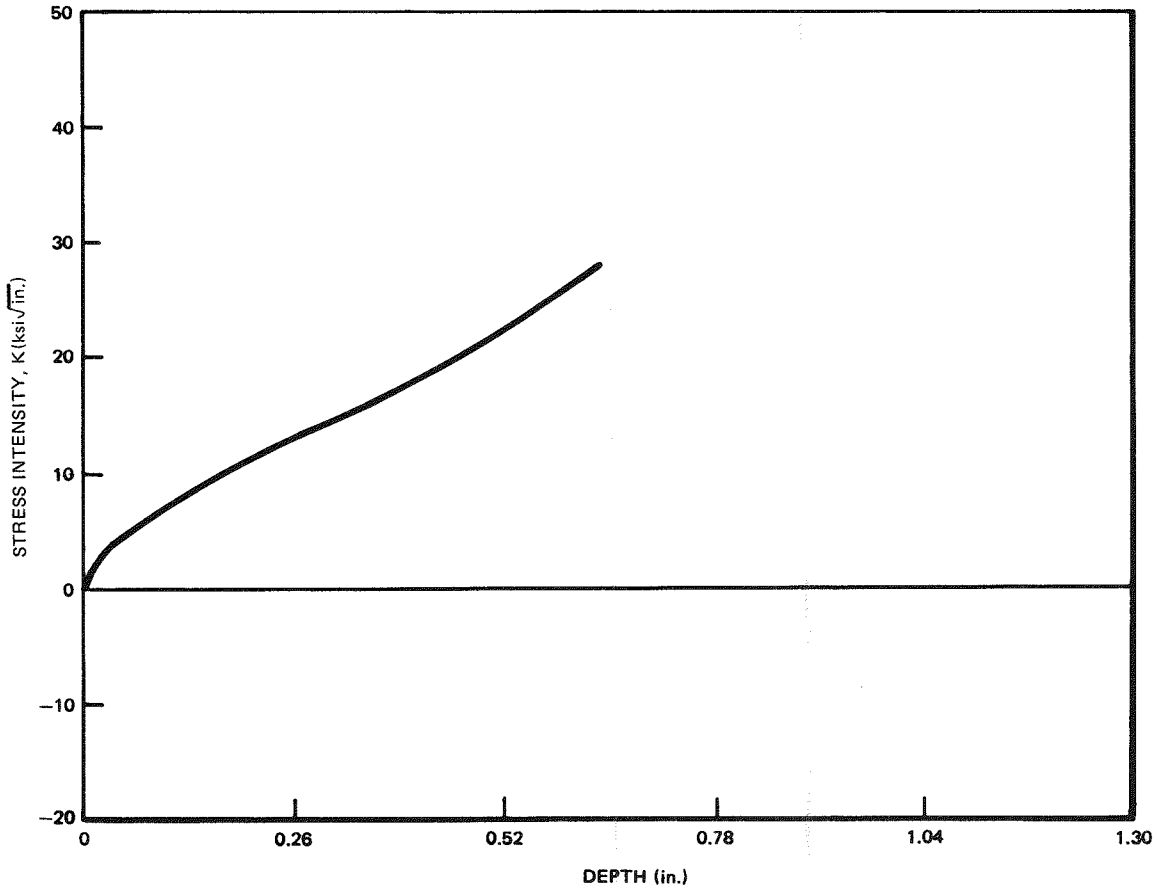

Figure F-10. Stress Intensity as a Function of Depth as Determined Using Buchalet and Bamford Finite Element Results

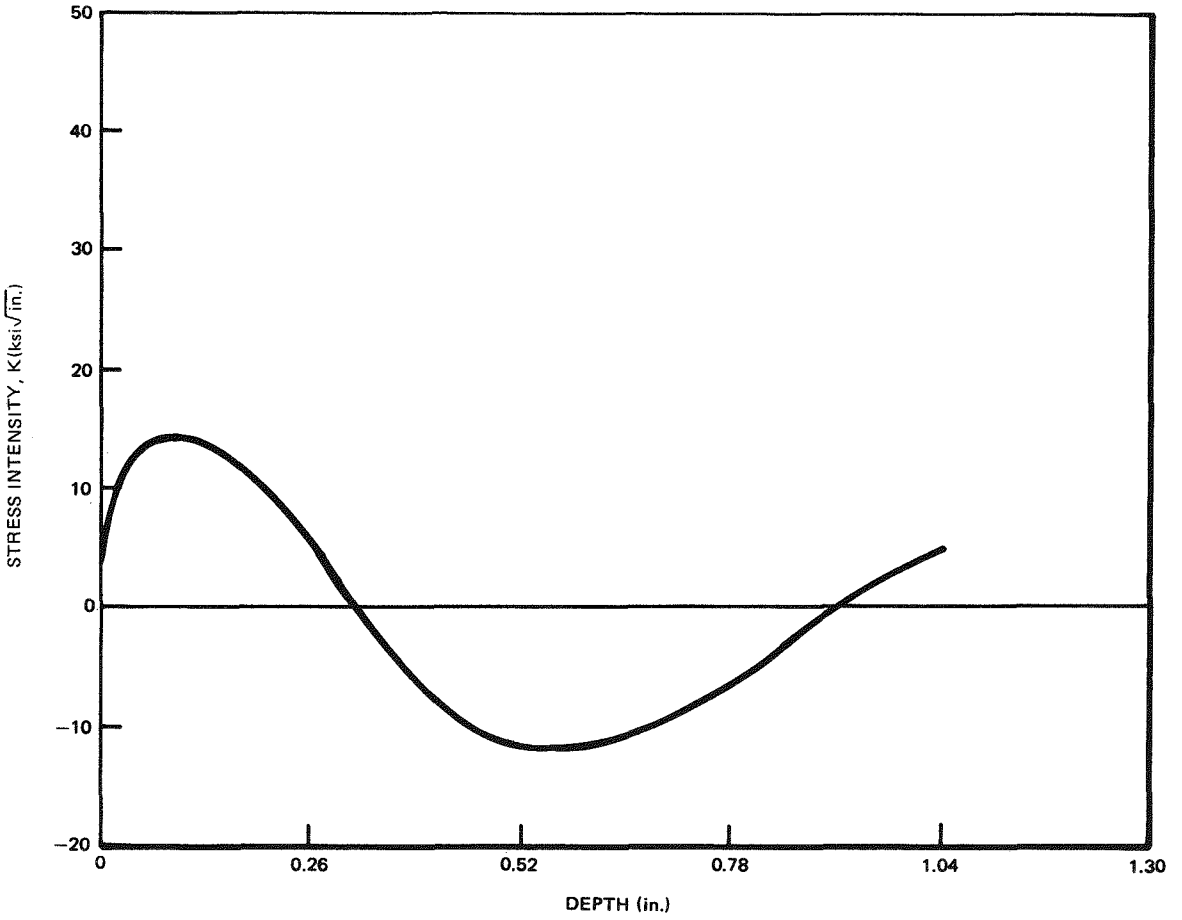

Figure F-11. Stress Intensity versus Depth for High Nonlinear Representative Weld Residual Stress, Determined Using Finite Element Methods

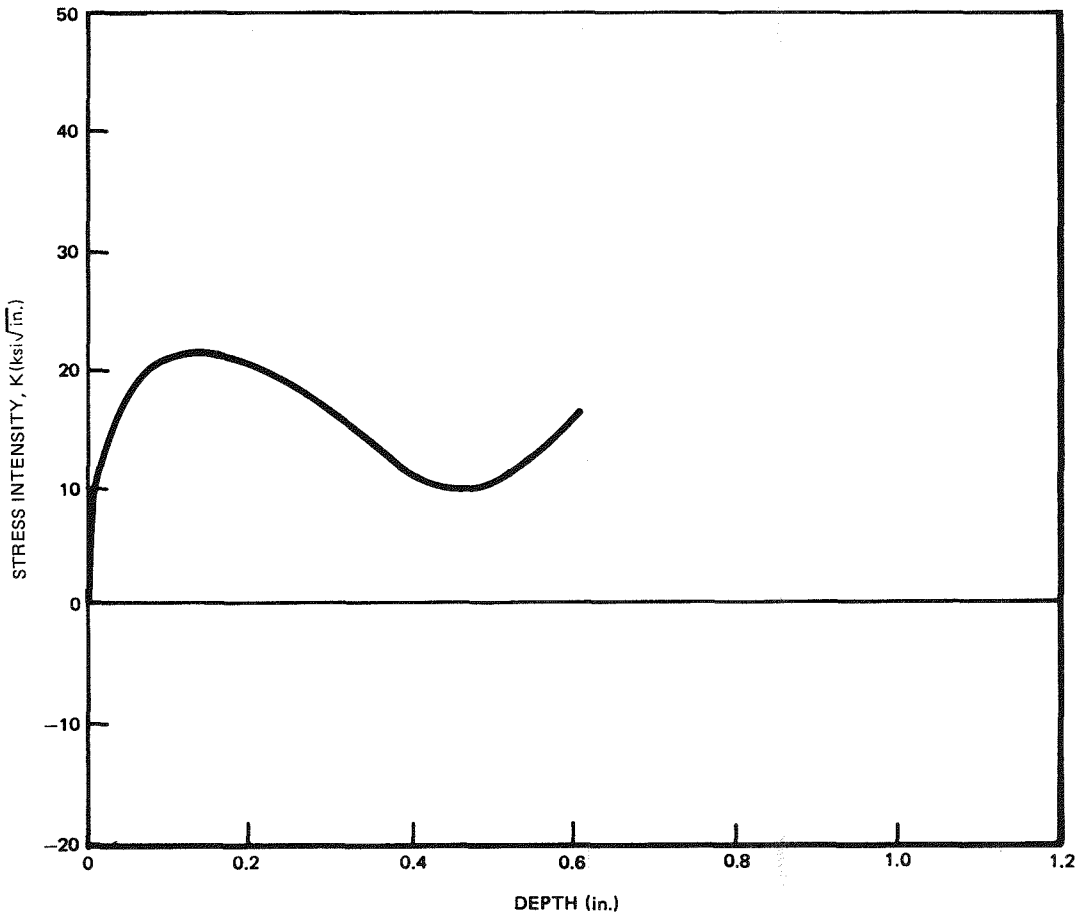

Figure F-12. Stress Intensity versus Depth for Stress State in Representative Large Pipe

Appendix G

WELD METAL CRACK ARREST EVALUATION
(C. W. Jewett)

G.1 SUMMARY AND CONCLUSIONS

A series of tests to investigate crack arrest in Type-308 Stainless Steel (SS) and Type-308L SS weld metals was completed. Tests were conducted on seven 1T-Wedge Open Loading (WOL) specimens fabricated from sensitized Type-304 SS base metal and either Type-308 SS weld metal with high (0.05%) or Type-308L SS weld metal with low (0.025%) carbon content, with one of three ferrite levels: 1.9-3.3% ferrite (low); 5.5-8.5% (medium); and 8.0-11.5% (high). Two weld geometries (90-deg crack intersection with weld metal and 30-deg crack intersection) were tested. The specimens were cycled in high temperature (550°F), high pressure (1,310 psig), 6 ppm O_2 demineralized water with an initial $\Delta K \tilde{=} 26$ ksi $\sqrt{in.}$ and R* = 0.05. The specimens were tested for 5448 hours, completing 1492 loading cycles.

Six of the seven specimens tested had cracks which penetrated the weld metal. Cracking in the weld metal tended to occur along the austenite/ferrite grain boundaries.

Test results show the 308L SS welds (5.5-11.5% ferrite) to be more resistant to cracking than the 308 SS welds. Crack arrest occurred in the 308L SS welds after less than 0.030 inch of penetration into the weld metal. Greater crack penetration occurred in the 308 SS welds with crack arrest occurring in the low and high ferrite content specimens after an average penetration of 0.104 inch and 0.045 inch, respectively. The crack in the mid-range ferrite level 308 SS weld had not arrested after 0.101 inch of penetration into the weld metal. No correlation between the weld metal ferrite content and weld metal crack arrest behavior was seen.

Even though most cracks that penetrated the weld metal appeared to arrest, Intergranular (IG) branch cracking continued to propagate along the base metal weld Heat-Affected Zone (HAZ) parallel to the weld/base metal interface.

*R = Minimum Load/Maximum Load

G.2 INTRODUCTION

Previous work has shown that carbon and ferrite content are important variables in controlling the susceptibility of Type-308 weld metal to stress corrosion cracking in a BWR environment. In general, it has been established that duplex alloys are indeed more resistant. The information developed about Type-308 weld metal has demonstrated the material's resistance to IGSCC initiation. In a pipe weld, however, it is important to evaluate whether weld metal is resistant to the propagation of an already existing stress corrosion crack. Because the weld metal's resistance to IGSCC initiation is a function of ferrite and carbon level, these variables will also influence the resistance to IGSCC propagation. Field experience has supported the premise that weld metal containing ferrite levels of 5% or greater will arrest a crack that has initiated in the HAZ.

The purpose of these tests was to investigate the factors influencing crack arrest. The combinations of weld metal carbon content and ferrite level that are necessary to arrest stress corrosion cracking in a sample that simulates a large-diameter pipe weld were identified. The effect of weld geometry relative to the propagating crack on this arrest behavior was also evaluated.

An initial test phase to investigate crack arrest in Type-308 SS weld metal was completed earlier and the results were reported in Reference G-1.

G.3 EXPERIMENTAL PROCEDURE

The test matrix for this work, Phase II, is presented in Table G-1. Seven 1T-WOL fracture mechanics-type specimens with a standard ASTM E-399 120-deg chevron notch and no side grooves were fabricated from specimen blanks of sensitized Type-304 SS base metal and Type-308 SS weld metal. Type-308 SS welds rod heats, selected to produce two carbon levels, and three ferrite levels were used to fabricate each specimen in two weld geometries (90-deg crack intersection with weld metal and 30-deg crack intersection with weld metal), as shown in Figures G-1 and G-2, respectively. Table G-1 shows the weld metal carbon content, weld metal ferrite level, and weld metal geometry for each of the seven specimens being tested in Phase II. Prior to testing, each of the seven specimens was fatigue pre-cracked to within 0.110-0.150 inch of the weld/base metal interface.

The sensitization treatment used was different for the two geometries. Whereas the 90-deg weld geometry's base material was furnace sensitized at 1,150°F for 24 hours, the 30-deg weld geometry's base material was sensitized at 1,150°F for 2 hours.

The reduced sensitization was picked to prevent crack path deviation due to extreme base material sensitization.

A closed-loop servo-hydraulic test machine cyclicly loaded the seven specimens in a series chain while they were immersed in a refreshed 550°F, 1,300 psig air-saturated (6 ppm O_2) demineralized environment. Dissolved oxygen content, pH, and conductivity of the water were monitored continuously and were controlled within the limits specified in Table G-2.

Cyclic testing was conducted at three loading waveforms/frequencies. These waveforms are detailed in Figures G-3a, b, and c. The test specimens were initially cycled using the same loading waveform as used in the Phase I tests and the nominal pipe tests (i.e., 5-min rising load, 75-min hold at maximum load, 5-min unload, 5-min hold at minimum load) (Figure G-3a). After 601 cycles, the waveform was changed to that shown in Figure G-3b (i.e., 4-hr rising load, 4-hr hold at maximum load and 5-min unload). This waveform was chosen to attempt to accelerate the specimen crack growth rate by greatly increasing the time spent during both rising load and maximum load, allowing greater interaction of the environment with the crack tip. After 70 cycles (i.e., 671 total cycles), this 8-hr per cycle waveform showed no apparent increase in crack growth rate, so the loading waveform was changed to the present 4-hour cycle shown in Figure G-3c. This waveshape was identical to the initial test waveshape (Figure G-3a), except the hold time at maximum load was extended from 75 minutes to 225 minutes and the maximum load was increased ∿7%.

A computerized Data Acquisition System (DAS) was used to monitor progress of the fatigue crack during environmental testing. The individual test specimens were equipped with a high-temperature Linear Variable Differential Transformer (LVDT) to measure the specimen Crack Opening Displacement (COD) during the rising load portion of the loading cycle. The resultant load/COD data (i.e., compliance) were then used to calculate crack lengths. A schematic of the complete test system is shown in Figure G-4.

G.4 RESULTS AND DISCUSSION - PHASE II

Specimen SS-431 was removed from test after 1311 cycles (4724 hours) when a visual side crack inspection showed that the crack had propagated into the weld metal. Specimen SS-431 was then sectioned as described in Subsection 6.4.2 and testing of the remaining six specimens continued until 1492 cycles (5448 hours) were completed.

G.4.1 Compliance and Crack Length Data

The 550°F compliance-based crack length versus cycles data for the seven specimens tested in Phase II are shown in Figures G-5 through G-11. Also shown in Figures G-5 through G-11 are several room temperature compliance-based crack lengths and the location of the weld/base metal interface as measured from the sides of the specimens. It should be noted that the location of the weld/base metal interface varied through the specimen thickness. The variation occurred during the laying of the manual weld beads and was accentuated in the 30-deg weld geometry specimens.

It should be noted that each test shutdown had a temporary effect on the compliance data. Figure G-12 shows the compliance-based crack length versus cycles data for Specimen SS-632 (replotted from Figure G-11) with all the test shutdowns that occurred throughout testing. A test shutdown is defined as a cooldown/depressurization of the environmental test loop which supplies the high-temperature and high-pressure demineralized water to the autoclave.

Figure G-12 shows that a shift in compliance occurred with each test startup/shutdown event. The magnitude of the compliance shift tended to gradually decrease once test cycling resumed until the compliance-based crack length approaches the value it had prior to the test shutdown. Although Specimen SS-632 (Figure G-12) was used to illustrate this trend, the apparent compliance shift with test shutdowns occurred for all seven specimens being tested in Phase II.

G.4.2 Metallography

Upon completion of testing, the seven specimens were sectioned as shown in Figure G-13. Five metallographic sections were cut from each specimen at 0, 25, 50, 75 and 100 percent of the specimen thickness. Composite photographs of all five sections for SS-333 and SS-431 are shown in Figures G-14 through G-18 and Figures G-19 through G-23, respectively. Composite photographs of the 50 percent sections from specimens SS-233, SS-534, SS-632, SS-223 and SS-324 are shown in Figures G-24 through G-28, respectively.

As previously observed in the Phase I tests, the heating of the sensitized base metal during welding resulted in a narrow recrystallized region of base metal adjacent to the weld which was less sensitized than the rest of the base metal. The in-plane cracking (i.e., cracking perpendicular to the loading plane) in this recrystallized region was predominately Transgranular (TG) in nature with sight mixed mode (i.e., transgranular/intergranular) cracking. Intergranular stress corrosion

(IGSCC) branch cracks are shown to initiate perpendicular to the precrack plane and tended to propagate parallel to the weld metal approximately 0.050 to 0.100 inch from the weld/base metal interface. The tendency for TG cracking toward the weld and IGSCC cracking parallel to the weld can be seen in Figure G-27 (90° weld geometry) and Figure G-26 (30° weld geometry).

The second observation which can be made from the metallography is that the cracks at the sides of the specimens tended to be more intergranular and propagate much further than they did in the specimen interiors. This can be seen in specimen SS-333 by comparing Figure G-14 which shows a section near the side of the specimen (i.e., Section 0) with Figures G-15 through G-17 which show sections through 25, 50 and 75 percent of the sample thickness, respectively. This observation is consistent with previous tests of the Type-304 stainless-steel 1T-WOL specimens in this environment. This phenomenon has been attributed to a different stress state at the sides of the specimen (i.e., non-plane strain) and a shorter mean free path to the refreshed oxygenated environment. The tendency for accentuated crack growth at the specimen sides has been observed in most crack growth specimens.

Table G-3 shows the average depth of crack penetration into the weld metal for the seven test specimens. Of the two 90-deg weld geometry specimens (SS-223 and SS-324), only one metallographic section (SS-223 Section 50) showed a crack that reached and penetrated ($\sim$0.031 in.) the weld metal. The crack penetration in the 30-deg geometry welds was greater in the high carbon content welds than in the low carbon content welds.

The cracks tended to penetrate the weld metal perpendicular to the weld/base metal interface and propagate along the columnar weld metal austenite/ferrite grain boundaries. Figure G-29 shows a crack that changed directions to follow the columnar austenite/ferrite boundaries as it propagated from one weld bead to the next. Micrographs (400x) of the weld metal crack tips for the six specimens with cracks propagating into the weld metal are shown in Figures G-30 through G-35.

One crack tip section sliced from each of three specimens (SS-333, SS-431, SS-534) was broken out of its metallographic mount and fractured in half to examine the specimen fracture surface. Scanning Electron Microscopy (SEM) fractographs of the weld metal fracture surface for specimens SS-333, SS-431, and SS-534 are shown in Figures G-36 through G-38, respectively.

G.4.3 Crack Growth Data

Table G-4 summarizes the change in specimen crack length, Δa, (i.e., final crack length - initial crack length) which occurred during environmental testing. The crack length measurements were made three ways: (1) calculated based upon 550°F compliance data; (2) measured from the metallographic sections; and (3) measured from the specimen fracture surface. The compliance-based crack length measurements tended to be longer than either the section or fracture surface measurements. The multiple branch cracks in the specimens made them more compliant and thus indicate more crack growth than was measured from the longest crack component perpendicular to the loading plane. In addition, the compliance-based crack growth measurements accounted for the longer cracks at the sides of the specimens while the section and fracture surfaces measurements did not since they were an average of measurements made only on the interior of the specimens.

Time and cycle based crack growth rates for the seven specimens are shown in Table G-5. The test average growth rates (i.e., $\Delta a/\Delta N$ and $\Delta a/\Delta t$) were obtained by dividing the total compliance-based crack growth by the total test cycles and total time, respectively. Incremental crack growth rates (i.e., da/dN) were also obtained by selecting regions of the compliance-based crack length versus cycles (i.e., da/dN) of a second order line fit through seven consecutive data points. The incremental crack growth rates tabulated in Table G-5 are representative numbers in the range of rates obtained from several regions of the a versus N curves. The a versus N curves for specimens S-324, SS-333, SS-431, and SS-632 (Figures G-8 through G-10, respectively) showed a decreased slope (i.e., crack growth) at the end of testing. The end of test incremental growth rates for these four specimens are shown in parentheses. The da/dt growth rates were obtained by multiplying the da/dN rates by the cyclic frequency.

Figures G-32, G-33, and G-35 show that the weld metal crack tips for specimens SS-333, SS-431, and SS-632 were filled with oxides, indicating that these cracks had arrested which correlates with the decreased crack growth rates in these specimens at the end of testing. Only specimen SS-534 showed (1) extensive cracking (>0.100 in.) in the weld metal, (2) a crack tip not plugged with oxides, and (3) no decrease in crack growth rate. It should be noted that even in the specimens showing arrest in the weld metal, IGSSC cracking continued to occur in the base metal heat-affected zone. This accounts for the finite, yet slower, compliance-based growth rates.

Figures G-39 through G-41 are SEM fractographs of specimens SS-431, SS-333, and SS-534, respectively, which show fatigue striations. Crack growth rates measured from the striation spacings are also tabulated in Table G-5.

G.4.4 Weld Metal Susceptibility and Cracking Mechanism

Crack arrest in the weld metal will occur when the driving stress intensity, ΔK, at the weld crack tip falls below the threshold value of K required for cracking in the particular as-welded material. The multiple crack branches and the unknown residual stress distributions in the specimens made it impossible to calculate ΔK at the crack tip. Therefore, it was not possible to quantify the susceptibility of the various welds based upon a relation of ΔK versus crack penetration into the weld. The K levels based on the external applied loads were higher than those expected in large pipes, and the branching was different from that behavior observed in the one overseas plant.

Devine (Reference G-2) investigated the influence of carbon content and ferrite morphology on the intergranular corrosion behavior of 308 stainless steel weld deposited alloys. His investigation concluded that there existed a critical distribution of austenite/ferrite (i.e., α-γ) boundary area above which the alloy was immune and below which it was susceptible to intergranular corrosion. Devine presented this critical distribution as a bounding line on a plot of $N_L^{\alpha-\gamma}$ versus carbon content, where $N_L^{\alpha-\gamma}$ is defined as the number of intercepts of a random test line with α-γ boundaries per unit length of the test line. Three to five $N_L^{\alpha-\gamma}$ measurements were made on each of the welds tested and the mean $N_K^{\alpha-\gamma}$ values with their corresponding one standard deviation error bars are plotted as a function of carbon content on Devine's curve shown in Figure G-42. Only the measurements from specimen SS-431 lay below the critical distribution line (i.e., sensitized region) and thus according to Devine's criteria was susceptible to intergranular corrosion. Since the other specimens lay above the line they should have been immune to sensitization and intergranular corrosion.

According to Devine's criteria for susceptibility of stainless steel weld metal to IGSCC, a difference in crack morphology between SS-431 (high carbon, low ferrite) and the rest of the specimens that experienced cracking in the weld metal would be expected. However, metallographic examination showed a marked similarity in weld metal crack morphology for all specimens tested. Although cracks sometimes did propagate through the austenite or ferrite gains, the over-all trend was for cracks to propagate along the austenite/ferrite grain boundaries which would indicate that these boundaries were more susceptible to cracking. It might be possible that the austenite/ferrite grain boundaries were more susceptible to mechanical fatigue damage, but that would not explain why cracks did not propagate as far in the low carbon content welds. It is much more likely that the austenite/ferrite were sensitized and that cracking occurred by corrosion fatigue. The low carbon content

weld material would be less likely to form chromium carbides at the grain boundaries (i.e., sensitized), except in a narrow region adjacent to the weld/base metal interface where the localized carbon content will be greater due to mixing during solidification with the high average carbon content of the base metal. This would explain why the cracks arrested after propagating a short distance into the low carbon content weld metal.

The tests were conducted at high ΔK's and K_{max}, and always had load cycling. If the conditions were nearer to those experienced by pipes in the field, i.e., constant load and lower K_{max}, the cracks might have arrested or grown extremely slowly, in all ferrite/carbon weldments. The depth of the crack in the heat-affected zone followed that of the weld metal. Therefore, the weld metal in actual pipes could lead to a significant reduction in crack growth rate through the pipe thickness.

G.5 REFERENCES

G-1. R. M. Horn, et al., "The Growth and Stability of Stress Corrosion Cracks in Large Diameter BWR Piping, First Semiannual Report, May - October 1979," November 1979 (NEDC-24750-1).

G-2. T. M. Devine, Metallurgical Transactions, Vol. 11A, No. 5, p. 791, 1980.

Table G-1

PHASE II TEST SPECIMENS

Specimen ID	Weld Metal Carbon Content (%)	Weld Metal Ferrite Level (%)	Weld Geometry (deg)	Base Metal[a]
SS-223	0.025	5.5 - 8.5	90	FS
SS-233	0.025	5.5 - 8.5	30	WS
SS-324	0.025	8.0 - 11.5	90	FS
SS-333	0.025	8.0 - 11.5	30	WS
SS-431	0.053	1.9 - 3.3	30	WS
SS-534	0.053	7.0 - 8.5	30	WS
SS-632	0.05	9.5 - 11.5	30	WS

[a]Metallurgical Condition

FS = Furnace Sensitized - 1,150°F/24 hours
WS = Weld Sensitized - 1,150°F/2 hours, air-cooled

Table G-2

ENVIRONMENTAL CONDITIONS FOR TESTING
IN AIR-SATURATED WATER

Temperature	550°F ± 10°F
Pressure	1,300 psi ± 20 psi
Oxygen	6.0 ppm ± 2.0 ppm
Conductivity	1.0 µmho ± 0.5 µmho at 25°C
pH	5.5 ± 0.5 at 25°C

Table G-3

WELD METAL CRACK PENETRATION - PHASE II

Specimen ID	Weld Geometry	Carbon Content	Ferrite Level	Weld Penetration[a] (in.)
SS-223	90°	0.025	5.5 - 8.5	0.031
SS-233	30°	0.025	5.5 - 8.5	0.010
SS-324	90°	0.025	8.0 - 11.5	--[b]
SS-333	30°	0.025	8.0 - 11.5	0.022
SS-431	30°	0.053	1.9 - 3.3	0.104
SS-534	30°	0.053	7.0 - 8.5	0.101
SS-632	30°	0.053	9.5 - 11.5	0.045

[a]Average length of crack penetration into weld as measured in Sections 25, 50, 75. Includes only those sections where the crack penetrates weld.
[b]Crack did not penetrate weld metal; however, some crack branches in HAZ went beyond interface depth.

Table G-4

CRACK LENGTH MEASUREMENTS - PHASE II

		Crack Length[a] (in.)	
Specimen ID	Compliance[b]	Section[c]	Fracture Surface[d]
SS-223	0.137	0.101	--
SS-233	0.120	0.118	--
SS-324	0.151	0.123	--
SS-333	0.140	0.097	0.115
SS-431	0.159	0.133	0.134
SS-534	0.193	0.173	0.153
SS-632	0.129	0.143	--

[a]Δa (i.e., final crack length - initial length)
[b]Based on 550°F compliance measurements
[c]Average of longest crack perpendicular to loading plane as measured from sections 25, 50, 75
[d]Average crack growth perpendicular to loading plane (<20% of total fracture surface measured)

Table G-5

CRACK GROWTH RATES - PHASE II

Specimen ID	$\Delta a/\Delta N$[a] (in./cycle)	$\Delta a/\Delta t$[b] (in./hour)	da/dN[c] (in./cycle)	da/dt[c] (in./hour)	$\Delta a/\Delta N$ Surface[d] (in./cycle)
SS-223	9.2×10^{-5}	2.5×10^{-5}	1×10^{-4}	3×10^{-5}	--
SS-233	8.0×10^{-5}	2.2×10^{-5}	7×10^{-5}	2×10^{-5}	--
SS-324	1.0×10^{-4}	2.8×10^{-5}	2×10^{-4} (8×10^{-5})	5×10^{-5} (2×10^{-5})	--
SS-333	9.4×10^{-5}	2.6×10^{-5}	1×10^{-4} ($<5 \times 10^{-5}$)	3×10^{-5} ($<1 \times 10^{-5}$)	1.7×10^{-4} (base metal)
SS-431	1.2×10^{-4}	3.4×10^{-5}	1×10^{-4}	3×10^{-5}	1.4×10^{-4} (base metal)
			($\sim 1 \times 10^{-5}$)	($\sim 3 \times 10^{-6}$)	7.0×10^{-5} (weld metal)
SS-534	1.3×10^{-4}	3.6×10^{-5}	1×10^{-4}	3×10^{-5}	3.2×10^{-4} (base metal)
SS-632	8.6×10^{-5}	2.4×10^{-5}	1×10^{-4} ($<1 \times 10^{-5}$)	3×10^{-5} ($<3 \times 10^{-6}$)	--

[a] Compliance-based crack growth/total cycles

[b] Compliance-based crack growth/total hours

[c] End of test rates are shown in parentheses if end of test rate changed

[d] Measured from fatigue striations

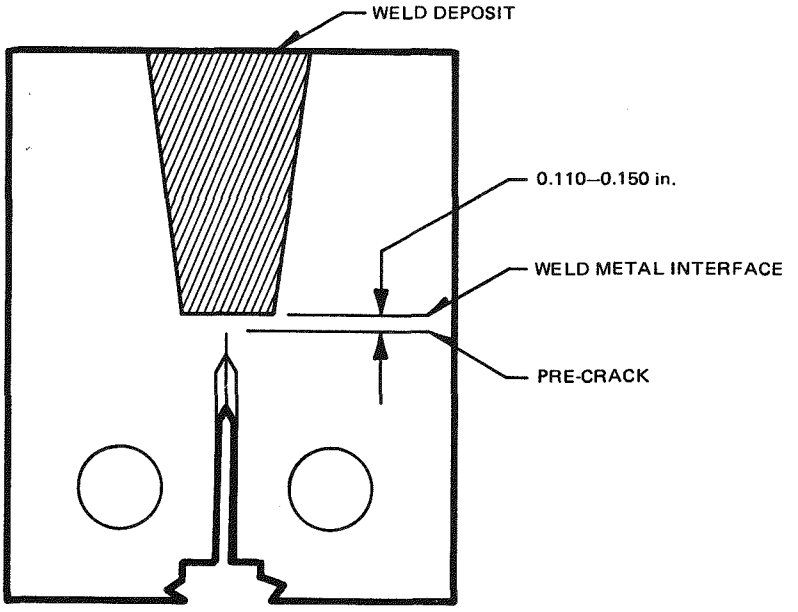

Figure G-1. WOL Test Specimen Designed to Investigate Crack Arrest for 90-Deg Crack Intersection

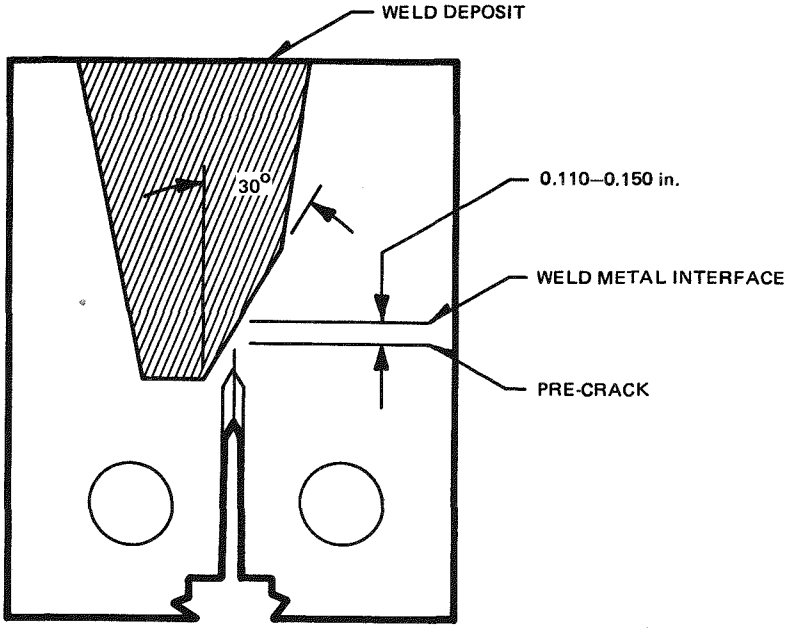

Figure G-2. WOL Test Specimen Designed to Investigate Crack Arrest for 30-Deg Crack Intersection

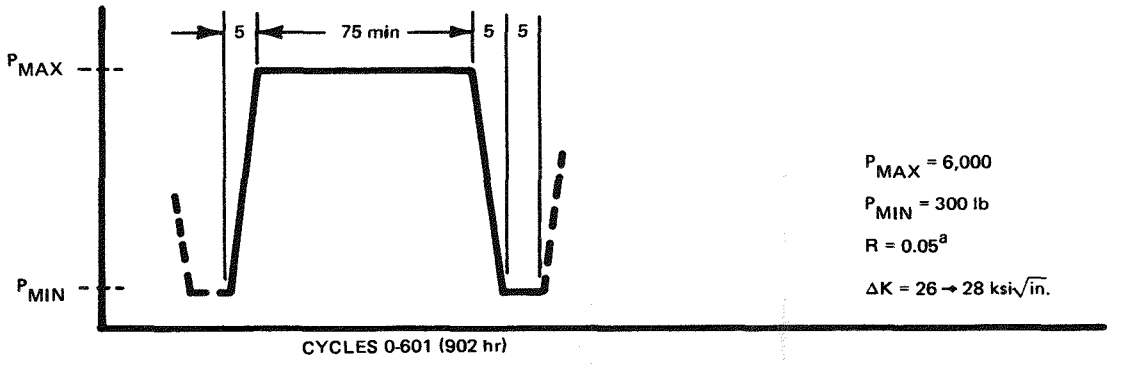

(a)

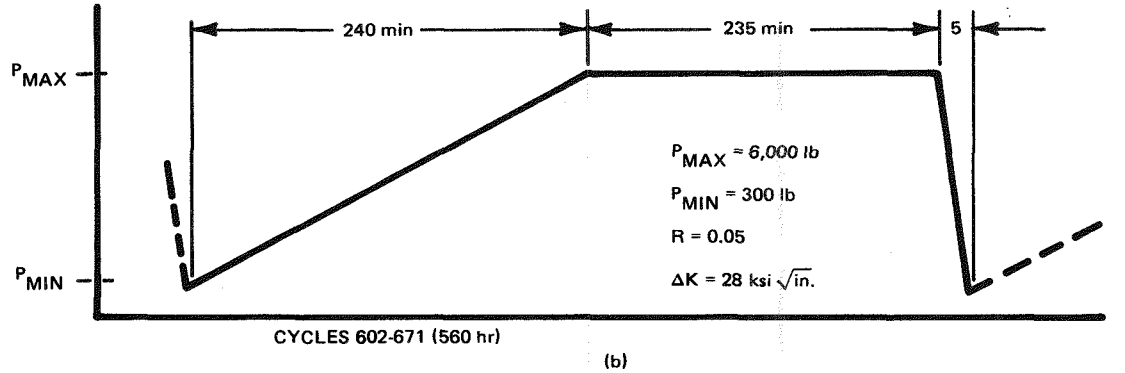

(b)

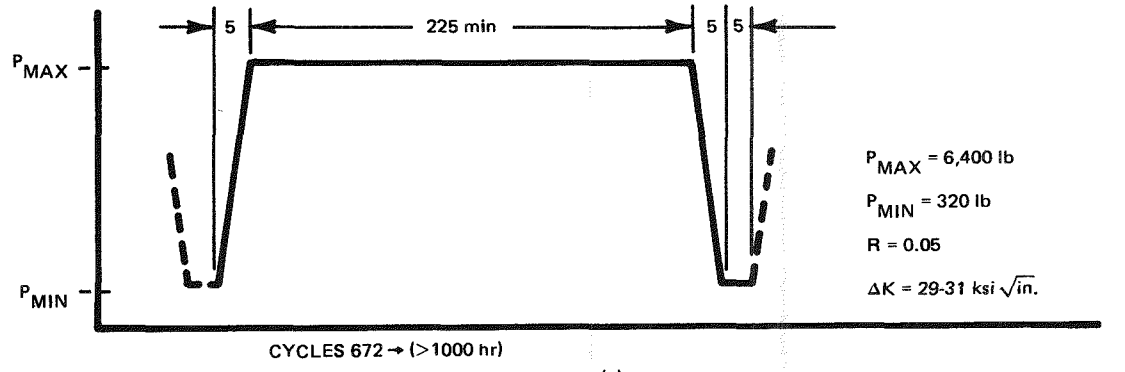

(c)

Figure G-3. Test Waveform

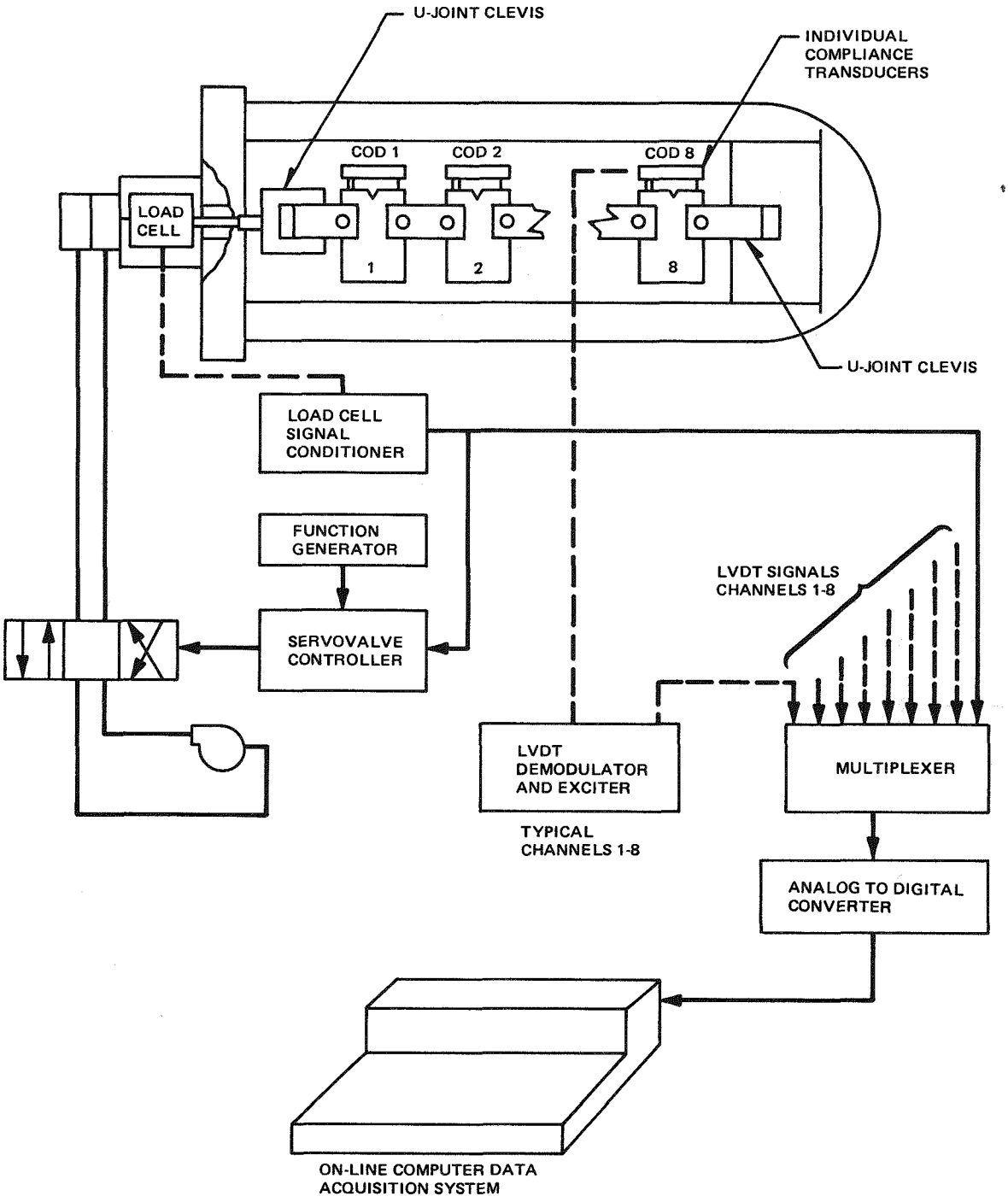

Figure G-4. Schematic of Test Vessel VI, Multispecimen Environmental Test Facility

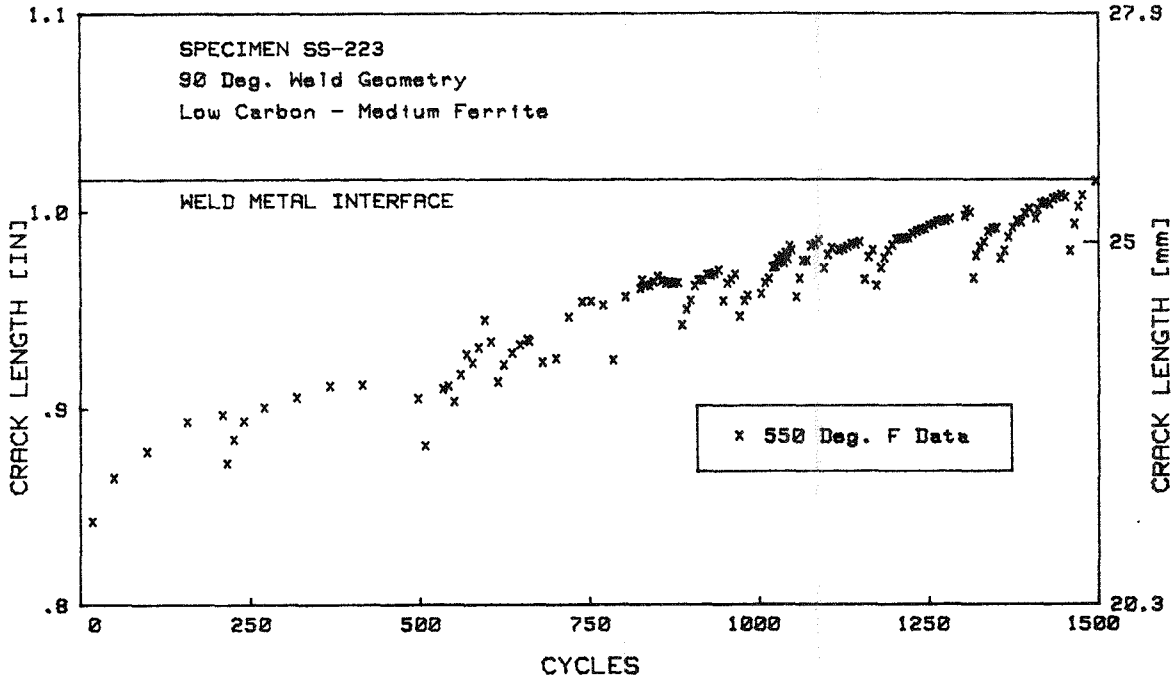

Figure G-5. Specimen SS-223 90-Deg Weld Geometry
Low Carbon - Medium Ferrite

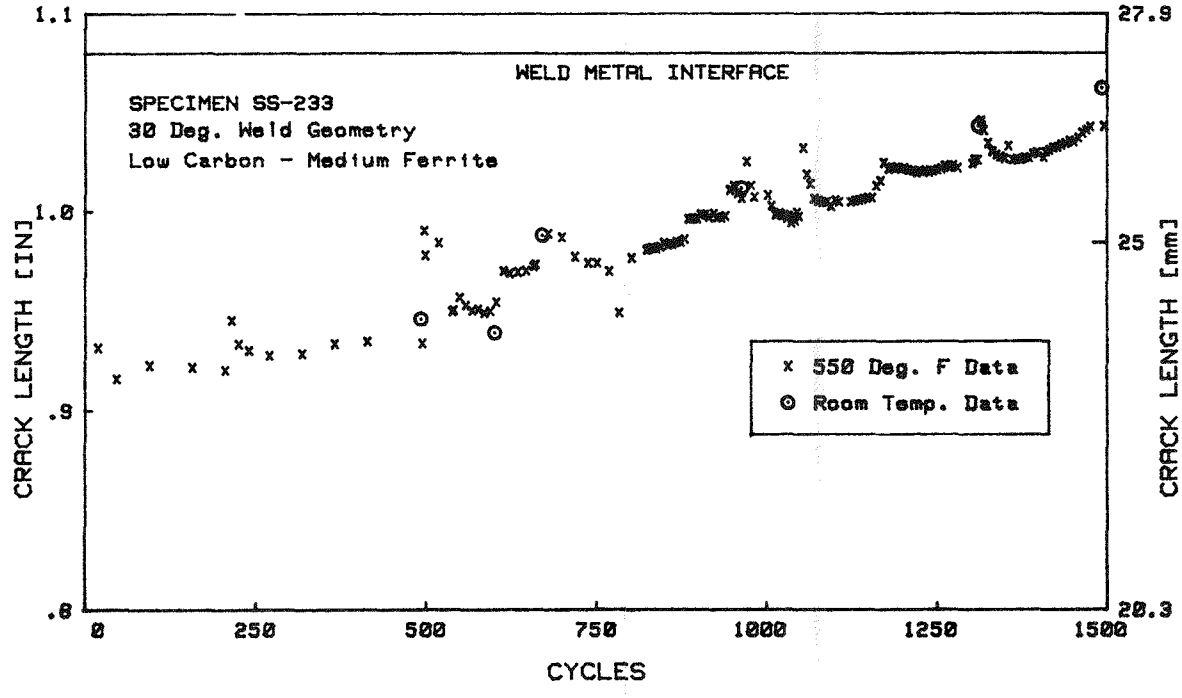

Figure G-6. Specimen SS-233 30-Deg Weld Geometry
Low Carbon - Medium Ferrite

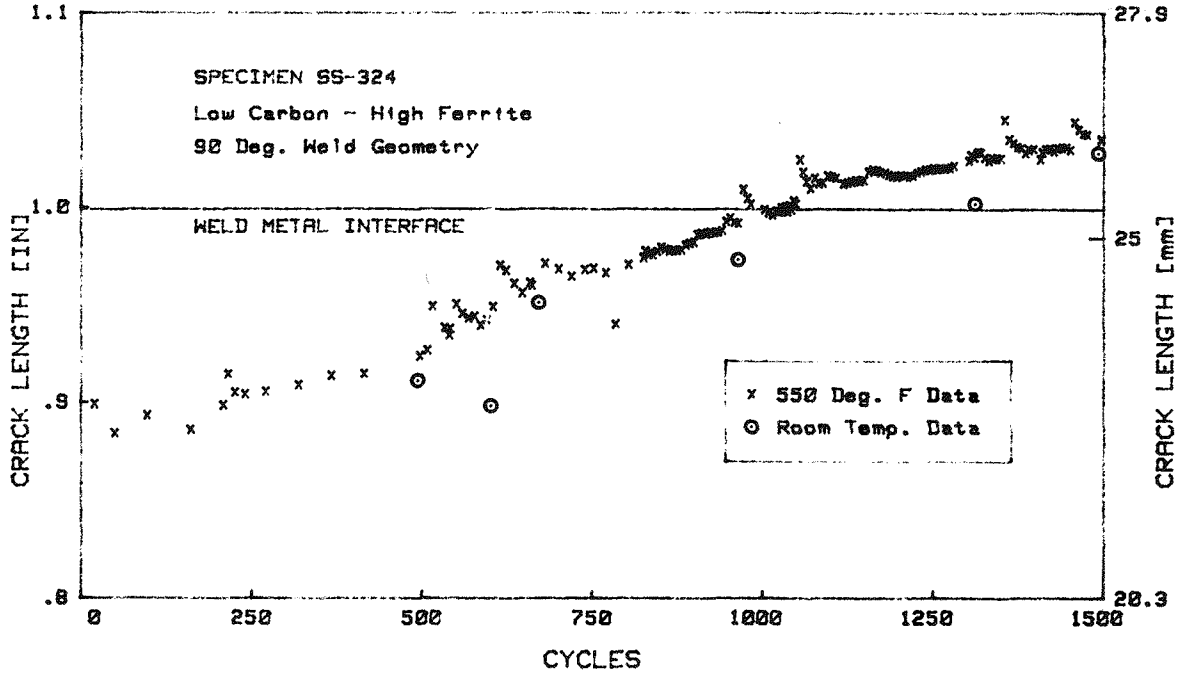

Figure G-7. Specimen SS-324 Low Carbon - High Ferrite 90-Deg Weld Geometry (Although crack never penetrated weld metal, some crack branches in HAZ were beyond interface.)

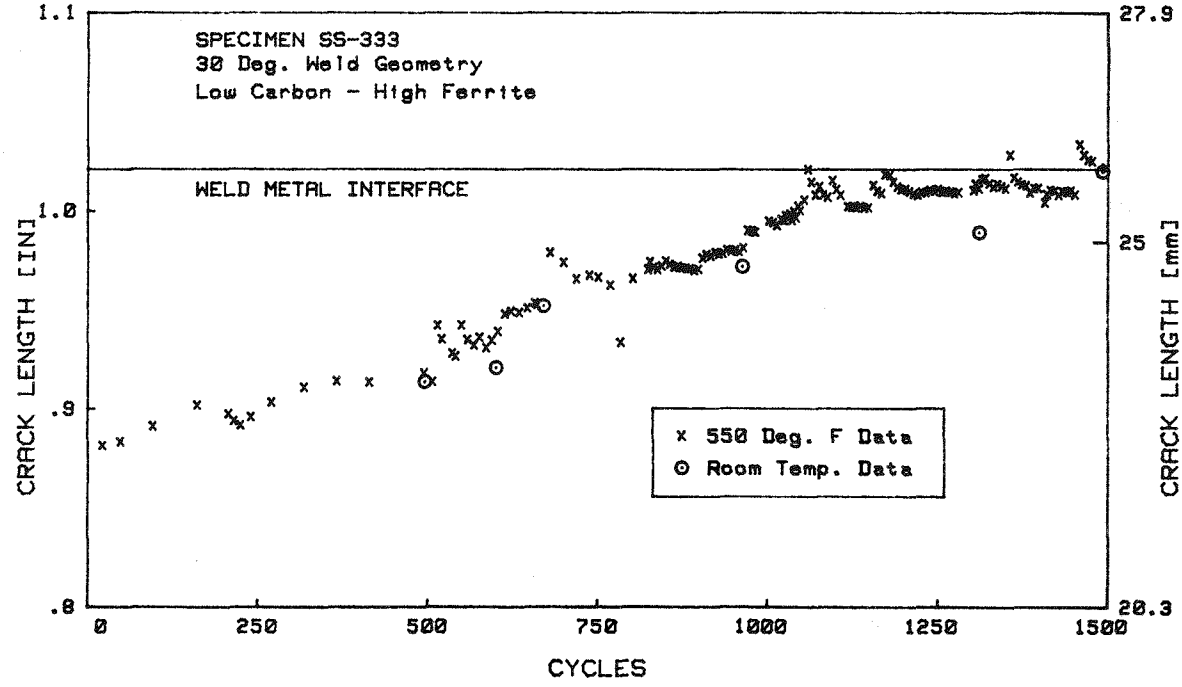

Figure G-8. Specimen SS-333 30-Deg Weld Geometry Low Carbon - High Ferrite

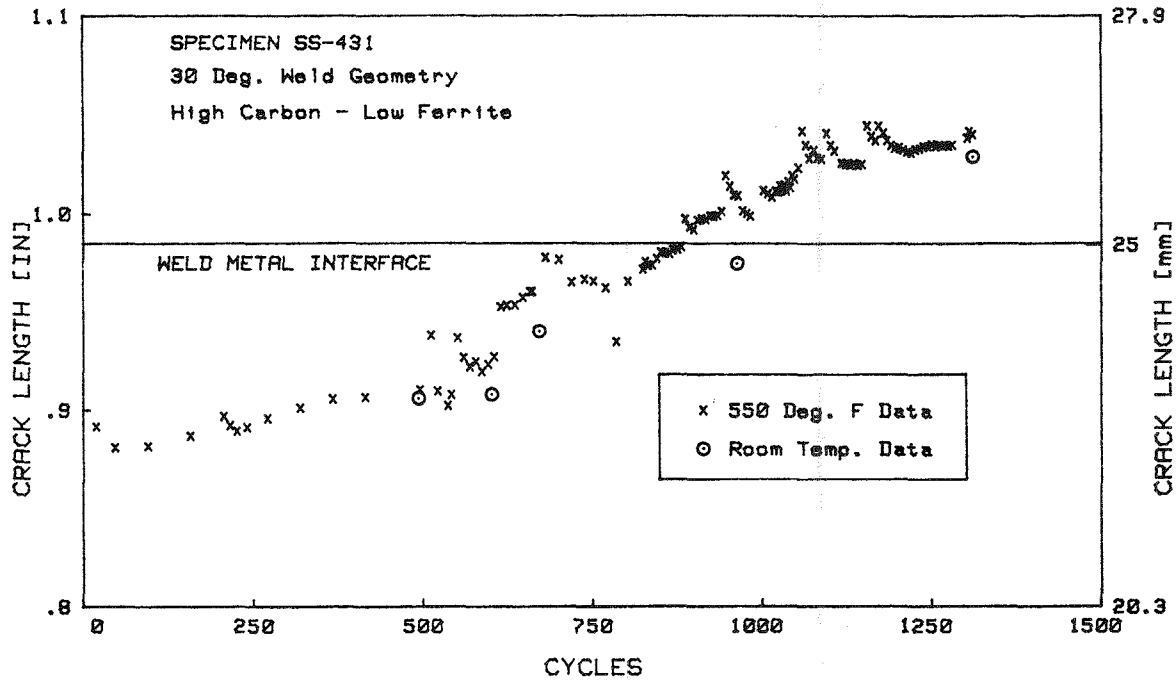

Figure G-9. Specimen SS-431 30-Deg Weld Geometry
High Carbon - Low Ferrite

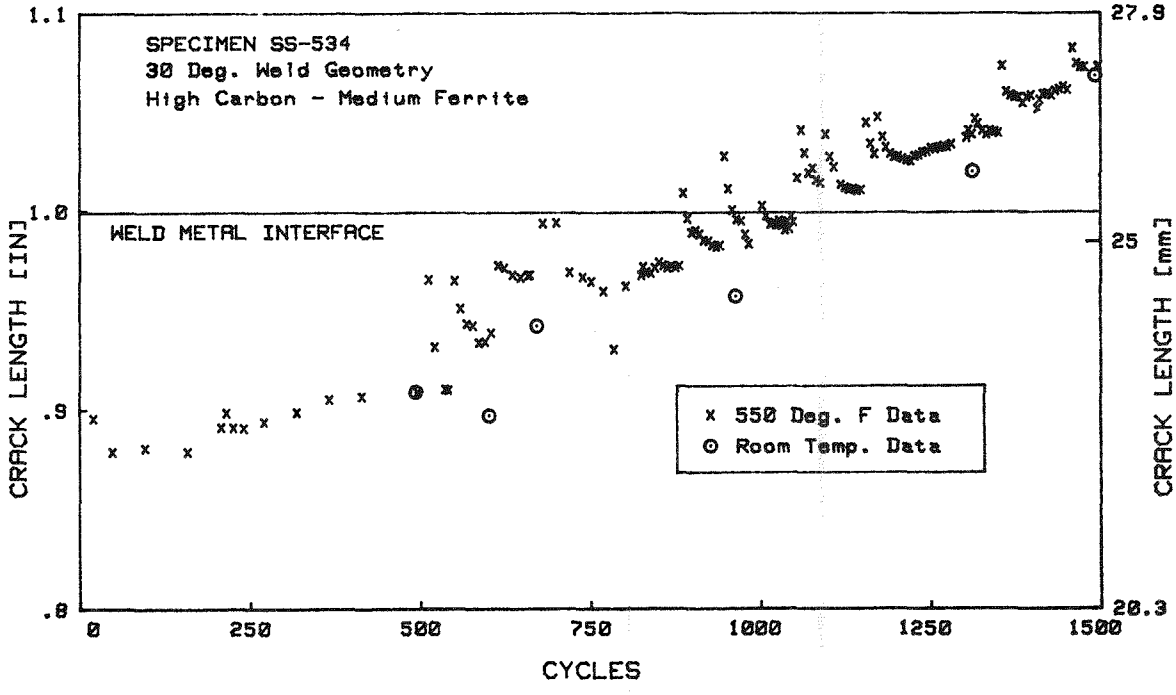

Figure G-10. Specimen SS-534 30-Deg Weld Geometry
High Carbon - Medium Ferrite

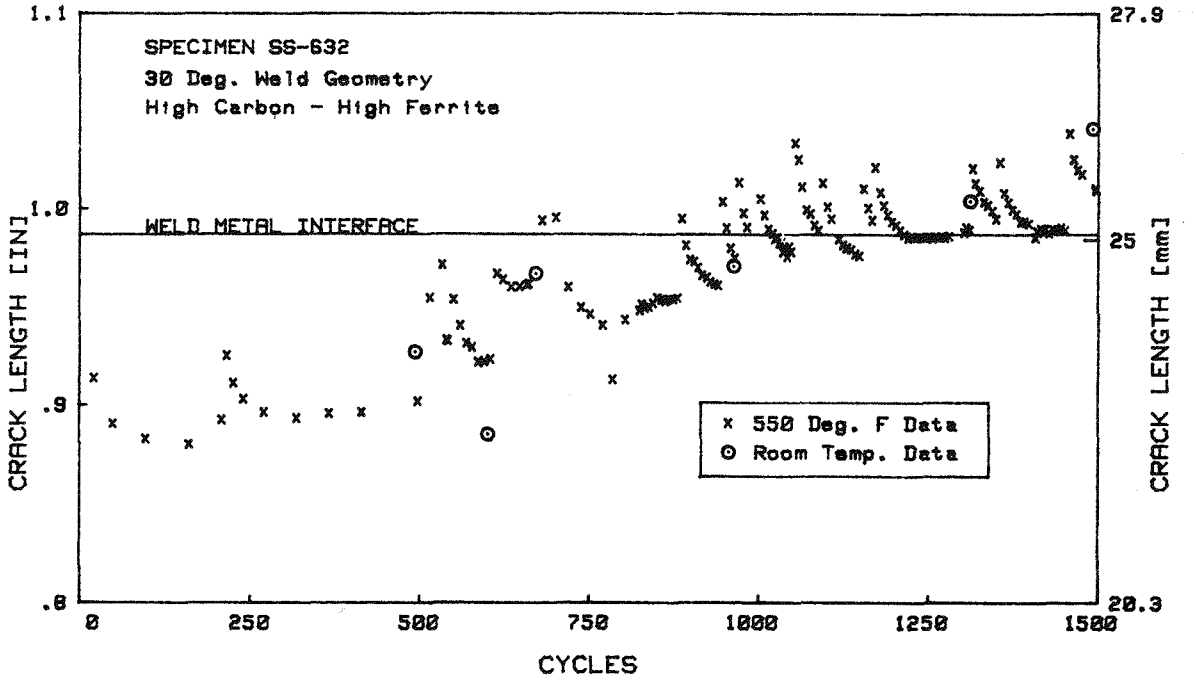

Figure G-11. Specimen SS-632 30-Deg Weld Geometry
High Carbon - High Ferrite

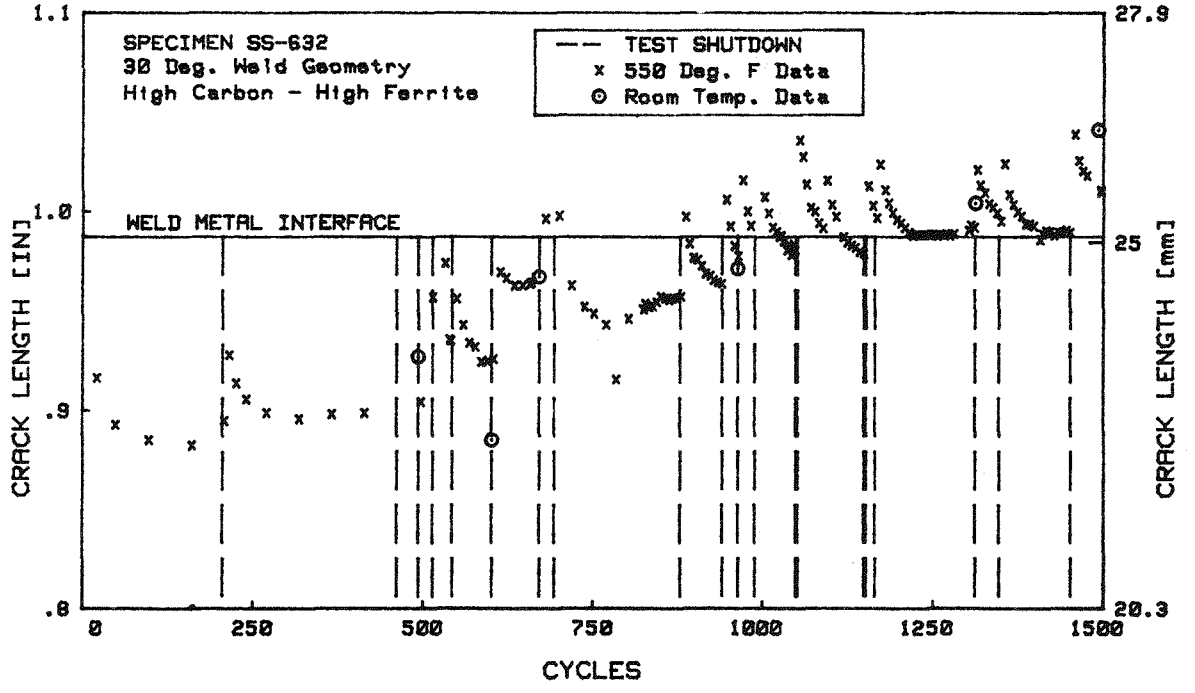

Figure G-12. Specimen SS-632 30-Deg Weld Geometry
High Carbon - High Ferrite

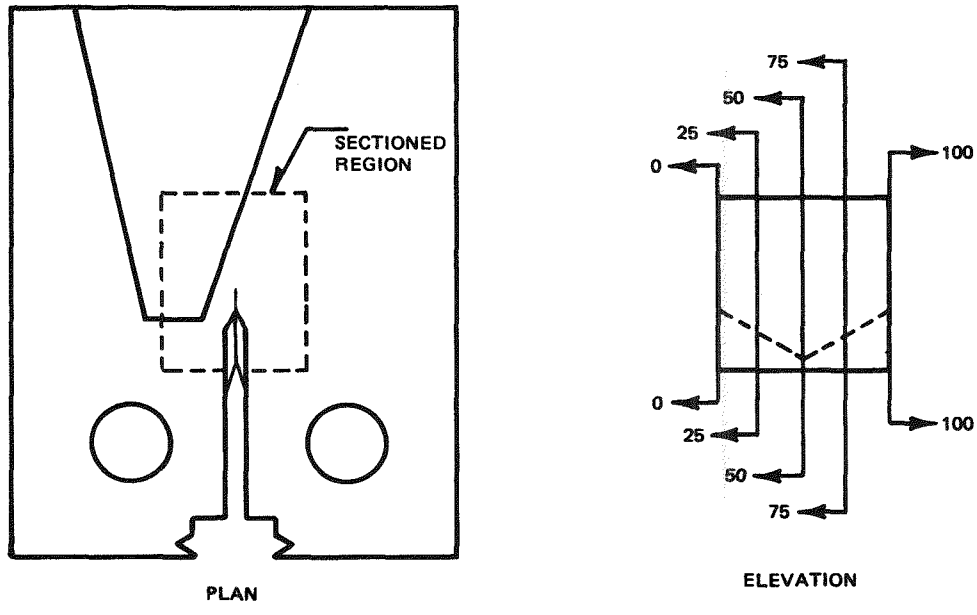

Figure G-13. Diagram Showing How WOL Specimens Were Sectioned (Labeling also indicated)

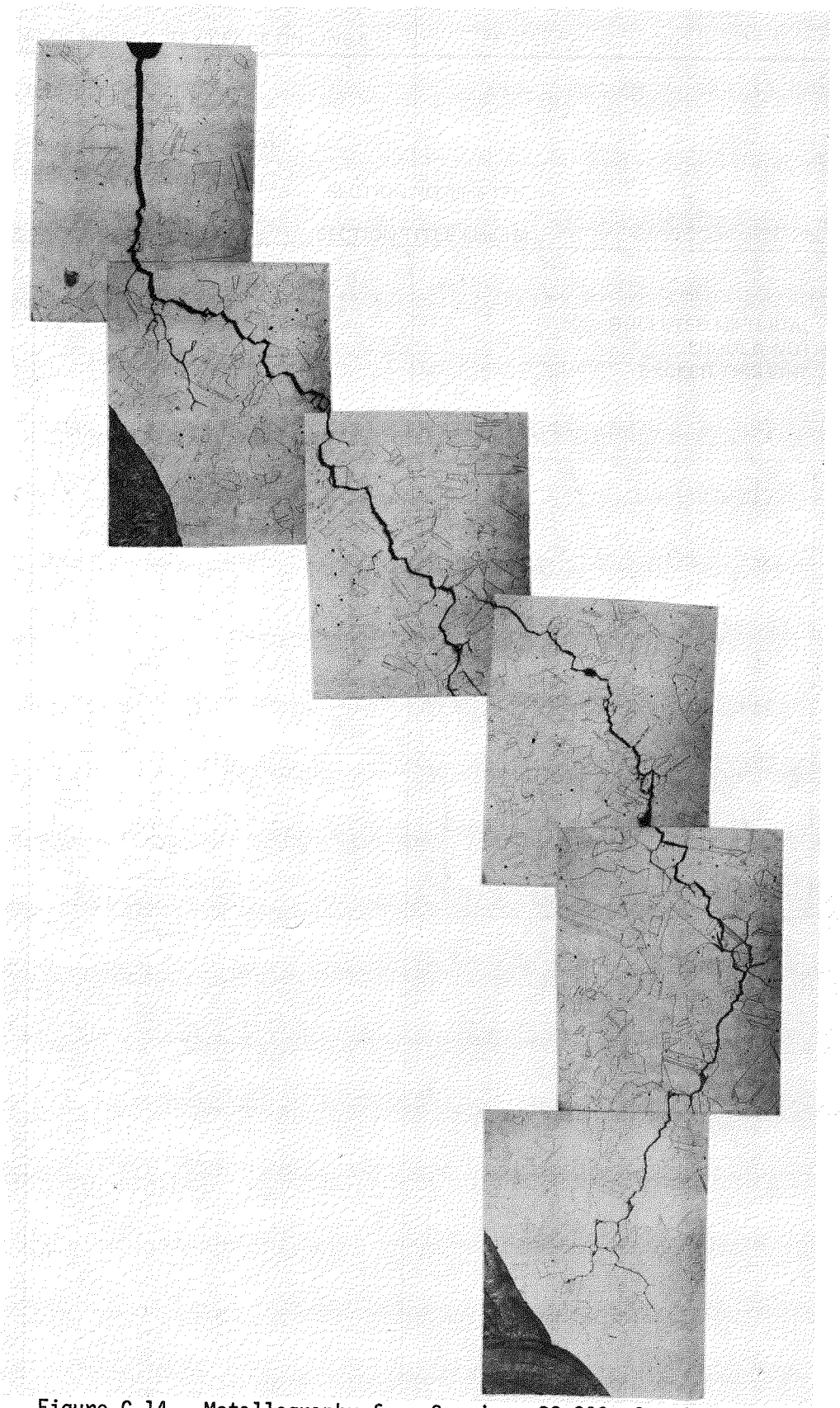

Figure G-14. Metallography from Specimen SS-333, Section O Location Showing IGSCC in HAZ Adjacent to Weld

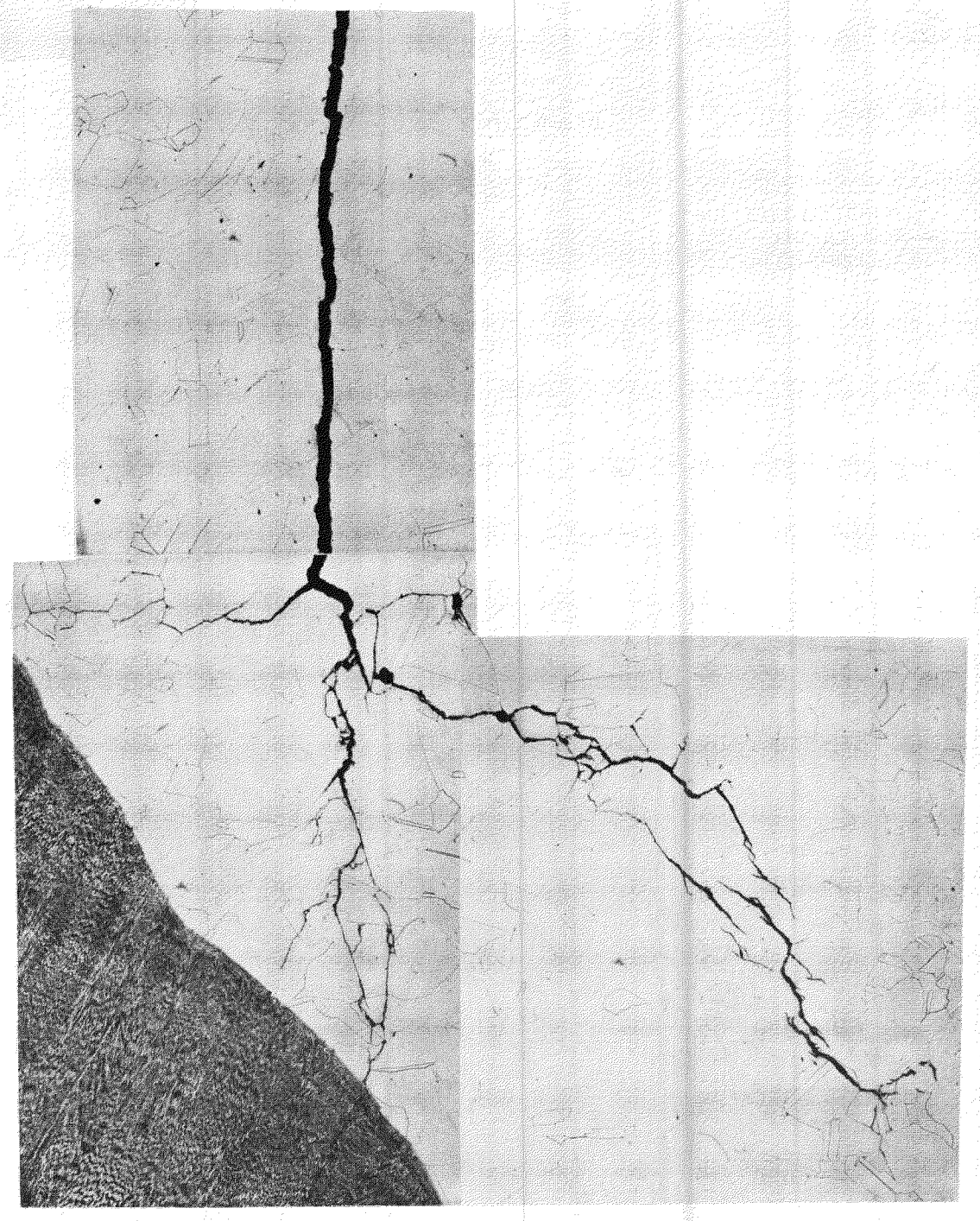

Figure G-15. Metallography from Specimen SS-333, Section 25

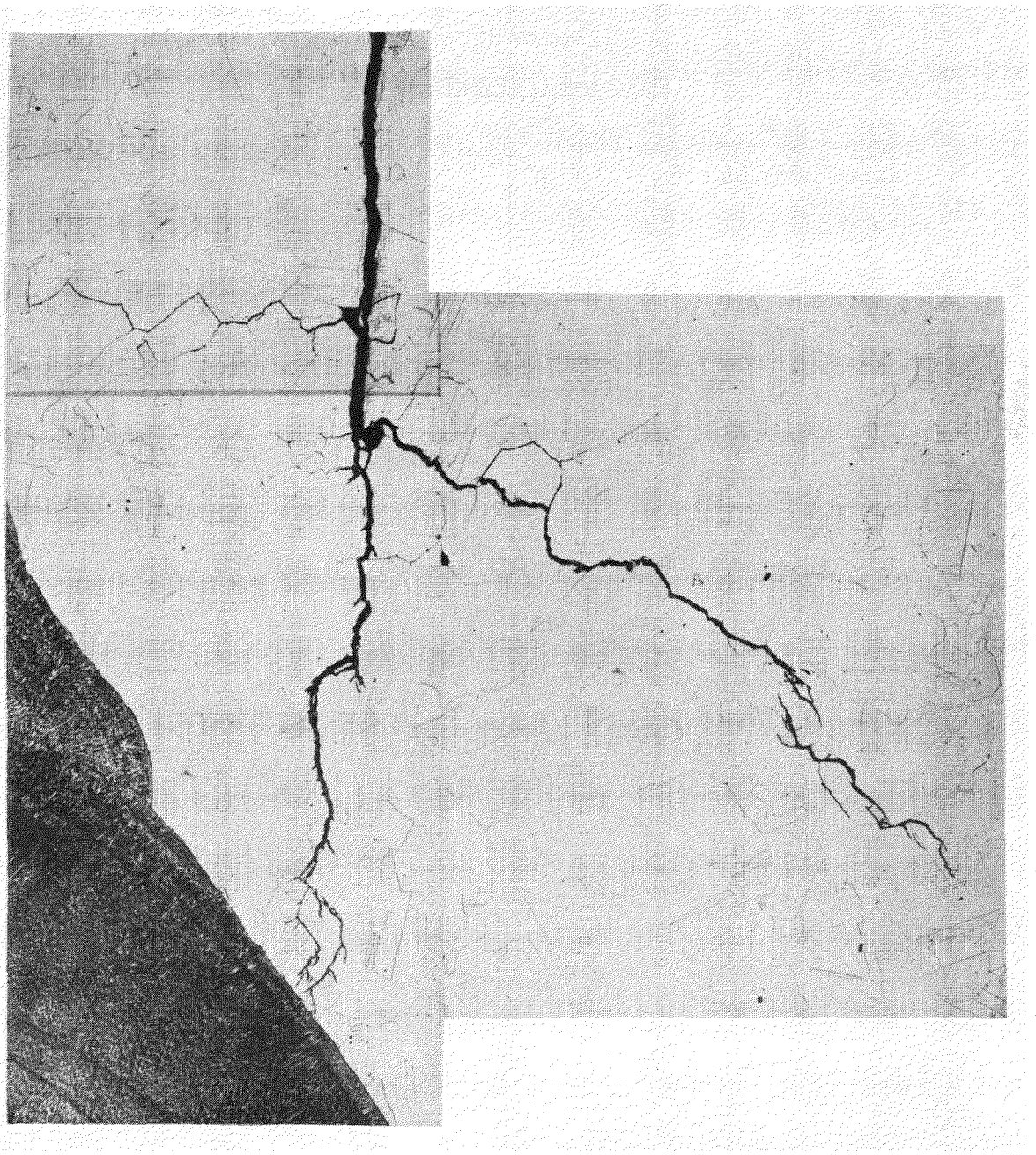

Figure G-16. Metallography from Specimen SS-333, Section 50 (at Specimen Center). Note crack does not penetrate weld.

Figure G-17. Specimen SS-333, Section 75 Metallography

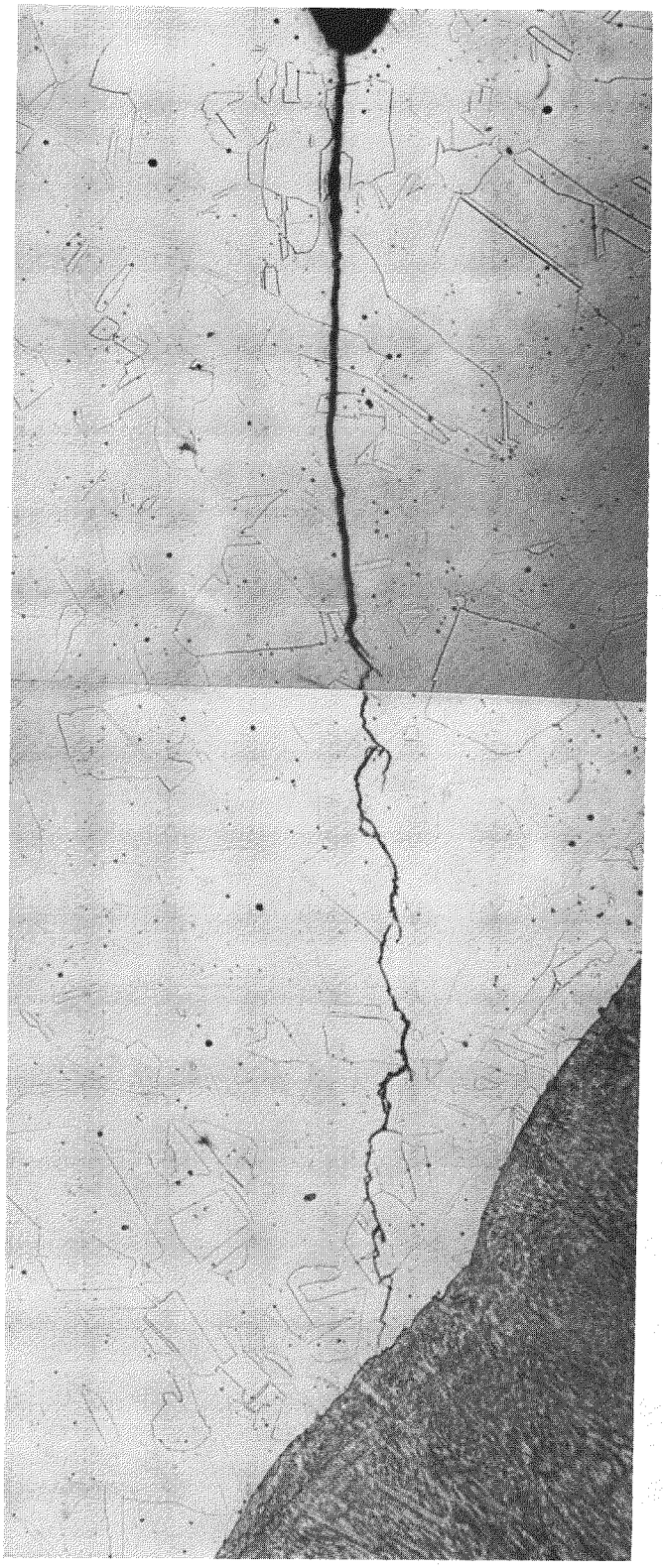

Figure G-18. Planar View of Specimen SS-333, Section 100 (Outer Edge)

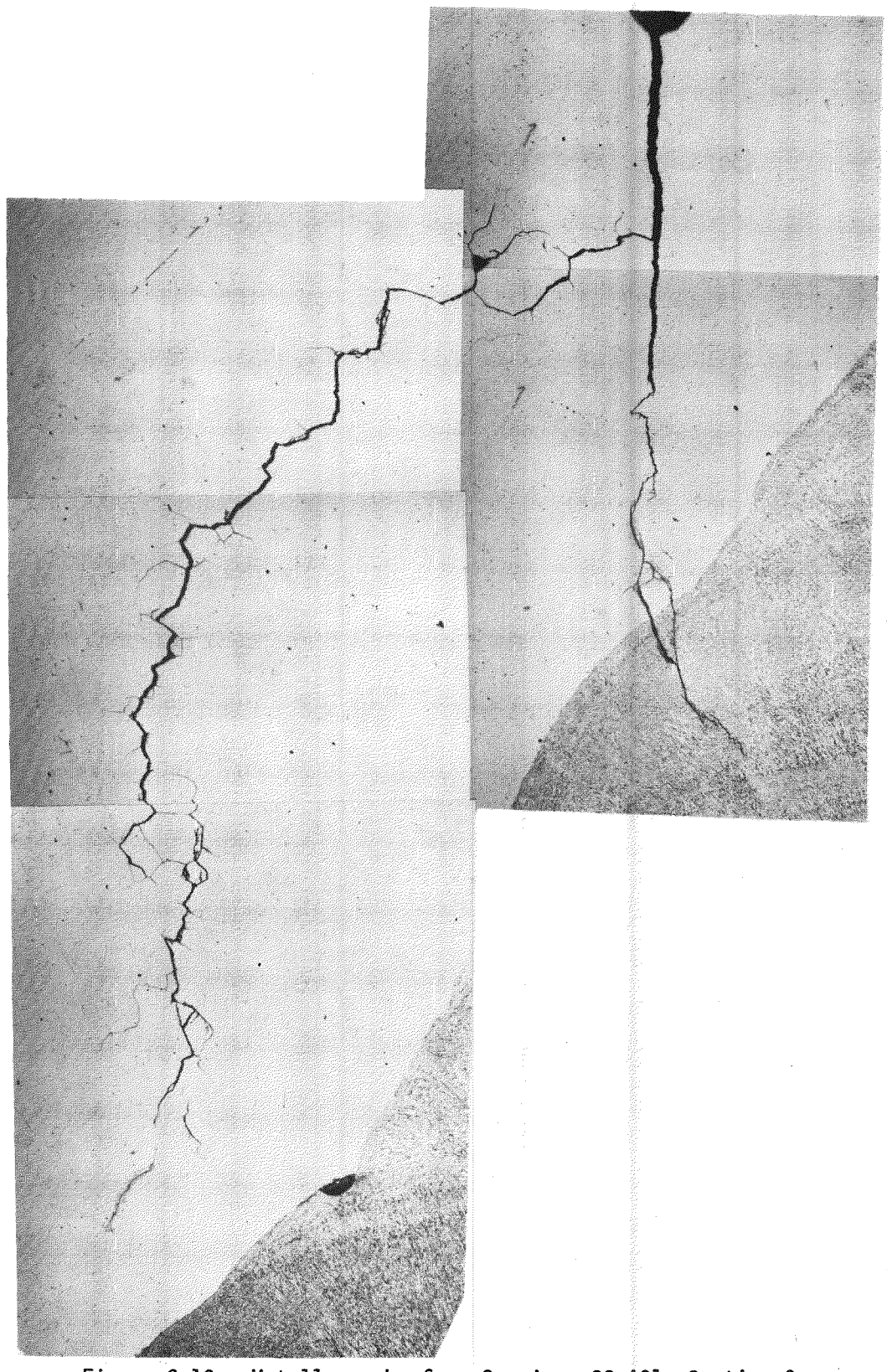

Figure G-19. Metallography from Specimen SS-431, Section O
(Crack penetrates weld metal.)

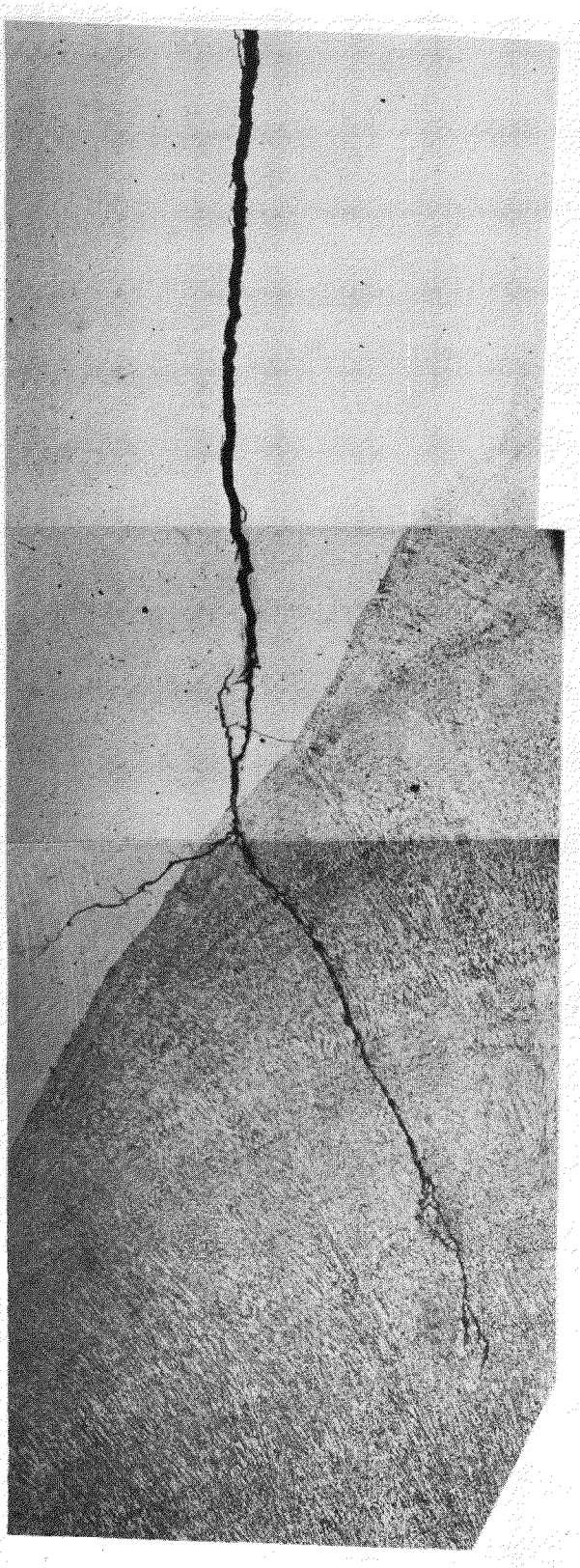

Figure G-20. Cracking in Specimen SS-431, at Section 25

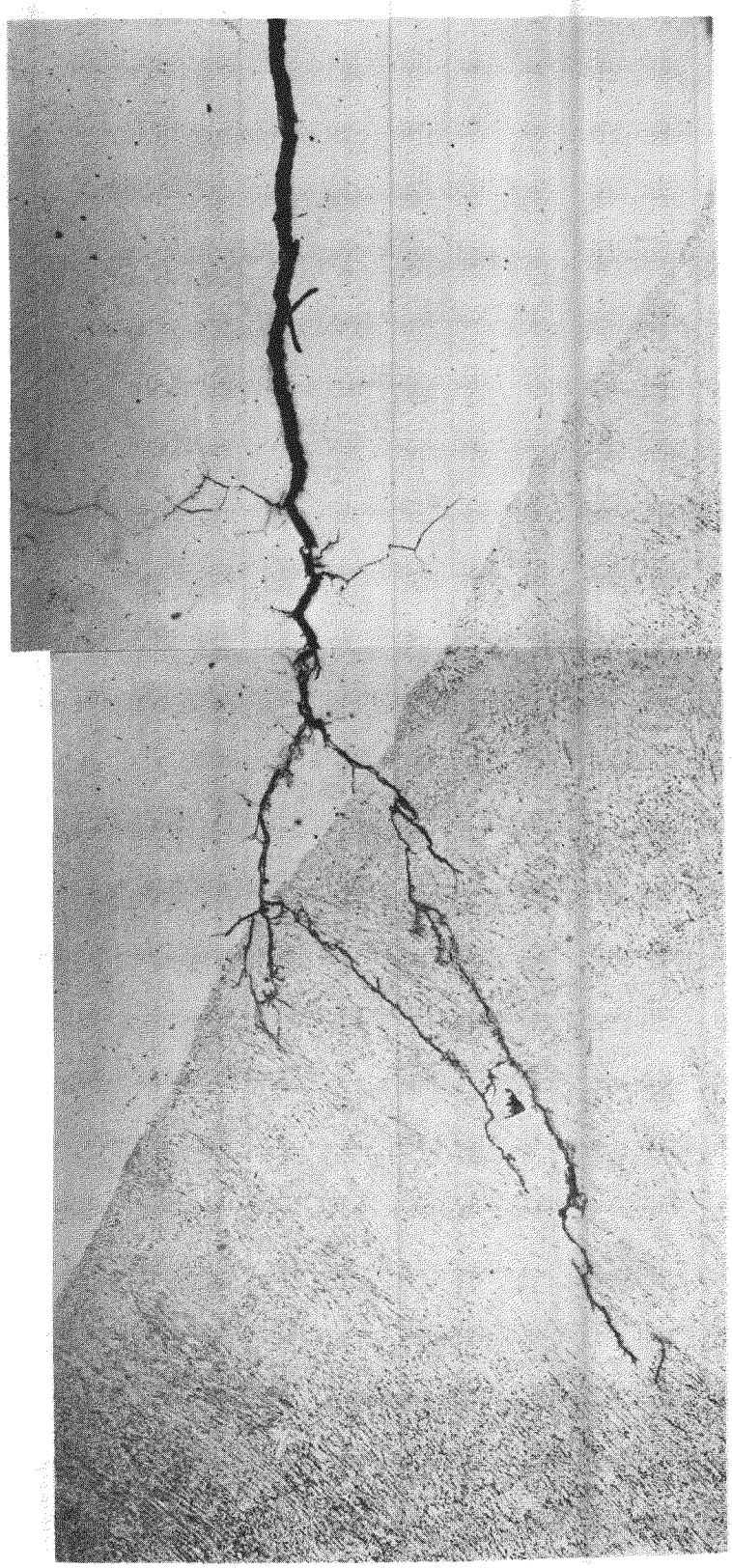

Figure G-21. Metallography from Specimen SS-431, Section 50 (Center cut) (Crack penetrates weld.)

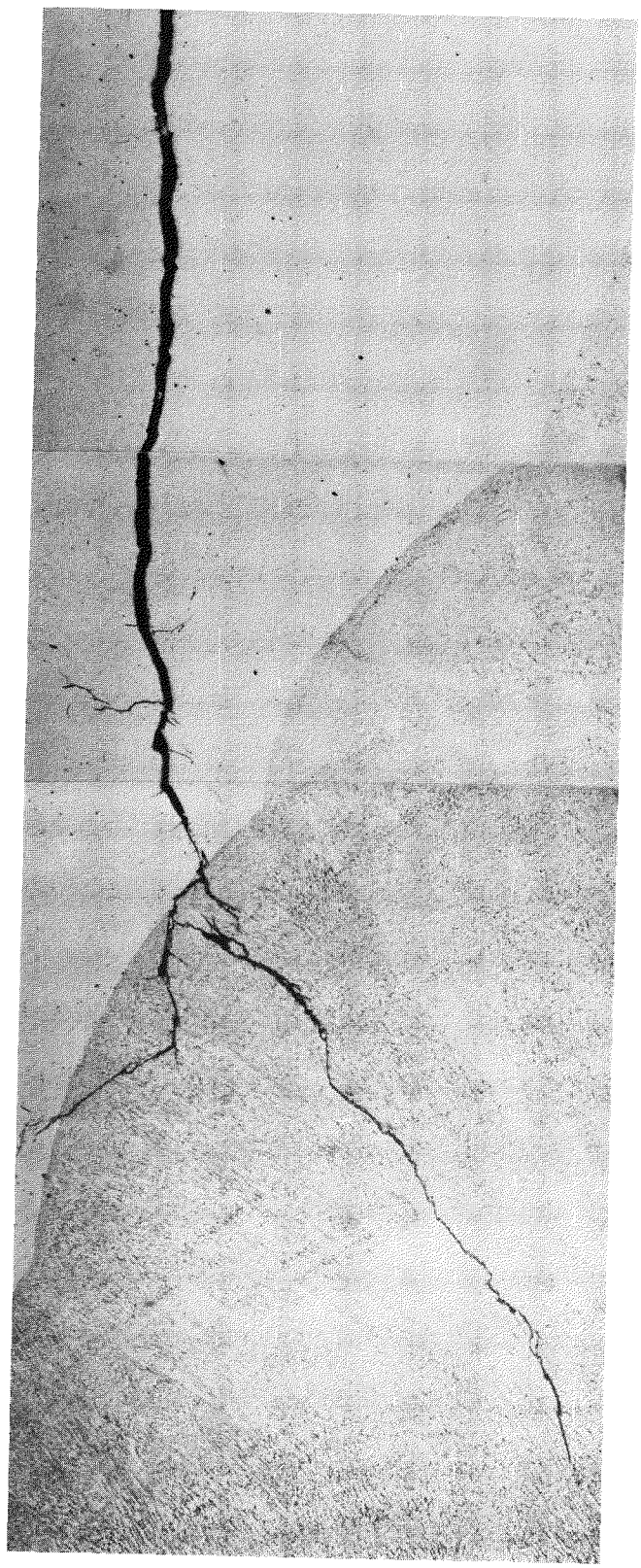

Figure G-22. Specimen SS-431, Section 75

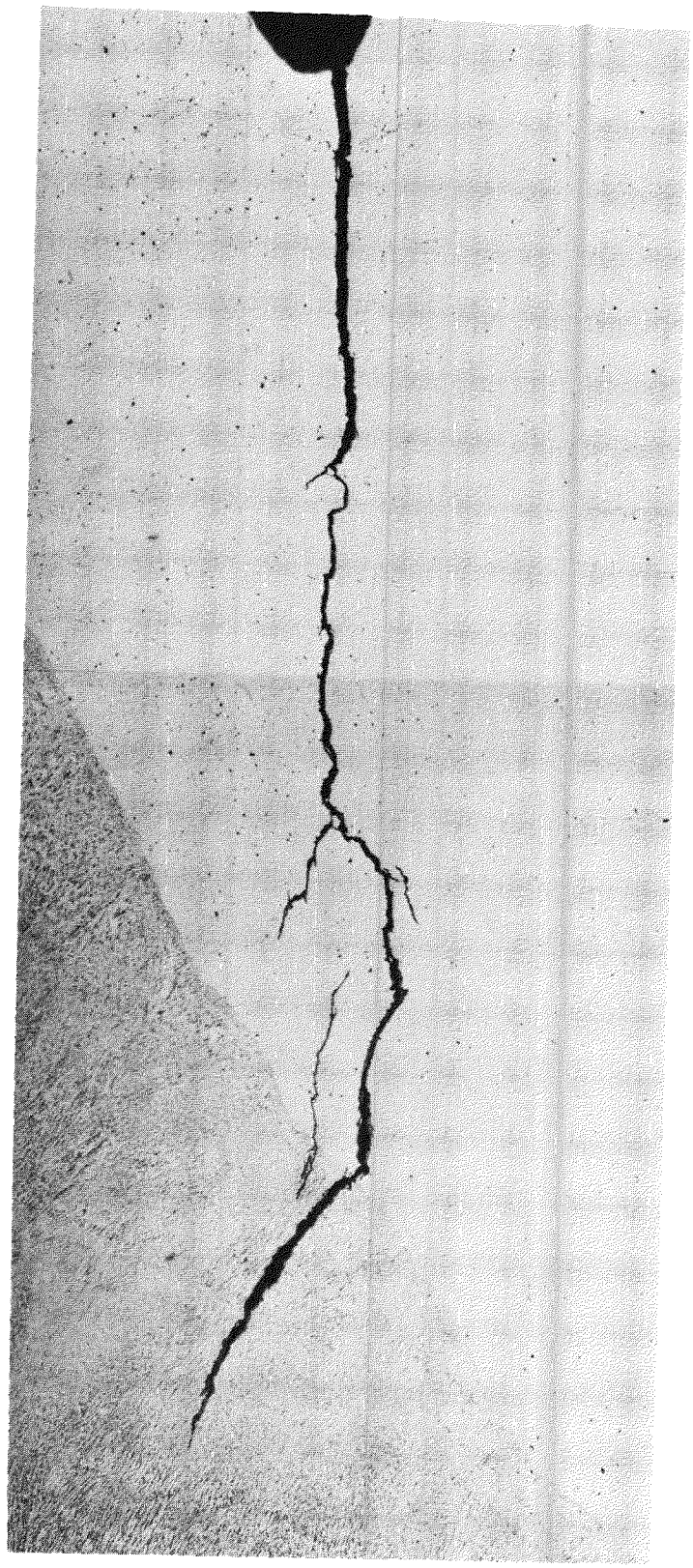

Figure G-23. Metallography from Specimen SS-431, Section 100

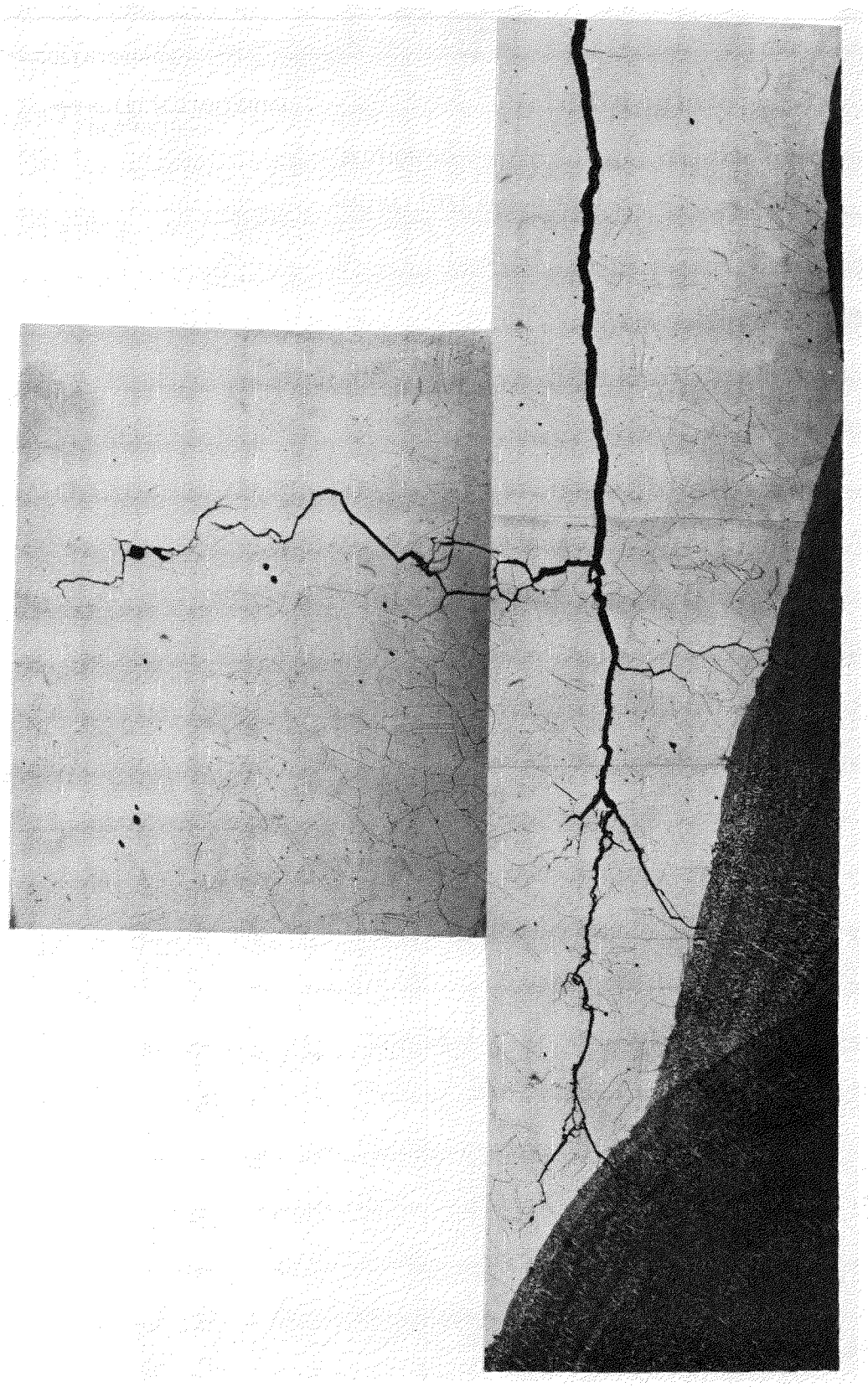

Figure G-24. Metallography from Mid-Plane of Specimen SS-233

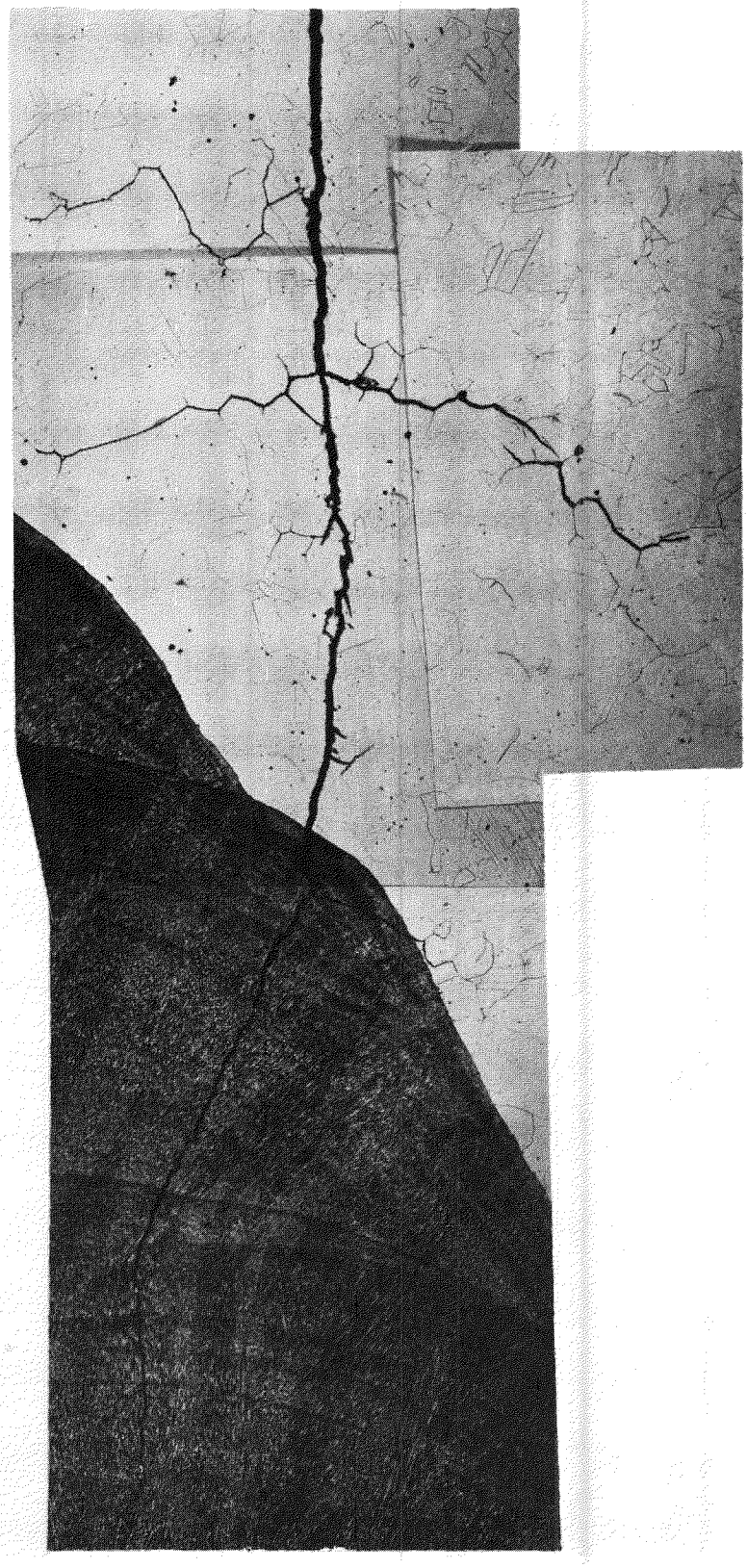

Figure G-25. Metallography from Specimen SS-534, Section 50 Where Crack Penetrates Weld Metal Significantly

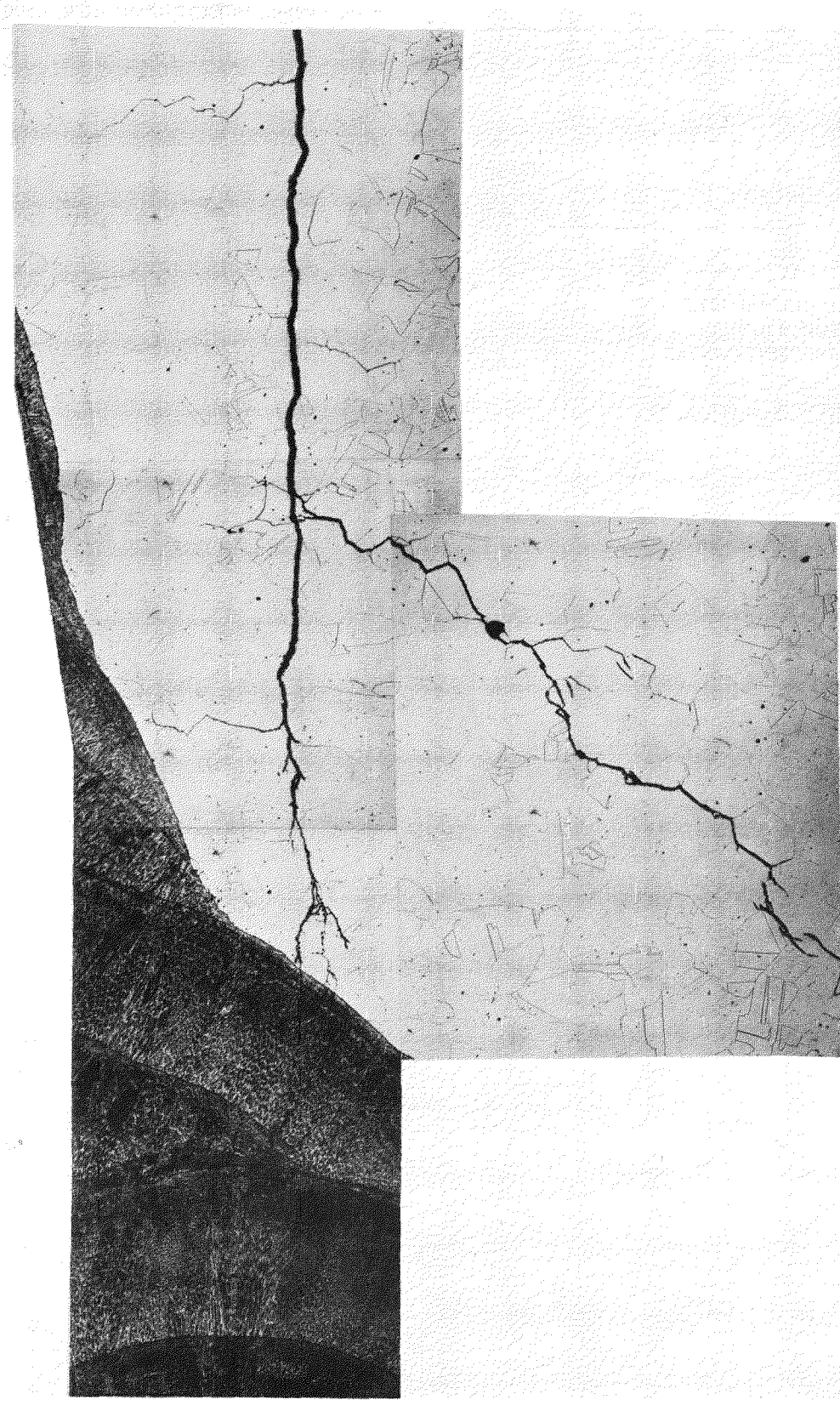

Figure G-26. Metallography from Specimen SS-632, Section 50

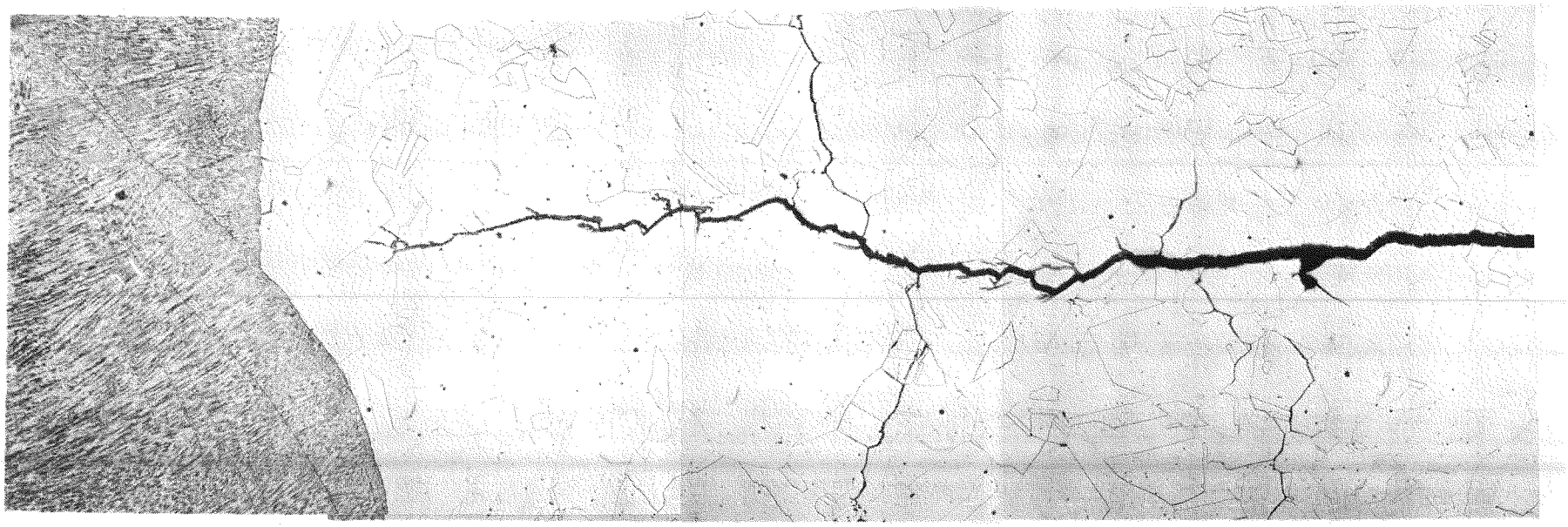

Figure G-27. Specimen SS-223, Section 50

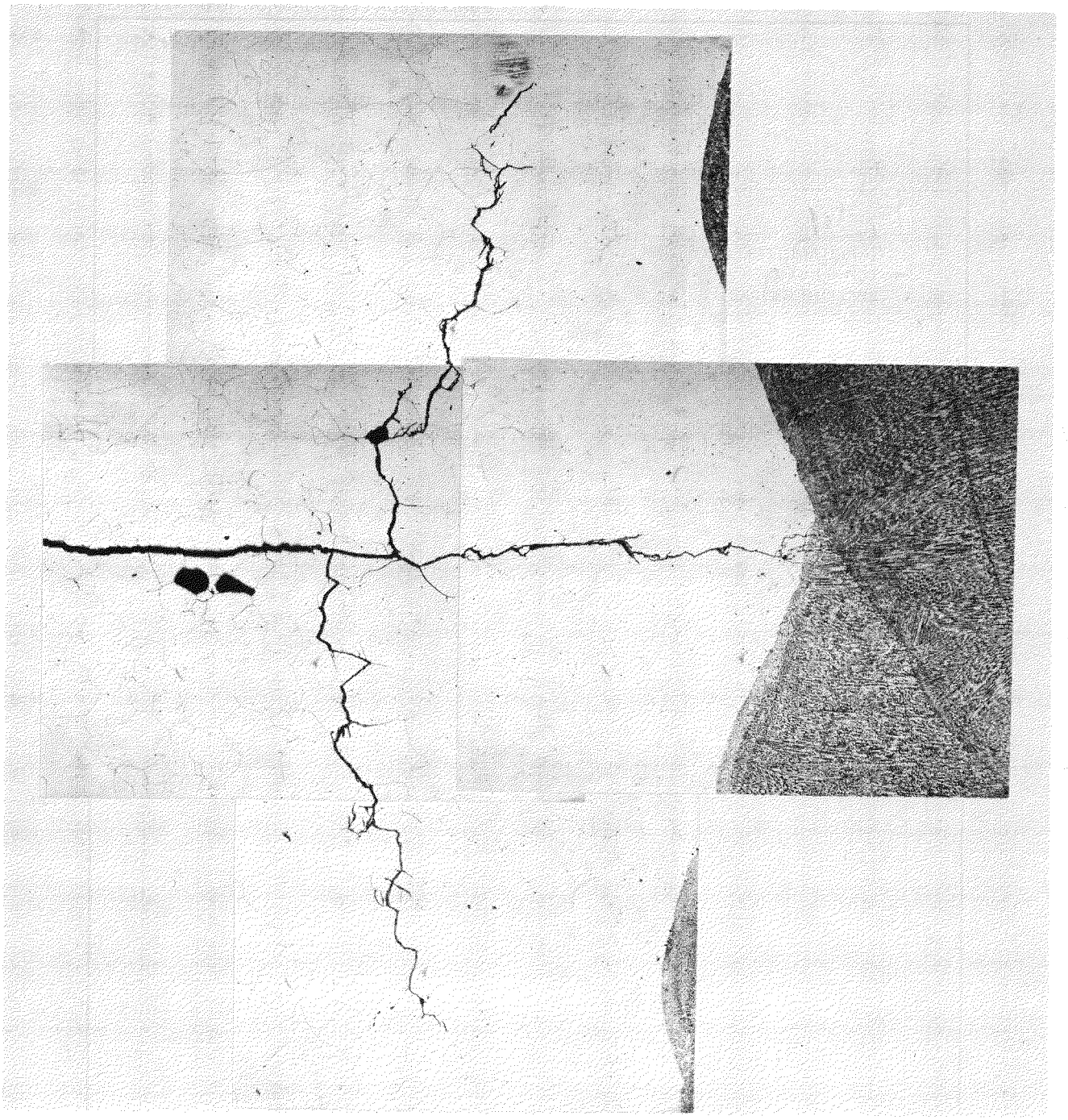

Figure G-28. Specimen SS-324, Section 50

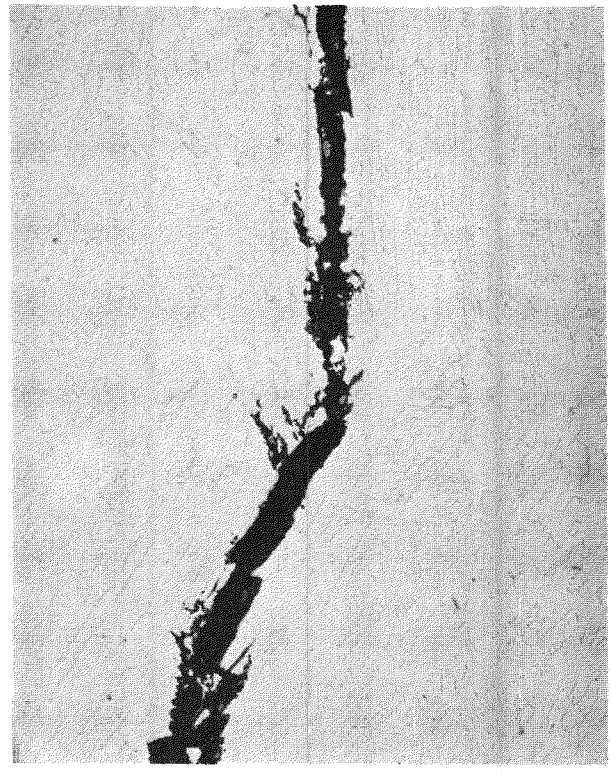

Figure G-29. Specimen SS-534, Section 50 - Weld Metal Cracking Along Ferrite-Austenite Boundaries

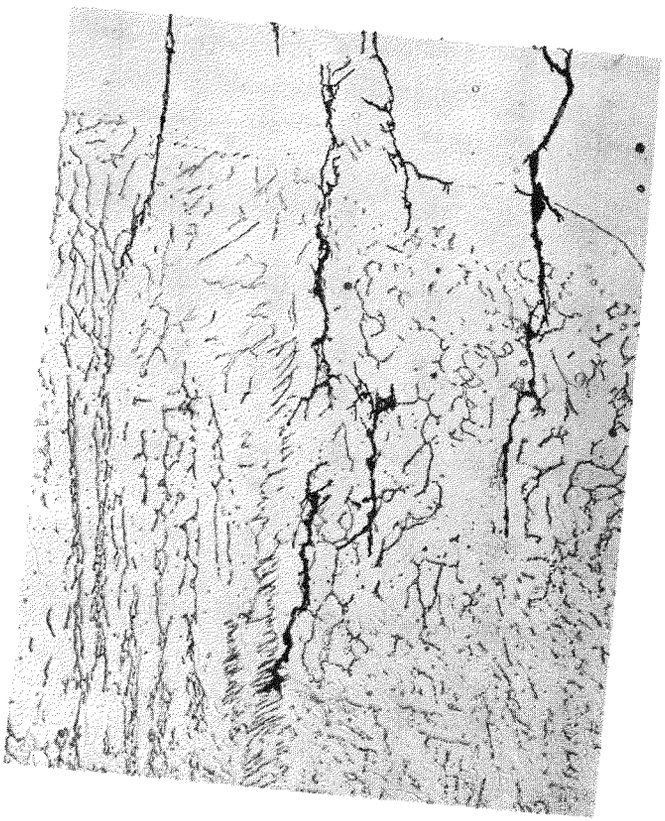

Figure G-30. Specimen SS-223, Section 50 (90° Weld Geometry, Low Carbon Content, Midrange Ferrite) Weld Metal Crack Tip

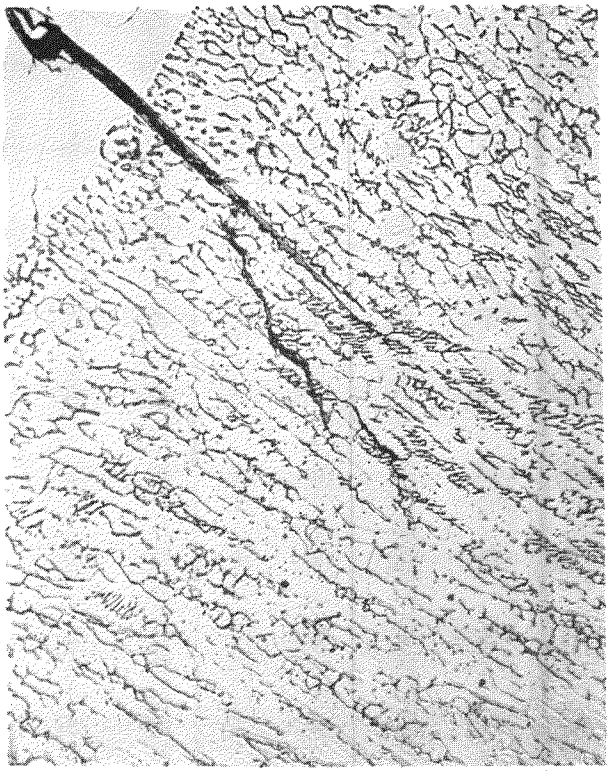

Figure G-31. Specimen SS-233, Section 50 (30-deg Weld Geometry, Low Carbon Content, Midrange Ferrite) Weld Metal Crack Tip

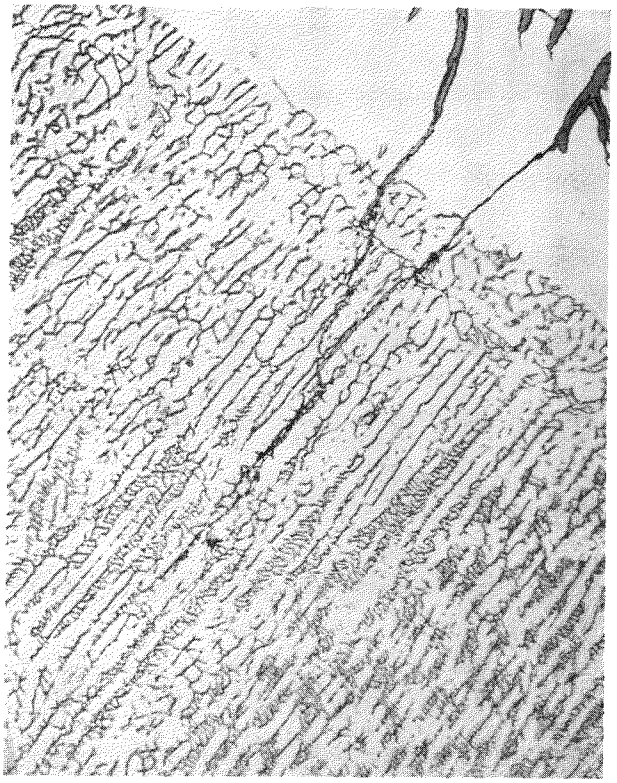

Figure G-32. Specimen SS-333, Section 50 (30-deg Weld Geometry, Low Carbon Content, High Ferrite) Weld Metal Crack Tip

Figure G-33. Specimen SS-431, Section 50 (30-deg Weld Geometry, High Carbon Content, Low Ferrite) Weld Metal Crack Tip

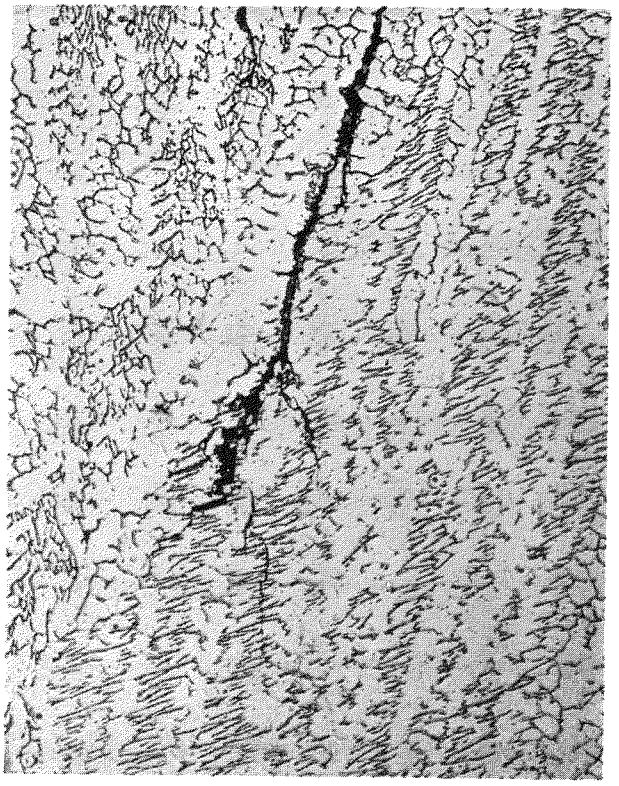

Figure G-34. Specimen SS-534, Section 50 (30-deg Weld Geometry, High Carbon Content, Midrange Ferrite) Weld Metal Crack Tip

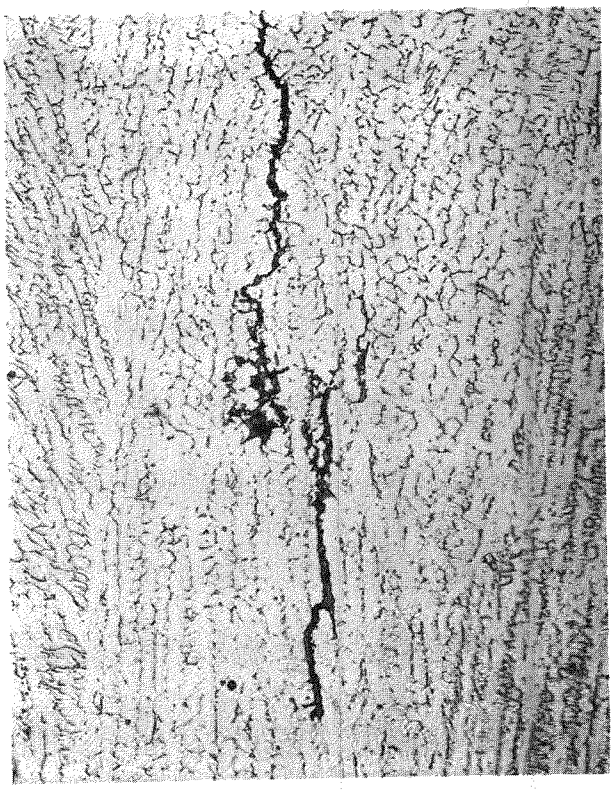

Figure G-35. Specimen SS-632, Section 50 (30-deg Weld Geometry, High Carbon Content, High Ferrite) Weld Metal Crack Tip

Figure G-36. SEM Fractograph of Specimen SS-333, Weld Metal Fracture Surface

Figure G-37. SEM Fractograph of Specimen SS-431, Weld Metal Fracture Surface

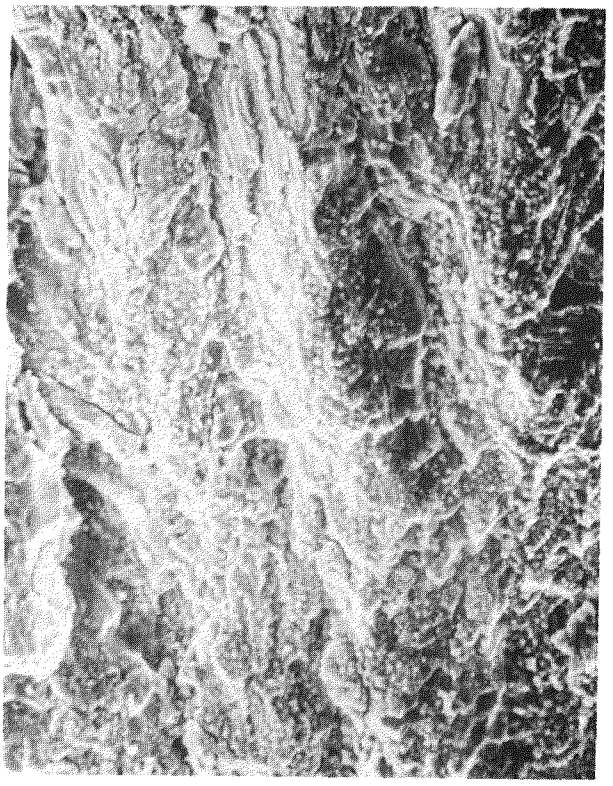

Figure G-38. SEM Fractograph of Specimen SS-534, Weld Metal Fracture Surface

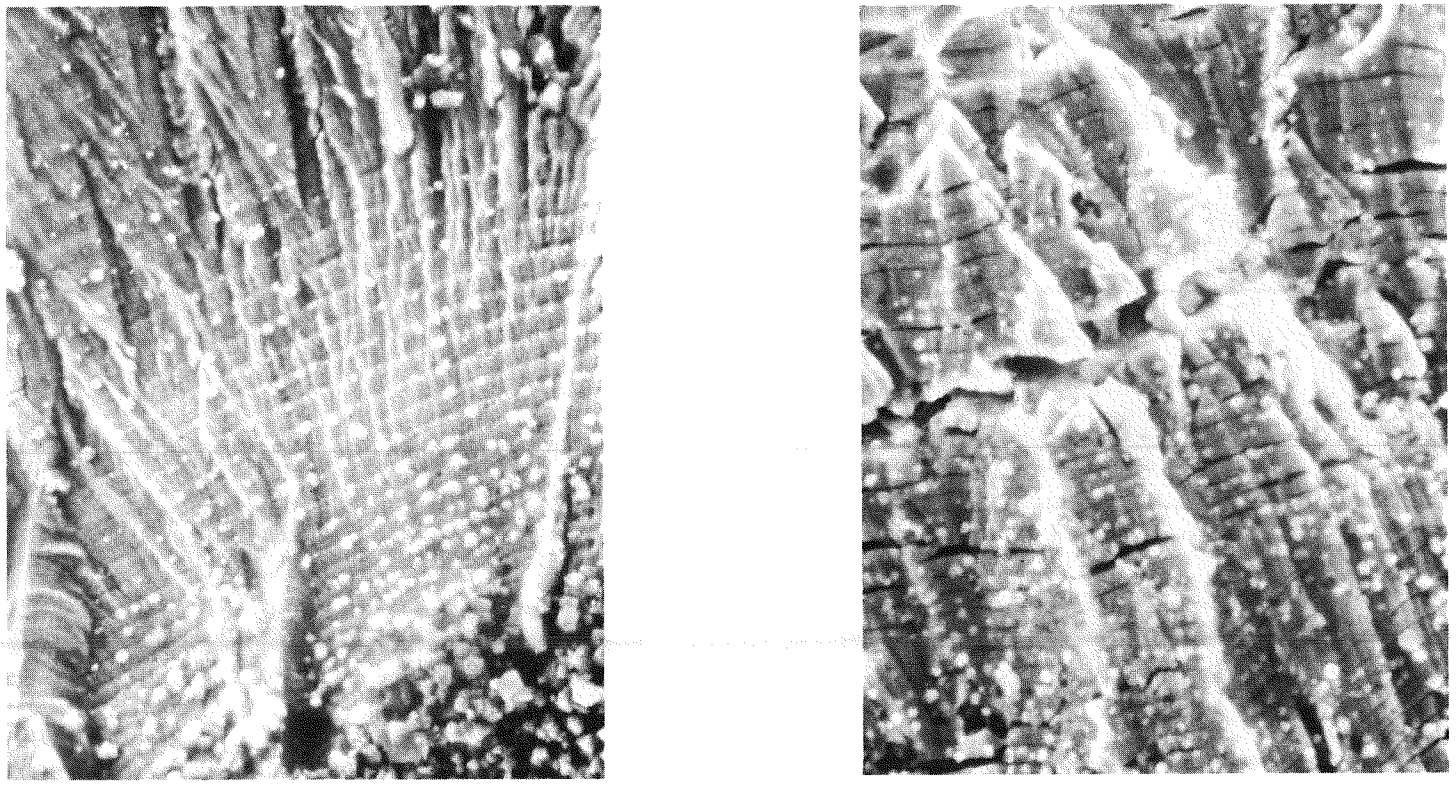

Figure G-39. Specimen SS-431 - SEM Fractographs Showing Fatigue Striations

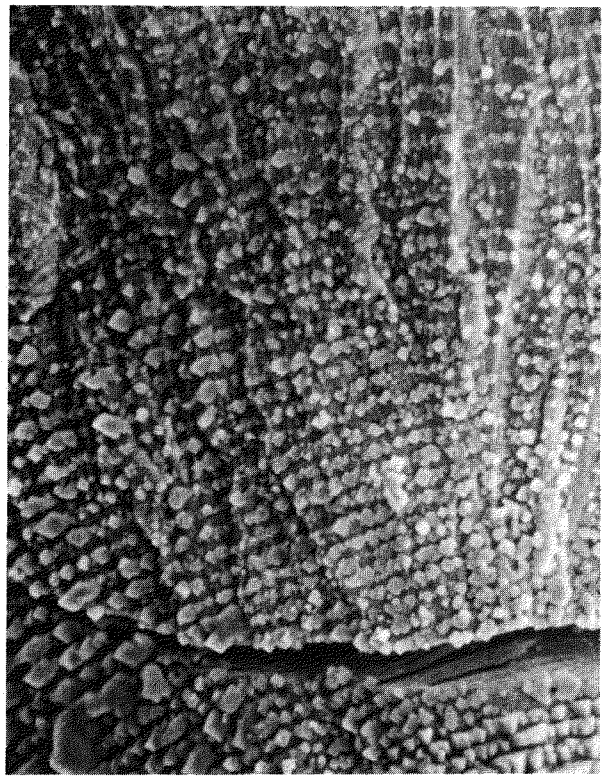

Figure G-40. Specimen SS-333 - SEM Fractography Showing Heavily Oxidized Fatigue Striations in Base Metal (1.7×10^{-4} in./cycle)

Figure G-41. Specimen SS-534 - SEM Fractography Showing Fatigue Striations in Base Metal (3.2×10^{-4} in./cycle)

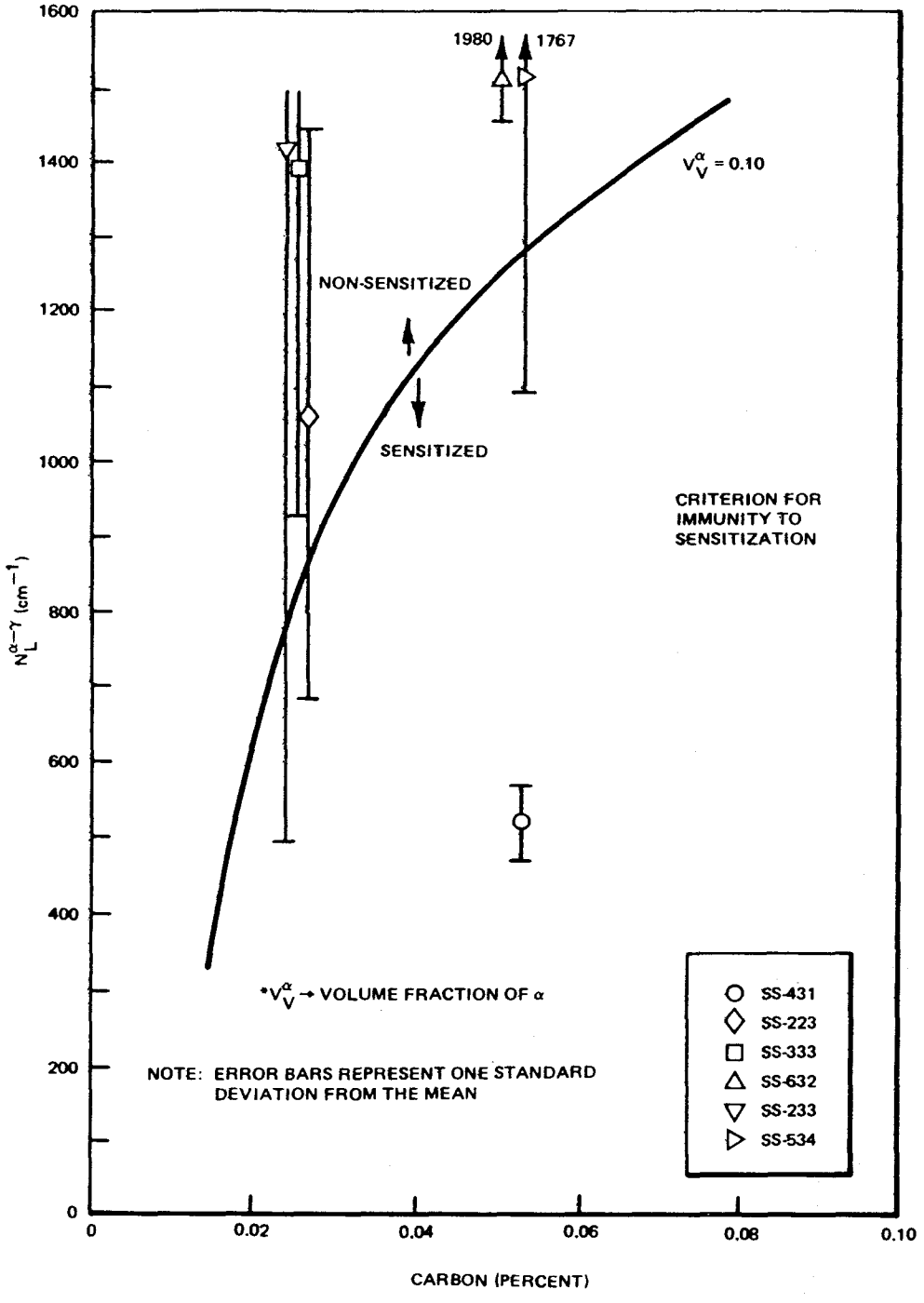

Figure G-42. Comparison of Ferrite-Intercept with Curve Developed by Devine to Determine Sensitization Susceptibility (Reference G-2)

Appendix H

EVALUATION OF CRACK GROWTH RATES FOR SERVICE CONDITIONS

(R. M. Horn, J. M. Kass, and D. A. Hale)

H.1 SUMMARY: CRACK GROWTH EVALUATION

Crack growth rates were measured as a function of several important parameters. Laboratory tests to evaluate crack growth were conducted under constant load, slow rising load, and slow cyclic loading. These tests summarized in following sections were conducted in 0.2 ppm O_2 and 8 ppm O_2 high temperature water. Emphasis was placed on the low oxygen environment in that this is representative of service conditions. Test specimens were heat treated to impart representative and high degree of sensization for evaluation.

Although crack growth rates were measured as a function of several parameters, the following conditions are most applicable as discussed in the methodology discussion:

1. Constant Load (CL)
   - -- 1150°F, 2-hr Sensitization, 0.2 ppm O_2 water (WS - 0.2 ppm O_2)
   - -- 1150°F, 24-hr Sensitization, 0.2 ppm O_2 water (FS - 0.2 ppm O_2)
   - -- 1150°F, 24-hr Sensitization, 8 ppm O_2 water (FS - 8 ppm O_2)
2. Slow Cyclic Load
   - -- 1150°F Isothermal Sensitization, 0.2 ppm O_2 water
   - -- 1150°F Isothermal Sensitization, 8 ppm O_2 water

Figures H-1 and H-2 present the data for these conditions. Included in Figure H-1 are two evaluation curves. The first bounds all the data. It could be used when sensitization due to post weld heat treatment or other treatment would be known to be high. It presents data generated primarily in 8 ppm oxygenated water which is more aggressive. Some 0.2 ppm oxygenated data is also included. In addition, the isothermal heat treatment used to impart sensitization was severe for the heats of stainless steel used as substantiated by CERT tests. The second curve represents data for more moderate degrees of sensitization and was generated in 0.2 ppm oxygenated water. The curve shape was selected to display characteristic stress corrosion cracking behavior. As the data base increases, this curve position might be

expected to shift. However, the curve shape would be expected to remain similar and the absolute position would fall below the upper bound data. The lower representative curve is not as strongly supported by the data as is the upper bound curve. However, as demonstrated in the summary, this data is the basis for predictions that explain field experience very well. For the constant loading mode, the data did demonstrate that sensitization level was the most important parameter controlling crack growth rate. In all cases an 1150°F, 24-hr treatment led to severe sensitization. However, an 1150°F, 2-hr treatment could be severe for one heat of material and representative of weld sensitization in another, leading to slower crack growth rates. For the constant loading mode, the data gathered demonstrated that sensitization level was the most important parameter controlling crack growth rate. Cyclic load crack growth rates given in Figure H-2 were most sensitive to frequency with sensitization and environment having less effect than found under constant load.

H.2 INTRODUCTION

The stress corrosion cracking behavior of Type-304 stainless steel in oxygenated high temperature water has been extensively studied. Excellent overviews have been provided by Cowan, Gordon, and Tedmon (H-1, H-2). The well-known chromium depletion model (H-3) has been successfully used to explain the observation that intergranular stress corrosion cracking will occur if the material is sensitized by thermal treatment and then exposed to high stress in the presence of oxygenated water. Most of the studies (H-4 - H-7) have involved the use of test specimens designed to assess crack initiation under constant load or constant extension rate using small tensile specimens, although recently studies involving welded pipes have been conducted. The fracture behavior has been found to depend on coolant oxygen, degree of sensitization, and load or loading rate.

There is also a need to assess the crack propagation resistance of this material using a fracture mechanics approach under various types of loading to assess the usefulness and examination frequency of in-service inspection programs that may potentially be implemented. As in any fracture mechanics study, information is needed on material properties, stress, and stress intensity factors in the component to be evaluated.

Some previous work in both high temperature and low temperature water has already been conducted (H-4 - H-9). Most of this work has been studies of fatigue crack growth. In Reference H-8, Kawakubo, et al. provided a comprehensive study of cycle frequency load waveshape and coolant oxygen effects on heavily sensitized material.

Slow cycle frequency and high coolant oxygen were found to enhance growth rates. In Reference H-9, Ford studied heavily sensitized material at 93°C/1.5 ppm oxygen. His studies were focused on an assessment of cycle frequency and mean stress. The influence of these parameters on the threshold stress intensity factor for cracking and on crack growth rates was amply discussed. However, only a very limited amount of test data has been generated to assess behavior (H-6, H-9) at 550°F (288°) in 0.2 ppm O_2 environment.

The purpose of this study was to assess the crack growth behavior of Type-304 stainless steel as a function of loading mode in high temperature high purity water conditions. The roles of degree of sensitization and coolant oxygen were assessed in addition to the role of loading mode. The methods used to generate crack growth rate data were developed during the course of the program. The series of crack growth studies on Type-304 stainless steel performed are as follows:

1. Constant stress intensity, constant load crack growth in 0.2 ppm oxygenated water.
2. Role of loading mode on crack growth in 8 ppm oxygenated water.
3. Slow rising load tests to evaluate crack growth in sensitized stainless steel - 8 ppm oxygenated water.
4. Slow rising load/constant load crack growth tests in 0.2 ppm oxygenated water.
5. Crack growth rates under cyclic loading in 0.2 ppm oxygenated water.
6. Constant load crack growth in 0.2 ppm oxygenated water.

Each independent study will be presented separately. The order of the non-cyclic tests is chronological.

H.3 IN-SERVICE CONSTANT LOAD CRACK GROWTH BEHAVIOR (R. M. Horn)

H.3.1 Summary

To support a methodology that will predict crack growth behavior in as-welded large pipes exposed to service environments, crack growth tests were run using tapered double cantilever beam specimens. These specimens were sensitized to represent the as-welded condition using a 1150°F (621°C), 2-hr treatment. Stress intensity levels of 20, 24, 28, and 32 ksi $\sqrt{in.}$ were investigated in the four specimens tested. The tests were conducted in 0.2 ppm O_2, 550°F high purity, high pressure water. The tests were run under constant load for 6630 hours with several interim

inspections. Intergranular stress corrosion cracking was developed in all specimens. The crack growth rates were much slower than those measured at similar stress intensity levels in specimens fully furnace sensitized isothermally at 1150°F for 24 hours and exposed to 8 ppm O_2 high temperature water. The crack growth rates were still a function of stress intensity with higher stress intensities leading to higher crack growth rates.

H.3.2 Experimental Procedures

H.3.2.1 Test Facilities and Test Environment. The high pressure/temperature water environment used for this program was provided by a high flow test loop (Environmental Fatigue Loop 1) in General Electric's Experimental Mechanics Laboratory. A schematic drawing of this loop is shown in Reference H-10. The loop included a canned rotor pump which provided sufficient flow (∿4 gallon/minute) to ensure that all specimens tested in the loop were subjected to a refreshed environment. Bypass demineralizer beds were provided to maintain the conductivity and pH of the demineralized water environment. The level of dissolved oxygen, conductivity, and pH of the loop water was continuously monitored during testing. Dissolved oxygen level was controlled by a gas control system that continuously purged a gas mixture through the makeup tank at a rate needed to establish the desired dissolved oxygen level in the makeup water which was added continuously to the loop.

The environment for the constant load tests was controlled to 0.2 ± 0.1 ppm during testing. The total environmental specifications are listed in Table H-1.

It was decided that these tests were best conducted under dead weight loading. An existing autoclave was modified to accommodate this test. Details of the autoclave are shown in Figures H-3 and H-4. The dead weight loading was accomplished in a conventional manner with 10:1 level arm providing the external load to the specimen chain. A load cell on the specimen chain axis measured the external load, which combined with the internal pressure load yielded the desired load. In-situ compliance monitoring was accomplished in the same manner as used at General Electric for cyclic crack growth tests (Subsection 4.7).

H.3.2.2 Material Condition. The material for testing was taken from one heat of Type-304 stainless steel. The composition is listed in Table H-2. The material was received in the solution annealed condition. The room temperature and 288°C (550°F) tensile properties are also listed in Table H-2. Prior to testing, the material received a heat treatment to sensitize the material to various desired levels. To select the heat treatment to impart this sensitization, a study was

performed on the heat to evaluate isothermal heat treatments. Using the results of Clarke to guide heat treatment parameters (H-11, H-12), an isothermal holding time was investigated. Electrochemical Potentiokinetic Reactivation (EPR) response of the heat was used to evaluate the heat treatment. Figure H-5 shows this response for the heat used. (Heat 03580, used for other studies, is also shown.) Using Clarke's data that showed than an EPR value of $\sim$15 C/cm^2 was typical of many weld heat-affected zones, the 1150°F (621°C) 2-hr treatment was chosen to represent the weld sensitization treatment. Following selection of this, a CERT test was performed on this heat in the 1150°F, 2-hr condition. Properties are listed in Table H-2. The properties verified sensitization with the fracture predominantly intergranular.

H.3.2.3 Test Specimens/Test Techniques. The constant load crack growth tests were performed under constant load using Tapered Double Cantilevered Beam (TDCB) specimens. The specimen is displayed in Figure H-4. The TDCB specimen was used to produce a stress intensity field that was only a function of the applied load and specimen thickness, and, therefore, independent of crack length. This specimen design has been used before by Mostovoy and others (H-13 - H-15).

It was decided that the constant stress intensity specimen geometry had the best change of producing reliable, quantitative crack growth data. For these specimens, the crack growth rates are independent of the crack length and, therefore, constant throughout the test. Multiple data points would be produced for each K-level investigated. The compliance of this tapered double cantilever beam specimen is a linear function of the crack length. The TDCB specimen depicted was designed such that a, the distance from the load line was related to the half specimen height, h, as follows:

$$\frac{3a^2}{h^2} + \frac{1}{h} = 4$$

This particular design had been successfully used at GE San Jose in the past by Wang (8).

By choosing this specimen design, the change in compliance with change in crack length is a constant because:

$$G = \frac{P}{2B} \frac{\partial C}{\partial a} \frac{K^2}{E}$$

where

C = compliance

a = Crack length

P = load

B = specimen thickness

G = crack release energy

K = stress intensity

Then

$$K = \text{constant if } \frac{\partial C}{\partial a} = \text{constant and P, B are fixed.}$$

To monitor crack growth, it was still necessary to measure changes in compliance. In-situ compliance readings were made with Linear Variable Differential Transformers (LVDTs) mounted on each specimen, using techniques previously developed.

The amount of crack growth indicated by the compliance change in the TDCB specimen was established by referring to previous work on the TDCB specimens by Wang (H-16). The calculated values of load-line compliance are listed in Table H-3, for the thickness of interest. In the range of crack length, 1% change in compliance indicated 0.010 inch (10 mils) of crack growth.

Following specimen manufacture, the specimens were precracked under tension-tension loading at room temperature. The precracking was conducted at ∿20 Hz under sine wave form. The R-ratio used was ∿0.1 and the maximum loading never exceeded 80% of the test load.

H.3.2.4 Test Matrix. A total of four TDCB specimens were tested. These specimens and their history are listed in Table H-4. One of the four specimens, 4904SS-4, yawed open extensively during the first 2923 hours of test. It was replaced with a Compact Tension (CT) specimen, SS-5, manufactured from heat 03580, as listed in Table H-4. The properties of this heat are listed in Table H-17, and preliminary crack growth information was detailed in Reference H-10. Destructive examination showed only IGSCC on the side. Therefore, the final report will only concentrate on the TDCB specimens.

H.3.3 Results

The loading history of the test is detailed schematically in Figure H-7 for the entire 6630-hr test period. The applied load decreased slightly at the end of

Phase III for ∿400 hours. This led to an approximate 3% decrease in stress intensity in all specimens for that 400-hr period or ∿1 ksi $\sqrt{in}$.

The total test time was divided into six smaller phases of the following duration: Phase I, 1021 hours; Phase II, 1902 hours; Phase III, 1224 hours; Phase IV, 792 hours; Phase V, 911 hours; and Phase VI, 780 hours. Specimen 4904 SS-4 was tested through Phase II and then destructively examined. Specimen SS-5 replaced 4904 SS-4 at that time and was tested through Phase VI. No significant IGSCC was found in SS-5 and it will not be discussed. The results for 4904 SS-4 will be presented first. Then, LVDT compliance, room temperature compliance, visual measurements, and final destructive examination will be presented for 4904 SS-1, 4904 SS-2, and 4904 SS-3.

H.3.3.1 Results - Specimen 4904 SS-1

This specimen was under test for the first two phases. Significant plasticity occurred early in the test, moving the LVDT core to a position out of the calibrated range. At the completion of the test time, 2939 hours, the specimen was examined for visual indications of IGSCC and then sectioned to establish crack growth. This examination showed significant IGSCC cracking at one edge and pockets of environmental cracking across the thickness of the specimen. This is shown in Figure H-8. The extent of IGSCC on the one side was significant. However, measured in from the side, the inward extent was limited to ∿0.100 inch.

Using nine points across the specimen thickness, the average growth was 0.031 inch. The maximum amount of growth was 0.162 inch at one side. It should also be noted that substantial IGSCC was observed at other locations (i.e., the specimen arms), as shown in Figure H-9 and detailed in Reference H-17. The stress state at these locations was significantly less severe than at the fatigue crack. However, the strain rate may have been higher because of the unchanging nature of the stress intensity at the sharp crack in these specimens.

H.3.3.2 Results - Specimens 4904 SS-1, 4904 SS-2, and 4904 SS-3. The crack growth behavior in these specimens was evaluated by several methods. In-situ LVDTs were used to measure compliance during testing. In addition, room temperature compliance measurements and visual measurements of the crack line were made at the ends of Phases II, III, IV, V and VI. Finally, a destructive examination was performed to evaluate fracture mode and final crack length. The results of these measurements will be summarized separately below.

H.3.3.2.1 In-Situ LVDT Compliance Measurements. LVDTs were attached to the front face of each specimen. These devices were used to monitor crack opening displacement as a function of applied load. At the test beginning, the hot compliance was adjusted to match the room temperature cold compliance. Table H-5 lists the measured 550°F compliance values as well as the corrected values for the entire test period. The raw compliance data was averaged from two readings on each day. The load range was evaluated from X-Y plots. This was necessary to eliminate the seal friction load. The correction factor contained a part for modulus change as well as a part for any change in gain that occurred in heating up the LVDT. At the beginning of each phase, the new compliance values were adjusted by a factor which matched the beginning value to the compliance values measured at the end of the previous phase. The values of compliance are plotted in Figures H-10, H-11, and H-12. It is immediately apparent that LVDT readings showed high variability for each specimen. The variability was present in each phase. Usually, over the course of a test phase, the compliance even tended to shift down. The data could not establish when initiation took place or establish actual growth rates.

A review of cold LVDT compliance data showed the same trend. There was scatter in the compliance values measured from test period to test period. It was not possible to reset LVDTs once the vessel was assembled to assure that the cold compliance values matched the room temperature clip gage compliance values corrected for distance from the load line.

H.3.3.2.2 Room Temperature Clip Gage Compliance Measurement. At the end of all phases, except Phase I, the specimens were removed for room temperature clip gage compliance measurements. These measurements were made using a clip gage attached to 0.125 inch from the front surface of the specimen. These measurements would be expected to be the most accurate measurements. The measurements made for the three specimens are tabulated in Table H-6. These values are also displayed on Figures H-10, H-11, and H-12. The values show a gradual increase over the entire period. (The compliance readings at 2923 hours were high for all specimens due to questionable clip gage calibration.) In particular, all three specimens showed an increase over the last 2500 hours. Least squares fits to the data showed that a linear fit to 4904 SS-1 and 4904 SS-2 compliance data (correlation coefficient $\geq$95%) was a good fit. The data for 4904 SS-3 showed a better fit from 4147 hours to the end (correlation coefficient equal to 93%). It was concluded that the room temperature

compliance measurements showed linear growth rate from 4147 hours for all three specimens.

From compliance calibrations given in Table H-3, 0.010-in. crack growth led to 1% change in load line compliance and, in turn, in clip gage measured compliance. This assumes a linear relation between the two values. Using these relationships, compliance-evaluated crack growth for the entire test period and crack growth from 4147 hours to the test end (2482 hours) were calculated and are listed in Table H-7.

H.3.3.2.3 Visual Observations and Measurements. During the inspections made at the end of the testing phases, visual observations and measurements were made for each specimen. In addition, destructive evaluation was performed at test end to calculate actual crack growth and fracture mode. These results will be presented separately.

The visual side measurements were made at all outages and are recorded in Table H-8. Precrack and final side crack lengths were measured on the fracture specimen. Intergranular cracking on the side occurred extensively in one side of each specimen. The cracking seemed to progress throughout the test on the intergranular side on each specimen. (It should be noted that this intergranular on the side was not due to bending, loading, or preferential flow. The chain had many U-joints to eliminate bending and the inlet flow came from four uniformly spaced spargers.) This indicated that initiation (at the surface) was quick and growth proceeded over the test period. Figure H-13 shows that initiation was clear in specimen 4904 SS-3 after 2923 hours. Specimens 4904 SS-1 and 4904 SS-2 were not as visually intergranular on the side even though the specimens were exhibiting changes in measured crack length throughout the test period.

At the end of the test, the specimens were removed from test, back cut, and then pulled apart. The cracking during testing was easily discernible from the ductile fracture region. Figures H-14, H-15, and H-16 are scanning electron microscope micrographs of the fracture surface, for the specimens 4904 SS-1, SS-2, and SS-3, respectively. The center portion of all the specimens exhibited intergranular fracture. There was additional cracking on the side at the free surface as found on 4904 SS-2 and displayed in Figure H-15b. The average crack growth for the specimens was determined by averaging 9 to 11 measurements evenly spaced across the thickness. These values are listed

in Table H-9. The average of a crack growth is a function of stress intensity and time.

H.3.4 Discussion of Crack Growth Results

The compliance and visual data from the four TDCB tests was evaluated for crack growth rates. These crack growth rates could be evaluated over the entire test period or over a specific test interval. Table H-9 lists the crack growth rates calculated this way. The visual evidence on the sides of the specimens 4904 SS-1, 4904 SS-2, and 4904 SS-3 indicated that crack growth had begun by 4147 hours. Using this starting time and the percentage of compliance changes during the last 2483 hours to evaluate the percent of total growth occurring in this time as a basis, end of test crack growth rates were also calculated. These rates are also listed in Table H-9. As discussed previously, the LVDT measurements could not support either set of crack growth rates determined from clip gage compliance measurements.

The data from the four tests performed under constant load are displayed in Figure H-17. This figure shows additionally the evaluation curve presented in reference H-17 for furnace sensitized material exposed to 8 ppm O_2 with purity, high temperature water where the crack growth rates continuously increase as the stress intensity increases over the range of 10 ksi $\sqrt{in.}$ to 34 ksi $\sqrt{in.}$ The data from the weld sensitized specimens exposed to 0.2 ppm O_2 high temperature water are significantly different. These tests, performed for several thousand hours, resulted in small but meaningful amounts of intergranular stress corrosion cracking. The room temperature compliance measurements and actual crack length measurements agreed well (Tables H-7 and H-9). These measurements as well as visual side measurements identified when crack initiation had taken place. The rates derived from these measurements were an order of magnitude slower than those measured in the furnace sensitized specimens.

The characteristics of the crack growth data on weld sensitized material may be similar to the classic three-stage stress corrosion behavior where a plateau region is exhibited (H-18). The furnace sensitized data shows similarities to other data generated by Ford on stainless steel in 1.5 ppm O_2, 93°C high purity water (H-9). It also is similar in rate to the cyclic crack growth data generated by this study and by Kawakubo (H-8). The data does not show a high dependence on the stress intensity which is characteristic of stress corrosion in a variety of systems (H-19 - H-22).

The weld sensitized data is more sparse. The growth rates at stress intensity levels of 20 and 24 ksi $\sqrt{in}$. are similar to one another. The specimens exposed at higher stress intensity levels exhibited some nonuniform cracking at the sides, increasing the average crack advancement and, in turn, the average crack growth rate. The data supplies evidence that coolant oxygen content and/or sensitization level has a very important influence on the magnitude of the growth rate. The growth rates for the lower coolant oxygen and weld sensitization level are much lower than that for the high oxygen and high degree of sensitization condition.

It is important then to determine the extent to which coolant oxygen and degree of sensitization, as separate variables, influence results. Two additional CT specimens were prepared with high sensitization (621°C/24 hours) and weld sensitization (621°C/3 hours) in a 0.2 ppm oxygenated water. These specimens were tested between 22 and 35 ksi $\sqrt{in}$. Results showed that the high sensitization sample has a growth rate higher than the weld sensitization samples, and an effect on coolant oxygen at high K's as discussed in Subsection H.6. Thus, both degree of sensitization and coolant oxygen content appear to be important in the determination of the crack growth rates for static load conditions.

Ford (H-23) has recently applied the slip-dissolution model of crack propagation to quantitatively predict observed crack growth rates in sensitized stainless steel tested in 1.5 ppm 100°C oxygenated water. The slip dissolution model is basically an electrochemical mechanism that considers the time period for formation of oxide at the crack tip and fracture of this oxide by mechanical loading. The crack velocity is expressed as:

$$V = \frac{M}{\rho FN} \cdot \frac{Q_f}{t_f}$$ (Reference H-24)

where

V = Crack growth rate

M, ρ = Atomic weight and density of metal

N = Valence change during oxidation process

F = Faraday's constant

t_f = periodicity of oxide rupture rate

Q_f = Oxidation charge density passed in t_f after the oxide rupture event

It is possible to qualitatively explain the principal observations of this study in terms of the above model.

At static loads where intergranular cracking is observed, there is sufficient time during the loading event for penetration into the grain boundary and oxide reformation. For this case, one would expect the observed effect of sensitization and coolant oxygen content in terms of the t_f and Q_f parameters described above. The periodicity of oxide rupture depends on the crack tip strain rate and the fracture strain of the oxide. The crack tip strain rate must be sufficiently slow that significant grain boundary penetration occurs before the significant fracture of the oxide is obtained. Constant extension rate tests conducted by Solomon (H-25) have shown that at slow extension rates, intergranular fracture morphology was promoted at high sensitization levels and that lower fracture strains were observed as the degree of sensitization increased. Hence, as the degree of sensitization increases, one would expect the periodicity of oxide rupture would decrease and the crack growth rate should increase as is observed. In a morphological sense, the continuous carbides and deep chromium deplation consistent with high sensitization would allow deeper intergranular penetration at each rupture event than the more discontinuous carbides associated with weld sensitization. The role of the coolant oxygen content is a little more complex because the crack tip is located in a crevice. The bulk water chemistry reflects only the extent of the potential gradient down the crevice. A steeper potential gradient would be expected to occur for 8 ppm oxygen than 0.2 ppm oxygen. With this in mind, more rapid growth rates would be expected in the 8 ppm oxygenated water solution since the corrosion potential is higher (more positive) than the 0.2 ppm oxygen case. Ford (H-23) has observed increased corrosion potentials with increased oxygen contents and consequent increase in crack growth rates at 288°C for sensitized stainless steel.

H.4 ROLE OF LOADING MODE ON CRACK GROWTH RATES IN SENSITIZED 304 STAINLESS STEEL (T. A. Caine and M. M. Bensch)

H.4.1 Introduction

Stainless steel reactor components are designed to endure several types of loading. Basic stress analyses consider primary loading or load controlled stress and secondary loading or displacement controlled stress. Cyclic loading becomes a factor in treating fatigue life.

Primary and secondary loadings are not categorized in analyzing crack growth rates of flawed components. The small cracks at such flaws deform very little to relieve

applied displacements, supporting the conservative assumption that all applied loading to a crack should be considered primary loading.

The test reported here had two main objectives: first, develop crack growth rate data in 304 stainless steel under constant and cyclic load control as well as under constant Crack-Opening Displacement (COD) control; second, compare constant load growth rates to constant COD rates to determine if any significant difference exists. The idea behind the comparison is that much of the loading considered in component analyses is attributed to secondary effects such as thermal stresses. Unpublished stress relaxation studies by Yukawa on fracture mechanics specimens showed that crack tip stresses dropped continually under displacement control in Type-304 stainless steel at 550°F. The corresponding creep rates would decrease as well when compared to those brought about by a constant applied load.

This data indicated that the creep controlled oxide rupture would be different for cracks subjected to secondary stresses (leading to a smaller or negative gradient in stress intensity). This difference in oxide rupture rates would lead to slower crack growth rates.

H.4.2 Test Description

Testing was conducted in the Small Environmental Fatigue Test (SEFT) machine which is a 100 kip capacity hydraulic test machine with the flexibility to operate in load control for constant and cyclic load and in strain control for constant COD operation. During the testing, SEFT was upgraded to include computerized data acquisition capability.

The SEFT test vessel was supplied with 550°F air saturated water from the Environmental Fatigue Loop I (EFL-I). Pressure, temperature, conductivity, pH, and oxygen levels were continuously monitored. These parameters were maintained at the values shown in Table H-10.

Three specimens were tested: TC-3, SS-21, and SS-24. All three were 1T-CT compact tension specimens depicted in Figure H-18. Details of material, heat treatment, and loading history are summarized for each specimen below.

TC-3. Specimen TC-3 was machined from 304 stainless steel heat 04904. Chemical and mechanical properties for this heat are listed in Table H-11. The specimen blank was heated in 1150°F air for 24 hours and air cooled. The first loading phase was cyclic loading at 2.0-cph using a load ratio

R* = 0.1. The waveform was a positive sawtooth, ramping to maximum load in 30 minutes and rapidly unloading. The cyclic testing phase developed stress intensities from 30 ksi $\sqrt{in.}$ initially to 34 ksi $\sqrt{in.}$ after 71 mils of crack growth. TC-3 was terminated with a short period of constant load testing during which the stress intensity changed from 34 ksi $\sqrt{in.}$ to 35 ksi $\sqrt{in.}$ as the crack grew another 20 mils.

SS-21. SS-21 was fabricated from heat 03580 of 304 stainless steel. The chemical and mechanical properties for heat 03580 are summarized in Table H-11. This specimen was used in a previous test described in Section H.7. Prior to that, it was heat treated for 15 hours in 1150°F air and air cooled. SS-21 was tested under controlled constant load at 3500 lbf in SEFT. The resulting stress intensity, K_{max}, was about 21 ksi $\sqrt{in.}$ During the testing reported in the later section, SS-21 developed stress intensities between 24 ksi $\sqrt{in.}$ and 27 ksi $\sqrt{in.}$

SS-24. This specimen was also machined from heat 03580 Type-304 stainless steel and heat treated for 24 hours in 1150°F air and air cooled. Slow rising load rates of 40 lbf/hr and 41 lbf/hr were used to raise the load from 1000 lbf to 2400 lbf and to 300 lb, respectively. At this point, cycling was begun at 0.72 cph and 4 = 0.48. The waveform was a positive sawtooth ramp. The final phase was run in COD (or strain) control. The cycling and COD controlled phases had stress intensity K_{max} levels between 23 and 24 ksi $\sqrt{in.}$

H.3.3 Results

Table H-12 lists crack length, crack growth rate, and stress intensity values versus time and cycles, where appropriate, for each of the three specimens tested. Figures H-19, H-20, and H-21 are plots of crack length versus time for each specimen. From these data, best fit lines were drawn to determine the crack growth rates given in Table H-12. These are plotted in Figure H-22 against maximum stress intensity K_{max}.

Post-test fracture surface inspections were made of each specimen. Figure H-23 shows the fracture surface of TC-3. The low magnification shot shows the precrack, transgranular, intergranular, and tensile rupture zones. The transgranular and intergranular crack growth zones are enlarged. The post-test inspections of SS-21 and SS-24 indicated that both experienced intergranular crack growth.

*R = minimum load/maximum load

H.3.4 Discussion

The crack growth rate versus time results shown on Figure H-22 are useful for some comparisons with prior data. Reference H-8 has cyclic data in 550°F, 8 ppm oxygenated water. Results from Reference H-8 for 0.72 cph and 7.2 cph cyclic testing are plotted on Figure H-22 for comparison to the cyclic test results from TC-3 and SS-24. The TC-3 data (2.0 cph, r = 0.1) falls below the rates from Reference H-8 by about a factor of two. The growth rate for SS-24 is not directly comparable because of the higher mean load (4 = 0.48).

The results for constant load and constant displacement appear to show no significant difference in growth rate. In Reference H-8, a "static component" of crack growth is extracted from the cyclic results. This component is estimated at 3×10^{-5} in./hr. The static load results from Reference H-23 are for testing in 1.5 ppm oxygenated water at 95°C (203°F). The rate at K_{max} = 25 ksi $\sqrt{in.}$ is 7×10^{-5} in./hr. These two values lie very close to the constant displacement result from SS-24 of 5×10^{-5} in./hr. Results compiled in Reference H-17 made in 8 ppm O_2, 550°F water are shown on Figure H-22. The over-all trend of the results is a fairly linear region on a log-log plot. These results include cyclic, constant load, slow rising load, and constant displacement test points.

In general, the cyclic results cause higher crack growth rates than the rates for the other modes of loading. This is due to the additional mechanical component of fatigue. The constant load, constant displacement, and slow rising load (H-26) results all lie in the same region of growth rate for the same K_{max}. The slow rising load testing performed in SS-24 resulted in no crack growth as the stress intensity was increased to about 25 ksi $\sqrt{in.}$ The loading rates of 40 lbf/hr followed by 4 lbf/hr may have been too rapid to allow growth to occur.

Figure H-23 shows the fracture surface of specimen TC-3 after test completion. The Transgranular (TG) and Intergranular (IG) regions are fairly clear in the low magnification pictures. As noted in Figure H-20, the transition from TG to IG occurred during the slow cycling phase. No noticeable change in growth rate occurred during the transition.

H.3.5 Conclusions

The following conclusions may be drawn from the results of this test:

1. There is no apparent difference in crack growth rates of load control testing and displacement (COD) control testing at the same stress intensity K_{max}.

2. Intergranular cracking may be initiated with slow cyclic loading (f = 2 cph, r - 0.1) in furnace sensitized 304 stainless steel. This was accomplished in specimens TC-3 and SS-24.

3. Slow rising load rates of 40 lbf/hr and 4.0 lbf/hr were too rapid to allow crack initiation to occur. At maximum stress intensities near K_{max} = 20 ksi $\sqrt{in.}$ the loading rate should be less than 4.0 lbf/hr. This corresponds to a K velocity below 0.03 ksi $\sqrt{in.}$/hr.

H.5 SLOW-RISING LOAD TESTS TO EVALUATE CRACK GROWTH IN SENSITIZED STAINLESS STEEL - 8 ppm O_2 ENVIRONMENT (J. N. Kass and W. L. Clarke, Jr.)

H.5.1 Summary and Conclusions

A new testing method was developed to evaluate the threshold stress intensity and crack growth rates in sensitized Type-304 stainless steel. This procedure involved loading a fracture mechanics-type specimen very slowly to promote IGSCC. The process is analogous to Constant Extension Rate Test (CERT) tensile testing which has been used to qualitatively evaluate the susceptibility to IGSCC of a lot of material. The test produced IGSCC in sensitized stainless-steel specimens exposed to a slow loading in 8 ppm O_2 water. The results produced a bound on the threshold stress intensity value and crack growth rates for values of K up to 21 ksi $\sqrt{in.}$

H.5.2 Introduction

The currently accepted methods of determining crack growth rate versus K and K_{ISCC} data for structural metals involve either the constant-load cantilever bend test or the constant displacement bolt-loaded compact toughness test (H-27, H-28). Although these procedures have advantages and limitations with respect to K_{ISCC} tests, they both have the same major limitation--testing times on the order of thousands of hours are required to obtain useful data. Some examples of bolt-loaded specimen tests are given in Reference H-25 and examples of constant load tests are given in Reference H-17. The experimental difficulties include "waiting out" the very long incubation time for nucleation of the stress corrosion crack as well as waiting a suitable length of time until the crack has grown far enough to allow measurements. For example, it is necessary to wait 5,000 hours to measure a growth rate of 10^{-6} in./hr if the minimum change in crack length that can be accurately measured is 0.005 inch.

In 1972, McIntyre and Priest (H-29) measured K_{ISCC} for high-strength steels (200-400 ksi yield strength) by conducting slow-rising load tests on fracture mechanics specimens in H_2S. Results of this testing showed that test times could be substantially reduced. Later, Clark and Landes (H-30) conducted similar testing and

utilized loading rates greater than 6,000 psi $\sqrt{in.}$/hr to measure growth rates as small as 6×10^{-2} in./hr. The test for K_{ISCC} must be conducted at a loading rate slow enough to allow detection of crack growth before the rising load increases greatly beyond the point where crack extension starts.

This subsection describes results of work to apply this Slow-Rising Load (SRL) technique for measurement of K_{ISCC} and crack growth rates on structural materials in oxygenated water. It was decided to apply the technique first to sensitized Type-304 stainless steel in air-saturated water for two reasons. First, the Reference H-30 tests on high-strength steel had a 100:1 ratio of loading rate to crack growth rate (6 ksi $\sqrt{in.}$/hr loading rate and 6×10^{-2} in./hr growth rate); similar ratios could be developed for sensitized stainless steel where loading rates could be 10×10^{-3} ksi $\sqrt{in.}$/hr and the corresponding crack growth rates are 10^{-4} to 10^{-5} in./hr. Second, the success of the technique in producing stress corrosion cracks would be easily verified by fractographic analysis--the presence of intergranular fracture would confirm IGSCC.

H.5.3 Test Development

Type-304 stainless steel from heat 03580 was used to manufacture the test specimen. The chemical content and mechanical properties are described in Section H.6. The sample was heat treated for 28 hours at 1,150°F to give an EPR value of 30 C/cm^2. A modified 1T-WOL specimen was used for testing. The specimen was the same as shown in Reference 3, except the W dimension was reduced to 2.30 inches to allow the specimen to fit in the autoclave used.

Testing was conducted in the Vallecitos Nuclear Center (VNC) Corrosion Laboratory. The test setup is shown schematically in Figure H-24. An in-situ compliance gage (LVDT) was attached to the specimen. In addition, an LVDT was attached to the loading rod to accurately monitor displacements. The specimen and LVDT were installed in an Instron Screw Driven Constant Extension Rate Test Machine. Extension rates are obtained by selecting appropriate gears by use of a digitized electronic control system. The tests were conducted in air-saturated water as described in Table H-10. The initial extension rate was 1 mil/hr, which produced 40 lb/hr and 100 psi $\sqrt{in.}$/hr up to 1,000 pounds. At this point, the applied K was about 7 ksi $\sqrt{in.}$ and the extension rate was reduced to 0.1 mil/hr, which produced 4 lb/hr and 10 psi $\sqrt{in.}$/hr for the remaining duration of the test. No attempt was made to measure growth rates below 7 ksi $\sqrt{in.}$

The remainder of the test was conducted with an extension rate of 0.1 mil/hr, except when the crack length was checked by taking a compliance reading. Compliance readings were taken in two ways. First, the hot specimen was unloaded from the maximum load to 200 pounds and then reloaded to the maximum load, all at a rapid rate of 10 to 50 mil/hr. Then the specimen was unloaded and cooled to ambient temperature. Compliance was again taken using another compliance gage by loading to 1,000 pounds and unloading to 0 pounds several times. Following this step, the specimen was reheated and returned to maximum load at 1.0 mil/hr.

Room temperature compliance data were taken during the course of the test. These data were used to calculate crack lengths and stress intensity values which are given in Table H-13. The K calculations were made using Reference H-31. At the end of the test, the specimen was fractured in air to expose the environmental cracking. As shown in Figure H-25, the environmental fracture is intergranular in nature and about 0.04 inch of crack extension occurred. This amount agrees with the Table H-13 results calculated from compliance changes. Note in Figure H-25 that much more crack extension has occurred at the specimen edges than in the central portion. In fact, photomicrographs of the specimen during a test interruption revealed at least 20 mils of cracking on the specimen edges before any change in compliance was noted.

H.5.4 Test Technique

Following this initially successful test, three additional specimens were prepared from heat 04904 to assess the effects of degree of sensitization and loading rate on results. The more conventional IT CT specimen (Figure H-18) geometry was utilized and all of the tests were conducted in 8 ppm O_2 oxygenated water at 288°C. The cold compliance measurements were eliminated since confidence in the hot measurements was established during the initial test. Specimen 1 was heat treated at 1150°F for 2 hours to produce a low degree of sensitization. An Electrochemical Potentiokinetic Reactivation (EPR) value of 10 C/cm^2 resulted. This specimen was tested at 100 psi $\sqrt{in.}$/hr up to 1000 pounds which produced about 6 ksi $\sqrt{in.}$ Thereafter it was loaded at about 10 psi $\sqrt{in.}$/hr with compliance readings taken every 500 pounds. Specimen 2 was heat treated at 1150°F for 8 hours to obtain a higher degree of sensitization. An EPR value of 20 C/cm^2 resulted. This specimen was also loaded at 100 psi $\sqrt{in.}$/hr up to 1000 pounds but was thereafter loaded at 40 psi $\sqrt{in.}$ with compliance readings taken at every 500 pounds. The third specimen was given the 1150°F/8 hour heat treatment and was loaded at the slower (10 psi $\sqrt{in.}$/hr) rate. In order to further validate the test data obtained, hold periods of up to 3 weeks duration were added to the test procedure for the third

specimen. These hold periods were added when the K values reached 12, 15, and 18 ksi $\sqrt{in}$. Compliance data was taken before and after each hold period. The hold period at 12 ksi $\sqrt{in}$. was 1 week in duration but the hold periods at 15 and 18 ksi $\sqrt{in}$. were 3 weeks long.

H.5.5 Results

There was no crack extension in the low degree of sensitization or in the higher loading rate test specimens. In the combined high degree of sensitization and slower loading rate test (specimen 3), however, data was obtained between about 12 and 18 ksi $\sqrt{in}$. Figure H-26 lists the compliance determined crack length and stress intensity for the test period. No growth indications were obtained below 12 ksi $\sqrt{in}$. The crack growth of 2, 10, and 15 mils was measured during the hold periods. The change in compliance corresponding to 2 mils of crack extension is extremely small and could not be measured consistently. That is, repeated attempts to measure the compliance did not yield consistent results. Hence only the latter two data points are considered to be reliable. They result in measured crack growth rates of 2×10^{-5} in./hr at 15 ksi $\sqrt{in}$. and about 3×10^{-5} in./hr at 18 ksi $\sqrt{in}$.

H.5.6 Discussion

The technique described in the preceding sections can be used to reliably produce intergranular cracking in a relatively short period of time. It is apparent that degree of sensitization and loading rate in the test strongly influence the results. More rapid crack growth rates and lower sensitization retard cracking. The results generated on the specimens where cracking was observed agree reasonably well with the other constant load test data obtained in 8 ppm oxygenated water and support the 8 ppm O_2, furnace sensitized crack growth curve presented in Reference H-17 and updated in a summary section of this appendix. The techniques developed were used to conduct tests in 0.2 ppm O_2 high temperature water. These tests, successful in generating test data, are reported in the next section.

H.6 SLOW RISING LOAD/CONSTANT LOAD CRACK GROWTH TESTS UNDER IN-SERVICE CONDITIONS (R. M. Horn)

H.6.1 Summary and Conclusions

Crack growth studies were conducted in sensitized stainless steel. The test was conducted for 1544 hours in 0.2 ppm O_2 high temperature water. Several conclusions were drawn from the studies aimed at developing crack growth data as well as assessing test techniques. The conclusions are as follows:

1. Crack growth rates in furnace sensitized stainless steel were faster than those measured in weld sensitized stainless steel under constant load and slow rising load.

2. Slow cyclic loading was effective in initiating crack growth prior to either slow rising load or constant load applications.

3. The furnace sensitized material showed a plateau in crack growth rates between K = 24 and 38 ksi $\sqrt{in}$. The rates were similar to those measured in furnace sensitized stainless steel exposed to 8 ppm O_2 BWR environment at K = 24 ksi $\sqrt{in}$. but slower at the higher K's.

4. The weld sensitized specimen exhibited slower crack growth at the low stress intensities, with crack growth rates higher at high K's. The data added to that measured in earlier studies.

H.6.2 Introduction

Reactor components experience both constant and cyclic loads during operation. However, the components are subjected to constant loading throughout most of plant operation. In order to evaluate the growth rates of an intergranular crack in a sensitized stainless steel component, it is necessary to develop laboratory data. It is also necessary to define the stress intensity needed for propagation, K_{TH}. It is difficult to get an IG crack initiated in a laboratory specimen. Environmental cracking has been most successfully initiated in fracture mechanics specimens using slow cyclic loading. Slow extension rate tests (CERT) have also been used to develop IGSCC in tensile specimen. The importance of slow loading in initiating IG, has led to the development of a slow loading test.

By using slow rising load in conjunction with a fracture mechanics specimen, it was hoped that IGSCC could be initiated and at the same time, accurate crack growth rates could be measured. The slow rising loading test was used successfully to estimate K_{ISCC} and to evaluate crack growth rates in furnace sensitized T-304 SS exposed to 8 ppm O_2 as discussed in the previous section.

This test had several objectives. The first was to develop the best methods for gathering crack growth data. Slow rising loading methods were the focus for this study. Comparison of slow cycling with slow rising load methods for initiation and slow rising load with constant load methods for gathering da/dt data were made. Finally, the test served to compare crack growth rates in weld sensitized material with rates in furnace sensitized material in the in-service, 0.2 ppm O_2 environment of primary interest.

H.6.3 Experimental Procedures

The specimens were both cut from heat 04904 supplied in the solution annealed condition. The chemistry and mechanical properties are given in Table H-2. Specimen FS-1 was given an 1150°F, 24 hour sensitization treatment, while specimen WS-1 was given an 1150°F, 2 hour sensitization treatment. These isothermal treatments represented furnace and weld sensitization, respectively. The tests were conducted in compact tension specimens. The design of the specimen is shown in Figure H-18. Prior to testing, the specimens were fatigue precracked to develop an initial crack length, a, of ∿1.00 inch.

The specimens were tested in General Electric's Test Vessel IV in 0.2 ppm O_2, high purity 550°F (288°C) water. The testing was conducted in several loading phases, including Slow Rising Load (SRL) at 3 lb/hr or ∿0.5 ksi $\sqrt{in.}$/day; slow cycling load (SCL) at 0.74 cycle per hour at ∿ΔK of 11.5 ksi $\sqrt{in.}$, K_{eff} = 17 ksi $\sqrt{in.}$; and Constant Load (CL). The detailed loading conditions and measured compliance values are given in Tables H-14 and H-15. Because the crack lengths were slightly different in each specimen, the maximum stress intensity levels developed during each phase are also listed.

Computer methods were used to develop in-situ compliance data for each specimen. On each of three unload-load cycles where a best fit line was fit through 100 load, COD data points is plotted to determine the compliance. These three values were then averaged to arrive at an over-all average compliance. The compliance was taken over the same load range through the last 800 hours. In the initial rising load portion, two different load ranges were used; however, at the times when the load range was changed, measurements over both ranges were made to interface the data.

H.6.4 Results

The test results, (crack length versus time) as determined using LVDT measurements, are displayed in Figure H-27 and Figure H-28 for specimens FS-1 and WS-1, respectively. The test phases are shown for each specimen. In addition, test shutdowns are denoted with arrows at the bottom of the figure. From these results, it is clear that specimen FS-1 experienced significant crack growth.

At the end of testing, the two specimens were destructively evaluated for crack growth. Figure H-29 displays the macroscopic appearance of the environmental crack growth. The average amount of crack growth for FS-1 and WS-1 determined by averaging 9 measurements across the width were 0.1211 inch and 0.051 inches, respectively. The edges did exhibit exaggerated crack growth, particularly in the

FS-1 specimen. This was averaged into the growth. Figures H-30 and H-31 display the crack growth behavior matching the beginning and end lengths and matching the crack lengths after shutdowns. It is clear that much more crack growth occurred in specimen FS-1.

H.6.5 Discussion

The slow rising load test conducted in 0.2 ppm O_2 service environment was successful in producing crack growth in both the furnace sensitized specimen FS-1 and the weld sensitized specimen WS-1. The furnace sensitized specimen exhibited more crack growth. The crack growth in this specimen was totally intergranular in nature as shown in Figure H-32. The crack growth in WS-1, while significant in amount, was primarily transgranular in appearance as shown in Figure H-33a. Figure H-33b does show a facet of IG that was occasionally present.

The test itself was divided into several test phases: (1) slow rising load, (2) slow cycling load, (3) constant load, (4) slow rising load, and (5) constant load. The slow rising loading rate, $\sim$0.5 ksi $\sqrt{in.}$ and the slow cyclic frequency were selected based on previous test experience to promote IG cracking. The first phase was directed at determining K_{ISCC} less than 24 ksi $\sqrt{in.}$ No systematic increase in compliance was seen for either specimen. At this point, slow cyclic loading was used to promote cracking. This was clearly successful in that there was a steady increase in compliance for both specimens. This is shown in Figures H-30 and H-31. With stress corrosion cracks initiated, the next three phases were used to evaluate the crack growth rates over a range of stress intensity levels. It can be noted that the crack growth rates, as determined from the adjusted compliance curves, were similar for both specimens under cyclic loading. This is consistent with cyclic crack growth data generated earlier and reported in Subsection H.7. The rates are listed in Table H-16. The rates are 6.5×10^{-5} in./cycle for FS-1 and 7×10^{-5} in./cycle for WS-1. These rates are similar to those measured earlier in the cyclic crack growth study.

The crack growth rates under constant load and slow rising load, the focus of this test, will be discussed for each specimen separately in the following sections. Specimen FS-1 will be discussed first.

H.6.5.1 Specimen FS-1: Furnace Sensitized, 1150°F, 24 Hours. Following crack initiation using slow cyclic loading, crack growth continued during all following test phases. Both Figure H-27 and Figure H-30, the uncorrected and corrected data, exhibit a steady increase in compliance measured crack length. The crack growth

was uniform for the constant load phase immediately following the slow cyclic loading, as well as the slow rising load phase where the stress intensity factor at the crack tip increased substantially. (The stress intensity was calculated using the average interior crack length, not the over-all average including side cracking that was used to calculate the crack growth rate.) During the last constant load phase, the crack may have slowed down but it was still growing as indicated by the compliance changes. It is difficult to determine different crack growth rates at different K levels. The data indicated a constant rate. The amount of growth was significant with an estimated 0.105 inch of crack growth during the last 842 hours of testing. This leads to an average rate of 1.2×10^{-4} in./hr. This value was listed in Table H-16 for each of these test phases. The rate for the highly sensitized material was the first determined in 0.2 ppm O_2 high temperature water. It indicates the existence of a plateau in crack growth. The crack growth data is plotted with other data in Figure H-32. The crack growth rate at K = 24 ksi $\sqrt{in.}$ is similar to that measured for furnace sensitized material in 8 ppm O_2 at that K level. However, the plateau behavior observed as K was increased is lower than that measured at the high stress intensities in earlier studies in 8 ppm O_2.

H.6.5.2 Specimen WS-1: Weld Sensitized, 1150°F, 2 Hours. The evaluation of the crack growth rate data for this specimen is much more difficult. First, the compliance determined crack length far underpredicted the actual crack length. Outages seem to shift compliance values as shown in Figure H-31 where the data was corrected. This makes crack growth at the lower stress intensities more difficult to evaluate. In addition, the cracking mode was predominantly transgranular in appearance. It was definitely environmentally assisted, however.

The crack growth rates are much more dependent on the applied stress intensity. During the constant load phase, following the cyclic loading period, there was little evidence of cracking. In this same phase, specimen FS-1 exhibited definite compliance changes. During the slow rising load phase, the adjusted data for WS-1 (Figure H-31) showed a more definite growth trend. The slowly increasing load was enough to start the environmental growth. Finally, during the last constant load phase, the growth continued at a stress intensity level of $\sim$35 ksi $\sqrt{in.}$

The over-all growth rate was not constant as observed in the companion specimen, FS-1. The growth during the first constant load portion was hard to measure. Growth of a few mils is hard to detect over the course of a few hundred hours.

However, as K increased the growth became measurable. To estimate crack growth rates, the compliance data as a function of time was empirically represented by different power laws. A quadratic fit proved to be best. This fit was used to estimate crack growth rates that are listed in Table H-16 for specimen WS-1.

The rates are plotted in Figure H-34. The rates are somewhat faster than those measured in an earlier study under constant load at 24 ksi in as reported in Subsection H.3. This could be due to the inability to measure the crack growth accurately enough over the test time. The crack growth rates measured under rising load conditions were also above previously measured data. Rising load tests conducted in 8 ppm O_2 also exhibited higher growth rates than constant load tests due to the enhancement of strain at the crack tip accelerating the film rupture process.

The final test phase, a constant load phase at 35 ksi $\sqrt{in.}$, led to definite growth with the rate being 7×10^{-5} in./hour. The uncorrected data (Figure H-26) and corrected data (Figure H-31) showed this definite upper trend.

The test was successful in generating environmental crack growth data. From the test results, it was clear that the furnace sensitized specimen exhibited faster crack growth than did the weld sensitized specimen under constant load and rising load conditions. The test demonstrated that slow cyclic loading was an effective method of generating a growing stress corrosion crack. The data generated supports the data generated earlier. However, the furnace sensitized material in the lower 0.2 ppm O_2 environment exhibited a plateau behavior similar to that seen by Ford in sensitized stainless steel exposed to 1.5 ppm O_2 93°C water (Reference H-23). The constant load data gathered from the weld sensitized specimen supported data generated earlier.

H.7 CRACK GROWTH RATES UNDER CYCLIC LOADING, IN-SERVICE CONDITIONS (D. A. Hale)

H.7.1 Summary and Conclusions

The fatigue crack growth behavior of Type-304 stainless steel was studied and the effects of high temperature, high purity oxygenated water, cycle frequency, mean stress, and degrees of sensitization were evaluated. Results of tests performed on 19 crack growth specimens indicate that the fatigue crack growth rates of non-sensitized stainless steel are not significantly affected by the environment for the range of conditions studied.

For sensitized specimens, the degree of sensitization is seen to have no marked influence on the environmental fatigue crack growth rates for the range of EPR values of 10 to 35. This is the range expected for most pipe welds using Type-304 stainless steel. Both intergranular and transgranular fracture modes were observed with the slower frequencies and higher oxygen concentration tending to produce intergranular cracking. Also, the crack growth rates of sensitized and nonsensitized stainless steel are very similar at higher frequencies (>18 cycles per hour (cph)); however, at slower frequencies (<18 cph), the crack growth rates of sensitized stainless steel are significantly enhanced by the environment. All tests but one in this study were in 0.2 ppm oxygenated water at 550°F. Literature data for 8 ppm oxygenated water was used to verify that both frequency and oxygen directly affect crack growth rates and fracture modes.

H.7.2 Introduction

The results summarized in this report were obtained as part of a program to generate environmental fatigue crack growth data for piping materials in high temperature, high purity, oxygenated water. The efforts of this study were focused specifically on developing a quantitative understanding of the effects of sensitization, frequency, mean load, and oxygen concentration on the crack growth behavior of Type-304 stainless steel.

This report covers results obtained from a total of 19 crack growth specimens including GE data generated prior to the inception of this program and reported in Reference H-32. Two different plates of Type-304 stainless steel were used to fabricate all of the specimens. Two specimens were made from the weld-heat affected zone of the stainless steel material. Sensitized specimens were made utilizing isothermal heat treatment.

The tests cover a wide range of frequencies and mean loads (R ratio).* The frequencies ranged from 300 cph to 0.74 cph and the R ratios varied from 0 to 0.78. A symmetric sawtooth or skewed sawtooth emphasizing the time spent under rising load was used as the loading waveshape in 18 of the tests. One test used a trapezoidal loading waveshape.

*Minimum stress/maximum stress

H.7.3 Test Description

H.7.3.1 Test Facilities. The high pressure, high temperature water environment used for this program was provided by a high flow test loop (Environmental Fatigue Loop 1 or 2) in General Electric's Experimental Mechanics Laboratory. A schematic drawing of this loop is shown in Figure H-35.

The loop includes a canned rotor pump which provides sufficient flow ($\sim$12 gal/min) to ensure that all specimens tested in the loop are subjected to a refreshed environment. Bypass demineralizer beds are provided to maintain the conductivity and pH of the demineralized water environment (Table H-1). The level of dissolved oxygen, conductivity, and pH of the loop water is continuously monitored. Dissolved oxygen level is controlled by a gas-controlled system that continuously purges a gas mixture through the makeup tank at a rate needed to establish the desired dissolved oxygen level in the makeup water which is being continuously added to the loop.

Specimen loading was accomplished using a closed loop, electrohydraulic test machine that applies a cyclic load to a group of up to six specimens arranged in a series chain inside a pressure vessel. A computer is available for use with this facility to acquire and analyze the data. A schematic drawing of this machine is shown in Figure H-36.

H.7.3.2 Test Specimen/Techniques. Both Wedge Open Loading (WOL) and CT crack growth test specimens were used for these tests. The geometry of each is shown in Figure H-18. Although the WOL and CT specimens are very similar, the CT is shorter and has a more rapid increase in applied K for given increase in crack length. Two techniques were used to monitor progress of the fatigue crack. The primary technique utilized a high temperature, high pressure LVDT to measure the specimen COD which accompanied specimen loading. The resultant load/COD data (i.e., compliance) was used to calculate crack lengths. The backup technique for monitoring crack lengths, which was used on 10 initial test specimens and has not been used for the last 3 years, consisted of a series of 0.028-in.-diameter holes drilled on 0.100-in. centers normal to the plane of fatigue crack growth. These holes were connected to external pressure switches with capillary tubing. This hole/capillary tube/switch system was evacuated and backfilled with an inert gas to a pressure slightly below the operating pressure in the test vessel. As the fatigue crack front intersects each hole, a pressure pulse was applied to an external pressure switch, stopping an individual cyclic load counter. The resultant data was incremental crack growth information representing the cycles required to extend

the fatigue crack in 0.100-in. increments. Figure H-37 shows a standard WOL specimen with capillary holes and an LVDT mounted on top. Extensive post-test fractography was performed on all specimens to obtain information on fracture modes and fatigue crack front geometries. A special 10X traversing microscope with x- and y-axes micrometer measuring capability was used to measure the crack length associated with each capillary hole, and, more importantly, to locate and define the shape of any artifacts present in the fracture surface.

H.7.3.3 Test Matrix. A total of 19 Type-304 stainless-steel specimens were tested. Eleven of these were made from the same plate material and were given specimen numbers containing the prefix (S-). The remaining eight specimens were made from another supply of plate material and were given specimen numbers containing the prefix (SS-). Six of these were tested as part of this program. Two of these specimens, SS-1 and SS-1A, were made from the weld heat-affected zone of the stainless steel material. The specimens were fabricated from the welded plate material with the crack propagation path lying along the HAZ (i.e., a sixteenth of an inch from the weld fusion line). The orientation of the WOL specimen with respect to the welded plate is schematically shown in Figure H-38. The physical and mechanical properties and chemical composition of all the materials included in the study are listed in Table H-17.

Of the 19 specimens tested, 8 of them received no heat treatment and were tested as nonsensitized specimens. The remaining 11 specimens were subjected to different isothermal heat treatments and subsequently had different Degrees of Sensitization (DOS). Table H-18 lists the heat treatment and EPR value associated with each specimen. The EPR value is an experimentally measured quantity (C^*/cm^2) that is directly related to degree of sensitization. The nonsensitized specimens had EPR values of 1.89, while the sensitized specimens had EPR values ranging from 5 (low DOS) to 35 (high DOS).

Several multispecimen tests were run. The pertinent parameters for these tests are listed in Table H-19. The tests covered a wide range of frequencies from 300 cph to 0.79 cph, and mean stresses from 0 to 0.78. All tests, except for one, were tested using either a symmetric or a skewed sawtooth loading waveshape. The skewed sawtooth emphasized the time spent under rising load and was used for most of the tests. The remaining test was examined using a trapezoidal loading waveshape.

*Coulomb

H.7.4 Test Results

An end of test fracture surface for Specimen SS-11 is shown in Figure H-39. The pronounced crack front curvature visible in this figure (dark portion is the environmental crack) is typical of all the stainless-steel specimens tested.

Crack length versus number of cycles data for all specimens* tested are presented in Figures H-40 through H-57. Notice that the abscissa for each of the curves is different and that the tests are at different loading conditions. Figures H-40 through H-51 show smoothed data for the 11 S-specimens while Figures H-51 through H-57 show the raw data collected for the 7 SS-specimens. The data were smoothed by deletion of the few "wild points" that typically occur when data are collected using LVDTs and connection of the remainder by smooth curves.

Examination of all a versus N plots, Figures H-40 through H-57, shows that generally the crack growth rates of stainless steel either stayed constant or increased as the crack grows. Specimen SS-6, Figure H-55, is a major exception to this generalization, but it is believed that this apparent behavior was due to LVDT failure partway through the test.

H.7.5 Discussion

In the preceding subsection, observations were made about the raw crack length versus cycles data contained in Figures H-40 through H-57, from which crack growth rates and stress intensities were calculated. A plot of crack growth rate, da/dt, versus stress intensity factor, K, provides a graphical representation of the crack growth behavior of the material under different test conditions. The effects of frequency, mean stress, and sensitization on crack growth behavior can then be observed by comparing the different da/dt versus K plots.

Figure H-58 is a crack growth rate versus an effective stress intensity factor of two Type-304 stainless-steel tests in 550°F air. One test was conducted at a high frequency of 36,000 cph, with a mean stress of R = 0.1. The air test will be used to make comparisons with the data presented in this report. The data is plotted versus an effective stress intensity factor, K_{eff}, because K_{eff} has been shown to normalize the effects of mean stress, making effects of frequency more pronounced.

*Sufficient data was not obtained for the SS-1 specimen and, therefore, no data is presented.

Figure H-59 is a crack growth rate versus an effective stress intensity factor plot of three nonsensitized, Type-304 stainless steel specimens tested in 550°F water, 0.2 ppm oxygen. The three specimens, S-15, S-10, and S-9, represent a wide range of frequencies and mean stress levels that are identified on the plot. Visual inspection of Figure H-59 shows that the higher frequencies clearly produced faster growth rates. This observation is also supported by Figure H-60, in which the air data, tested at a very fast frequency (36,000 cph) had very fast growth rates associated with it. This in itself is not surprising since, for this case, the time-based growth rates, da/dt, are merely the product of the cyclic-based growth rates, da/dN, and the loading frequency, f. Therefore, even in an environment such as air, the growth rates, da/dt, should increase linearly with frequency; i.e., a "pure fatigue" line on a log-log plot (Figure H-60) would have a slope of 1.

A quantitative comparison between the air data (Figure H-58) and the nonsensitized crack growth data (Figure H-59) is made in Figure H-60. At an effective stress intensity factor level of 30 ksi$\sqrt{\text{in.}}$, crack growth rates, da/dt, were picked off the corresponding graphs. Figure H-60 plots these growth rates versus frequency. Notice that the air data from Reference H-8 is plotted and is identified as pure fatigue. The nonsensitized data tested in 0.2 ppm oxygen plots near the pure fatigue point, with a slope of 1, suggesting that crack growth rates of nonsensitized stainless steel are not enhanced by the 550°F 0.2 ppm oxygenated water environment. Figure H-60 also includes a plot of the estimated crack growth rates of the nonsensitized data tested in 0.2 ppm at an effective stress intensity factor level of 20 ksi$\sqrt{\text{in.}}$ versus frequency. It was necessary to estimate the crack growth rates at K_{eff}^{*} = 20 ksi$\sqrt{\text{in.}}$ because the data plotted in Figure H-59 only covers a K_{eff} range from 27 ksi$\sqrt{\text{in.}}$ to 38 ksi$\sqrt{\text{in.}}$ This curve is used to make comparisons with data discussed later in this report.

In order to observe the effects of sensitization of fatigue crack propagation rates, groups of specimens having different degrees of sensitization, but tested at the same frequency and mean stress, are plotted on the same graph. Figure H-61 is a plot of two such groups of specimens. Three specimens, SS-10, SS-11, and SS-12, represent varying degrees of sensitization tested at 7.5 cph and R = 0.6. Table H-18 shows that the three specimens had EPR values ranging from 10.5 C/cm^2 (SS-11) to 27 C/cm^2 (SS-10). The points have been plotted as crack growth rate versus maximum stress intensity factor, K_{max}, in Figure H-61. Notice that all the points plot in

$^{*}K_{eff} = K_{max}(1-R)^{0.5}$

the same location indicating that degree of sensitization did not influence the environmental crack growth rate of Type-304 stainless steel. This conclusion is supported by specimens SS-7 and SS-21, both tested at 0.74 cph and R = 0.6. They represent two different degrees of sensitization: SS-7 at 13 C/cm^2 and SS-21 at 27 C/cm^2. As seen in Figure H-61, these points also plot in the same location again showing no effect of degree of sensitization.

There are, however, differences in fracture morphology related both to the differences in DOS among Specimens SS-10, -11, and -12, and to the change in load level for a given specimen. Specimen SS-10 showed considerable areas of mixed mode (intergranular + transgranular) morphology corresponding to the first phase of testing when low loads were used (Figure H-62). Corresponding areas on Specimen SS-11 (Figure H-62) were predominantly transgranular with a slight indication of IG. The corresponding areas on Specimen SS-12 were totally transgranular in nature (Figure H-64). Specimen SS-10 (high DOS) also showed small patches of IG morphology near both sides, immediately behind the fatigue precrack (Figure H-65). No purely IG cracking was observed anywhere in Specimens SS-11 (medium DOS) or SS-12 (low DOS).

On the other hand, all three specimens (SS-10, -11, and -12) experienced transgranular cracking during the second part of testing (Phase II) when much higher loads were used (Figure H-66). This same effect of DOS on fracture morphology was observed in the 0.75 cph specimens (SS-7 with medium DOS, and SS-21 with high DOS; see Figure H-67). Specimen SS-7 exhibited behavior very similar to SS-11; i.e., transgranular cracking with slight indications of IG. Specimen SS-21 was totally intergranular, as shown in Figure H-68. Much more IG was noted in Specimen SS-21 than SS-10, which was expected since SS-21 was run at a slower frequency. Thus, slower frequencies and/or higher DOS promote intergranular cracking.

The DOS does not significantly affect macroscopic crack growth rates (Figure H-61), yet it does dramatically change fracture morphology. However, it should be noted that the crack growth data (Figure H-61) represents macroscopic growth rates derived from compliance measurements. By its very nature, the compliance technique averages out microscopic events, such as local secondary cracking, and crack branching. Therefore, it is possible that higher crack growth rates were occurring on a microscopic scale under IG conditions, and were not showing up as planar extensions of the primary crack; i.e., a large part of the system energy which was creating fresh crack surface area on each loading cycle was going into secondary cracking and/or crack branching.

Figure H-62 is a typical photo of the mixed mode portion of specimen SS-10, in which a significant amount of secondary cracking is noted. Little or no secondary cracking was observed in corresponding areas of Specimens SS-11 or SS-12. The effects of frequency and oxygen concentration on the mode of fracture of sensitized stainless steel are described by data presented in Reference H-8. The data are representative of tests run at different frequencies and different oxygen concentrations and are plotted as crack growth rate versus maximum stress intensity factor in Figure H-69. Notice that at the fast frequencies, 72 cph and 720 cph, there is no difference between the 0.2 ppm and the 8 ppm oxygen concentration data. Furthermore, it is pointed out in Reference H-8 that the fracture mode at these two frequencies was purely transgranular. At the slowest frequency, 0.72 cph, however, the 8 ppm O_2 data had much faster growth rates than the 0.2 ppm O_2 data. Reference H-8 points out that the 0.2 ppm O_2 data was transgranular while the 8 ppm O_2 data was intergranular at this frequency. The 7.2 cph data, then, represents a transition for the two types of crack growth behavior exhibited by the slow and fast frequencies. These Reference H-8 data show that frequency and oxygen concentration affect the fracture mode with slower frequencies and higher oxygen concentrations, promoting intergranular cracking.

Figure H-70 shows General Electric fatigue crack propagation data for highly sensitized Type-304 stainless steel tested in 550°F water, 0.2 ppm oxygen at high mean stress levels. The four specimens, S-4, S-8, SS-10, and SS-21, are representative of four different frequencies as identified on the plot.

Figure H-71 compares the General Electric highly sensitized data of Figure H-70 with the 0.2 ppm oxygen concentration data of Reference H-8 (Figure H-69). The Reference H-8 data was obtained at low mean stress levels while the GE sensitized data was obtained at high mean stress levels. In order to make the comparison meaningful, the crack growth rates were plotted versus effective stress intensity factor to normalize the mean stress effects. At the three higher frequencies, 300 cph, 18 cph, and 7.5 cph, the GE sensitized data agree reasonably well with the data from Reference H-8. However, the data for the slowest frequency specimen (SS-21) do not compare as favorably to the Reference H-8 data. This lack of agreement may be due to the very limited range of K_I values studied in the General Electric low frequency data.

Further observations on the effect of fracture mode (transgranular or intergranular) of sensitized stainless steel can be made. The crack growth rates of the 0.2 ppm and 8 ppm data corresponding to an effective stress intensity value of 20 ksi$\sqrt{\text{in}}$.

are taken from Reference H-8. Data for 8 ppm level off at a consistent value of about 10^{-4} in./hr at frequencies less than 10 cph. On a growth rate per cycle basis, the rate increases below this frequency. It is at these low frequencies that Reference H-8 reports intergranular cracking for the 8 ppm data. The General Electric highly sensitized data in 0.2 ppm oxygenated water from Figure H-68 agrees very well with both the 0.2 and 8 ppm Reference H-8 data. Specimen SS-21, run at 0.74 cph, showed this leveling off agreeing with the 8 ppm data, which is consistent with its observed intergranular fracture morphology.

A final generalization about the behavior of sensitized and nonsensitized stainless steel can be made from Figure H-72. The estimated crack growth rate (at K_{eff} = 20 ksi$\sqrt{in.}$) per cycle is plotted as a function of frequency. This plot displays the impact of cyclic loading on plant operation. It is seen that only at slow frequencies (<10 cph) is the crack growth rate strongly accelerated for the sensitized steel. The rate increased about 10 times on a per cycle basis as the frequency was decreased below 1 cph. These increased rates would only extend the crack during the few slow loading cycles experienced by the piping during startups.

H.8 CONSTANT LOAD CRACK GROWTH TESTS IN 0.2 ppm OXYGENATED WATER (M. M. Bensch and R. M. Horn)

H.8.1 Summary and Conclusions

Five Type-304 weld sensitized stainless steel 1T-WOL specimens, and one furnace sensitized 304 stainless steel 1T-CT specimen were exposed to a 550°F, 0.2 ppm dissolved oxygen, demineralized water environment for over 1400 hours. These tests were conducted to determine the threshold stress intensity for stainless steel and crack growth rates. The specimens were subjected to cyclic loading for 374 hours to initiate cracking, then held at a constant load of 2700 pounds until test termination. The five stainless steel specimens were precracked to different lengths to obtain a range of stress intensity, K, values from 12 to 23 ksi$\sqrt{in.}$ The furnace-sensitized stainless steel specimens had a K of 19.6 ksi$\sqrt{in.}$ The test methods were developed based on earlier crack growth studies reported in Sections H.3 through H.6.

Two out of the five Type-304 stainless steel specimens experienced minimal IGSCC crack growth (4.4×10^{-6} to 6.0×10^{-6} in./hr). These were at the lowest K levels (12 to 15 ksi$\sqrt{in.}$). The remaining three Type-304 stainless steel specimens exhibited IGSCC crack growth rates under constant load of 4.0×10^{-5} in./hr to 6.0×10^{-5} in./hr (K = 17.7 to 23.4 ksi$\sqrt{in.}$), respectively. The crack growth rate

of the furnace-sensitized Type-304 stainless steel specimen was 5.2×10^{-5} in./hr. All specimens cracked substantiating that the threshold stress intensity was below 12 ksi$\sqrt{in}$.

The crack growth rate fell on or below the upper bound evaluation curve developed earlier. The data substantiated that in severely sensitized material, crack growth rates in 0.2 ppm oxygenated water are similar to those in 8 ppm oxygenated water. Significant differences were found in sensitization response of the two heats investigated. These differences were used to explain crack growth rates measured. The rates measured in one heat, 04904, which was sensitized to a lesser degree by the 1150°F, 2-hr isothermal heat treatment, supported the representative crack growth curve.

H.8.2 Introduction

In order to predict the subsequent behavior of cracked (SCC) Sensitized Stainless Steel piping it is necessary to characterize the crack growth behavior. Typically, during normal BWR plant operation, the recirculation piping is subjected to constant loads and is exposed to 0.2 ppm O_2 high purity, high temperature water. The objective of this test program was to measure the threshold stress intensity and constant load crack growth rates for stainless steel in the sensitized condition under these typical in-service conditions. The data obtained would then be suitable for use in development of an evaluation curve to determine the crack growth rate as a function of stress intensity. The test matrix design and test methods were developed based on earlier data and tests.

H.8.3 Experimental Procedures

Five 1T-WOL and one 1T-CT Type-304 stainless steel specimens were tested. Table H-20 lists the associated heat numbers and material heat treatment. Tables H-1 and H-11 list the chemistry and mechanical properties for both heats.

In five of the six specimens, a moderate-to-high level of sensitization was imparted to the material prior to machining by a 1150°F, 2-hr isothermal heat treatment followed by air cooling. The response of the two heats used to this heat treatment was characterized by Electrochemical Potentiokinetic Reactivation (EPR) earlier and discussed in Subsection H.3. This heat treatment was expected to impart a sensitization level similar to that of as-welded pipe. Constant extension rate tests were used to characterize Intergranular Stress Corrosion Cracking (IGSCC) behavior of the material from the two heats in this condition and the results are listed in Table H-21. The other specimen tested was fully furnace sensitized by an

1150°F, 24-hr heat treatment. The specimens were tested in Test Vessel VI of the Mechanics of Materials (MOM) Laboratory which has associated with it a 10-kip closed loop electrohydraulic test machine. The specimens were fatigue precracked in air and inserted into the test vessel in a series chain arrangement. The following 0.2 ppm oxygenated water environment was supplied from the Environment Fatigue Loop II (EFL-II):

Temperature	550°F
Pressure	1230 psig
Conductivity	0.5 ± 0.2 μmho/cm at 25°C
Dissolved oxygen content	100-300 ppb

The loading was applied at two rates shown in Figure H-73.

Rate 1: Slow cyclic loading at 0.74 cph
Positive Sawtooth - 80-min rise, 1-min fall
P_{max} = 2678 lb, P_{min} = 250 lb

Rate 2: Constant Load
P_{max} = 2678 lb

The total load included external load in addition to a 1000-lb pressure load. Rate 1 was used to initiate environmental Stress Corrosion Cracking (SCC) from the precrack. This was applied for approximately 2 weeks, then followed by constant load (Rate 2).

A computerized Data Acquisition System (DAS) was used to monitor progress of the fatigue crack during environmental testing. The individual test specimens were equipped with a high-temperature Linear Variable Differential Transformer (LVDT) to measure the specimen Crack Opening Displacement (COD) during the rising load portion of the daily compliance cycles. The resultant load/COD data (i.e., compliance) are then used to calculate crack lengths. A schematic of the complete test system was displayed in Figure H-36.

H.8.4 Test Results

The total time in test for the six stainless steel specimens was 1422 hours, with the initial 374 hours under cycle loading (Rate 1).

The daily LVDT compliance measurements are plotted in Figure H-74 through H-79. There were two outages during the constant load period, one at 611 hours and one

at 1056 hours. The crack growth rates were determined from the middle interval (650 - 1032 hours), and are listed in Table H-22. Specimen SS-70 exhibited a shift in apparent crack length of 0.011 inch during this interval. The data was corrected in Figure H-74 to compensate for the shift. It was also noted that the crack growth rates were slightly decreased in the final test interval (1060 through 1422 hours).

At the test completion, the specimens were broken apart (Figures H-80 through H-85) and the total crack growth was measured using a x-y traversing bed optical microscope. The results correlate well with the computerized DAS compliance-based measurements, with the exception of specimen SS-72, as seen in Table H-23. Scanning Electron Microscopy (SEM) photographs were made of the fracture surfaces. These indicated predominantly IGSCC crack growth in the stainless steel specimens.

H.8.5 Discussion of Crack Growth Behavior

The objective of these tests was to develop crack growth data to support an evaluation methodology to be applied to piping components under normal operation conditions. Consequently, this series of tests was conducted under 0.2 ppm oxygen, high purity, high temperature water and constant loading conditions. All but one specimen were given a heat treatment which produced sensitization expected to be similar to that produced in the pipe heat-affected zone by welding. The other specimen, which was fully furnace sensitized, would yield data useful for evaluating the role of oxygen level on crack growth rates in severely sensitized material. This last treatment was the basis for the upper bound evaluation curve generated using tests conducted in 8 ppm oxygenated BWR water and reported first in Reference H-17. The crack growth rates for all the specimens are listed in Table H-22. The results of the furnace sensitized specimen will be discussed first, followed by the discussion on the other five tests.

H.8.5.1 Full Furnace Sensitized (1150°F, 24 hours) Crack Growth Rates - 0.2 ppm Oxygenated Water. The data from specimen FS-2 is plotted in Figure H-86, which also displays crack growth curves presented earlier. The upper bound evaluation curve was developed for fully furnace sensitized specimens (1150°F, 24 hours) tested in 8 ppm O_2, BWR water. It is clear from these tests that the growth rates measured at a stress intensity level of 20 ksi$\sqrt{in.}$ in this severely sensitized material are the same in 0.2 ppm O_2 as rates measured in similar material exposed to 8 ppm O_2. This was observed earlier and reported in Subsection H.6. Sensitization level and its impact on crack growth rates outweigh any oxygen effect at levels down to 0.2 ppm O_2.

H.8.5.2 Sensitized (1150°F, 2 hours) Crack Growth Rates - 0.2 ppm Oxygenated Water. Five of the six specimens tested were given an 1150°F, 2-hr heat treatment, picked as a heat treatment characteristic of as-welded pipe. The specimens were manufactured from two different heats, both of which were used to generate data reported in the other crack growth studies. Table H-22 again, lists the crack growth rates determined from compliance measurements. In addition, the data are displayed in Figure H-86 with different symbols used for the two heats. It is clear that the data all fall on or below the Upper Bound Curve. However, the heat treatment used is identical to that used for the specimens that were used to generate the reference evaluation curve, also shown in Figure H-86. Closer examination of the data shows that the growth rates measured for heat 04904 were significantly slower than those measured in heat 03580. This is partly a function of the stress intensity level used. However, the data from SS-70 and SS-71 (04904) was clearly below the upper bound curve, while the data from SS-72, SS-73, and SS-74 (03580) were on the curve. Both 04904 specimens exhibited small but measurable amounts of IGSCC. Resolution of crack growth rate, a function of the absolute amount of growth and test time, was difficult and might suggest that these data were not significantly different from that used to define the Representative Curve.

The data from the 03580 material was definitely much faster than the Representative Evaluation Curve. Therefore, a clear distinction must exist for the two heats. In heat 04904, and 1150°F, 2-hr treatment produced moderate crack growth rates while in heat 03580, it produced rates indistinguishable from those measured in material given a full 1150°F, 24-hr furnace sensitization. In turn, these rates support the upper bound evaluation curve.

The kinetics of sensitization are obviously different for the two heats. Chemically, the only difference is the manganese content, which would not be expected to significantly influence sensitization. The 550°F yield strength was lower and the grain size was finer (ASTM 2 to 3 versus ASTM 1) for heat 04904. The biggest difference, however, was in the CERT results, also given in Table H-21. Heat 03580 exhibited a total IGSCC failure and only 6.0% reduction in area compared to a partial IGSCC failure and 12.3% reduction in area for heat 04904. The failure of 04904 seems to be more typical of as-welded pipe associated with field failures as supported by Reference H-34.

Separate EPR tests were performed on material from each test specimen. The grain-size corrected values are listed in Table H-24. The values do not appear

different for the two heats. The etched surface following EPR showed more grain boundary decoration for the 03580 material. Ptting also occurred on the 04904 material, possibly inflating the EPR values.

In order to further evaluate the sensitization produced in these two heats by the 1150°F, 2-hr treatment, an ASTM A262 practice E corrosion test was performed. Although only one 72-hr exposure was used, heat 03580 showed severe sensitization. Figure H-87a displays the microscopic appearance of a coupon from SS-72 following exposure and bending. Severe IGSCC over the entire piece was observed. Figure H-87b displays the appearance of a coupon from SS-70 (04904) exposed to the same history. Only limited edge cracking and grain boundary fissuring could be observed.

The over-all IGSCC response of the two heats is very different. The explanation for this difference is not clear. However, it is not surprising that the crack growth rates measured in SS-72, SS-73, and SS-74 are faster than those rates measured in SS-70 and SS-71, even after considering stress intensity differences. The 1150°F, 2-hr treatment leads to severe sensitization in heat 03580; a severity that is similar to that produced by a full furnace sensitization treatment of 1150°F, 24 hours. The sensitization imparted to 04904 by this same heat treatment is less severe, and based on CERT results more characteristic of field weld sensitization. The new data from SS-70 and SS-71 essentially support the representative evaluation curve. This data from SS-72, SS-73, and SS-74 supports the upper bound evaluation curve and demonstrates that growth rates in 0.2 ppm oxygen are similar to the rates in 8.ppm oxygen in severely sensitized material.

H.9 REFERENCES

H-1. R. L. Cowan, II, and D. S. Tedmon, Jr., "Intergranular Corrosion of Iron-Nickel-Chromium Alloys," Advanced in Corrosion Science and Technology, Vol. 3, ed. M. G. Fontana and R. W. Staehle, 1973.

H-2. R. L. Cowan, II, and G. M. Gordon, "Intergranular Stress Corrosion Cracking and Grain Boundary Composition of Fe-Ni-Ci Alloys," General Electric Company, 1973 (NEDO-12399).

H-3. H. H. Klepfer, et al., "Cause of Cracking in Austenitic Stainless Steel Piping," General Electric Company, 1975 (NEDO-2100).

H-4. W. Berry, Corrosion, Vol. 29, No. 12, 1973.

H-5. D. Vermilyea, Corrosion, Vol. 29, No. 1, 1973.

H-6. W. Clarke, Corrosion, Vol. 29, No. 1, 1973.

H-7. J. N. Kass, Corrosion, Vol. 36, No. 6, 1980.

H-8. T. Kawakubo, et al., "Crack Growth Behavior of T-304SS in Oxygenated 290°C Pure Water Under Low Frequency Cyclic Loading," Corrosion, 36, 11, November 1980.

H-9. F. P. Ford, Corrosion, Vol. 36, No. 11, 1980.

H-10. R. M. Horn, et al., "The Growth and Stability of Stress Corrosion Cracks in Large Diameter BWR Piping," Third Semiannual Report, General Electric Company, December 1980 (NEDC-27450-3).

H-11. W. Clarke, "The EPR Method for the Detection of Sensitization in Stainless Steel," General Electric Company, February 1981 (GEAP-24888).

H-12. W. Clarke, "Comparative Methods for Measuring Degree of Sensitization in Stainless Steel ASTM STP 656 Intergranular Corrosion of Stainless Alloys," R. Stergerwald (ed.), 1978.

H-13. S. Mostovoy, P. B. Crosley, and E. J. Ripling, "Use of Crack Line Loaded Specimens for Measuring Plant Strain Fracture Toughness," Journal of Materials, Vol. 2, 1967.

H-14. W. A. VanDerSlys, "Engineering Fracture Mechanics," Vol. 1, 1969.

H-15. P. B. Crosley and E. J. Ripling, "Nuclear Engineering Design," Vol. 17, 1971.

H-16. W. T. Wang, unpublished results, General Electric Company, San Jose.

H-17. R. M. Horn, et al., "The Growth and Stability of Stress Corrosion Cracks in Large Diameter BWR Piping," Second Semiannual Report, General Electric Company, June 1980 (NEDC-24750-2).

H-18. M. O. Speidel, M. J. Blackburn, T. R. Beck, and J. A. Feeney, Corrosion Fatigue: Chemistry, Mechanics and Microstructure, National Association of Corrosion Engineers, 1972, pp. 324-345 (NACE02).

H-19. M. O. Speidel, Hydrogen Embrittlement and SCC of Iron-Base Alloys, Firmany, France, 1973.

H-20. M. Speidel, Met. Trans., Vol. 6A, 1975, pp. 631-51.

H-21. A Russell, Met. Trans., Vol. 10A, No. 9, 1979.

H-22. M. Landkof, Corrosion, Vol. 36, No. 5, 1980.

H-23. F. P. Ford, "Mechanism of Environmentally Controlled Crack Growth of Fractured Steels in High Temperature Water," IAEAA Meeting on Environmental Cracking, Freiburg, West Germany, May 11-15, 1981.

H-24. R. Parkins, Metal. Sci., Vol. 465, August 1977.

H-25. J. Alexander, "Alternate Pipe Alloy for BWR Pipe Applications," Sixth Semi-Annual Report, General Electric Company, September 1980 (NEDO-23750-6).

H-26. I. Masaoki, et al., Hitachi Research Laboratories, private communication.

H-27. B. F. Brown, Matls. Res. Stan., 6, 3, 129-33, March 1966.

H-28. S. R. Novak, J. Matls., 4, 3, 701-28, September 1969.

H-29. P. McIntyre, "Accelerated Test Techniques for Determination of K_{ISCC} in Steels," British Steel Corporation, 1972 (MG/31/71).

H-30. W. Clarke, "Evaluation of Rising Load K_{ISCC} Tests," ASTM, November 1976 (ASTM 610).

H-31. H. Tada, P. C. Paris, and G. R. Irwin, "The Stress Analysis of Cracks Handbook," Del Research Corporation, 1979.

H-32. D. A. Hale, C. W. Jewett, J. N. Kass, J. Eng. Matls. and Tech., p. 191, July 1979.

H-33. H. D. Solomon, unpublished results.

H-34. W. L. Clarke, R. L. Cowan, and J. C. Danko, "Dynamic Straining Stress Corrosion Test for Predicting BWR Materials Performance," The Slow Strain Rate Technique, ASTM, 1979, ASTM STP 665, p. 1949.

H-35. D. A. Hale and A. E. Pickett, "First Semiannual Progress Report, Materials Performance in a Startup Environment, May 1981 - January 1982," April 1982 (NEDO-24392-1).

H-36. J. Y. Park and W. J. Shack, "Corrosion Studies in Nuclear Piping in BWR Environments," Semiannual Report, Electric Power Research Institute, July 1980 (EPRI T117-1).

H-37. R. D. Caligiuri, L. E. Eiselstein, and M. L. Fox, "Low Temperature Sensitization of Weld Heat-Affected Zones in Type-304 Stainless Steel," IAAEA Meeting on Environmental Cracking, Freiburg, West Germany, May 11-15, 1981.

Table H-1

ENVIRONMENTAL CONDITIONS FOR TESTING IN SIMULATED BWR SERVICE CONDITIONS

Temperature	550°F ± 10°F
Pressure	1230 psi ± 20 psi
Oxygen	0.2 ppm ± 0.1 ppm
Conductivity	0.5 μmho ± 0.2 μmho
pH	6.5 ± 0.5 at 25°C

Table H-2

PROPERTIES OF HEAT 04904

A. COMPOSITION OF TYPE-304 STAINLESS STEEL MATERIAL - Heat No. 04904

	Percent Alloy Addition							
Heat No.	C	Mn	Cr	Ni	Mo	P	S	Si
04904 (ladle)	0.067	0.94	18.67	8.09	0.44	0.022	0.022	0.37
(check)	0.071	0.97	18.65	8.15	0.41	0.023	0.026	0.37

B. MECHANICAL PROPERTIES - Heat No. 04904

Test Temperature	0.2% Yield Strength (ksi)	Ultimate Tensile Strength (ksi)	% Elongation	% Reduction in Area
Room Temperature[a]	37.1	89.0	73	67.2
550°F[a]	20.9	65.7	46	57.2

[a]Average of two specimens

C. CERT PROPERTIES - Heat No. 04904 (heat treated for 2 hours at 1150°F)

Strain Rate	Maximum Stress	Time to Fail	% Elongation	% Reduction Area
4.4×10^{-5} in./in./min.	45.3 ksi	101.5 hr	12.3	25.9

Table H-3

COMPLIANCE AS A FUNCTION OF CRACK LENGTH
FOR CONSTANT LOAD CRACK GROWTH TESTS

Crack Length (in.)	Load Line Compliance - 304 SS			
	B = 0.7 in. (in./lb) (31 ksi$\sqrt{in.}$)	B - 0.8 in. (in./lb) (27 ksi$\sqrt{in.}$)	B - 0.9 in. (in./lb) (24 ksi$\sqrt{in.}$)	B = 1.1 in. (in./lb) (19 ksi$\sqrt{in.}$)
1.26	2.29×10^{-6}	2.00×10^{-6}	1.78×10^{-6}	1.46×10^{-6}
1.27	2.32×10^{-6}	2.03×10^{-6}	1.80×10^{-6}	1.47×10^{-6}
1.28	2.34×10^{-6}	2.05×10^{-6}	1.82×10^{-6}	1.49×10^{-6}
1.29	2.37×10^{-6}	2.07×10^{-6}	1.84×10^{-6}	1.51×10^{-6}
1.30	2.39×10^{-6}	2.09×10^{-6}	1.86×10^{-6}	1.52×10^{-6}
1.31	2.41×10^{-6}	2.11×10^{-6}	1.87×10^{-6}	1.54×10^{-6}
1.32	2.44×10^{-6}	2.13×10^{-6}	1.90×10^{-6}	1.55×10^{-6}
1.33	2.46×10^{-6}	2.16×10^{-6}	1.92×10^{-6}	1.57×10^{-6}
1.34	2.49×10^{-6}	2.18×10^{-6}	1.94×10^{-6}	1.58×10^{-6}
1.35	2.51×10^{-6}	2.20×10^{-6}	1.95×10^{-6}	1.60×10^{-6}
1.37	2.54×10^{-6}	2.22×10^{-6}	1.97×10^{-6}	1.62×10^{-6}

B = thickness

Table H-4

SPECIMEN HISTORY - IN-SERVICE CONSTANT LOAD TESTS

Specimen	Heat Number	Heat Treatment	Stress Intensity (ksi$\sqrt{in.}$)	Hours Under Test	Test Status
SS-1	4904	1150°F, 2 hours	20.0	6630	Total Time
SS-2	↓	↓	24.7	↓	↓
SS-3			28.1		
SS-4			32.5	2,923	Complete 2923 hr
SS-5*	03850		27.9	3,707	Complete 3707 hr

*Replaced 4904 SS-4; CT specimen; at test end only cracking on side to ∿1-2 mils deep.

Table H-5

CORRECTED COMPLIANCE FROM LVDT MEASUREMENTS

Average of Daily Values

	4904 SS-1			4904 SS-2			4904 SS-3		
Hours	Co.*	$\delta/p \times 10^{-6}$	Corrected δ/p	Co.*	$\delta/p \times 10^{-6}$	Corrected δ/p	Co.*	$\delta/p \times 10^{-6}$	Corrected δ/p
Phase I									
0	---	3.025	3.025		3.285	3.285		3.810	3.810
288	0.64288	4.709	3.025	0.96988	3.387	3.285		12.965	3.810
456		4.808	3.088		3.425	3.322	0.29387	12.819	3.767
552		4.743	3.047		3.372	3.270		12.674	3.724
624		4.726	3.036		3.347	3.246		12.712	3.736
720		4.734	3.041		3.372	3.271		12.632	3.712
792		4.671	3.000		3.349	3.248		12.455	3.660
888		4.674	3.002		3.348	3.247		12.161	2.573
984		4.701	3.020		3.314	3.314		12.081	3.550
Phase II									
1261	0.62858	4.804	3.020	0.9899	3.347	3.314	0.3192	11.121	3.550
1453		4.816	3.028		3.374	3.341		11.371	3.629
1525		4.864	3.057		3.362	3.328		11.064	3.704
1675		4.985	3.134		3.439	3.404		12.237	3.906

*Multiplier used to match end and beginning measurements.

Table H-5

CORRECTED COMPLIANCE FROM LVDT MEASUREMENTS (Continued)

Average of Daily Values

	4904 SS-1			4904 SS-2			4904 SS-3		
Hours	Co.*	$\delta/p \times 10^{-6}$	Corrected δ/p	Co.*	$\delta/p \times 10^{-6}$	Corrected δ/p	Co.*	$\delta/p \times 10^{-6}$	Corrected δ/p
Phase II (Continued)									
1843		4.905	3.083		3.399	3.365		11.969	3.821
1939		4.829	3.035		3.316	3.282		11.609	3.705
2011		4.800	3.017		3.402	3.368		12.011	3.834
2083		4.841	3.043		3.350	3.317		11.588	3.699
2179		4.813	3.026		3.336	3.303		11.633	3.713
2275		4.841	3.074		3.366	3.333		12.148	3.877
2347		4.744	3.001		3.302	3.269		11.630	3.712
2419		4.810	3.023		3.325	3.292		11.833	3.777
2515		4.738	2.978		3.271	3.238		11.499	3.671
2587		4.841	3.043		3.337	3.303		11.729	3.744
2683		4.861	3.055		3.339	3.305		12.232	3.904
2779		4.786	3.088		3.297	3.264		12.180	3.888
2923		4.760	2.992		3.284	3.251		11.828	3.776

*Multiplier used to match end and beginning measurements.

Table H-5

CORRECTED COMPLIANCE FROM LVDT MEASUREMENTS (Continued)

Average of Daily Values

	4904 SS-1			4904 SS-2			4904 SS-3		
Hours	Co.*	$\delta/p \times 10^{-6}$	Corrected δ/p	Co.*	$\delta/p \times 10^{-6}$	Corrected δ/p	Co.*	$\delta/p \times 10^{-6}$	Corrected δ/p
Phase III									
3019	0.6856	4.364	2.992						
3091		4.365	2.993						
3187		4.401	3.018						
3259		4.372	2.997						
3355		4.392	3.011						
3427		4.501	3.086						
3499		4.460	3.058						
3595	0.6856	4.383	3.005						
3691		4.306	2.952						
3763		4.533	3.108						
3853		4.476	3.068						
3931		4.474	3.068						
4027		4.519	3.093						
4099		4.489	3.077						
4147		4.515	3.096						

Large variability in LVDT

LVDT shifting over test period

*Multiplier used to match end and beginning measurements.

Table H-5

CORRECTED COMPLIANCE FROM LVDT MEASUREMENTS (Continued)

Average of Daily Values

	4904 SS-1			4904 SS-2			4904 SS-3		
Hours	Co.*	$\delta/p \times 10^{-6}$	Corrected δ/p	Co.*	$\delta/p \times 10^{-6}$	Corrected δ/p	Co.*	$\delta/p \times 10^{-6}$	Corrected δ/p
Phase IV									
4147	0.6803	4.551	3.096	1.4104	2.305	3.251	0.9003	4.194	3.776
4195		4.553	3.097		2.309	3.257		4.166	3.751
4267		4.473	3.043		2.285	3.223		4.121	3.710
4339		4.413	3.002		2.257	3.183		4.097	3.689
4459		4.507	3.066		2.305	3.252		4.218	3.798
4531		4.434	3.016		2.267	3.198		4.125	3.714
4603		4.430	3.013		2.259	3.187		4.097	3.689
4699		4.419	3.006		2.243	3.164		4.074	3.668
4771		4.444	3.024		2.252	3.177		4.101	3.692
4867		4.419	3.006		2.247	3.169		4.131	3.719
4939		4.398	2.992		2.331	3.147		4.109	3.699
Phase V**									
4937	0.991			0.991	3.177	3.147	0.870	4.250	3.699
5002					3.134	3.104		4.289	3.733
5018					3.072	3.043		4.134	3.598
5195					3.051	3.022		4.105	3.573

*Multiplier used to match end and beginning measurements.
**LVDT on 4904 SS-1 went bad at start of Phase V.

Table H-5

CORRECTED COMPLIANCE FROM LVDT MEASUREMENTS (Continued)

Average of Daily Values

	4904 SS-1			4904 SS-2			4904 SS-3		
Hours	Co.*	$\delta/p \times 10^{-6}$	Corrected δ/p	Co.*	$\delta/p \times 10^{-6}$	Corrected δ/p	Co.*	$\delta/p \times 10^{-6}$	Corrected δ/p
Phase V** (Continued)									
5195					3.007	2.978		4.042	3.518
5273					3.007	2.978		4.031	3.508
5345					3.040	3.011		4.079	3.550
5435					3.061	3.032		4.091	3.561
5514					3.037	3.008		4.082	3.553
5608					3.108	3.078		4.160	3.621
5674					3.088	3.059		4.119	3.585
5729					3.059	3.030		4.108	3.575
5850					3.064	3.035		4.136	3.599
Phase VI									
5850				1.004	3.024	3.035	0.900	4.000	3.599
5965					3.000	3.011		4.078	3.670
6036					3.054	3.065		4.132	3.718
6108					3.010	3.021		4.083	3.674
6196					3.020	3.031		4.079	3.671

*Multiplier used to match end and beginning measurements.
**LVDT on 4904 SS-1 went bad at start of Phase V.

Table H-5

CORRECTED COMPLIANCE FROM LVDT MEASUREMENTS (Continued)

Average of Daily Values

	4904 SS-1**			4904 SS-2			4904 SS-3		
Hours	Co.*	$\delta/p \times 10^{-6}$	Corrected δ/p	Co.*	$\delta/p \times 10^{-6}$	Corrected δ/p	Co.*	$\delta/p \times 10^{-6}$	Corrected δ/p
Phase VI (Continued)									
6273					2.080	2.991		4.028	3.625
6369					2.985	2.996		4.040	3.636
6441					2.981	2.992		4.042	3.638
6537					3.067	3.078		4.169	3.750
6630					2.996	3.007		4.041	3.637

*Multiplier used to match end and beginning measurements.
**LVDT on 4904 SS-1 went bad at start of Phase V.

Table H-6

ROOM TEMPERATURE CLIP GAGE COMPLIANCE READINGS

Specimen ID	K-level ($ksi\sqrt{in.}$)	Room Temperature Compliance (in./lb x 10^{-6}) Test Start	2,923* Hours	4,147 Hours	4,939 Hours	5,850 Hours	6,630 Hours
4904 SS-1	20.1	3.025	3.198	3.079	3.089	3.102	3.104
4904 SS-2	24.7	3.285	3.422	3.358	3.380	3.362	3.379
4904 SS-3	28.1	3.810	3.837	3.826	3.887	3.888	3.927

*Clip gage calibration questionable due to change in signal conditioning gain.

Table H-7

CRACK GROWTH EVALUATED FROM ROOM TEMPERATURE COMPLIANCE CHANGES

Specimen	0→6630 Hours Compliance Change (%)	0→6630 Hours Δa (in.)	4147→6630 Hours Compliance Change (%)	4147→6630 Hours Δa (in.)
4904 SS-1	2.61	0.026	0.83	0.008
4904 SS-2	2.86	0.028	0.64	0.006
4904 SS-3	3.07	0.030	2.65	0.026

Table H-8

VISUAL MEASUREMENTS - CRACK LENGTH

Specimen	Test Start*	2923 hr	4147 hr	4937 hr	5850 hr	6630 hr
4904 SS-1	0.127	0.144	0.137	0.167	0.170	0.177 (IG)
	0.146	0.146	0.136	0.137	0.157	0.159
4904 SS-2	0.084	0.084	0.094	0.091	----	0.090
	0.050	0.072	----	0.075	0.132	0.120 (IG)
4904 SS-3	0.077	0.094	0.093	0.101	0.115	0.093
	0.098	0.136	0.135	0.175	0.180	0.210 (IG)

*Measured at test end from broken specimen.

Table H-9

MEASURED CRACK LENGTH AND CALCULATED CRACK GROWTH RATES

Specimen	Stress Intensity	Average Crack Length	Maximum Side Length	Crack Growth Rates (in./hr)	
				Total Test Time	Last 2483 hr*
4904 SS-1	20.1	0.022	0.050	3.3×10^{-6}	3.2×10^{-6}
4904 SS-2	24.7	0.023	0.070	3.5×10^{-6}	2.4×10^{-6}
4904 SS-3	28.1	0.031	0.113	4.7×10^{-6}	1.04×10^{-5}
4904 SS-4	32.5	0.031	0.162	1.06×10^{-5}	----------

*Using % compliance change to evaluate % of final cracking that occurred in period from 4147 hours to 6630 hours.

Table H-10

HIGH TEMPERATURE/PRESSURE OXYGENATED WATER ENVIRONMENT (EFL-I)

Temperature	550°F
Pressure	1320 psig
Conductivity	1.0 ± 0.5 μmho/cm at 25°C
Dissolved Oxygen Content	6 ± 2 ppm
pH	5.5 ± 0.5 at 25°C
Chloride	<0.1 ppm
Fluoride	<0.1 ppm

Table H-11

SPECIMEN PLATE MATERIAL - CHEMICAL ANALYSES

Material Specification	Chemical Composition ASTM Requirements[a] (%)	Vendor Certified Analysis (%)	Check Analysis (%)	ASTM Requirements	Vendor Test Results[b] (psi)	GE Check Results[b] (psi)	GE Check Results[c] (psi)
ASTM-A-240 Type-304 (Heat 04904)	C - 0.08 maximum	0.067	0.071	Minimum Tensile Strength 75,000 psi	----	89,000	65,700
	Si - 1.00 maximum	0.37	0.37				
	P - 0.045 maximum	0.022	0.023				
	Ch - 18.00 - 20.00	18.67	18.65				
	N - 8.00 - 12.00	8.09	8.15	Minimum Yield Strength 30,000 psi	----	37,100	20,900
	S - 0.030 maximum	0.022	0.026				
	Mn - 2.00 maximum	0.94	0.97				
	Mo	0.44	0.41				
ASTM-A-240 Type-304 (Heat 03580)	C - 0.08 maximum	0.068	0.066	Minimum Tensile Strength 75,000 psi	84,700	85,300	64,700
	Si - 1.00 maximum	0.39	0.4				
	P - 0.045 maximum	0.029	0.029				
	Ch - 18.00 - 20.00	18.45	18.54				
	N - 8.00 - 12.00	8.16	8.16	Minimum Yield Strength 30,000 psi	40,300	42,600	27,800
	S - 0.030 maximum	0.022	0.025				
	Mn - 2.00 maximum	1.78	1.84				
	Mo	0.39	0.38				

[a]Material Code

C - Carbon Ch - Chromium Mn - Manganese
Si - Silicon N - Nickel Fe - Iron
P - Phosphorus S - Sulfur Mo - Molybdenum

[b]Room Temperature

[c]500°F

Table H-12

CRACK GROWTH TEST RESULTS

a (in.)	t (hr)	N (cycles)	$\Delta a/\Delta t$ (in./hr)	$\Delta a/\Delta N$ (μ in./cycle)	K_{max} (ksi$\sqrt{in.}$)	ΔK (ksi$\sqrt{in.}$)
SPECIMEN TC-3						
0.995	0		2.4×10^{-4}	120	30.2	27.2
1.016	23	46			31.2	28.1
1.036	97	194			32.2	29.0
1.044	148	296			32.5	29.3
1.050	166	332			32.9	29.6
1.052	180	360			33.0	30.0
1.066	255	510			33.7	30.3
1.086	308	---	3.8×10^{-4}		34.8	CL[a]
SPECIMEN SS-24						
1.054	0	---	0	0	7.8	SRL[b]
1.054	48				18.9	SRL
1.054	192				23.3	12.0
1.054	322				23.3	12.0
1.058	337	104	7×10^{-5}	10	23.5	12.1
1.058	362	122			23.5	12.1
1.061	384	138			23.6	12.2
1.063	456	190			23.7	12.2
1.072	624	---	6×10^{-5}		23.6	CD[c]
1.080	696	---			23.5	CD[c]
SPECIMEN SS-21						
0.852	0	0			20.41	All CL
0.852	22				20.41	
0.855	79				20.49	
0.855	161				20.49	
0.861	161				20.65	
0.861	238				20.65	
0.858	329				20.57	
0.867	329				20.82	

[a] CL = constant load
[b] SRL = slow rising load
[c] CD = constant displacement

Table H-12

CRACK GROWTH TEST RESULTS (Continued)

a (in.)	t (hr)	N (cycles)	$\Delta a/\Delta t$ (in./hr)	$\Delta a/\Delta N$ (μ in./cycle)	K_{max} (ksi$\sqrt{in.}$)	ΔK (ksi$\sqrt{in.}$)
SPECIMEN SS-21 (Continued)						
0.846	377				20.26	
0.842	442				20.15	
0.852	464				20.41	
0.855	488				20.49	
0.858	513				20.57	
0.858	632				20.57	
0.864	656				20.74	
0.864	777				20.74	
0.873	777				20.98	
0.867	799		5×10^{-5}		20.82	
0.876	824				21.07	
0.870	831				20.90	
0.873	847				20.98	
0.879	949				21.15	
0.876	966				21.07	
0.882	990				21.23	
0.873	1017				20.98	
0.855	1081				21.32	
0.876	1105				21.07	

Table H-13

SPECIMEN SSW-E CRACK GROWTH UNDER RISING LOADING

Load (lb)	Time (hr)	Δa (in.)	K (ksi$\sqrt{in.}$)	da/dt (in./hr)
1,850	0	0	11.0	5×10^{-5}
2,100	62.5	0.003	12.5	9×10^{-5}
2,500	162.5	0.009	15.1	1.0×10^{-4}
3,000	287.5	0.013	18.1	1.0×10^{-4}
3,470	405.0	0.015	21.3	1.3×10^{-4}

Note: Total measured crack extension = 0.040 inch.

Table H-14

SPECIMEN FS-1

1T-CT (LVDT position) 39 Data Points

B = 0.949 inches W = 2.000 inches Initial a = 1.002 inches Eapp = 25.97 Mpsi

Data Point	Time (hr)	Compliance (in./lb)	Loading Mode	Max. Stress Intensity (ksi$\sqrt{in.}$)	Crack Length (in.)
1	26	3.208E-06	SRL	14.0	1.003
2	100	3.205E-06			1.003
3	196	3.186E-06			1.000
4	263	3.199E-06			1.002
5	263*	3.215E-06			1.004
6	336	3.197E-06	SCL	23.3	1.002
7	456	3.196E-06			1.002
8	504	3.197E-06			1.002
9	600	3.209E-06			1.003
10	672	3.225E-06			1.006
11	672*	3.189E-06			1.001
12	702	3.204E-06	CL	23.8	1.003
13	828	3.249E-06			1.009
14	846	3.261E-06			1.011
15	869	3.265E-06			1.011
16	934	3.294E-06	SRL	24.3	1.015
17	958	3.309E-06			1.017
18	988	3.306E-06			1.017
19	1010	3.328E-06			1.020
20	1029	3.336E-06			1.021
21	1100	3.366E-06		28.9	1.025
22	1124	3.382E-06			1.027
23	1150	3.377E-06			1.026
24	1155	3.369E-06			1.025
25	1160	3.358E-06		30.7	1.024
26	1162	3.469E-06			1.038
27	1183	3.473E-06			1.038
28	1206	3.488E-06			1.040
29	1231	3.484E-06		33.5	1.040
30	1256	3.494E-06			1.041
31	1277	3.457E-06			1.036
32	1328	3.475E-06			1.038
33	1349	3.474E-06	CL	37.4	1.038
34	1376	3.497E-06			1.041
35	1396	3.497E-06			1.041
36	1422	3.463E-06			1.037
37	1493	3.506E-06			1.042
38	1520	3.511E-06			1.043
39	1544	3.515E-06			1.043

*Same time, different load range

Table H-15

SPECIMEN WS-1

1T-CT (LVDT position) 39 Data Points

B = 0.949 inch W = 2.00 inches Initial a = 1.060 inches Eapp = 26.38 Mpsi

Data Point	Time (hr)	Compliance (in./lb)	Loading Mode	Max. Stress Intensity (ksi$\sqrt{in.}$)	Crack Length (in.)
1	26	3.616E-06	SRL	13.7	1.062
2	100	3.598E-06			1.060
3	196	3.516E-06			1.060
4	263	3.572E-06			1.057
5	263*	3.587E-06			1.060
6	336	3.598E-06	SCL	23.0	1.060
7	456	3.593E-06			1.059
8	504	3.588E-06			1.059
9	600	3.610E-06			1.061
10	672	3.625E-06			1.063
11	672*	3.596E-06			1.059
12	702	3.601E-06	CL	23.5	1.060
13	828	3.606E-06			1.061
14	846	3.599E-06			1.160
15	869	3.593E-06			1.059
16	934	3.611E-06	SRL	23.6	1.061
17	958	3.599E-06			1.060
18	988	3.593E-06			1.059
19	1010	3.613E-06			1.062
20	1029	3.607E-06			1.061
21	1100	3.631E-06		27.8	1.064
22	1124	3.635E-06			1.064
23	1150	3.616E-06			1.062
24	1155	3.617E-06			1.062
25	1160	3.609E-06		29.2	1.061
26	1162	3.592E-06			1.059
27	1183	3.610E-06			1.061
28	1206	3.619E-06			1.062
29	1231	3.624E-06			1.063
30	1256	3.633E-06		31.5	1.064
31	1277	3.592E-06			1.059
32	1328	3.609E-06			1.061
33	1349	3.612E-06	CL	34.8	1.061
34	1376	3.621E-06			1.062
35	1396	3.607E-06			1.061
36	1422	3.601E-06			1.060
37	1483	3.642E-06			1.065
38	1520	3.629E-06			1.063
39	1544	3.648E-06			1.066

*Same time, different load range

Table H-16

CRACK GROWTH RATES

Test Phase	WS-1 K-Range ksi$\sqrt{in.}$	WS-1 Δa (in.)	WS-1 da/dt (in./hr)	FS-1 K-Range (ksi$\sqrt{in.}$)	FS-1 Δa	FS-1 da/dt (in./hr)
Slow Rising Load	13→23	---	----	13→23	---	----
Slow Cyclic Load	12→23.5	0.018	7×10^{-5}	12→24	0.016	6.5×10^{-5}
Constant Load	23.5→24	0.002	$<7 \times 10^{-6}$	24→24.5		1.2×10^{-4}
Slow Rising Load	24→35	0.020	4×10^{-5}	24.5→37.5	0.103	1.2×10^{-4}
Constant Load	35+	0.015	7×10^{-5}	37.5+	(total)	1.2×10^{-4}

Table H-17

SPECIMEN PLATE MATERIAL - CHEMICAL ANALYSES

Material Specification	Chemical Composition: ASTM Requirements[a] (%)	Chemical Composition: Vendor Certified Analysis (%)	Chemical Composition: Check Analysis (%)	ASTM Requirements	Vendor Test Results[b] (psi)	GE Check Results[b] (psi)	GE Check Results[c] (psi)
ASTM-A-240 Type-304 (S Specimens)	C - 0.080 maximum	0.06	0.065	Minimum Tensile Strength 75,000 psi	79,830	79,100	63,100
	Si - 1.00 maximum	0.66	0.656				
	P - 0.045 maximum	0.024	0.023				
	Ch - 18.00 - 20.00	18.68	18.25				
	N - 8.00 - 12.00	9.95	10.06	Minimum Yield Strength 30,000 psi	33,350	34,300	21,800
	S - 0.030 maximum	0.013	0.022				
	Mn - 2.00 maximum	1.43	1.37				
	Mo	0.17					
ASTM-A-240 Type-304 (SS Specimens) (Heat 03580)	C - 0.08 maximum	0.068	0.066	Minimum Tensile Strength 75,000 psi	84,700	85,300	64,700
	Si - 1.00 maximum	0.39	0.4				
	P - 0.045 maximum	0.029	0.029				
	Ch - 18.00 - 20.00	18.45	18.54				
	N - 8.00 - 12.00	8.16	8.16	Minimum Yield Strength 30,000 psi	40,300	42,600	27,800
	S - 0.030 maximum	0.022	0.025				
	Mn - 2.00 maximum	1.78	1.84				
	Mo	0.39	0.39				

[a]Material Code

C - Carbon Ch - Chromium Mn - Manganese
Si - Silicon N - Nickel Fe - Iron
P - Phosphorus S - Sulfur Mo - Molybdenum

[b]Room Temperature

[c]500°F

Table H-18

HEAT TREATMENT AND EPR VALUES OF STAINLESS-STEEL SPECIMENS

Specimen	Heat Treatment	EPR (C/cm^2)
S-15	None	1.84
S-11[a]		
S-5		
S-7		
S-10		
S-12		
S-14		
S-9		
S-13	40 hours at 1150°F, FC[b]	58.0[c]
S-4[d]		
S-8		36.5
SS-10	16 hours at 1150°F, AC[b]	27
SS-11	2 hours at 1150°F, AC	10.5
SS-12	1 hour at 1150°F, AC	16.1
SS-6	2 hours at 1150°F, AC	13[e]
SS-1	As welded plus 1 hour @ 1150°F	5
SS-7	2 hours at 1150°F, AC	13[e]
SS-21	16 hours at 1150°F, AC	27[e]
SS-1A	As welded plus 24 hours at 932°F	5

[a] An EPR analysis was performed on Specimen S-11 and the result (1.84 C/cm^2) was used as a characteristic value for all as-received specimens.

[b] FC = furnace cool, AC = air cool.

[c] EPR value obtained from coupon from same heat of material which was heat treated with specimen S-13.

[d] An EPR analysis performed on Specimens S-13 and S-8 is used as a bound for Specimen S-4.

[e] Obtained from EPR study of heat 03580.

Table H-19

FATIGUE CRACK GROWTH TESTS[a]

Specimen ID	Material	Frequency (cph)	Waveshape	R[b]	K_{max} Initial ΔK Initial ksi $\sqrt{in.}$ (MPa $\sqrt{m}$)	K_{max} Final ΔK Final ksi $\sqrt{in.}$ (MPa $\sqrt{m}$)	Total Crack Growth in. (mm)	Measurement	
								COD	Capillary
S-15	304	300	Skewed[c] Sawtooth	0.05	27/26 (30/29)	64/61 (70/67)	1.0 (25)	Yes	Yes
S-11			Sawtooth	0.78	40/9 (44/10)	51/11 (56/12)	0.3 (8)	No	No[d]
S-5				0.78	39/8.6 (43/9)	50/11 (55/12)	0.28 (7)	No	Yes
S-7				0.78	44/9.6 (48/11)	76/17 (84/19)	0.56 (14)	No	Yes
S-10		75	Skewed[c] Sawtooth	0.6	41/16 (45/18)	69/15 (76/17)	0.56 (14)	No	Yes
S-12		18		0.05	45/43 (49/47)	59/56 (65/62)	0.34 (9)	No	Yes
S-14				0.05	21/30 (23/22)	26/25 (29/27)	0.24 (6)	Yes	Yes
S-9				0.6	41/16 (45/18)	58/23 (64/25)	0.39 (10)	No	Yes
S-13	Type-304 High DOS	300		0.05	21/20 (23/22)	30/28 (33/31)	0.40 (10)	No	Yes
S-4		300	Sawtooth	0.78	39/8.5 (43/9)	63/14 (69/15)	0.54 (14)	No	Yes
S-8		18	Sawtooth	0.6	40/16 (44/18)	58/23 (64/25)	0.43 (11)	No	Yes
SS-10		7.5	Skewed[c] Sawtooth	0.6	24/95 (27/10.5)	33/13[e] (36/14)	0.134 (3.4)	Yes	No
SS-11	Type-304 Medium DOS				23/9.4 (26/14)	34/14[e] (37/15)	0.185 (4.7)	Yes	No
SS-12	Type-304 Low DOS				23/9.4 (26/10.4)	34/14[e] (37/15)	0.178 (4.5)	Yes	No
SS-6	Type-304 Medium DOS				36/19 (39/15)	49/20[e] (54/22)	0.102 (2.6)	Yes	No
SS-1	Type-304 Weld HAZ Low DOS	6.7			24/9.6[f] (27/10.6)	26/11[f] (29/12)	0.050[f] (1.3)	Yes	No
SS-7	Type-304 Medium DOS	0.74			26/10 (29/11)	29/11 (32/12)	0.070 (1.8)	Yes	No
SS-21	Type-304 High DOS	0.74			26/10[g] (29/11)	29/11[g] (32/12)	0.070[g] (1.8)	Yes	No
SS-1A	Type-304 HAZ Low DOS	4.44[h]	Trapezoidal[i]	0	10/10 (11/11)	40/40 (44/44)	0.185 (4.7)	Yes	No

[a] Environment for all specimens except SS-1A is 0.2 ppm O_2, 550°F Water

[b] $R = \frac{K_{min}}{K_{max}}$

[c] Skewed Sawtooth

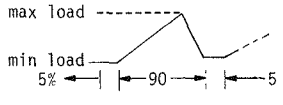

[i] Trapezoidal

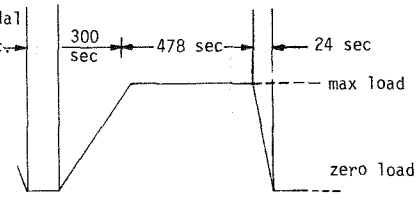

[d] Crack length measurements based on beginning and end point and, where present, fracture surface artifacts

[e] Load levels increased at 12,500 cycles

[f] Sufficient data not obtained for this specimen

[g] Preliminary results only

[h] Test run in three phases; f_{max} = 2,200 lb for 0-900 cycles; P_{max} = 7,000 lb for 990-2196 cycles; P_{max} = 7,500 lb for 2196-2262 in 8 ppm O_2, 500°F water

Table H-20

SPECIMENS AND THEIR ASSOCIATED HEAT AND HEAT TREATMENT

Specimen ID*	Heat Number	Material Heat Treatment
SS-70	04904	1150°F, 2 hours, 1.0-in. thick 1T-CT
SS-71	04904	
SS-72	03580	1150°F, 2 hours, 1.0-in. thick 1T-WOL
SS-73	03580	
SS-74	03580	
FS-2	04904	1150°F for 24 hours (1.0-in. thick 1T-CT furnace sensitization)

*SS - Type-304 stainless steel
FS - Furnace sensitized Type-304 stainless steel

Table H-21

CERT RESULTS** - 8 ppm O_2, 550°F WATER

Heat	Strain Rate	Max Stress	Time to Fail	% R.A.	% Elongation
03580	4.4×10^{-5} in./in./min.	41.1 ksi	18 h	6.0	4.9
04904	4.4×10^{-5} in./in./min.	45.3 ksi	101.5 h	12.3	25.9

**1150°F, 2-hr heat treatment

Table H-22

APPLIED STRESS INTENSITY AND MEASURED CRACK GROWTH RATES

Specimen ID	Average K $ksi\text{-}in.^{1/2}$ (initial-final)	Crack Growth Rates During Constant Load (in./hr)
SS-70	12.06 (11.98-12.16)	4.4×10^{-6}
SS-71	15.08 (15.00-15.17)	6.0×10^{-6}
SS-72	17.66 (17.35-17.99)	4.0×10^{-5}
SS-73	21.24 (20.66-21.89)	6.0×10^{-5}
SS-74	23.44 (22.75-24.07)	5.6×10^{-5}
FS-2	19.59 (19.02-20.03)	5.2×10^{-5}

Table H-23

CRACK LENGTH MEASUREMENTS

Specimen ID	Δa (in.) from DAS Measurements	Δa (in.) from Fracture Surface Measurements
SS-70	0.004	0.005 (few grains)
SS-71	0.021	0.009 (few grains)
SS-72	0.050	0.089
SS-73	0.082	0.081
SS-74	0.005	0.061
FS-2	*	0.097

*Due to LVDT malfunction, initial crack length was unknown when specimen began constant load test period. Therefore, Δa measurements were input from fracture surface measurements, not determined from DAS.

Table H-24

EPR VALUES OF TEST SPECIMENS

Specimen ID	Average Q (C)	P_a (Average)(C/cm^2)
SS-70[a]	0.128	9.4
SS-71[a]	0.129	11.0
SS-72[b]	0.042	5.4
SS-73[b]	0.031	3.9
SS-74[b]	0.082	13.0
FS-2[a,c]	0.31	29.6

[a]Grain Size - ASTM 2.5 to 3.5
[b]Grain Size - ASTM 1
[c]Furnace Sensitized (1150°F, 24 hours)

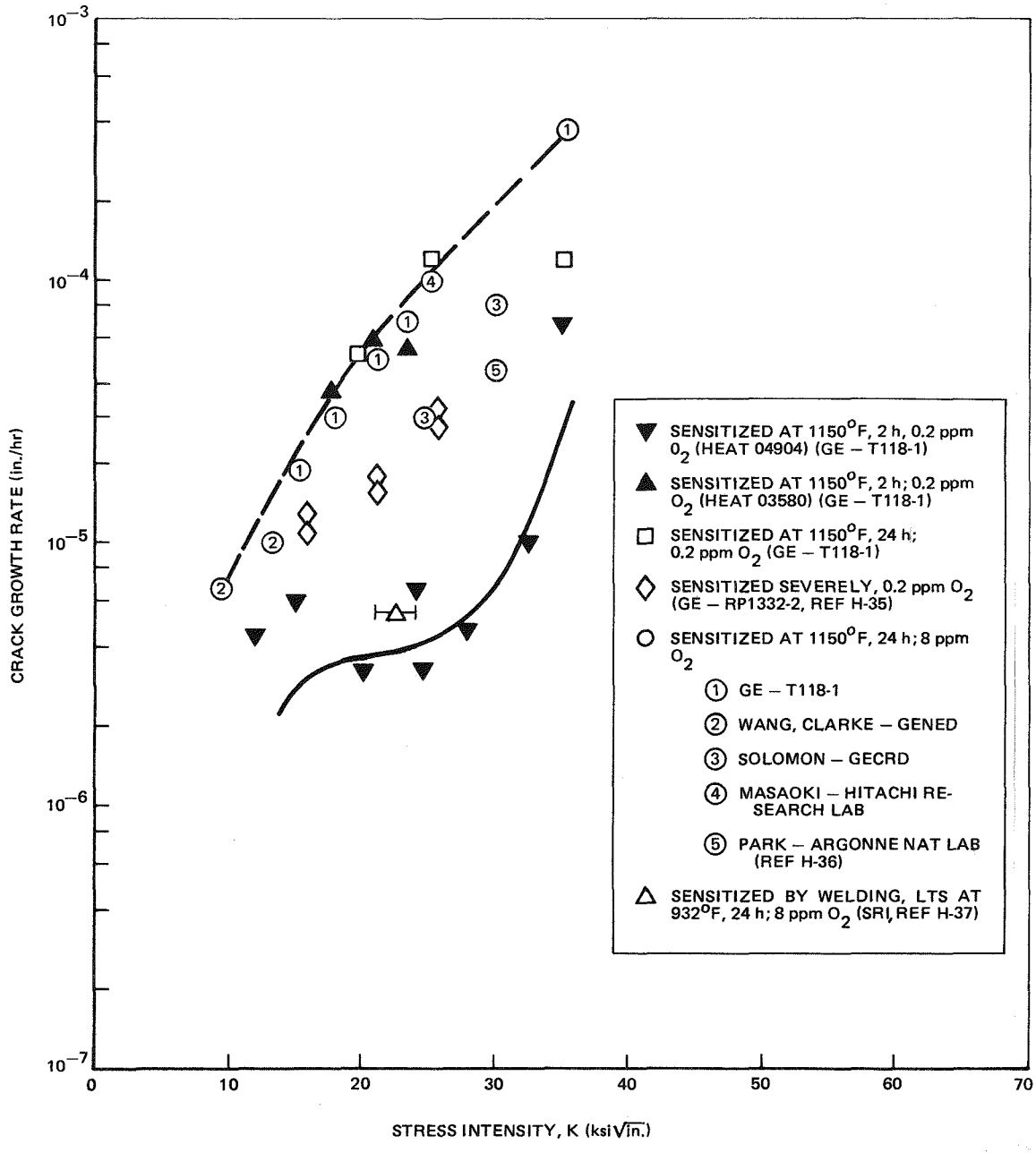

Figure H-1. Summary of Constant Load Crack Growth Data (Curves are evaluation curves.) Data collected in 0.2 ppm O_2 and 8 ppm O_2 water. Different levels of sensitization examined.

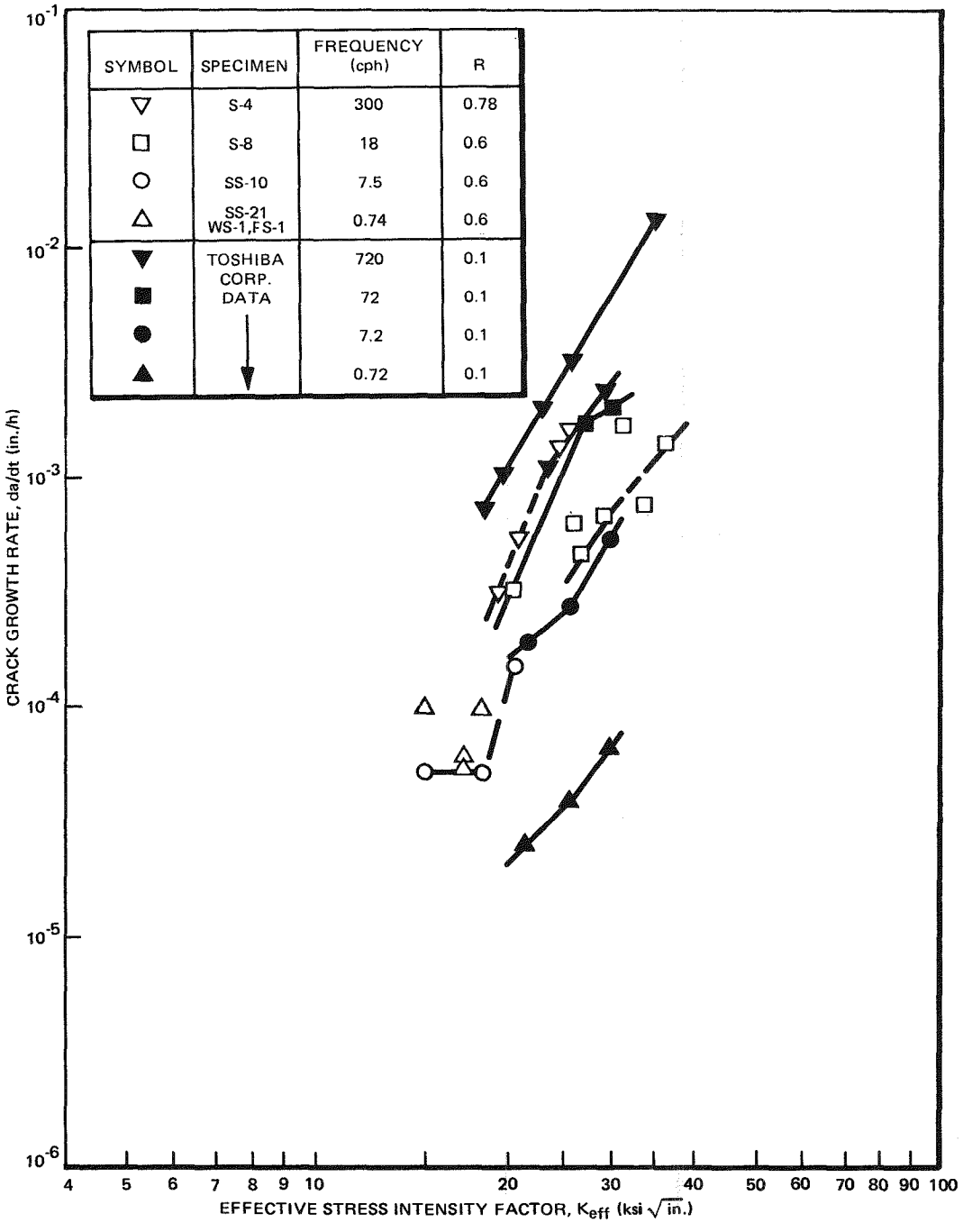

Figure H-2. Cyclic Crack Growth Data in 0.2 ppm O_2 High Temperature High Purity Water (Data from GE and Toshiba)

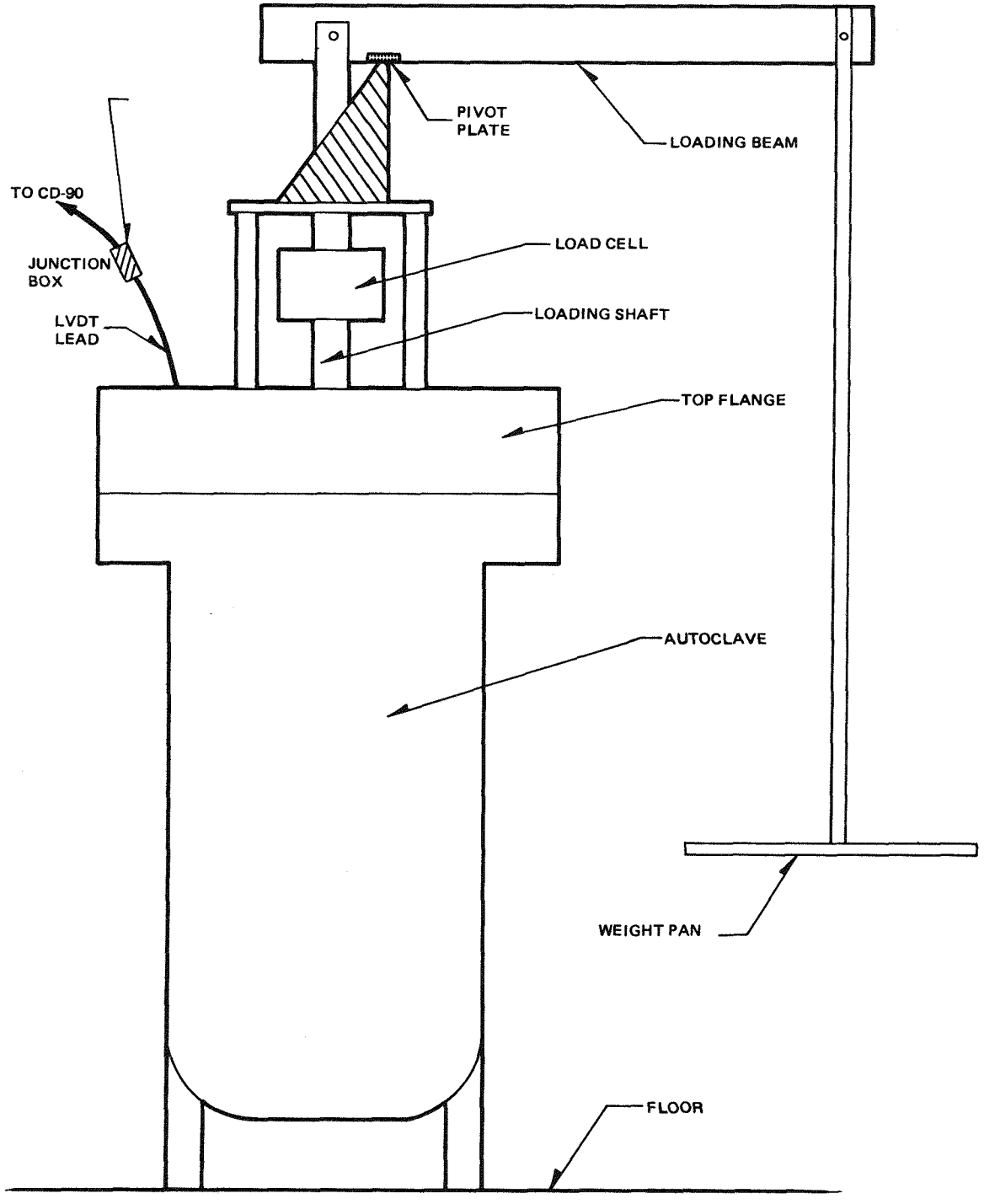

Figure H-3. Schematic - Test Vessel V with Dead Weight Loading

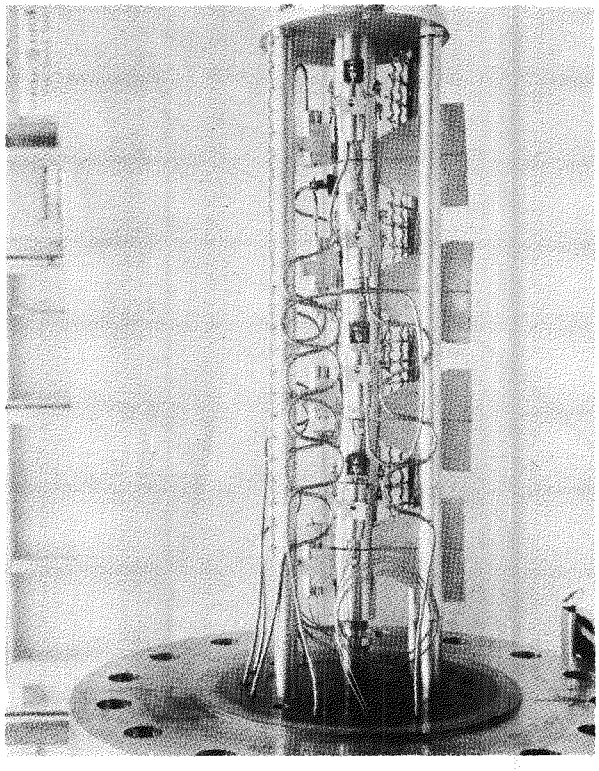

Figure H-4. Photograph of Internal Structure of Test Vessel V with TDCB Specimens in Place and LVDTs Attached

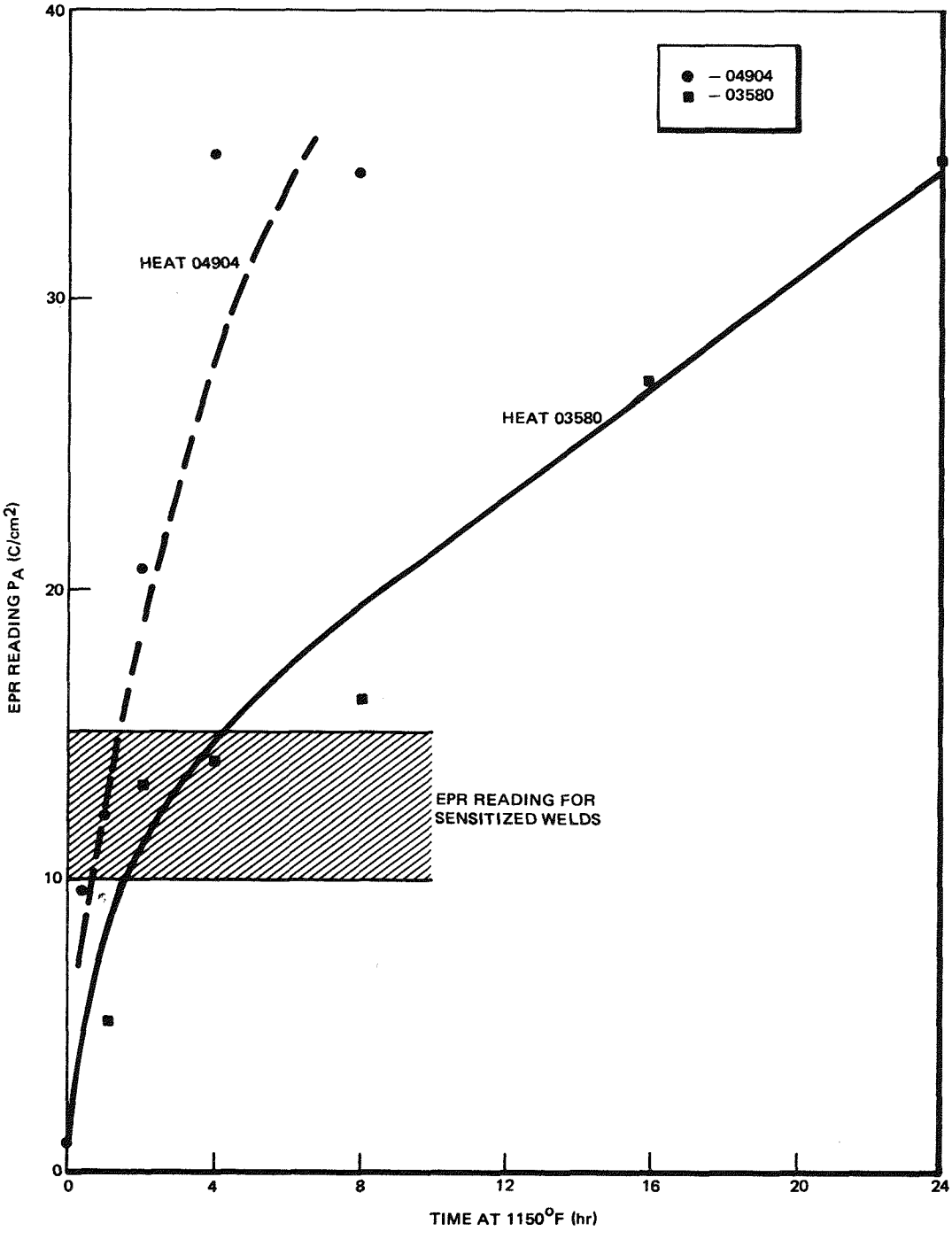

Figure H-5. EPR Readings as a Function of Isothermal Holding Time at 1150°F (621°C) for Heat 04904 and Heat 03580

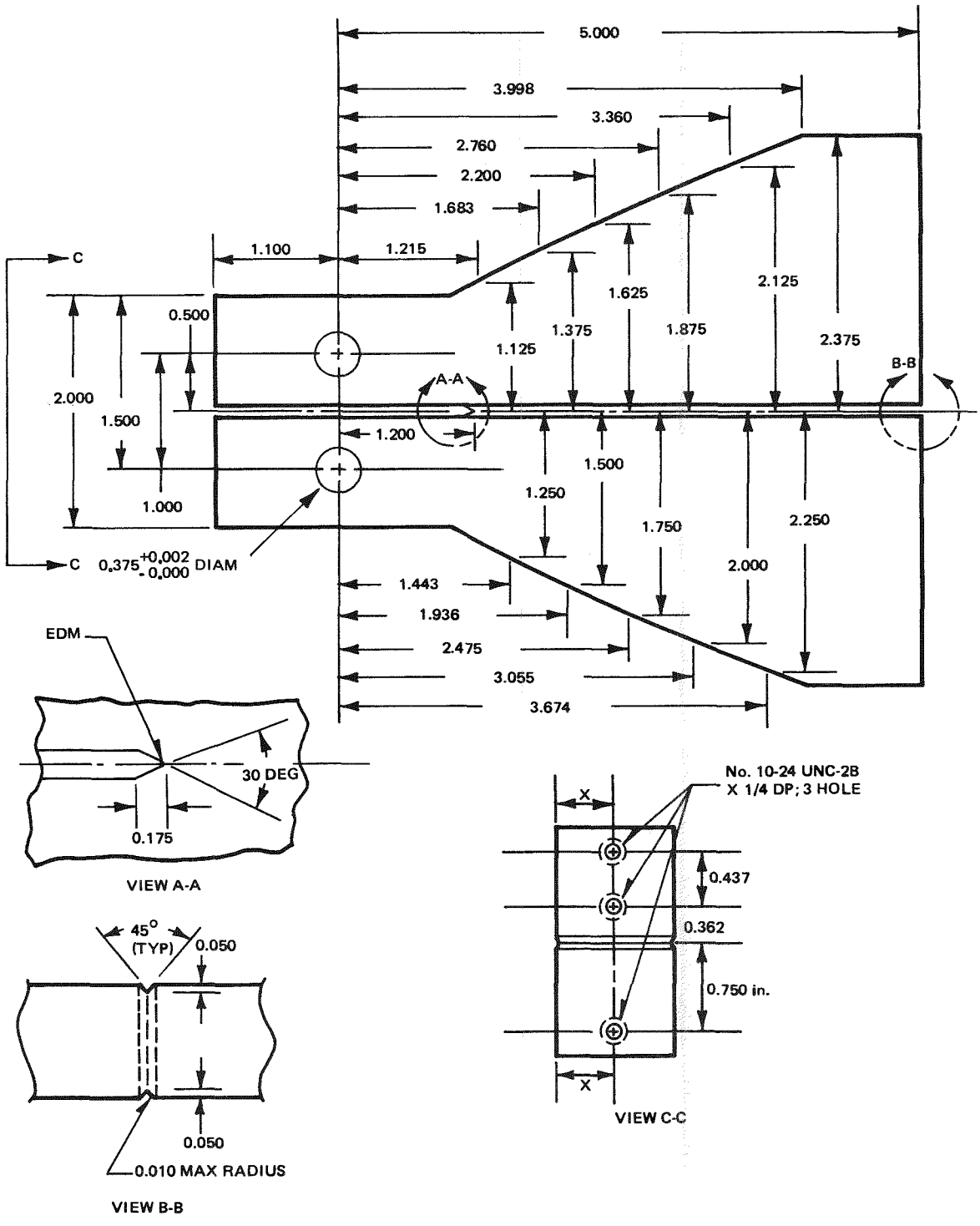

Figure H-6. Tapered Double Cantilever Beam Specimen Used for Constant Load Crack Growth Tests

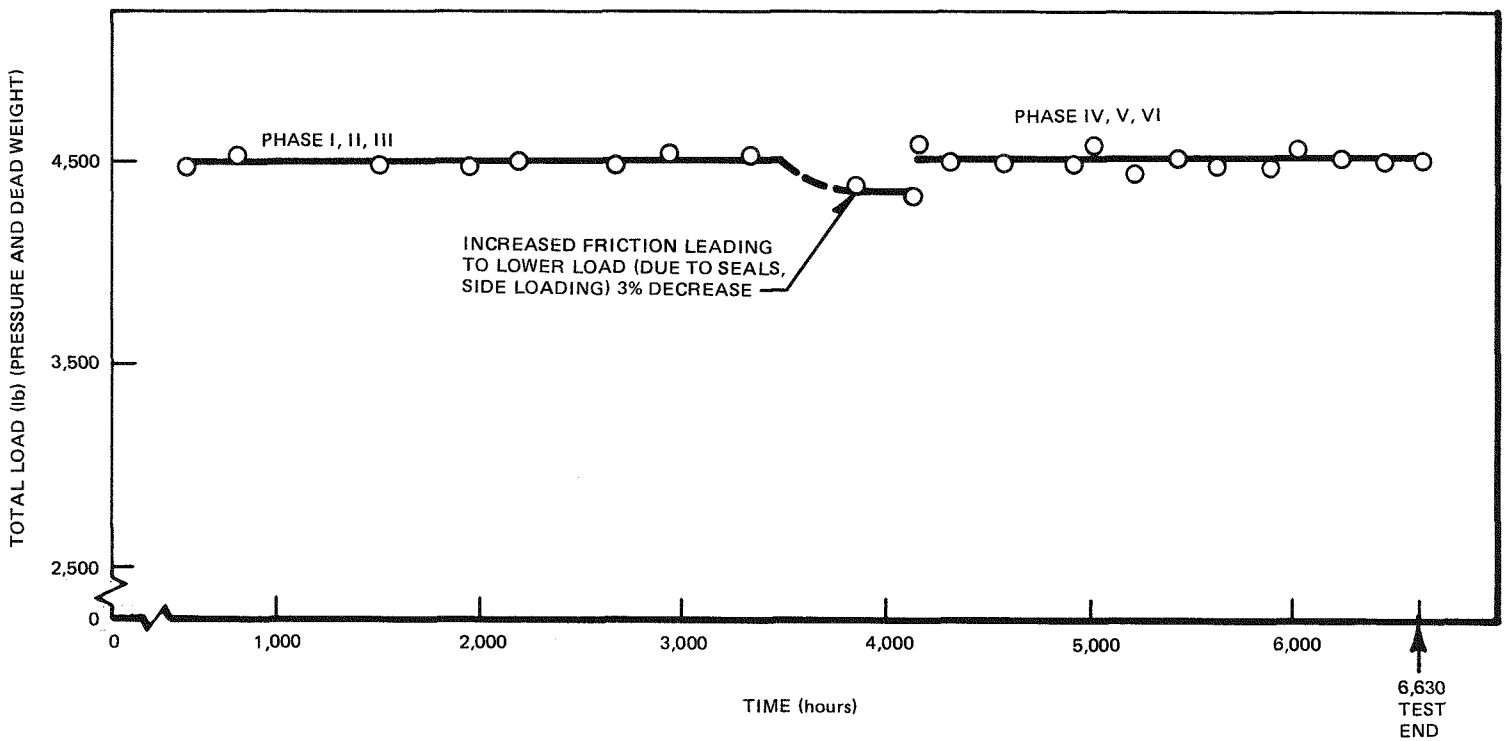

Figure H-7. Load History versus Test Time

*Please note that the illustration(s) on this page has been reduced 10% in printing.

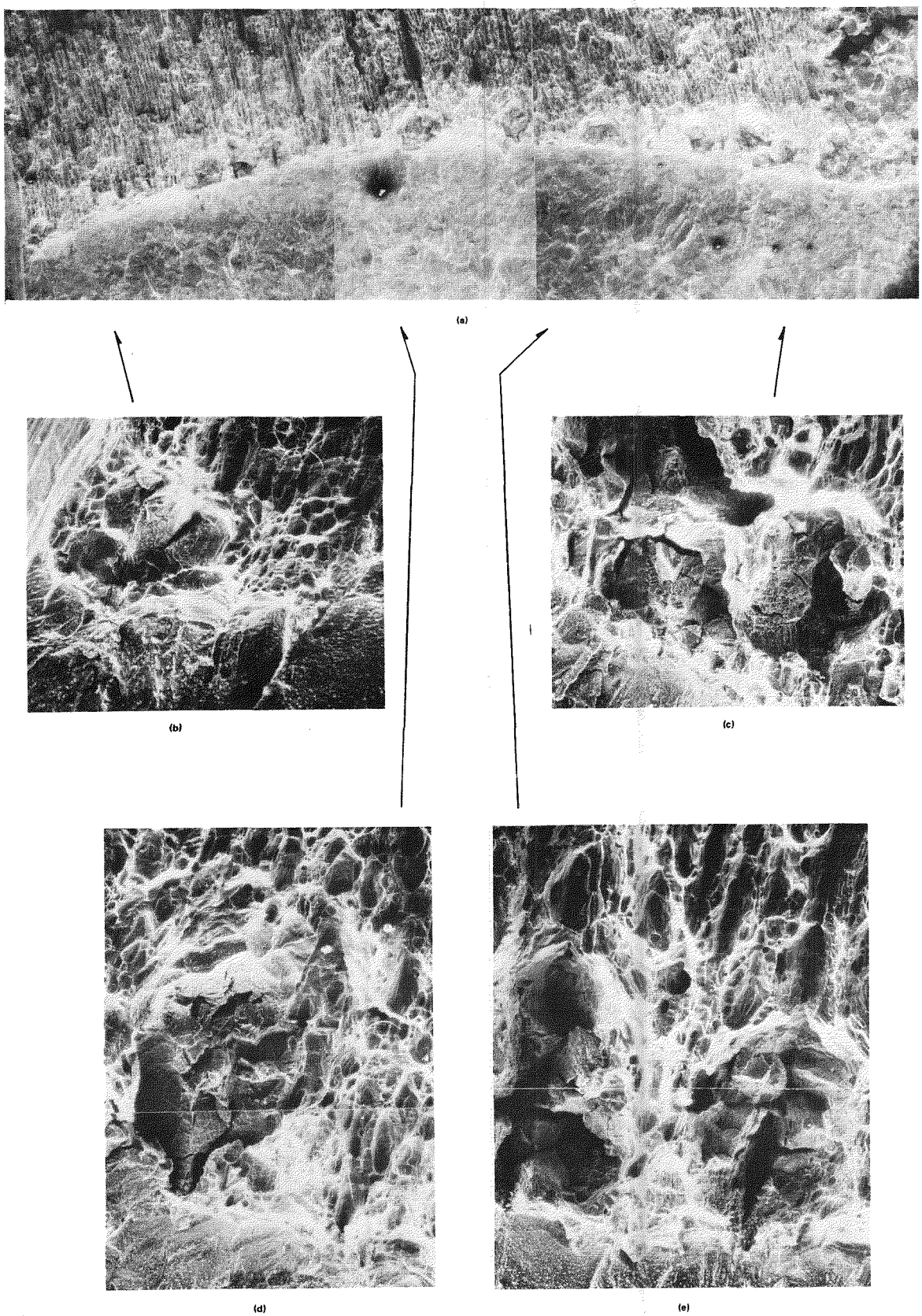

Figure H-8. Fracture Surface from Specimen 4904 SS-4 Reveal Environmental Cracking Features; Note Pockets of Intergranular Fracture; (a) = 15X, (b), (c), (d), (e) = 100X (Reduced in reproduction to 65%)

*Please note that the illustration(s) on this page has been reduced 10% in printing.

(a)

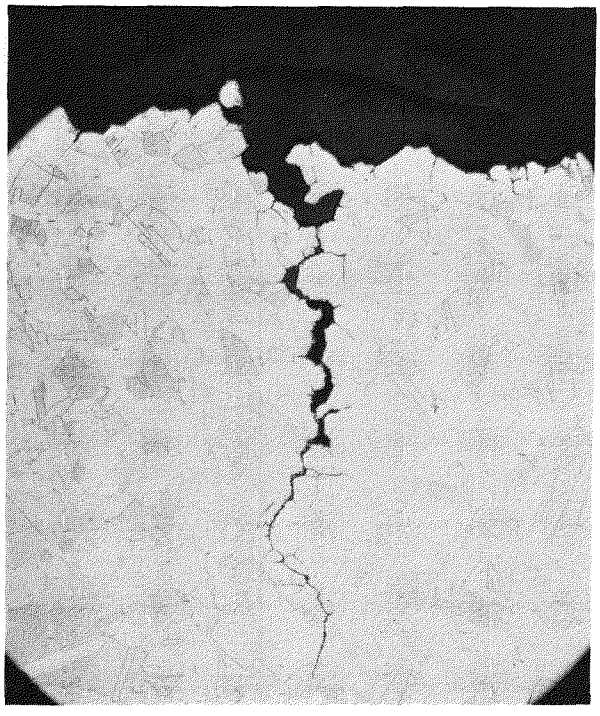

(b)

Figure H-9. Intergranular Cracking in Areas Remote from Crack Tip, Specimen 4904 SS-4, 26X

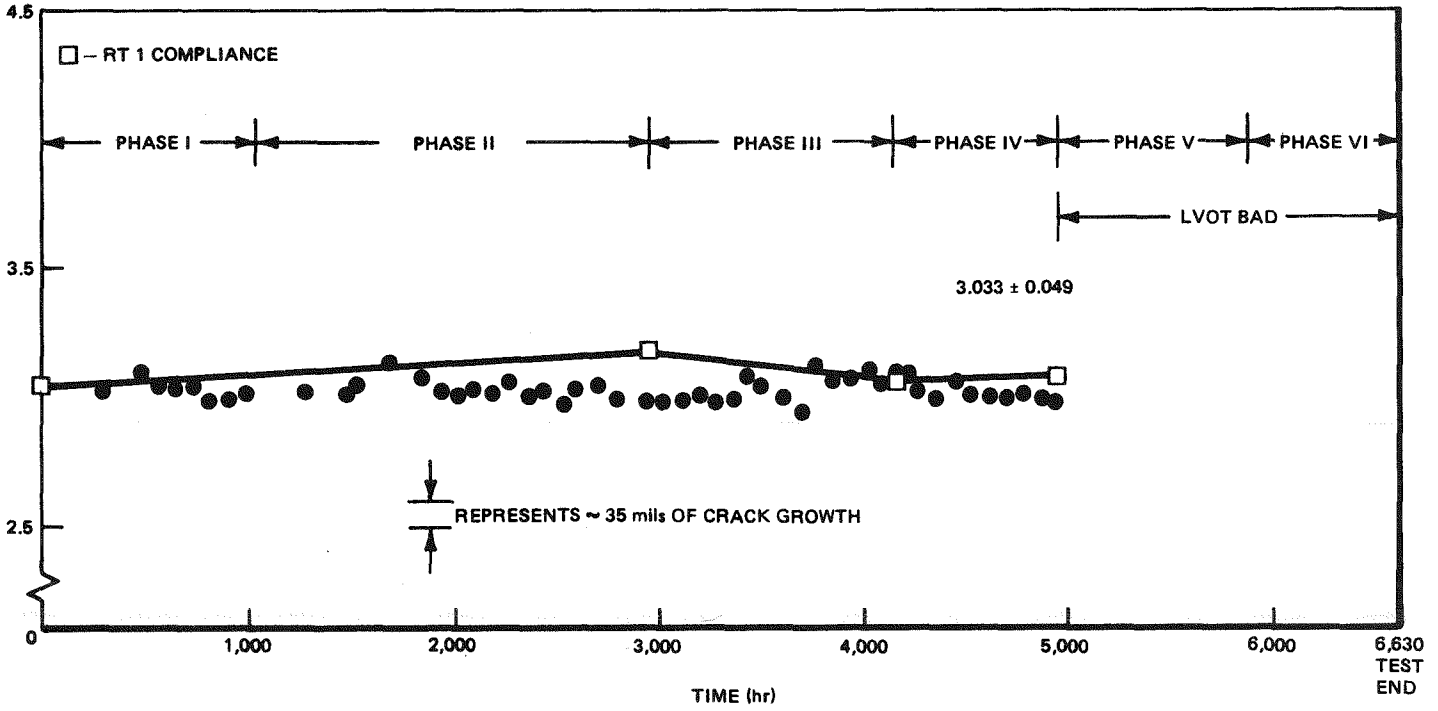

Figure H-10. LVDT Compliance versus Time, Specimen 4904 SS-1 ($K = 20$ ksi $\sqrt{in.}$)

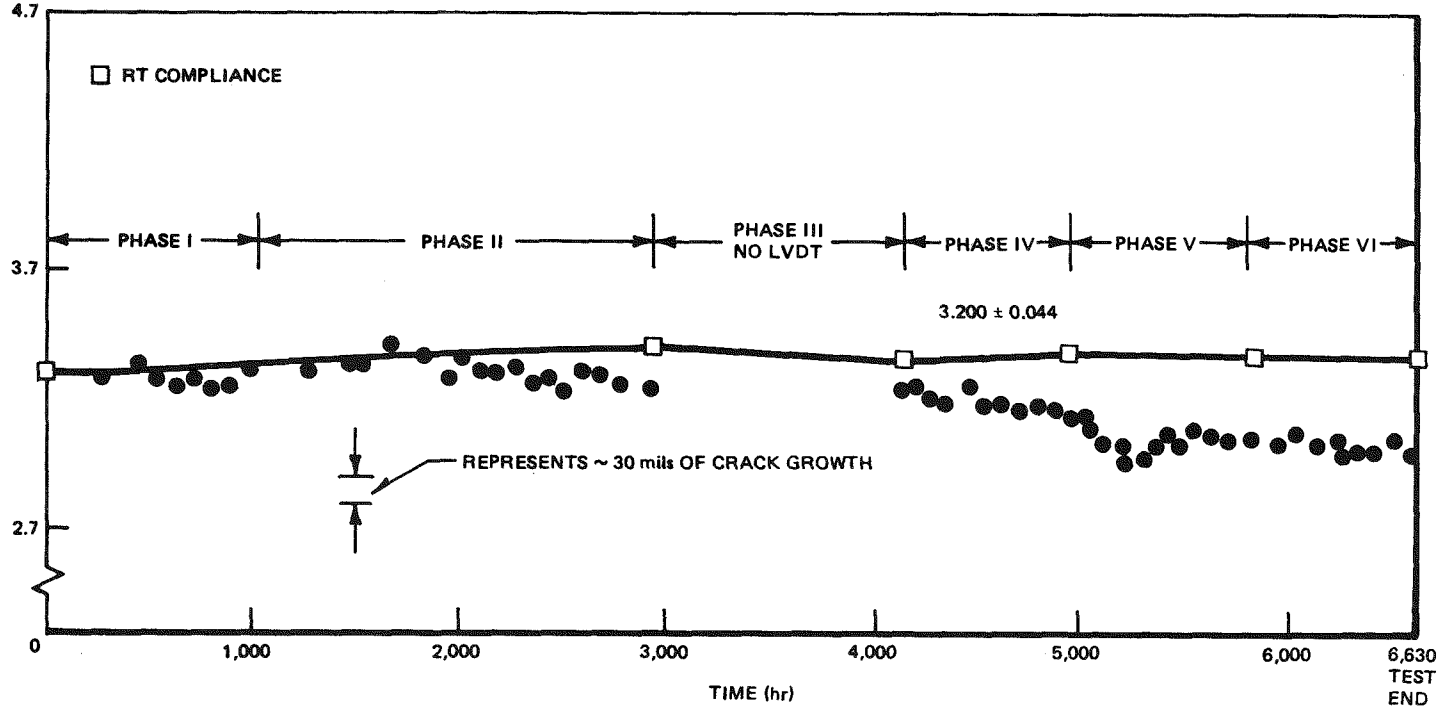

Figure H-11. LVDT Compliance versus Time, Specimen 4904 SS-2
($K = 24.7$ ksi $\sqrt{in.}$)

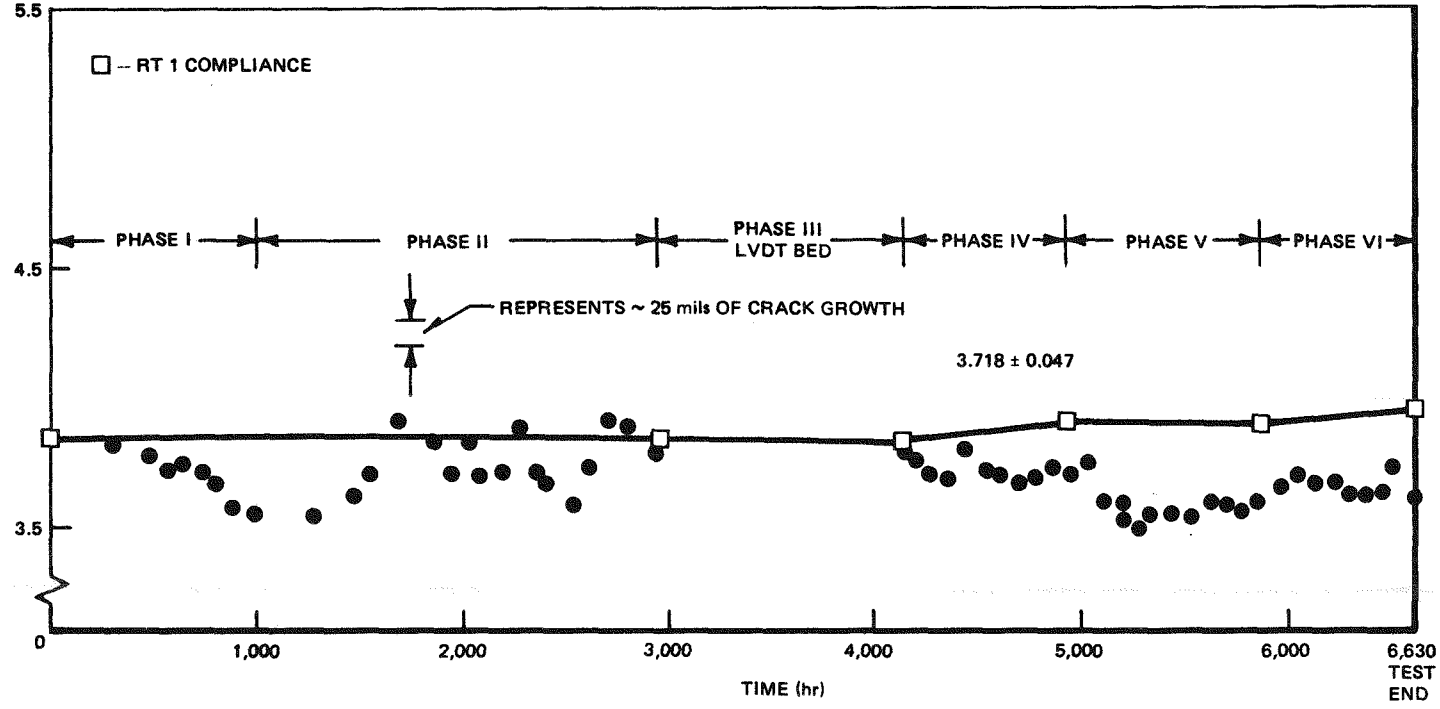

Figure H-12. LVDT Compliance versus Time, Specimen 4904 SS-3
(K = 28 ksi $\sqrt{in.}$)

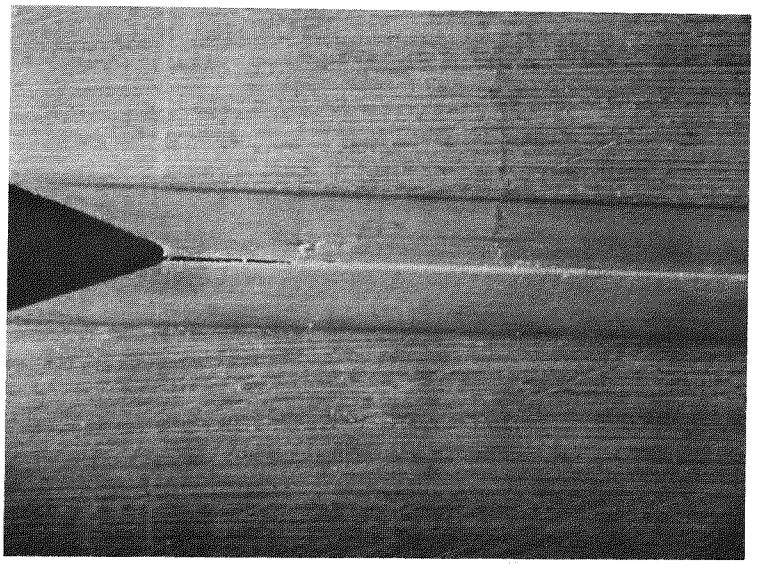

(a)

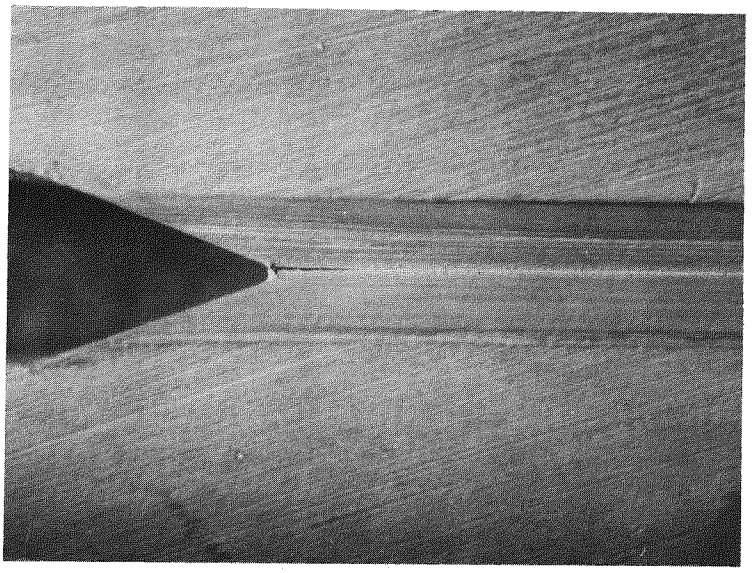

(b)

Figure H-13. Macrographs of Side View of Crack in Specimen 4904 SS-3

*Please note that the illustration(s) on this page has been reduced 10% in printing.

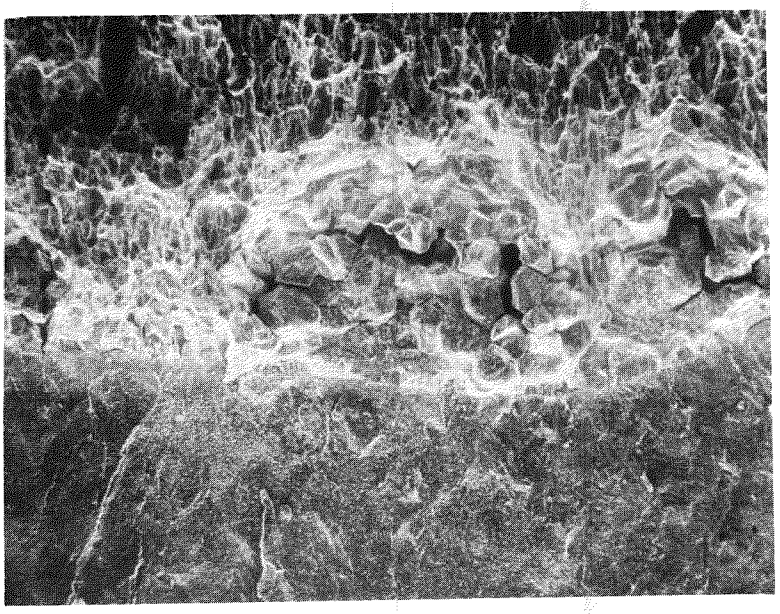

Figure H-14. SEM Photograph of Fracture Surface from Specimen 4904 SS-1 Showing IGSCC (35X)

*Please note that the illustration(s) on this page has been reduced 10% in printing.

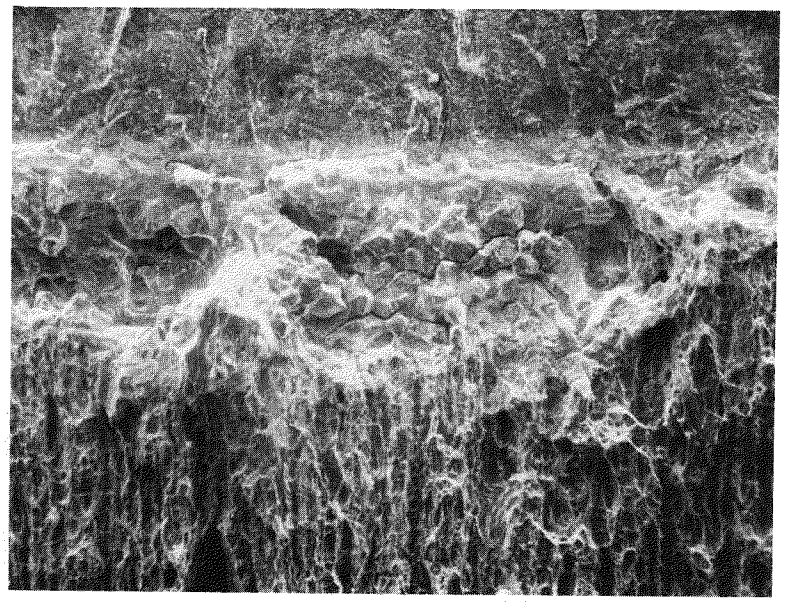

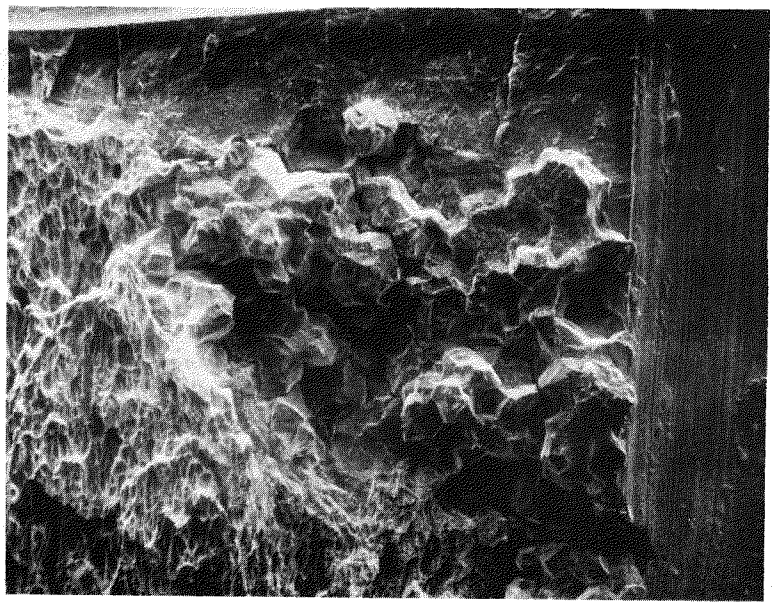

Figure H-15. SEM Photographs of IGSCC Fracture in Specimen 4904 SS-2 (a) Center of Specimen; (b) Specimen Edge (35X)

*Please note that the illustration(s) on this page has been reduced 10% in printing.

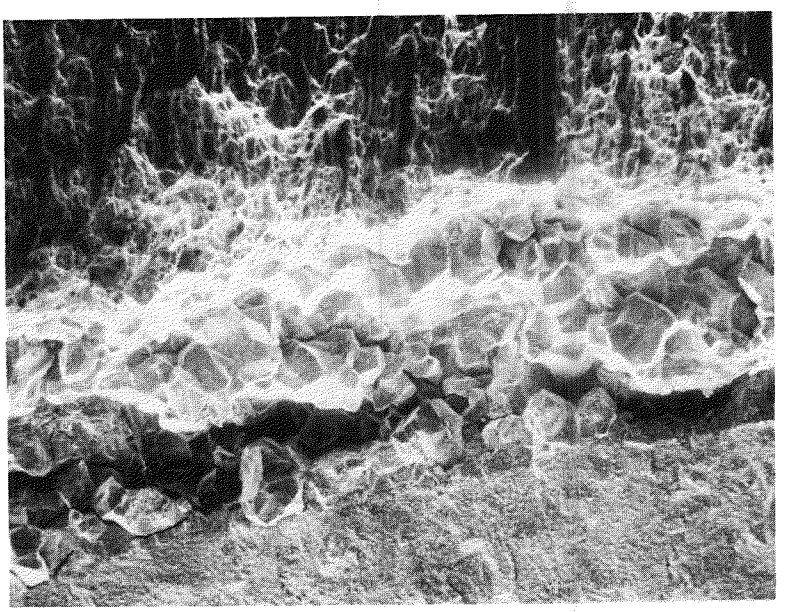

Figure H-16. SEM Photograph of Specimen 4904 SS-3 Showing IGSCC (35X)

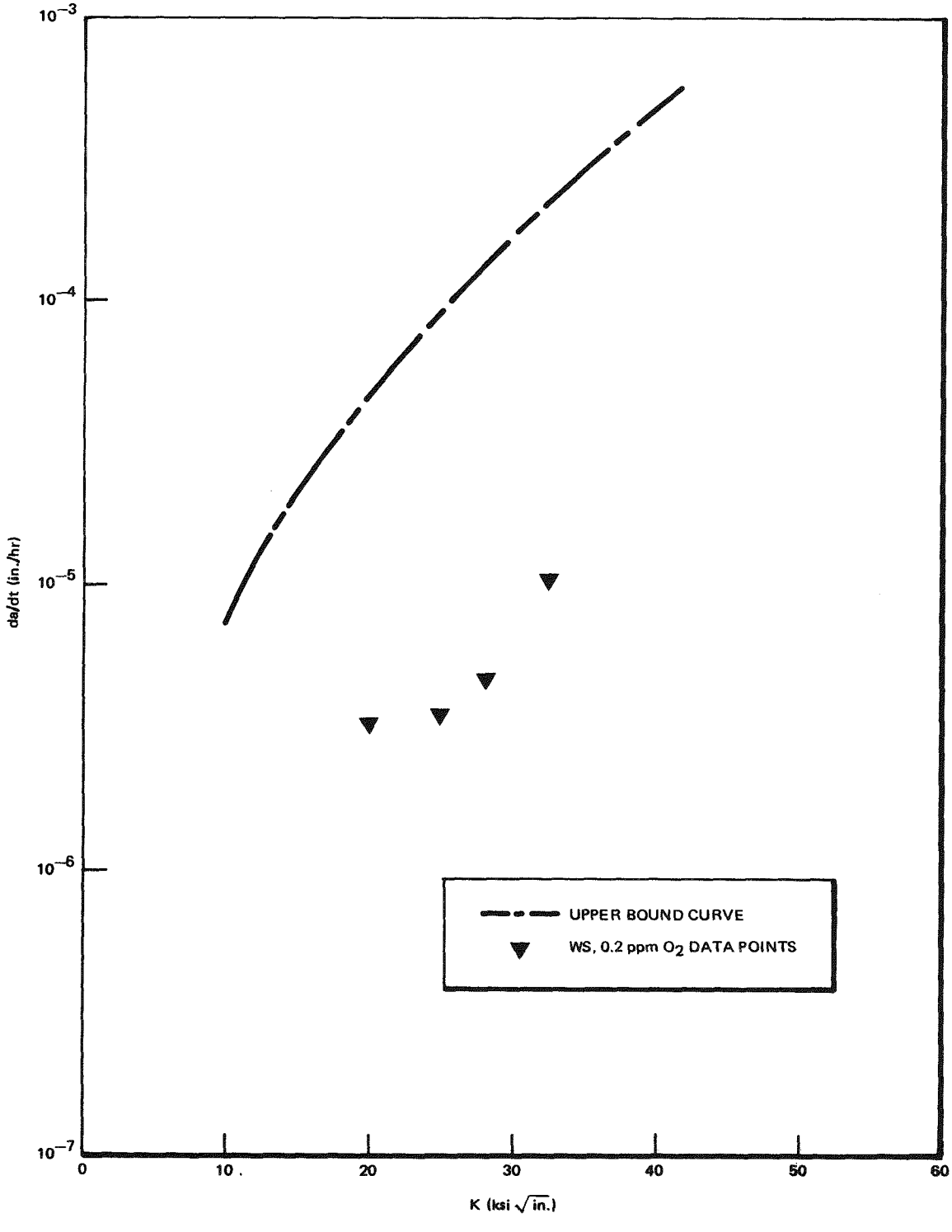

Figure H-17. Constant Load Crack Growth Rates Measured as a Function of Stress Intensity. Material sensitized at 1150°F, for hours (WS) tested in 0.2 ppm O_2 environment. Rates are averages.

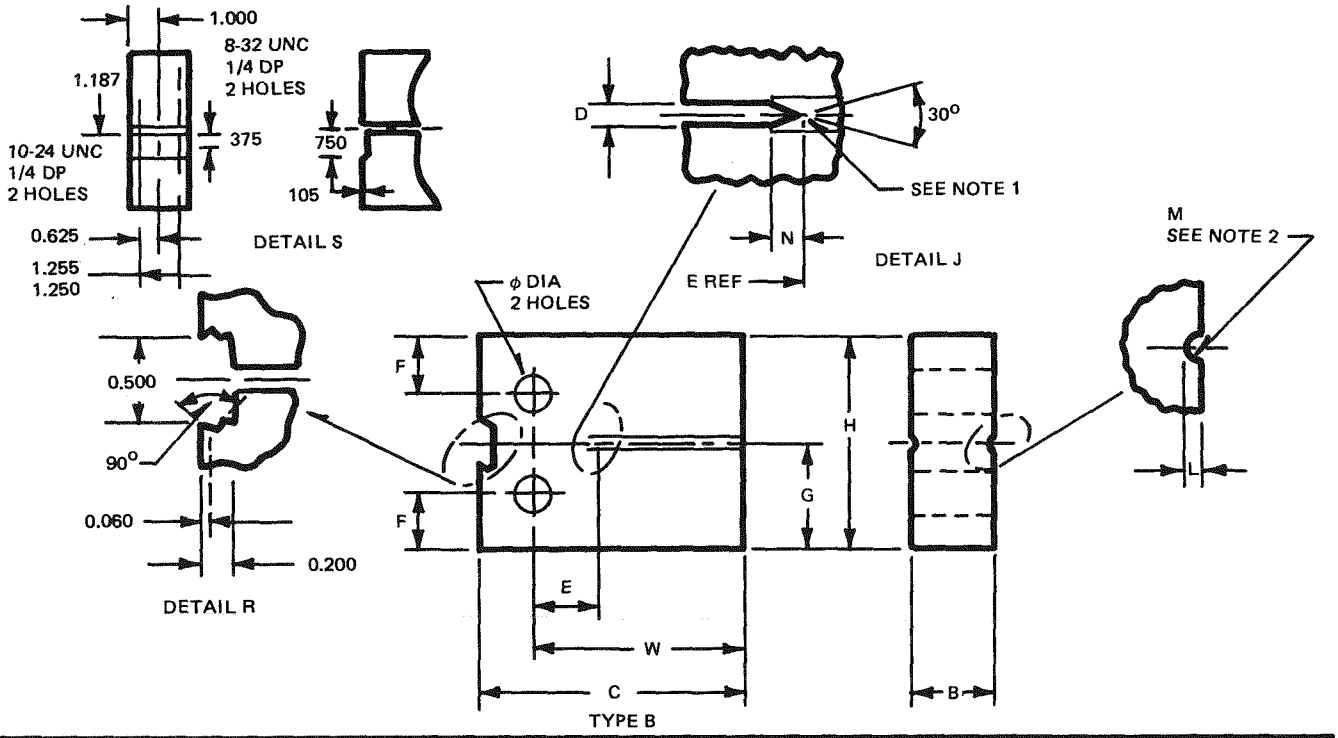

SPEC No.	B	W	C	D	E	F	G	H	L	M	N	O	P	R	S
1T-WOL	$1.000^{\pm 0.010}$	2.55	3.200	0.094	0.767	0.650	1.240	2.480	0.060	0.047	$0.175^{\pm 0.020}$	$0.500^{+0.005}_{-0.000}$	—	YES	NO
1T-CT	$1.000^{\pm 0.010}$	2.00	2.65	0.094	0.850	0.650	1.200	2.400	0.050	0.047	$0.175^{\pm 0.020}$	$0.500^{+0.005}_{-0.000}$	—	YES	NO

NOTES:

1. 0.007 in. MAXIMUM RADIUS (EDM)
2. LAY MARKS TO FALL PARALLEL TO AXIS OF RADIUS SURFACE FINISH TO BE 32

Figure H-18. WOL or Compact Tension Specimen for Crack Growth Rate Study

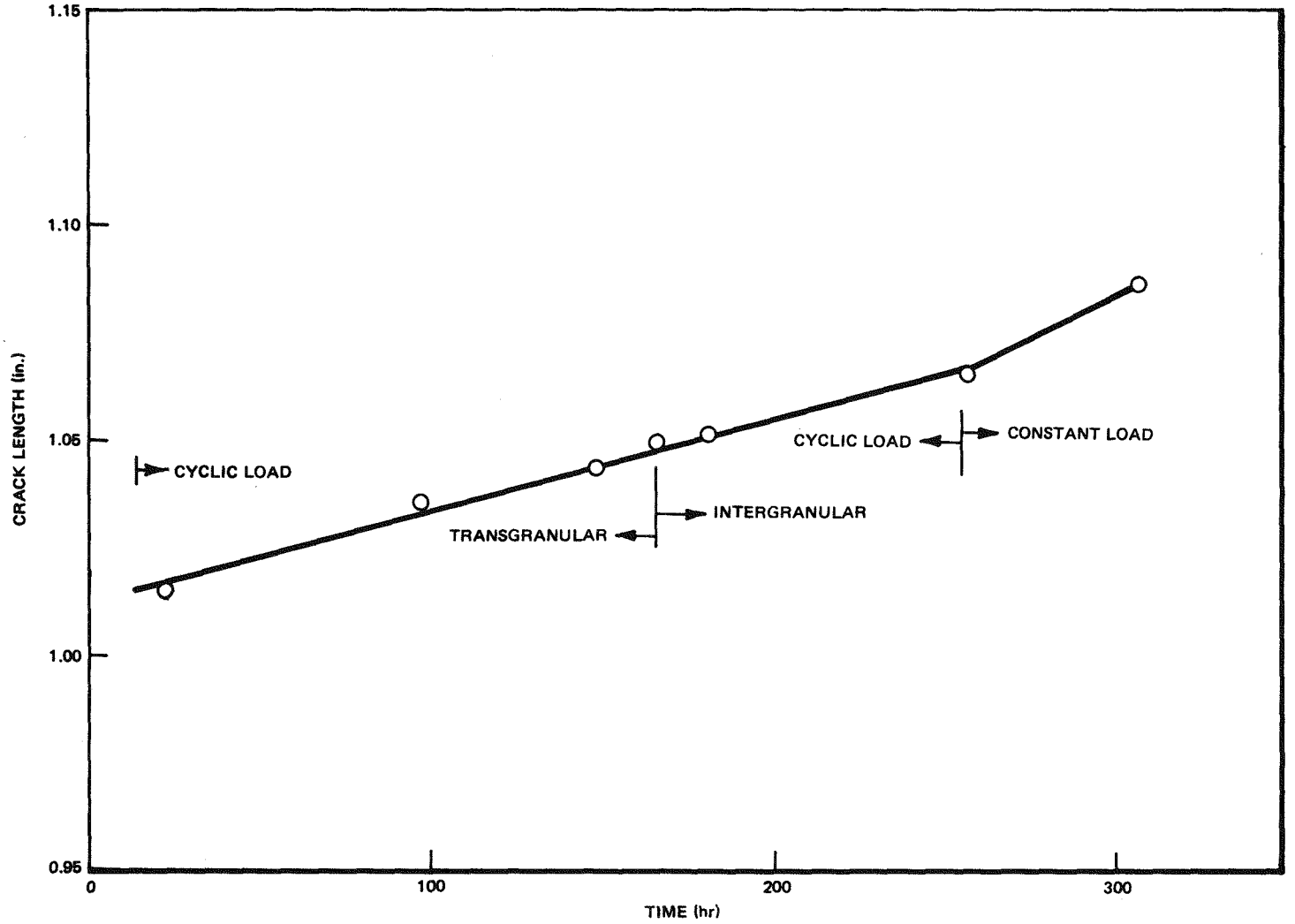

Figure H-19. Crack Length versus Time for Specimen TC-3

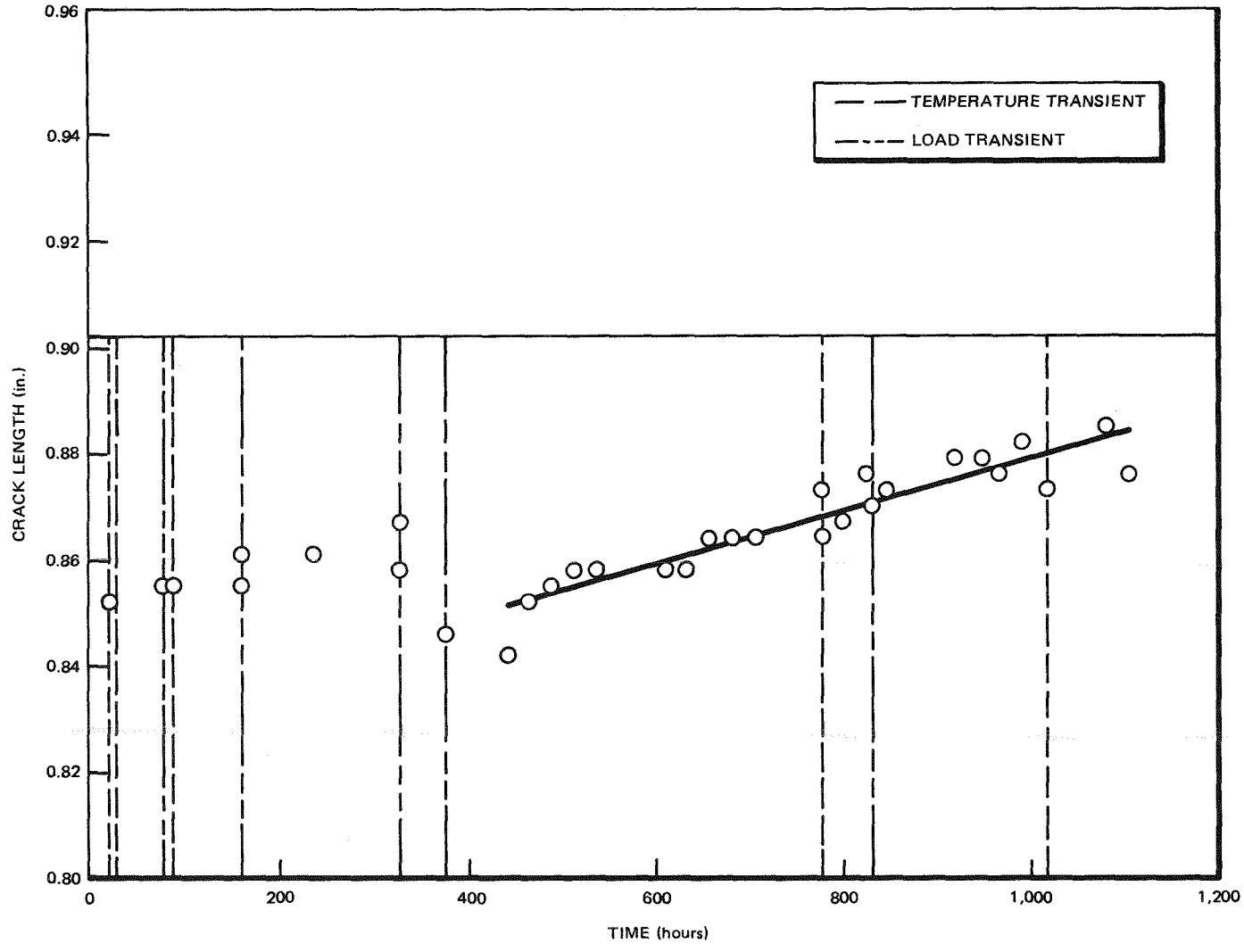

Figure H-20. Crack Length A versus Time, Specimen SS-21 (Constant Load)

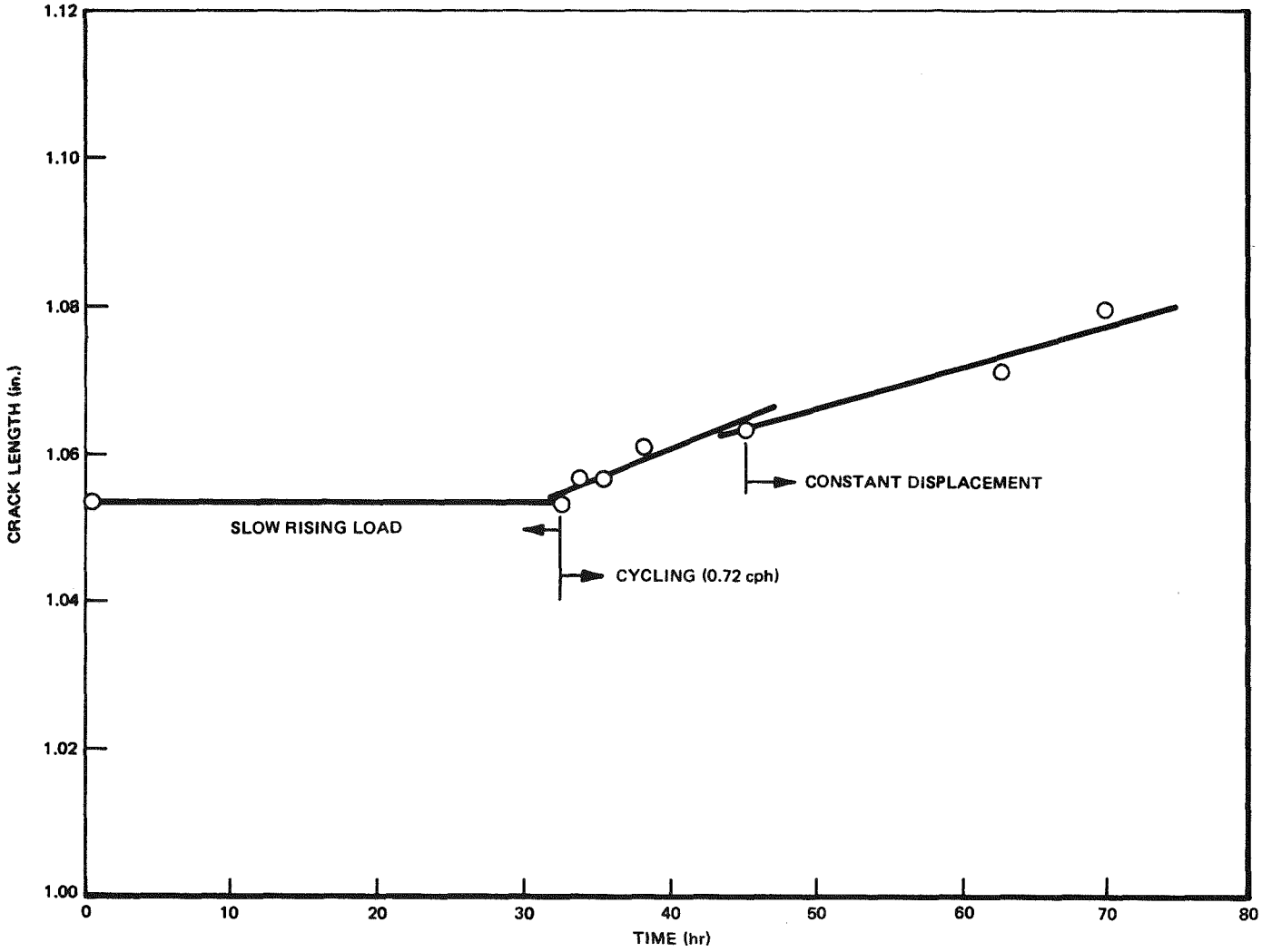

Figure H-21. Crack Length, a, versus Time, Specimen SS-24

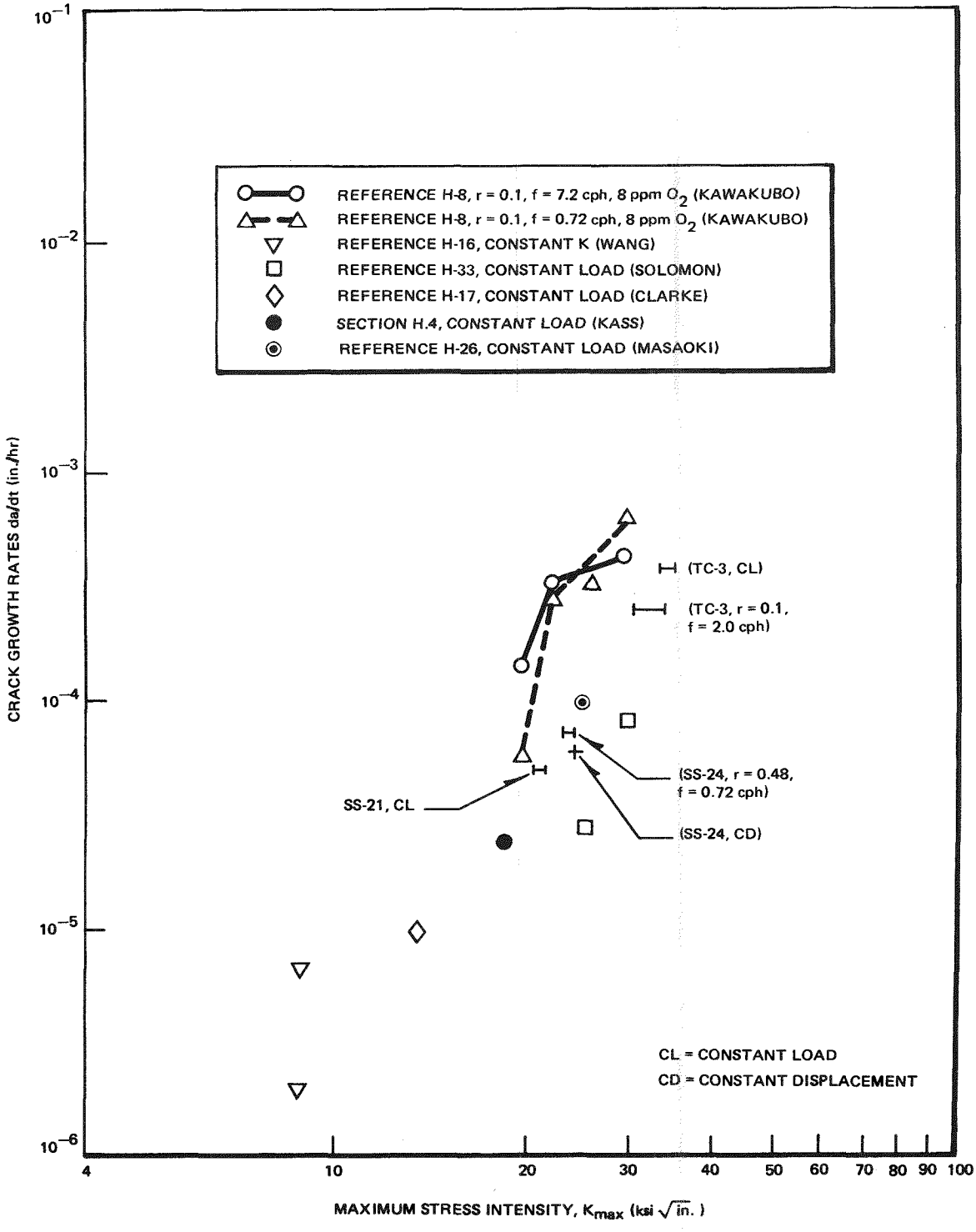

Figure H-22. Crack Growth Rate Data in 550°F, 8 ppm O_2 Water

*Please note that the illustration(s) on this page has been reduced 10% in printing.

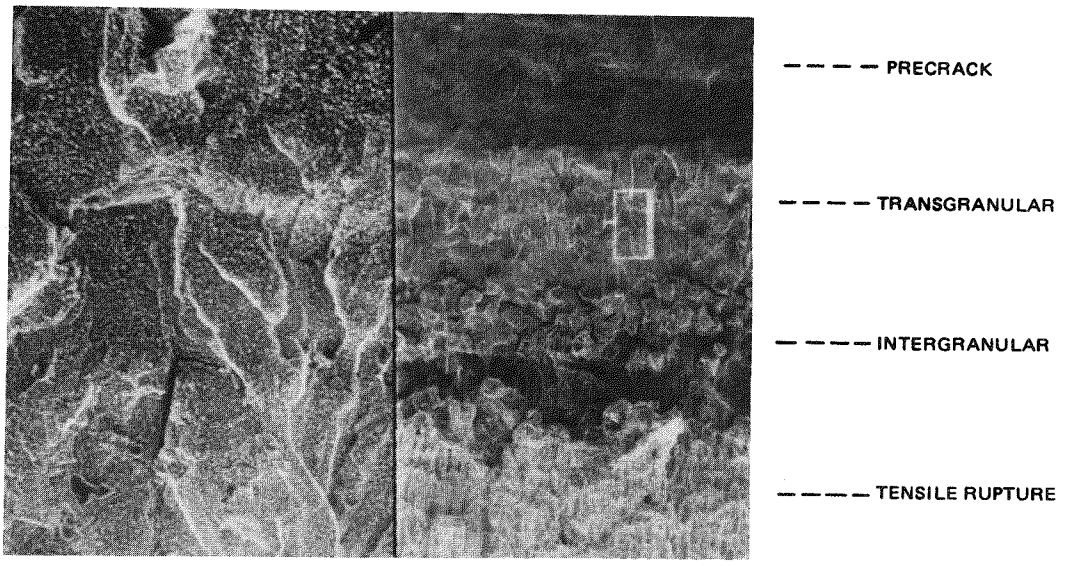

(a)

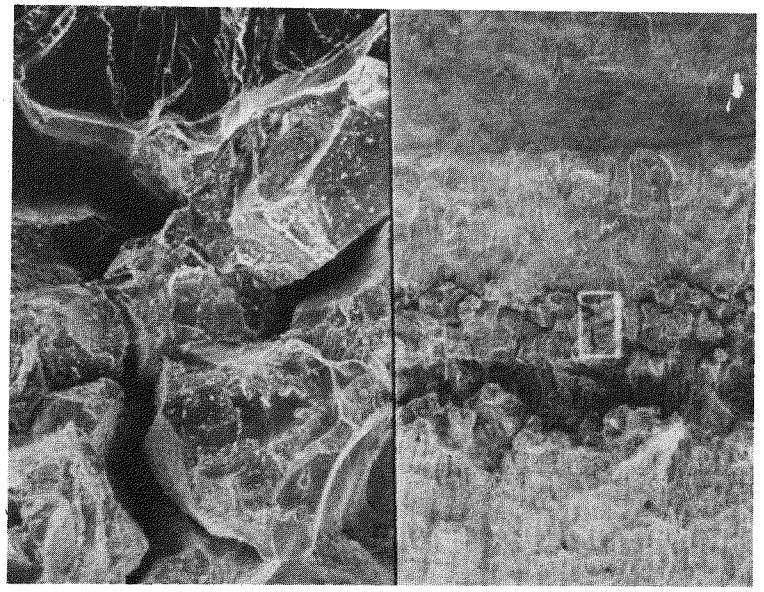

(b)

Figure H-23. Fracture Surface of Specimen TC-3 (15X/150X)

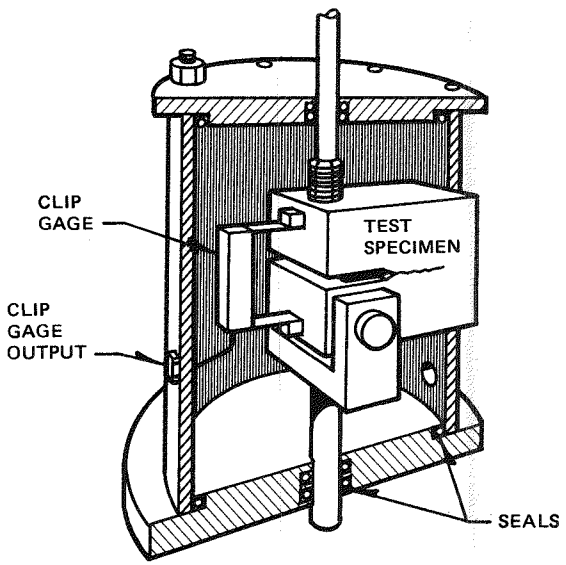

Figure H-24. Slow-Rising Load
Test Schematic

*Please note that the illustration(s) on this page has been reduced 10% in printing.

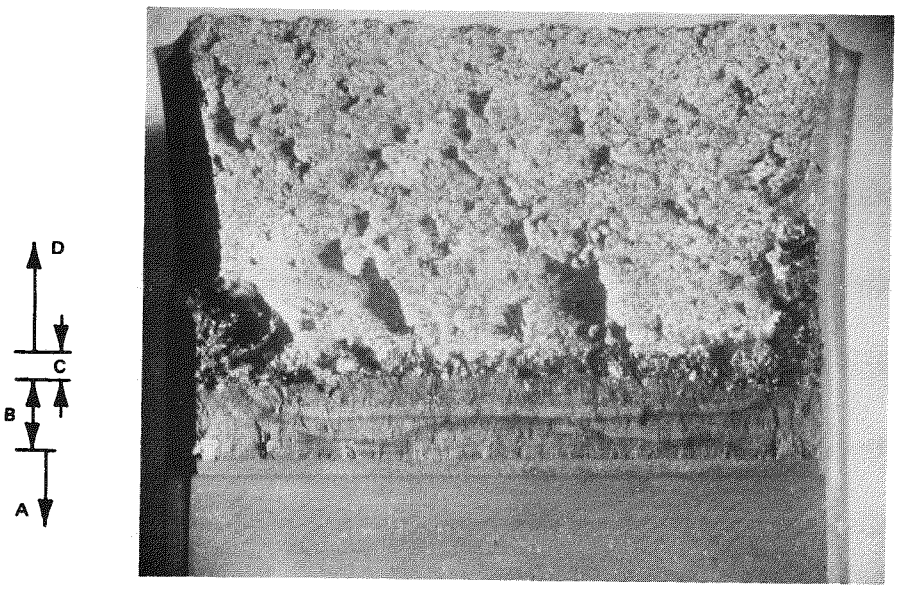

A – MACHINED NOTCH; C – INTERGRANULAR CRACK;
B – FATIGUE PRECRACK; D – AIR FRACTURE

(a)

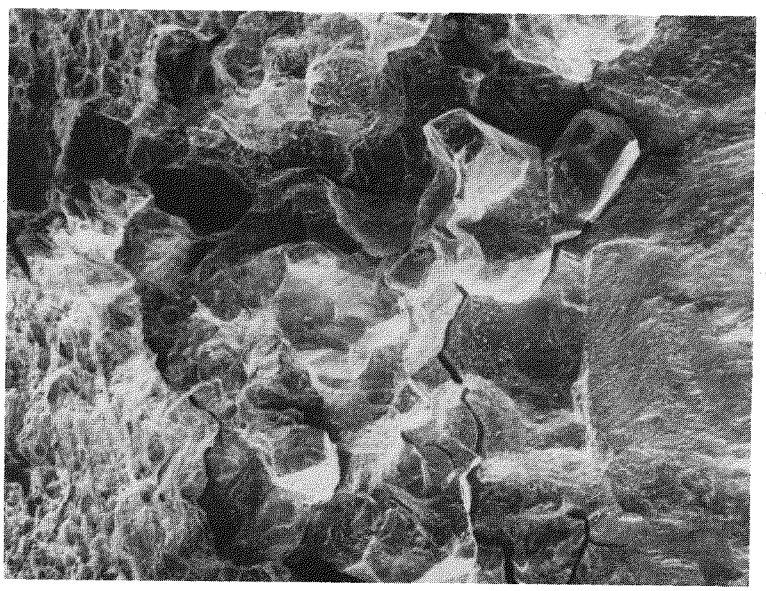

ENLARGEMENT OF AREA B ABOVE

(b)

Figure H-25. Intergranular Fracture in Slow Rising Load Specimen SSW-E; (a) = 4X, (b) = 50X

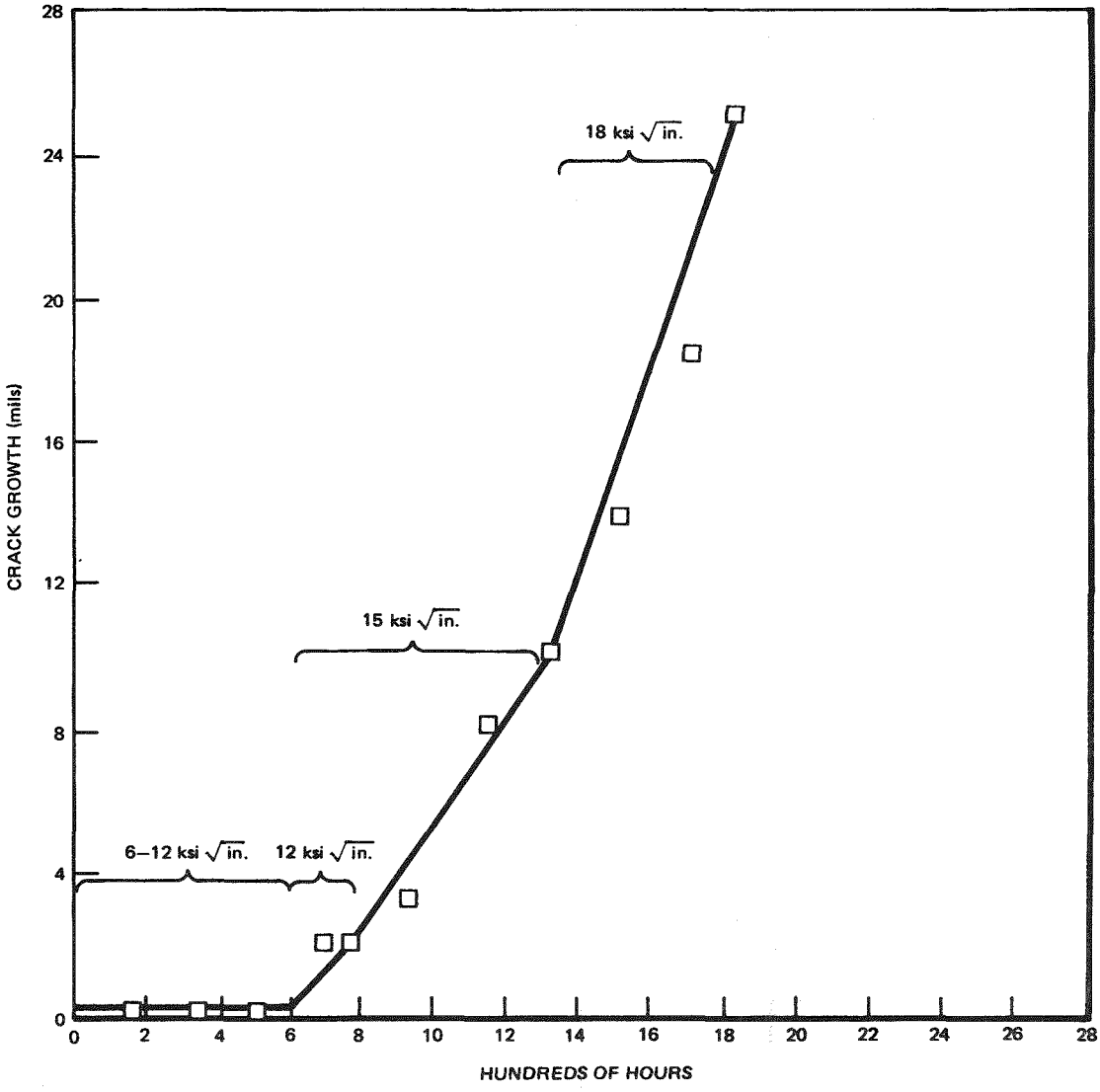

Figure H-26. Crack Growth, Δa, As a Function of Time in Final Slow Rising Load Specimen; Determined from Compliance

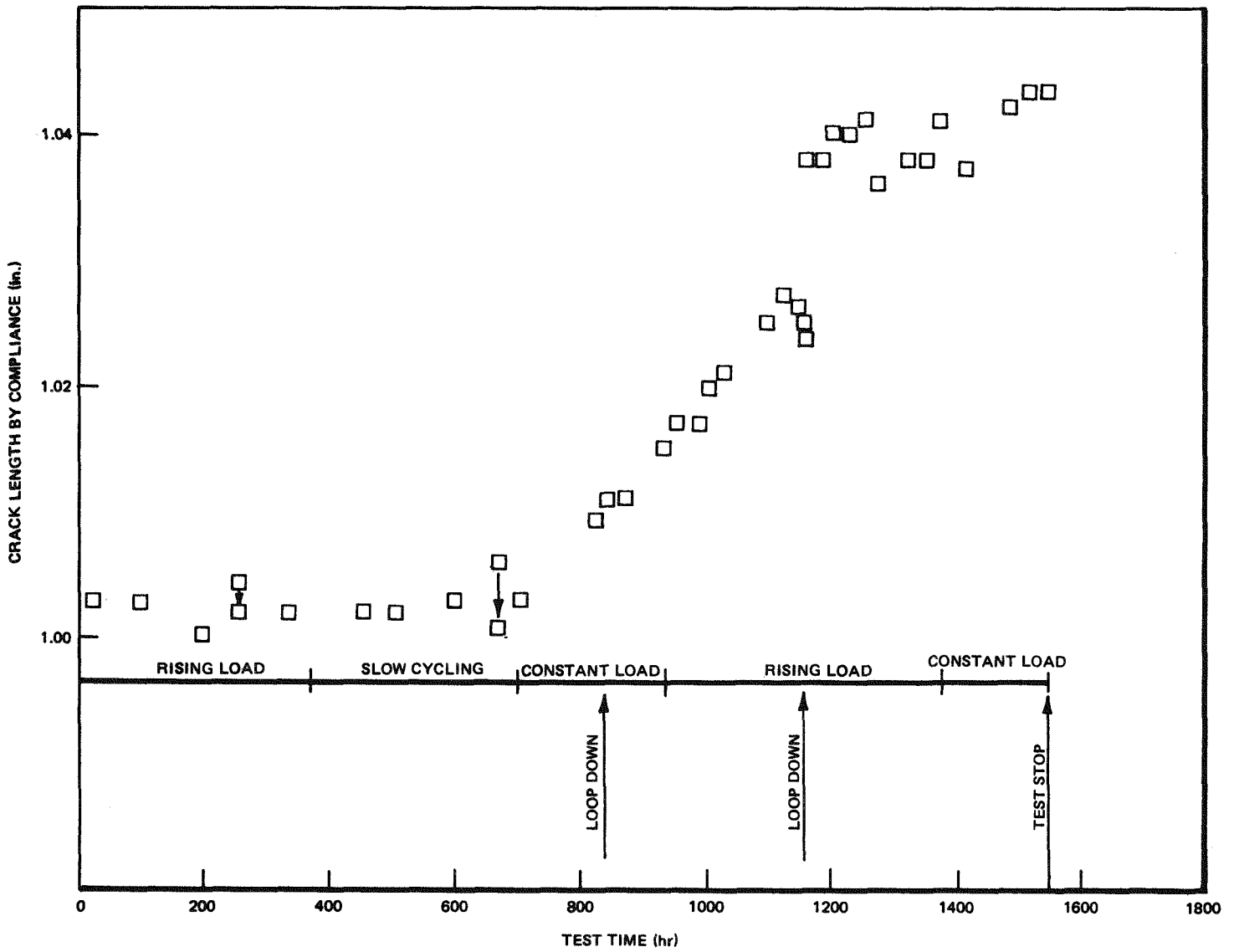

Figure H-27. Specimen FS-1: Crack Length versus Time; Determined from Compliance

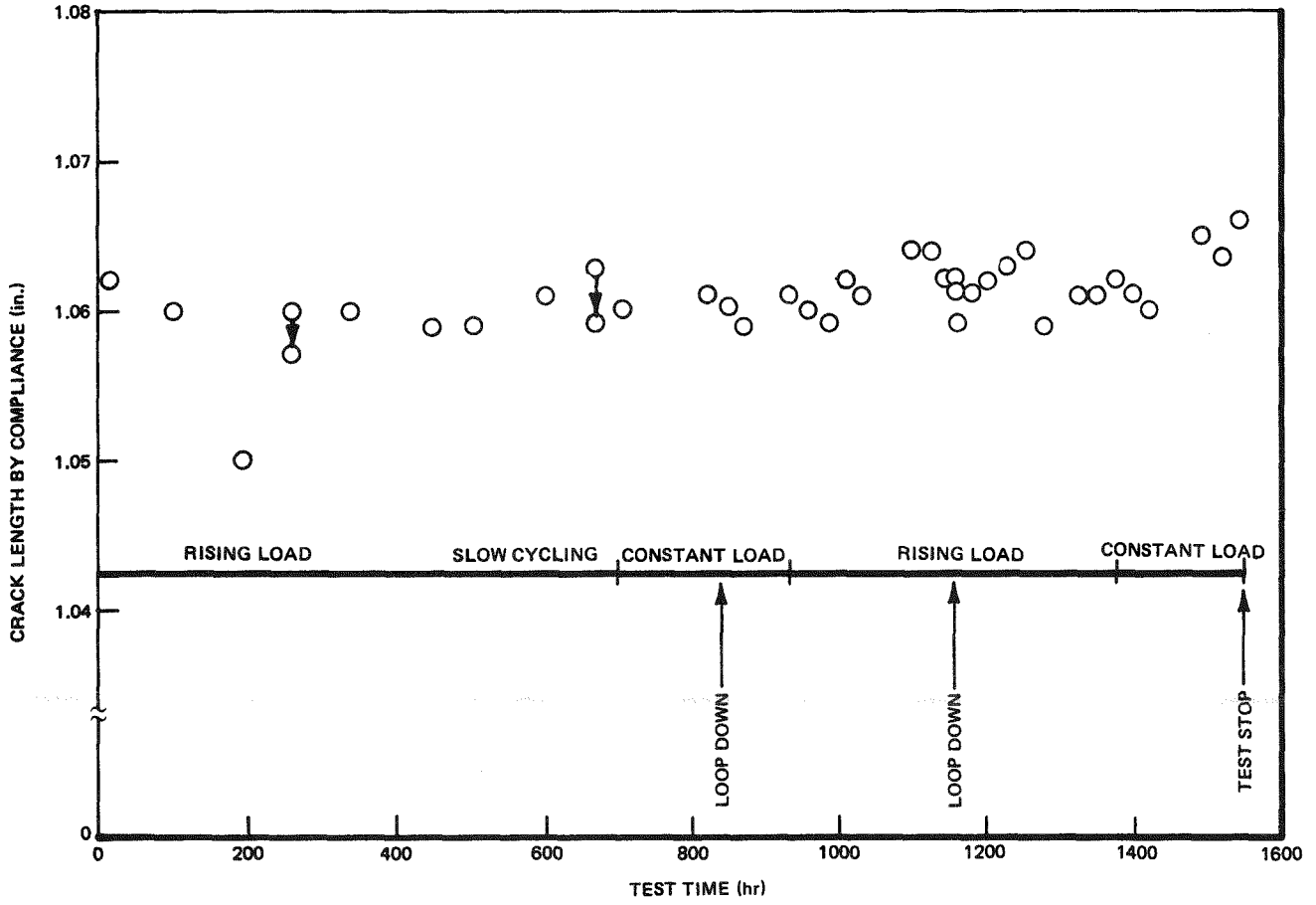

Figure H-28. Specimen WS-1: Crack Length versus Time - Uncorrected

*Please note that the illustration(s) on this page has been reduced 10% in printing.

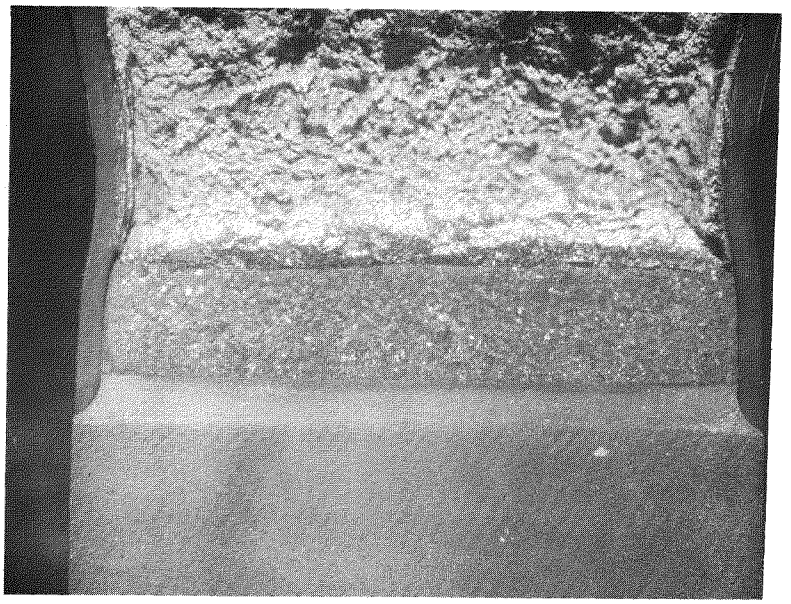

(a)

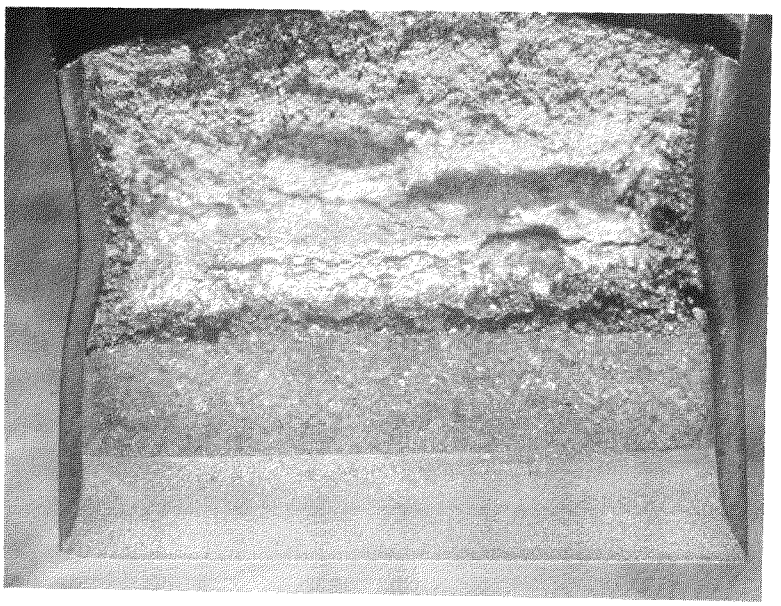

(b)

Figure H-29. Macrographs of Fracture Surface from (a) Specimen WS-1 and (b) Specimen FS-1 (4X)

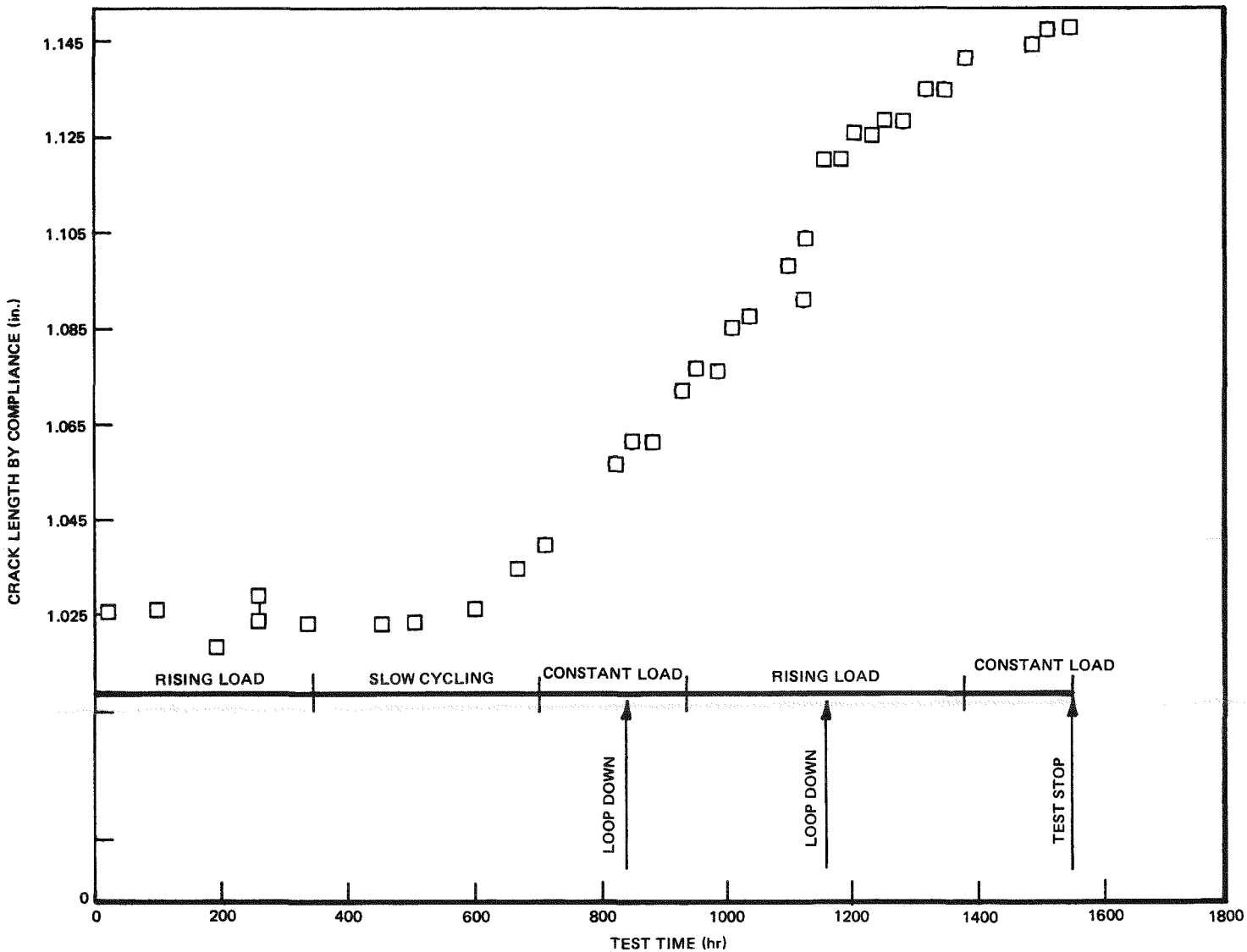

Figure H-30. Specimen FS-1: Crack Length versus Time - Corrected

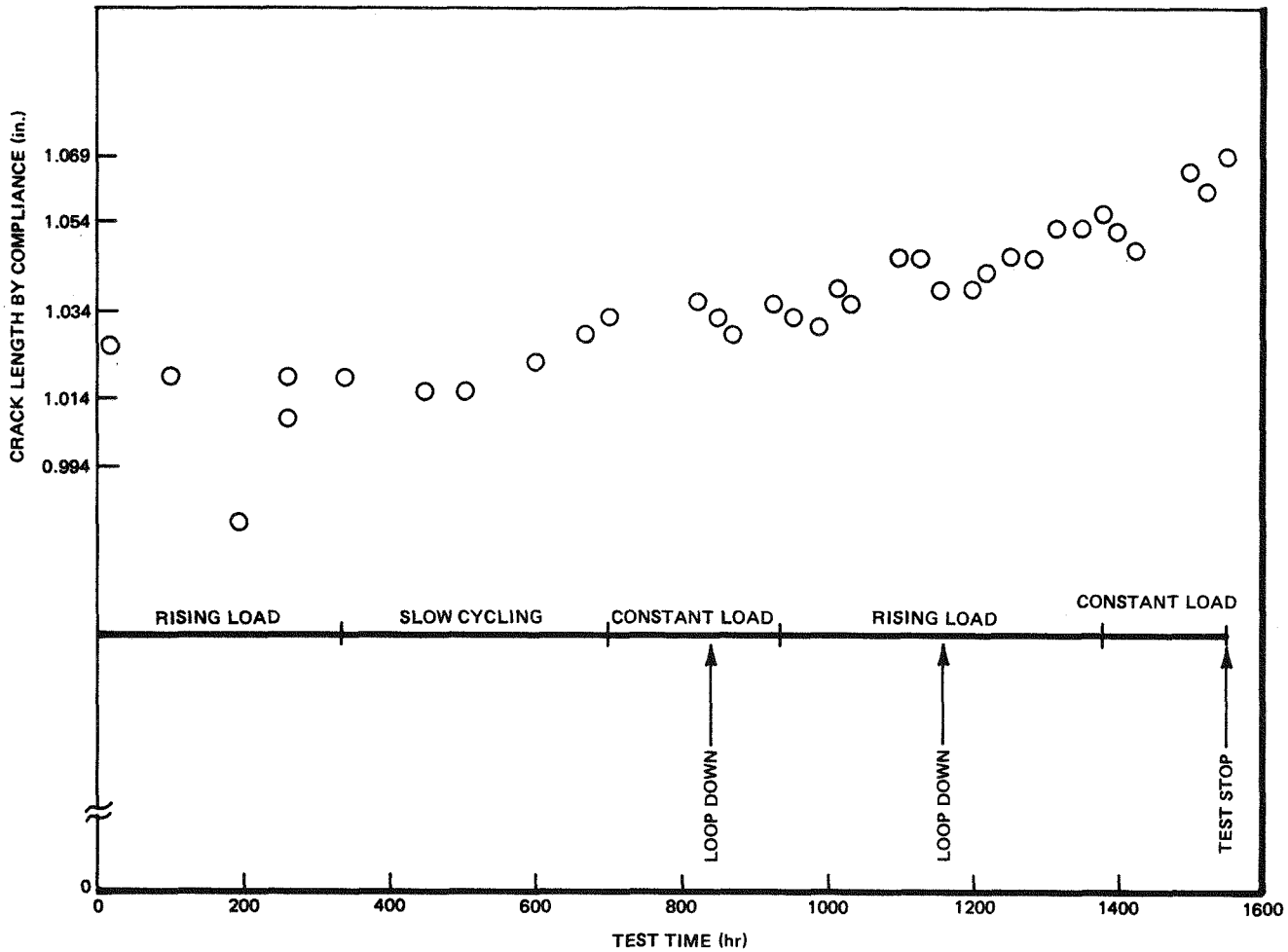

Figure H-31. Specimen WS-1: Crack Length versus Time - Corrected

*Please note that the illustration(s) on this page has been reduced 10% in printing.

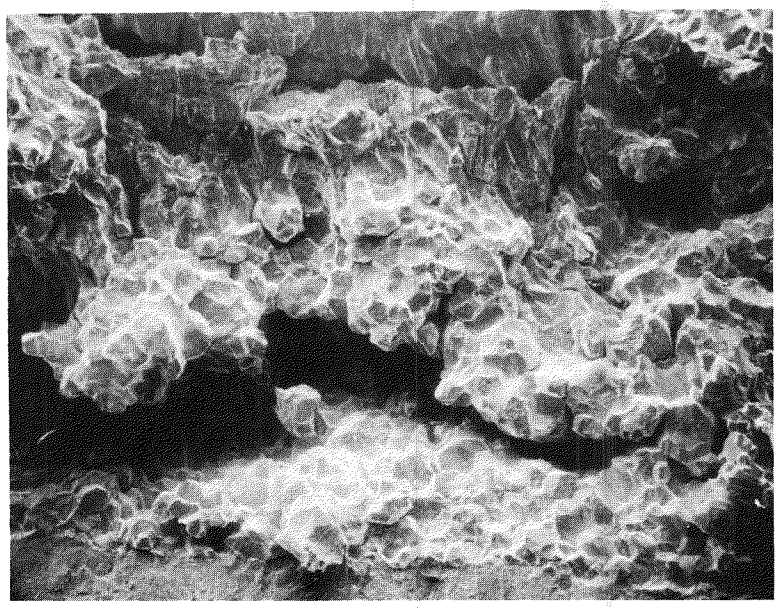

(a)

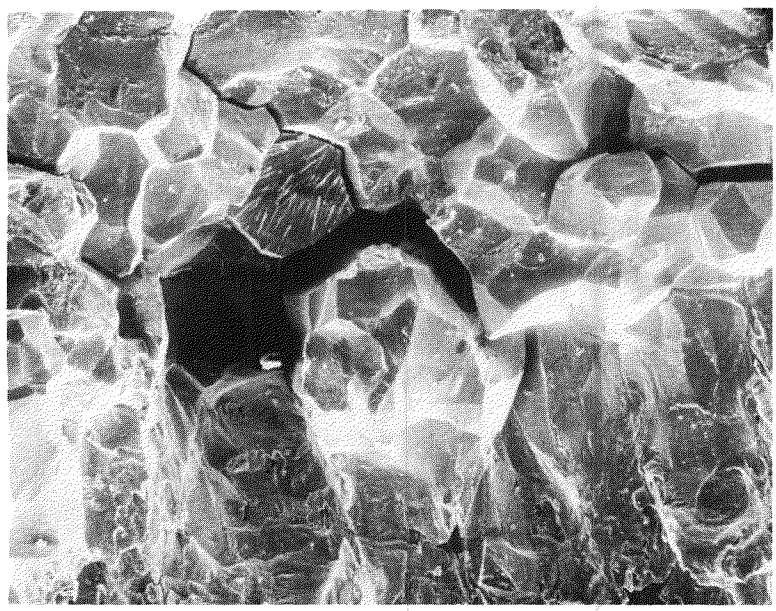

(b)

Figure H-32. SEM Micrographs of IG Fracture in FS-1
(a) 21X, (b) 105X

*Please note that the illustration(s) on this page has been reduced 10% in printing.

(a)

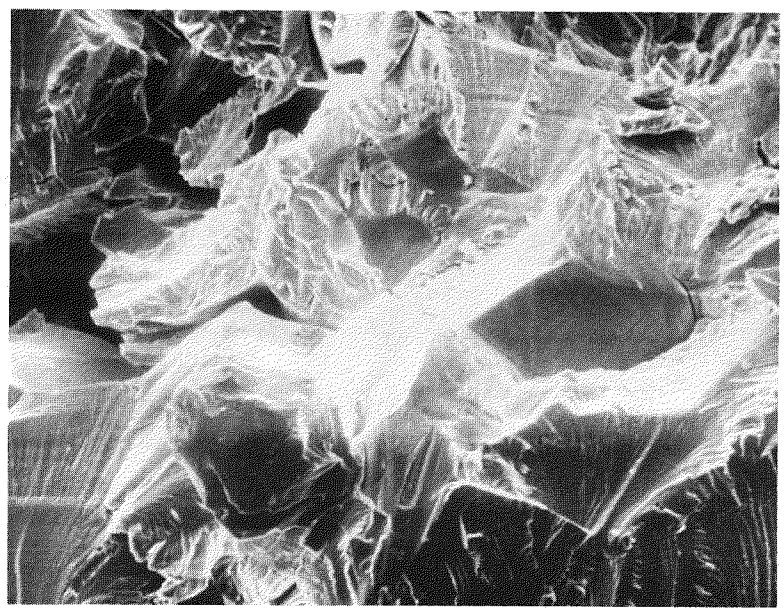

(b)

Figure H-33. SEM Micrographs from Specimen WS-1 Showing Mixed Mode Fracture (a) 140X, (b) 350X

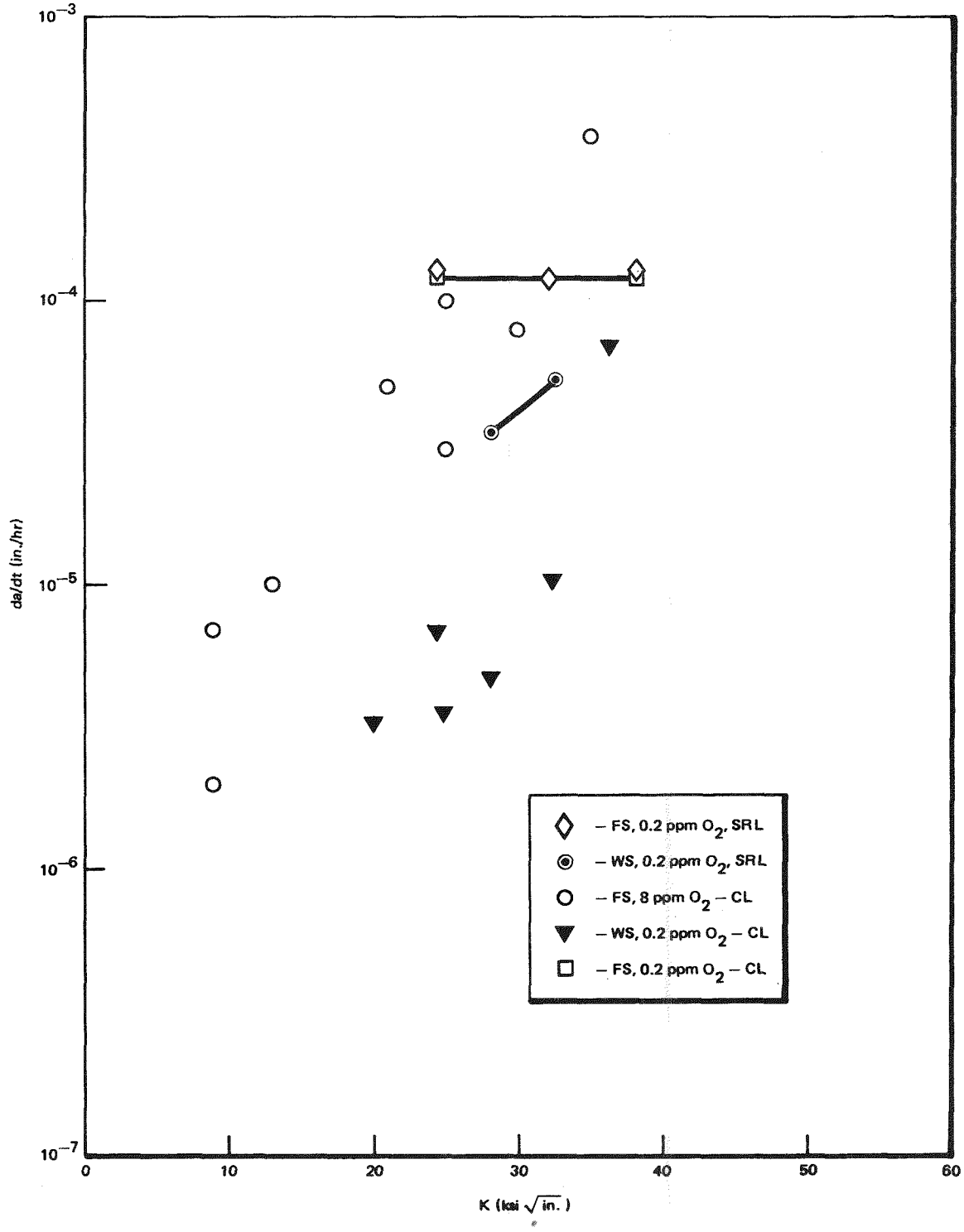

Figure H-34. Crack Growth Rate Data for Slow Rising Load (SRL) and Constant Load (CL) Tests. (1150°F, 24-hr sensitization treatment represented by FS; 1150°F, 2-hr sensitization treatment represented by WS.)

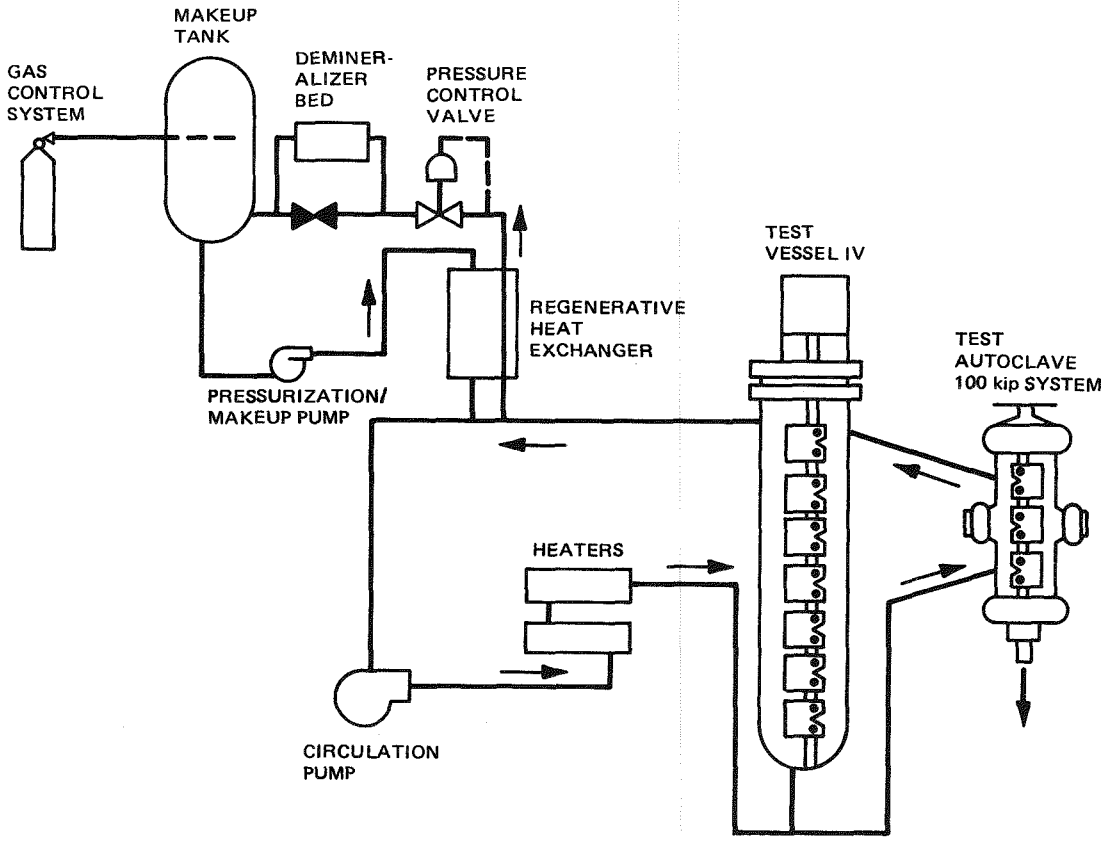

Figure H-35. Simulated BWR Water Test Loop

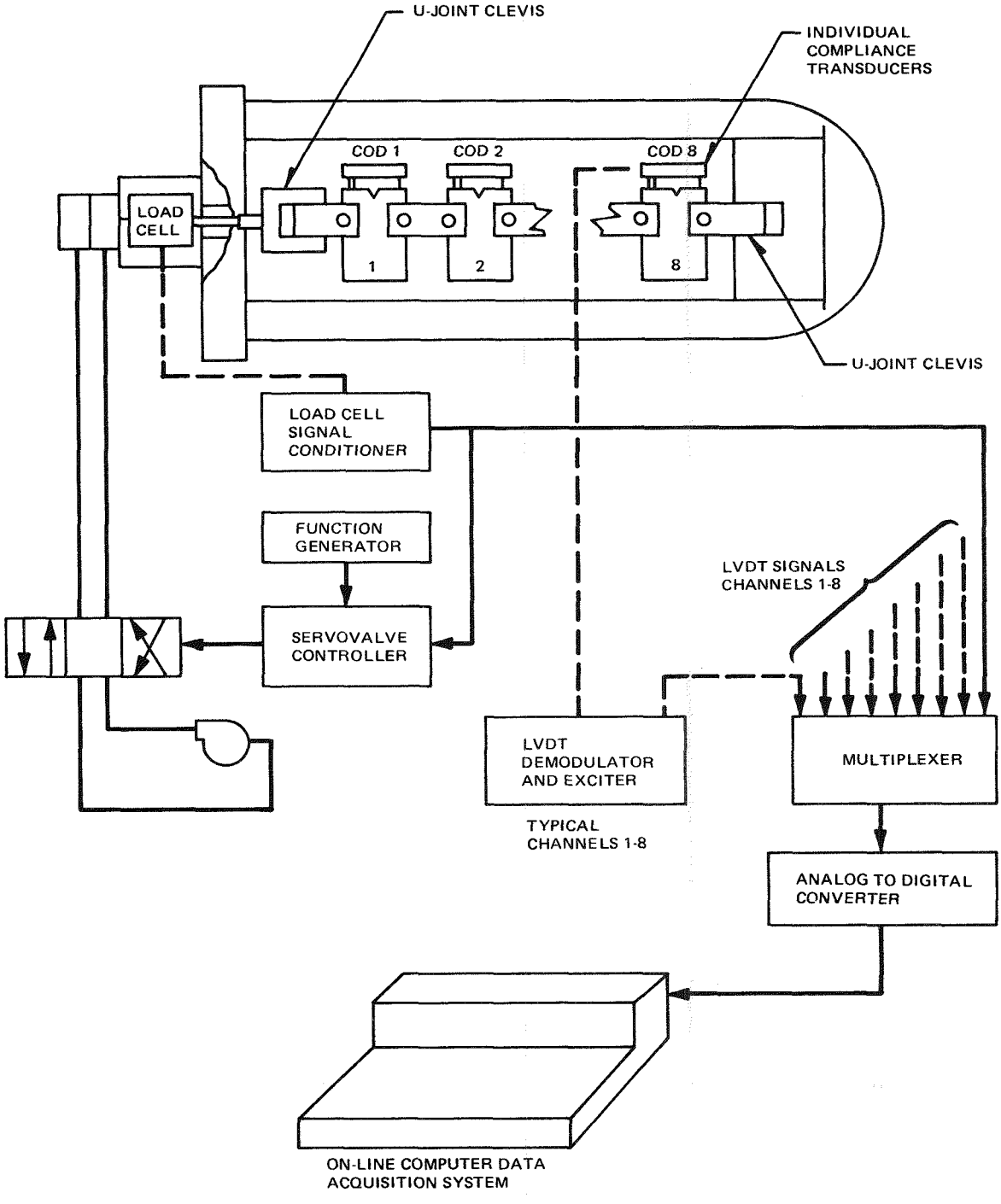

Figure H-36. Schematic of Test Vessel VI, Multispecimen Environmental Test Facility

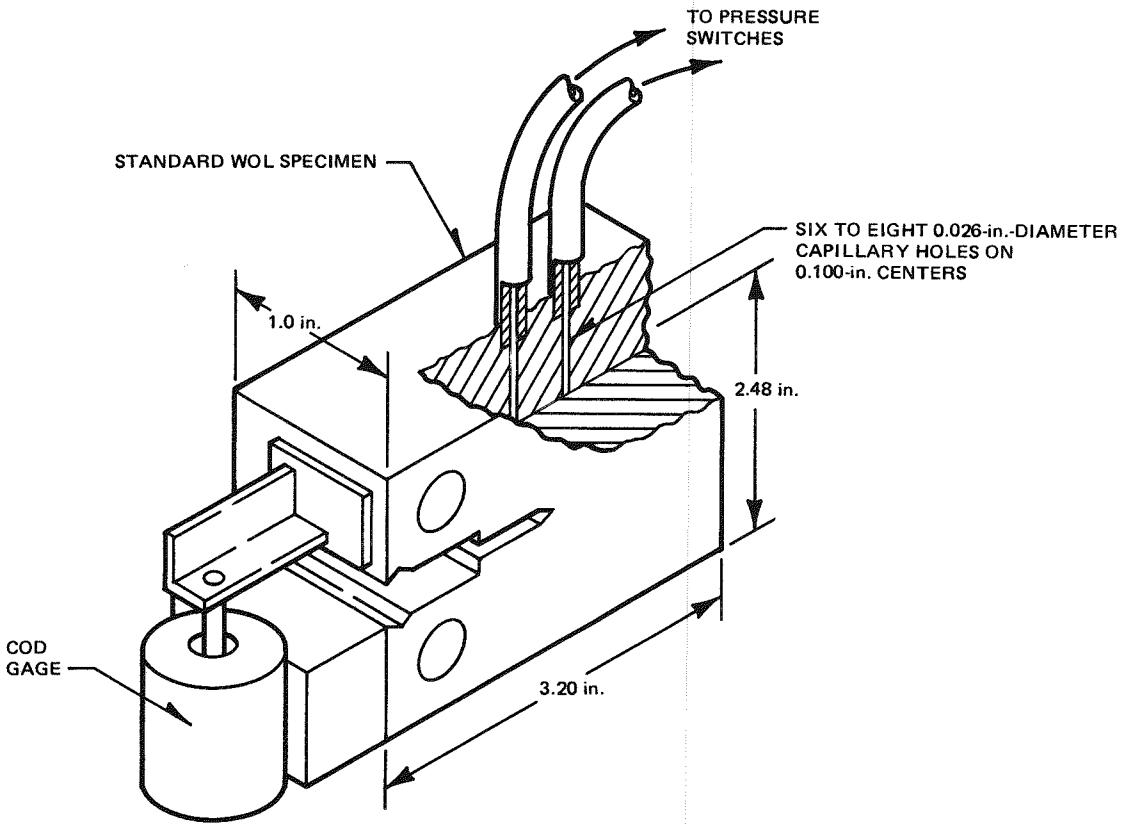

Figure H-37. Specimen Modifications for Remote Crack Length Measurement Capability

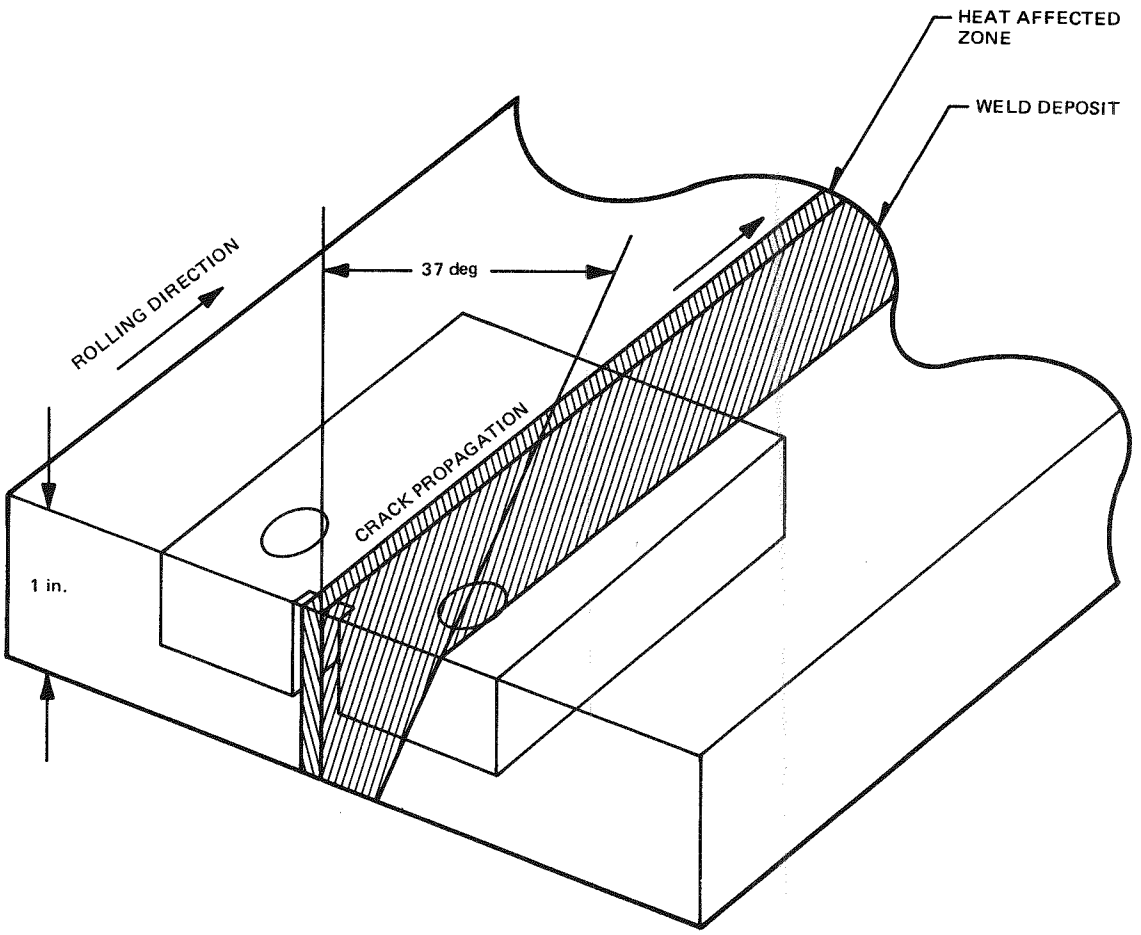

Figure H-38. 1T-WOL Specimen Orientation With Respect to Welded Plate and HAZ

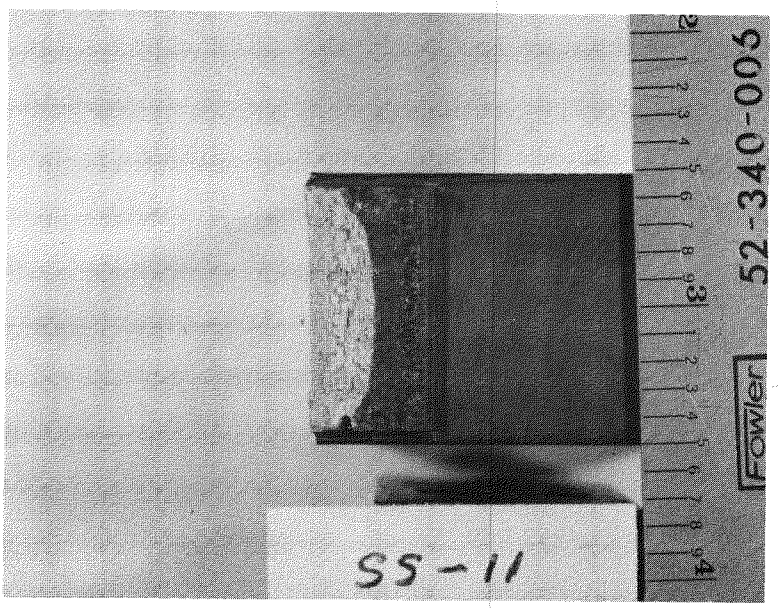

Figure H-39. End of Test Fracture Surface for Specimen SS-11

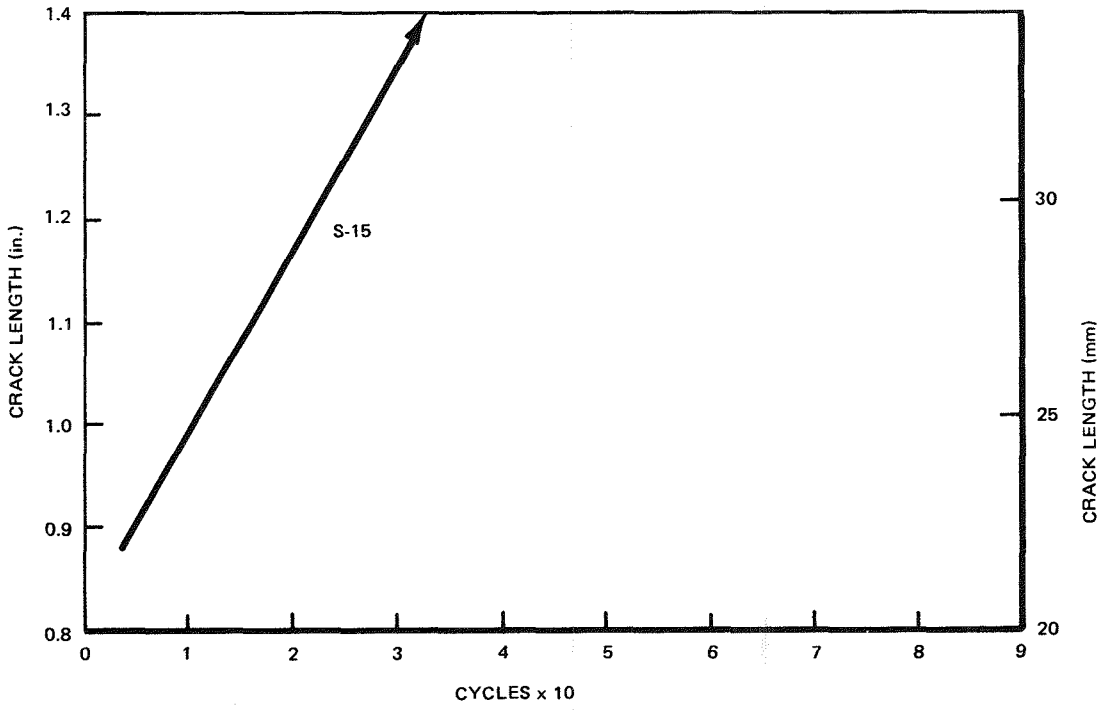

Figure H-40. Crack Length versus Number of Cycles for Stainless Steel at 300 cph, Specimen S-15

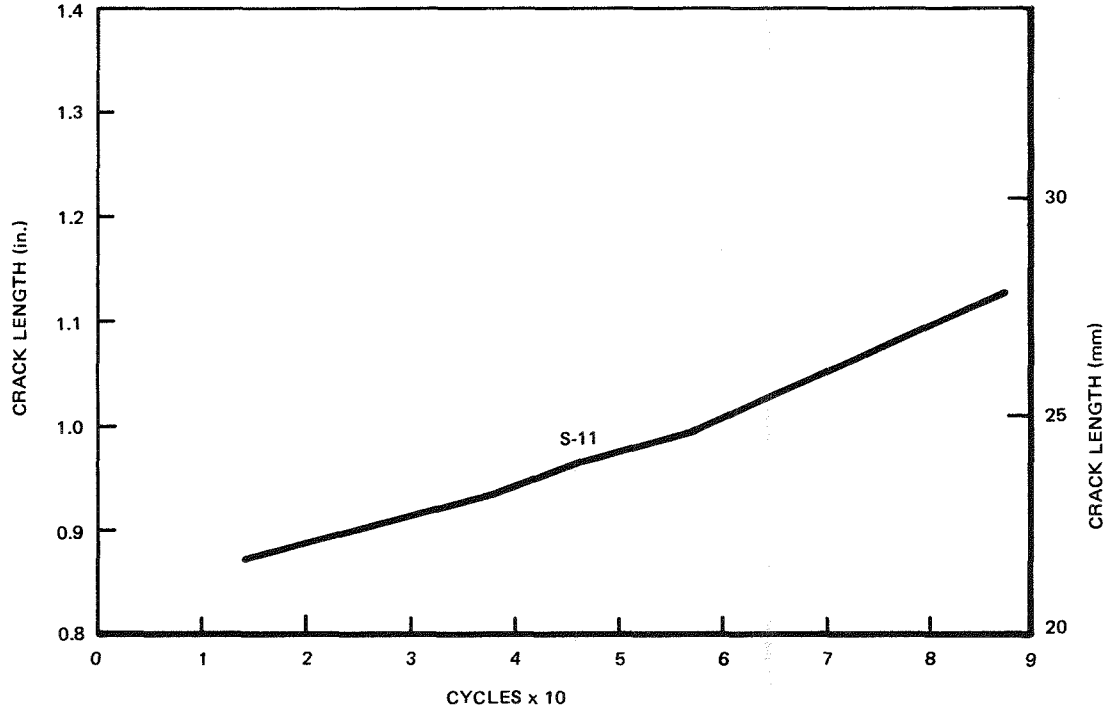

Figure H-41. Crack Length versus Number of Cycles for Stainless Steel at 300 cph, Specimen S-11

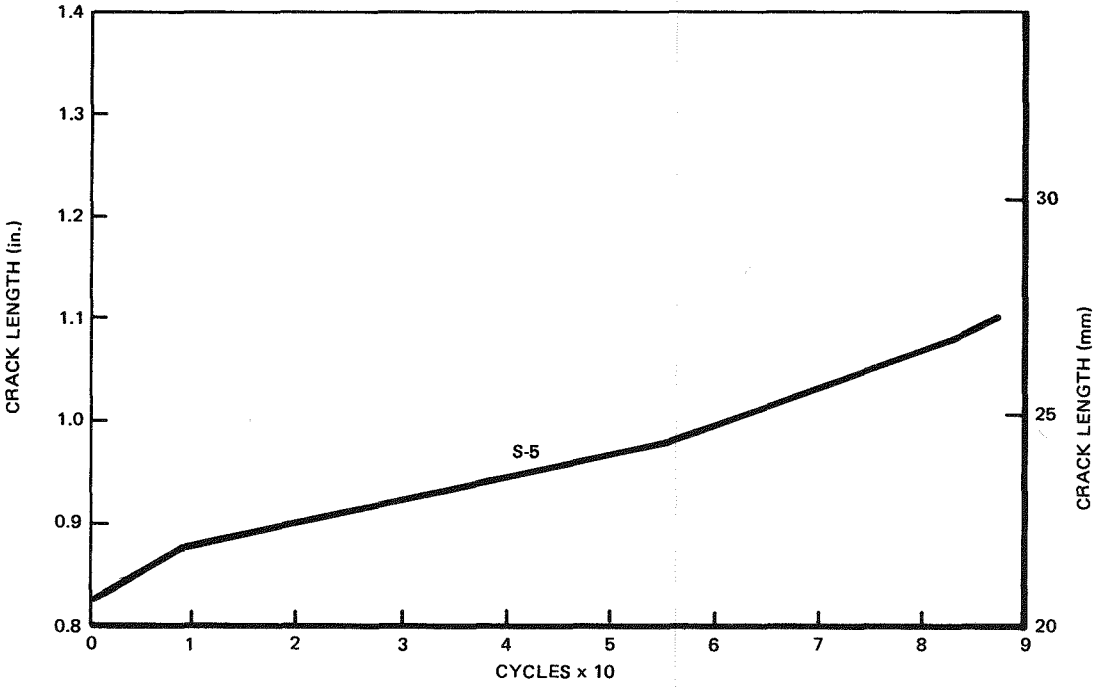

Figure H-42. Crack Length versus Number of Cycles for Stainless Steel at 300 cph, Specimen S-5

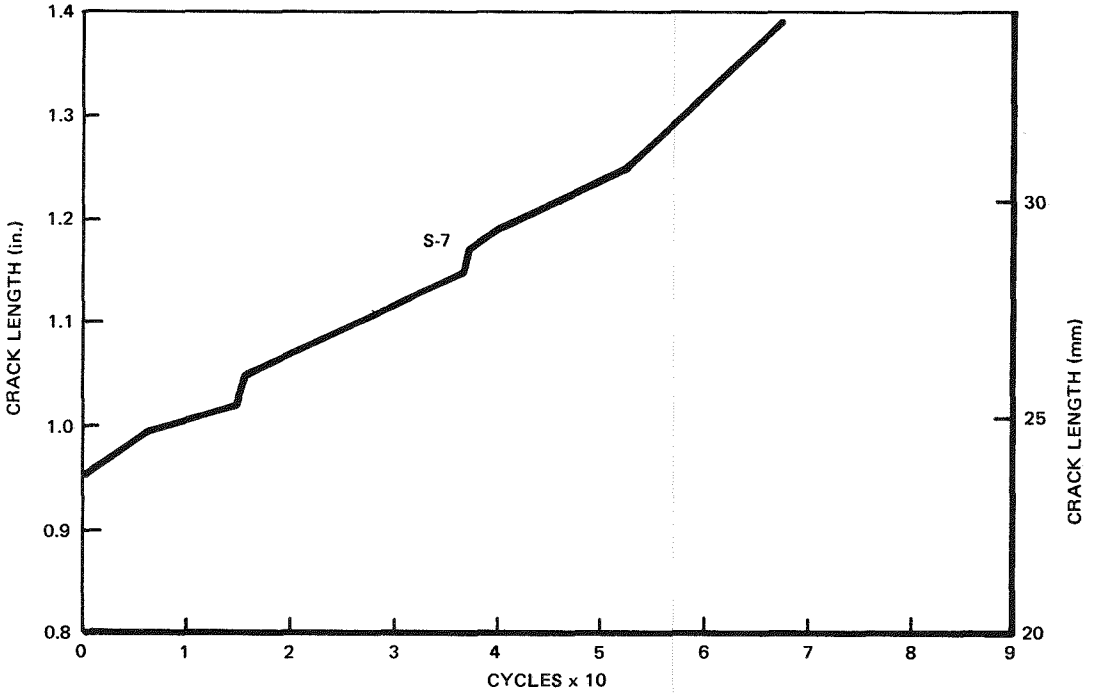

Figure H-43. Crack Length versus Number of Cycles for Stainless Steel at 300 cph, Specimen S-7

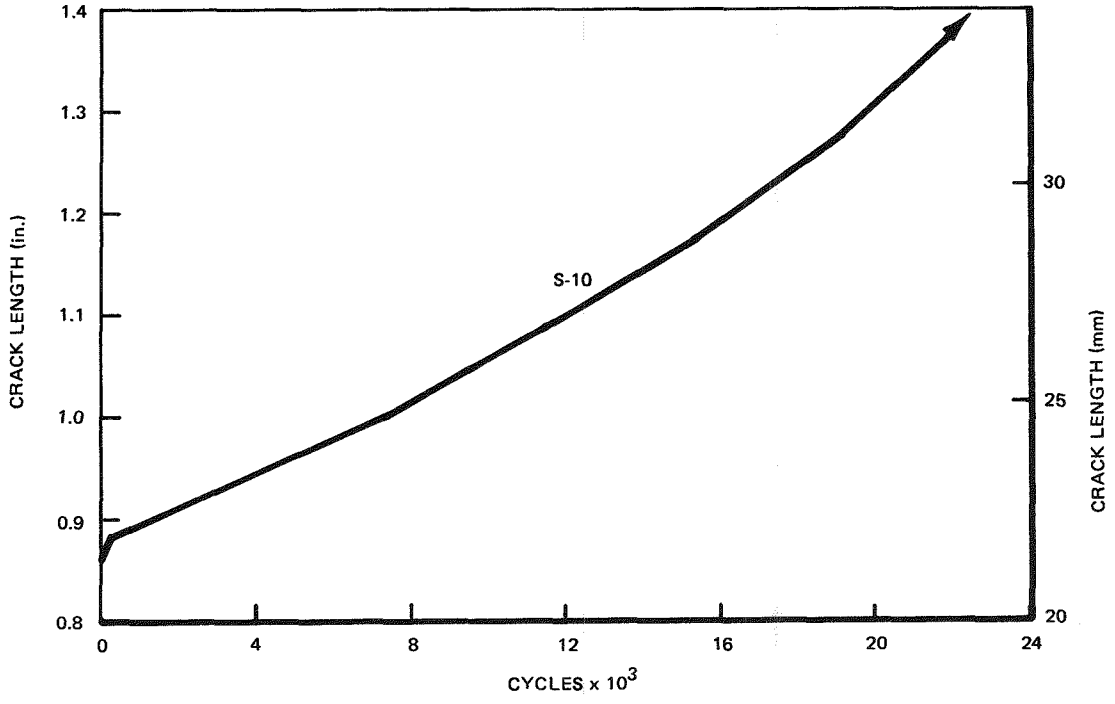

Figure H-44. Crack Length versus Number of Cycles for Stainless Steel at 75 cph, Specimen S-10

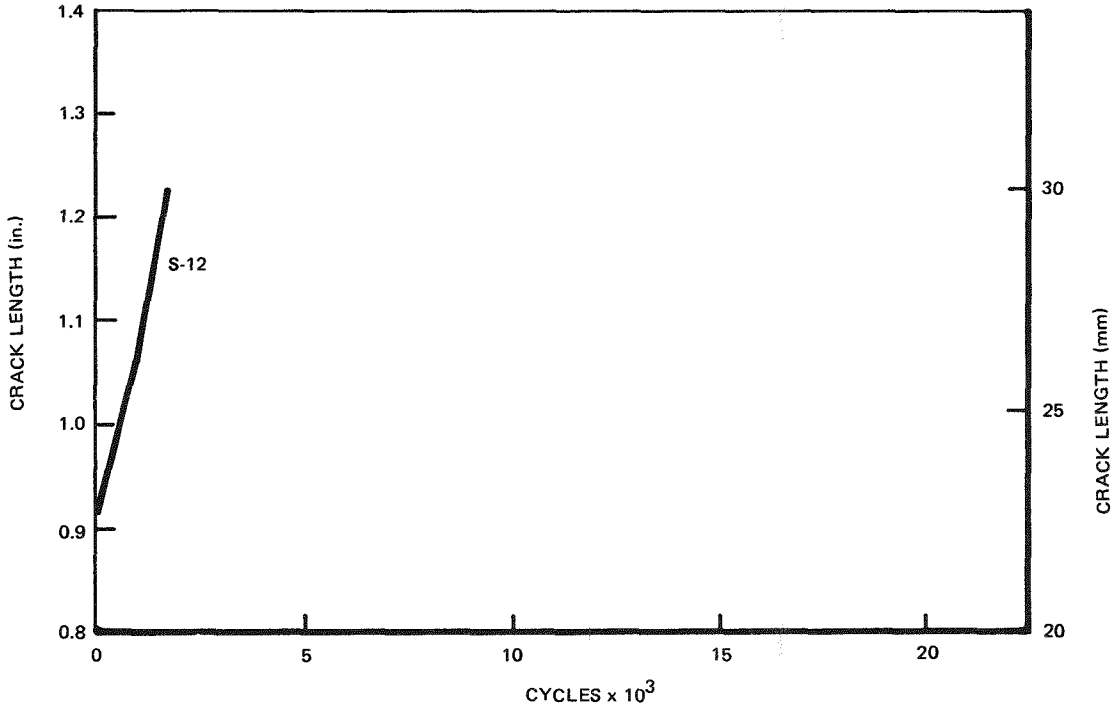

Figure H-45. Crack Length versus Number of Cycles for Stainless Steel at 18 cph, Specimen S-12

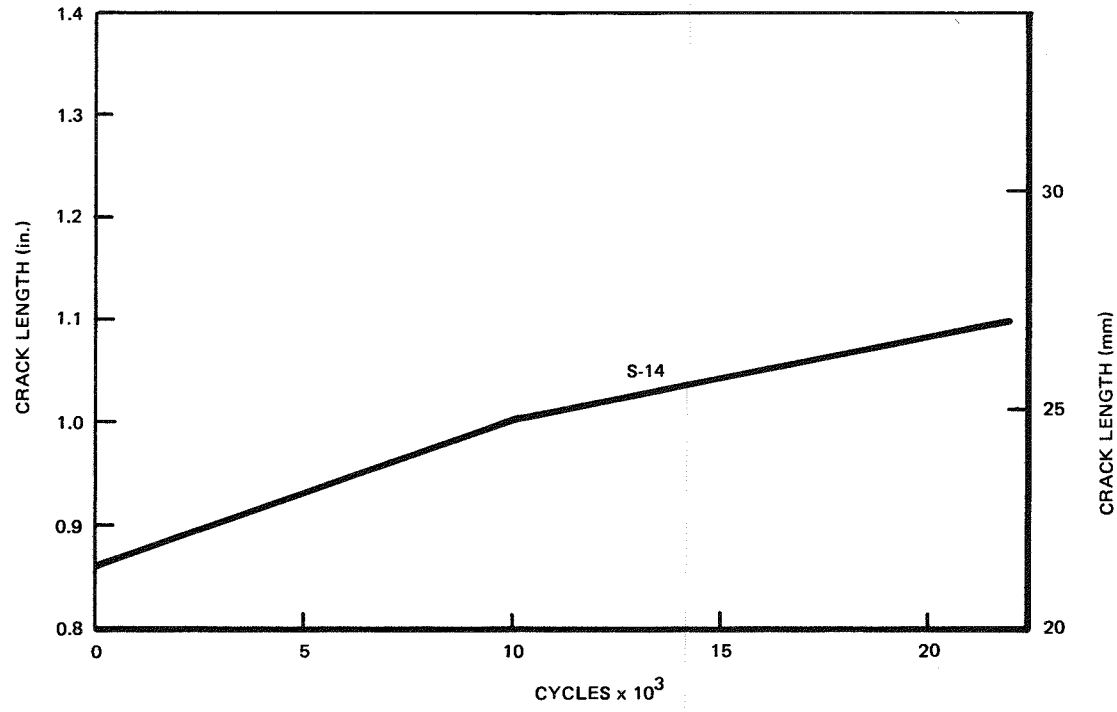

Figure H-46. Crack Length versus Number of Cycles for Stainless Steel at 18 cph, Specimen S-14

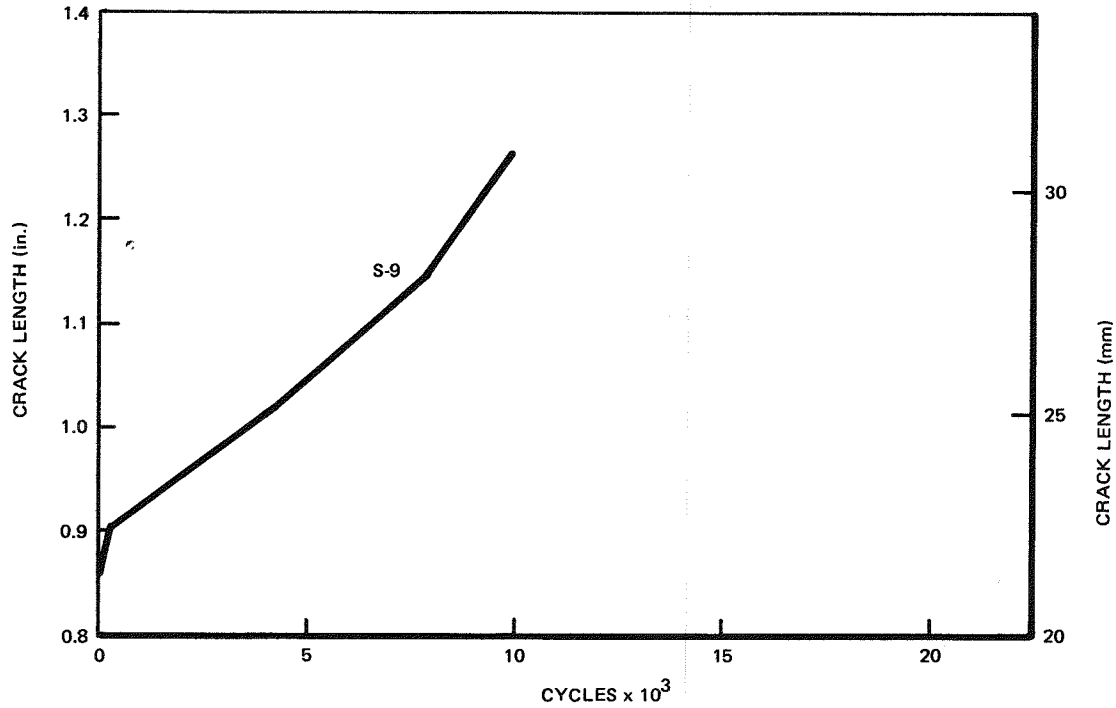

Figure H-47. Crack Length versus Number of Cycles for Stainless Steel at 18 cph, Specimen S-9

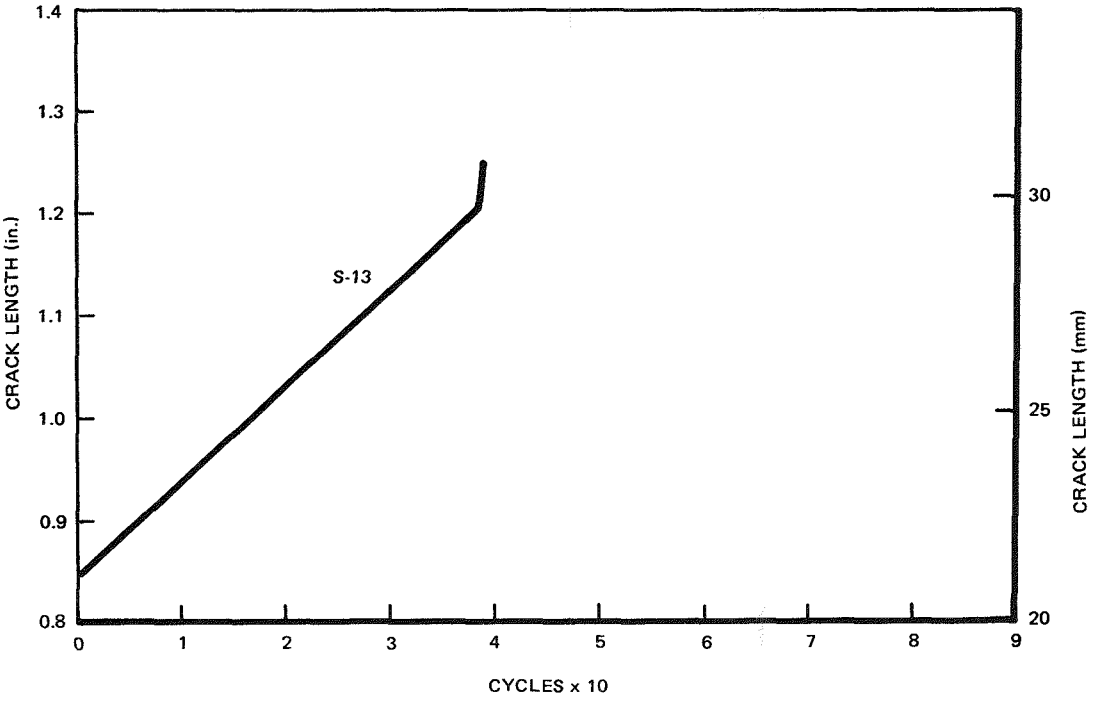

Figure H-48. Crack Length versus Number of Cycles for Stainless Steel at 300 cph, Specimen S-13

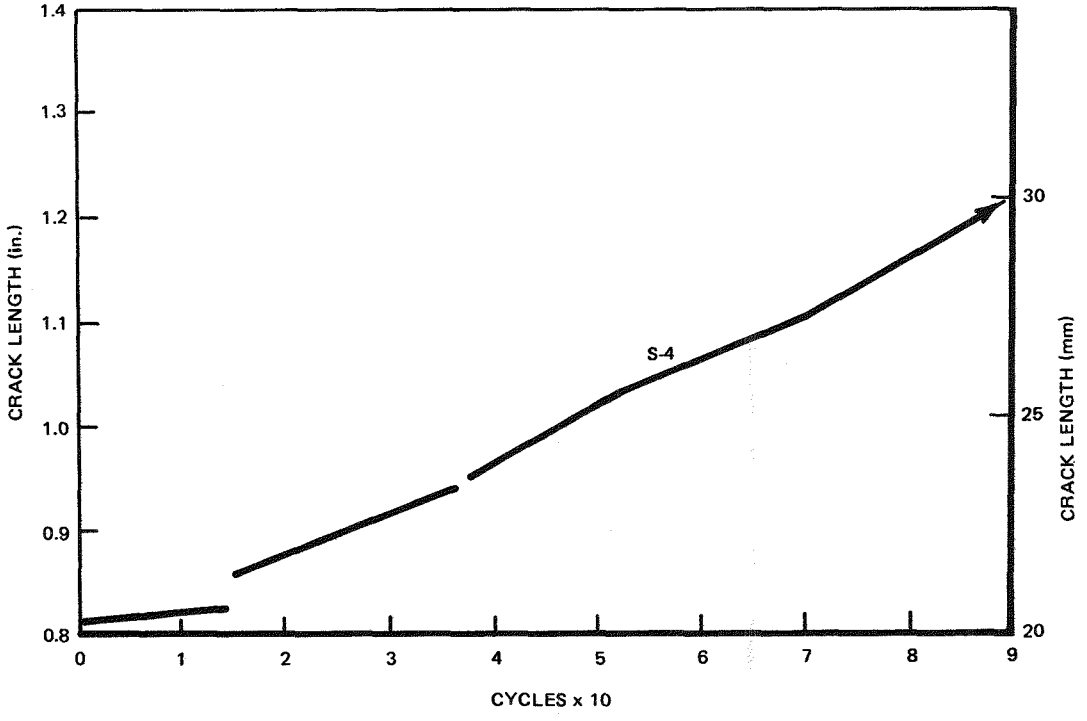

Figure H-49. Crack Length versus Number of Cycles for Stainless Steel at 300 cph, Specimen S-4

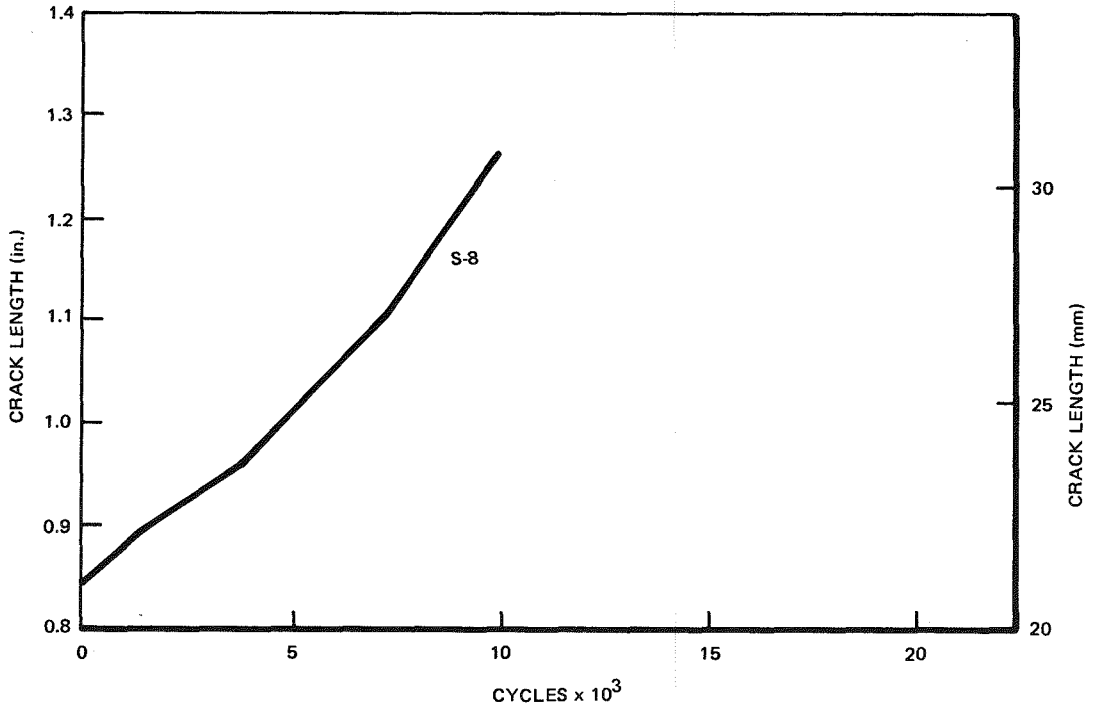

Figure H-50. Crack Length versus Number of Cycles for Stainless Steel at 18 cph, Specimen S-8

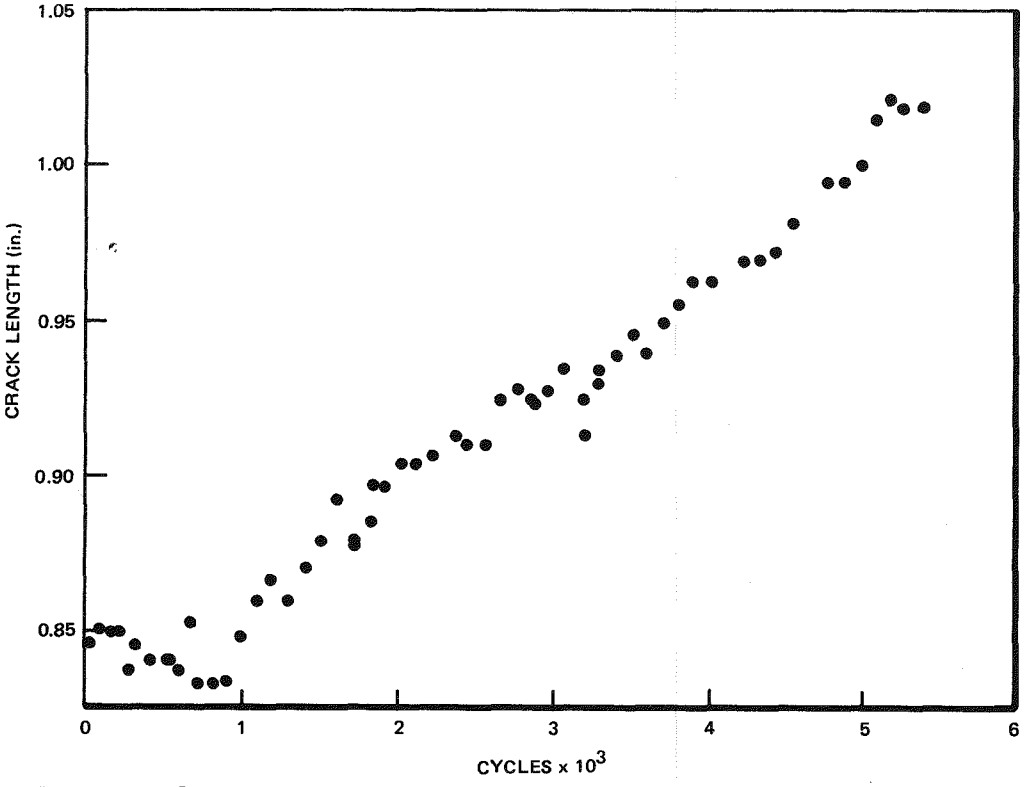

Figure H-51. Crack Length versus Number of Cycles for Stainless Steel at 4.4 cph, Specimen SS-1A

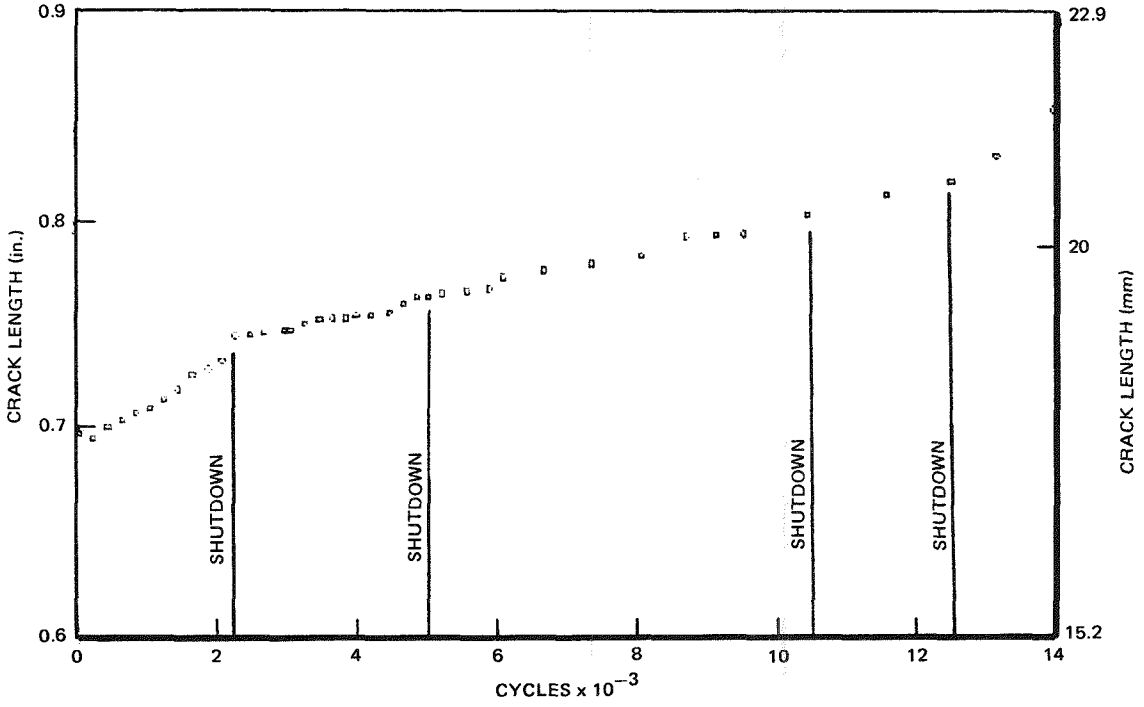

Figure H-52. Crack Length versus Number of Cycles for Stainless Steel at 7.5 cph, Specimen SS-10

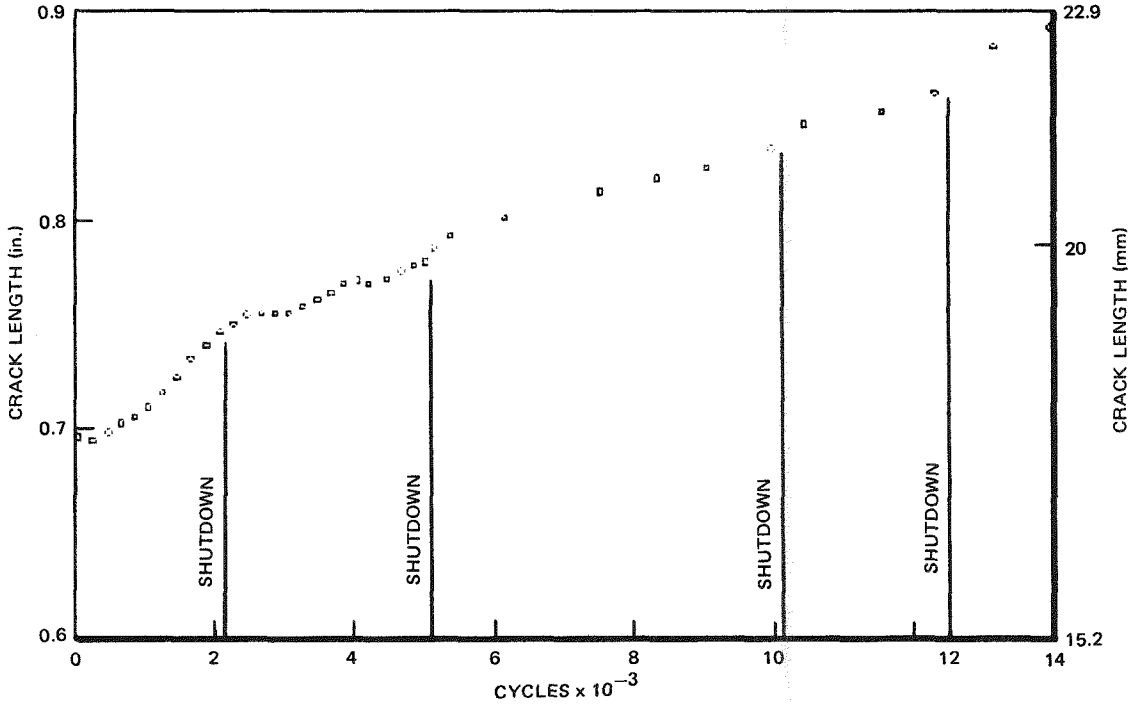

Figure H-53. Crack Length versus Number of Cycles for Stainless Steel at 7.5 cph, Specimen SS-11

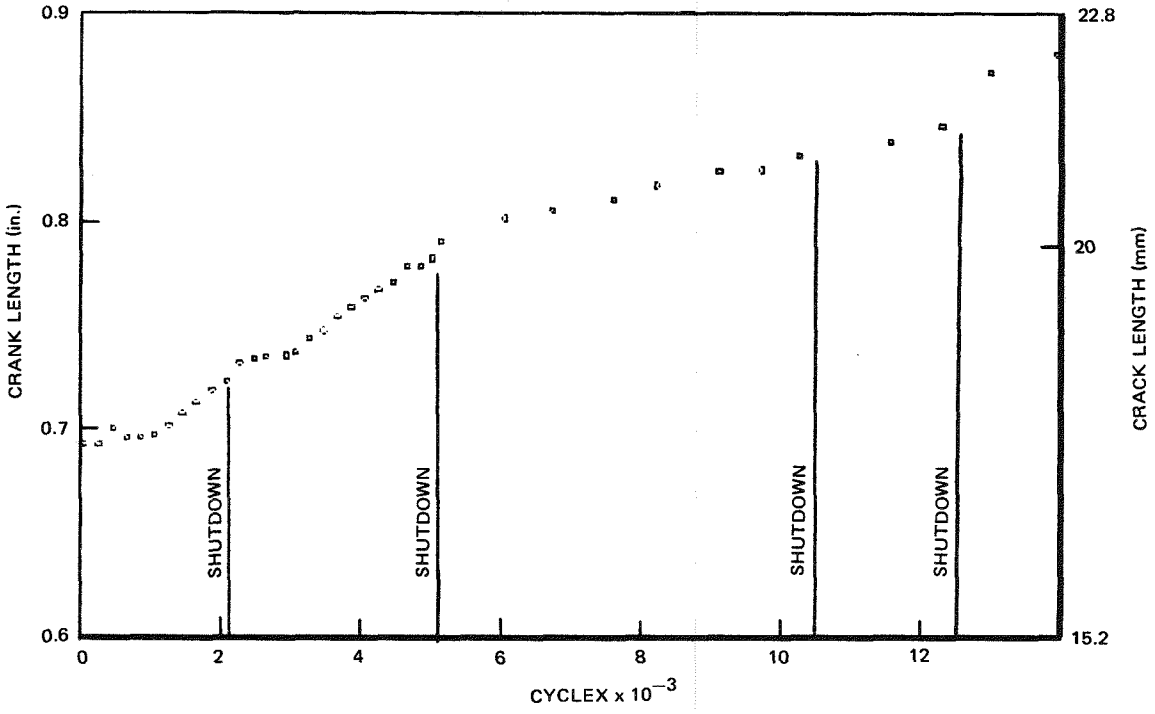

Figure H-54. Crack Length versus Number of Cycles for Stainless Steel at 7.5 cph, Specimen SS-12

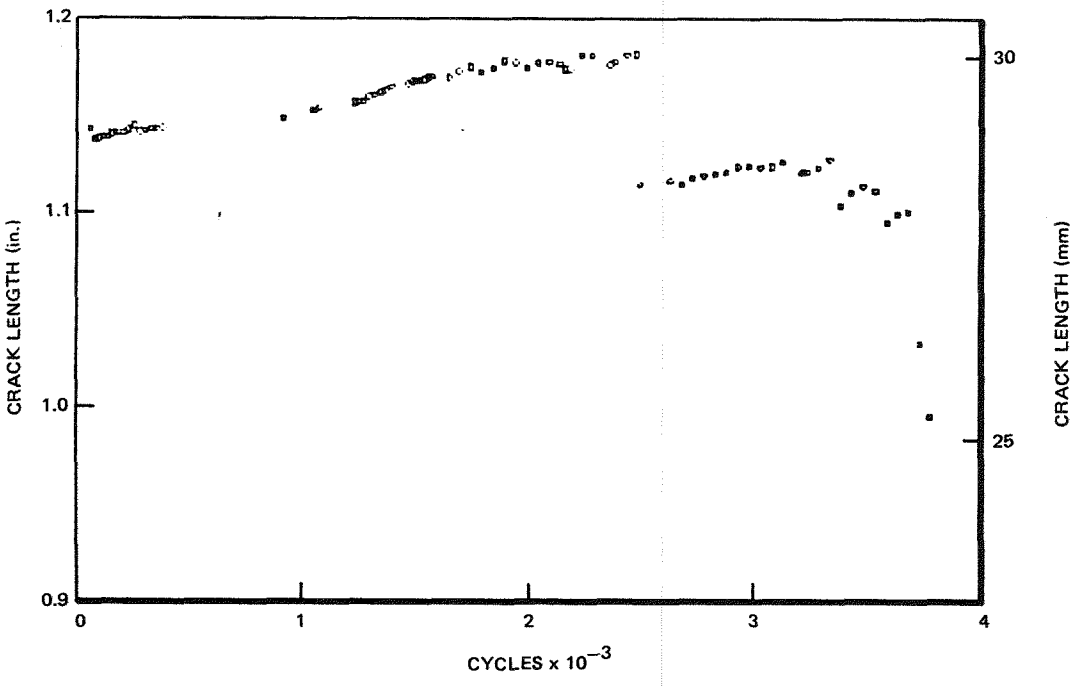

Figure H-55. Crack Length versus Number of Cycles for Stainless Steel at 7.5 cph, Specimen SS-6

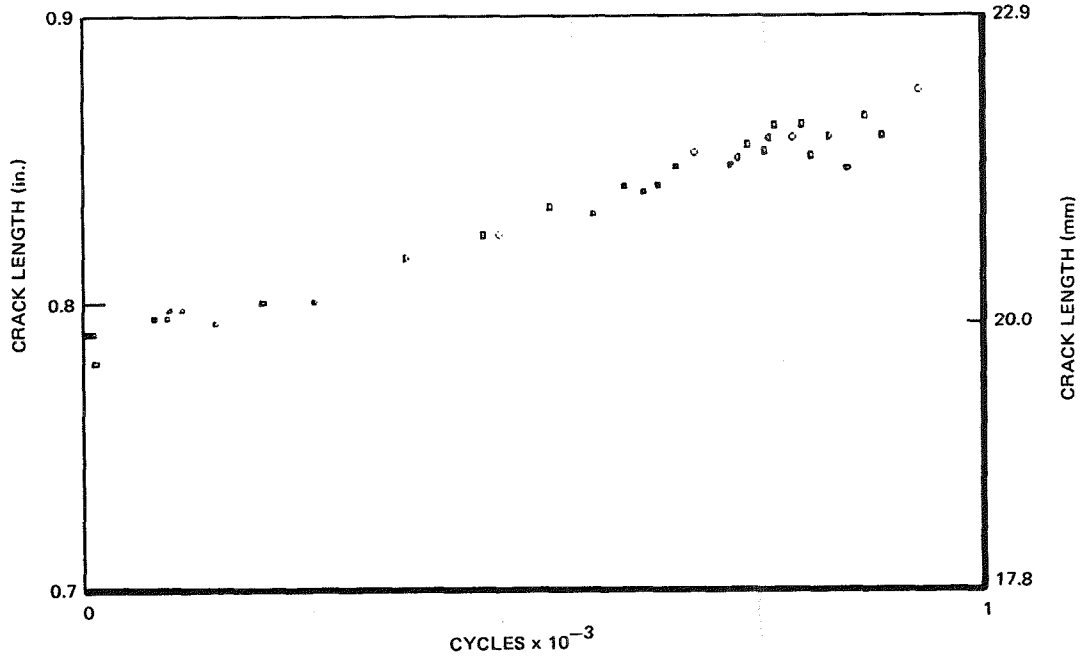

Figure H-56. Crack Length versus Number of Cycles for Stainless Steel at 0.74 cph, Specimen SS-7

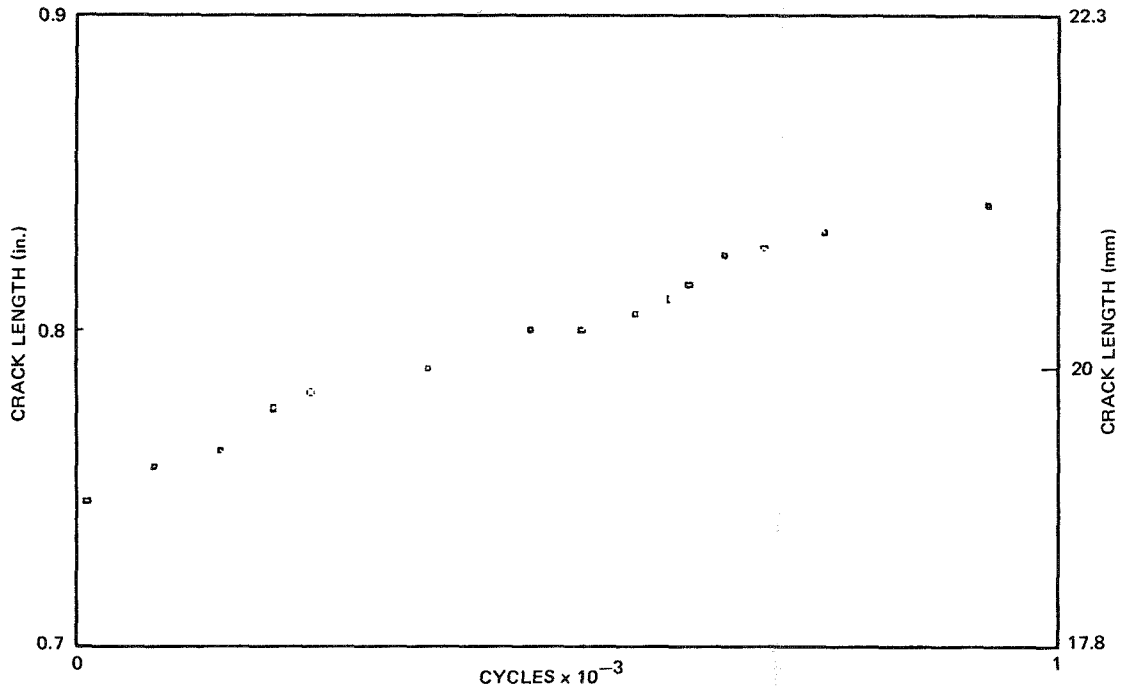

Figure H-57. Crack Length versus Number of Cycles for Stainless Steel at 0.74 cph, Specimen SS-21

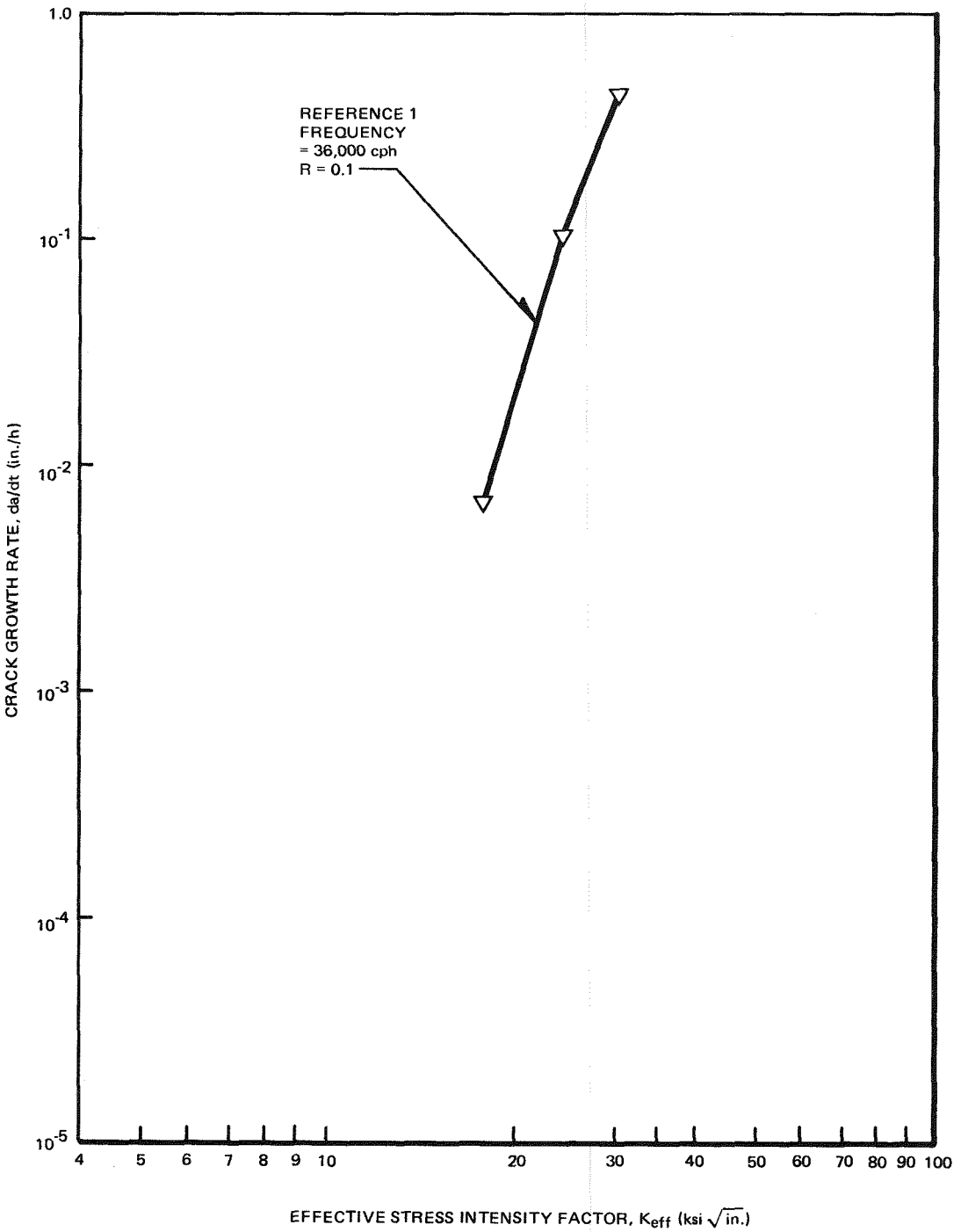

Figure H-58. Fatigue Crack Propagation Rates of Type-304 Stainless Steel Tested in 550°F Air - Nonsensitized

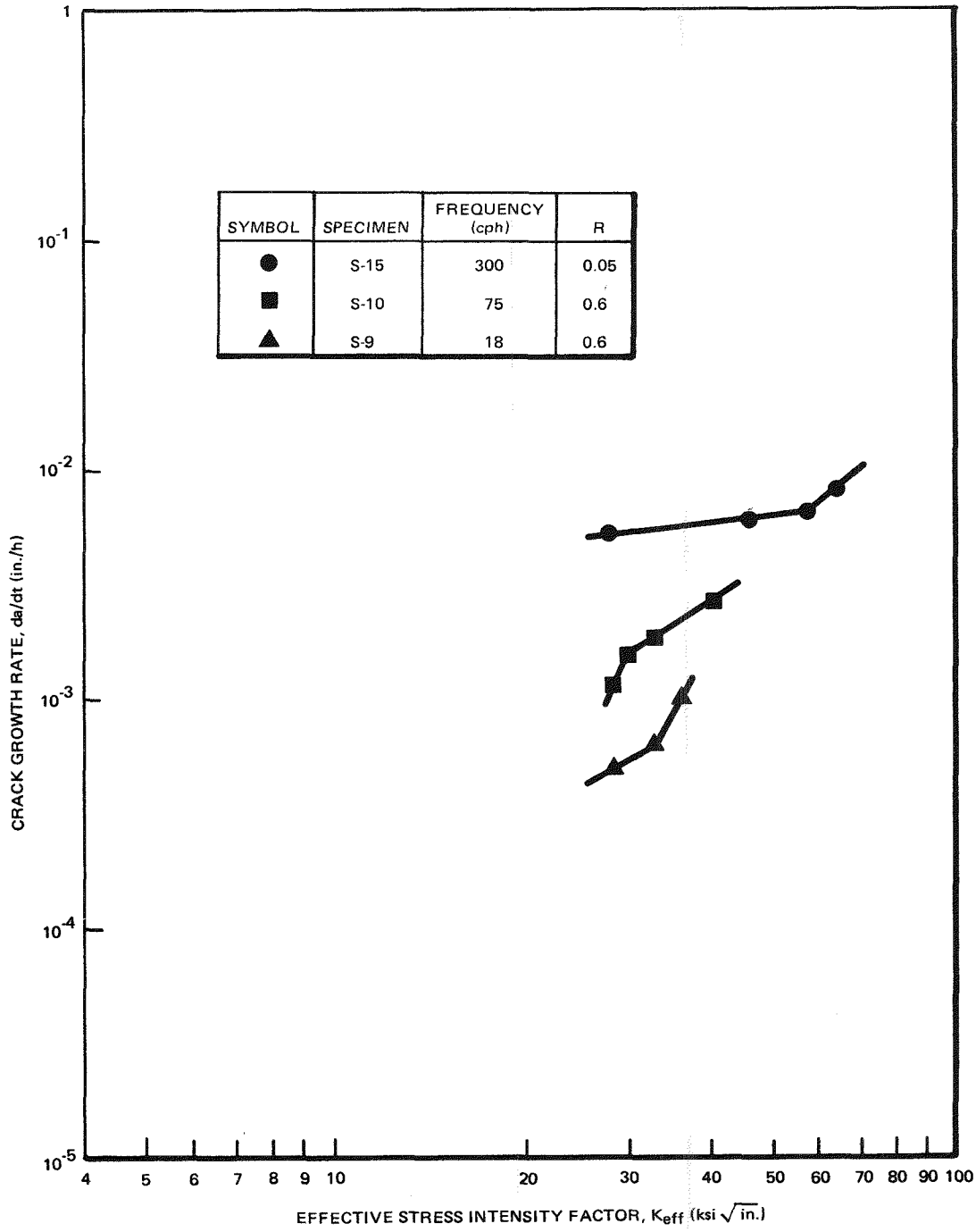

Figure H-59. Fatigue Crack Propagation Rates of Nonsensitized Type-304 Stainless Steel Tested in 550°F Water, 0.2 ppm Oxygen

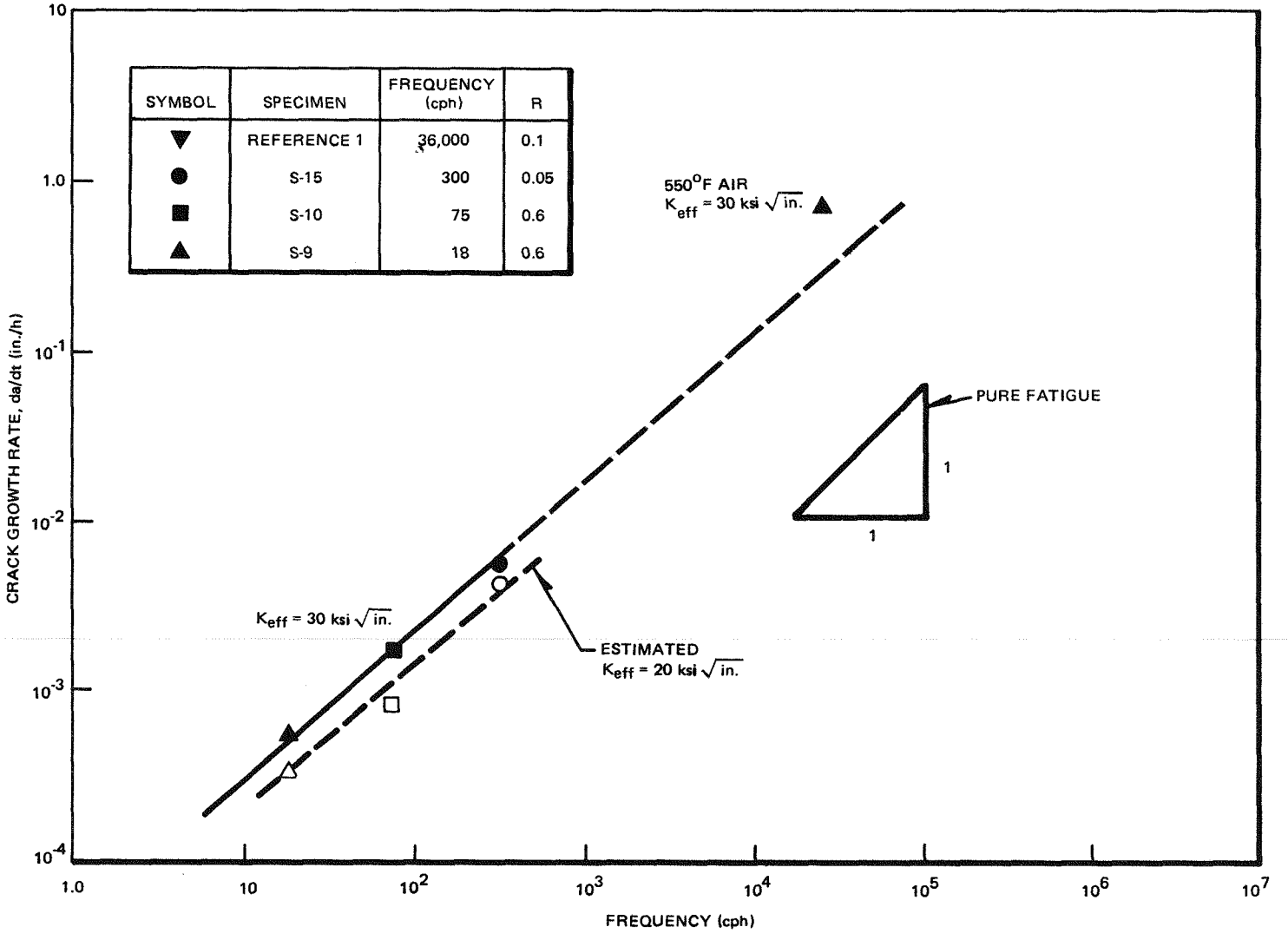

Figure H-60. Fatigue Crack Propagation Rates versus Frequency at K_{eff} = 30 ksi $\sqrt{in.}$ for Type-304 Stainless Steel Tested in 550°F Water

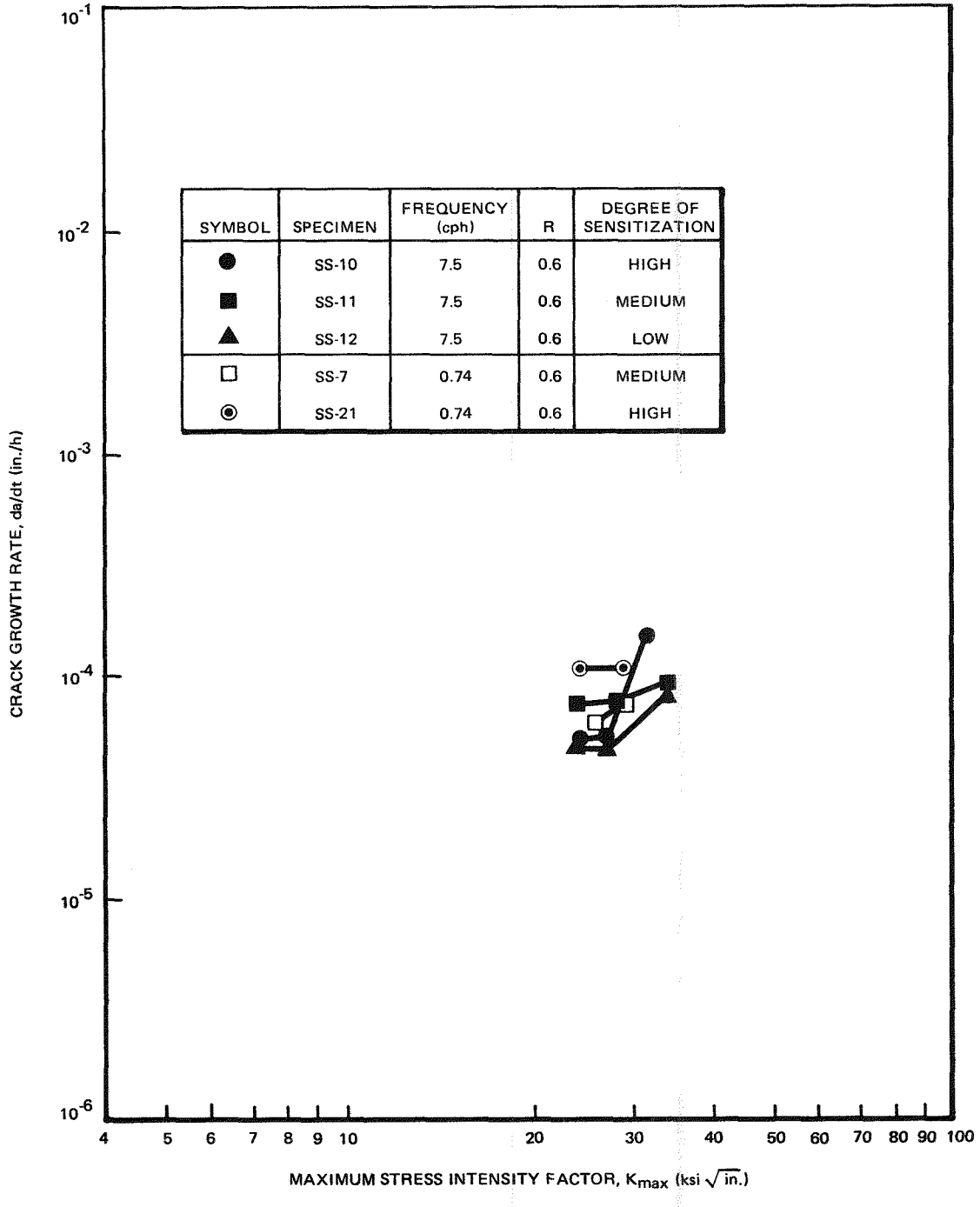

Figure H-61. Effect of Degree of Sensitization on Fatigue Crack Propagation Rates of Type-304 Stainless Steel Tested in 550°F Water, 0.2 ppm Oxygen

*Please note that the illustration(s) on this page has been reduced 10% in printing.

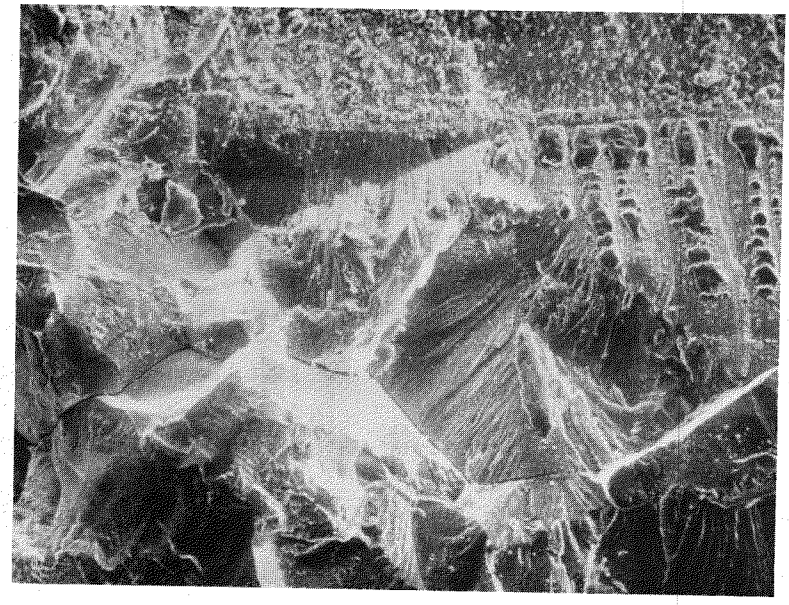

Figure H-62. Fracture Surface of Specimen SS-10 (High DOS), 150X

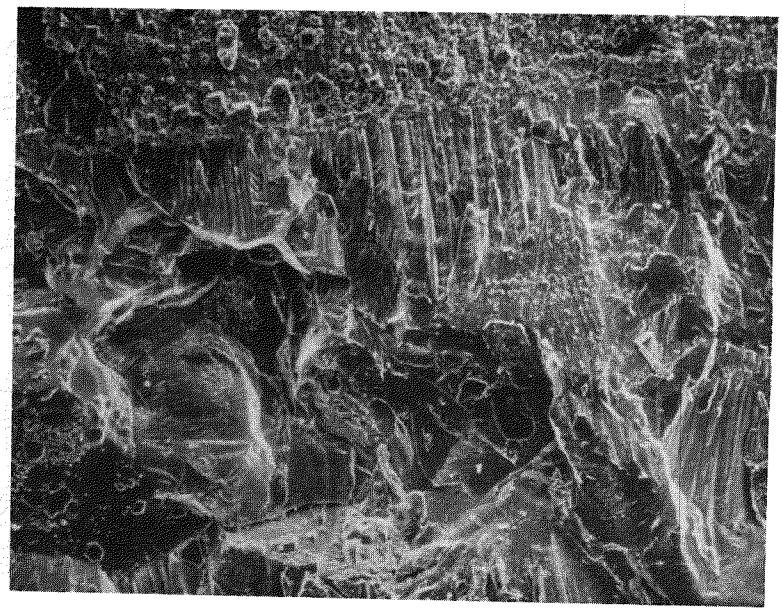

Figure H-63. Fracture Surface of Specimen SS-11 (Medium DOS), 150X

*Please note that the illustration(s) on this page has been reduced 10% in printing.

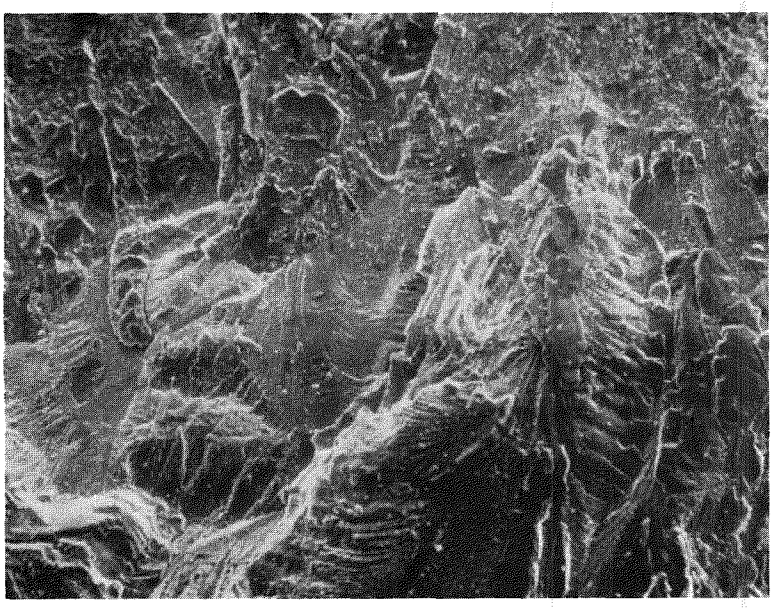

Figure H-64. Fracture Surface of Specimen SS-12 (Low DOS), 100X

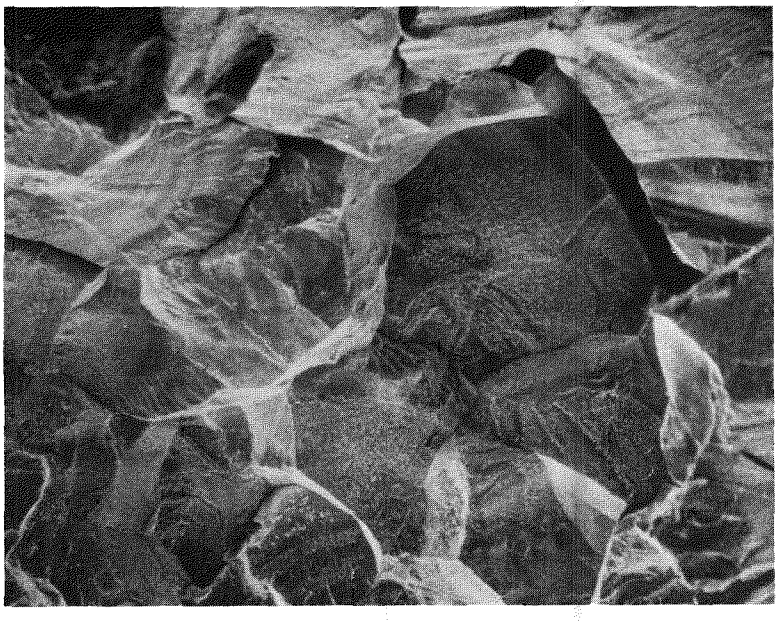

Figure H-65. Fracture Surface of Specimen SS-10 as Seen Near the Sides of Specimen, 100X

*Please note that the illustration(s) on this page has been reduced 10% in printing.

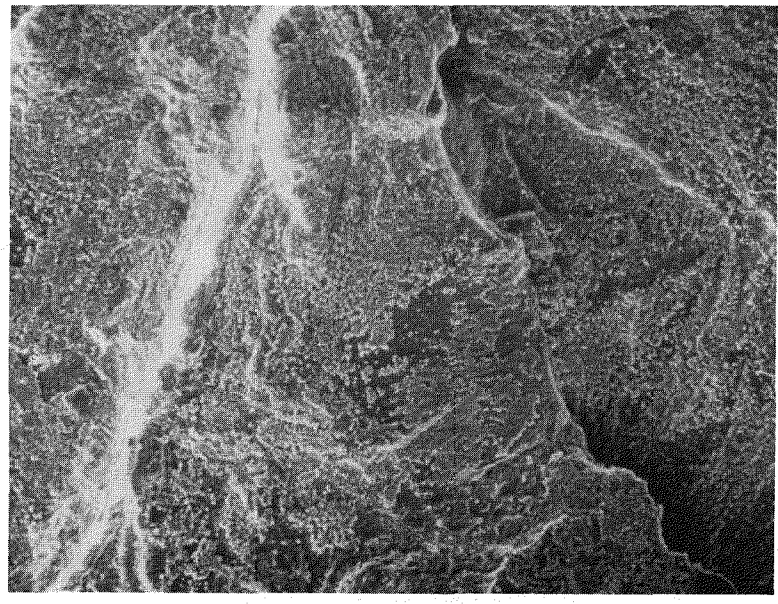

Figure H-66. Fracture Surface of Specimen SS-10, 150X; Photo Taken of Growth Region Associated with the High-Load Test Phase in Environment

Figure H-67. Fracture Surface of Specimen SS-7 (Medium DOS), 100X

*Please note that the illustration(s) on this page has been reduced 10% in printing.

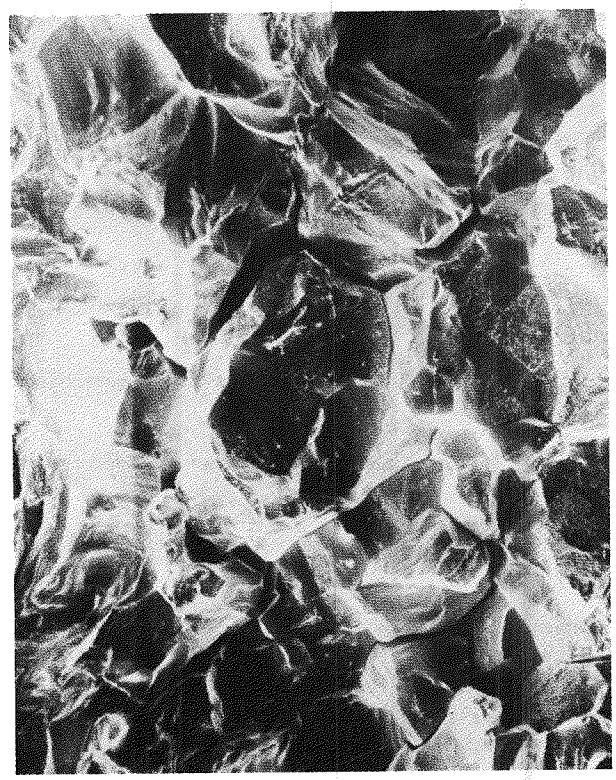

Figure H-68. SEM Micrograph of Specimen SS-21 Showing IGSCC, 4X

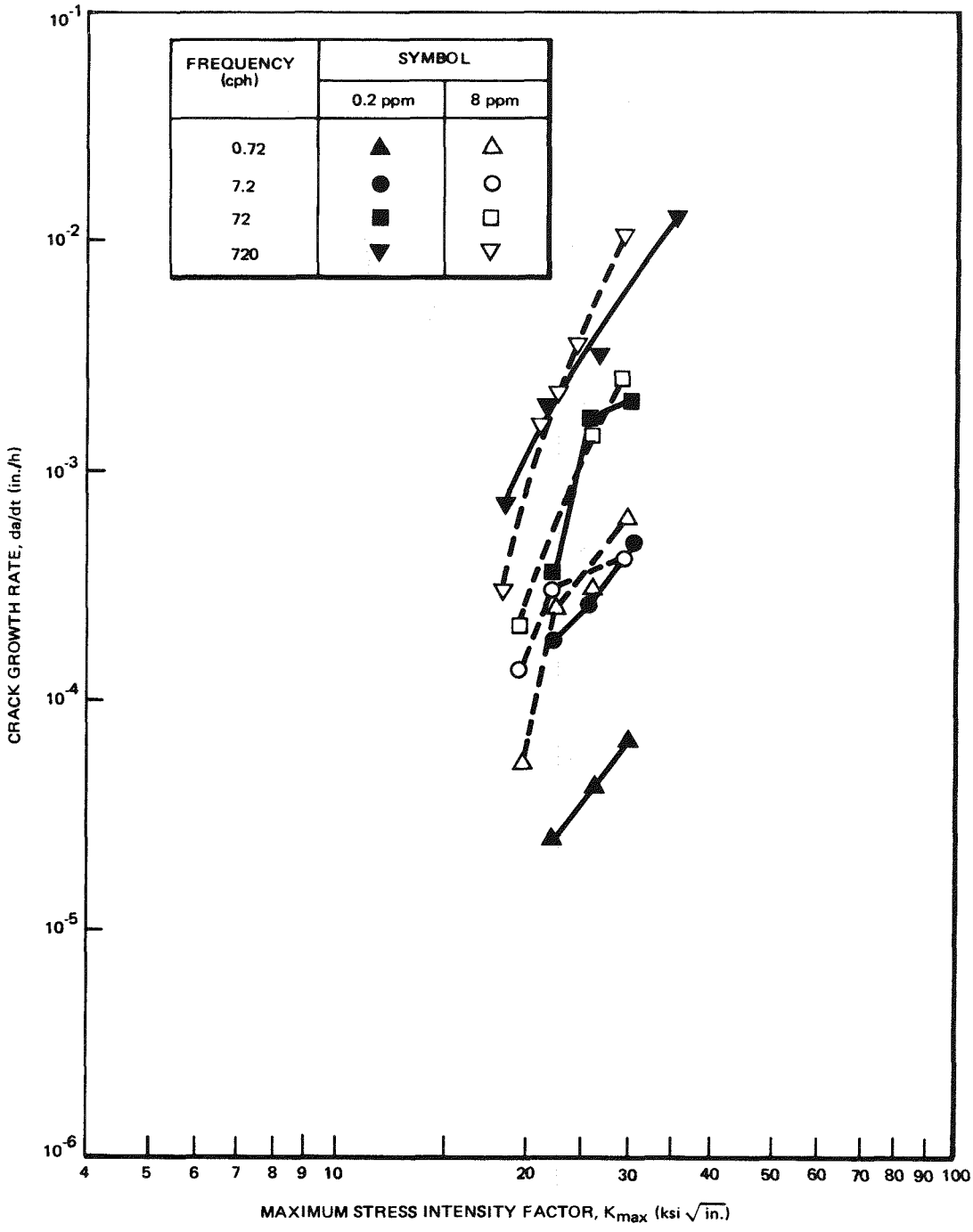

Figure H-69. Effect of Oxygen Concentration on Fatigue Crack Propagation Rates of Sensitized Type-304 Stainless Steel in 550°F Water with R-0.1, All Tests (Reference H-8)

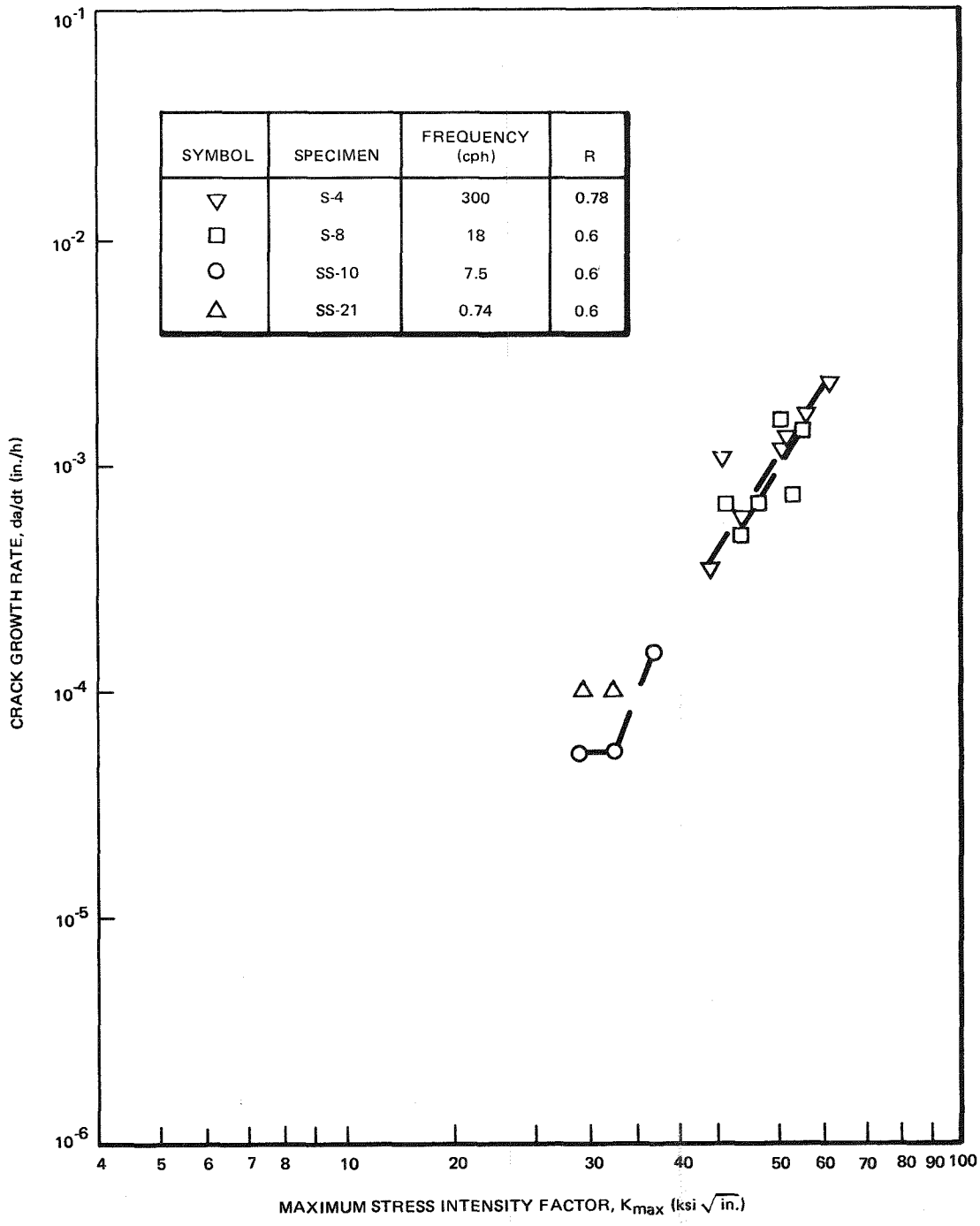

Figure H-70. Fatigue Crack Propagation Rates of Highly Sensitized Type-304 Stainless Steel Tested in 550°F Water, 0.2 ppm O_2

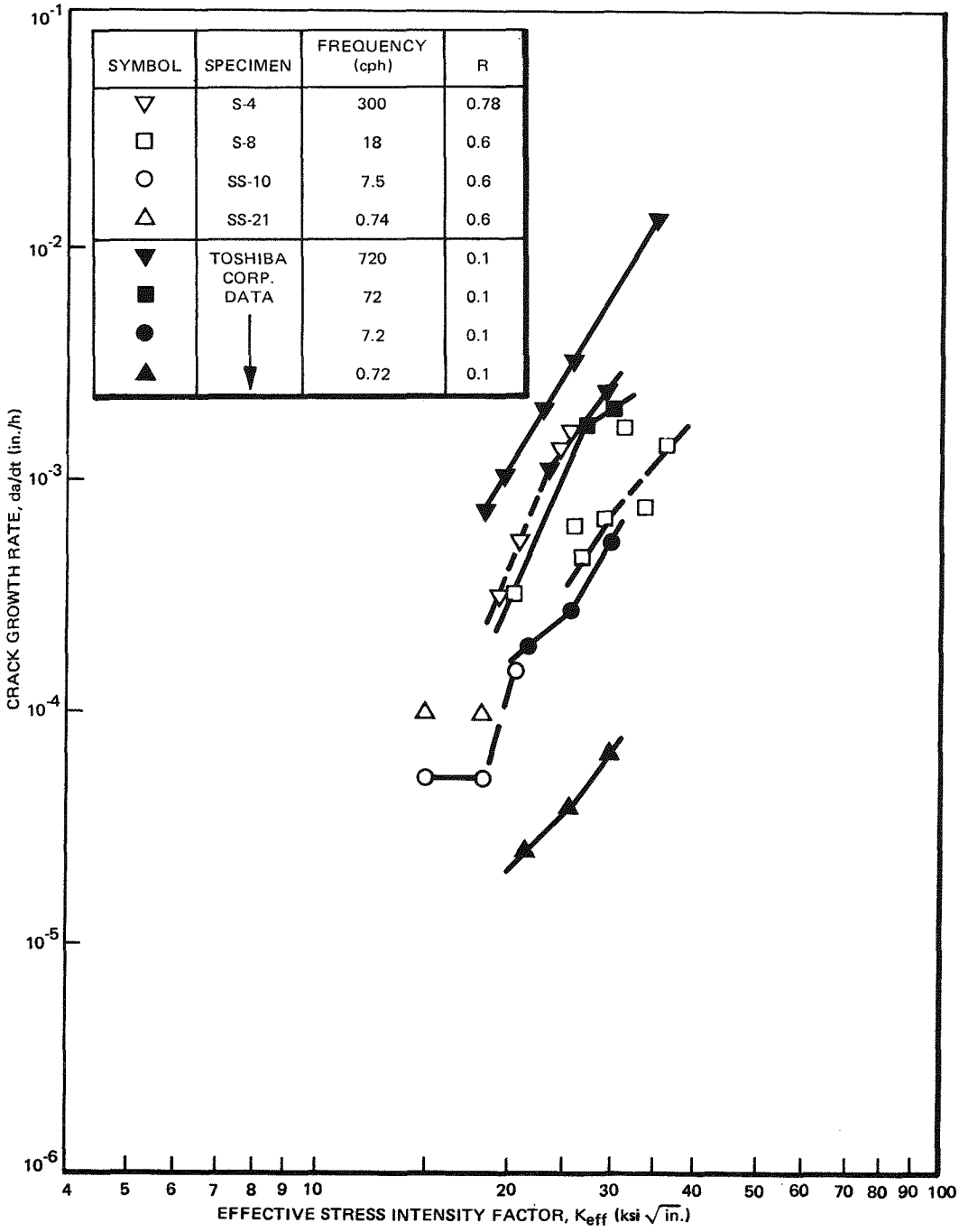

Figure H-71. Comparison of Fatigue Crack Propagation Rates with Toshiba Corp. Data for Sensitized Type-304 Stainless Steel Tested in 550°F Water, 0.2 ppm O_2 (Reference H-8)

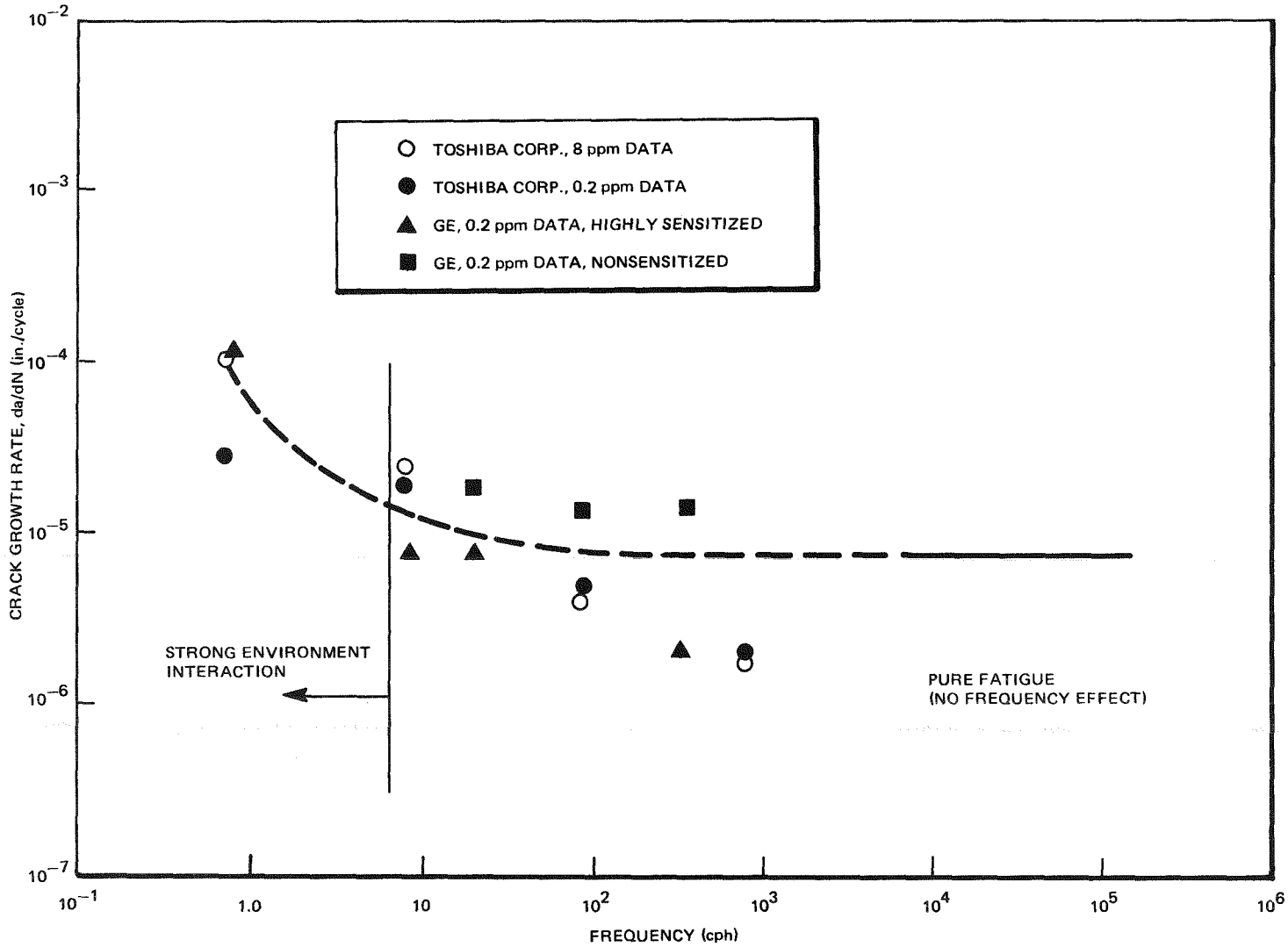

Figure H-72. Fatigue Crack Propagation Rates versus Frequency at K_{eff} = 20 ksi $\sqrt{in.}$ for Sensitized Type-304 Stainless Steel Tested in 550°F Water

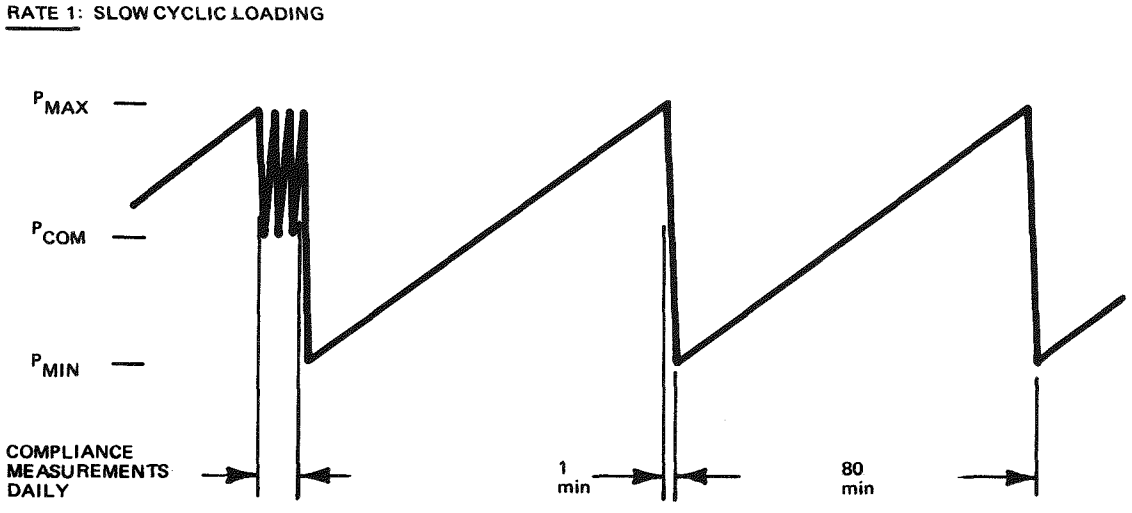

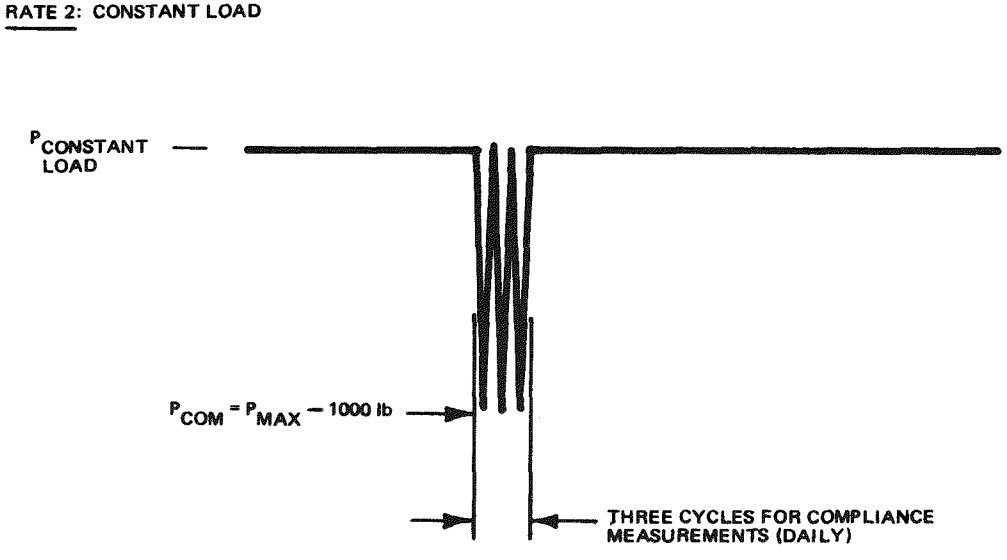

Figure H-73. Loading Schematic Constant Load SCC Crack Growth Test

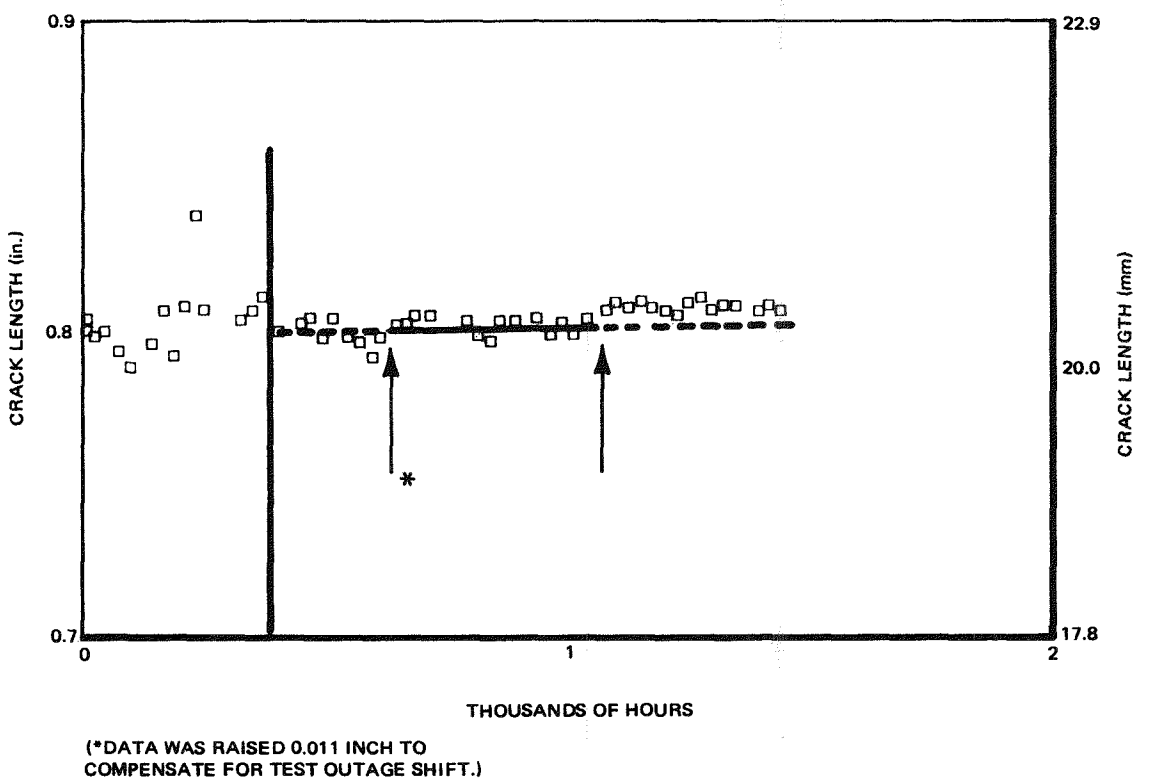

(*DATA WAS RAISED 0.011 INCH TO COMPENSATE FOR TEST OUTAGE SHIFT.)

Figure H-74. Compliance Determined Crack Length as a Function of Test Time: Specimen SS-70

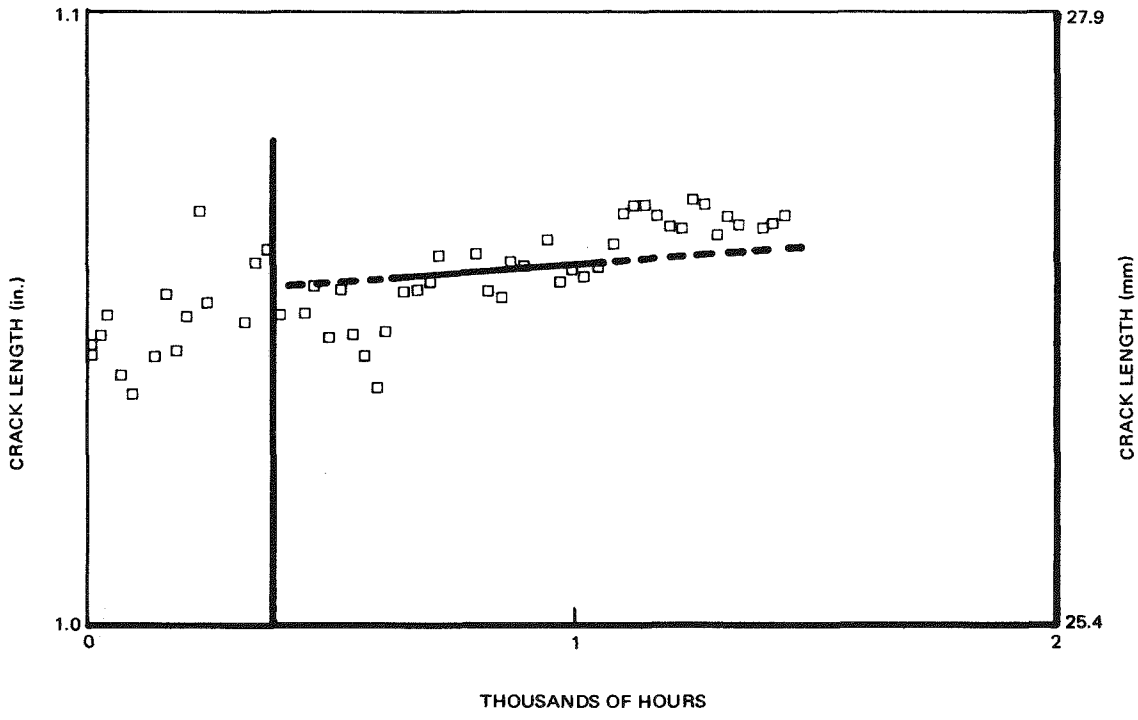

Figure H-75. Compliance Determined Crack Length versus Time: Specimen SS-71

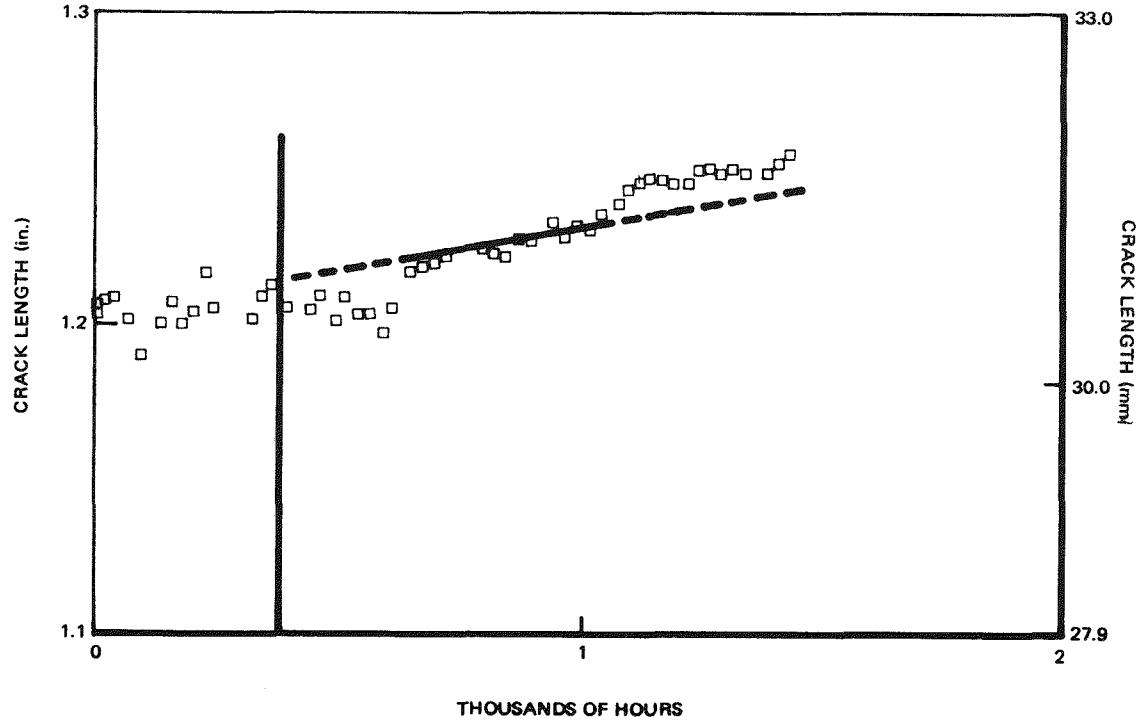

Figure H-76. Compliance Determined Crack Length versus Time: Specimen SS-72

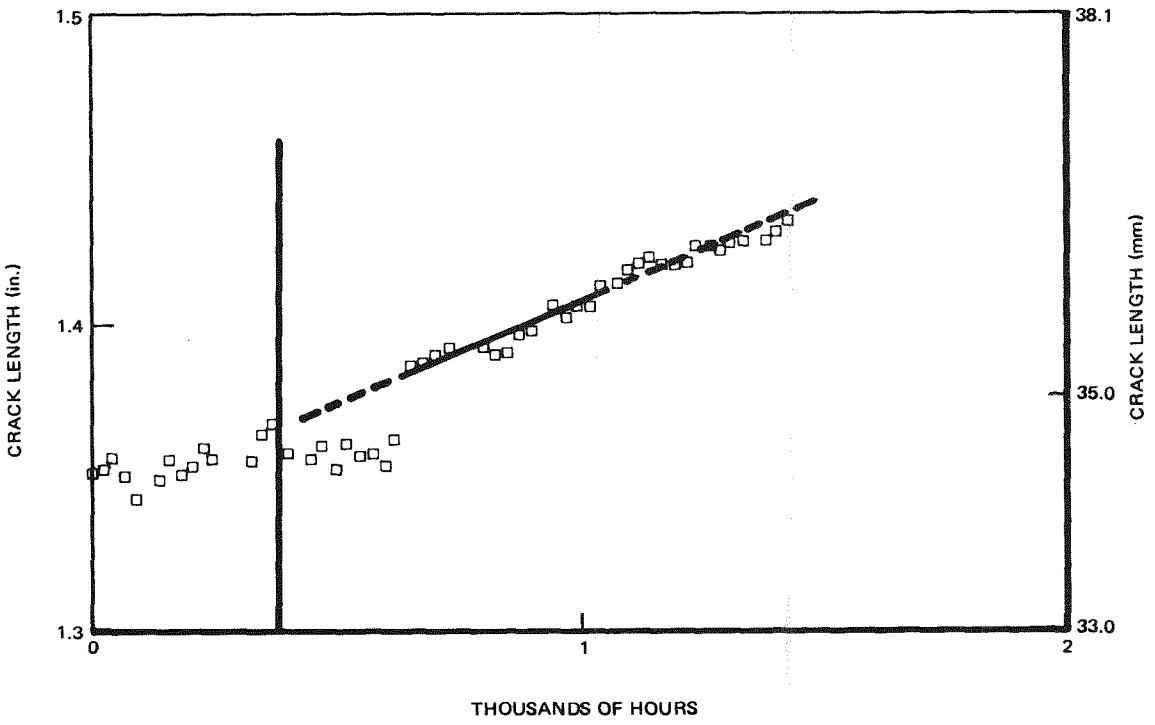

Figure H-77. Crack Length versus Time: Specimen SS-73

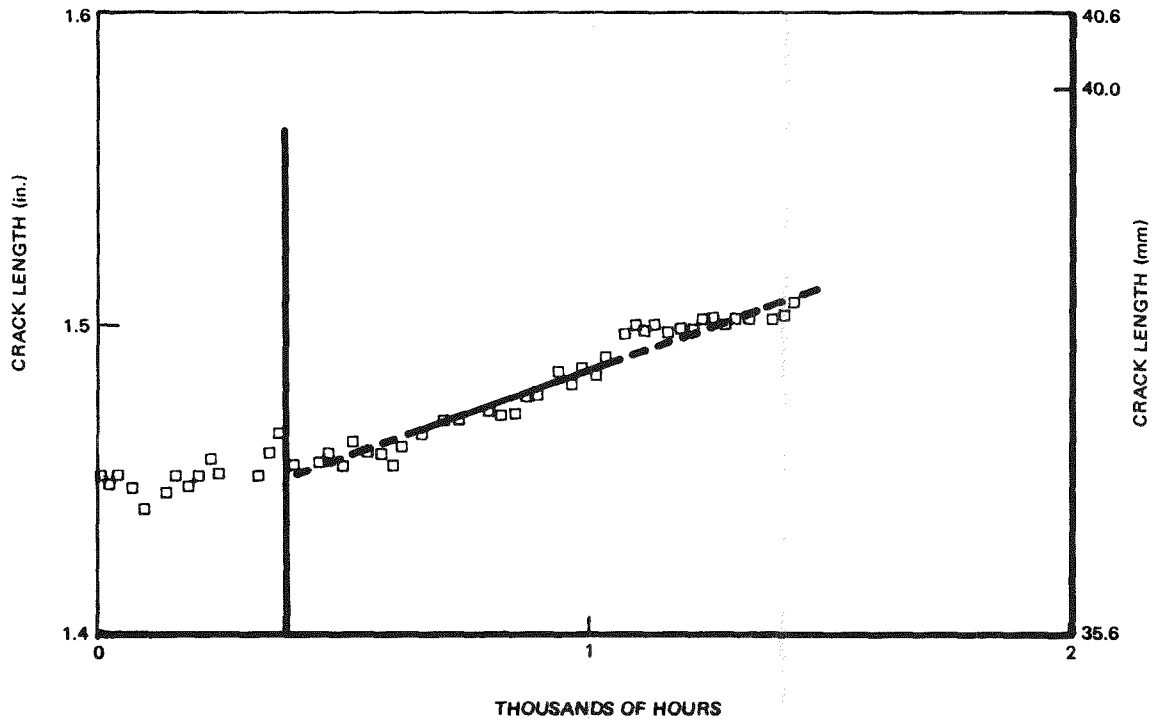

Figure H-78. Crack Length versus Time: Specimen SS-74

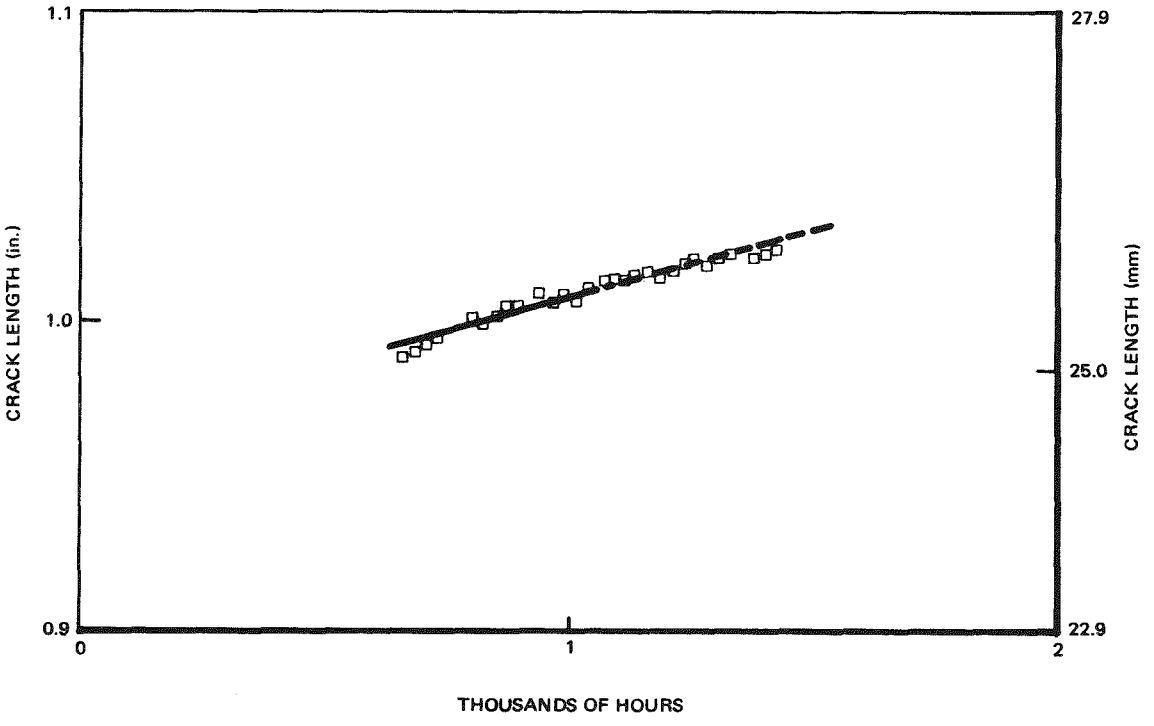

Figure H-79. Compliance Determined Crack Length versus Time: Specimen FS-2 (furnace sensitized at 1150°F for 24 hours)

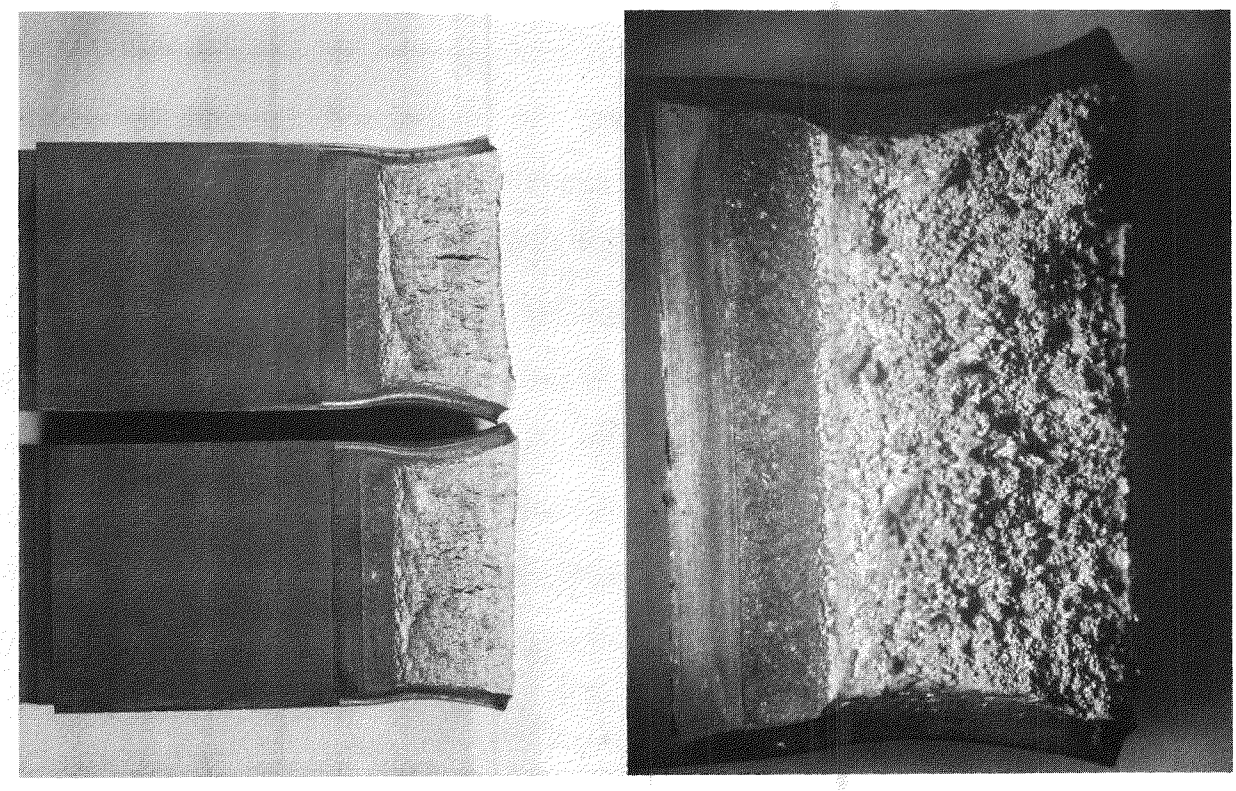

Figure H-80. Specimen SS-70 Fracture Surface Showing Thin Line of IGSCC Between Fatigue Precrack and Final Ductile Fracture

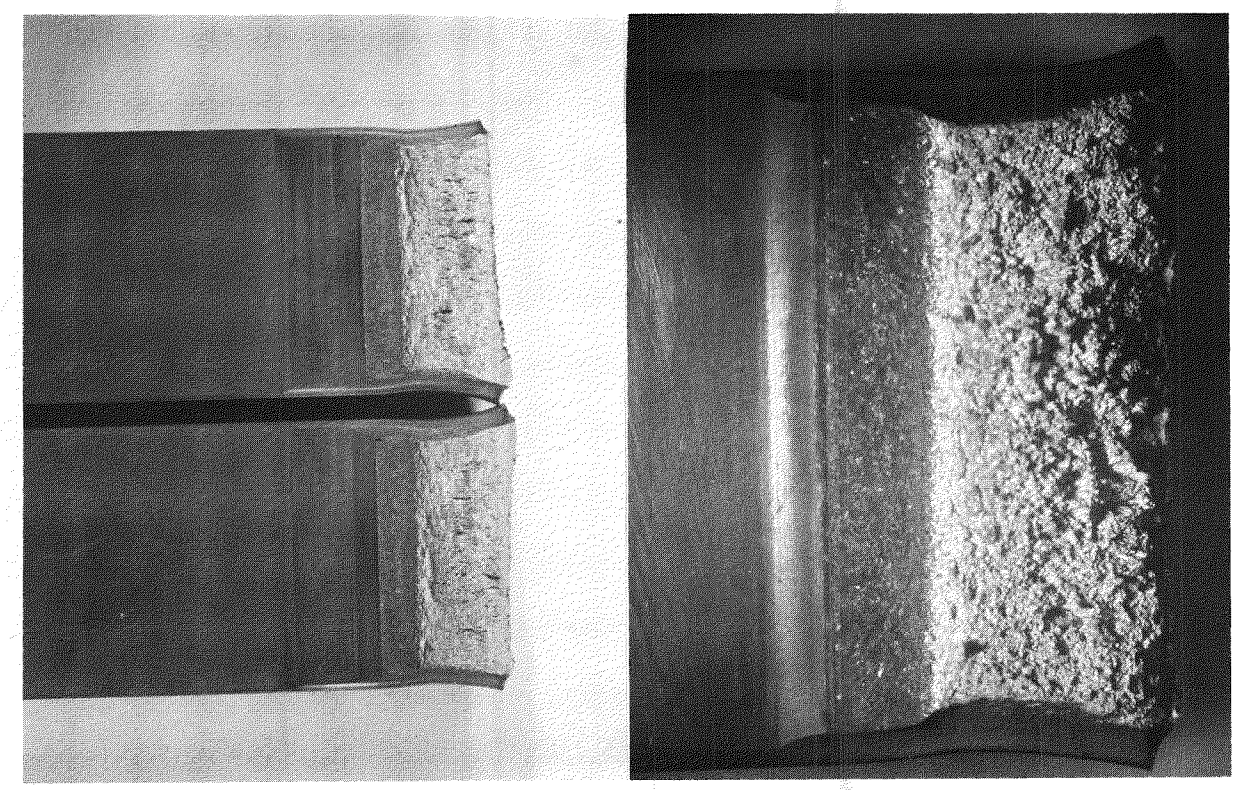

Figure H-81. Specimen SS-71 Fracture Surface Showing Limited IGSCC

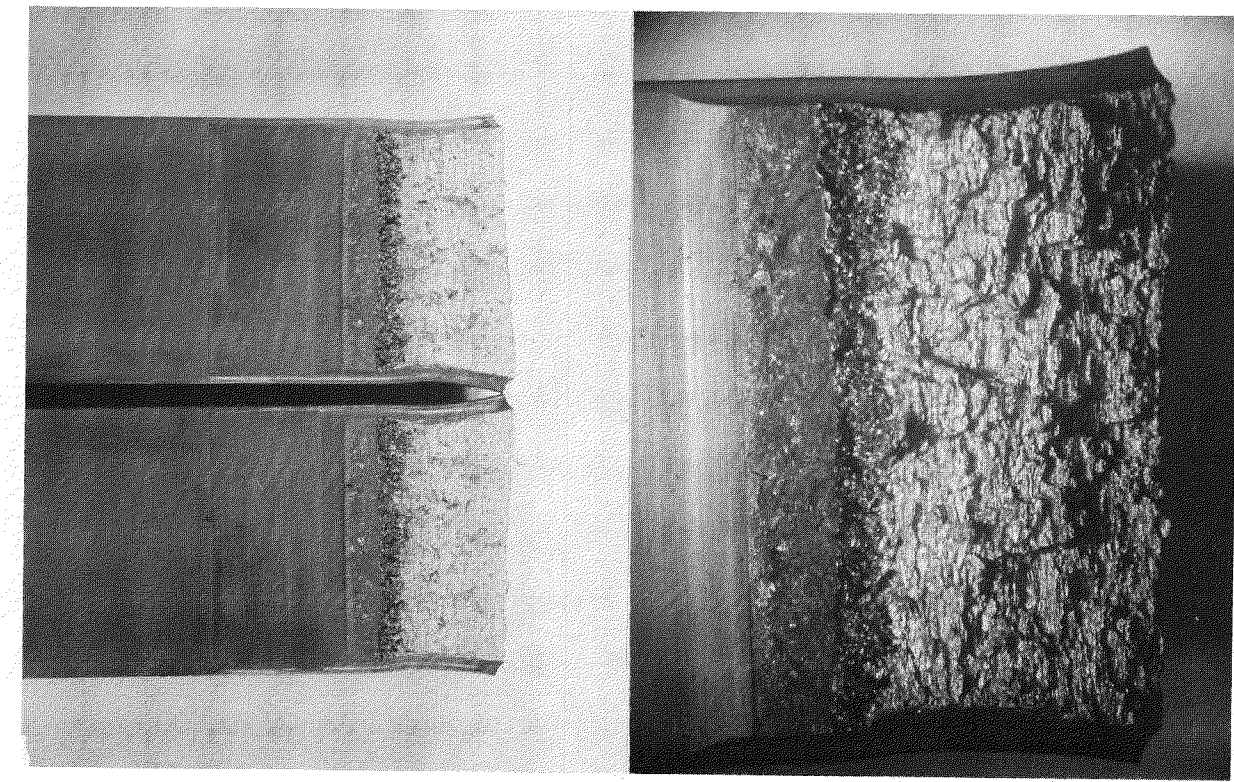

Figure H-82. Specimen SS-72 Fracture Showing Significant IGSCC

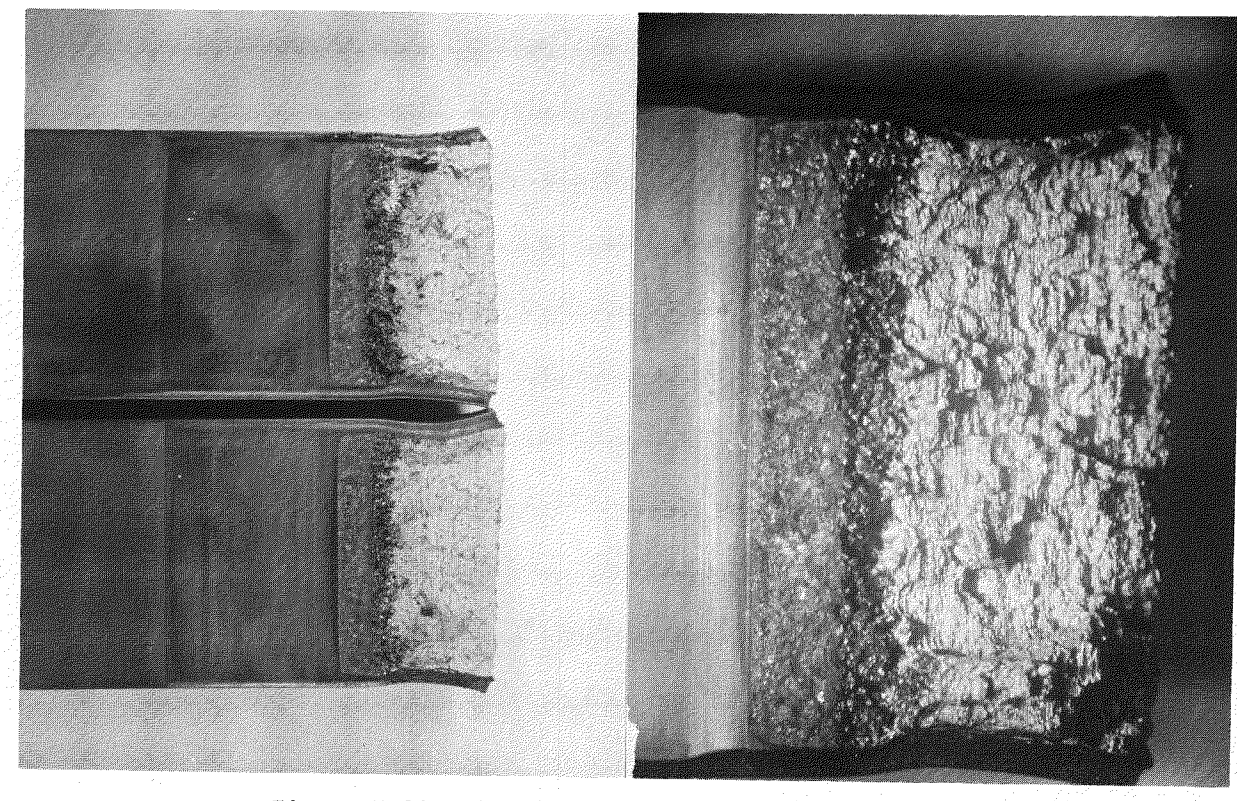

Figure H-83. Specimen SS-73: IGSCC Fracture

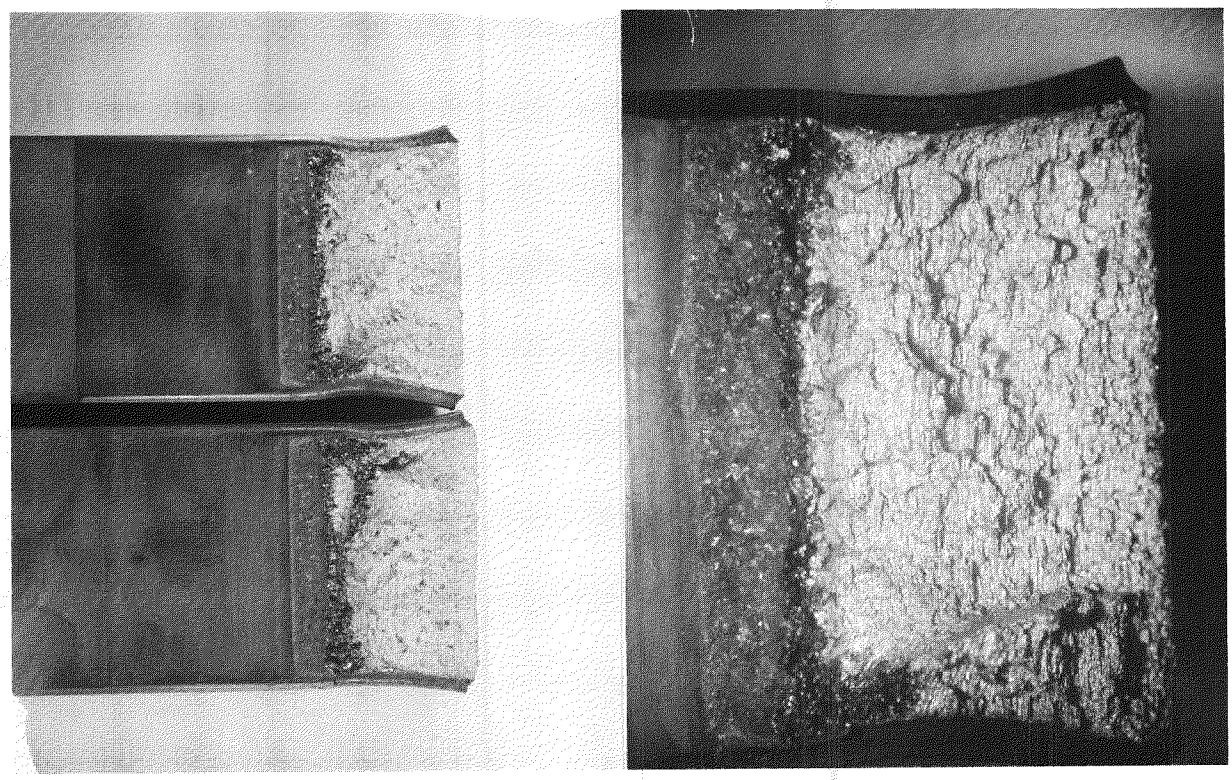

Figure H-84. Specimen SS-74 Fracture Surface

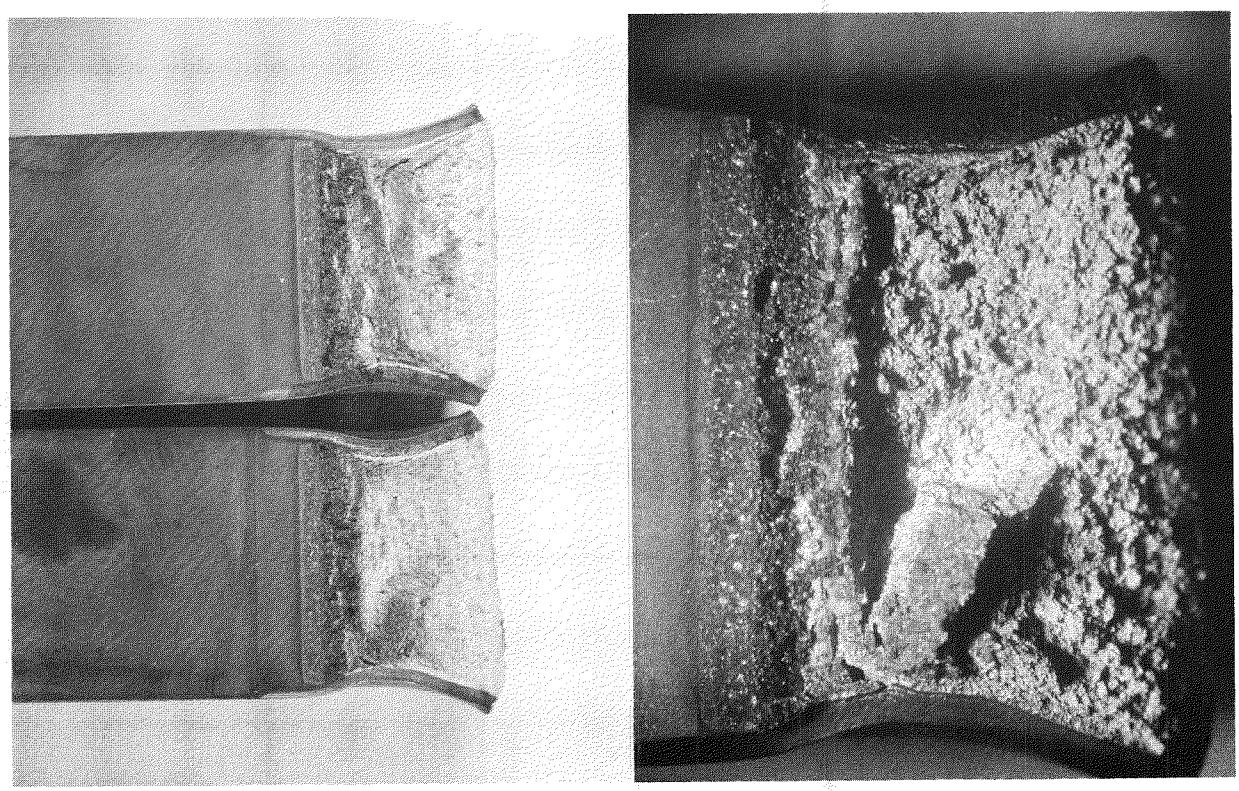

Figure H-85. Specimen FS-2 Fracture Surface

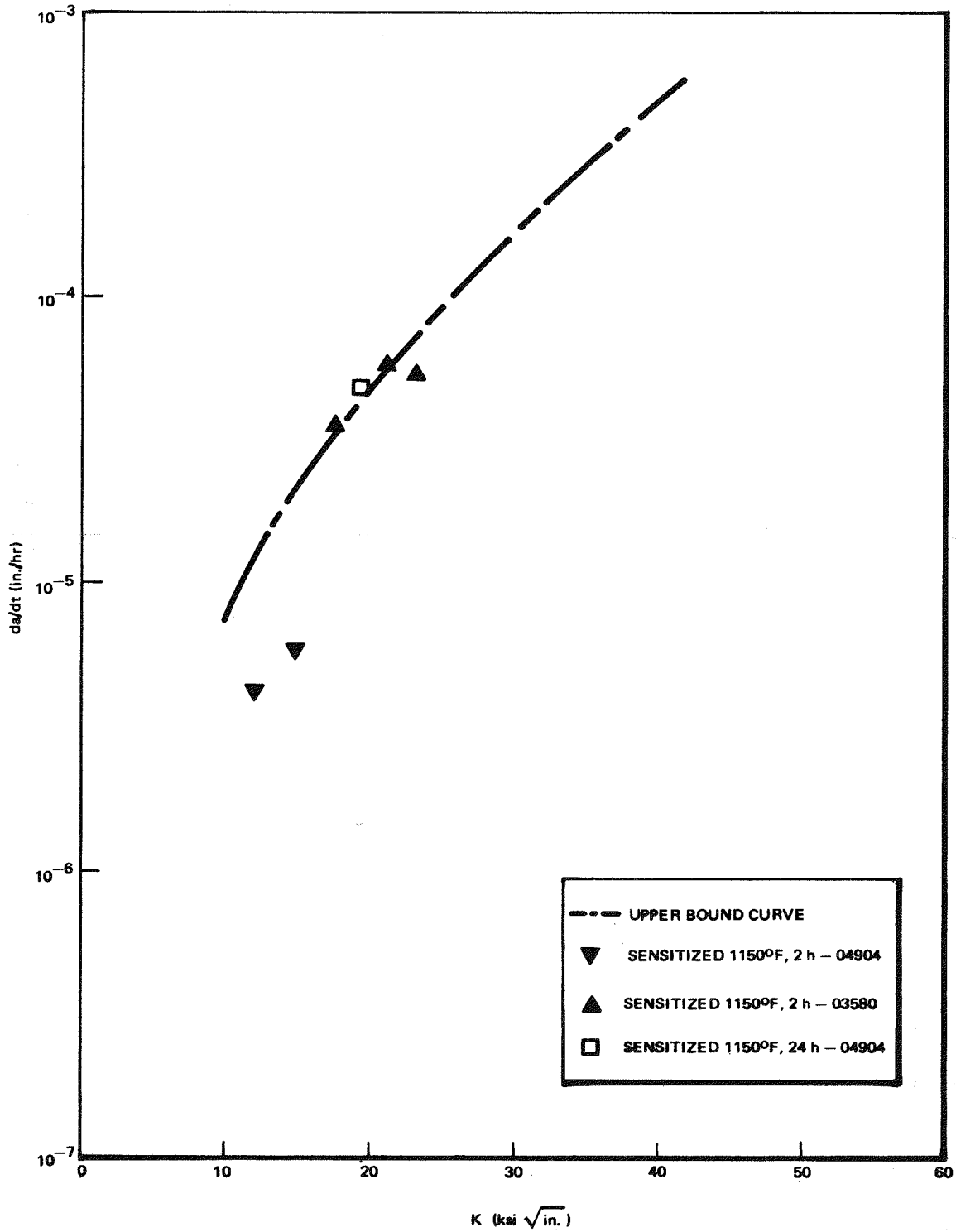

Figure H-86. Constant Load Crack Growth Rates Measured as a Function of Stress Intensity in Sensitized Material Tested in 0.2 ppm O_2 Environment. Rates are average rates. Data from heats 03580 and 04904 compared to upper bound crack growth curve.

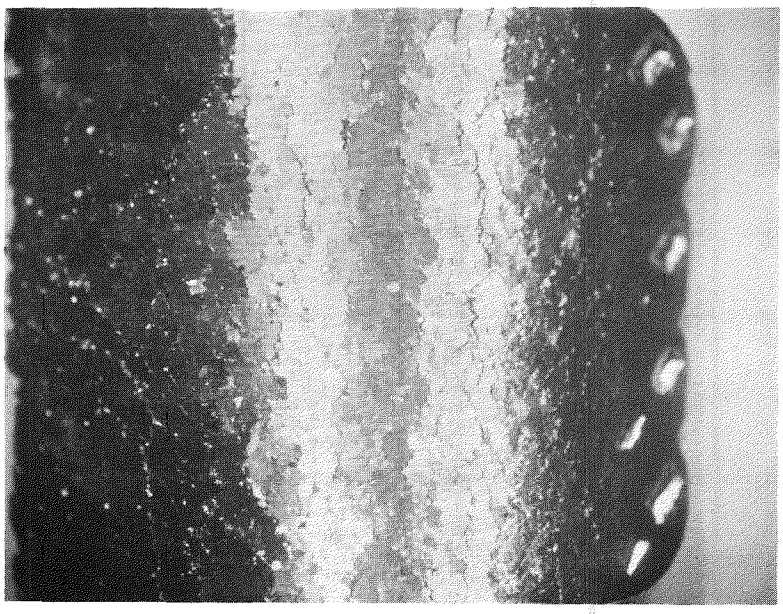

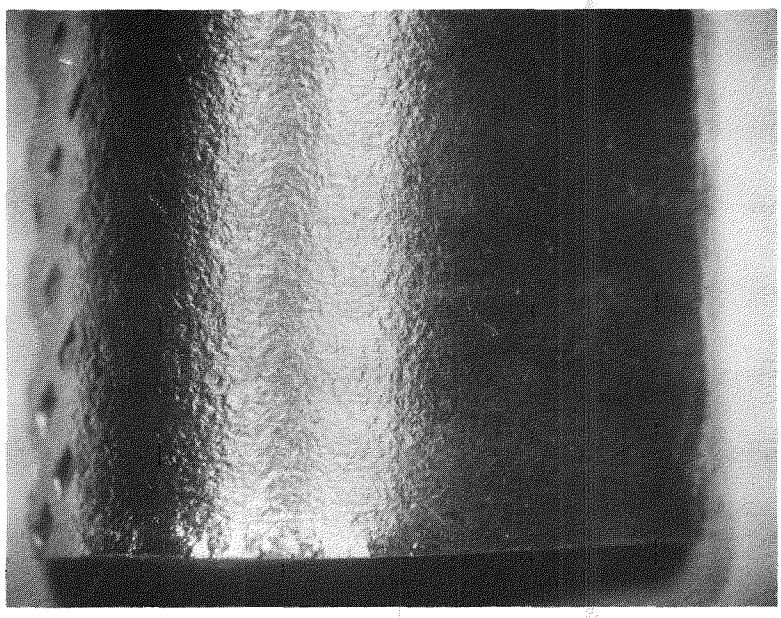

Figure H-87. Surface of Bent Coupons after A26E, Practice E Test from (a) Specimen SS-72, (b) Specimen SS-70

Appendix I

CONFIRMATORY PIPE TESTS
(R.M. Horn)

I.1 SUMMARY OF TEST PROGRESS

In order to confirm the predictive methodology, full size component tests are being conducted. A total of three tests are being conducted: two 4-in. Schedule 80 pipe tests and one 16-in. Schedule 140 pipe test. The tests' objective is to benchmark the crack growth predictions as well as to evaluate the crack/arrest concept in the 16-in. diameter pipe. Several parts of the pipe tests have been completed. First the pipe material was characterized for mechanical properties and for susceptibility to intergranular stress corrosion cracking (IGSCC). After verification that the pipe heats represented susceptible field material, test pipes were constructed. The pipes were built containing graphite wool compressed against selected heat-affected zones to form a crevice and promote IGSCC in oxygenated high temperature water. The pipes were exposed for up to 1200 hours and ultrasonic testing (UT) indicated cracks at selected locations. The next phase of testing, to be conducted in a contract extension, will perform the model verification.

I.2 INTRODUCTION

The work reported in Appendices E through H was generated to support a method capable of predicting the behavior of cracked stainless steel piping. These appendices present work that evaluates the effects of applied stress, residual stress, weld metal, loading mode, and degree of sensitization on crack growth of intergranular (IG) cracks in piping. Each variable is addressed separately. The objective of work described in this task was to perform a component test to verify the applicability of the prediction methods, synthesized from this laboratory data, to field pipes. To perform this verification, the pipes had to be manufactured to match field pipes. The confirmatory pipes had to respond to the welding manufacturing processes similar to field pipes, so that the sensitization level would be realistic. The sensitization would affect the crack growth rates adversely if an additional heat treatment was performed to overly sensitize the pipe material through the thickness. Secondly, because of the important role of residual stresses in the methodology, efforts to assure characteristic welded residual stresses had to be taken. Although the first

two requirements could normally be satisfied, it was necessary to precrack the pipes without compromising the representative nature of the pipes prior to benchmarking the model. This could be accomplished by using graphite wool to act as a crevice to promote IGSCC initiation as demonstrated by Ishikawajima-Harima Heavy Industries, Ltd. (IHI) (I-1). Electrodischarge machining could be used to produce cracks that could be used to benchmark the depth of cracking, but would probably relieve residual stresses necessary to start IGSCC. The methodology could work for any size pipe. Two different sizes of pipe have been selected for this task: 4-in. Schedule 80 and 16-in. Schedule 140 pipe. The 4-in. pipes will be used to verify crack growth rates alone. The IGSCC will initiate out of the shadow of the weld and will eventually grow through the wall. The large 16-in. Schedule 140 pipe simulates an actual large diameter recirculation system pipe. Because its wall thickness and weld geometry match those found in the field, this test will verify both crack growth and crack arrest. This appendix reviews the characterization, manufacturing and precracking phases of the test pipes. The actual testing is being conducted as an extension to the program and will be reported as an addendum to this document.

I.3 CHARACTERIZATION OF PIPE MATERIAL

The steels' chemical and mechanical properties as well as sensitization response were characterized for the heats used in the pipe tests. Heat 04836 was used for the 4-in. Schedule 80 test pipes. It has been used previously as the base heat in the Parametric Pipe program, EPRI Contract T112-1 (formerly RP1169-1). Heat 816208 was obtained for use in the large diameter test pipe, the focal test of this program. The properties are discussed below. Care was taken to be certain that the properties are typical of field material.

I.3.1 Chemical and Mechanical Properties

The chemical composition of the two heats of interest, 04836 and 816208, are listed in Table I-1. Both heats have 0.06% carbon minimum to ensure that the steel would sensitize readily. Both heats also meet the specification for Type-304 stainless steel. The mechanical properties measured at room temperature and at 550°F (288°C) are listed in Table I-2. The properties were reported for heat 04836 in earlier reports. The properties for the 16-in. Schedule 140 heat was measured from tensile specimens taken from the pipe material along the axial direction. These properties are typical of those measured in actual pipe material.

I.3.2 Characterization of Heat 04836: Susceptibility to IGSCC

The heat used for the 4-in.-diameter test pipes was used for pipe testing as part of RP 968 (I-2) and T112-1 (I-3). The heat was first characterized using standard methods to ensure that the material was susceptible to IGSCC in the as-welded condition. The pipe testing portion of T112-1 which has been aimed at investigating stress and environmental variables on IGSCC used this heat to differentiate the effect of these variables on IGSCC. The heat is susceptible to IGSCC.

I.3.3 Characterization of Heat 816208: Susceptibility to IGSCC

I.3.3.1 Creviced Bent Beam Tests. Creviced bent beam tests with graphite wool crevices were performed to determine the IGSCC susceptibility of heat 816208 and to estimate the exposure time needed to introduce defects in specimen LPT-16-1. The carbon content of 0.06% was picked to assure susceptibility. The material conditions tested were (1) as-received base metal, (2) base metal plus low temperature sensitization (LTS), (3) as-welded, and (4) welded plus LTS. The welded conditions were cut from a full-thickness ring weld made from the heat of interest. Tests were conducted at 0.5% strain for the as-welded condition and at 1.0% strain for all four material conditions. The exposure time to 8 ppm O_2 water at 288°C ranged from 150 to 600 hours, as shown in the test matrix of Table I-3. No cracking was produced in any condition in the 150 and 300-hour exposure. Both transgranular (TG) and IG cracks were observed in the as-welded specimens (Figure I-1) for specimens strained to 0.5% and 1.0% with IG being limited to the heat-affected zone.

The maximum IG depth (24 mils) in a 1.0% strain as-welded specimen was 10 times the maximum depth of IG in the 0.5% strain, as-welded specimen. Transgranular cracking occurred in both base metal and LTS-treated base metal exposed for 600 hours. Based on these results, the pipe test phase to introduce defects in Specimen LPT-16-1 was expected to produce IG cracks in the heat-affected zone. The cracks initiated in the heat-affected zone location, even at the 0.5% strain level. It is expected that the strain levels in the pipe due to residual stresses plus applied stresses would promote IG in the proper areas under the compressed graphite wool.

I.3.3.2 EPR Sensitization Tests. EPR measurements were made on the inner diameter surface of the same welded joint from which creviced bent beam (CBB) specimens were removed. Three measurements were made at about a 0.125-in. increment from the Weld Fusion Line (WFL) and a fourth was taken in the base metal 2 inches from the WFL as depicted in Figure I-2. The first measurement, covering the weld HAZ, yielded an EPR reading of 12.2 C/cm^2, while the successive readings were 1.1, 0.3, and 0.1 C/cm^2. These results indicate that the weld HAZ is sensitized and should be

susceptible to IGSCC, which was verified by the graphite wool CBB tests. The base metal is not sensitized.

I.3.3.3 Constant Extension Rate (CERT) Tests. CERT tests were also performed on material with conditions similar to those of the CBB tests. The test matrix and results are presented in Table I-4. Testing was completed on the as-welded specimens. Two specimens exhibited mixed transgranular and intergranular cracking; one failed by ductile overload and another had TGC initiation, followed by ductile overload. Figures I-3 and I-4 display the fracture surfaces of the mixed-mode failed specimens. Cracking occurred in the weld HAZ, as expected. Figure I-5 shows the fracture surface of the 100% ductile overload specimen. It was apparent from examination that the gage section of the specimen consisted of weld metal indicating that the specimen was machined from material at the location of the longitudinal seam of the pipe. This explains the fracture mode, since neither TG nor IG cracking would be expected to occur in weld metal. Finally, Figure I-6 shows the fracture surface of the specimen with TG and ductile overload. Failure occurred in the base metal about 1 inch away from the weld. The above results indicate that the weld heat-affected zone of heat 816208 (1.3-in.-thick) was susceptible to IGSCC, although there is a risk that mixed-mode failure could occur.

I.4 CHARACTERISTICS OF IGSCC SUSCEPTIBILITY OF ACTUAL LARGE DIAMETER PIPE

The results of the CBB, EPR and CERT tests indicated that the large diameter pipe material in the as-welded condition was susceptible to environmental cracking in the as-welded condition. The location of maximum susceptibility on the inside surface as determined by EPR measurements appeared to be adjacent to the weld fusion line. It is important that this behavior be representative or bounding to the behavior found in actual large diameter piping in the field. Table I-5 details EPR measurements made on other test pipes and field pipes. It can be seen that the values measured on heat 816208 were higher than the values for other pipes indicating upper bound sensitization. The location also matched the location of highest sensitization point as measured in field pipes.

I.5 MANUFACTURE OF TEST PIPES

I.5.1 Specimens LPT4-1 and LPT4-2: 4-In. Schedule 80 Pipes

Each of the two test pipes was made with five test welds containing a total of eight heat-affected zones. Figure I-7 details the layout of the test pipe and the dimensions of the test sections. The pipes were made in two parts prior to final assembly. Welds A and B were joined together while D and E were joined (A and E

were transition pieces). The welding procedure is detailed in Table I-6. The welds were manufactured using a consumable insert and Type-308L weld wire. Prior to completing weld C, the weld heat-affected zones A2 and B2 were notched using electro-discharge machining (EDM). Two defects 180° apart were placed in each HAZ. The notches were located 0.225 in. axially from the weld fusion line, with each slot 0.050 in. deep and 1 in. long around the circumference. The specification called for 0.002 in. radius at the bottom of each notch. Figure I-8 shows the location and flow geometry schematically. These notches were placed in the pipes to act as standards for UT and as potential IGSCC initiators. Concurrent with EDM notching, graphite wool was compressed over the two heat-affected zones associated with the D weld. The wool was compressed to a 6:1 ratio using a brake-shoe fixture displayed in Figure I-9. The final thickness was determined using a teflon spacer. The procedure for placing the wool was determined through interactions with IHI personnel. Once the wool was installed, the final test weld and the end cap welds were completed.

I.5.2 Specimen LPT16-1: 16-in. Schedule 140 Test Pipe

The single test pipe, constructed from heat 816208, was manufactured to contain four 12-in. test sections of pipe. As with the 4-in. pipes, a total of five test welds containing eight HAZs were made. Two of these HAZs were adjacent to the XM-19 material transition pieces. Figure I-10 displays the test pipe configuration with the dimensions of test sections also shown. The test sections unlike the 4-in. pipe pieces were manufactured without any reduced thickness adjacent to the weld. The weld procedures and fabrication sequence differed from that used for the 4-in. pipes. Automatic welding techniques were used with the heat input for each pass kept at a level of ∿40 KJ/in. Table I-7 details the procedures. Standard weld design was used. Type-308L consumable inserts were used for all welds. Type-308 weld wire was used for joints A and B while Type-308L weld wire was used for the remaining welds. Figure I-11 details the specific fabrication sequence. Joints B, C, D, and E were made conventionally with ∿30 consecutive weld passes. Joint A was welded using a special procedure to enhance the degree of sensitization on the inside surface in the HAZ. This enhancement was expected to promote nucleation of IGSCC. Following the buildup of three layers (∿0.3 in.), a thickness similar to that of a 4-in. pipe, the partially welded pipe piece consisting of a transition piece and the test piece was given a 500°C (932°F), 24-hour low temperature sensitization heat treatment. Following this heat treatment, the weld was then completed using an additional ∿23 passes to induce the standard residual stress pattern characteristic of a large diameter pipe. With the completion of all welds except B, EDM notches were introduced in weld HAZs C1 and E1 as indicated in Figure I-12. Four flaws spaced at

90° around the circumference were placed on two weld HAZs 0.050 in. from the weld fusion line. The flaws were 0.060 in. deep, 1.5 in. long and had a 0.002 in. radius at the flaw bottom.

Upon the completion of weld B, graphite wool was installed in the pipe in a manner similar to that used for the 4-in. pipes. The fixtures used were different than those used for the 4-in. pipes as shown in Figure I-13. The four part fixtures allowed graphite wool to be placed almost continuously around the circumference. The fixtures were installed on welds A and D with wool only placed on the A2 HAZ on the A weld. The wool was compressed 6:1 to a 0.040 in. final thickness. Figure I-14 shows the wool/fixture as installed in the pipe. At this point the end caps were welded on and the pipe was ready for precracking. The finished pipe is shown in Figure I-15.

I.6 TESTING: PRECRACKING

The 4-in. pipes and 16-in. large diameter pipe were placed in the Pipe Test Laboratory and exposed to 8 ppm O_2 high temperature water. The only load was present due to the operating pressure stress. Experience at IHI indicated that these conditions would be sufficient to initiate IGSCC.

The presence of the graphite wool would be sufficient to create the proper conditions for IGSCC nucleation. In addition, the increased sensitization on A2 HAZ would certainly promote IGSCC in the large diameter pipe. The 16-in.-diameter pipe was exposed for 1000 hours while the 4-in. pipes were exposed for 600 hours under pressure loading. Following these exposures, all pipes were ultrasonically tested to determine if any cracks were present. While the 16-in. diameter pipe had clear indications, the 4-in. pipes did not and were placed on test under a total axial stress of 11.5 ksi for 600 additional hours. After this exposure these pipes were again inspected for evidence of cracks.

I.7 ULTRASONIC INSPECTION: EVALUATION OF PRECRACKING TEST PHASE

At the end of the precracking phase UT was performed to verify the presence of IGSCC. Figures I-16 through I-18 show reproductions of the UT records for the 16-in. pipe before and after testing for joint HAZs' A2, D1, and D2. At these locations there were definite changes in signal, indicating cracking. There were other changes on other HAZ's as well. The signal from the EDM notches did not change significantly. This is expected due to the effect of machining in relieving residual stress at the notch tip. There were some evidences of radial growth however. The changes found in A2 HAZ were significant around the entire circumference.

The behavior was expected in that the i.d. material received added sensitization by the LTS treatment. The D weld (both D1 and D2 HAZ) were covered with graphite wool. While these HAZs were not as sensitized, some cracking appears to have taken place.

The 4-in.-diameter pipes showed less evidence of cracking. Figure I-19 and I-20 show the UT traces before and after exposure on the D weld. There appears to be evidence of cracking. The extent was far less than that in the 16-in. large pipe.

I.8 FUTURE TEST PLANS

Following testing to determine evidence of cracking, the pipe end caps will be cut off to remove the graphite wool and fixtures and then re-welded for the actual test phase to confirm the methodology. The stress level will be chosen to induce stresses bounding those found in field pipes. The results will be discussed in a topical report issued at the end of the testing phase.

I.9 REFERENCES

I-1 Y. G. Nakagawa, Ishikawajima-Harima Heavy Industries Co., Ltd., private communication.

I-2 J. E. Alexander, et al., "Alternate Alloy for BWR Pipe Applications," Fourth Semiannual Progress Report, April - September 1979, November 1979 (NEDC-23750-6).

I-3 T. P. Diaz, et al., "Parametric Studies for Stress Corrosion in Type-304 Stainless Steel Pipe," First Semiannual Progress Report, September 1978 - March 1979, March 1979 (NEDC-24187-1).

Table I-1

CHEMICAL COMPOSITION

Pipe Size	Heat No.	C	Si	Mn	Cr	Ni	P	S	Mo
4-in. Schedule 80	04836	0.07	0.42	1.80	18.30	8.12	0.024	0.021	0.31
	(Check analysis)	0.066	0.42	1.83	18.20	8.07	0.026	0.020	0.31
16-in. Schedule 140	816208	0.06	0.60	1.63	18.20	8.34	0.028	0.007	--
	(Check analysis)	0.06	0.58	1.78	18.48	8.12	0.033	0.011	0.21

Table I-2

PHYSICAL PROPERTIES FOR PIPE HEATS

Heat No.	Test Temperature	YS (ksi)	UTS (ksi)	Elongation (%)	R. A. (%)
04836 (4-in. Schedule 80)	RT	39.0	86.4	54	--
	550°F	24.5	69.1	32	--
861208 (16-in. Schedule 140)	RT	36.9 37.4	84.8 86.3	69 69	80.1 81.5
	550°F	19.8 20.4	65.2 65.5	49 54	74.0 76.3

Table I-3

CBB TEST MATRIX FOR HEAT 816208
(16-in.-diameter Pipe)

Specimen ID	Material Condition	Time of Exposure (hours)	Strain (%)	Cracking	Maximum Depth (mils)
LPB1	Base Metal	300	1.0	No	-
LPB2	Base Metal	300	1.0	No	-
LPB3	Base Metal	600	1.0	TG	2.8
LPB4	Base Metal	600	1.0	TG	3.6
LHB1	Base Metal plus LTS	300	1.0	No	-
LHB2	Base Metal plus LTS	300	1.0	No	-
LHB3	Base Metal plus LTS	600	1.0	TG	4.0
LHB4	Base Metal plus LTS	600	1.0	TG	4.8
WPB1	As-welded	150	0.5	No	-
WPB2	As-welded	150	0.5	No	-
WPB3	As-welded	150	1.0	No	-
WPB4	As-welded	150	1.0	No	-
WPB5	As-welded	300	1.0	No	-
WPB6	As-welded	300	1.0	No	-
WPB7	As-welded	300	0.5	No	-
WPB8	As-welded	300	0.5	No	-
WPB9	As-welded	600	0.5	TG	2.4
WPB10	As-welded	600	0.5	IG/TG	2.4
WPB11	As-welded	600	1.0	IG/TG	24.0
WPB12	As-welded	600	1.0	TG	2.8
WHB1	Welded + LTS	150	1.0	No	-
WHB2	Welded + LTS	150	1.0	No	-
WHB3	Welded + LTS	300	1.0	No	-
WHB4	Welded + LTS	300	1.0	No	-

Table I-4

CERT TEST RESULTS FOR HEAT 816208 (AS-WELDED CONDITION)
IN 8 ppm O_2 550°F WATER AT 3 mil/h EXTENSION RATE

Specimen ID	Strain Rate (in./min)	Maximum Stress (ksi)	TTF (hours)	RA (%)	EL (%)	Failure Mode
WPC1	5×10^{-5}	68.6	73.5	21.4	15.5	IG and TG
WPC2	5×10^{-5}	76.0	77	38.3	16.4	Ductile shear
WPC3	5×10^{-5}	69.9	48.5	27.7	11.1	TG and ductile
WPC4	5×40^{-5}	70.45	38.5	15.7	8.3	IG and TG

Table I-5

EPR MEASUREMENTS ON CONFIRMATORY PIPE AND OTHER TEST/FIELD PIPES

Pipe	EPR Reading in Cross Section (C/cm^2)*
Confirmatory Pipe - Heat 816208	12
Recirc - Pipe Side (Plant) 24-in. Sch 80	4
1-in. Thick Plate 26-in. Weld Parameters	4
Recirc - Pipe Side (Plant) 24-in. Sch 80	5-10
26-in. Sch 80 (GEAP-21382)	4
26-in. Sch 80 (GEAP-12697)	2

*>2 Susceptible to Crack

Table I-6

WELD PROCEDURE WD-2

BASE METAL:	ASME/ASTM SA312, Type 304, 347, CF8 (P-No. 8 to P-No. 8)
SIZE:	4-in. Schedule 80 (4.5 in o.d. x 0.337 in wall)
FILLER METALS:	
CONSUMABLE INSERT:	1/16-in. x 3/16-in. Grinnell per SFA 5.9 Type ER 308L, 8 FN Minimum
BARE WIRE:	3/32-in. x 36-in. per SFA 5.9 Type 308L, 8 FN Minimum
COVERED ELECTRODE:	1/8-in. Diameter per SFA 5.4 Type 308L-16 8 FN Minimum
WELD POSITION:	1G (Axis Horizontal, Rotate Pipe)
PREHEAT TEMPERATURE:	Ambient
MAX. INTERPASS TEMP:	350F (177C) Measured with Contact Pyrometer
POST WELD HEAT TREAT:	None
ROOT CONTOUR:	Standard
CROWN CONTOUR:	Standard
WELD TECHNIQUE:	Oscillate all filler passes.

Table I-7

WELD PROCEDURE
MODIFIED FOR 16-in. PIPE

BASE METAL:	ASME/ASTM - Type 304
SIZE:	16-in. Schedule 120
JOINT DESIGN:	N/R
FILLER METALS:	
CONSUMABLE INSERT:	1/16-in. x 3/16-in. Grinnell per SFA 5.9 Type ER 308L, 8 FN Minimum
BARE WIRE:	3/32-in. x 36-in. per SFA 5.9 Type 308 (308L), 8 FN Minimum
COVERED ELECTRODE:	1/8-in. Diameter per SFA 5.4 Type 308L-16 8 FN Minimum 5/32-in. Diameter per SFA 5.4 Type 308L-16 8 FN Minimum
WELD POSITION:	1G (Axis Horizontal, Rotate Pipe)
PREHEAT TEMPERATURE:	Ambient
MAX INTERPASS TEMP:	350F (177C) Measured with Contact Pyrometer
POST WELD HEAT TREAT:	LTS on Subassembly A after first 3 layers only
ROOT CONTOUR:	Hand Grind
CROWN CONTOUR:	Hand Grind
WELD TECHNIQUE:	Oscillate all filler passes
WELD PROCESS:	GTAW using automatic and pulse
VOLTAGE:	Primary arc volts 10.0 to 9.0 Background arc volts 9.0 to 7.6
AMPS:	Primary current - 240 to 115 Background current - 120 to 50
TRAVEL SPEED:	3.0 in./min

*Please note that the illustration(s) on this page has been reduced 10% in printing.

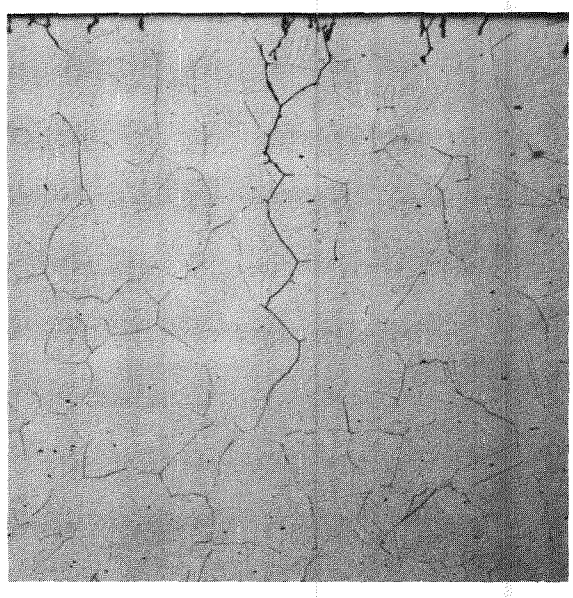

DEEPEST INTERGRANULAR CRACK
OBSERVED ON HAZ

(a)

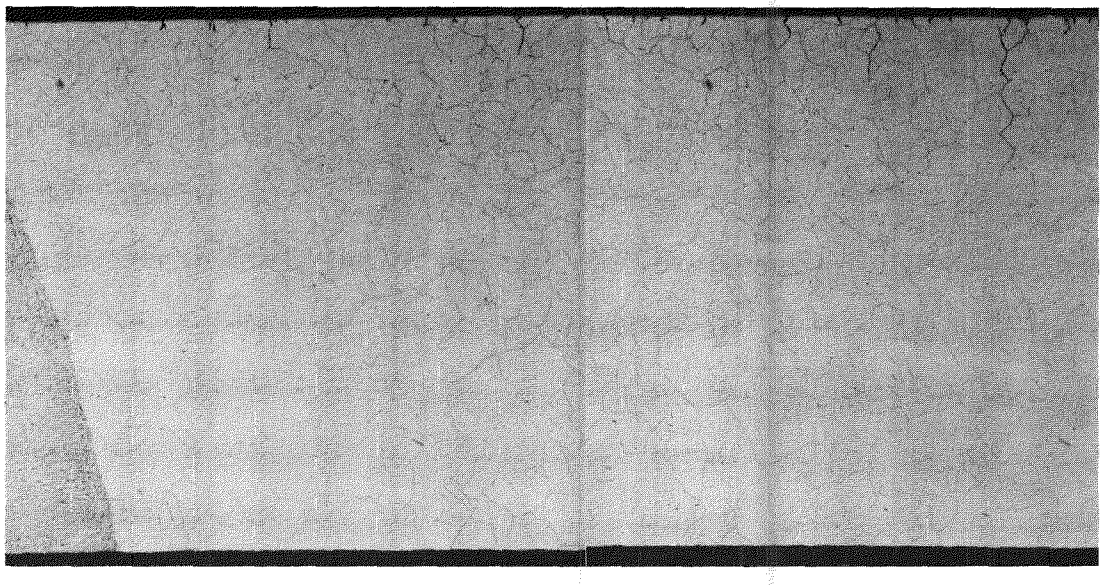

(b)

Figure I-1. Intergranular and Transgranular Cracking on Graphite Wool CBB Specimen WPB 11 after 600-Hour Exposure in 8 ppm O_2 550°F Water at 1.0% Strain: (a) = 400X, (b) = 40X

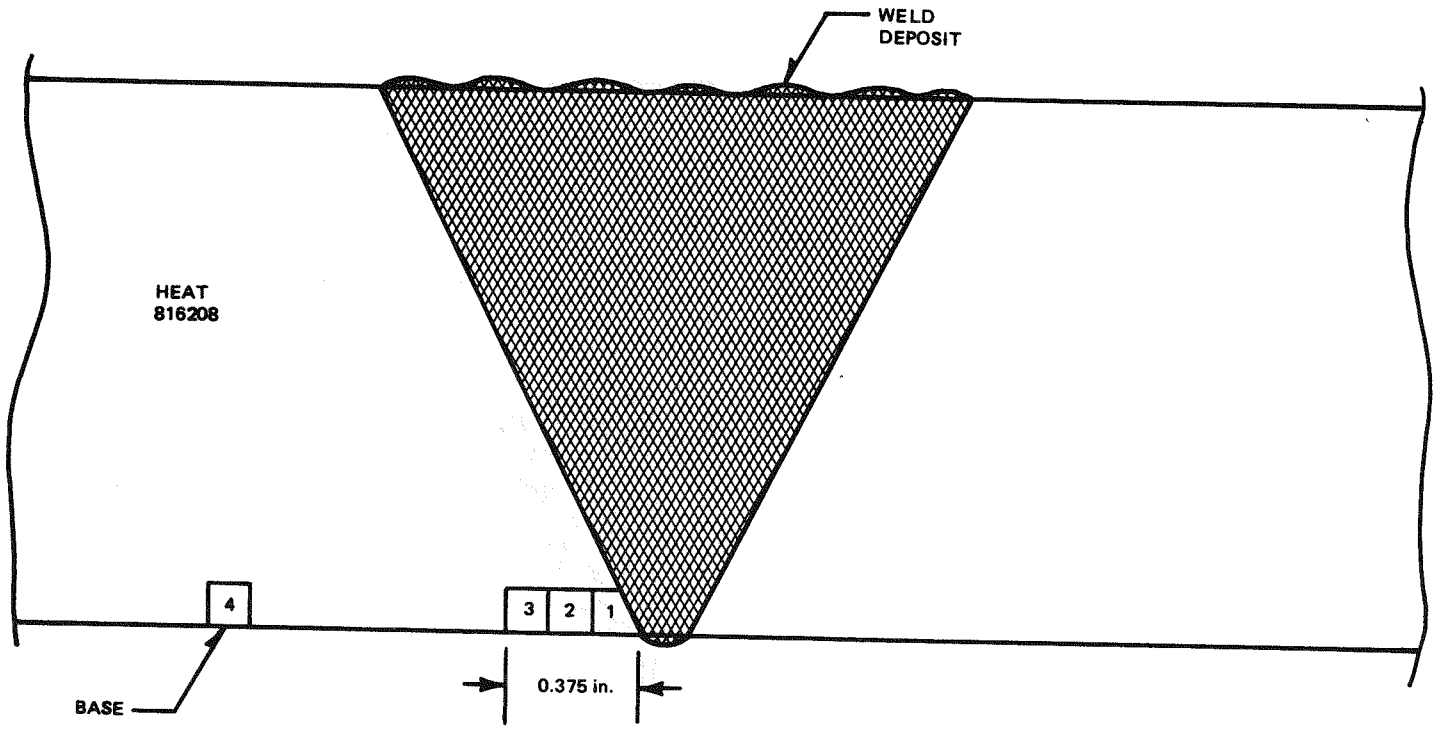

Figure I-2. Location of EPR Measurements on Test Weld, Heat 816208

*Please note that the illustration(s) on this page has been reduced 10% in printing.

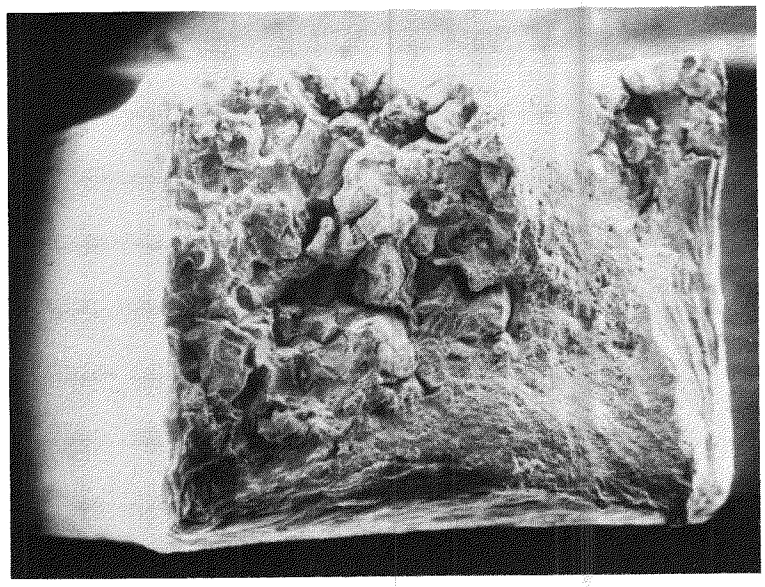

(a)

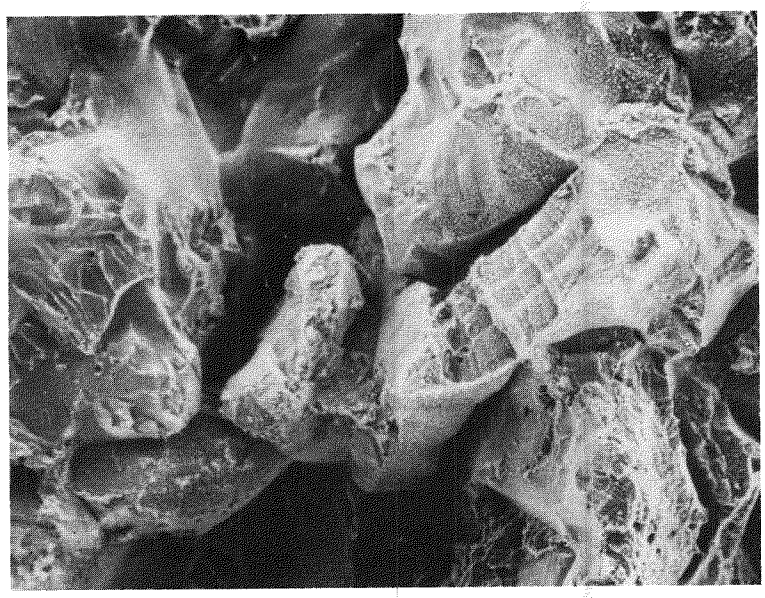

(b)

Figure I-3. CERT Specimen WPC1, Intergranular and Transgranular Cracking Failure Mode: (a) = 30X, (b) = 150X

*Please note that the illustration(s) on this page has been reduced 10% in printing.

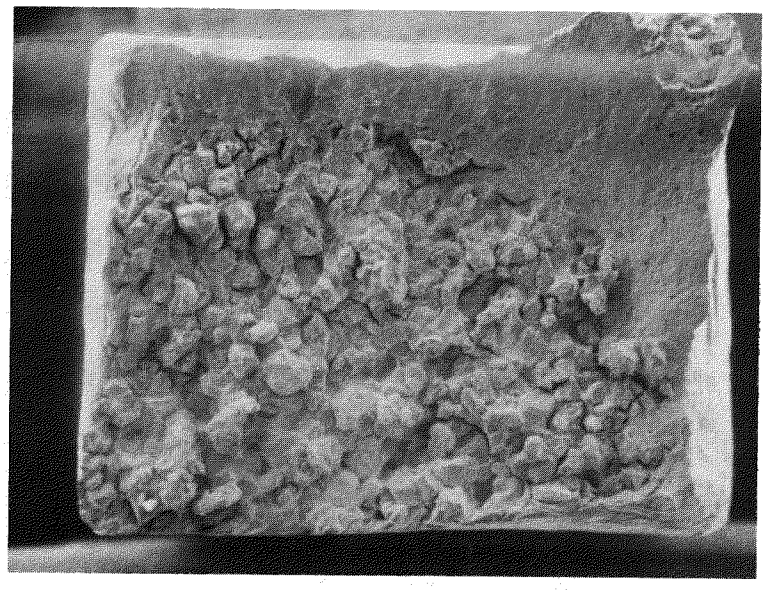

(a)

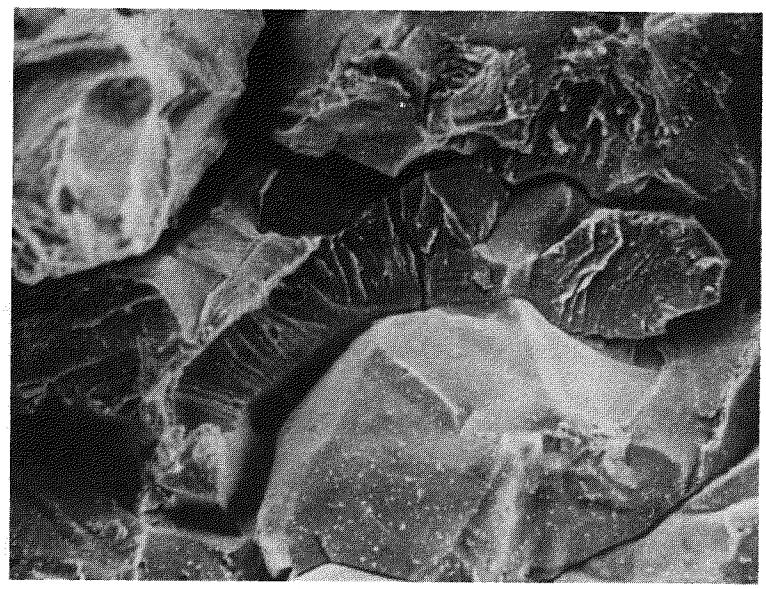

(b)

Figure I-4. CERT Specimen WPC4, Intergranular and Transgranular Cracking Failure Mode: (a) = 30X, (b) = 500X

*Please note that the illustration(s) on this page has been reduced 10% in printing.

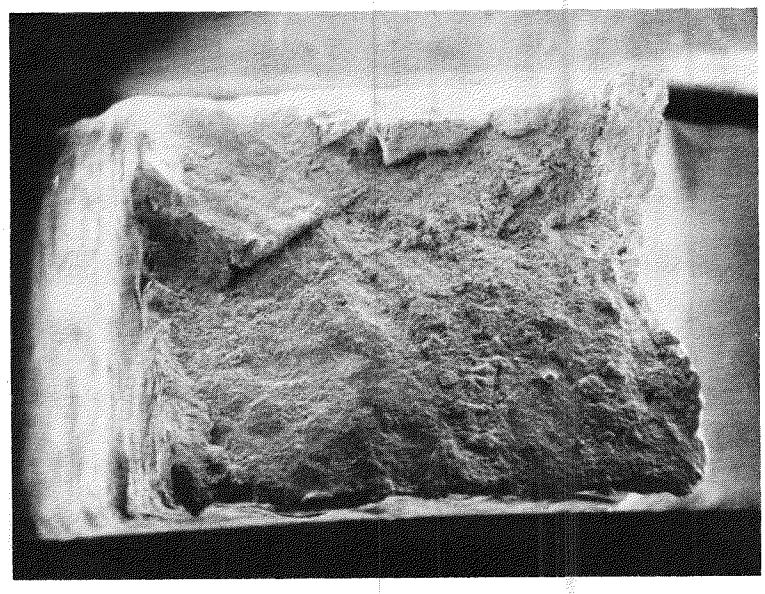

(a)

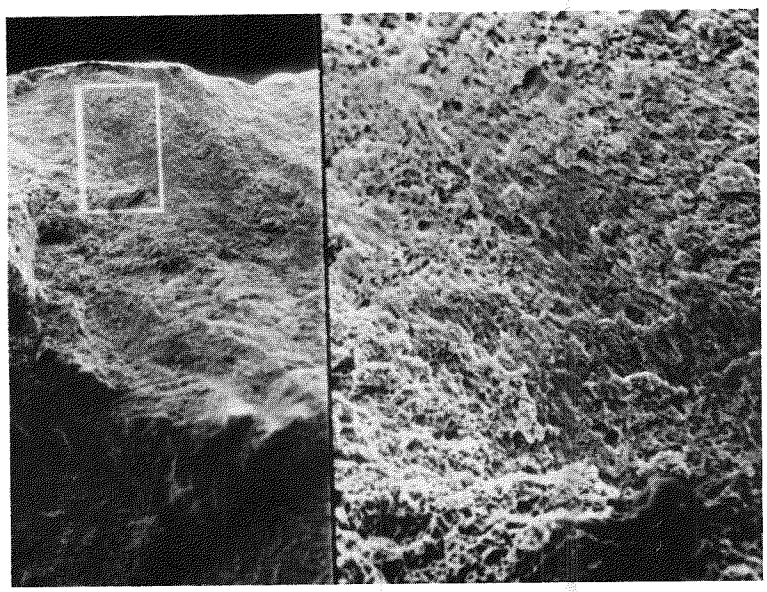

(b)

Figure I-5. CERT SPECIMEN WPC2, Ductile Shear Failure Mode: (a) = 30X, (b) = 100X/500X

*Please note that the illustration(s) on this page has been reduced 10% in printing.

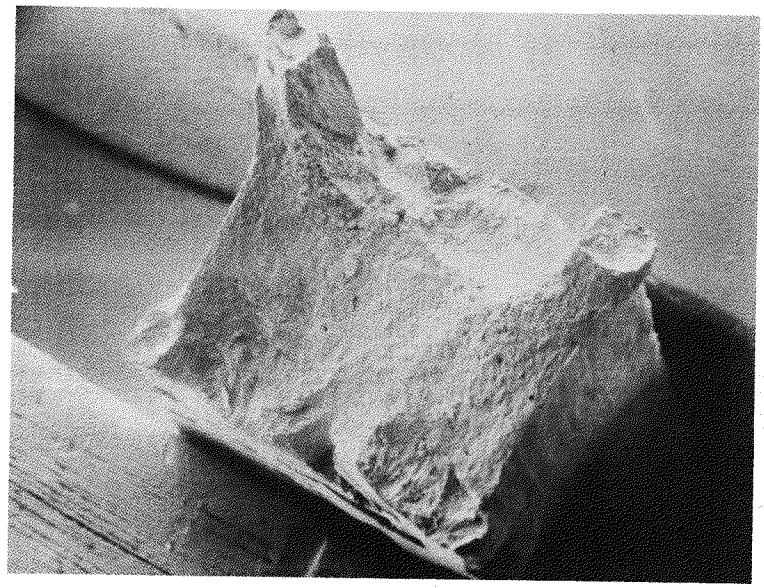

Figure I-6. CERT Specimen WPC3, Transgranular Cracking Initiation and Ductile Overload: (a) = 21X, (b) = 350X

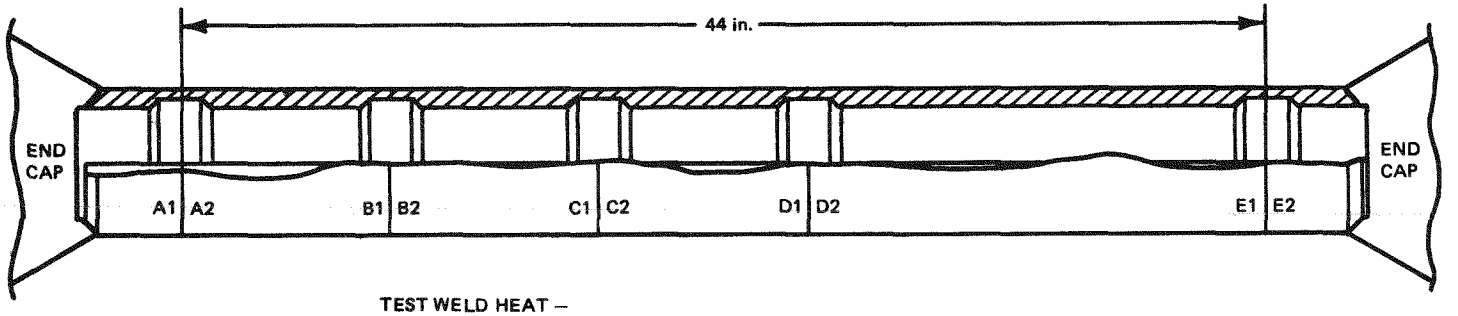

Figure I-7. 4-in.-Diameter Test Piece Configuration

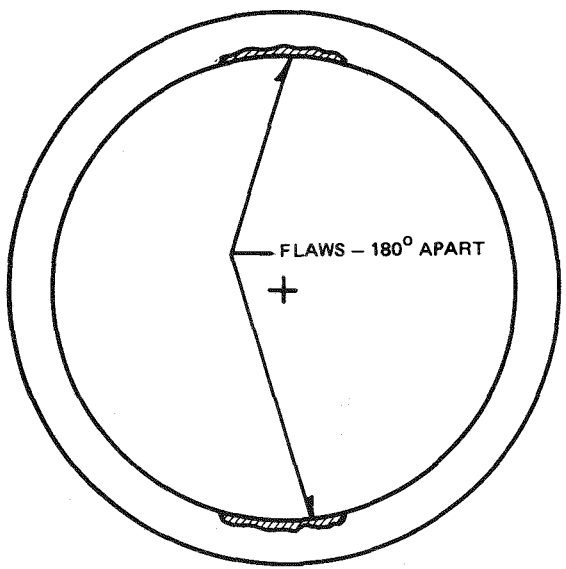

a) LOCATION AROUND CIRCUMFERENCE

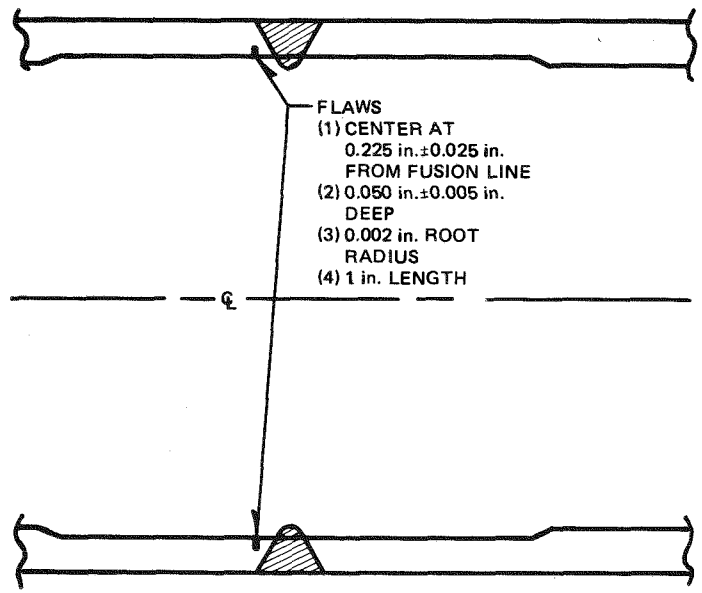

LOCATION WITH RESPECT TO FUSION LINE ALONG AXIS OF PIPE

Figure I-8. Schematic of EDM Notching

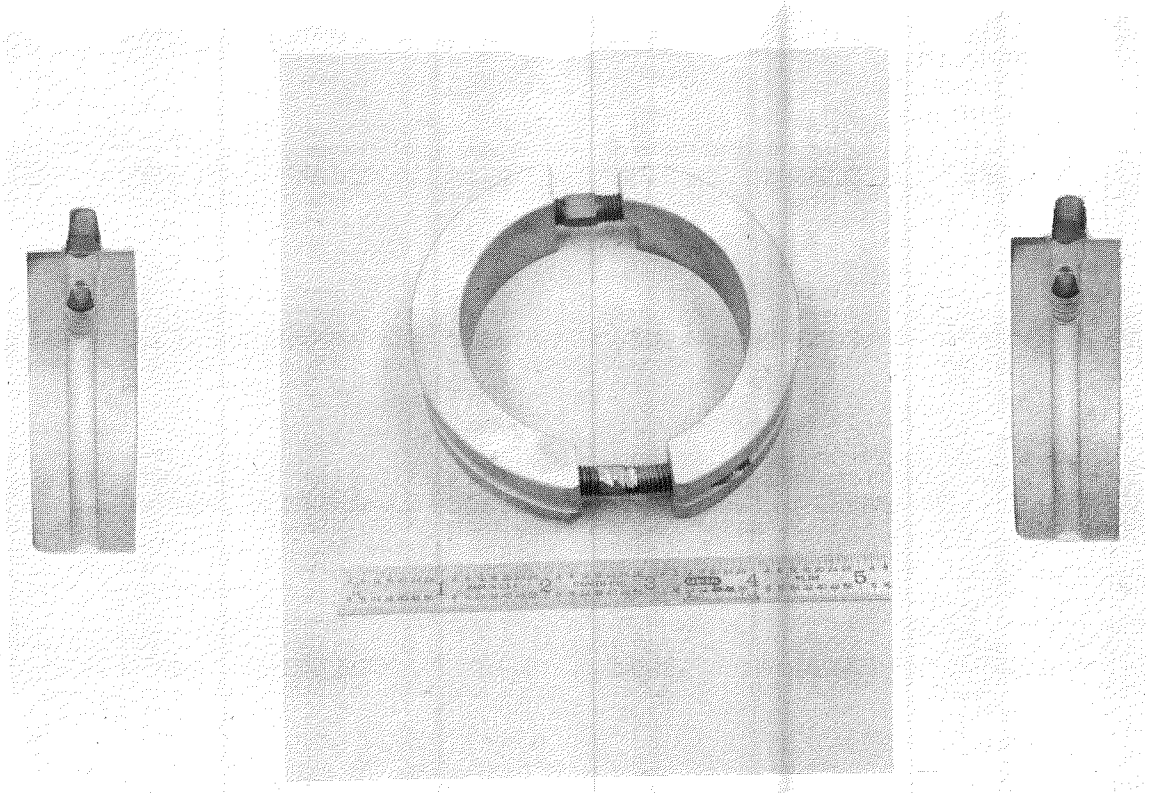

Figure I-9. Fixtures for Compressing Graphite Wool in 4-in. Pipes

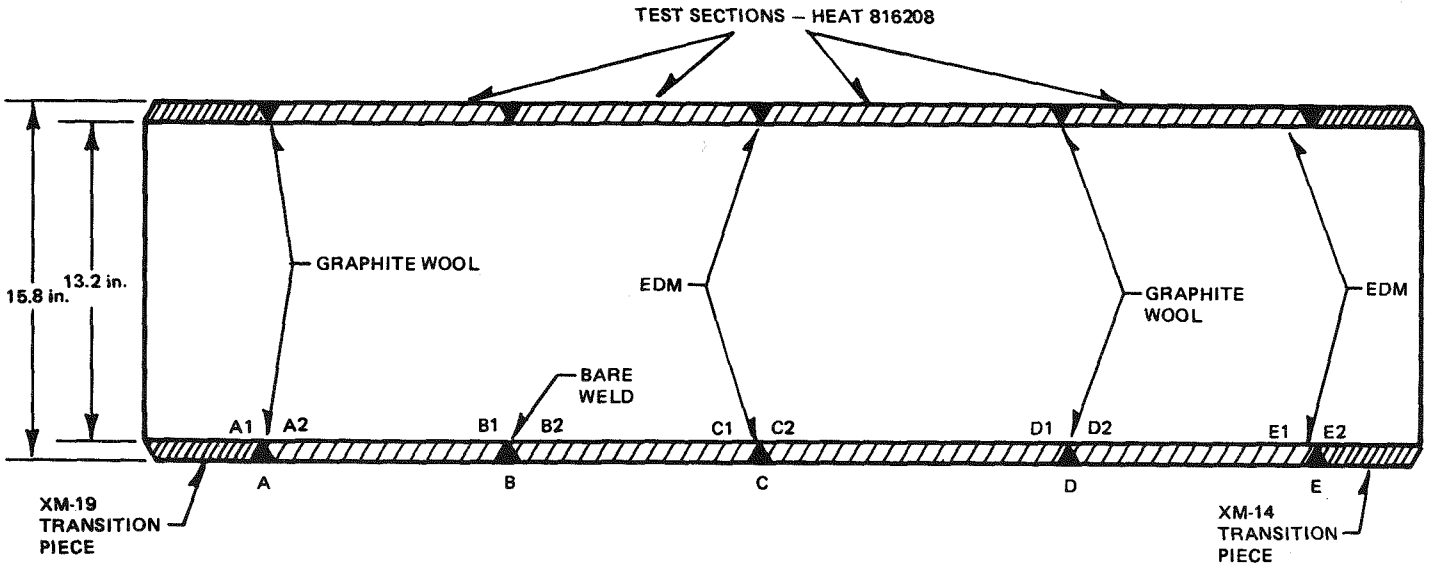

Figure I-10. Schematic of Test Pipe without End Caps - Large Pipe

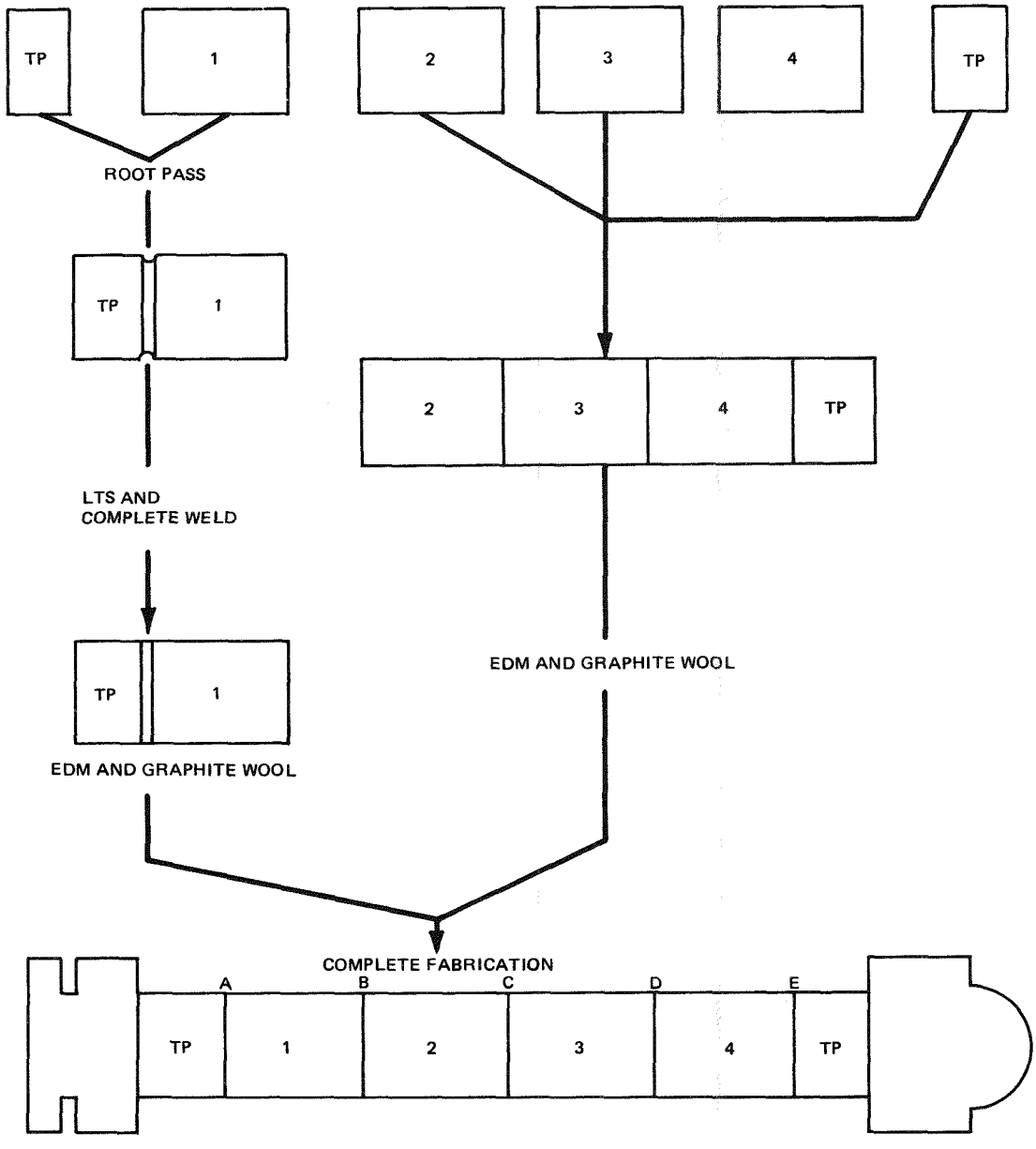

Figure I-11. Fabrication Sequence, Large Pipe Specimen LPT-16-1

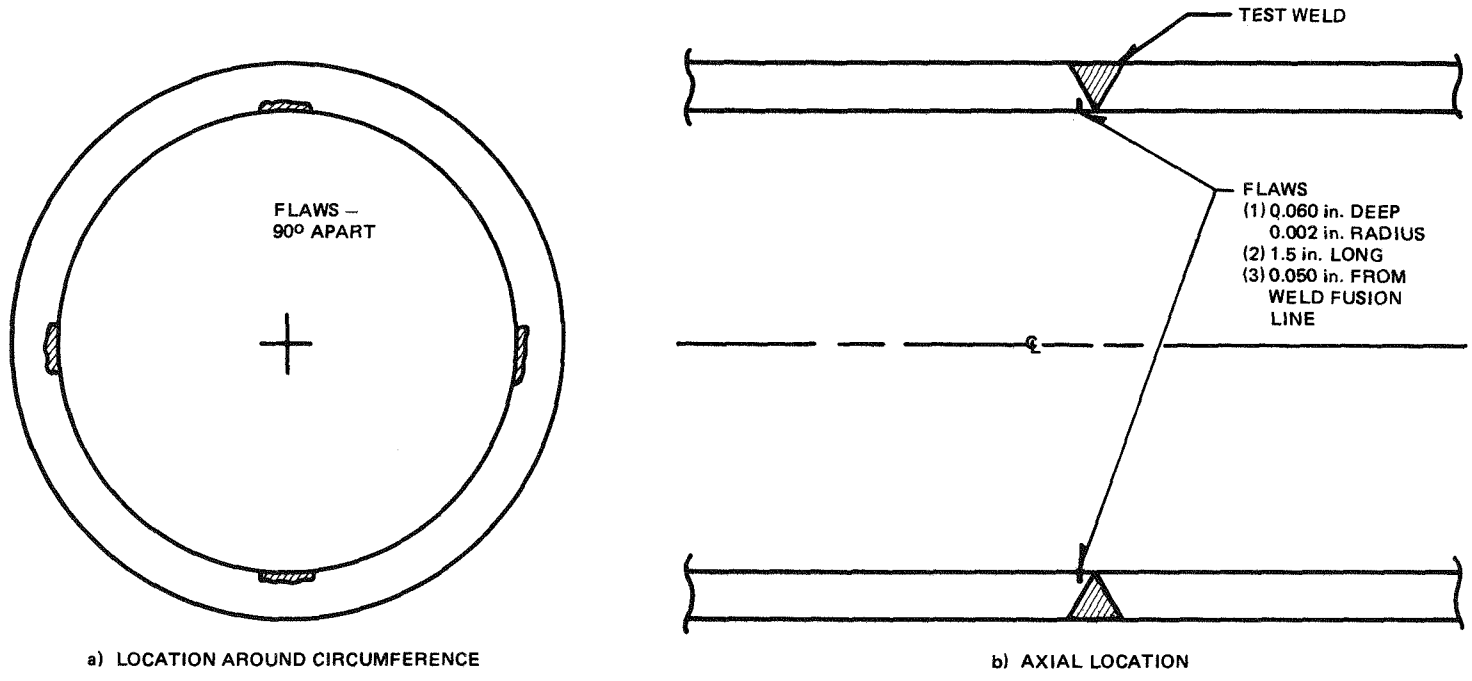

a) LOCATION AROUND CIRCUMFERENCE

b) AXIAL LOCATION

Figure I-12. Schematic of EDM Notches - 16-in. Pipe

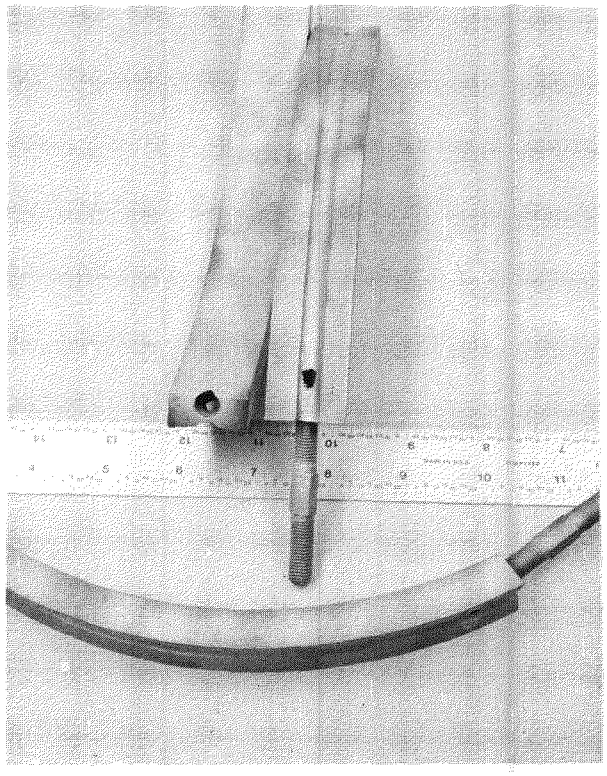

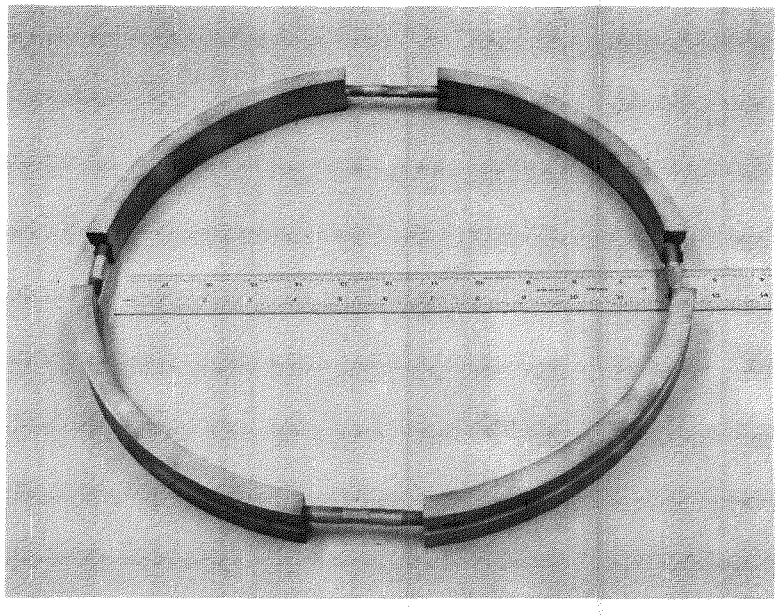

Figure I-13. Fixtures for Compressing Graphite Wool in Large Diameter Confirmatory Pipe

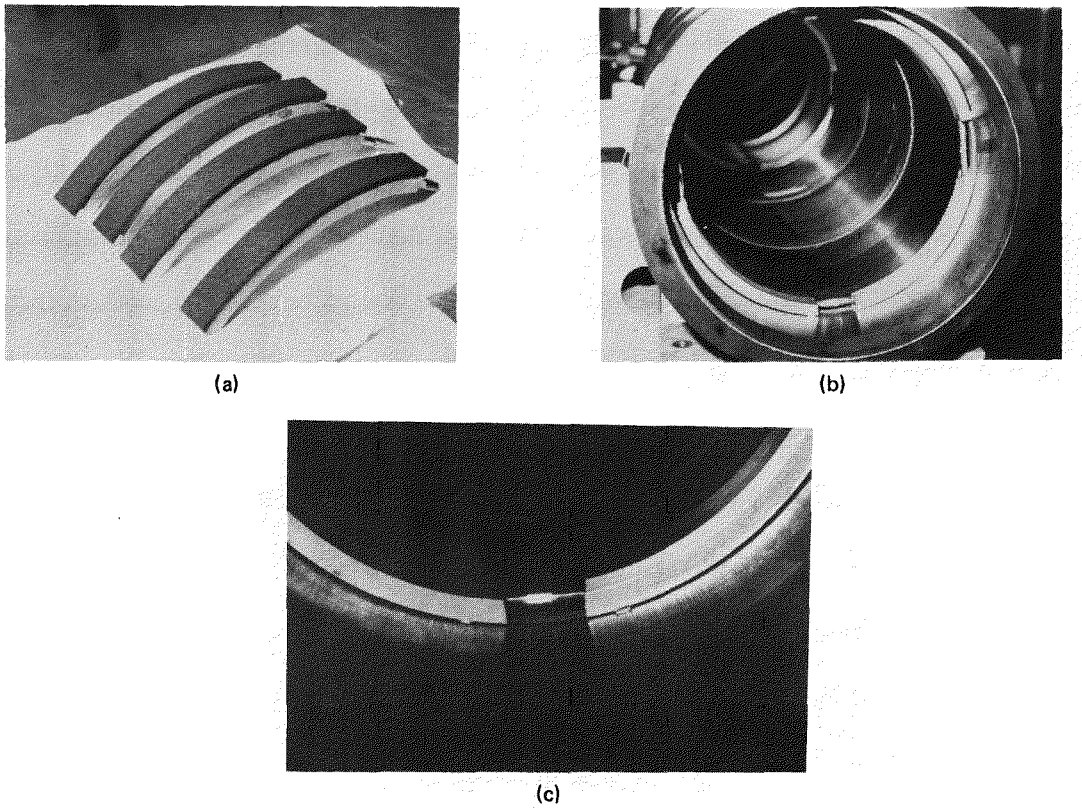

Figure I-14. (a) Fixture Parts with Graphite Wool Prior to Installation
(b) Fixtures Installed Compressing Wool
(c) Close-up of Fixture/Compressed Wool

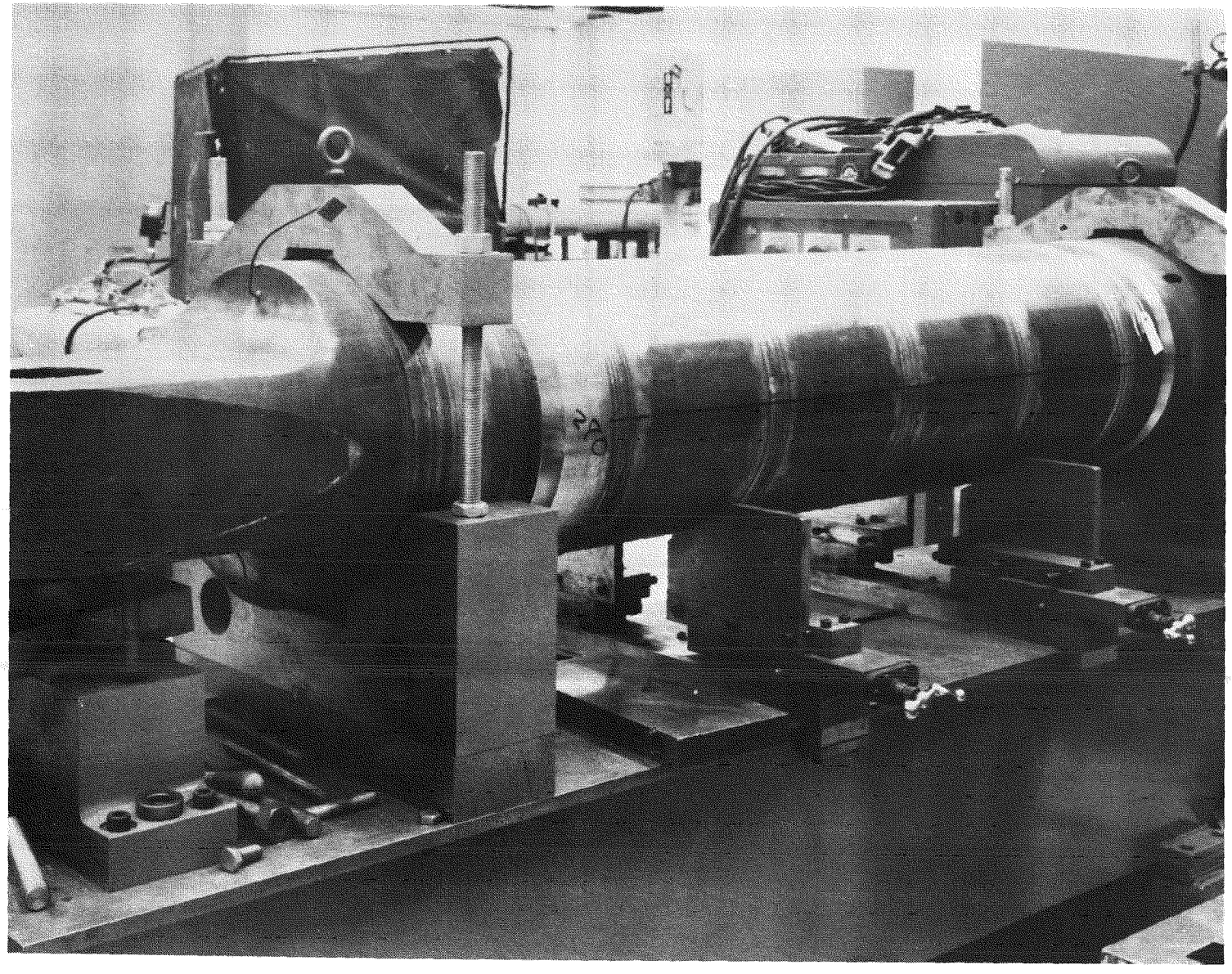

Figure I-15. Photograph of Completed Large Diameter Test Pipe

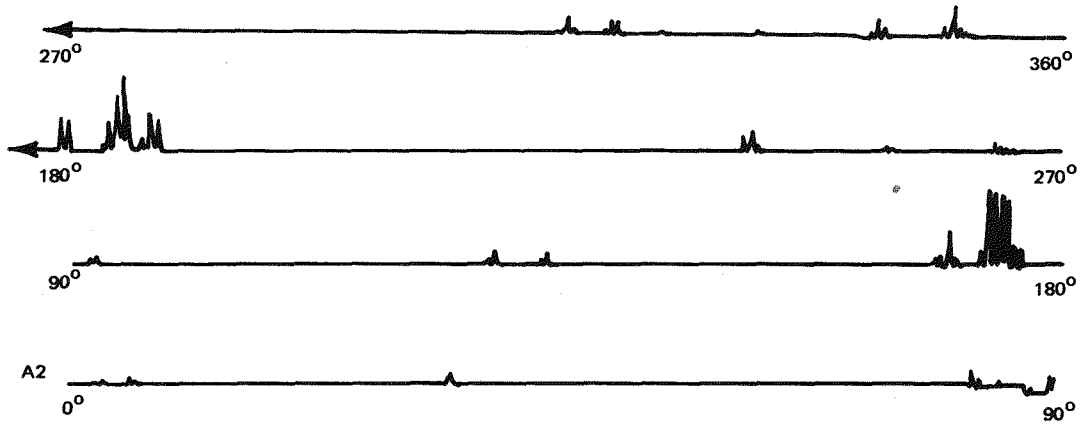

90° SECTOR UT TRACES – PRIOR TO EXPOSURE – AZ HAZ

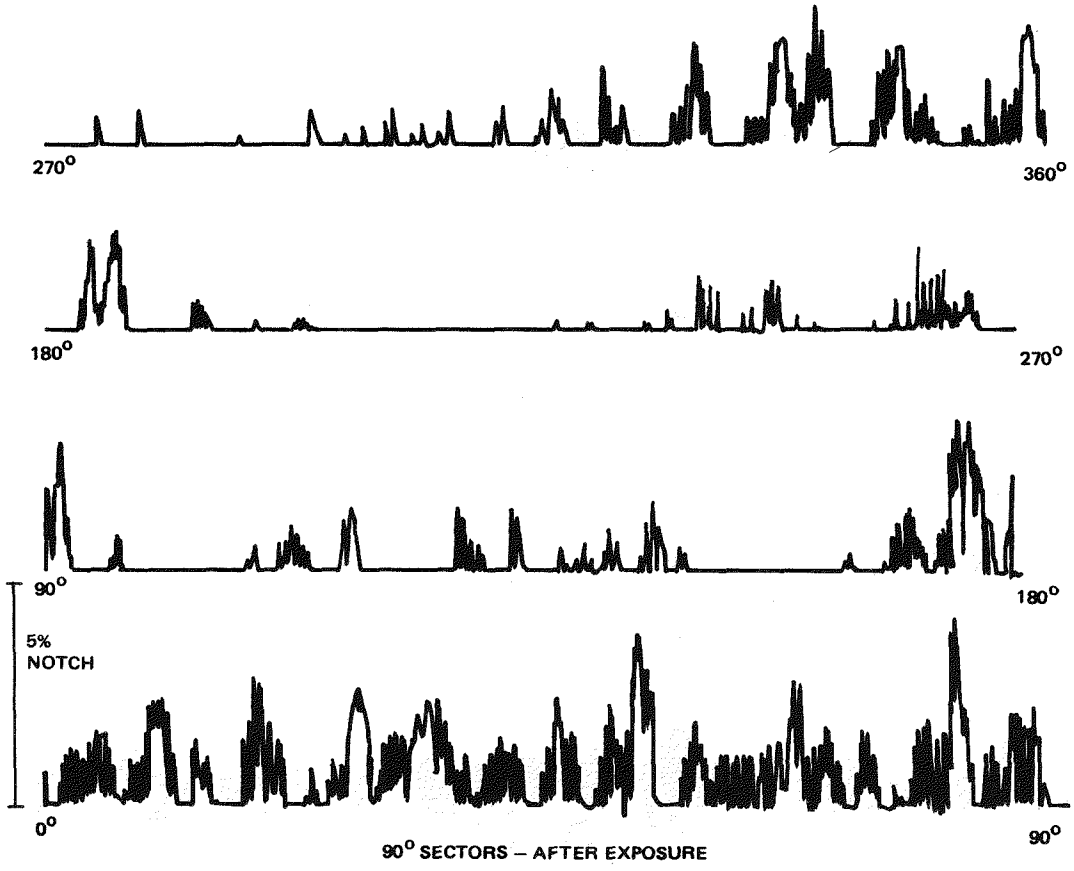

90° SECTORS – AFTER EXPOSURE

Figure I-16. Ultrasonic Traces - Large Pipe: Joint A_2 (HAZ)

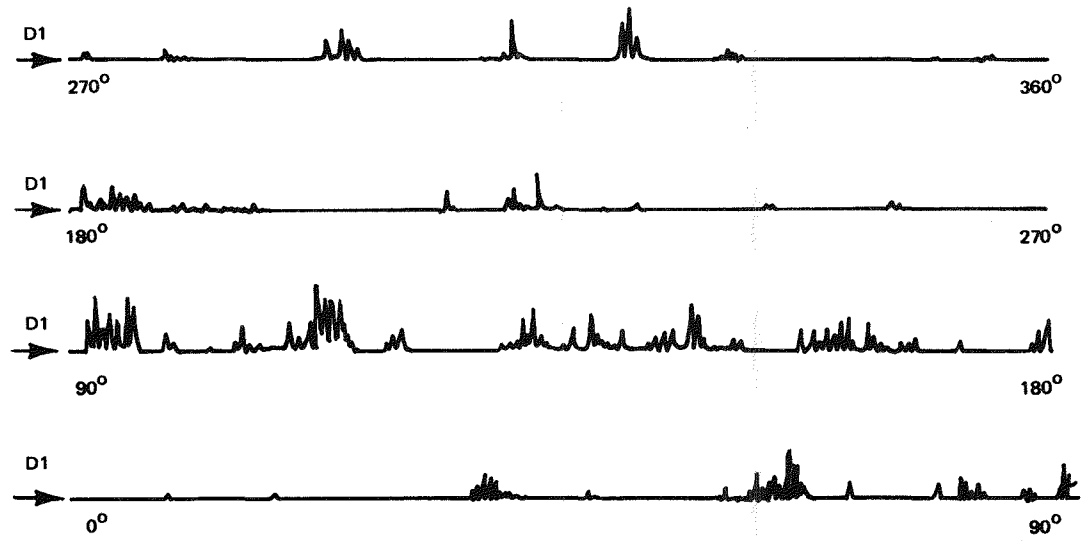

90° SECTOR SCANS – BEFORE EXPOSURE – D1 HAZ

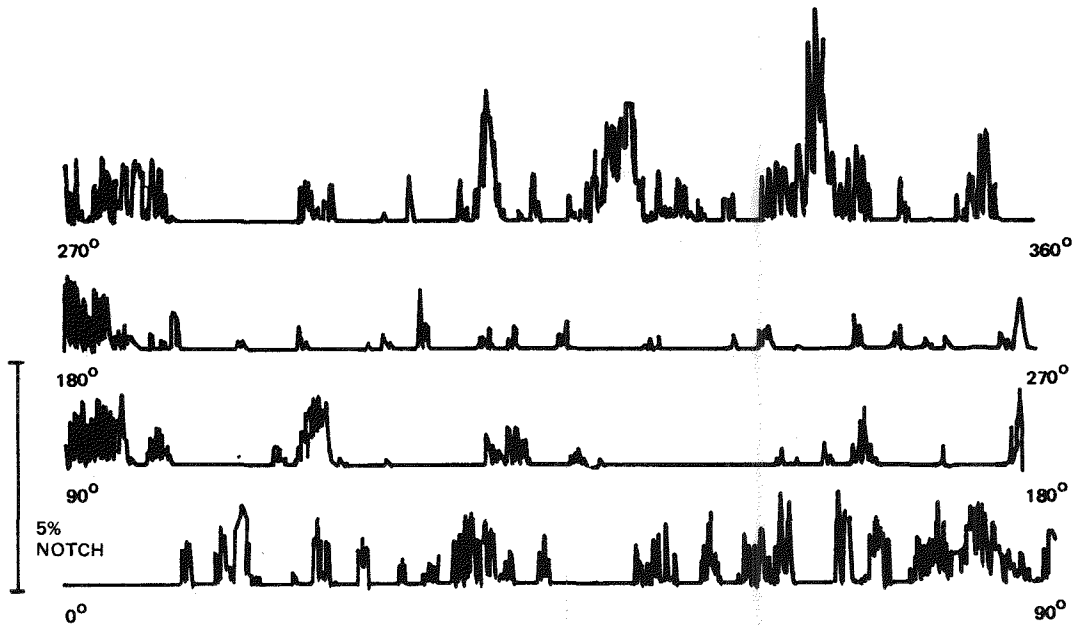

90° SECTOR SCANS – AFTER EXPOSURE

Figure I-17. Ultrasonic Traces - Large Pipe: Joint D1

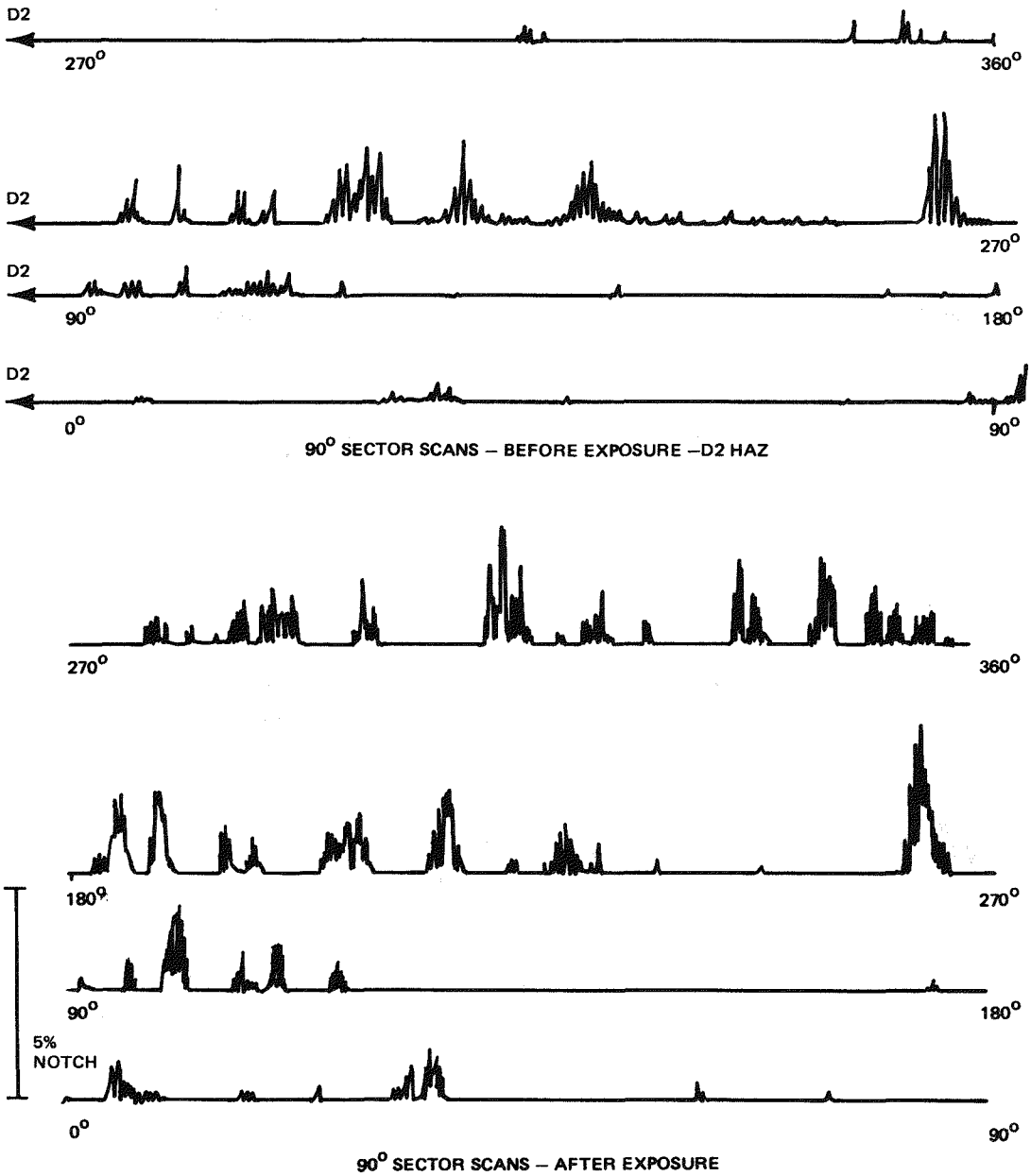

Figure I-18. Ultrasonic Traces - Large Pipe: Joint D2

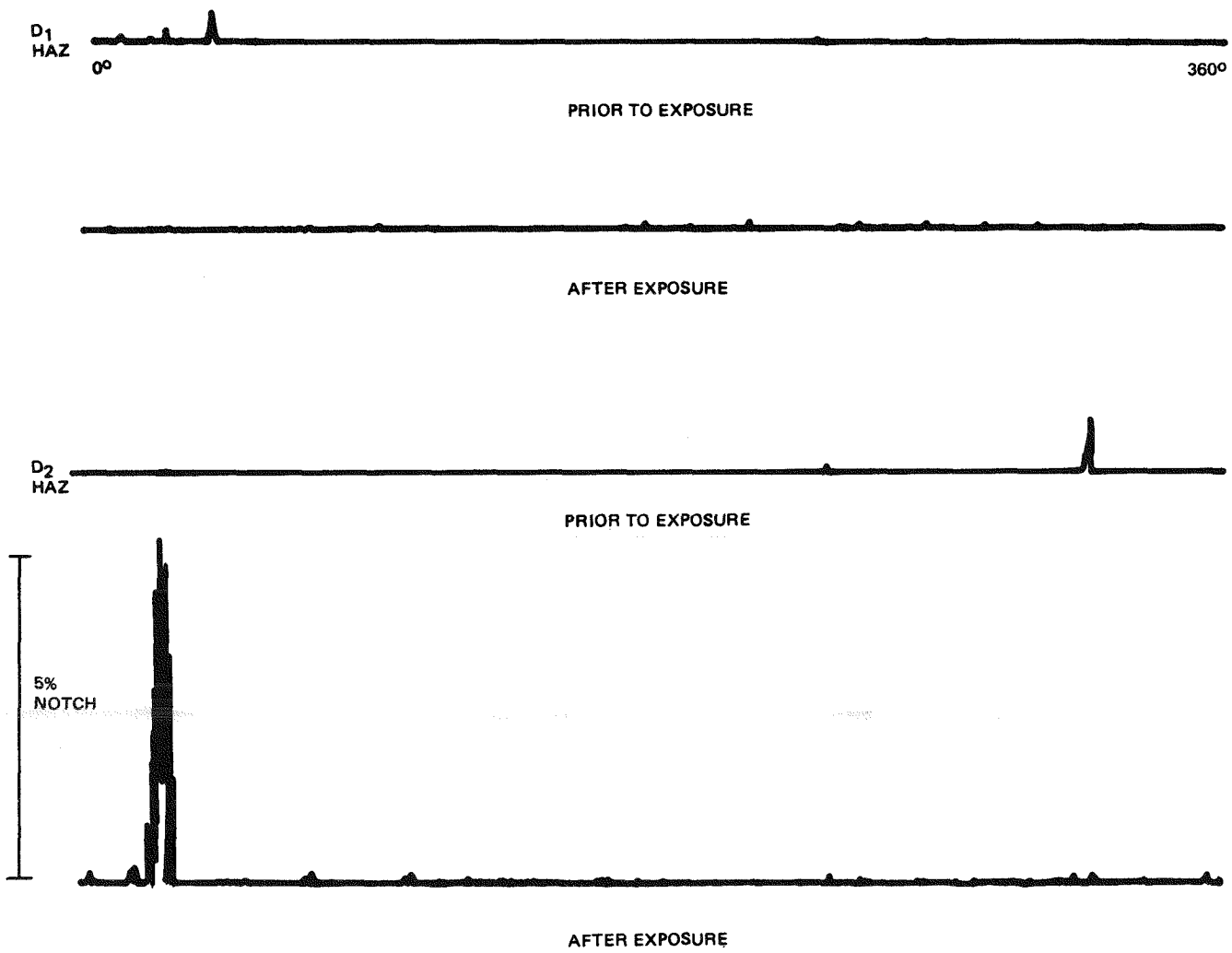

Figure I-19. Ultrasonic Traces - 4-in. Pipe: Joint D (LPT4-1)

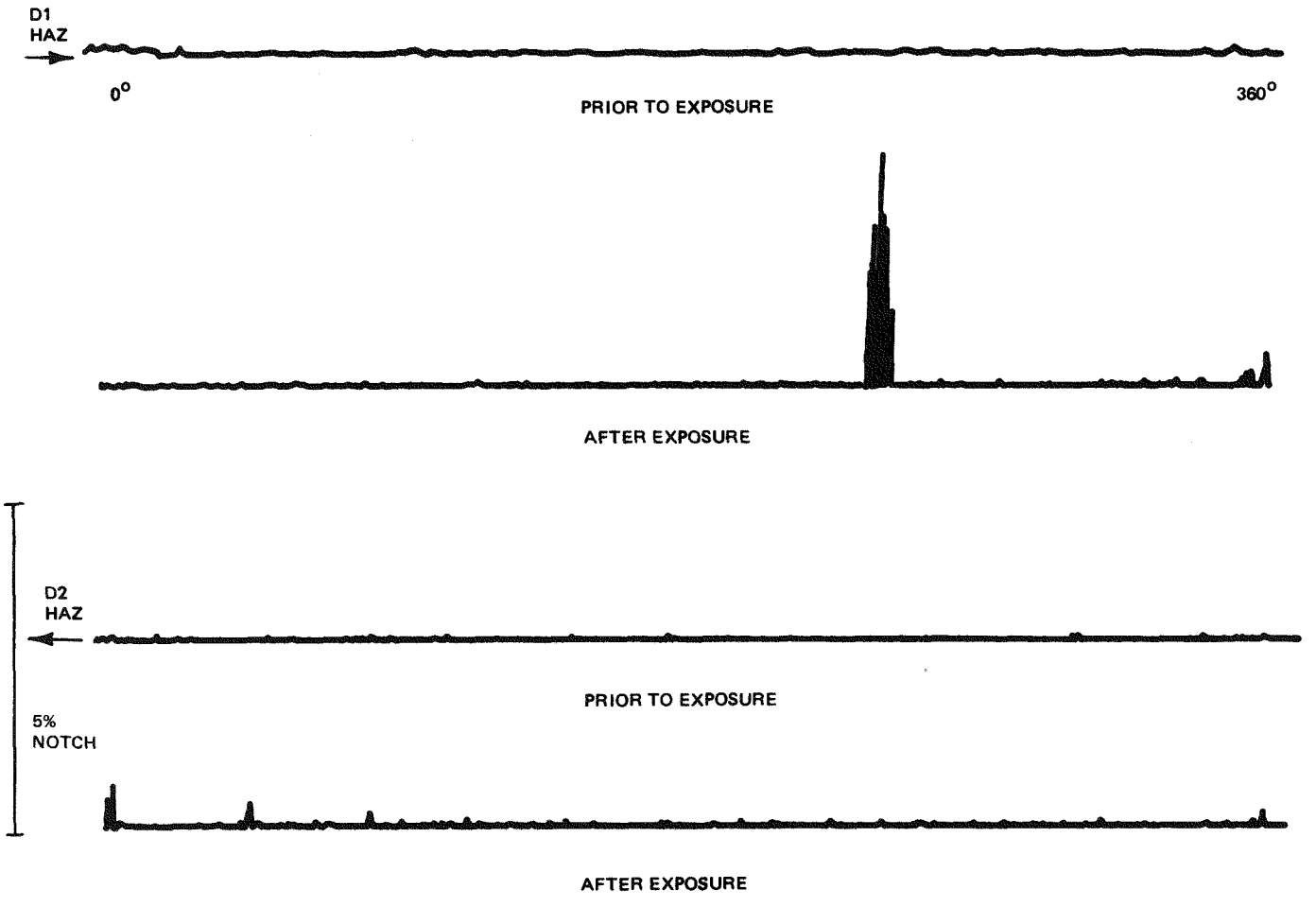

Figure I-20. Ultrasonic Traces - 4" Pipe: Joint D (LPT4-2)

Appendix J

IN-SERVICE INSPECTION METHODOLOGY
(A. J. Jacobs)

J.1 INTRODUCTION

Installed piping systems are currently inspected in accordance with Section XI of the ASME Code. The code requires inspection of each Class 1 weld at least once during plant life and of 25 percent of all Class I welds within each of four consecutive 10-year periods.

The increasing incidence in recent years of IGSCC in BWR Type-304 stainless steel (SS) piping has led to a variety of remedial measures. Steadily growing implementation of these measures has reduced the incidence of IGSCC but has not eliminated it due to remaining untreated pipe systems. To further reduce the incidence, the NRC established augmented in-service inspection (ISI) requirements for Type-304 SS piping in BWRs not fully in conformance with the material selection and processing guidelines listed in NUREG-0313 (J-1). The degree of inspection depends on whether specific piping runs are classified as "service-sensitive" or not. "Service-sensitive" lines are defined as those that have experienced cracking in service (e.g., core spray and recirculation riser lines), or are considered particularly susceptible to cracking because of high stress, or contain relatively stagnant, intermittent, or low flow coolant. The service-sensitive lines are subject to more intensive inspection than the non-service-sensitive lines. Since any augmented ISI plan has to be superimposed on ASME Code requirements, even non-service-sensitive welds are inspected on an accelerated basis (J-1), "at least once in no more than 80 months" initially, and subsequently in 120 months or less as prescribed in Section XI of the Code. Welds in service-sensitive lines are inspected at shorter intervals than the non-service-sensitive lines. In addition, those service-sensitive welds meeting certain stress criteria are examined at each inspection, instead of only once during plant life as are non-service-sensitive welds.

The General Electric Company has recently developed a new approach for formulating an alternative augmented ISI plan. This approach was developed in response to two factors: (1) the NRC recommendation in NUREG-0531 (J-2) that "an improved focused in-service program based on stress rule index, material of construction, history of

cracking, etc." be developed and implemented; and (2) the fact that compliance with NUREG-0313, Rev. 1, is now mandatory. The latter factor makes this approach to augmented ISI an attractive alternative for utilities, since it can be optimized with respect to plant availability, inspection cost, or exposure to radiation. The main features are discussed in the next section.

J.2 FEATURES OF THE ALTERNATIVE ISI PLAN

The alternative plan is the first one to recognize and apply (1) the known dependence of IGSCC rate on stress rule index (SRI) and carbon content of Type-304 SS; and (2) the increasing rate of IGSCC failure with time in the field, hence the need for increasing or constant (i.e., not decreasing, as proposed by NUREG-0313) inspection effort with time. These and other factors are discussed below.

J.2.1 Weld Selection

The welds targeted for inspection in the alternative plan are those having high stress rule indices and/or high carbon contents. All the documented BWR weld cracking incidents have occurred where the stress rule indices were greater than 1.2, and in all but two incidents, the carbon content was greater than 0.05 wt%. In laboratory, full-scale pipe tests using 4-in. Schedule 80 pipe, a dramatic increase in time-to-failure was observed as the carbon content approached and dropped below 0.05 wt% (J-3 - J-5). Recent attempts to demonstrate a correlation between pipe test data and other chemical components of Type-304 SS have met with either limited success (Mn, N) or no success (Mo, Cr) (J-6). The effects of Mn and N present within specification were secondary to those of C. An attempt to correlate IGSCC susceptibility with the number of plant startups also met with limited success.

J.2.2 Statistical Model

Statistical methods were used in developing the alternative plan for two reasons: (1) to permit a minimization of IGSCC incidence in terms of number of welds inspected and inspection frequency, and (2) to facilitate a quantitative comparison of the alternative plan with the NRC and ASME plans.

The main criteria for comparison of the various ISI plans are the probability of leakage between two successive inspections and a so-called "Leakage Index," which is the area under the probability versus time curve over any desired time interval. The statistical model on which the alternative plan is based incorporates the

following independent variables (leakage probability and Leakage Index are functions of these):

1. Number of welds inspected.
2. Time between inspections.
3. Stress corrosion crack propagation time (time period from which a crack is first detectable by ultrasonic techniques until leakage). This time would be developed using predictive methods developed here and reported in the summary.
4. Weibull shape and scale parameters (field leakage data are observed to follow a Weibull distribution function).
5. Plant age at time of inspection.
6. Number of welds in piping system and subsystems (as follows).

The underlying cracking distribution of a piping system (e.g., recirculation system) may vary over the system. Thus, different size pipes or size ranges within a system may exhibit different cracking distributions. A "piping subsystem" has been defined to include all piping in the over-all system having the same cracking distribution. In order to simplify the model, it is assumed that cracking in one part of the subsystem requires replacement of the entire subsystem.

Three distinct cases were developed, depending on the relationship between inspection frequency and crack propagation time:

1. Case I - the time period between inspections is greater than the crack propagation time.
2. Case II - the crack propagation time is greater than one but less than two inspection periods.
3. Case III - the crack propagation time is greater than two but less than three inspection periods.

One of these cases (Case I) is illustrated in Figure J-1.

In this case, a detectable crack may propagate to a leak in the period between inspections (denoted by a shaded box in Figure J-1) or it may be found in one and only one inspection (denoted by the open box in Figure J-1). In Cases II and III, no leakage may occur prior to the first and second inspections, respectively, because of the relationships between inspection frequency and crack propagation time. Also, a detectable crack can be found in as many as two (Case II) or three (Case III) consecutive inspections.

J.2.3 Some Scheduling Guidelines

Some important trends emerge from the model (Figure J-2) which are applicable to the development of a specific alternative plan. First, for a given (total) number of welds inspected, leakage due to IGSCC can be reduced by increasing the inspection frequency. Figure J-2 shows that a Case I schedule (Point C) will result in the highest probability of leakage, and a Case III schedule (Point E) in the lowest probability. In other words, many inspections of a few welds each time are more effective than a few inspections of many welds each time. Secondly, a similar improvement in availability can be obtained by increasing the inspection frequency within a given ISI plan. Figure J-2 shows that a Case I/Case II/Case III sequence (Point A) is more effective in reducing IGSCC incidence than the alternative sequence Case III/Case II/Case I (Point B), even though the total number of welds inspected and the number of inspections remain the same. The increasing inspection frequency is also more effective than the constant inspection rate (Case II, Point D) for approximately the same number of inspections.

J.2.4 Inspection Costs and Exposure to Radiation

The alternative ISI plan also permits the calculation of costs incurred in execution and of man-Rem of radiation exposure accumulated during inspections. For this purpose, the plan uses a methodology developed from the Atomic Industrial Forum's National Environment Studies Project for determining the cost of work in radiation areas. This methodology simulates the progress of a maintenance job by determining the number of ingresses/egresses to the job site until the job is finished, the amount of productive work accomplished during each ingress/egress, and the exposures received. The total manhours, Rem, clock time, costs, and number of crews and men required to complete the job can be calculated. Thus, a base case, such as ISI per Section XI of the ASME Code, can be compared with alternative actions, such as the NRC and alternative augmented ISI plans.

Inherent in the alternative plan, therefore, are the options to meet specific utility needs. By using an iterative process similar to the one used to minimize IGSCC incidence, either one or the combination of both man-Rem exposure and inspection cost can be minimized. The optimum combination of all three quantities (IGSCC incidence, man-Rem exposure, and inspection cost) can also be obtained, if that is what is desired by a given utility. It should be noted that since the cost of inspection is insignificant compared to the costs of replacement power and repairs (estimated by IGSCC incidence), it is the latter costs that emerge as the most important cost factor in evaluating a given ISI plan.

J.3 SUMMARY

The General Electric Company has developed an approach for formulating an optimized in-service inspection plan that addresses the issue of stress corrosion cracking in welded piping. The new approach can be customized to meet specific utility needs regarding plant availability, inspection cost, and man-Rem exposure. The key to optimization lies in the sampling procedure. The welds targeted for inspection are those having stress rule indices and/or high carbon contents, which are known to correlate with IGSCC susceptibility. (Other parameters such as number of plant startups and elemental contents including Mo, Cr, Si, Ni, P, S, Mn, and N have been considered and rejected.) Furthermore, the inspection frequency is not allowed to decrease, since the probability of IGSCC is known to increase with plant age. The newly developed methodology calculates the IGSCC incidence associated with a given inspection plan, as well as the radiation exposure and the costs incurred in the execution of the plan. It is immediately adaptable to any Type-304 stainless steel piping system and can be carried out at nominal engineering cost.

J.4 REFERENCES

J-1 "Technical Report on Material Selection and Processing Guidelines for BWR Coolant Pressure Boundary Piping," U. S. Nuclear Regulatory Commission, July 1977 (NUREG-0313).

J-2 "Investigation and Evaluation of Stress Corrosion Cracking in Piping of Light Water Reactor Plants," U. S. Nuclear Regulatory Commission, February 1979 (NUREG-0531).

J-3 J. C. Lemaire, "Alternative Alloy for BWR Pipe Applications, Second Semi-annual Progress Report, April to October 1978," General Electric Company, December 1978 (NEDC-23750-4).

J-4 J. E. Alexander, "Alternative Alloys for BWR Welded Piping, EPRI/GE Contract No. RP968 Monthly Progress Letter for Period Ending 31 March, 1979," General Electric Company, March 1979.

J-5 N. R. Hughes and A. J. Giannuzzi, "Evaluation of Near-Term BWR Piping Remedies," EPRI Report No. NP122, May 1979.

J-6 R. S. Tunder, Personal Communication, March 1981.

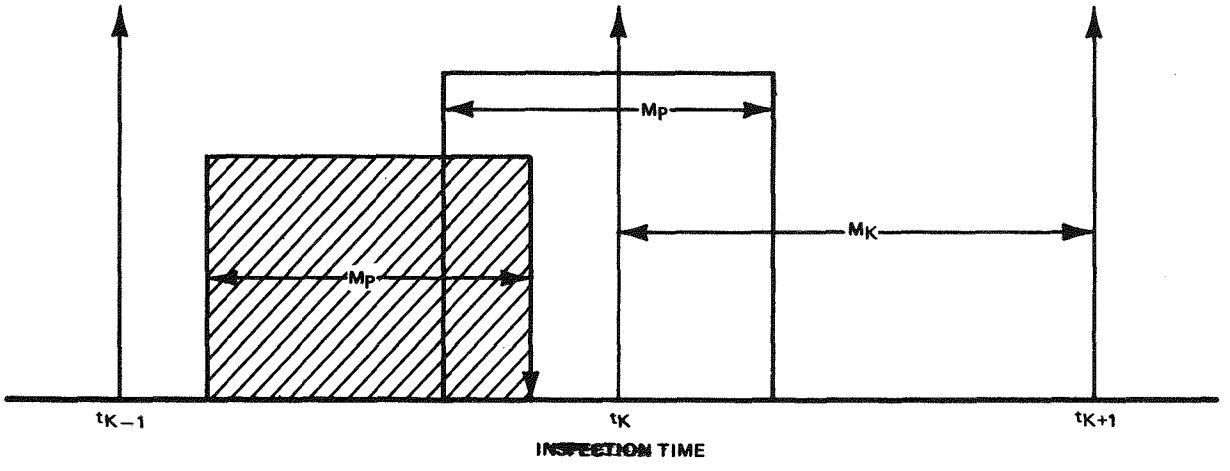

Figure J-1. Relationship Between Crack Propagation Time (Mp) and Time Between Inspections (M_K) for Case I

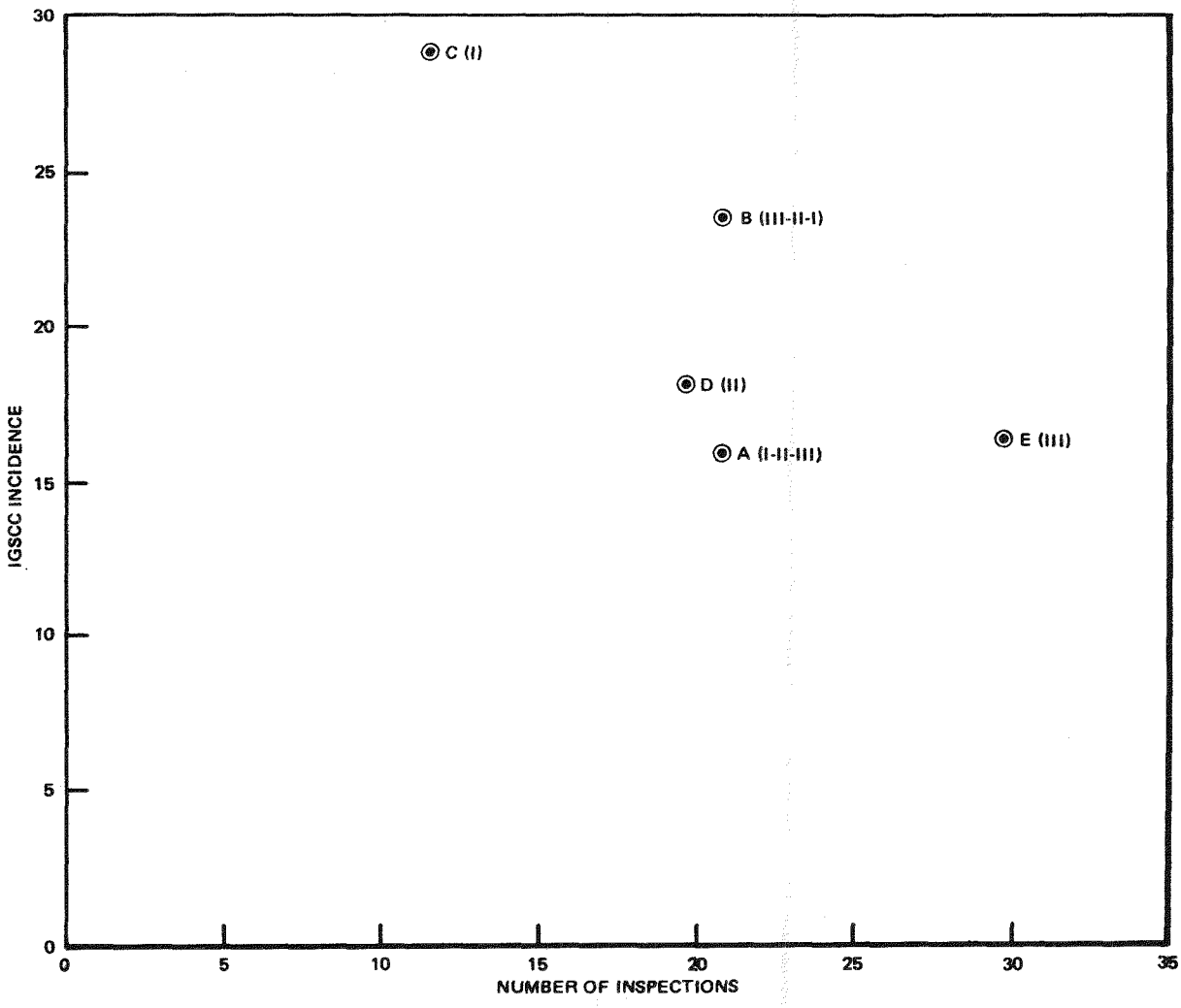

Figure J-2. IGSCC Probability versus Number of Inspections for Five Different Inspection Schedules. Total number of welds inspected remains the same in each schedule. (Roman numerals in parenthesis refer to statistical cases in GE model.)